General Disclaimer

One or more of the Following Statements may affect this Document

- This document has been reproduced from the best copy furnished by the organizational source. It is being released in the interest of making available as much information as possible.

- This document may contain data, which exceeds the sheet parameters. It was furnished in this condition by the organizational source and is the best copy available.

- This document may contain tone-on-tone or color graphs, charts and/or pictures, which have been reproduced in black and white.

- This document is paginated as submitted by the original source.

- Portions of this document are not fully legible due to the historical nature of some of the material. However, it is the best reproduction available from the original submission.

1974 NASA-ASEE
SUMMER FACULTY FELLOWSHIP
AERONAUTICS AND SPACE RESEARCH
PROGRAM

**RESEARCH
REPORTS**

GEORGE C. MARSHALL SPACE FLIGHT CENTER

conducted by

**SCHOOLS OF ENGINEERING
AUBURN UNIVERSITY
and
UNIVERSITY OF ALABAMA**
in cooperation with

SEPTEMBER, 1974

1974 NASA/ASEE SUMMER FACULTY FELLOWSHIP
AERONAUTICS AND SPACE RESEARCH
PROGRAM

conducted by
Auburn University
and
University of Alabama
at
George C. Marshall Space Flight Center
under
NASA Grant No. NGT 01-003-045

RESEARCH REPORTS

by
Mr. J. Fred O'Brien, Jr., University Co-Director
Associate Director, Engineering Extension Service
Auburn University

Mr. Charles O. Jones, NASA/MSFC Co-Director
Electronics and Controls Laboratory
Marshall Space Flight Center

Dr. Bobby F. Barfield, Associate Director
Director, Thermal Fluid Sciences Division
University of Alabama, Tuscaloosa

SEPTEMBER 1974

PREFACE

For the tenth consecutive year, the NASA/ASEE Summer Faculty Fellowship Aeronautics and Space Research Program was conducted at the Marshall Space Flight Center. The program was conducted by the Engineering Extension Service of Auburn University with assistance from the College of Engineering, University of Alabama, Tuscaloosa. This activity was one of six similar programs under the auspices of the Space Engineering Committee of the American Society for Engineering Education. The national program is financially supported by the Office of University Affairs, NASA Headquarters, Washington, D. C.

The basic objectives of the program, which is in its eleventh year of operation nationally, are:

(1) To further the professional knowledge of qualified engineering and science faculty members.

(2) To stimulate an exhange of ideas between participants and NASA engineers and scientists.

(3) To enrich and refresh the research activities of the participants' institutions.

The Faculty Fellows spent ten weeks at the Marshall Space Flight Center engaged in a research project commensurate with their interests and background and in collaboration with an assigned NASA/MSFC Colleague. During this period he also attended specially arranged seminars on topics related to the collective interests of the group, usually Space related. In addition, tours of other nearby government facilities were conducted to provide an additional facet of orientation. The official period of the program was June 3, 1974 to August 9, 1974.

This document is a compliation of each Fellow's report assembled by J. Fred O'Brien, Jr., University Co-Director, who has exercised certain administrative editorial prerogatives to produce this report. The reader is also referred to NASA CR-120337 for the administrative details of the Summer Program.

1974 NASA/ASEE SUMMER FACULTY RESEARCH FELLOWS

MARSHALL SPACE FLIGHT CENTER

1.	Dr. A. M. Martin, III	10.	Dr. A. E. Traver	19.	Prof. L. A. Holmes
2.	Dr. D. R. Pitts	11.	Dr. J. R. McDonald	20.	Dr. R. E. Oberly
3.	Dr. M. E. Crandell	12.	Dr. J. E. Sergent	21.	Dr. J. F. Trahan
4.	Mr. J. F. O'Brien, Jr.*	13.	Dr. R. M. Cosby	22.	Dr. T. R. Rogge
5.	Dr. T. D. Fay	14.	Dr. J. O. Nichols	23.	Mr. C. O. Jones*
6.	Dr. E. Logan, Jr.	15.	Dr. J. A. Biesbrock	24.	Dr. J. C. Conway
7.	Dr. E. H. Perry	16.	Dr. R. E. Bozeman	25.	Dr. G. C. Bucher (NASA)
8.	Dr. W. B. Newbolt	17.	Dr. W. G. Hopkins, III	26.	Dr. B. F. Barfield*
9.	Dr. W. B. Hall	18.	Dr. H. K. Liu	27.	Dean E. P. Segner

* PROGRAM DIRECTORS

-iii-

List of 1974 Participants

1. **Second Year Fellows**

Dr. Joseph C. Conway
  Ph.D., Associate Professor, 35
  Engineering Science and Mechanics, The Pennsylvania State University
  MSFC Assignment: Strength Analysis
                           Engineering Analysis
                           Structures and Propulsion Lab.
  Research Topic : Stress Intensity Factors by the Finite Element
                           Method
  NASA Colleague : J. E. Key

Dr. Merrell E. Crandell
  Ph.D., Associate Professor, 36
  Physics, Muskingum College
  MSFC Assignment: Surface Science
                           Physics and Instrumentation
                           Space Sciences Lab.
  Research Topic : Optical Properties of ZnTe in the Vacuum Ultra-
                           violet
  NASA Colleague : R. C. Linton

Dr. Hua-Kuang Liu
  Ph.D., Associate Professor, 34
  Electrical Engineering, University of Alabama
  MSFC Assignment: Optics and Electro Optics
                           Physics and Instrumentation
                           Space Sciences Lab.
  Research Topic : The Effects of Programmed Dislocations on the
                           Inteference Fringes in a Mobil Laser HNDT System
  NASA Colleague : R. L. Kurtz

Dr. Earl Logan, Jr.
  Ph.D., Professor, 47
  Mechanical Engineering, Arizona State University
  MSFC Assignment: Environmental Dynamics
                           Aerospace Environment
                           Space Sciences Lab.
  Research Topic : Atmospheric Wind and Stress Profiles in a Two-
                           Dimensional Internal Boundary Layer
  NASA Colleague : G. H. Fichtl

Dr. John R. McDonald
    Ph.D., Assistant Professor, 35
    Engineering Mechanics, South Dakota School of Mines and Technology
    MSFC Assignment: Solid-State Sciences
                        Astronomy and Solid-State Physics
                        Space Sciences Lab.
    Research Topic :   Temperature Requirements for the Floating Zone
                        Crystal Growing Technique in a Space Environment
    NASA Colleague :   M. C. Davidson

Dr. James O. Nichols
    Ph.D., Associate Professor, 44
    Aerospace Engineering, Auburn University
    MSFC Assignment: Propulsion Systems Branch
                        Sub-Systems Design
                        Program Development
    Research Topic :   Computer Program for Preliminary Design of Cryo-
                        genic Propellant Pressurization Systems for Space
                        Vehicles
    NASA Colleague :   James L. Sanders/James F. Thompson

Dr. Donald R. Pitts
    Ph.D., Professor, 45
    Mechanical Engineering, Tennessee Technological University
    MSFC Assignment: Life Support and Environmental
                        Engineering Analysis
                        Structures and Propulsion Lab.
    Research Topic :   Transient Analysis of a Thermal Capacitor Element
    NASA Colleague :   Randy Humphries

Dr. Thomas R. Rogge
    Ph.D., Associate Professor, 38
    Engineering Science and Mechanics, Iowa State University
    MSFC Assignment: Strength Analysis
                        Engineering Analysis
                        Structures and Propulsion Lab.
    Research Topic :   Stress Concentrations via Finite Element Analysis
    NASA Colleague :   J. E. Key

2. First Year Fellows

Dr. Joseph A. Biesbrock
    Ph.D., Assistant Professor, 38
    Biology, North Georgia College
    MSFC Assignment: Earth Resources Office
                        Data Systems Lab.
    Research Topic :   Multispectral Imagery for Detecting Southern Pine
                        Beetle Infestations
    NASA Colleague :   Sanford Downs

Dr. Robert E. Bozeman
Ph.D., Assistant Professor, 28
Mathematics, Morehouse College
MSFC Assignment: Flight Mechanics
                 Mission Analysis
                 System Analysis and Integration Lab.
Research Topic : Trajectory Optimization Techniques for Low Thrust
                 Vehicles
NASA Colleague : Hugo Ingram

Dr. Billy D. Carroll
Ph.D., Assistant Professor, 33
Electrical Engineering, Auburn University
MSFC Assignment: Design Techniques
                 Electronics Development
                 Electronics and Control Lab.
Research Topic : Test Pattern Generation for Sequential Logic
                 Circuits
NASA Colleague : J. M. Gould

Dr. Ronald M. Cosby
Ph.D., Assistant Professor, 30
Physics and Astronomy, Ball State University
MSFC Assignment: Propulsion Systems Analysis Branch
                 Engineering Analysis Division
                 Structures and Propulsion Laboratory
Research Topic : Concentration Characteristics of a Fresnel Solar
                 Strip Reflection Concentrator
NASA Colleague : Leon Hastings

Dr. Theodore D. Fay
Ph.D., Visiting Professor, 33
Astronomy and Physics, Louisiana State University
MSFC Assignment: Astronomy
                 Astronomy and Solid-State Physics
                 Space Sciences Lab.
Research Topic : Calibration and Reduction of Video Camera Date
NASA Colleague : E. R. Miller

Dr. William B. Hall
Ph.D., Associate Professor, 44
Chemical Engineering, Mississippi State University
MSFC Assignment: Ceramics and Coating
                 Non-Metallic Materials
                 Materials and Processes Lab.
Research Topic : Fracture Mechanics of Cer-Vit C101 Glass Ceramic
NASA Colleague : H. M. King

Professor LeRoy A. Holmes
  M.S., Engineering Instructor, 33
  Engineering and Physical Science, Modesto Junior College
  MSFC Assignment: Thermal Engineering
                    Engineering Analysis
                    Structures and Propulsion Lab.
  Research Topic : Space Shuttle External Propellant Tank Prelaunch
                    Heat Transfer
  NASA Colleague : Farouk Huneidi

Dr. Walter G. Hopkins, III
  Ph.D., Associate Professor and Acting Chairman, 32
  Engineering Technology, Alabama A&M University
  MSFC Assignment: Navigation and Control
                    Sub-System Design
                    Program Development
  Research Topic : Analysis of Fine Guidance Pointing Stability for
                    Space Craft
  NASA Colleague : Onis Green

Dr. Ashley M. Martin, III
  Ph.D., Associate Professor and Chairman, 31
  Physics, Athens College
  MSFC Assignment: Optics and Electro Optics
                    Physics and Instrumentation
                    Space Sciences Lab.
  Research Topic : HNDT of Shuttle Engine
  NASA Colleague : R. L. Kurtz

Dr. William B. Newbolt
  Ph.D., Professor, 40
  Physics, Washington and Lee University
  MSFC Assignment: Space Physics Group
                    Payload Studies Office
                    Program Development
  Research Topic : Neutralization of a Charged Spacecraft in the
                    Ionosphere
  NASA Colleague : Jim Ballance

Dr. Ralph E. Oberly
  Ph.D., Assistant Professor and Chairman, 33
  Physics, Marshall University
  MSFC Assignment: Optics and Electro Optics
                    Physics and Instrumentation
                    Space Sciences Lab.
  Research Topic : Holographic Techniques for Cloud Chamber Studies
  NASA Colleague : R. L. Kurtz

Dr. Edward H. Perry
   Ph.D., Assistant Professor, 30
   Mechanical Engineering, Memphis State University
   MSFC Assignment: Life Support and Environmental
                      Engineering Analysis
                      Structures and Propulsion Lab.
   Research Topic :   Theoretical Performance of Continuous and Inter-
                      mittent Lithium Bromide-Water Absorption Refriger-
                      ation Cycles
   NASA Colleague :   Joe Cody

Dr. Jerry E. Sergent
   Ph.D., Assistant Professor, 34
   Electrical Engineering, University of South Florida
   MSFC Assignment: Electronics Packaging
                      Electronics Development
                      Electronics and Control Lab.
   Research Topic :   Stability and Dispersion of High Ohmic Value Thick
                      Film Resistors
   NASA Colleague :   S. V. Caruso

Dr. Jeffery F. Trahan
   Ph.D., Assistant Professor, 33
   Physics, Centenary College
   MSFC Assignment: Low Temperature and Gravitation Sciences
                      Radiation and Low Temperature Sciences
                      Space Sciences Lab.
   Research Topic :   Electrical and Superconducting Properties of
                      Lead-Zinc Immiscible Alloys
   NASA Colleague :   Lew Lacy

Dr. Alfred E. Traver
   Ph.D., Associate Professor, 34
   Mechanical Engineering, Tennessee Technological University
   MSFC Assignment: Mission Operations
                      Mission Operations and Integration
                      Program Development
   Research Topic :   Investigation of Optimal Project Scheduling Under
                      Resource Constraints with Resource Leveling
   NASA Colleague :   John Cole

RESEARCH REPORTS

Report No.	Title	Faculty Fellow
1	Multispectral Imagery For Detecting Southern Pine Beetle Infestations	Dr. Joseph A. Biesbrock
2	Trajectory Optimization Techniques For Low Thrust Vehicles	Dr. Robert E. Bozeman
3	Test Pattern Generation for Sequential Logic Circuits	Dr. Billy D. Carroll
4	Stress Intensity Factors By The Finite Element Method	Dr. Joseph C. Conway
5	Concentration Characteristics Of A Fresnel Solar Strip Reflection Concentrator	Dr. Ronald M. Cosby
6	Optical Properties Of The II-VI Compound Semiconductor ZnTe In The Vacuum Ultraviolet	Dr. Merrell E. Crandell
7	Calibration and Reduction of Video Camera Data	Dr. Theodore D. Fay, Jr.
8	Fracture Mechanics Of Cer-Vit Glass-Ceramic	Dr. William B. Hall
9	Space Shuttle External Propellant Tank Prelaunch Heat Transfer	Prof. LeRoy A. Holmes
10	Analysis Of Fine Guidance Pointing Stability For Spacecraft	Dr. Walter G. Hopkins, III
11	On The Meaning Of The Holographic Interferometric Fringes	Dr. Hua-Kuang Liu
12	Atmospheric Wind And Stress Profiles In A Two-Dimensional Internal Boundary Layer	Dr. Earl Logan, Jr.

RESEARCH REPORTS (Continued)

Report No.	Title	Faculty Fellows
13	Holographic Nondestructive Testing	Dr. Ashley M. Martin, III
14	Temperature Requirements For The Floating Zone Crystal Growing Technique In A Space Environment	Dr. John R. McDonald
15	Natural Neutralization Of A Charged Spacecraft In The Ionosphere	Dr. W. Barlow Newbolt
16	Computer Program For Preliminary Design Or Cryogenic Propellant Pressurization Systems For Space Vehicles	Dr. James O. Nichols
17	Holographic Techniques For Cloud Chamber Studies	Dr. Ralph E. Oberly
18	Theoretical Analysis Of Continuous And Intermittent Lithium-Bromide-Water Absorption Refrigeration Cycles	Dr. Edward H. Perry
19	Numerical Analysis Of A Two-Dimensional Thermal Capacitor Element	Dr. Donald R. Pitts
20	Stress Concentration Factors Via The Finite Element Method	Dr. Thomas R. Rogge
21	Stability And Dispersion Of High Ohmic Value Thick Film Resistors	Dr. Jerry E. Sergent
22	Electrical And Superconducting Properties Of Lead-Zinc Composite Materials	Dr. Jeffery F. Trahan
23	Investigation Of Optimal Project Scheduling Under Resource Constraints With Resource Leveling	Dr. Alfred E. Traver

1974

ASEE - NASA SUMMER FACULTY FELLOWSHIP PROGRAM

MARSHALL SPACE FLIGHT CENTER

(AUBURN UNIVERSITY - UNIVERSITY OF ALABAMA)

MULTISPECTRAL IMAGERY FOR DETECTING
SOUTHERN PINE BEETLE INFESTATIONS

Prepared by: Joseph A. Biesbrock, Phd.

Academic Rank: Associate Professor

Department and College: Department of Biology
North Georgia College

NASA/MSFC Assignment:
    (Laboratory)   Data Systems Laboratory
    (Office)   Earth Resources Office

NASA Research Colleague: Sanford Downs

Date: August 9, 1974

Contract No.:   NGT-01-003-045

MULTISPECTRAL IMAGERY FOR DETECTING
SOUTHERN PINE BEETLE INFESTATIONS

BY

JOSEPH A. BIESBROCK

ABSTRACT

A research investigation has been designed and partially imple-
mented to study the feasibility of multispectral imagery for detecting
southern pine beetle infestations. Background and specific rationale
with respect to multispectral imagery and remote sensing applica-
tions are outlined. Considerations for the development of procedures
for designing, administering and analyzing photo interpretation tests
that yield quantitative results and permits objective evaluation of
multispectral imagery for beetle detection are outlined. Photo
interpretive tests of a dependent and independent construction are
developed. Regards for test administration and analyses are
discussed; however, no results can be reported at this date. Ground
survey data acquisition methodology is outlined and a form for
recording suspect silvical, biological, climatological and geophysical
factors linked with southern pine beetle outbreaks is presented.
Arrangements for a continuing research effort are treated.

INTRODUCTION
(Background Inference Rationale)

Remote Sensing

Multispectral imagery for forest insect detection constitutes but one small facet of the broader topic "remote sensing of earth resources". Generally defined, the term "remote sensing" refers to any process of obtaining information about an object without actually making contact with that object. Modern "platforms" for viewing-from-afar include aircraft, spacecraft and satellite. Modern remote sensors may be photographic or non-photographic. Even though photographs imply the use of the visible portion of the electromagnetic spectrum; photo-like images can be obtained over a wider spectral range including ultraviolet, infrared, microwave and radar wavelengths.

Objects in nature are composed of specific substances that have distinct spectral absorbence and reflectance properties. The conventional photographic image is depicted as it is "seen" by a filter-lens-film configuration. The technique most widely used for color photography employs three-layer-color film. When white light illuminates a three-layer-color print, some wavelengths are absorbed; the color viewed results from those wavelengths that are reflected.

Multispectral Photography

In multispectral photography the light that is reflected or emitted from a scene is simultaneously separated and recorded in different spectral regions. Normally for this purpose a camera loaded with black and white infrared film and equipped with four lens systems that are boresighted to view the same scene and that are equipped with filters to divide the spectrum into four separate spectral regions, is employed. The most widely used multispectral configuration records in the blue (400-480 nm.), green (480-590 nm.), red (590-700 nm.) and infrared 730-900 nm.) spectral regions. In order to utilize multispectral imagery to fullest advantage the imagery must be viewed in an additive color projector. When projected for

registration the blue, green and red images can be combined with
filters of the same color to form a natural color image. Likewise
a false-color image can be formed by projecting the green, red
and infrared images through blue, green and red filters, respectively.

Infrared Sensing

Infrared imagery's most valuable application is in the areas of
agriculture and forestry; herein, it is employed in the false-color
mode for evaluating plant species, relative vigor and disease. The
green color of healthy leaves as perceived by the human eye is a
result of the chlorophyll molecule's high absorbence in the blue and
red spectral bands and strong reflection in the green spectral band.
What can not be detected by the human eye is the comparatively
higher infrared reflectance of stressed and diseased leaves. In
healthy leaves, abundant water within the tissues serves to absorb
infrared wavelengths. When previously healthy leaves become
stressed or diseased the loss of internal water and dehydration
result in a reduction of infrared absorbence and a subsequent
increase in infrared reflectance. Even before the visible fading of
chlorophyll results in obvious discoloration, this water loss can be
detected by infrared sensing.

Earth Resources Applications

In the broad context the term "earth resources" conveys much
more than knowledge of the earth's valuable minerals; it implies all
the conditions on the earth's surface that are of economic, social or
cultural interest to man. Since its inception the Earth Resources
Survey Program of the National Aeronautics and Space Administra-
tion has addressed itself to the following disciplines and their broad
objectives:

1. Oceanography and Marine Resources--to aid ocean transpor-
   tation and better utilization of fisheries,

2. Hydrology and Water Resources--to aid the location and
   better usage of water,

3. Geology and Mineral Resources--to aid the discovery of
   minerals and petroleum,

4. Geography, Cartography, and Cultural Resources--to update topographic base maps and census inventories and aid the formulation of land use plans for rural and urban land areas,

5. Agriculture and Forest Resources--to aid the increase of agriculture and forest production.

The Agriculture and Forest Resources application can, in turn, be categorized into the following sub-disciplines and their specific objectives:

A. Agriculture--to aid in estimating crop type, acreage and yield and detecting plant stress situations,

B. Range Management--to aid in conducting grassland and livestock surveys,

C. Forest Management--to aid in determining timber types and areas, estimating timber volumes and combating forest fires, disease and insects.

Southern Pine Beetle

Early detection of damaging forest insects is important to prompt remedial action and is especially important where reoccurring insect damage and threat of damage extend over large areas of complex topographic and ownership patterns. The southern pine beetle is the most widespread and destructive insect in the South, particularly in loblolly, slash, and Virginia pine stands. Outbreaks have been recorded since the late 1800's; some of which have encompassed the entire range of the southern pines. Recent attacks in epidemic proportions have caused foresters, landowners and home owners to be concerned.

As a result of their life style the southern pine bark beetles are extremely difficult to combat. Southern pine bark beetles spend most of their lives in the inner bark of host trees. The adult female constructs winding tunnels beneath the bark and lays her egg along the sides of the tunnels; subsequently, the trees are killed by the feeding of the larvae in the cambial areas. The larvae mature and emerge in approximately four weeks and as many as five generations

may develop in a single year. In the first year after successful infestation the foliage fades and changes from green to red; in the second year the needles drop. Sprays are ineffectual in combating the southern pine beetle and the only control is prevention by prompt detection and immediate removal of infested trees.

Photo Interpretive Test Development

Historically, early beetle detection efforts were made entirely by ground surveillance, later aerial surveillance and aerial photography became an adjuct to the ground survey. The results of a recent study carried out at Marshall Space Flight Center give credence to the use of multispectral imagery as a feasible technique for detecting southern pine beetle infestations. Remote sensing applications in the area of southern pine beetle detection like remote sensing applications in any of the other aforementioned resource disciplines or sub-disciplines involves the development of data acquisition methodology for a coordinated ground, aircraft and spacecraft observation program. Paramount to the whole applications area is the development of procedures for designing and administering interpretation tests that yield quantitative results and that permit objective evaluations of the capabilities of sensing techniques employed.

INTRODUCTION
(Specific Task Rationale)

The southern pine beetle is a prolific, destructive, widespread, reoccurring pest that causes millions of dollars of damage to the pine forests of the South. Historically the southern pine beetle has been the reason for and the means by which entomological aerial survey technology has developed. Aerial mapping techniques were first perfected for locating and appraising timber losses caused by the southern pine beetle (Heller, et. al. 1955, 1958). The first reported evaluative test of black-and-white and normal color aerial photography for forest insect detection was accomplished in southern pine beetle infestations (Heller et. al. 1959). Subsequent evaluative tests comparing normal color and infrared color aerial photographs for forest insect detection were also carried out in areas damaged by the southern pine beetle (Ciessla et. al. 1967). Recently the

application of multispectral imagery has been demonstrated to be feasible for detecting southern pine beetle infestations (Downs 1973). This aforementioned application of multispectral imagery remains to be evaluated in a quantitative interpretation.

OBJECTIVES

The primary objective of this study was to compare the relative merits of multispectral, color and color-infrared imagery in detecting southern pine beetle infestations..

A secondary objective was the development of ground survey methodology to aid in identification of sivical, biological, climatological and geophysical factors correlated with southern pine beetle outbreaks.

PROCEDURE

Study Area (Photo Interpretive Task)

A north Georgia area of approximately 40,000 acres with approximately 100 active southern pine beetle infestations was selected for investigation. This area near Gainesville in Hall County is situated in the Georgia piedmont immediately south of the Blue Ridge Mountains. About one-half of this area is forested, mostly farm woodland; the main forest type is pine which loblolly, shortleaf or Virginia pine predominate.

Aerial Imagery (Photo Interpretive Task)

Multispectral, color and color-infrared for evaluative comparisons was collected during the same reconnaissance mission, utilizing the same flight lines. However, only the color-infrared and the multispectral imagery were of simultaneous origin. The mission was flown in August at a scale of 1:12,000 by a NASA-Marshall Space Flight Center remote sensing C-45. Multispectral imagery was obtained employing an I^2S Mark I camera with a 150 mm focal length lens and Kodak 2424 film. Color-infrared and conventional color photography were obtained employing a Wild-Heerbrugg RC-10 camera with a 150 mm focal length lens and Kodak 2443 and Kodak 2453 film, respectively.

Field Procedure (Photo Interpretive Task)

After imagery was obtained selected beetle damaged areas
ranging in size from single trees to stands covering several acres
were identified and their respective ground truths established. All
trees within the identifiable area 6.0 inches d.b.h. and larger were
tallied and ranked according to the following disease conditions:
(1) symptomless, (2) fading, (3) red-topped and (4) snag.

Test and Laboratory Procedure (Photo Interpretive Task)

In an effort to objectively appraise and compare imagery, photo
interpretive performance tests of two types were developed. The
first test was of relative simple design and of dependent construction.
In addition to functioning as a preliminary test, it was also to serve
as a training aid to administered prior to the independent test.
Beetle damaged areas and corresponding non-infested areas of the
same size, silvical and topographical character were delineated in
grease pencil at a ratio of approximately 1 to 4 on standardized
photographic positives of the corresponding study imagery. After a
brief orientation in which the interpreters were shown a series of
35 mm Kodachrome slides depicting various sizes and stages of
southern pine beetle infestations, they were instructed to select
the beetle infestations present in each of 30 test frames (10
corresponding frames for each type of imagery). The test frames
were administered in a Latin square presentation.

The second photo interpretive test was of complex design and of
independent construction. Within the framework of this test no
attempt was made to standardize the image format; moreover, the
test was administered in an operational manner. Color and color-
infrared transparencies were interpreted with the aid of a light table
and a scanning stereoscope; multispectral imagery was interpreted
with the aid of an I^2S additive viewer. Transparent templets with a
delineated central area of 6 x 6 inches, sub-divided into 9 sequent-
ially numbered 2 inch squares, were prepared for the photo test
frames and the viewer screen. Interpreters were instructed to
scan the imagery in an orderly manner and to locate and outline all
the suspected beetle infested areas; and in addition, to tabulate the
number of discolored and defoliated trees within each of the infested
areas. The independent test contained 30 test frames, 10 frames

for each type of imagery. The simulated operational procedure prevented the presentation of the individual test frames in a Latin square arrangement; however, the sequence of the type imagery was presented to the individual interpreters in a Latin square arrangement.

Experimental Design (Photo Interpretive Task)

At the onset of the study a need for a comparison of inexperienced (naive) and experienced interpreters was recognized as imagery preferences among our available experienced interpreters were already in evidence. In an effort to identify and isolate interpreter preferences, inexperienced interpreters selected from students enrolled in a military science map reading and pre-flight course taught at North Georgia College--Dahlonega and experienced interpreters selected from the staff of the Earth Resources Office, Marshall Space Flight Center--Huntsville were utilized in the interpretive phases of the study. Resulting data were examined statistically by means of an imagery x interpreter (3 x 2) factorial ANOV and Duncan's Multiple Range Test; thereby, facilitating the statistical inferences involving the imagery effect alone, the interpreter effect alone and the imagery x interpreter interaction.

Ground Survey Methodology Development (Correlation Task)

A search of the literature for the purpose of identifying the silvical, biological, climatological and geophysical factors implicated with southern pine beetle infestations was conducted.

RESULTS

Photo Interpretive Task (Progress Report)

The literature pertaining to the photo interpretive task has been reviewed. Preliminary ground and aerial surveys have resulted in the selection of a primary study area. Low altitude flight requests were submitted to and approved by MSFC's Flight Board. At this date August 9, 1974 partial coverage cf the study area has been attained and is being processed. Development, administration, and analysis of the photo interpretive tests are pending and no results can be reported at this stage of the research task.

Correlation Task (Progress Report)

The review of the literature revealed that southern pine beetle outbreaks are frequently associated with drought, fire, overcrowding and over-maturity. Lightning damage, severe weather conditions, poor drainage, logging and building activities and off-site plantings have also been implicated with southern pine beetle infestations. In an attempt to focus attention on these suspected contributing factors a data sheet for field and laboratory analysis of southern pine beetle infestations was developed (Refer Figure 1-A and 1-B). Explanations of specific designations and directions for collecting and recording the specific plot data are also included with the data form. This information is to be gathered in part from the primary study area when imagery becomes available.

DATA SHEET FOR FIELD AND LABORATORY--SOUTHERN

PLOT DATA: AREA _____ FLIGHT D

1) Plot # _____   6) Land use _____   11) Distb _____
2) Photo # _____   7) Slope _____   12) Injury _____
3) Inf size _____   8) Aspect _____   13) Pl Pat* _____
4) Std type _____   9) Drain _____   14) B A _____
5) Std org _____   10) Soil Tx* _____   15) x DBH _____

31	32	33	34	35	36	37	38	39	40
Azmth	Dist	Tree #	Cwn Cl	Spp	Injry	Pl Pat	DBH	Ht	Age

MSFC - One-Time Form 41 (July 1974)

Figure 1-A: Data Sheet for Ground Survey

1-11

PINE BEETLE INFESTATIONS

ᵂATE _____   GROUND CHECK DATE _____

	16) x HT		21) Cl Y-R		26) Emrg	
17) x Age		22) Cl Fd		27) MFSD	
18) x Bk Tk		23) Cl Rd		28) Db Den	
19) x R/O in		24) Cl Bl		29) Bk Con	
20) x An Inc		25) Inf #		30) Act Ix	

41	42	43	44	45	46	47	48	49	50
Bk Tk	R/O in	An Inc	Color	Emrg	MFSD	Bd Den	Bk Con	Sc Inv	Rmrks

Figure 1-B: Data Sheet for Ground Survey (Cont'd)

PLOT DIRECTIONS

1) Plot number--record plot numbers consecutively.

2) Photo number--record photo numbers from index numbers.

3) Infestation size--record as either (1) single tree, (2) .1 acre, (3) .25 acre, (4) .50 acre, (5) .75 acre, (6) 1.0 acre, (7) 2.5 acres, (8) 5.0 acres, (9) 7.5 acres, (10) 10.0 acres, or actual acreage to whole acre for areas larger than 10 acres.

4) Stand type--record as either (1) pine or (2) mixed pine-hardwood.

5) Stand origin--record as either (1) natural or (2) planted.

6) Land use--record as either (1) urban, (2) farm woodlot, or (3) forest.

7) Slope--record in degrees.

8) Aspect--record as either (1) no obvious slope, (2) N, (3) NE, (4) E, (5) SE, (6) S, (7) SW, (8) W, (9) NW, or (10) panoramic effect.

9) Drainage--record as either (1) bottom, (2) flat, (3) side slope, or (4) ridgetop.

10) Soil Texture--procure soil for laboratory analysis, record from textural triangle as either (1) clay, (2) silty clay, (3) sandy clay) (4) clay loam, (5) silty clay loam, (6) sandy clay loam, (7) loam, (8) silt loam, (9) sandy loam, (10) silt, (11) loamy sand, or (12) sand.

11) Disturbance--record as either (1) undisturbed, (2) adjacent to logged or cleared land, (3) adjacent buildings or building site, (4) adjacent agricultural practices, or (5) fire, (plot designations).

12) Injury--record as either (1) no obvious injury-sign lacking, (2) wind or sleet as evidenced by broken, bent, or toppled stems, (3) lightening as evidenced by sear marks, or (4) bark wounds.

13) Plant pathogens--record as (1) no pathogens-signs lacking, (2) above ground fruiting structures evident, or (3) root rotting organisms detected in lab analysis.

14) Basal area--record number of trees times 10.

15) Average diameter breast height--average tree data and record to nearest one-tenth inch.

16) Average height--average tree data and record to nearest foot.

17) Average age--average tree data and record to nearest year.

18) Average bark thickness-average tree data and record to nearest mm.

19) Average number of rings per outer inch--average and record to nearest whole number.

20) Average annual increment--average tree data and record to nearest mm.

21) Color-yellow-green--tally number of trees with slight discoloration to obvious yellow green.

22) Color-fading (yellow-pink)--tally number of trees with yellow to light red discoloration.

23) Color-red--tally number of trees with red to redish brown discolorations.

24) Color-black--tally number of trees without or in the act of loosing needles and small branches.

25) Infestation number--tally all discolored trees.

26) Emergence--record either (1) pre-emergence or (2) post emergence as evidenced by number of holes and pitch tubes.

27) Most frequent stage of development--record as either (1) egg, (2) larva, (3) pupa, or (4) adult.

28) Brood density--record as either (1) light, (2) moderate, or (3) heavy (ball park estimate).

29) Bark condition--record as either (1) firm bark, (2) bark with woodpecker damage in evidence, (3) peeling or slipping bark, or (4) bark sloughing in large patches.

30) Activity index--record as either (1) non-active, (2) low level activity, (3) moderate level of activity, (4) high level of activity (activity index is a function of color data, stage of development, and brood density).

31) Azimuth--record the degrees of individual tally trees from true North.

32) Distance-- measure distance of individual tally trees from plot center.

33) Tree number--assign numbers to individual tally trees in clock-wise fashion from plot center.

34) Crown class--record as either (1) dominant, (2) codominant, (3) intermediate, or (4) suppressed.

35) Species--record as either (1) slash pine, (2) loblolly pine, or (3) Virginia pine.

36) Injury--code as in #12.

37) Plant pathogens--code as in #13.

38) DBH--code as in #15.

39) Height--code as in #16.

40) Age--code as in #17.

41) Bark Thick--code as in #18.

42) R/O inch--code as in #19.

43) An Inc--code as in #20.

44) <u>Color</u>--code as in #21, 22, 23, or 24.

45) <u>Emerg</u>--code as in #26.

46) <u>MFSD</u>--code as in #27.

47) <u>Bd den</u>--code as in #28.

48) <u>Bk con</u>--code as in #29.

49) <u>Secondary invaders</u>--record as either (1) fungi or (2) other insects.

50) <u>Remarks</u>: Address remarks to past history and reconstruction of initial attack; focus attention on plot center.

DISCUSSION

Future Considerations

Tentative arrangements to loan a MSFC's I^2S additive viewer to my institution have been formulated. My NASA colleague and I are hopeful that we will be able to obtain complete imagery coverage and ground truth data by early fall. Preparation and administration of the test for the first time can be scheduled within the fall school term.

LITERATURE CITED

.1. Aldrich, R. C., R. C. Heller and W. F. Baily. 1958. Observation limits for aerial sketch mapping southern pine-beetle damage in the southern Appalachians. Jour. Forestry 56:200-202.

2. Ciesla, W. M., J. C. Bell and J. W. Curlin. 1967. Color photos and the southern pine beetle. Photogrammetric Engineering 33:883-888.

3. Downs, S. W., 1973. Feasibility of using multispectral imagery for determining infestations of southern pine beetles. First Annual Research and Technology Review. National Aeronautics and Space Administration, Marshall Space Flight Center, AL

4. Draeger, W. C., and D. M. Carneggie. 1974. Test procedures for remote-sensing data. Photogrammetric Engineering 40:175-181.

5. Driscoll, R. S. and M. D. Coleman. 1974. Color for shrubs. Photogrammetric Engineering 40:451-459.

6. Gausman, H. W. 1974. Leaf reflectance of near-infrared. Photogrammetric Engineering 40:183-191.

7. Heller, R. C., and R. V. Bega. 1973. Detection of forest insects by remote sensing. Jour. Forestry 71:18-21.

8. Hall, R. C., 1973. Application of ERTS-1 imagery and underflight photography in the detection and monitoring of forest insect infestations in the Sierra Nevada Mountains of California. In Symposium on Significant Results Obtained from the Earth Resources Technology Satellite-1, Volume I: Technical Presentations Section A: pp. 135-142. National Aeronautics and Space Administration, Goddard Space Flight Center, Greenbelt, MD.

9. Heller, R. C., R. C. Aldrich and W. F. Baily 1959. An evaluation of aerial photography for detecting southern pine beetle damage. Photogrammetric Engineering 25:595-606.

10. Heller, R. C., J. F. Coyne and J. L. Bean. 1955. Airplanes increase effectiveness of southern pine beetle surveys. Jour. Forestry 53:483-487.

11. Klein, W. H., 1973. Beetle-killed pine estimates. Photogrammetric Engineering 39:385-388.

12. Leachtenauer, J. C., 1973. Photo interpretation test development. Photogrammetric Engineering 39:1187-1195.

13. Meyer, M. P. and D. W. French. 1967. Detection of diseased trees. Photogrammetric Engineering 33:1035-1040.

14. Ross, D. S., 1973. Simple multispectral photography and additive color viewing. Photogrammetric Engineering 39:583-591.

15. Wear, J. F., and J. W. Bongberg. 1951. The use of aerial photographs in forest insect surveys. Jour. Forestry 49:632-633.

1974

ASEE - NASA SUMMER FACULTY FELLOWSHIP PROGRAM

MARSHALL SPACE FLIGHT CENTER

(AUBURN UNIVERSITY - UNIVERSITY OF ALABAMA)

TRAJECTORY OPTIMIZATION TECHNIQUES

FOR LOW THRUST VEHICLES

Prepared by: Robert E. Bozeman, Ph.D.

Academic Rank: Assistant Professor

Department and University: .   Department of Mathematics
                                    Morehouse College

NASA/MSFC Assignment:
      (Laboratory)   Systems Analysis & Integration
      (Division)   Mission Analysis
      (Branch)   Flight Mechanics

NASA Research Colleague: Hugo Ingram

Date: August 9, 1974

Contract No.:   NGT-01-003-045

TRAJECTORY OPTIMIZATION TECHNIQUES
FOR LOW THRUST VEHICLES

by

Robert E. Bozeman

ABSTRACT

A minimum fuel orbital transfer problem of a low thrust vehicle is posed and discussed. Trajectory optimization theory is applied to the system to yield a two point boundary value problem in ordinary differential equations. The differential equations and boundary conditions are nonlinear and a Newtonian iterative scheme is employed to obtain a numerical solution.

The original equations of motion of the model vehicle are approximated by a new system which is solved in closed form. This closed form solution is suggested for use in a variation of parameters technique to integrate the original equations of motion. This technique would avoid some of the time-consuming numerical procedures that are necessary to solve the boundary value problem.

ACKNOWLEDGMENTS

INTRODUCTION

The low thrust of ion engines which are now being considered for space missions produces a particularly difficult trajectory optimization problem. The application of optimization theory to most problems of trajectory analysis usually results in a boundary value problem in ordinary differential equations. In these problems unknown initial conditions must be determined so that they cause the results of the integration of the differential equations to satisfy pre-specified conditions at the initial time, the final time, and at a finite number of intermediate times. In most cases the differential equations and the boundary conditions are non-linear and consequently numerical methods are employed to find a solution to the boundary value problem. In the study of low thrust trajectories, the numerical integration of the corresponding system of nonlinear differential equations is a time consuming procedure. For this reason, approximate solutions which take much less time to evaluate are often used for trajectory analysis purposes.

In this report a minimum fuel orbital transfer problem for a low thrust vehicle is posed and a numerical technique for obtaining an exact solution to the modeling system of nonlinear differential equations is explained. This technique uses an approximate closed-form solution to the system of differential equations and a variation of parameters idea to obtain a computationally efficient exact numerical solution to the system of differential equations. Also, the variation of parameters technique allows the partial derivative matrices needed for the numerical solution of the boundary value problem to be obtained in a very efficient manner.

THE MATHEMATICAL MODEL

The equations of motion for this problem in an inertial three-dimensional Cartesian coordinate system will be represented by the differential equations

$$\dot{\bar{X}} = \bar{V} \qquad \bar{X} = (x, y, z), \quad \bar{V} = (\dot{x}, \dot{y}, \dot{z})$$

$$\dot{\bar{V}} = \left(\frac{F}{m}\right)\frac{\bar{c}}{|\bar{c}|} - \frac{GM}{R^3}\bar{X}, \quad R = (x^2 + y^2 + z^2)^{\frac{1}{2}} \tag{1}$$

where $\bar{x}$ is the position vector, $\bar{v}$ is the velocity vector and GM is the

gravitational constant. Also in these equations the unit vector $\dfrac{\bar{c}}{|\bar{c}|}$

is a control vector which defines the direction of the constant thrust

F. The quantity m is the mass of the vehicle and at any time is de-

fined by $m = m_o - \dot{m}(t-t_o)$ with $\dot{m}$ a positive constant. The boundary con-

straints for the problem are given as

$$\bar{V}_i \cdot \bar{V}_i - \frac{2GM}{\sqrt{\bar{x}_i \cdot \bar{x}_i}} + \frac{GM}{a_i} = 0$$

$$(\bar{x}_i \times \bar{V}_i) \cdot (\bar{x}_i \times \bar{V}_i) - GM a_i (1 - e_i^2) = 0 \qquad (i = o, f)$$

$$(\bar{x}_i \times \bar{V}_i) \cdot \bar{d} - \left(\sqrt{GM a_i (1 - e_i^2)}\right) \cos \theta_i$$

where $\bar{d}$ is a unit vector perpendicular to the equatorial plane. The

subscript i = 0 denotes that the functions are to be evaluated at the

initial time t_o with constants a_o, e_o and θ_o being specified; similarly

when i = f, the functions are again evaluated at the final time t_f with

specified values of the constants a_f, e_f and θ_f.

The mass m has important physical significance for this problem

so its identity will be retained by defining q=m and adjoining the

equation $\dot{q} = -\dot{m}$ to the set of differential equations. The optimization

problem can now be stated as follows. Determine a time varying control

vector, $\bar{c}$, that satisfies the system of differential equations

$$\dot{\bar{x}} = \bar{v}$$

$$\dot{\bar{v}} = \left(\frac{F}{m}\right)\frac{\bar{c}}{|\bar{c}|} - \frac{GM}{R^3}\bar{x}$$

$$\dot{q} = -\dot{m}$$

(2)

with boundary constraints

$$F_i(\bar{x}_o, \bar{v}_o, t_o) = 0 \qquad (\bar{x}_o = \bar{x}(t_o),\ \bar{v}_o = \bar{v}(t_o)) \qquad (i = 1, 2, 3, 4)$$

$$G_j(\bar{x}_f, \bar{v}_f, t_f) = 0 \qquad (\bar{x}_f = \bar{x}(t_f),\ \bar{v}_f = \bar{v}(t_f)) \qquad (j = 1, 2, 3)$$

and that minimizes the quantity $\varphi(x_f,\ v_f,\ q_f,\ t_f)$. The F_i are defined by

$$F_1(\bar{x}_o, \bar{v}_o, t_o) \equiv \bar{v}_o \cdot \bar{v}_o - \frac{2GM}{\sqrt{\bar{x}_o \cdot \bar{x}_o}} + \frac{GM}{a_o}$$

$$F_2(\bar{x}_o, \bar{v}_o, t_o) \equiv (\bar{x}_o \times \bar{v}_o) \cdot (\bar{x}_o \times \bar{v}_o) - GMa_o(1 - e_o^2)$$

(3)

$$F_3(\bar{x}_o, \bar{v}_o, t_o) \equiv (\bar{x}_o \times \bar{v}_o) \cdot \bar{d} - \left[\sqrt{GMa_o(1 - e_o^2)}\right] \cos \theta_o$$

$$F_4(\bar{x}_o, \bar{v}_o, q_o, t_o) = q(t_o) - m_o.$$

The functions $G_1(\bar{x}_f,\ \bar{v}_f,\ t_f)$, $G_2(\bar{x}_f,\ \bar{v}_f,\ t_f)$, and $G_3(\bar{x}_f,\ \bar{v}_f,\ t_f)$ are defined analogous to F_1, F_2, and F_3 respectively simply by changing

the subscript "0" to "f".

DERIVATION OF THE NECESSARY CONDITIONS FOR

THE OPTIMIZATION OF $\varphi(\bar{x}_f, \bar{v}_f, q_f, t_f)$

In this section it is advantageous to define the vector

$$\tilde{X}^T(t) = (x, y, z, \dot{x}, \dot{y}, \dot{z}, q)$$

and write the differential equations appearing in (2) as

$$\dot{\tilde{X}}(t) = f(\tilde{X}(t), \bar{c}(t), t)$$

where f is a vector of dimension seven, and $\bar{c}$ is a vector of dimension three.

To minimize $\varphi(\tilde{X}_f, t_f)$, an optimization criteria, J, that adjoins the constraints of the problem to $\varphi(\tilde{X}_f, t_f)$ is defined. The expression J will be equal to φ when the constraints are satisfied. The definition is

$$J = \varphi(\tilde{X}_f, t_f) + p^T F(\tilde{X}_o, t_o) + \rho^T G(\tilde{X}_f, t_f)$$

$$+ \int_{t_o}^{t_f} \lambda^T(t) \left[\dot{\tilde{X}} - f(\tilde{X}(t), \bar{c}(t), t) \right] dt. \tag{4}$$

In the above expression p, ρ and $\lambda(t)$ are the multipliers associated with this problem. They are vectors of dimension four, three, and seven, respectively. A minimization of J and satisfaction of the constraints will produce a minimum of $\varphi(\tilde{X}_f, t_f)$. (In this report a vector

say p, will be considered a column, so the transpose of p denotes the row vector.) In order for J to be a local minimum, δJ, a small variation in J produced by the free or independent parameters must be zero and δ^2J must be positive for this small variation. Satisfaction of these requirements yields the necessary conditions for local optimality. An expression for δJ can be obtained as follows:

$$\delta J = \frac{\partial \varphi}{\partial \tilde{X}_f} \delta \tilde{X}_f + \dot{\varphi}\delta t_f + p^T \frac{\partial F}{\partial \tilde{X}_o} \delta \tilde{X}_o + p^T \dot{F}\delta t_o + p^T \frac{\partial G}{\partial \tilde{X}_f} \delta \tilde{X}_f$$

$$+ p^T \dot{G}\delta t_f + \int_{t_o}^{t_f} \lambda^T(t)\left[\delta \dot{\tilde{X}} - \frac{\partial F}{\partial \tilde{X}}\delta \tilde{X}(t) - \frac{\partial f}{\partial \bar{c}}\delta \bar{c}(t)\right]dt .$$

The term $\int_{t_o}^{t_f}\lambda^T \delta \dot{\tilde{X}}(t)\,dt$ in the above equation can be integrated by parts to give

$$\int_{t_o}^{t_f}\lambda^T \delta \dot{\tilde{X}}\,dt = \lambda^T(t_f)\delta \tilde{X}(t_f) - \lambda^T(t_o)\delta \tilde{X}(t_o) - \int_{t_c}^{t_f}\dot{\lambda}^T(t)\delta \tilde{X}(t)\,dt .$$

Substitution of this result back into the expression for δJ and requiring that δJ=0 for arbitrary variations in

$$\delta \tilde{X}_f, \quad \delta t_f, \quad \delta t_o, \quad \delta \tilde{X}(t), \quad \delta \tilde{X}_o \quad and \quad \delta \bar{c}(t) \quad \left(\tilde{X}_\kappa = \tilde{X}(t_\kappa)\right)$$

results in the following necessary conditions:

(a) $\dot{\lambda}^T(t) + \lambda^T(t)\left[\dfrac{\partial f(\tilde{X}(t),\,\bar{c}(t))}{\partial \tilde{X}(t)}\right] = 0$

(b) $\lambda(t_o) - p^T\left[\dfrac{\partial F(\tilde{X}_o, t_o)}{\partial \tilde{X}_o}\right] = 0$

(c) $p^T \dot{F}(\tilde{X}_o, t_o) = 0$

(d) $\lambda^T(t_f) + \dfrac{\partial \varphi}{\partial \tilde{X}_f} + p^T\left[\dfrac{\partial G(\tilde{X}_f, t_f)}{\partial \tilde{X}_f}\right] = 0$

(e) $\quad \dot{\psi}(\tilde{X}_f, t_f) + \rho^T \dot{G}(\tilde{X}_f, t_f) = 0$

(f) $\quad \lambda^T(t) \left[\dfrac{\partial f(\tilde{X}(t), \bar{c}(t))}{\partial \bar{u}(t)} \right] = 0$.

In addition to the preceding requirements, the condition $\delta^2 J > 0$ must be satisfied. This condition can be combined with condition (f) above to say that

$$ H(t) = \bar{\lambda}^T \dot{\bar{X}} + \bar{u}^T \dot{\bar{v}} + \gamma \dot{\bar{q}} \tag{5} $$

must be a local maximum with respect to $\bar{c}(t)$ for $t_o \leq t \leq t_f$. Here the seven dimensional vector λ has been written in the form $\lambda^T = (\bar{\lambda}^T, \bar{u}^T, \gamma)$ where $\bar{\lambda}^T$ and $\bar{u}^T$ are both three dimensional and γ is a scaler. It is advantageous for later computations to rewrite the above conditions using $\bar{\lambda}^T$, $\bar{u}^T$, and γ to replace λ^T. The resulting system, after some simplifications, can be arranged in the following form. The differential equations are written as

$$ \dot{\bar{\lambda}}^T = -\dfrac{\partial H}{\partial \bar{X}}, \qquad \dot{\bar{u}}^T = -\dfrac{\partial H}{\partial \bar{v}}, \qquad \dot{\gamma} = -\dfrac{\partial H}{\partial \bar{q}} $$

with boundary conditions

(a) $\quad F(\bar{x}_0, \bar{v}_0, t_0) = 0$

(b) $\quad \bar{\lambda}^T(t_0) - \bar{p}^T \dfrac{\partial F}{\partial \bar{x}_0} = 0 \quad (\bar{p}^T = (p_1, p_2, p_3)) \tag{6}$

(c) $\quad \bar{p}^T \dot{F}(\bar{x}_0, \bar{v}_0, t_0) = 0$

(d) $\quad \bar{u}^T(t_0) - \bar{p}^T \dfrac{\partial F}{\partial \bar{v}_0} = 0$

(e) $\quad \gamma(t_0) = P_4$

and

(a) $\quad G(\bar{x}_f, \bar{v}_f, t_f) = 0$

(b) $\quad \bar{\lambda}^T(t_f) + \dfrac{\partial \psi}{\partial \bar{x}_f} + \rho^T \dfrac{\partial G}{\partial \bar{x}_f} = 0 \qquad (\rho^T = (P_1, P_2, P_3))$

(c) $\quad \bar{u}^T(t_f) + \dfrac{\partial \psi}{\partial \bar{v}_f} + \rho^T \dfrac{\partial G}{\partial \bar{v}_f} = 0$

(d) $\quad \gamma(t_f) + \dfrac{\partial \psi}{\partial q_f} = 0$

(e) $\quad \dot{\psi} + \rho^T \dot{G}(\bar{x}_f, \bar{v}_f, t_f) = 0.$

(7)

The requirement that the function H(t) be a local maximum with respect to $\bar{c}(t)$ can be replaced by the equivalent relations that $\dfrac{\partial H}{\partial \bar{c}} = 0$ and that $\dfrac{\partial^2 H}{\partial \bar{c} \partial \bar{c}}$ be negative definite. The first relation can be solved to give the control vector $\bar{c}$ in terms of $\bar{\lambda}$ at every $t_0 \le t \le t_f$. Now replacing $\dot{\bar{v}}$ from equation (1), H(t) can be written as

$$H(t) = \bar{\lambda}^T \dot{\bar{x}} + \bar{u}^T \left[\dfrac{F}{q} \dfrac{\bar{c}}{|\bar{c}|} - \dfrac{GM}{R^3} \bar{x} \right] + \gamma \dot{q} .$$

Then

$$\dfrac{\partial H}{\partial \bar{c}} = \bar{u}^T \dfrac{F}{q} \left[\dfrac{1}{|\bar{c}|} I_{3 \times 3} - \dfrac{\bar{c}\,\bar{c}^T}{|\bar{c}|^3} \right]$$

$$= \dfrac{F}{q} \left[\dfrac{\bar{u}^T}{|\bar{c}|} - \dfrac{\bar{u}^T \bar{c}\,\bar{c}^T}{|\bar{c}|^3} \right].$$

By examining the expression for $\frac{\partial H}{\partial \bar{c}}$ it can be seen that $\bar{c} = \bar{u}$ is

sufficient to assure that $\frac{\partial H}{\partial \bar{c}} = 0$. Also one can verify that this

selection for $\bar{c}$ will also make the matrix $\frac{\partial^2 H}{\partial \bar{c} \partial \bar{c}}$ be negative definite.

Now this result for $\bar{c}$ can be substituted back into the differential

equations and the formulation of the necessary conditions associated

with this optimal trajectory problem is complete.

FORMULATION OF THE BOUNDARY VALUE PROBLEM

In the last section the control vector $\bar{c}$ necessary to optimize

the quantity J listed in equation (4) was found to be $\bar{c} = \bar{u}$. Replacing

this value of $\bar{c}$ in all of the differential equations results in the new

system

$$\dot{\bar{x}} = \bar{v}$$

$$\dot{\bar{v}} = \left(\frac{F}{q}\right)\frac{\bar{u}}{|\bar{u}|} - \frac{GM}{R^3}\bar{x}, \qquad R = (x^2 + y^2 + z^2)^{\frac{1}{2}}$$

$$\dot{q} = -\dot{m} \tag{8}$$

$$\dot{\bar{\lambda}} = \left(\frac{GM}{R^3}\right)\bar{u} - \frac{3GM}{R^5}(\bar{x}\cdot\bar{u})\bar{x}$$

$$\dot{\bar{u}} = -\bar{\lambda}$$

$$\dot{\gamma} = \left(\frac{F}{q^2}\right)|\bar{u}|.$$

These differential equations are to connect the boundary conditions

listed in equations (6) and (7) of the last section. These conditions

will now be rewritten by giving explicit expressions for the matrices

$$\left[\frac{\partial F}{\partial \bar{x}_0}\right], \qquad \left[\frac{\partial F}{\partial \bar{v}_0}\right], \qquad \left[\frac{\partial G}{\partial \bar{x}_f}\right], \qquad \left[\frac{\partial G}{\partial \bar{v}_f}\right]$$

$$\dot{F}(\bar{x}_0, \bar{v}_0, t_0) \quad \text{and} \quad \dot{G}(\bar{x}_f, \bar{v}_f, t_f).$$

Using the definitions of F_1, F_2, F_3 and F_4 given in (3), it is straight-forward to verify that

$$\left[\frac{\partial F_1}{\partial \bar{x}_0}\right] = \frac{2GM\bar{x}_0^T}{(\bar{x}_0^T \bar{x}_0)^{3/2}} ; \qquad \left[\frac{\partial F_1}{\partial \bar{v}_0}\right] = 2\bar{v}_0^T$$

$$\left[\frac{\partial F_2}{\partial \bar{x}_0}\right] = 2\left[\bar{v}_0 \times (\bar{x}_0 \times \bar{v}_0)^T\right]; \quad \left[\frac{\partial F_2}{\partial \bar{v}_0}\right] = 2\left[\bar{x}_0 \times (\bar{v}_0 \times \bar{x}_0)\right]^T \qquad (9)$$

$$\left[\frac{\partial F_3}{\partial \bar{x}_0}\right] = (\bar{v}_0 \times \bar{J})^T; \quad \left[\frac{\partial F_3}{\partial \bar{v}_0}\right] = (\bar{J} \times \bar{x}_0)^T; \quad \left[\frac{\partial F_4}{\partial \bar{x}_0}\right] = \left[\frac{\partial F_4}{\partial \bar{v}_0}\right] = \bar{0}.$$

Similarly, using the definitions of G_1, G_2 and G_3, one finds analogous expressions for

$$\left[\frac{\partial G_1}{\partial \bar{x}_f}\right], \qquad \left[\frac{\partial G_2}{\partial \bar{x}_f}\right], \qquad \left[\frac{\partial G_3}{\partial \bar{x}_f}\right]$$

$$\left[\frac{\partial G_1}{\partial \bar{v}_f}\right], \qquad \left[\frac{\partial G_2}{\partial \bar{v}_f}\right] \quad \text{and} \quad \left[\frac{\partial G_3}{\partial \bar{v}_f}\right].$$

The relation

$$\dot{F}(\bar{x}_0, \bar{v}_0, t_0) = \frac{\partial F}{\partial \bar{x}_0} \dot{\bar{x}}_0 + \frac{\partial F}{\partial \bar{v}_0} \dot{\bar{v}}_0 + \frac{\partial F}{\partial t_0}$$

when used together with equations (b) and (d) of (6) transforms the equation

$$\bar{p}^T \dot{F}(\bar{x}_0, \bar{v}_0, t_0) = 0$$

into

$$\bar{\lambda}_o^T \dot{\bar{x}}_o + \bar{u}_o^T \dot{\bar{v}}_o = 0 \tag{10}$$

In a similar fashion equation (e) of system (7) can be replaced by the equation

$$\bar{\lambda}_f^T \dot{\bar{x}}_f + \bar{u}_f^T \dot{\bar{v}}_f + \gamma_f \dot{q} - \frac{\partial \varphi}{\partial t_f} = 0$$

$$(\bar{\lambda}_k = \bar{\lambda}(t_k), \quad \bar{u}_k = \bar{u}(t_k), \quad \gamma_k = \gamma(t_k)). \tag{11}$$

The boundary value problem can now be formulated in a compact form. First, the following definition is made. Let

$$X(t) = (\bar{x}(t), \bar{v}(t))^T \quad \text{and} \quad P(t) = (\bar{\lambda}(t), \bar{u}(t), \gamma(t))^T. \tag{12}$$

Then the optimization problem consists of solving the system of non-linear differential equations

$$\dot{X}(t) = f(X(t), P(t), t)$$

$$\dot{P}(t) = g(X(t), P(t), t) \tag{13}$$

$$\dot{q} = -\dot{m}$$

and satisfying the boundary conditions from (6) and (7) now written in the form

$$D(t_o, X_o, P_o, q_o, \bar{p}) = 0 \tag{14}$$

$$E(t_f, X_f, P_f, q_f, p) = 0.$$

In equation (13) above

$$f_1 = \vec{v}; \qquad f_2 = \left(\frac{F}{q}\right)\frac{\vec{u}}{|\vec{u}|} - \frac{GM}{R^3}\vec{x};$$

$$g_1 = \left(\frac{GM}{R^3}\right)\vec{u} - \frac{3GM}{R^5}(\vec{x}\cdot\vec{u})\vec{x}; \quad g_2 = -\vec{\lambda}; \quad g_3 = \left(\frac{F}{q^2}\right)|\vec{u}|.$$

Also, in (14) D is a twelve dimensional vector defined by

$$D_k(t_o, X_o, P_o, q_o, \vec{p}) = F_k(X_o, t_o) \qquad (k=1,2,3)$$

$$\begin{bmatrix} D_4 \\ D_5 \\ D_6 \end{bmatrix} = \vec{\lambda}(t_o) - \left\{ \frac{2GM\vec{x}_o}{(\vec{x}_o^T\vec{x}_o)^{3/2}}, 2[\vec{v}_o \times (\vec{x}_o \times \vec{v}_o)], (\vec{v}_o \times \vec{d}) \right\}\vec{p}$$

$$\begin{bmatrix} D_7 \\ D_8 \\ D_9 \end{bmatrix} = \vec{u}(t_o) - \left\{ 2\vec{v}_o, 2[\vec{x}_o \times (\vec{v}_o \times \vec{x}_o)], (\vec{d} \times \vec{x}_o) \right\}\vec{p} \qquad (15)$$

$$D_{10} = \vec{\lambda}_o^T \dot{\vec{x}}_o + \vec{u}_o^T \dot{\vec{v}}_o$$

$$D_{11} = \gamma(t_o) - P_4$$

$$D_{12} = q(t_o) - m_o.$$

The vector $E(t_f, X_f, P_f, q_f, \rho)$ is eleven dimensional and is defined by

$$E_k = G_k(X_f, t_f) \qquad (k=1,2,3)$$

$$\begin{bmatrix} E_4 \\ E_5 \\ E_6 \end{bmatrix} = \bar{\lambda}(t_f) + \left\{ \frac{2GM\bar{x}_f}{(\bar{x}_f^T \bar{x}_f)^{3/2}}, \ 2[\bar{v}_f \times (\bar{x}_f \times \bar{v}_f)], \ (\bar{v}_f \times \bar{d}) \right\} \rho + \left(\frac{\partial \varphi}{\partial \bar{x}_f} \right)^T$$

$$\begin{bmatrix} E_7 \\ E_8 \\ E_9 \end{bmatrix} = \bar{u}(t_f) + \left\{ 2\bar{v}_f, \ 2[\bar{x}_f \times (\bar{v}_f \times \bar{x}_f)], \ (\bar{d} \times \bar{x}_f) \right\} \rho + \left\{ \frac{\partial \varphi}{\partial \bar{v}_f} \right\}^T \qquad (16)$$

$$E_{10} = \gamma(t_f) + \frac{\partial \varphi}{\partial q_f}$$

$$E_{11} = \bar{\lambda}_f^T \dot{\bar{x}}_f + \bar{u}_f^T \dot{\bar{v}}_f + \gamma(t_f)\dot{q}(t_f) - \frac{\partial \varphi}{\partial t_f} \ .$$

Two of the above boundary conditions

$$D_{11}(t_o, X_o, P_o, q_o, \bar{p}) = 0 \quad \text{and} \quad D_{12}(t_o, X_o, P_o, q_o, \bar{p}) = 0$$

can be solved by selecting $q(t_o)$ to be equal to the constant m_o and by

choosing $\gamma(t_o)$ and p_4 to be the same value. Therefore the problem now

is to determine values of t_o, X_o, P_o, $\bar{p}$, ρ, and t_f so that when t_o, X_o,

P_o, (and q_o selected above) are used as initial values for the differen-

tial equations in (13), the resulting solution $X(t)$, $P(t)$ and $q(t)$ when

evaluated at t_o and t_f will satisfy the twenty-one conditions

$$D_j(t_o, X_o, q_o, P_o, \bar{p}) = 0 \qquad j = 1, 2, 3, \ldots, 10$$

$$E_k(t_f, X_f, q_f, P_f, \rho) = 0 \qquad k = 1, 2, 3, \ldots, 11.$$

The solution of the boundary conditions involves the expansion of

the vector functions $D(t_o, X_o, q_o, P_o, \bar{p})$ and $E(t_f, X_f, P_f, \rho)$ into Taylor

series about a set of guessed values (denoted by $t_o^*, X_o^*, P_o^*, \bar{p}^*, \rho^*$ and t_f^*)

for the parameters t_o, X_o, P_o, $\bar{p}$, ρ, and t_f. By truncating these
series expansions after first-order terms, a set of correction vectors

$$\Delta t_o, \quad \Delta X_o, \quad \Delta P_o, \quad \Delta \bar{p}, \quad \Delta \rho \quad \text{and} \quad \Delta t_f$$

can be determined which when added to t_o^*, X_o^*, P_o^*, $\bar{p}^*$, ρ^* and t_f^* will
produce values of $D_j(t_o, X_o, q_o, P_o, p)$ and $E_k(t_f, X_f, q_f, P_f, \rho)$ nearer zero.
The entire procedure can be repeated with the corrected values as the
estimated (*) values. This process is well documented (see [1], [7],
[8]) and the result is the development of a modified Newton's iteration
formula for the correction vectors. The formula for the problem con-
sidered here is

$$
\begin{bmatrix} \Delta t_o \\ \Delta X_o \\ \Delta P_o \\ \Delta \bar{p} \\ \Delta \rho \\ \Delta t_f \end{bmatrix}_{n+1}
= (-K)
\begin{bmatrix} [\dot{D}] & [\frac{\partial D}{\partial X_o}] & [\frac{\partial D}{\partial P_o}] & [\frac{\partial D}{\partial \bar{p}}] & [0] & [0] \\ \\ [\frac{\partial E}{\partial t_o}] & [\frac{\partial E}{\partial X_o}] & [\frac{\partial E}{\partial P_o}] & [0] & [\frac{\partial E}{\partial \rho}] & [\dot{E}] \end{bmatrix}_n
\begin{bmatrix} D \\ \\ \\ E \end{bmatrix}_n
$$

where n and n+1 denote the iteration number. This formula for
the correction vector is used repetitively until the boundary conditions

$$D(t_o, X_o, q_o, P_o, \bar{p}) \quad \text{and} \quad E_k(t_f, X_f, q_f, P_f, p)$$

are zero to a desired tolerance.

Explicit expressions for the matrices

$$[\dot{D}], \quad \left[\frac{\partial D}{\partial X_o}\right], \quad \left[\frac{\partial D}{\partial P_o}\right] \quad \text{and} \quad \left[\frac{\partial D}{\partial \bar{p}}\right]$$

appearing in Newton's formula can be obtained by chain rule differentiation of the vectors, D , given in (15). To obtain numerical values for the matrices involving the E_k's, chain rule differentiation is again used and results in the following equations:

$$\frac{\partial E}{\partial t_o} = \left[\frac{\partial E}{\partial X_f}\right]\left[\frac{\partial X_f}{\partial t_o}\right] + \left[\frac{\partial E}{\partial P_f}\right]\left[\frac{\partial P_f}{\partial t_o}\right]$$

$$\frac{\partial E}{\partial X_o} = \left[\frac{\partial E}{\partial X_f}\right]\left[\frac{\partial X_f}{\partial X_o}\right] + \left[\frac{\partial E}{\partial P_f}\right]\left[\frac{\partial P_f}{\partial X_o}\right]$$

$$\frac{\partial E}{\partial P_o} = \left[\frac{\partial E}{\partial X_f}\right]\left[\frac{\partial X_f}{\partial P_o}\right] + \left[\frac{\partial E}{\partial P_f}\right]\left[\frac{\partial P_f}{\partial P_o}\right]$$

$$\dot{E} = \frac{\partial E}{\partial t_f} + \frac{\partial E}{\partial X_f}\dot{x}(t_f) + \frac{\partial E}{\partial P_f}\dot{P}(t_f)$$

All matrices on the right-hand side of the above equations can be explicity represented, except for

$$\left[\frac{\partial X_f}{\partial t_o}\right], \quad \left[\frac{\partial P_f}{\partial t_o}\right], \quad \left[\frac{\partial X_f}{\partial X_o}\right], \quad \left[\frac{\partial P_f}{\partial X_o}\right], \quad \left[\frac{\partial X_f}{\partial P_o}\right] \quad \text{and} \quad \left[\frac{\partial P}{\partial P_o}\right]. \qquad (17)$$

These "transition" matrices must be obtained from the numerical integration of the following set of matrix differential equations

$$\frac{d}{dt}\left[\frac{\partial X}{\partial t_0}\right] = \left[\frac{\partial \dot{X}}{\partial t_0}\right] = \left[\frac{\partial f}{\partial X}\right]\left[\frac{\partial X}{\partial t_0}\right] + \left[\frac{\partial f}{\partial P}\right]\left[\frac{\partial P}{\partial t_0}\right] + \left[\frac{\partial f}{\partial q}\right]\left[\frac{\partial q}{\partial t_0}\right]$$

$$\frac{d}{dt}\left[\frac{\partial P}{\partial t_0}\right] = \left[\frac{\partial \dot{P}}{\partial t_0}\right] = \left[\frac{\partial g}{\partial X}\right]\left[\frac{\partial X}{\partial t_0}\right] + \left[\frac{\partial g}{\partial P}\right]\left[\frac{\partial P}{\partial t_0}\right] + \left[\frac{\partial g}{\partial q}\right]\left[\frac{\partial q}{\partial t_0}\right]$$

$$\frac{d}{dt}\left[\frac{\partial X}{\partial X_0}\right] = \left[\frac{\partial \dot{X}}{\partial X_0}\right] = \left[\frac{\partial f}{\partial X}\right]\left[\frac{\partial X}{\partial X_0}\right] + \left[\frac{\partial f}{\partial P}\right]\left[\frac{\partial P}{\partial X_0}\right]$$

$$\frac{d}{dt}\left[\frac{\partial P}{\partial X_0}\right] = \left[\frac{\partial \dot{P}}{\partial X_0}\right] = \left[\frac{\partial g}{\partial X}\right]\left[\frac{\partial X}{\partial X_0}\right] + \left[\frac{\partial g}{\partial P}\right]\left[\frac{\partial P}{\partial X_0}\right] \qquad (18)$$

$$\frac{d}{dt}\left[\frac{\partial X}{\partial P_0}\right] = \left[\frac{\partial \dot{X}}{\partial P_0}\right] = \left[\frac{\partial f}{\partial X}\right]\left[\frac{\partial X}{\partial P_0}\right] + \left[\frac{\partial f}{\partial P}\right]\left[\frac{\partial P}{\partial P_0}\right]$$

$$\frac{d}{dt}\left[\frac{\partial P}{\partial P_0}\right] = \left[\frac{\partial \dot{P}}{\partial P_0}\right] = \left[\frac{\partial g}{\partial X}\right]\left[\frac{\partial X}{\partial P_0}\right] + \left[\frac{\partial g}{\partial P}\right]\left[\frac{\partial P}{\partial P_0}\right].$$

The initial conditions for these matrix equations are

$$\left[\frac{\partial X(t_0)}{\partial X_0}\right] = I, \quad \left[\frac{\partial X(t_0)}{\partial P_0}\right] = [0], \quad \left[\frac{\partial X(t_0)}{\partial t_0}\right] = \dot{X}(t_0^-) - \dot{X}(t_0^+)$$

$$\left[\frac{\partial P(t_0)}{\partial X_0}\right] = [0], \quad \left[\frac{\partial P(t_0)}{\partial P_0}\right] = I, \quad \left[\frac{\partial P_0}{\partial t_0}\right] = \dot{P}(t_0^-) - \dot{P}(t_0^+).$$

The expressions for the matrices

$$\left[\frac{\partial X(t_0)}{\partial t_0}\right] \quad \text{and} \quad \left[\frac{\partial P_0}{\partial t_0}\right]$$

above results from the fact that t_0 is a "switching" time, i.e., slightly before t_0 the motion is governed by two-body equations (no thrust) and slightly after t_0 the thrusting force appears and perturbed motion results. A mathematical justification of these conditions are given in reference [2].

Numerical integration of equation (18) on the interval $t_o \leq t \leq t_f$
will produce values for the matrices appearing in (17) and consequently
all entries in the iteration formula will have been computed. Also the
differential equations appearing in equation (13) must be numerically
integrated along each trial in the iteration process and this together
with the partial derivative matrices will result in an accurate solution
to the boundary value problem. It is clear that to obtain this solution
a number of numerical integration schemes must be employed. In the
next section a brief description of how a closed-form solution of an
approximating system of differential equations can be used to avoid
some of the numerical computation is given.

DEVELOPMENT OF A CLOSED FORM SOLUTION

The low thrust of the model vehicle considered in this report
enables the equations of motion listed in equation (1) to be approxi-
mated by a two-body problem

$$\dot{\bar{x}} = \bar{v}$$

$$\dot{\bar{v}} = - \frac{GM}{R^3} \bar{x} .$$

Also differential equations for the multipliers, $\bar{\lambda}$ and $\bar{u}$ associated
with the two-body problem can be written and used to approximate the
corresponding equations in system (8). However, the approximating
system considered here consists of the addition of a thrust term, that
has some dependence on the initial values of the multipliers, to the
two-body problem. Let $\bar{x}_2 = (x_2, y_2, z_2)$ and $\bar{v}_2 = (\dot{x}_2, \dot{y}_2, \dot{z}_2)$ represent
a solution of the two-body problem. Then the approximating system for

the equations of motion will be taken to be

$$\dot{\bar{x}} = \bar{v}$$

$$\dot{\bar{v}} = \left(\frac{F}{m}\right)\bar{c} - \frac{GM}{R_2^3}\bar{x}_2, \quad R_2 = (x_2^2 + y_2^2 + z_2^2)^{1/2} \tag{19}$$

where

$$\bar{c} = \bar{a}\,\sin\left[\frac{2\pi}{T}(t - t_0)\right] + \bar{b}\,\cos\left[\frac{2\pi}{T}(t - t_0)\right] \tag{20}$$

with

$$\bar{b} = \frac{\bar{u}_0}{|\bar{u}_0|}, \qquad \bar{a} = \frac{(\bar{b} \times \bar{\lambda}_0) \times \bar{b}}{|(\bar{b} \times \bar{\lambda}_0) \times \bar{b}|} \qquad (T = \text{period}).$$

It is straightforward to verify that a solution to system (19) above is

$$\bar{x}(t) = \bar{x}_2(t) + \int_{t_0}^{t}\left[\int_{t_0}^{t}\frac{F}{m}\bar{c}\,dt\right]dt \tag{21}$$

$$\bar{v}(t) = \bar{v}_2(t) + \int_{t_0}^{t}\frac{F}{m}\bar{c}\,dt.$$

Since $\bar{x}_2(t)$ and $\bar{v}_2(t)$ are known solutions of the two-body problem, the integrals need only be evaluated in order to have explicit representations of $\bar{x}(t)$ and $\bar{v}(t)$. Recall that the mass m is a function of time defined by $m = m_0 - \dot{m}(t - t_0)$. Then

$$\frac{F}{m} = \frac{F}{m_0}\left\{1 + \frac{\dot{m}}{m_0}(t - t_0) + \left(\frac{\dot{m}}{m_0}\right)^2(t - t_0)^2 + \cdots + \left(\frac{\dot{m}}{m_0}\right)^N(t - t_0)^N + \cdots\right\}$$

$$\left(\left|\frac{\dot{m}}{m_0}(t - t_0)\right| < 1\right).$$

For ease of computation in evaluating the above integrals, this series will be truncated after second order terms. (Of course a closed form solution of greater accuracy can be obtained by truncating at some higher power). The first integral to be evaluated now has the form

$$\frac{F}{m_0} \int_{t_0}^{t} \bar{c} \left(1 + \left(\frac{\dot{m}}{m_0}\right)(t - t_0) + \left(\frac{\dot{m}}{m_0}\right)^2 (t - t_0)^2 \right) dt =$$

$$\frac{F}{m} \int_{t_0}^{t} \left\{ \bar{a} \sin \alpha(t-t_0) + \bar{b} \cos \alpha(t-t_0) + \left(\frac{\dot{m}}{m_0}\right)\left[\bar{a}(t-t_0) \sin \alpha(t-t_0) \right.\right.$$

$$\left. + \bar{b}(t-t_0) \cos \alpha(t-t_0)\right] + \left(\frac{\dot{m}}{m_0}\right)^2 \left[\bar{a}(t-t_0)^2 \sin \alpha(t-t_0)\right.$$

$$\left.\left. + \bar{b}(t-t_0)^2 \cos \alpha(t-t_0)\right]\right\} dt, \qquad \alpha = \frac{2\pi}{T}.$$

The above integral can be evaluated using standard integration formulas

and the results can be written in terms of sines and cosines as follows:

$$\int_{t_0}^{t} \bar{c}\left[1 + \left(\frac{\dot{m}}{m_0}\right)(t-t_0) + \left(\frac{\dot{m}}{m_0}\right)^2(t-t_0)^2\right] dt = A \sin \alpha(t-t_0) + B \cos \alpha(t-t_0) \qquad (22)$$

where A and B are defined by

$$A = \frac{\bar{a}}{\alpha^2}\left[\frac{\dot{m}}{m_0} + 2\left(\frac{\dot{m}}{m_0}\right)^2(t-t_0)\right] + \frac{\bar{b}}{\alpha}\left[1 - \frac{2}{\alpha^2}\left(\frac{\dot{m}}{m_0}\right)^2\right]$$

$$+ \frac{\bar{b}}{\alpha}\left[\left(\frac{\dot{m}}{m_0}\right)^2(t-t_0)^2 + \left(\frac{\dot{m}}{m_0}\right)(t-t_0)\right] \qquad (23)$$

$$B = \frac{\bar{a}}{\alpha}\left[\frac{2}{\alpha^2}\left(\frac{\dot{m}}{m_0}\right)^2 - \left(\frac{\dot{m}}{m_0}\right)^2(t-t_0)^2 - \left(\frac{\dot{m}}{m_0}\right)(t-t_0) - 1\right]$$

$$+ \frac{\bar{b}}{\alpha^2}\left[\frac{\dot{m}}{m_0} + 2\left(\frac{\dot{m}}{m_0}\right)^2(t-t_0)\right].$$

Now integrating the expression in (22) yields

$$\int_{t_0}^{t}\left[\int_{t_0}^{t} \bar{c}\left[1 + \left(\frac{\dot{m}}{m_0}\right)(t-t_0) + \left(\frac{\dot{m}}{m_0}\right)^2(t-t_0)^2 dt\right]\right] dt = C \sin \alpha(t-t_0) + D \cos \alpha(t-t_0)$$

with C and D given by

$$C = \frac{\bar{a}}{\alpha^2}\left[\frac{6}{\alpha^2}\left(\frac{\dot{m}}{m_0}\right)^2 - \left(\frac{\dot{m}}{m_0}\right)(t-t_0) - \left(\frac{\dot{m}}{m_0}\right)^2(t-t_0)^2 - 1\right]$$

$$+ \frac{\bar{b}}{\alpha^3}\left[2\left(\frac{\dot{m}}{m_0}\right) + 4\left(\frac{\dot{m}}{m_0}\right)^2(t-t_0)\right] \qquad (24)$$

$$D = \frac{\bar{b}}{\alpha^2}\left[\frac{6}{\alpha^2}\left(\frac{\dot{m}}{m_0}\right)^2 - \left(\frac{\dot{m}}{m_0}\right)(t-t_0) - \left(\frac{\dot{m}}{m_0}\right)^2(t-t_0)^2 - 1\right]$$

$$- \frac{\bar{a}}{\alpha^3}\left[2\left(\frac{\dot{m}}{m_0}\right) + 4\left(\frac{\dot{m}}{m_0}\right)^2(t-t_0)\right], \qquad \left(\alpha = \frac{2\pi}{T}\right).$$

The solution of the system given in (19) with $\frac{F}{m}$ replaced by

$$\frac{F}{m_0}\left(1 + \left(\frac{\dot{m}}{m_0}\right)(t-t_0) + \left(\frac{\dot{m}}{m_0}\right)^2(t-t_0)^2\right)$$

can now be represented by

$$\bar{x}(t) = \bar{x}_2(t) + \frac{F}{m_0}\left[C \sin \alpha(t-t_0) + D \cos \alpha(t-t_0)\right]$$

$$\bar{v}(t) = \bar{v}_2(t) + \frac{F}{m_0}\left[A \sin \alpha(t-t_0) + B \cos \alpha(t-t_0)\right].$$

(25)

An approximating system for the full set of equations appearing in (8) will be taken to be

$$\dot{\bar{x}} = \bar{v}$$

$$\dot{\bar{v}} = \left[\frac{F}{m_0}\left(1 + \left(\frac{\dot{m}}{m_0}\right)(t-t_0) + \left(\frac{\dot{m}}{m_0}\right)^2(t-t_0)^2\right)\right]\bar{c} - \frac{GM}{R_2^3}\bar{x}_2$$

$$\dot{\bar{\lambda}} = \left(\frac{GM}{R_2^3}\right)\bar{u} - \frac{3GM}{R_2^5}(\bar{x}_2 \cdot \bar{u})\bar{x}_2$$

$$\dot{\bar{u}} = -\bar{\lambda}$$

$$\dot{q} = -\dot{m}$$

$$\dot{r} = 0$$

(26)

Solutions for the adjoint variables $\bar{\lambda}(t)$ and $\bar{u}(t)$ are available from Ingram's work [9]. Also cartesian coordinate closed form expressions for $\bar{x}_2(t)$ and $\bar{v}_2(t)$ needed for the complete representation of the solution $\bar{x}(t), \bar{v}(t)$ in (25), are available from Goodyear's work on the two-body problem, [5]. Therefore, a closed form solution for the above system of differential equations can be obtained. This closed form solution can be combined with a variation of parameters technique developed by H. L. Ingram [8] to integrate the equations given in (8). A detailed explanation of this procedure is given in reference [8] and will not be reproduced here. Also the transition matrices of the closed form solution can be evaluated by explicit differentiation of the expressions for $\bar{x}$, $\bar{v}$, q, $\bar{\lambda}$, $\bar{u}$, and r with respect to $\bar{x}_0$, $\bar{v}_0$, q_0, $\bar{\lambda}_0$, $\bar{u}_0$,

2-22

and $\overline{\gamma}_o$. These matrices can be used to approximate the ones appearing in (17) that are needed in the iteration formula. The effect of this approximation is the elimination of the necessity of having to numerically integrate the system of equations in (18).

CONCLUSIONS

A boundary value formulation of a low thrust trajectory optimization problem has been developed and a Newton's method iteration has been applied in order to solve the resulting two point boundary value problem. Closed form representations for the major parts (state variables) of the solution to an approximating system of differential equations have been given. What is now needed is the development of a computer program that would test the efficiency of the closed form solution when used in the variation of parameters technique developed by H. L. Ingram. Such a program would indicate whether or not the closed form solution proposed in this report provided (significantly) rapid numerical integration of the original equations of motion.

REFERENCES

1. Baker, C. C., Causey, W. E. and Ingram, H. L., "Mathematical Concepts and Historical Development of the Mascot Guidance Techniques for Space Vehicles", NASA TM-X-64608, July 20, 1971.

2. Brown, K. R., Harrold, E.F. and Johnson, G. W., "Rapid Optimization of Multiple - Burn Rocket Flights", NASA-CR-1430, September, 1969, 15-17.

3. Danby, J. H. A., Fundamentals of Celestial Mechanics, MacMillan, New York (1962).

4. Goodyear, W. H., "A General Method of Variation of Parameters for Numerical Integration", Astronomical Journal, 70(1965), 524-526

5. _____, "Completely General Closed Form Solution for Coordinates and Partial Derivatives of the Two-Body Problem", Astronomical Journal, 70(1965), 187-192.

6. Hunt, R. W., and Silber, R., "Space Vehicle Guidance - A Boundary Value Formulation", NASA TM-X-53059, June 8, 1964.

7. Ingram, H. L., "Boundary Value Problems Associated with Optimization Theory", NASA TM-X-53365, December, 1965.

8. _____, "Closed-Form Solutions for Atmospheric Flight with Applications to Shuttle Guidance", NASA TM-X-64694, September, 1972.

9. _____, "Optimal Guidance with Transition Partial Derivative Matrices", Proceedings of the 19th Congress of the International Astronautical Federation, Vol. 2, Astrodynamics and Astrionics, Pergamon Press, New York, 1970.

10. _____, "The Automation of Optimization Problems", The American Astronautical Society of Science and Technology Series, Vol. 2, Space Flight Mechanics Specialist Symposium, 1967.

11. Keller, Herbert B., Numerical Methods for Two-Point Boundary - Value Problems, Blaisdell Publishing Co., Waltham, Mass.,1968.

12. Luenberger, David G., Optimization by Vector Space Methods, John Wiley and Sons, Inc., New York, 1969.

1974

ASEE - NASA SUMMER FACULTY FELLOWSHIP PROGRAM

MARSHALL SPACE FLIGHT CENTER

(AUBURN UNIVERSITY - UNIVERSITY OF ALABAMA)

TEST PATTERN GENERATION

FOR SEQUENTIAL LOGIC CIRCUITS

Prepared by: B.D. Carroll, Ph.D.

Academic Rank: Assistant Professor

Department and University: Electrical Engineering Department
                                 Auburn University

NASA/MSFC Assignment:
    (Laboratory)   Electronics and Control
    (Division)   Electronics Development
    (Branch)   Design Techniques

NASA Research Colleague: John M. Gould

Date: August 9, 1974

Contract No.:   NGT-01-003-045

TEST PATTERN GENERATION FOR SEQUENTIAL LOGIC CIRCUITS

by

B. D. CARROLL

ABSTRACT

The problem of test pattern generation (TPG) for sequential logic circuits is studied. In particular, several aspects of the TPG problem are discussed for the case of asynchronous sequential circuits and single stuck-at faults. A circuit model is first developed for use in TPG procedures. Homing sequence and TPG procedures are then presented.

The effect of gate delays in logic circuit performance is discussed in relation to the TPG problem. It is shown that insertion of delay elements at critical points in the Huffman sequential circuit model yields a useful model for TPG purposes. Edge-sensitive circuits are represented very satisfactorily by the model. A procedure for delay element placement is described.

A homing sequence generation procedure is developed for use with the circuit model. The procedure yields an input sequence that will take a circuit from an unknown starting state to a specified final state if such a sequence exists. Stability conditions are imposed for each input in the sequence.

The TPG procedure given is based on a unique adaptation of the homing sequence procedure. A test pattern sequence for a given fault is obtained in a single iterative process. The test sequence does not require the circuit under test to be in a known starting state.

ACKNOWLEDGEMENT

TEST PATTERN GENERATION
FOR SEQUENTIAL LOGIC CIRCUITS

INTRODUCTION

Test pattern generation (TPG) for sequential logic circuits is an important practical problem for which no adequate solution has been presented. Several aspects of the test pattern generation problem will be discussed in this report along with proposed solutions. Many of the sequential circuit TPG procedures that have been developed have evolved from procedures originally intended for combinational logic circuits. Hence the procedures do not adequately handle the memory characteristics inherent in sequential circuits.

Clocked or synchronous sequential circuits may be handled reasonably well for TPG when certain assumptions are made. Assumptions usually made are that memory elements are all clocked flip-flops, that circuit inputs do not change while the clock signal is high, and that faults do not affect the internal behavior of the flip-flops. These assumptions eliminate the need to consider asynchronous behavior of the circuit including the effects of element delays, races, and hazards. Timing problems associated with TPG are therefore minimized and TPG procedures are straightforward.

The assumptions mentioned above cannot always be justified in which case circuits must be handled as asynchronous circuits. Even when the assumptions are applicable it is often desirable to treat the circuits as asynchronous devices for purposes of testing. Hence, TPG procedures for asynchronous circuits are required.

TPG for asynchronous circuits is more complex than for synchronous circuits primarily due to the need to consider circuit transient states caused by time delays and the related problems of races and hazards. A TPG procedure must be able to handle circuits that are edge-sensitive as well as circuits that contain both local and global feedback loops.

An asynchronous circuit TPG procedure will be developed in this report that is designed to handle the following cases.

    1. Asynchronous logic

    2. Edge-sensitive logic

    3. Local and global feedback.

The report is organized into five sections including an introduction, a section on circuit models, a section on "homing" sequence generation, a section describing the TPG procedure, and a conclusion.

ASYNCHRONOUS CIRCUIT MODELS FOR TPG

Two asynchronous circuit models for use in TPG will be described in this section. First, a basic model will be described. The basic model is then augmented to overcome some inadequacies that arise in TPG.

Basic Asynchronous Model (BAM)

It is well known that any asynchronous sequential circuit can be drawn in the form shown in Figure 1. This model is due to Huffman. The combinational logic in the model is assumed to have no feedback loops and to have zero propagation delay. All delays in the circuit are assumed to be lumped together in the feedback paths.

Variables shown in Figure 1 are related at time t by the following Boolean equations.

$$z_i^t = f_i (x_1^t, \ldots, x_n^t, y_1^t, \ldots, y_r^t), \quad i = 1, \ldots, m \tag{1}$$

$$Y_j^t = g_i (x_1^t, \ldots, x_n^t, y_1^t, \ldots, y_r^t), \quad j = 1, \ldots, r \tag{2}$$

$$y_j^{t+\Delta t_j} = Y_j^t, \quad j = 1, \ldots, r \tag{3}$$

where each z_i is referred to as an <u>output variable</u>, each x_i an <u>input variable</u>, each y_i a <u>secondary variable</u> and each Y_i an <u>excitation variable</u>. The combined values of $(x_1 \ldots, x_n)$ is called the circuit <u>input state</u>, of $(z_1, \ldots, z_m)$ the circuit <u>output state</u>, of $(y_1, \ldots, y_r)$ the circuit <u>secondary state</u>, and of $(Y_1, \ldots, Y_r)$ the circuit <u>excitation state</u>. The <u>total state</u> of the circuit is given by the values of $(x_1, \ldots, x_n, y_1, \ldots, y_r)$. Hence by (1) and (2), the output state and the excitation state at time t are each functions of the total state at time t. A circuit is in a <u>stable state</u> if $(y_1^t, \ldots, y_r^t) = (Y_1^t, \ldots, Y_r^t)$. If $(y_1^t, \ldots, y_r^t) \neq (Y_1^t, \ldots, Y_r^t)$, then the circuit is in an <u>unstable</u> or <u>transient</u> state.

For a given sequential circuit, there exists a minimum number of secondary variables necessary to represent the circuit by the Huffman model. A circuit model containing the minimum number of secondary variables will be referred to as the <u>basic asynchronous model</u> (BAM)

Figure 2 shows an asynchronous circuit with its corresponding BAM. The equations given by the BAM are as follows.

$$z_1 = x_1 \bar{x}_2 + x_1 y + \bar{x}_2 y$$

$$z_2 = \bar{x}_1 x_2 + \bar{y}$$

$$Y = z_1$$

$$y^{t+\Delta t} = Y^t$$
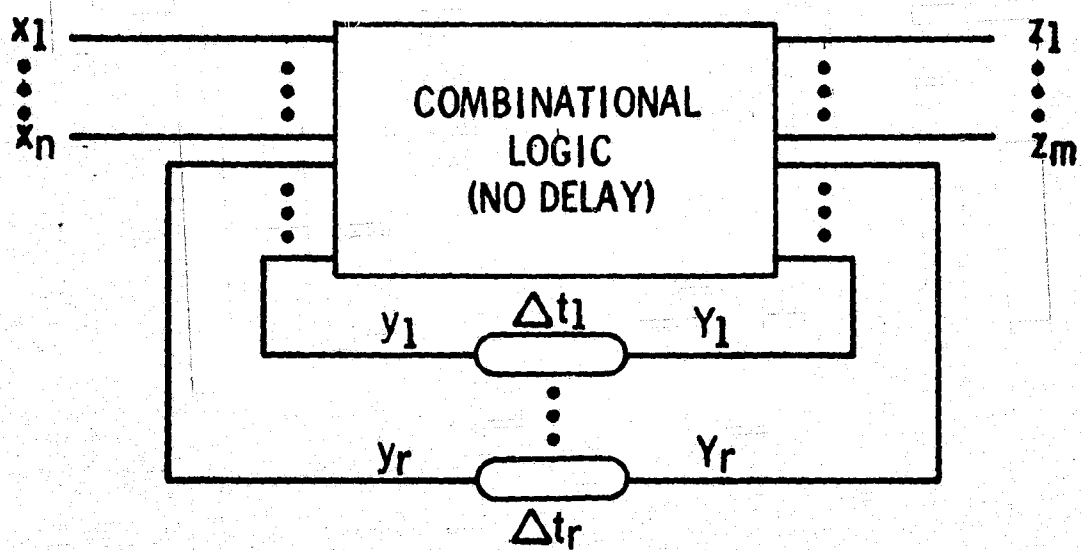
Figure 1. General Huffman model.
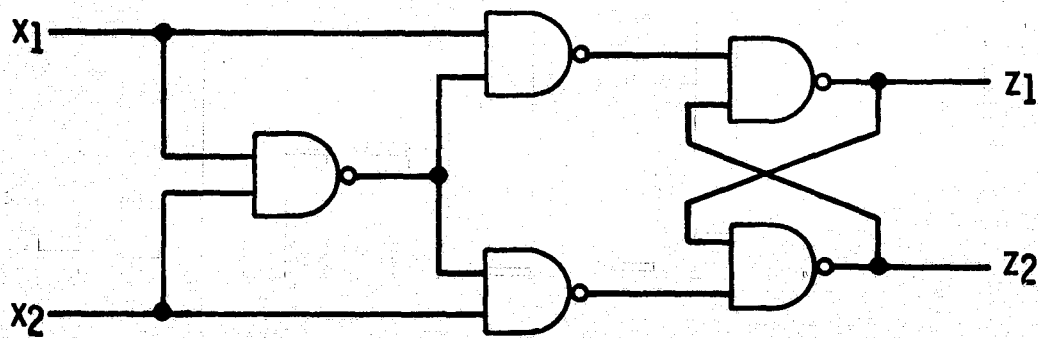
(a) Logic Diagram
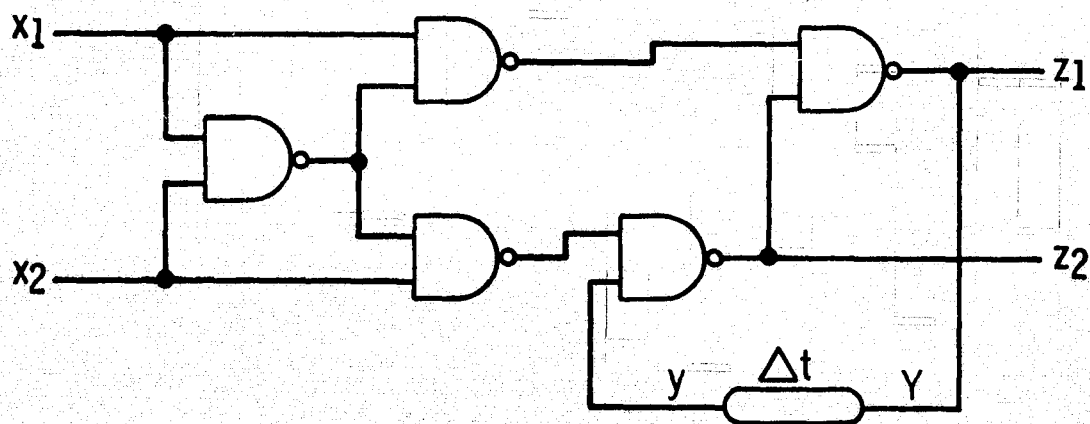
(b) Basic Asynchronous Model (BAM)

Figure 2. Basic Asynchronous Model Example

		$x_1 x_2$						$x_1 x_2$	
		00	01	11	10	00	01	11	10
y	0	⓪	⓪	⓪	1	01	01	01	11
	1	①	0	①	①	10	01	10	10
			Y					$z_1 z_2$	

Table 1. Flow table for Figure 2(b).

A tabular representation of the above set of equations is shown in Table 1. This table is called a _flow_ table or _excitation_ table. Stable states are circled.

The BAM of a given circuit is not necessarily unique. Figure 3 shows an alternate BAM for the circuit in Figure 2(a). A procedure for identifying a minimum set of secondary variables along with the resulting excitation and output equations is given in Pai and Lewin[1].

Problems Encountered with the BAM

The BAM does not always represent an adequate model for asynchronous circuits as will now be shown by two examples. An augmented model will then be described for overcoming these problems.

Consider the cross-coupled NAND latch and the corresponding BAM shown in Figure 4. When $x_1 = x_2 = 0$, it follows that $z_1 = z_2 = 1$ and that if this condition is held a sufficiently long time then the circuit reaches a stable state of $y = Y = 1$. Now if both inputs are simultaneously changed to 1 ($x_1 = x_2 = 1$), then, by the BAM, z_1 will remain unchanged while z_2 changes to 0. The circuit remains stable at $y=Y=1$ during this period. This sequence of events can easily be followed in Table 2.

An actual cross-coupled NAND latch may not respond as indicated in the above analysis. For example if the response time of the gate producing z_1 is faster than the gate producing z_2, then the $x_1 = x_2 = 0$ to $x_1 = x_2 = 1$ input change will produce a final output of $z_1 = 0$, $z_2 = 1$. The $z_1=1$, $z_2=0$, output will be produced when the z_1 gate is slower than the z_2 gate. When the gate delays are precisely the same, the $x_1=x_2=0$ to $x_1=x_2=1$ input change will produce an oscillating condition where the outputs alternate between the $z_1 = z_2 = 1$ and the $z_1 = z_2 = 0$ states until one or both inputs are changed to 0.

The above analysis of an actual cross-coupled NAND latch indicates that the behavior of the circuit to the input change from $x_1=x_2=0$ to $x_1=x_2=1$ is a function of the relative response times of the NAND gates. This fact is not evident in the BAM.

Explanation of the inadequacy of the BAM lies in the fact that all delays are assumed to be lumped in the feedback paths and that no delay is present in any gate. Hence, there is no way of taking into account relative gate delays but only relative loop delays in circuits with more than one feedback loop.

Input changes that produce a response dependent on relative
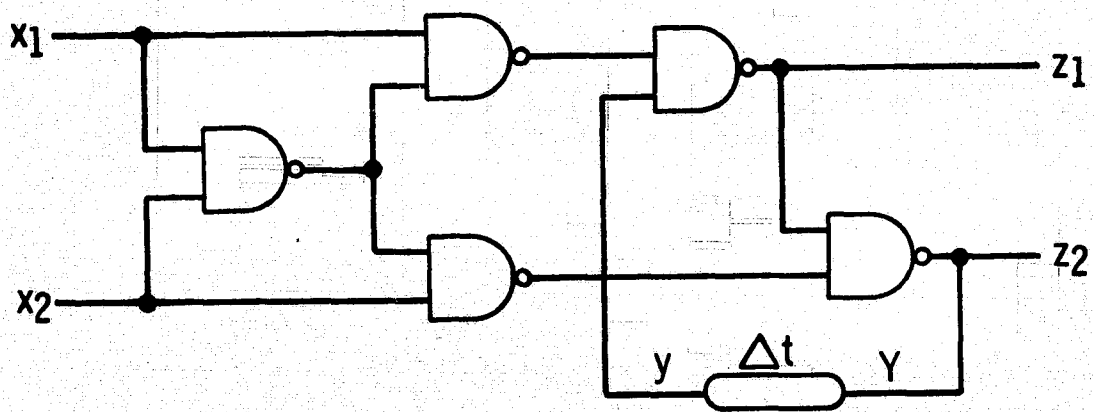
Figure 3. Alternate SAM for Figure 2(a).
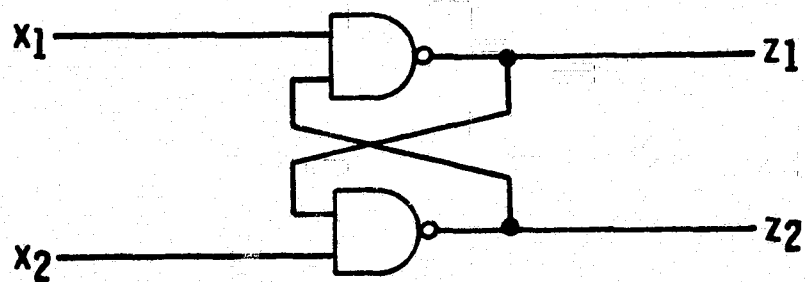
(a) Logic Diagram
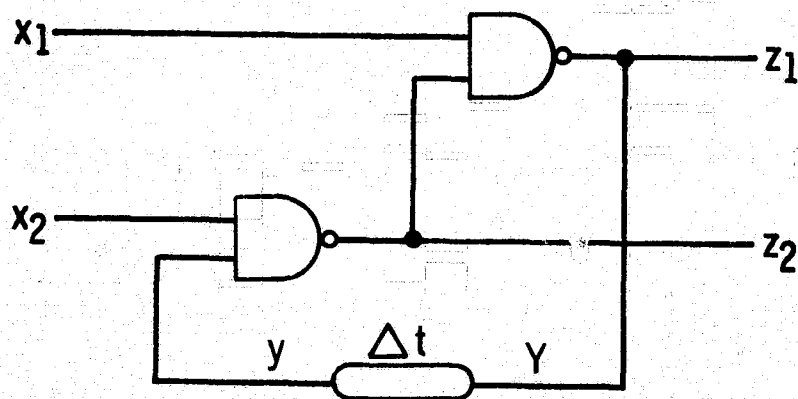
(b) RAM

Figure 4. Cross-coupled NAND Latch

		00	01	$x_1 x_2$ 11	10	00	01	$x_1 x_2$ 11	10
y	0	1	1	(0)	(0)	11	11	01	01
	1	(1)	(1)	(1)	0	11	10	10	01
				Y				$z_1 z_2$	

Table 2. Flow table for NAND latch RAM.

3-10

time delays should be avoided in general. Hence, a circuit model that will give an indication of such a condition is desirable. Augmentation of the NAND latch BAM as shown in Figure 5 will provide such a model. Table 3 gives the corresponding flow table.

The augmented BAM has been obtained by inserting a delay element and defining a secondary variable for each leg of cross-coupled latch. In essence, a discrete delay has been inserted for each gate in the circuit that may affect the response to input changes.

Analysis of the $x_1 = x_2 = 0$ to $x_1 = x_2 = 1$ input change using the augmented BAM shows an oscillation when both delays are the same. This oscillation can be taken as an indication of an input change that should be avoided.

Another shortcoming of the BAM can be illustrated using the circuit shown in Figure 6(a). This circuit has positive edge-sensitive inputs obtained by the utilization of the delay times of physical gates. Figure 6(b) shows the augmented BAM of the circuit, and Table 4 clearly shows the inadequacy of the model since no input change will cause a state change. Again this can be explained by recalling that gates are assumed to have zero delay in the model. Hence the output of gates G1 and G2 is always logic one for any value of x_1 and x_2.

In an actual circuit, however, gate delays will be present. Therefore, if x_1, is changed from $x_1 = 0$ to $x_1 = 1$, the output of G1 will momentarily change to 0 before stabilizing at 1. This follows since there is more delay along the path from x_1 through the inverter to G1 than from x_1 through a wire to G1. Hence when x_1 changes from 0 to 1, both inputs to G1 are 1 until the change propagates through the inverter placing a 0 on the lower G1 input. When the delay through the inverter is sufficiently long, a 0 to 1 change on x_1 will cause the latch to be set to the state $z_1 = 1$, $z_2 = 0$. Similarly, a 0 to 1 change on x_2 will place the latch in state $z_1 = 0$, $z_2 = 1$.

Figure 7 shows a further modification of the BAM that will properly represent the edge-sensitive nature of the circuit. The corresponding flow table is given in Table 5. It should be pointed out that this model gives the proper transitions only if $\Delta t_3 \geq 2\Delta t_1$, and $\Delta t_4 \geq 2\Delta t_2$. However, these relative delays must also be satisfied in the actual circuit. Hence the model does not impose any artificial constraints. An explicit representation of the criticality of the relative delay times is required by the procedures presented in later sections. This can be accomplished by inserting two delay elements in the appropriate paths as shown in Figure 8. The model shown in Figure 8 for the edge-sensitive latch is an example of the augmented asynchronous model (AAM) to be described in the following sections.
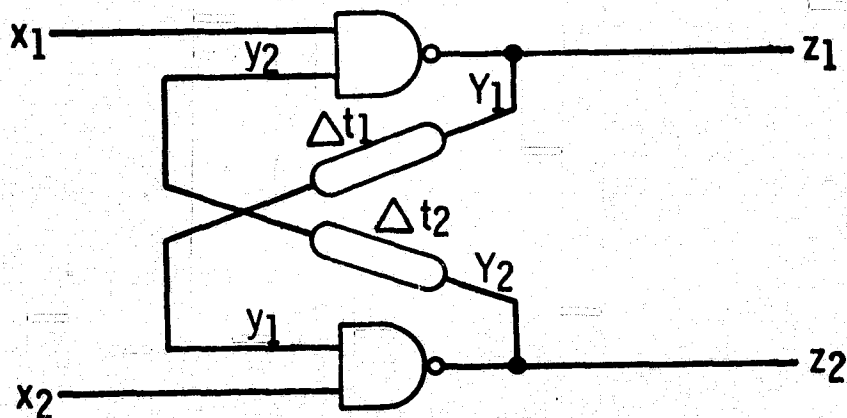
Figure 5. Augmented PAM for NAND Latch

Table 3. Flow table for NAND latch augmented PAM.
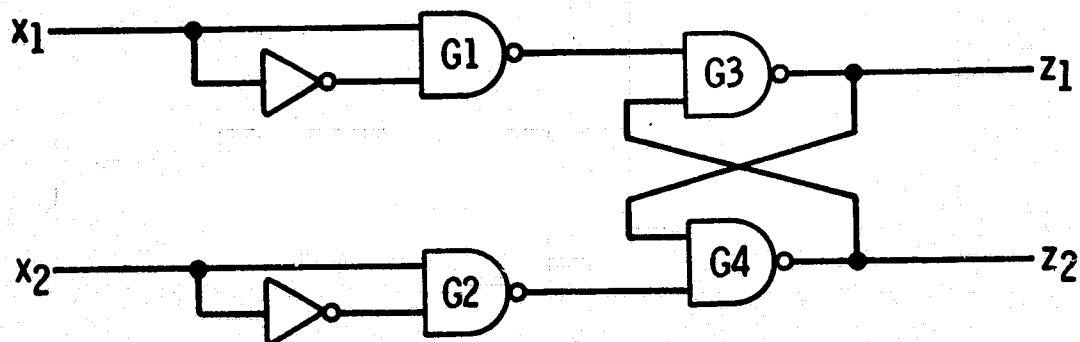
(a) Logic Diagram.
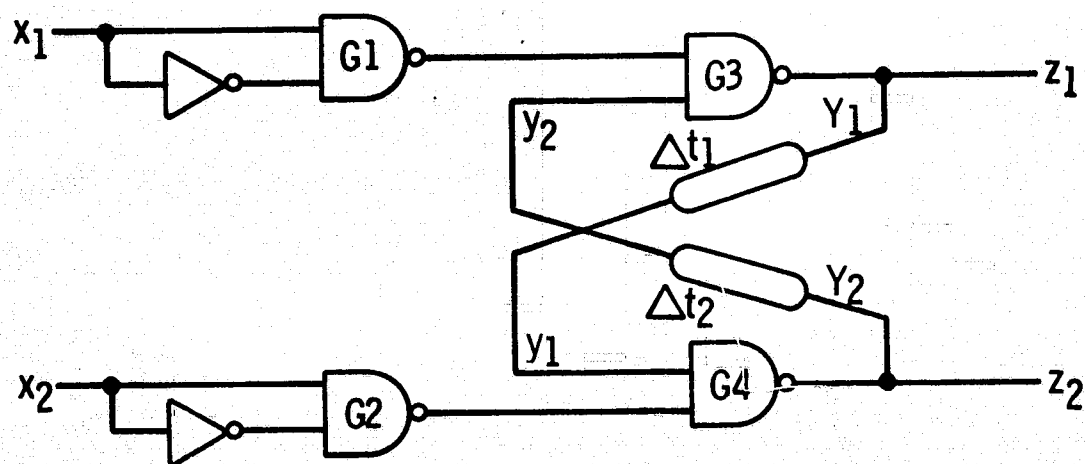
(b) Augmented RAM

Figure 6. Edge-sensitive NAND Latch

$$x_1 \; x_2$$

	00	01	11	10
00	11	11	11	11
01	⟨01⟩	⟨01⟩	⟨01⟩	⟨01⟩
11	00	00	00	00
10	⟨10⟩	⟨10⟩	⟨10⟩	⟨10⟩

$y_1 \; y_2$

$$Y_1 \; Y_2$$

Table 4. Flow table for augment BAM of edge-sensitive NAND latch.
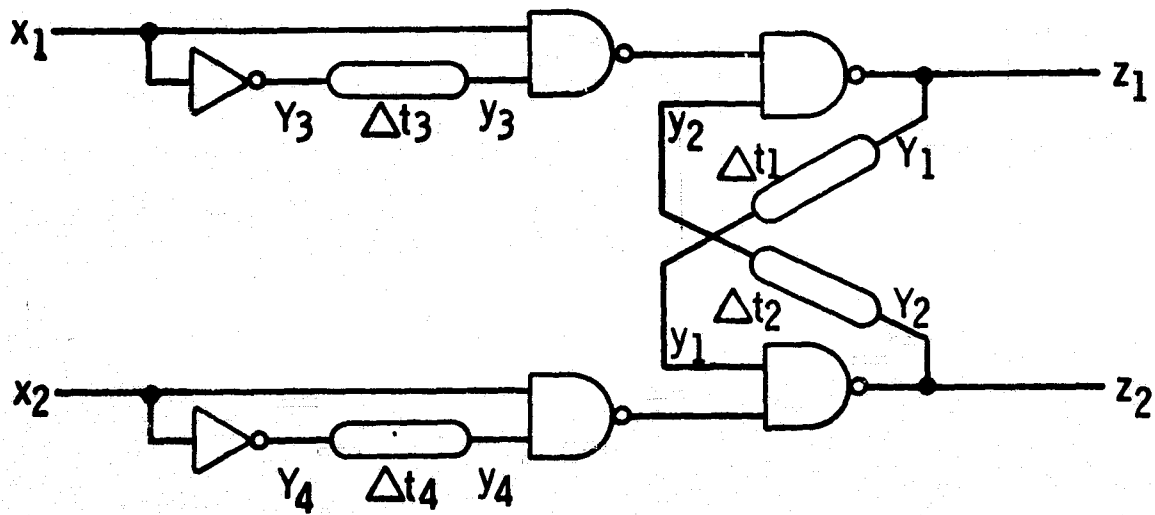
Figure 7. Augmented Asynchronous Model (AAM) for
Edge-sensitive NAND Latch
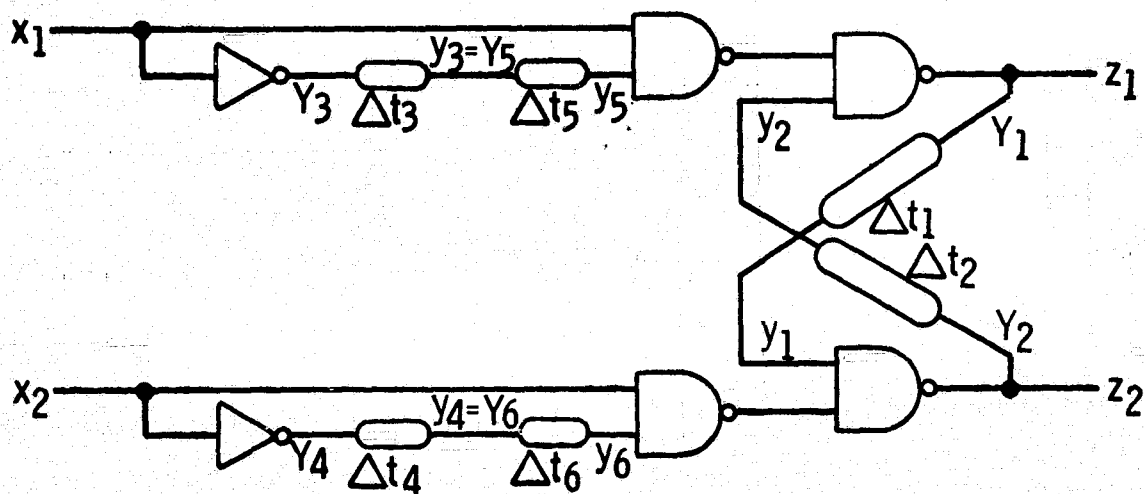
Figure 8. AAM for edge-sensitive Latch with Critical
Delays Inserted.

$$x_1 \; x_2$$

	00	01	11	10
0000	1111	1110	1100	1101
0001	1111	1110	1100	1101
0010	1111	1110	1100	1101
0011	1111	1110	1100	1101
0100	0111	0110	(0100)	0101
0101	0111	0110	0100	(0101)
0110	0111	(0110)	1100	1101
0111	(0111)	0110	1100	1101
1000	1011	1010	(1000)	1001
1001	1011	1110	1100	(1001)
1010	1011	(1010)	1000	1001
1011	(1011)	1110	1100	1001
1100	0011	0010	0000	0001
1101	0011	0110	0100	0001
1110	0011	0010	1000	1001
1111	0011	0110	1100	1001

The row labels on the left are $y_1 y_2 y_3 y_4$.

$$Y_1 \; Y_2 \; Y_3 \; Y_4$$

Table 5. Flow table for edge-sensitive latch.

Augmented Asynchronous Model (AAM)

The previous examples illustrate the importance of considering gate delay times in the analysis of asynchronous sequential logic circuits. TPG is a form of analysis and therefore a consideration of delay times is needed for this process. However, it is not necessary to consider all delays in many cases as seen in the earlier examples. The circuit model to be described in this section is a generalization of the model shown in Figure 8.

The Augmented Asynchronous Model (AAM) is obtained by inserting delays into the BAM to account for critical gate delays. A set of Boolean equations that represent the circuit consists of an output equation for each circuit output and an excitation equation for the input to each inserted delay element. These equations are written in terms of the circuit input variables and the secondary variables representing delay element outputs.

A model for a given circuit can be obtained from the following general procedure.

1. Identify all feedback paths and insert a delay element in each path.

2. Identify all reconvergent fan-out paths and insert delay elements to provide the proper relative path delays.

3. Insert delay elements as required for any critical delay values.

4. Assign a unique input variable to each circuit input.

5. Assign a unique output variable to each circuit output.

6. Assign a unique excitation variable to the input of each delay element and the corresponding secondary variable to each delay element output.

7. Generate a Boolean equation for each output variable and for each excitation variable in terms of only input and secondary variables.

The AAM of the circuit shown in Figure 9 (a) is given in Figure 9 (b). An algebraic description of the model is contained in the following set of Boolean equations.

$$z = Y_1 = \bar{x}_1 \ y_4 + y_4 \ \bar{y}_5$$

$$Y_2 = \bar{x}_1 \ \bar{y}_1 + \bar{x}_2 \ \bar{y}_1$$

$$Y_3 = \bar{y}_2$$

$$Y_4 = \bar{y}_3$$

$$Y_5 = \bar{y}_2$$

All steps of the procedure outlined above can be automated except for step 3. This poses no problem, however, since establishment of critical delay paths must be handled during design, and the insertion of delays into the AAM to reflect this can be specified in advance by the designer.
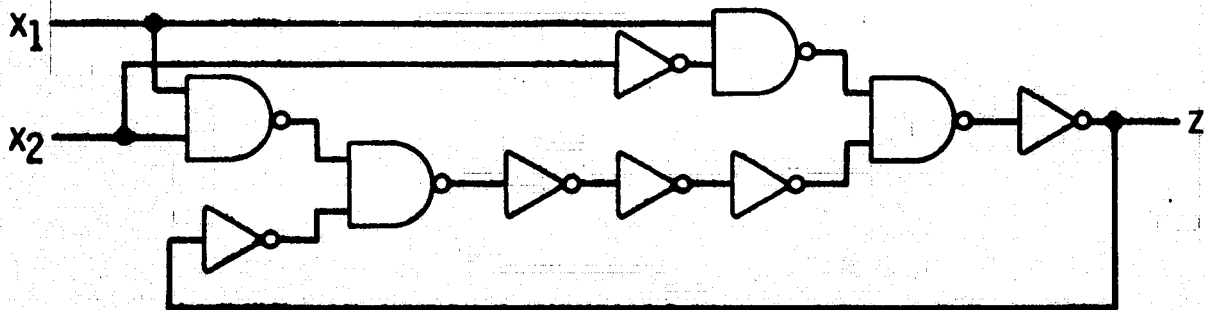
(a) Logic Diagram
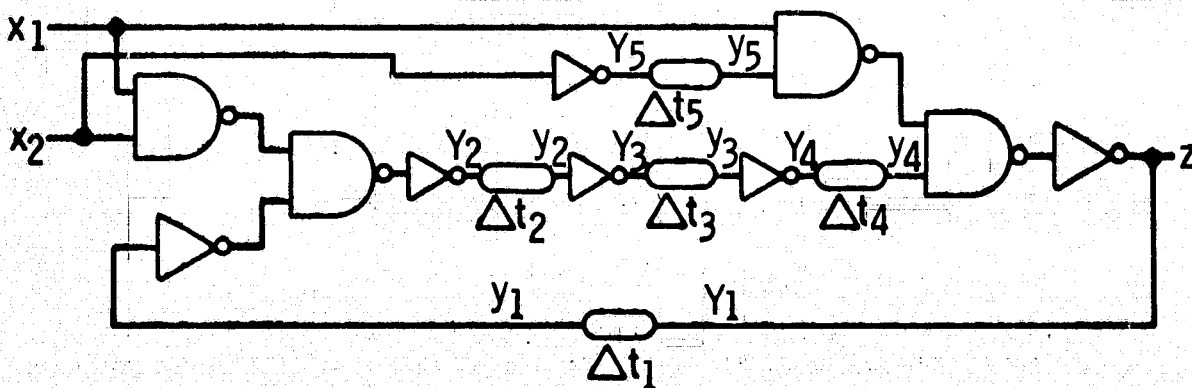
(b) AAM

Figure 9.   Example of Augmented Asynchronous Model.

HOMING SEQUENCE GENERATION

It is often necessary or desirable to place a sequential circuit in a specified stable secondary state from an unknown starting state by applying a sequence of input patterns. Such an input sequence is sometimes referred to as a "Homing" sequence. A procedure for determining a homing sequence for a given state of a circuit modelled using the AAM will be described in this section. The procedure is a generalization of an approach described by Chia and Hsiao [2].

Basic Approach

The procedure to be described is algebraic in nature using the equations that describe the AMM and their complements. First, the desired final state is used as a criteria to develop an equation that describes prior state conditions that will lead to the desired state. Next, one of the possible conditions is selected and the process repeated on the selected condition. The process is repeated until, finally a condition that is independent of any secondary state is found. Stability conditions are imposed at each step as discussed below. This procedure will be illustrated by example before a detail description is given.

The circuit shown in Figure 8 can be described by the following Boolean equations.

$$Y_1 = \bar{y}_2 + x_1 y_5 \qquad\qquad \overline{Y_1} = \bar{x}_1 y_2 + y_2 \bar{y}_5 \qquad (4a\text{-}b)$$

$$Y_2 = \bar{y}_1 + x_2 y_6 \qquad\qquad \overline{Y_2} = \bar{x}_2 y_1 + y_1 \bar{y}_6 \qquad (5a\text{-}b)$$

$$Y_3 = \bar{x}_1 \qquad\qquad\qquad \overline{Y_3} = x_1 \qquad\qquad\qquad (6a\text{-}b)$$

$$Y_4 = \bar{x}_2 \qquad\qquad\qquad \overline{Y_4} = x_2 \qquad\qquad\qquad (7a\text{-}b)$$

$$Y_5 = y_3 \qquad\qquad\qquad \overline{Y_5} = \bar{y}_3 \qquad\qquad\qquad (8a\text{-}b)$$

$$Y_6 = y_4 \qquad\qquad\qquad \overline{Y_6} = \bar{y}_4 \qquad\qquad\qquad (9a\text{-}b)$$

Complements of the secondary state equations are redundant but have been included because of their usefulness in the example that follows.

A homing sequence to place the circuit shown in Figure 8 in state $x_1 = 1$, $x_2 = 1$, $y_1 = 1$, $y_2 = 0$ will be developed. The equation $Y_1 \overline{Y}_2$ will yield conditions that produce the desired secondary state and is given below in an "input factor" form.

$$Y_1 \overline{Y}_2 = \bar{x}_1 \bar{x}_2 y_1 \bar{y}_2 + \bar{x}_1 x_2 y_1 \bar{y}_2 \bar{y}_6 + x_1 \bar{x}_2 (y_1 \bar{y}_2 + y_1 y_5)$$
$$+ x_1 x_2 (y_1 \bar{y}_2 \bar{y}_6 + y_1 y_5 \bar{y}_6)$$

The procedure is continued by selecting the term $x_1 x_2 (y_1 \bar{y}_2 \bar{y}_6 + y_1 y_5 \bar{y}_6)$ since the input state is the same as in the desired final state and since the secondary state is different than in the desired final state.

Stability of the selected terms is checked as follows.

$$x_1 \, x_2 (y_1 \bar{y}_2 \bar{y}_6 + y_1 y_5 \, \bar{y}_6) \, [Y_1 \bar{Y}_2 \bar{Y}_6 + Y_1 \, Y_5 \, \bar{Y}_6]$$

$$= x_1 x_2 \, (y_1 \bar{y}_2 \bar{y}_6 + y_1 y_5 y_6) \, [\bar{x}_1 \bar{x}_2 y_1 \bar{y}_2 \bar{y}_4 + \bar{x}_1 x_2 y_1 \bar{y}_2 \bar{y}_4 \bar{y}_6 + x_1 \bar{x}_2 y_1 \bar{y}_2 \bar{y}_4$$

$$+ x_1 \bar{x}_2 y_1 \bar{y}_4 y_5 + x_1 x_2 y_1 \bar{y}_2 \bar{y}_4 \bar{y}_6 + x_1 x_2 y_1 \bar{y}_4 y_5 \bar{y}_6 + \bar{y}_2 y_3 \bar{y}_4 + x_1 \, y_3 \bar{y}_4 y_5]$$

$$= x_1 x_2 \, (y_1 \bar{y}_2 \bar{y}_4 \bar{y}_6 + y_1 \bar{y}_4 y_5 \bar{y}_6)$$

Note that $\bar{y}_4$ was necessary to produce a stable condition on the selected term.

Next conditions that lead to $y_1 \bar{y}_2 \, \bar{y}_4 \bar{y}_6 + y_1 \bar{y}_4 y_5 \bar{y}_6$ are computed as follows.

$$Y_1 \bar{Y}_4 \bar{Y}_6 \, (\bar{Y}_2 + Y_5) = \bar{x}_1 x_2 \, (y_1 \bar{y}_2 \bar{y}_4 \bar{y}_6 + \bar{y}_2 y_3 \bar{y}_4)$$

$$+ x_1 x_2 (y_1 \bar{y}_2 \bar{y}_4 \bar{y}_6 + \bar{y}_2 y_3 \bar{y}_4 + y_1 \bar{y}_4 y_5 \bar{y}_6 + y_3 \bar{y}_4 y_5)$$

The second term is again selected since the input state is the same as in the previous step but the secondary state is different. After factoring, stability is checked as follows.

$$x_1 x_2 \bar{y}_4 (\bar{y}_2 + y_5) \, (y_1 \bar{y}_6 + y_3) [\bar{Y}_4 \, (\bar{Y}_2 + Y_5) \, (Y_1 \bar{Y}_6 + Y_3)]$$

$$= x_1 x_2 \bar{y}_4 \, (\bar{y}_2 + y_5) \, (y_1 \bar{y}_6 + y_3)$$

Hence all terms are stable.

Conditions producing the chosen secondary state are given by the following equation.

$$\bar{Y}_4 (\bar{Y}_2 + Y_5) \, (Y_1 \bar{Y}_6 + Y_3) = \bar{x}_1 x_2 (y_1 \bar{y}_6 + y_3)$$

$$+ x_1 x_2 (y_1 \bar{y}_2 \bar{y}_4 \bar{y}_6 + y_1 \bar{y}_4 y_5 \bar{y}_6$$

$$+ \bar{y}_2 y_3 \bar{y}_4 + y_3 \bar{y}_4 \, y_5)$$

The first term in the above equation is selected to continue the procedure because the second term is a repeat of the previously selected term.

The selected term is checked for stability and found to be stable.

$$\bar{x}_1 x_2 (y_1 \bar{y}_6 + y_3) \left[Y_1 \bar{Y}_6 + Y_3 \right] = \bar{x}_1 x_2 (y_1 \bar{y}_6 + y_3)$$

Computation of the new state requirements produces the following equation.

$$Y_1 \bar{Y}_6 + Y_3 = \bar{y}_2 \bar{y}_4 + x_1 \bar{y}_4 y_5 + \bar{x}_1$$

The above equation contains a term that is independent of any secondary variables. Hence, this term is selected and the procedure is terminated.

Input states of the terms selected, correspond to the input patterns in the homing sequence. Recalling that terms are selected backward in time, the homing sequence produced is $x_1 = 0$ followed by $x_1 = 0$, $x_2 = 1$ followed by $x_1 = x_2 = 1$. Hence $00 \rightarrow 01 \rightarrow 11$ or $01 \rightarrow 11$ are acceptable homing sequences. It should be noted that other input sequences are also homing sequences. These can be obtained by starting with a different term in the first equation produced in the procedure.

Detailed Description

A step-by-step description of the procedure illustrated in the previous section will now be presented.

    1. Obtain the state condition desired.

    2. Check stability of the given state condition.

    3. Is the state stable? if no, terminate. If yes, continue.

    4. Select a stable state (S_o) consistent with the given state.

    5. Let $i=0$.

    6. Compute the S_i predecessor equation (P_i).

    7. Express P_i as a sum of prime implicants.

    8. Does P_i have a prime implicant containing only input variables? If yes, go to step 29, if no, continue.

    9. Express P_i in input state factored form.

    10. Does P_i contain a term with an input state the same as in S_i? If yes, continue. If no, go to step 12.

    11. Let T_i represent the term of P_i. Is the secondary state

factor of T_i the same as the secondary state factor of S_i? If yes, continue. If no, go to step 13.

12. Does P_i contain a term whose input state differs from the input state of S_i in only one variable? If yes, call this term T_i and continue. If no, go to step 25.

13. Has T_i been selected previously? If no, continue. If yes, go to step 22.

14. Check the stability of T_i.

15. Is T_i stable? If yes, continue. If no, go to step 22.

16. Record the input state of T_i as term i of the homing sequence.

17. Does i exceed max (i)? If no, continue. If yes, go to step 21.

18. Let $S_{i+1} = T_i$.

19. Let $i = i + 1$.

20. Go to step 6.

21. Homing sequence exceeds the maximum specified length. Terminate.

22. Does P_i contain other terms whose input state differs from the input state of S_i in only one variable? If yes, select this term, call it T_i', and continue. If no, go to step 25.

23. Let $T_i = T_i'$.

24. Go to step 13.

25. Does i=0? If no, continue. If yes, go to step 28.

26. Let $i = i - 1$.

27. Go to step 22.

28. No homing sequence exists that satisfies the single input change criteria.

29. Select a secondary state independent prime implicant as term i of the homing sequence and terminate the procedure.

This concludes the discussion of homing sequence generation. Attention will now be focused on TPG procedures.

TEST PATTERN GENERATION PROCEDURE

A TPG procedure that follows from the homing sequence generation procedure will now be described. The procedure guarantees that a stable state is reached for each input pattern in the test sequence. This is consistent with a commonly used testing philosophy where only static output conditions are considered significant during test. In other words, momentary output changes such as spikes or dips are ignored during tests and are therefore not considered during TPG. This static testing philosophy may not always be justified since it can be envisioned that faults causing only transient errors can occur [3]. However, faults of this type are considered rare and are not investigated here.

The TPG procedure given below will yield one test pattern sequence for a specified fault. When complete fault coverage is desired, the following approach is recommended for TPG rather than applying the TPG procedure for each fault class.

    1. Generate the test pattern sequences for stuck-at-0 and stuck-at-1 faults on each circuit input line using the TPG procedure.

    2. Use a fault simulator to determine all faults that would be detected by the sequences obtained in step 1.

    3. Identify all faults not covered.

    4. Generate test pattern sequences using the TPG procedure for each fault identified in step 3.

BASIC APPROACH

The TPG procedure will now be illustrated by a specific example in this section and with a step-by-step outline given in the following section.

Consider the circuit shown in Figure 8. Equations (4) through (9) describe the circuit for the fault-free case. The following set of equations represent the circuit when a stuck-at-0 fault is present at Y_3.

$$Y_1^* = \bar{y}_2^* + x_1 y_5^* \qquad\qquad \bar{Y}_1^* = \bar{x}_1 y_2^* + y_2^* \bar{y}_5^* \qquad (10\ a\text{-}b)$$

$$Y_2^* = \bar{y}_1^* + x_2 y_6^* \qquad\qquad \bar{Y}_2^* = \bar{x}_2 y_1^* + y_1^* y_6^* \qquad (11\ a\text{-}b)$$

$$Y_3^* = 0 \qquad\qquad\qquad\qquad \bar{Y}_3^* = 1 \qquad\qquad\qquad (12a\text{-}b)$$

$$Y^*_4 = \bar{x}_2 \qquad\qquad \bar{Y}^*_4 = x_2 \qquad\qquad \text{(13 a-b)}$$

$$Y^*_5 = y^*_3 \qquad\qquad \bar{Y}^*_5 = \bar{y}^*_3 \qquad\qquad \text{(14 a-b)}$$

$$Y^*_6 = y^*_4 \qquad\qquad \bar{Y}^*_6 = \bar{y}^*_4 \qquad\qquad \text{(15 a-b)}$$

It should be noted that no distinction is made between input variables for the fault-free circuit and for the faulty circuit. This is done because input values are fault independent and can be the same for both fault-free and faulty circuits. On the other hand, secondary and excitation variables are fault dependent. Hence , a distinction is made between fault-free and faulty circuits for these variables. Also note that in the following example, Y_1 is assumed to be the only circuit output.

An input sequence is a test sequence for a given fault if and only if the output sequence produced in response to the input sequence is a function of the presence of the fault. Conditions that yield such a result are given by the following expression for the example.

$$Y_1 \oplus Y^*_1 = x_1(\bar{y}_2\, y^*_2\, \bar{y}^*_5 + y_2\bar{y}^*_2\, \bar{y}_5 + y^*_2\, y_5\bar{y}^*_5 + y_2 y^*_5\, \bar{y}_5)$$
$$+\bar{x}_1\, (\bar{y}_2 y^*_2 + y_2\bar{y}^*_2)$$

One term in the above expression is chosen and new requirements are computed. The first term implies $x_1 = 1$ and the following (only the term to be selected in succeeding steps is shown).

$$\bar{Y}_2 Y^*_2 \bar{Y}^*_5 + Y_2\bar{Y}^*_2 Y_5 + Y^*_2 Y_5\bar{Y}^*_5 + Y_2 Y^*_5 \bar{Y}_5$$
$$= \bar{x}_2\, \bar{y}^*_1\bar{y}^*_3(y_1+y_3) + \bar{y}_1\bar{y}_3\, (y^*_1+y^*_3)+\ldots$$

Requirements given above are $x_2 = 0$ and the following.

$$\bar{Y}^*_1\bar{Y}^*_3\, (\bar{Y}_1\, \bar{Y}_3\, (Y^*_1 + Y^*_3) = \bar{x}_1\, y^*_2 + \ldots$$

New requirements are $x_1 = 0$ and those given by the following equation.

$$Y^*_2 = \bar{y}^*_1 = x_2 y^*_6 = \bar{y}^*_1 + x_2\, (\bar{y}^*_1 + y^*_6)$$

The second term in the above equation is chosen implying $x_2 = 1$ and the following.

$$\bar{Y}^*_1 + Y_6 = \bar{x}_1\, (y^*_2 + y^*_4) + y^*_2\bar{y}^*_5 + y^*_4$$

Selecting the first term of the above equation produces $x_1 = 0$ and the following.

$$Y^*_2 + Y^*_4 = \bar{y}^*_1 + y^*_6 + \bar{x}_2$$

A term in the above equation is secondary variable independent and is therefore chosen which yields $x_2 = 0$. The process is thus complete.

Recalling that the above procedure is worked backward in time, the test sequence produced is $x_1 x_2$: $\_0 \rightarrow 0 \_ \rightarrow \_1 \rightarrow 0 \_ \rightarrow \_0 \rightarrow 1 \_$.

Careful assignment of the don't care conditions yields the test sequence $x_1 x_2$: $00 \rightarrow 01 \rightarrow 00 \rightarrow 10$ which can easily be verified as a valid test for the fault under consideration.

It should be mentioned that stability conditions were not imposed in the process illustrated above. This was done because of the complex computations involved. Further study of a means to impose stability constraints is clearly indicated.

DETAILED DESCRIPTION

Let C represent the set of equations describing a fault free sequential circuit, and let C* represent the set of equations that represent the same circuit with a specified fault. Let Z and Z* represent subsets of C and C*, respectively, that contain circuit output equations. A test sequence for a specified fault is computed as follows.

1. Compute $P = (z_1 \oplus z^*_1) + (z_2 \oplus z^*_2) + \ldots + (z_m \oplus z^*_m)$

where $z_i \in Z$, $z^*_i \in Z^*$, $i = 1, \ldots, m$.

2. Express P_o as a sum of prime implicants.

3. Does P_o have a prime implicant containing only input variables? If yes go to step 33. If no, continue.

4. Express P_o in input factor form.

5. Select a term (S_1) from P_o.

6. Is S_1 stable? If yes, go to step 9. If no, continue.

7. Does P_o have unselected terms? If yes, continue. If no, go to step 32.

8. Select a new S_1 and go to step 6.

9. Let $i = 1$.

10. Compute the S_i predecessor equation (P_i).

11. Express P_i as a sum of prime implicants.

12. Does P_i have a prime implicant containing only input variables? If yes, go to step 33. if no, continue.

13. Express P_i in input state factored form.

14. Does P_i contain a term with an input state the same as in S_i? If yes, continue. If no, go to step 16.

15. Let T_i represent the term of P_i. Is the secondary state factor of T_i the same as the secondary state factor of S_i? If yes, continue. If no, go to step 17.

16. Does P_i contain a term whose input state differs from the input state of S_i in only one variable? If yes, call this term T_i and continue. If no, go to step 29.

17. Has T_i been selected previously? If no, continue. If yes, go to step 26.

18. Check the stability of T_i.

19. Is T_i stable? If yes, continue. If no, go to step 26.

20. Record the input state of T_i as term i of the homing sequence.

21. Does i exceed max (i)? If no, continue. If yes, go to step 25.

22. Let $S_{i+1} = T_i$.

23. Let i=i+1.

24. Go to step 10.

25. Test sequence exceeds the maximum specified length. Terminate.

26. Does P_i contain other terms whose input state differs from the input state of S_i in only one variable? If yes, select this term, call it T_i', and continue. If no, go to step 29.

27. Let $T_i = T_i'$.

28. Go to step 17.

29. Does i=0? If no, continue. If yes, go to step 7.

30. Let i = i-1.

31. Go to step 26.

32. No test sequence exists that satisfies the single input change criteria.

33. Select a secondary state independent prime implicant as term i of the test sequence and terminate the procedure.

TPG algorithms that differ significantly in approach to the above are described in references [4], [5], and [6].

CONCLUSION

The concepts described above represent reasonable approaches to the problem of TPG for asynchronous sequential logic circuits. However, further study is needed to fully develop and evaluate the ideas presented.

In particular, the circuit model should be evaluated for validity for numerous physical examples and for practicality in terms of computer storage requirements and processing time. Methods of implementing the homing sequence and TPG algorithms must be developed and the algorithms programmed. The algorithms should then be evaluated for validity of the sequences generated and for computer memory and processing time requirements.

REFERENCES

1. D. Pai and D. Lewin, "Analysis of Sequential Logic Circuits," The Computer Journal, vol. 17, no. 1, pp. 64-68.

2. D.K. Chia and M.Y. Hsiao, "A Homing Sequence Generation Algorithms for Fault Detection in Asynchronous Sequential Circuits," Proceedings of the 1972 Fault Tolerant Computing Symposium, pp. 137-142.

3. M.A. Breuer, "The Effect of Races, Delays, and Delay Faults on Test Generation," IEEE Computer Society Repository, No. R73-290.

4. M.Y. Hsiao and D.K. Chia, "Boolean Difference for Fault Detection in Asynchronous Sequential Machines," IEEE Transactions on Computers, vol. C-20, no. 11, November 1971, pp. 1356-1361.

5. G.R. Putzolu and J.P. Roth, "An Algorithm and a Program for Generation of Test Patterns for Sequential Circuits," Proceedings of Third Hawaii International Conference on Systems Science, Jan. 1970, pp. 64-67.

6. W.G. Bouricius, et.al., "Algorithms for Detection of Faults in Logic Circuits," IEEE Transactions on Computers, vol. C-20, no. 11, November 1971, pp. 1258-1264.

1974

ASEE - NASA SUMMER FACULTY FELLOWSHIP PROGRAM

MARSHALL SPACE FLIGHT CENTER

(AUBURN UNIVERSITY - UNIVERSITY OF ALABAMA)

STRESS INTENSITY FACTORS

BY THE FINITE ELEMENT METHOD

Prepared by: Joseph C. Conway, Phd.

Academic Rank: Associate Professor

Department and University: Department of Engineering Science
                                      and Mechanics
                                      Pennsylvania State University

NASA/MSFC Assignment:
    (Laboratory)   Structures and Propulsion
    (Division)   Engineering Analysis
    (Branch)   Strength Analysis

NASA Research Colleague: J. E. Key

DATE: August 9, 1974

Contract No.:   NGT-01-003-045

STRESS INTENSITY FACTORS BY THE FINITE ELEMENT METHOD

By

Joseph C. Conway

ABSTRACT

The usefulness of the displacement and J-integral methods for the computation of extensional stress intensity factor K_I for cracks approaching material and geometric singularities is established. Selected singularities investigated are a colinear crack, a circular penetration, and a notched circular penetration. Stress intensity factors numerically generated for each case compare favorably to those experimentally obtained in a photoelastic investigation.

Results indicate that the magnitude of the stress intensity factor is strongly influenced by the geometry of the singularity. A maximum stress intensity factor is obtained for a crack approaching a colinear crack. The stress intensity factor is reduced by approximately 10 percent for a crack approaching a notched circular penetration and by approximately 20 percent for a crack approaching a circular penetration indicating a substantial strength increase for a given critical extensional stress intensity factor K_{IC}.

ACKNOWLEDGEMENTS

LIST OF FIGURES

LIST OF TABLES

NOMENCLATURE

E = modulus of elasticity (psi)

G = shear modulus (psi)

ν = Poisson's ratio

w = width of rectangular plate (in.)

h = height of rectangular plate (in.)

t = thickness of rectangular plate (in.)

a = crack length (in.)

b = distance from crack tip to singularity (in.)

c = length of notch (in.)

d = diameter of circular penetration (in.)

x,y = Cartesian coordinates at crack tip

u = displacement in x-direction (in.)

v = displacement in y-direction (in.)

θ = angle from x-axis to radius vector (deg.)

r = radius vector from crack tip (in.)

K_I = extensional stress intensity factor (psi $\sqrt{in.}$)

K_{IC} = critical extensional stress intensity (psi $\sqrt{in.}$)

J = path independent integral

Γ = circular path around crack tip

Γ^* = complementary path around boundary of plate

W = strain energy density $\frac{(in.-lb.)}{in^3}$

σ = uniaxial tensile stress applied to crack axis (psi)

τ = maximum shear stress (psi)

$\vec{T}$ = traction vector

$\vec{u}$ = displacement vector

N = photoelastic fringe order (order)

f_σ = stress fringe coefficient (psi/order/in.)

INTRODUCTION

Accelerated use of high-strength metallic, composite and brittle materials in engineering structures has focused increased interest on problems in the area of fracture mechanics. Many of these materials do not obey classical theories of failure based on computed strain or stress levels, but fracture catastrophically when subjected to critical static, cyclic or thermal loading. Fracture, in most cases, is initiated at geometric or material singularities such as notches, reentrant corners, crack tips, voids, and inclusions. Prediction of fracture initiation at a given singularity is complicated by the fact that extremely high strain and stress gradients exist at such a point. Critical strain and stress levels at the singularity may, therefore, not be accurately determined, and fracture criteria based on these parameters are not applicable.

Recent investigations in the area of fracture mechanics have utilized an indirect approach to assess the effect of geometric or material singularities on the strength of a material or structure. The approach consists of defining a parameter which reflects the redistribution of stress and energy levels in a body caused by the introduction of a singularity and to indicate the type and magnitude of force transmission through the body. These parameters, K_I, K_{II}, and K_{III} are defined as stress intensity factors for extensional, inplane shear, and antiplane shear loading. They may be used to generate strain, stress, or displacement fields surrounding a given singularity and to predict fracture initiation in a material or structure. Fracture is initiated when the magnitude of the stress intensity reaches a critical value, the critical stress intensity factor K_{IC}, whose magnitude is determined by specimen testing.

In the engineering application of the concepts of linear fracture mechanics to the prediction of strength and life of structures, a knowledge of the crack tip stress intensity factor as a function of applied load and geometry of the structure is necessary. This information, when combined with the experimentally determined critical stress intensity factor for the structural material, make such predictions possible. Existing theoretical stress intensity factors are the product of highly sophisticated mathematical analyses for idealized model configurations and loading conditions (1,2). These are very valuable for limited geometries and loading conditions but are impossible to apply in many real situations.

For real situations involving complex geometric and loading conditions, the need for relatively straight forward numerical and experimental methods is apparent in order to accurately estimate stress intensity factors. Two numerical methods are currently finding wide

application, the displacement method and the J-integral method (3,4).
Both methods rely on finite element techniques, as the necessary para-
meters are easily generated for a wide range of geometries, materials,
and loading conditions. Stress intensity factors can be experimentally
generated by using interferrometric or photoelastic techniques. Photo-
elastic techniques are most easily applied to two-dimensional problems
and relate the stress intensity factor to shear stress distribution at
the crack tip (5).

The numerical and experimental techniques cited above also allow
the inclusion of material and geometric singularities which strongly
influence the fracture mechanism. This influence is here examined
for simplified geometry and loading conditions. Crack tip stress
intensity factors are generated for a crack approaching a colinear
crack, a circular penetration, and a notched circular penetration in a
rectangular plate.

OBJECTIVE AND SCOPE

The objective of this investigation was to apply two recent numer-
ical approaches for the generation of stress intensity factors to the
problem of a crack approaching a geometric or material singularity and
to determine the effect of selected singularities on the magnitude of
the crack tip stress intensity factor. Numerical approaches applied
were the displacement method which is based on geometry changes of
the crack configuration and the path independent integral concept which
considers variations in strain energy density along a path surrounding
the crack tip. Singularities investigated consisted of a colinear
crack tip, a circular penetration, and a notched circular penetration.
Results for each case investigated were compared to those experimental-
ly determined from a photoelastic analysis.

NUMERICAL AND EXPERIMENTAL MODEL

The configuration and dimensions of the model used in the numeri-
cal and experimental investigation can be seen in figure 1. It con-
sists essentially of a doubly-cracked rectangular plate with inclusions
introduced on the vertical centerline between the crack tips. Three
cases involving selected inclusions were investigated: colinear cracks
approaching each other, colinear cracks approaching a circular penetra-
tion, and colinear cracks approaching a notched circular penetration.
The plate was subjected to a uniform tensile stress of 100 psi so that
only the extensional stress intensity factor K_I was generated and
conditions of generalized plane stress were assumed.

For the numerical investigation, the plate material was assumed
as 6061-T6 aluminum having a Young's modulus of 10×10^6 psi and a
Poisson's ratio of 0.33. In the photoelastic investigation, the exper-
imental plates were constructed from PS-5 photoelastic plastic. The
cracks were sawed to within 50 percent of final length and then fatig-
ued to final length.
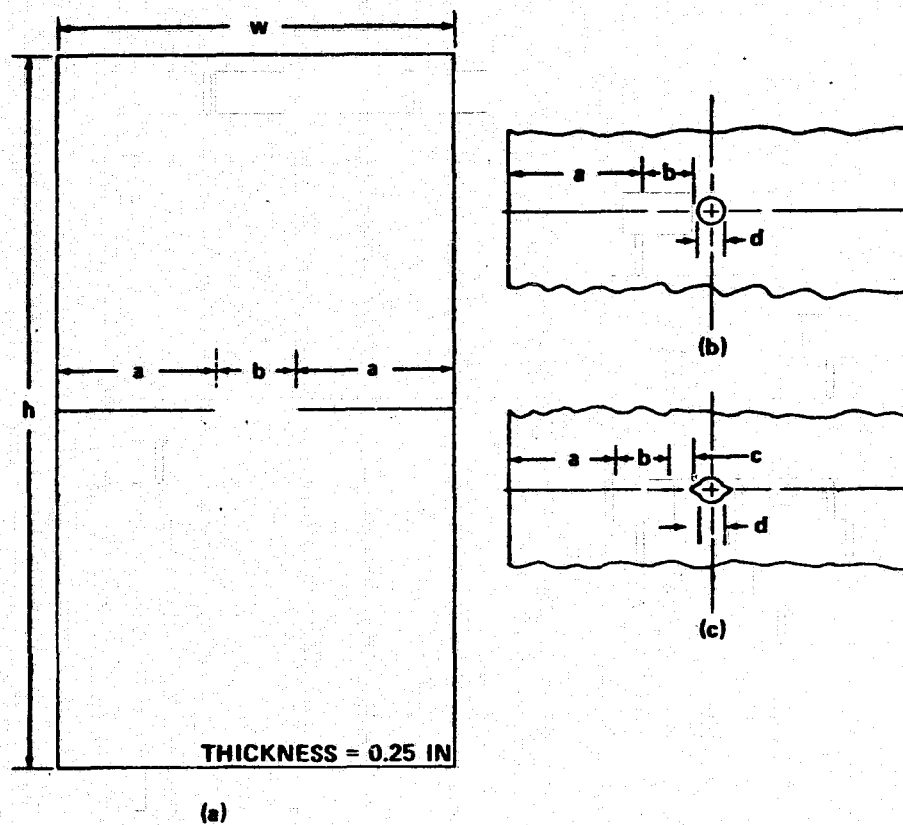
CASE	b/a	b IN	a IN	w IN	h IN	d IN	c IN
1	0.125	0.280	2.235	4.750	10.0		
	0.250	0.528	2.111				
	0.500	0.950	1.900				
	1.000	1.584	1.583				
2	0.125	0.250	2.000	4.750	10.0	0.250	
	0.250	0.457	1.800				
	0.500	0.750	1.500				
	1.000	1.125	1.125				
3	0.125	0.250	2.000	5.000	10.0	0.250	0.125
	0.250	0.457	1.800				
	0.500	0.750	1.500				
	1.000	1.125	1.125				

Figure 1 Plate Model :(a) Case 1, (b) Case 2, (c) Case 3 And (d) Dimensions

NUMERICAL PROCEDURE

The extensional stress intensity factor K_I was generated for each case investigated by utilizing both the displacement and J-integral methods and standard finite element techniques (6). The displacement method is based on the well known crack tip displacement equations for generalized plane stress (1). Referring to figure 2:

$$u = \frac{K_I}{G}\left(\frac{r}{2\pi}\right)^{1/2} \cos\frac{\theta}{2}\left[\frac{1-\nu}{1+\nu} + \sin^2\frac{\theta}{2}\right]$$
$$+ \frac{K_{II}}{G}\left(\frac{r}{2\pi}\right)^{1/2} \sin\frac{\theta}{2}\left[\frac{2}{1+\nu} + \cos^2\frac{\theta}{2}\right]$$
$$\nu = \frac{K_I}{G}\left(\frac{r}{2\pi}\right)^{1/2} \sin\frac{\theta}{2}\left[\frac{2}{1+\nu} - \cos^2\frac{\theta}{2}\right]$$
$$+ \frac{K_{II}}{G}\left(\frac{r}{2\pi}\right)^{1/2} \cos\frac{\theta}{2}\left[\frac{\nu-1}{1+\nu} + \sin^2\frac{\theta}{2}\right]$$

(1)

Along the free flank of the crack ($\theta = \pi$), the displacement functions reduce to:

$$u = \frac{K_{II}}{E}\left(\frac{x}{2\pi}\right)^{1/2}$$
$$\nu = \frac{K_I}{E}\left(\frac{x}{2\pi}\right)^{1/2}$$

(3)

Assuming a crack length a and discretizing equations 3, we obtain:

$$\frac{u_i/a}{\sqrt{x_i/a}} = \frac{K_{II}}{E}\left(\frac{8}{\pi a}\right)^{1/2}$$

$$\frac{\nu_i/a}{\sqrt{x_i/a}} = \frac{K_I}{E}\left(\frac{8}{\pi a}\right)^{1/2}$$

(4)

By matching equations 4 to the nodal displacements along the crack flank resulting from a finite element solution, we obtain the desired stress intensity factors. The technique is applied by plotting the left sides of equations 4 as a function of distance from the crack tip and extrapolating the resultant slope to $r \rightarrow 0$ as shown in figure 3.

A typical finite element discretization of a quarter plate section of the model considered in this investigation is shown in figure 4. Case 3 is pictured with the crack approaching a circular penetration and b/a = 0.125. As the precision of this method depends on the density and arrangement of the nodes along the crack flank, a high nodal density was utilized in this region, and the density was gradually reduced at increased distance from the crack flank. Nodal density was
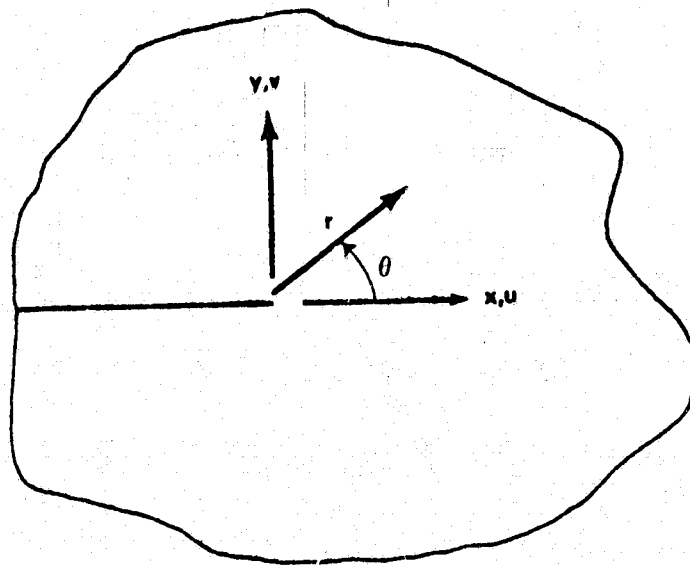
Figure 2   Coordinate Axes At Crack Tip
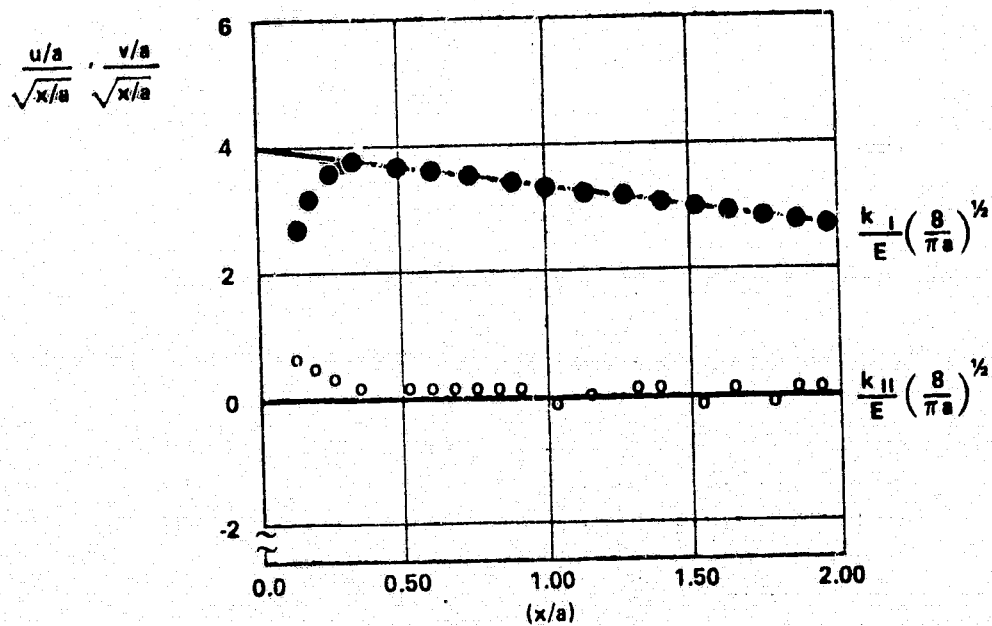
Figure 3   Graphical Solution For Stress Intensity
Factors By Displacement Method.

CRACK TIP
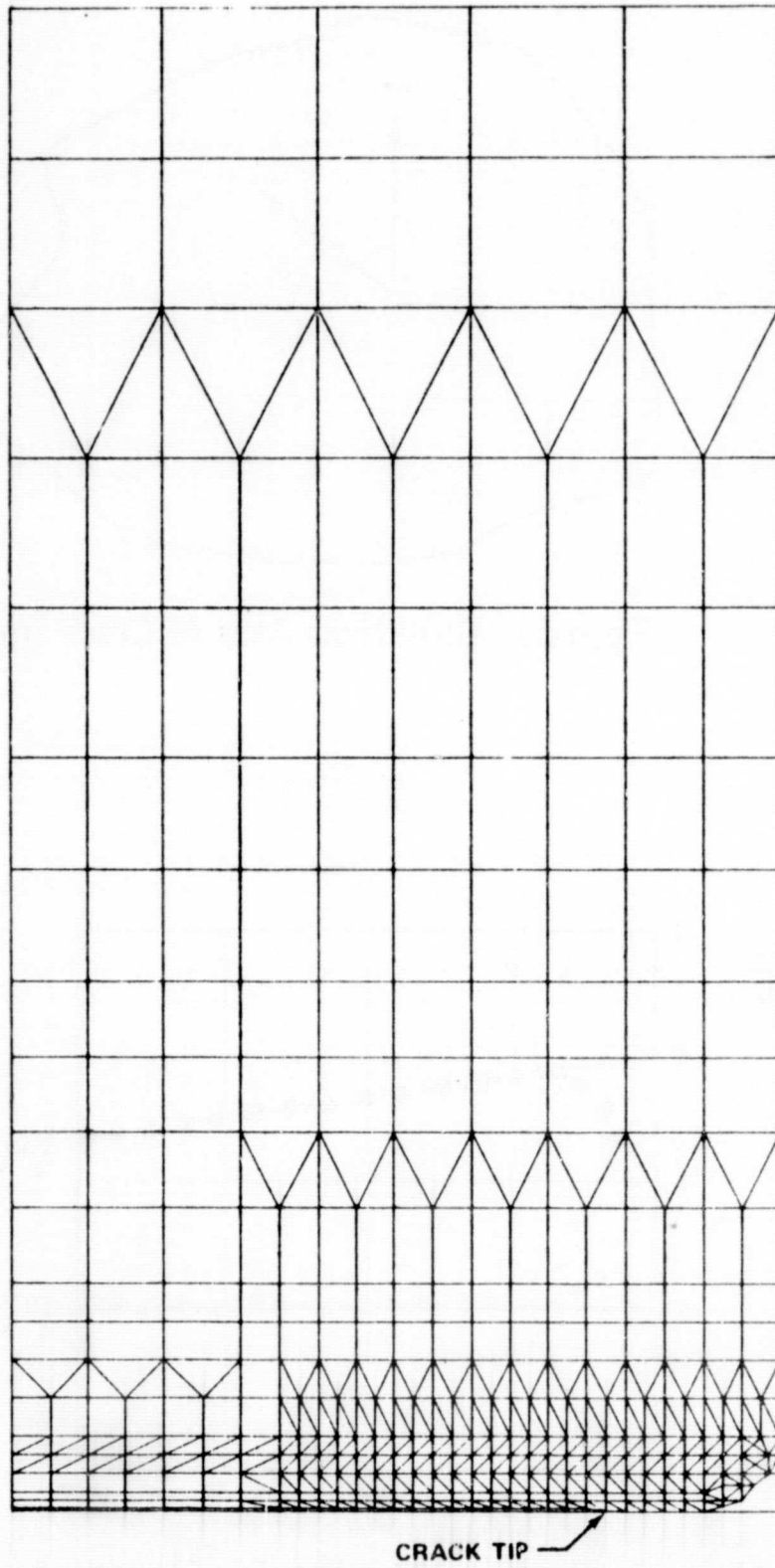
Figure 4 Displacement Model Grid For Case 3, B/A = 0. 125

set to ensure acceptable accuracy according to procedures outlined in a prior investigation (3).

The J-integral is based on the evaluation of an energy line integral

$$J = \int_{\Gamma} \left(w \, dy - \vec{T} \frac{\partial \vec{u}}{\partial x} \, ds \right)$$

(5)

where Γ is an arbitrary contour around the crack tip, w is the strain energy density, $\vec{T}$ is the traction vector defined according to the outward normal along the path Γ, $T_i = \sigma_{ij} n_j$, and $\vec{u}$ is the displacement vector. The integral has been shown to be path independent so that two complementary paths selected around a notch or crack tip yield the same value for the integral, figure 5.

The J-integral can be evaluated analytically by assuming that the stress field for large r has the asymptotic boundary condition from linear elasticity which reads, for example, in the tensile mode

$$\sigma_{ij} = \frac{K_I}{(2\pi r)^{1/2}} f_{ij}(\theta) \qquad as \ r \rightarrow \infty$$

(6)

Evaluation of the integral assumes the relationship expressed in equation 6 and a circular path of constant radius with origin at the crack tip (4). The end result for small-scale yielding and the assumption of generalized plane stress is

$$J = \frac{K_I^2}{E}$$

(7)

Similar expressions can be generated for inplane shear and antiplane shear loading.

In view of path independence, the integral can be evaluated along a more convenient path such as path Γ^* along the specimen boundary shown in figure 5 and this result equated to equation 7 resulting in the determination of the extensional stress intensity factor K_I.

Integration along the complementary path Γ^* is best performed numerically with the aid of the finite element method. Nodal density is not as much of a problem for this method since the complementary path Γ^* follows a line of low strain and stress gradient. The integration expressed in lumped form is expressed as

$$J = 2\sum_i \left[W_i(b-a, Y_i) - W_i(-a, Y_i) \right] \Delta Y_i$$

(8)

$$+ 2\sum_j \left[\sigma_{j\infty}(X_j, h/2) \Delta u_j(X_j, h/2) \right]$$

where the energy density W_i is given in terms of stress and strain at element i along Γ^* as

$$W_i = \frac{1}{2} \sigma_i \varepsilon_i$$

(9)
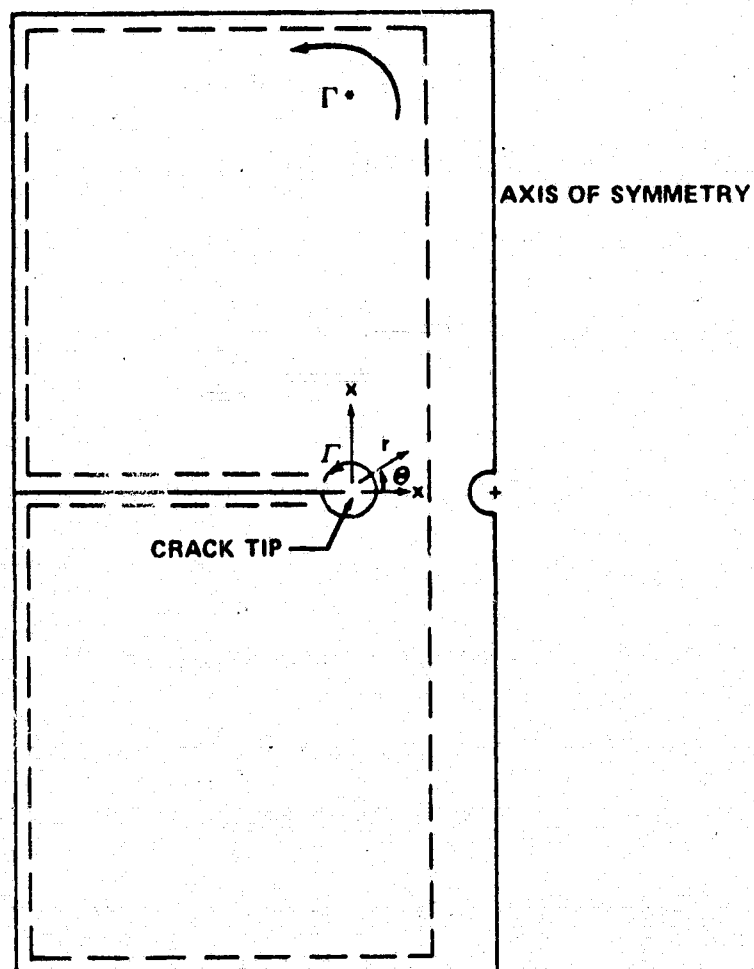
Figure 5 Two Complementary Path Integrals Around
The Crack Tip For J-Integral Method.

A typical finite element discretization for a quarter plate section of the model considered in this investigation is shown in figure 6. Case 3 is pictured with the crack approaching a circular penetration and b/a = 0.125. The integration path is shown by the shaded elements and is in a counterclockwise direction.

EXPERIMENTAL PROCEDURE

In order to verify numerical results, the extensional stress intensity factor K_I was generated for each case investigated by using a photoelastic technique developed in a previous investigation (5). Photoelastic specimens dimensionally similar to those used in the numerical investigation were loaded in a dark field circular polariscope and the resultant isochromatic fringes at the crack tip were photographed. A typical set of isochromatics can be seen in figure 7.

Selecting a point on each of the isochromatic fringe loops (r_1, θ) and (r_2, θ), the corresponding maximum shear stresses τ_1 and τ_2 were photoelastically determined by using

$$\tau_i = \frac{N_i f_\sigma}{2h} \tag{10}$$

and were related to the extensional stress intensity factor through the relation

$$K_I = \frac{2\sqrt{2\pi}\,(\tau_2 - \tau_1)\sqrt{r_1 r_2}}{f_2\sqrt{r_1} - f_1\sqrt{r_2}} \tag{11}$$

where

$$f_i = \left(\sin^2\theta_i + \frac{\sqrt{2 r_i}}{a} \sin\theta_i \, \sin\frac{3\theta_i}{2} + \frac{2 r_i}{a} \right)^{1/2}$$

Isochromatic data were obtained by scanning the photographs with a densitometer and stress intensity factors were computed using equation 11.

NUMERICAL AND EXPERIMENTAL RESULTS

Numerical and experimental results are shown for each case investigated in table 1 for b/a ratios ranging from 0.125 to 1.000. Figure 8 shows extensional stress intensity factors as a function of distance from a colinear crack tip. Excellent correlation is shown between an analytical solution developed by Paris and Sih (1) and numerical and experimental results. Some scatter is evident in numerical and experimental values for small b/a ratios but this is to be expected as the crack approaches a region of high strain or stress gradient.

Figure 9 shows the stress intensity factor as a function of distance from a circular penetration. Excellent correlation of numerical and experimental results is again shown. The circular penetration is shown to reduce the stress intensity factor by approximately 20 percent over that obtained for two approaching colinear cracks.
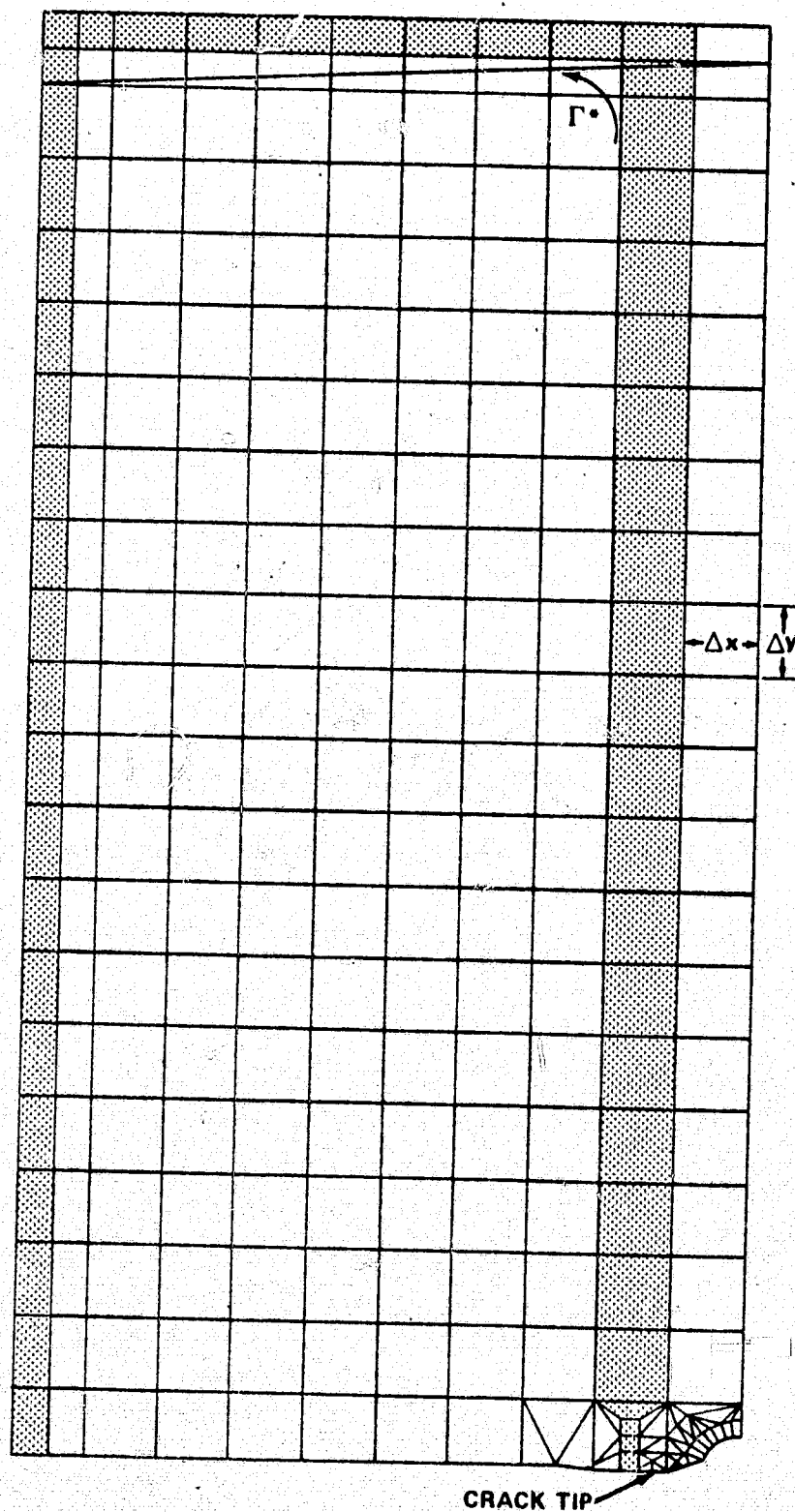
Figure 6   J-Integral Model Grid For Case 3, Bia = 0. 125
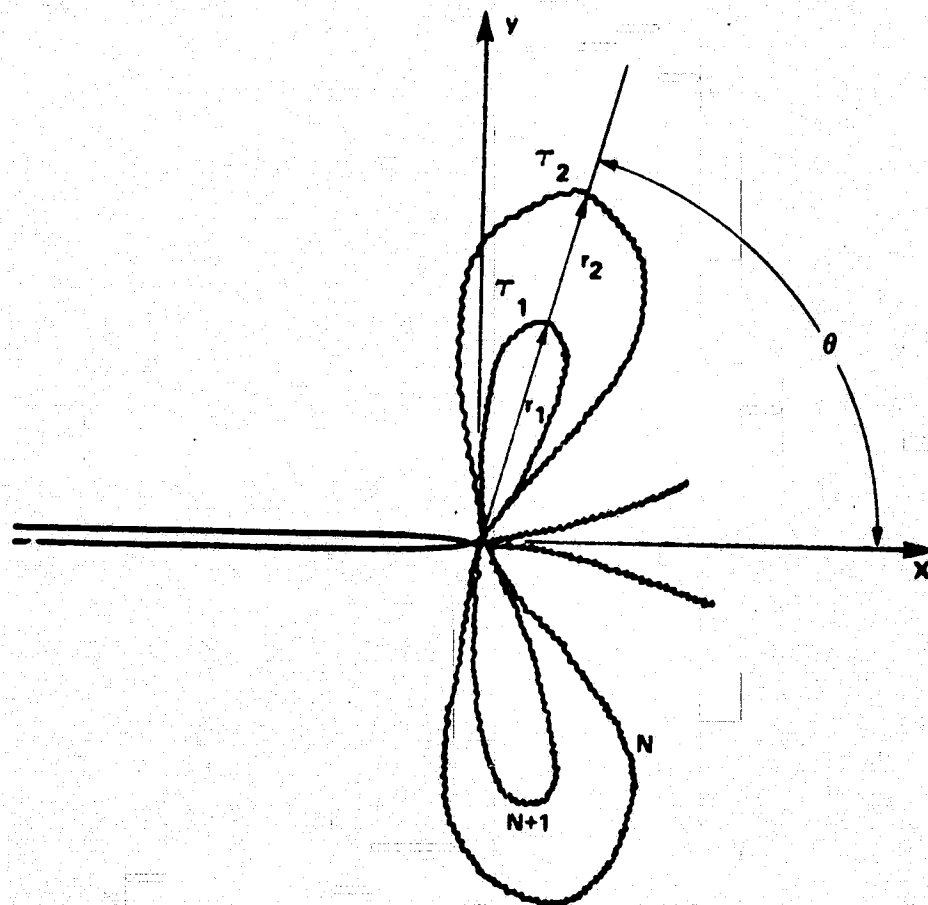
Figure 7   Isochromatic Fringes At Crack Tip

TABLE I NUMERICAL AND EXPERIMENTAL STRESS INTENSITY FACTORS

EXTENSIONAL STRESS INTENSITY FACTOR K_1 (PSI $\sqrt{IN.}$)									
b/a	CASE 1				CASE 2			CASE 3		
	PARIS AND SIH	DISPL. METHOD	J-INTEGRAL	PHOTO-ELASTIC	DISPL. METHOD	J-INTEGRAL	PHOTO-ELASTIC	DISPL. METHOD	J-INTEGRAL	PHOTO-ELASTIC
0.125	717	554	645	615	449	493	451	497	521	496
0.250	534	435	510	480	356	376	370	404	383	380
0.500	381	352	390	364	297	288	282	343	289	332
1.000	287	263	297	280	220	220	190	269	226	282
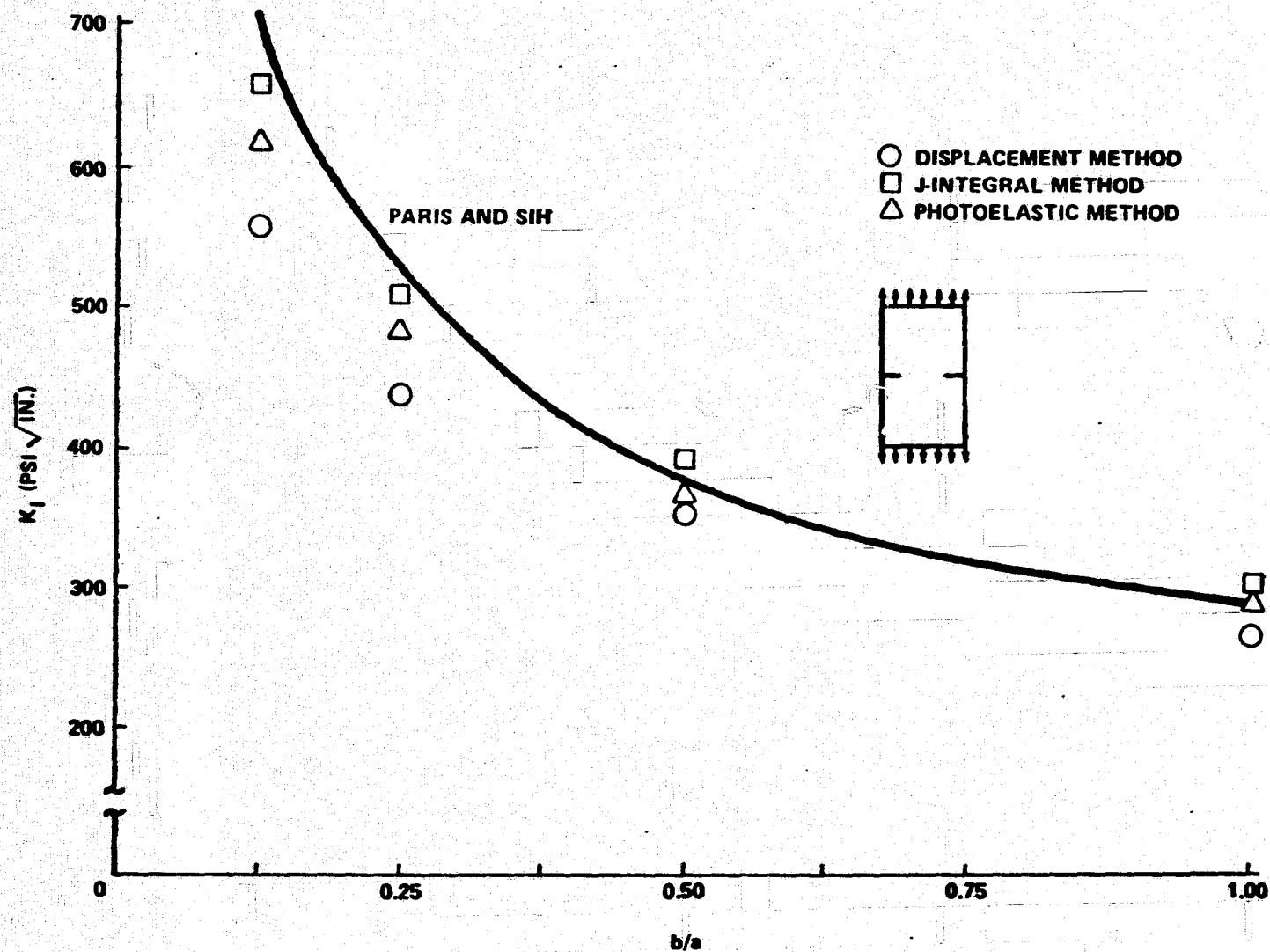
FIGURE 8. Extensional Stress Intensity Factor Versus Distance From Collinear Crack Tip
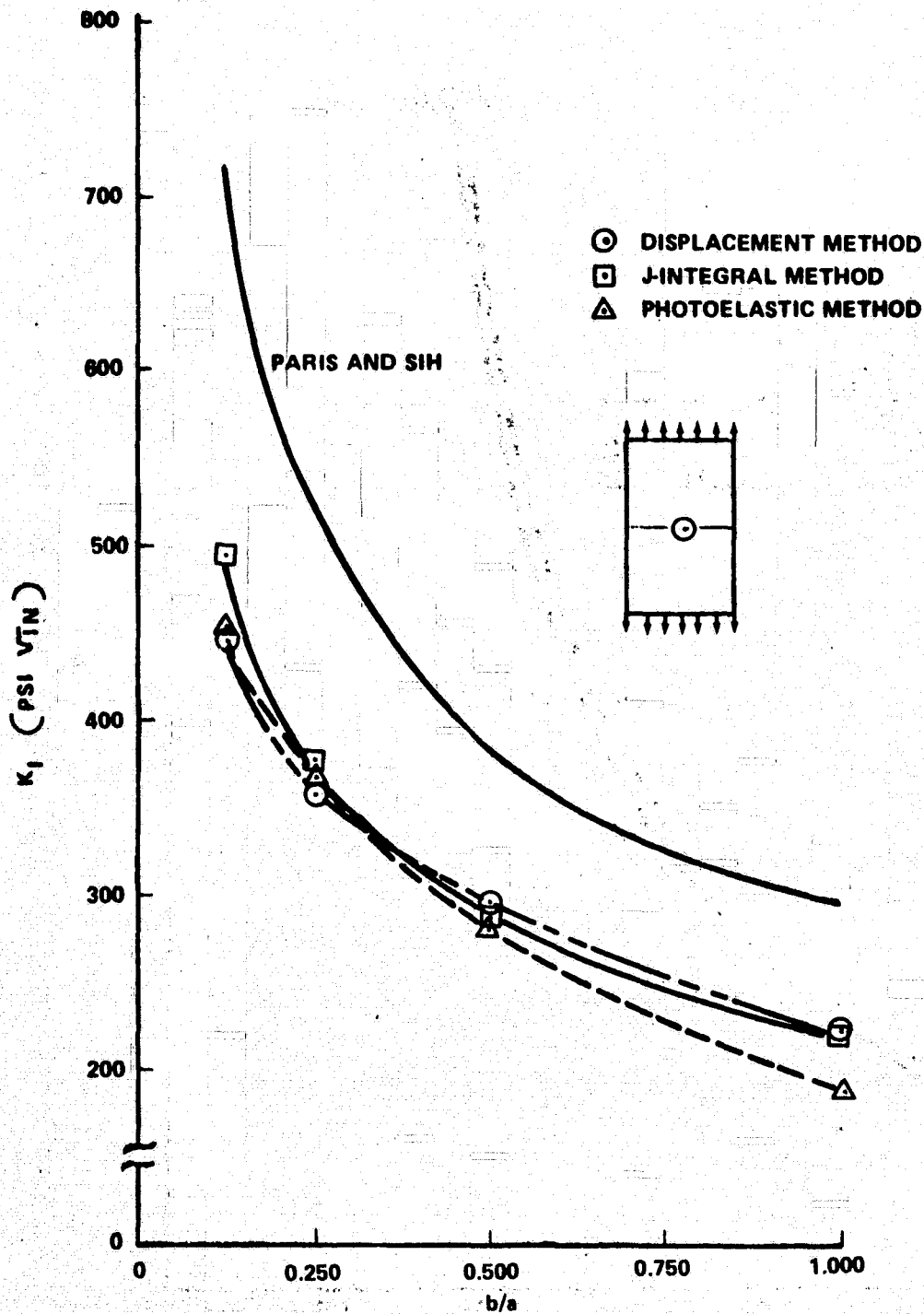
Figure 9 Extensional Stress Intensity Factor
Versus Distance From Circular Void

Figure 10 shows the stress intensity factor as a function of distance from a notched circular penetration. Correlation between numerical and experimental values is acceptable though not as close as that obtained for the prior two cases. The notched circular penetration is shown to reduce the stress intensity factor by approximately 10 percent over that obtained for two approaching colinear cracks.

CONCLUSIONS AND RECOMMENDATIONS

The displacement and J-integral methods used in conjunction with finite element techniques adequately predicted extensional stress intensity factors for cracks approaching selected singularities. Numerical stress intensity factors compared favorably to those experimentally obtained in a photoelastic analysis.

Stress intensity factors were found to decrease as the square root of the inverse of the distance from the crack tip for each case investigated. In addition, the singularities were found to substantially affect the magnitude of the stress intensity factor at the crack tip. Maximum stress intensity factors were found for the case of two approaching colinear cracks. The stress intensity factor was reduced by 10 percent for the case of a crack approaching a notched circular penetration and by 20 percent for a crack approaching a circular penetration indicating an increase in fracture resistance for a given critical extensional stress intensity factor K_{IC}.

This dependence leads to the conclusion that the fracture resistance of a material or structure can be optimized by controlling the configuration of material or geometric singularities. This can be of extreme importance in high-strength metallic or brittle materials where the size and shape of voids and inclusions can be regulated to some extent. It can also lead to a more comprehensive understanding of the fracture mechanisms operative in fiber reinforced composite materials where the singularity would be the tip of a fiber or a flaw introduced in the fabrication process.

Future efforts should be spent in applying the stress intensity factor approach to more realistic structures and materials. Accurate determination of fracture strength should be possible through a knowledge of resultant stress intensity factors and the experimentally determined critical stress intensity factor for the material.
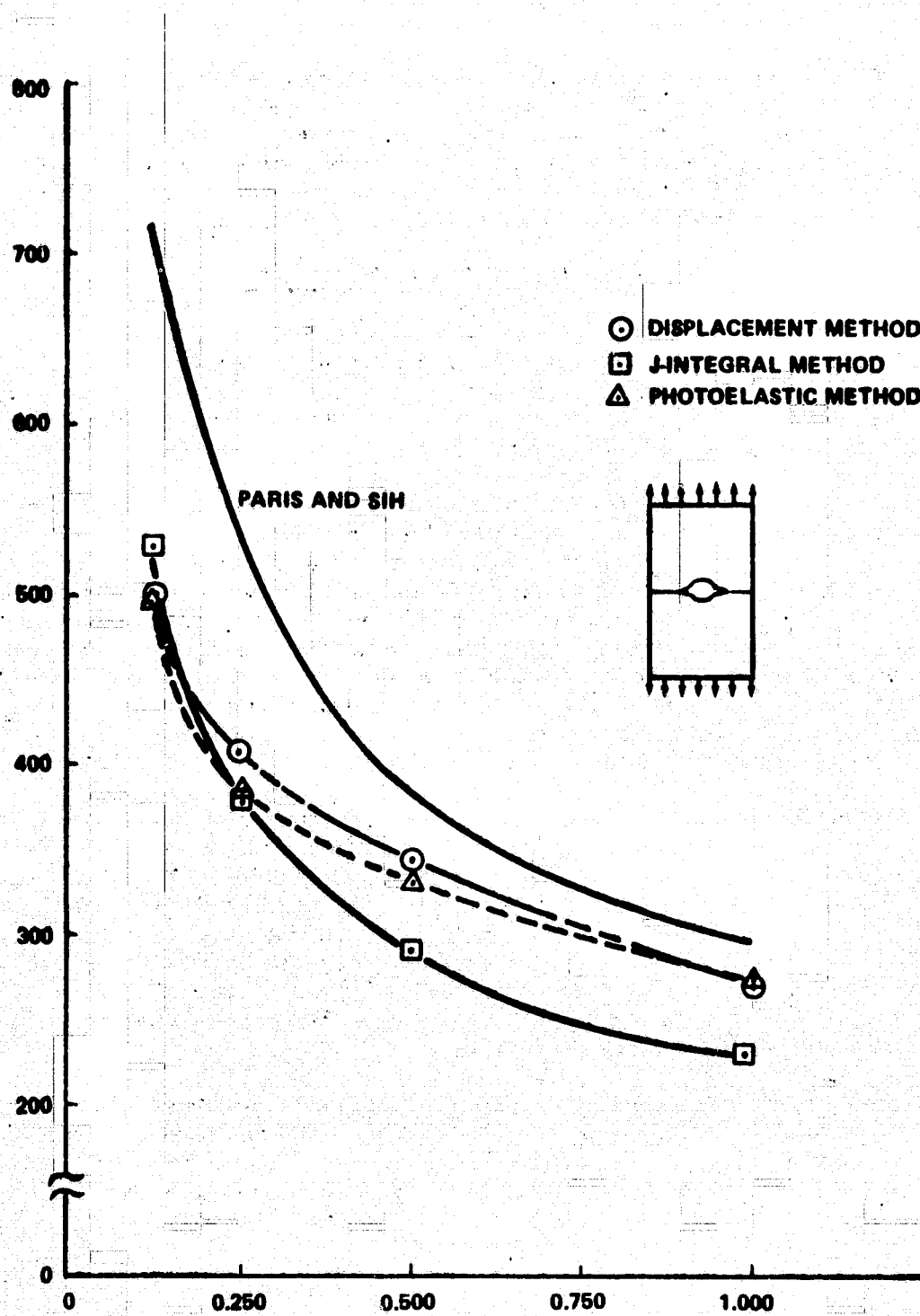
Figure 10 Extensional Stress Intensity Factor Versus
Distance From Notched Circular Void

REFERENCES

1. Paris, P. C. and G. C. Sih, "Stress Analysis of Cracks," _Fracture Toughness Testing and Its Applications_, ASTM Special Publication No. 381, pp 30 - 83, April 1965.

2. Hofer, K. E., "Fracture Mechanics," _Machine Design_, pp 109 - 113, February 1968.

3. Chan, S. K., I. S. Tuba, and W. K. Wilson, "On the Finite Element Method in Linear Fracture Mechanics, " _Engineering Fracture Mechanics_, v2, pp 1 - 17, 1970.

4. Rice, J. R., "A Path Independent Integral and the Approximate Analysis of Strain Concentration by Notches and Cracks," _J. Appl. Mech._, 35, pp 379 - 386, 1968.

5. Bradley, W. B. and A. S. Kobayashi, "An Investigation of Propagating Cracks by Dynamic Photoelasticity," _Experimental Mechanics_, pp 106 - 113, March 1970.

6. Desai, C. S. and J. S. Abel, "Introduction to the Finite Element Method," Von Nostrand - Reinhold (1972).

1974

ASEE-NASA SUMMER FACULTY FELLOWSHIP PROGRAM

MARSHALL SPACE FLIGHT CENTER

(AUBURN UNIVERSITY–UNIVERSITY OF ALABAMA)

CONCENTRATION CHARACTERISTICS

OF A

FRESNEL SOLAR STRIP REFLECTION CONCENTRATOR

Prepared by: Ronald M. Cosby, Ph.D.

Academic Rank: Assistant Professor

Department and University: Department of Physics & Astronomy
                                    Ball State University

NASA/MSFC Assignment:
    (Laboratory)   Structures and Propulsion
    (Division)   Engineering Analysis
    (Branch)   Propulsion System Analysis

NASA Research Colleague: Leon Hastings

Date: August 9, 1974

Contract No.:   NGT-01-003-045

CONCENTRATION CHARACTERISTICS
OF A
FRESNEL SOLAR STRIP REFLECTION CONCENTRATOR

By
Ronald M. Cosby

ABSTRACT

The development of an economically competitive solar power plant for the generation of electrical power depends largely on the introduction of low cost, high performance solar concentrators. Fresnel-type concentrators are considered as possible alternatives to the usual parabolic reflector concentrators.

An analysis of the concentration characteristics of an ideal Fresnel solar strip reflection concentrator is presented. Required reflection surface angles are calculated as a function of position and concentrator focal length. The intensity distribution of the concentrated solar radiation in the focal plane is determined and characterized by a maximum intensity, a central solar image width, a full width at half-maximum, and a maximum beam spread. The fraction of the total concentrated solar flux intercepted by a target placed in the concentrator focal plane is determined as a function of target width.

Results of the analysis provide theoretical limits on the concentration performance of the Fresnel solar strip reflection concentrator. The optimum concentration characteristics determined may be compared with those of other concentrators and may serve as a basis for subsequent cost-performance trade-off studies. Further, for solar power plants using the Fresnel-type reflection concentrator, the required concentrator sizes and the preliminary design of plant subsystems may be based on these results.

ACKNOWLEDGMENTS

NOMENCLATURE

SYMBOL	DEFINITION
C	concentration ratio; dimensionless
f	focal length; inches
F	target intercept fraction; dimensionless
$I(Y)$	radiation intensity in the focal plane as a function of position; Btu/ft^2 · hr
I_o	radiation intensity in central solar image; Btu/ft^2 · hr
I_p	radiation intensity in zone p of the focal plane; Btu/ft^2 · hr
ΔI_n	radiation intensity contribution from the nth reflector strip; Btu/ft^2 · hr
L	maximum beam spread in focal plane; inches
L_{min}	minimum of L with respect to focal length; inches
L_n	spread width in focal plane of beam from nth reflector strip; inches
q_s	solar radiation intensity incident on the concentrator; Btu/ft^2 · hr
W	concentrator width; inches
x_n	distance from reflector support surface to center of nth reflector strip; inches
y, y_n	distance from axis of FSSRC to center of nth reflector strip; inches
Y	focal plane distance variable; inches
Δy_n	width of nth reflector strip projected on y axis; inches
Y_l^n, Y_r^n	focal plane intercepts of beam from nth relfector strip; inches
Y_t	target width; inches
ΔY	full width at half-maximum of intensity distribution curve; inches

SYMBOL	DEFINITION
Z	limit of integration; inches
2α	apparent angular diameter of the sun; radians
γ	reflectivity of concentrator surfaces; dimensionless
ϵ	concentration efficiency; dimensionless
θ_n	reflector surface angle for the nth reflector strip; radians

LIST OF ILLUSTRATIONS

I. INTRODUCTION

The use of solar energy as the heat source for electrical power generating stations is receiving increasing attention as a possible solution to future energy requirements. Since power plants require relatively high temperature heat sources, concentrating devices must be used to collect incident sunlight and create high energy densities in regions where heat transfer devices are placed. The most widely investigated concentrator for power plant applications is the cylindrical parabolic mirror[1].

While the concentration characteristics of the cylindrical parabolic mirror[2] make it highly desirable, the initial manufacturing costs of this relatively complex shape are large compared with those for flat mirrors. Further, it may be speculated that maintenance costs may be excessive if periodic recoating of the reflective surfaces is necessary to maintain proper concentration efficiencies. Instability of shape over long periods of time and through many ambient temperature cycles may also cause problems. A practical and perhaps not minor difficulty is that of proper washing and cleaning of large cylindrical parabolic mirrors without damage to the surface and with minimum costs (implying automatic washing machinery). These difficulties make it of interest to investigate other concentrator designs which minimize the envisioned problems.

An alternative to the cylindrical parabolic reflection concentrator for a solar power plant is the Fresnel Solar Strip Reflection Concentrator (FSSRC). This report deals with the concept of such a concentrator and, through analysis, explores the optimum performance characteristics of a flat plate FSSRC design. The usefulness of the FSSRC for power plant applications depends in large part on its concentration characteristics. A major objective of the present study is to determine the concentration characteristics of an ideal FSSRC, thus establishing limits on the expected characteristics of a real system. The results permit performance comparisons with the better known cylindrical parabolic reflector and may serve as a basis for cost performance trade-off studies in view of the expected lower manufacturing and maintenance costs for the FSSRC.

Segmented mirror solar reflectors and Fresnel-type reflectors of various designs have previously been described, though sparsely, in the literature. For example Tyler and McClure[3] detail the construction and testing of a 4-foot diameter Fresnel reflector with circular mirror surfaces orbited in the U.S. Air Force Project EROS. Segmented or arrayed mirror reflectors are briefly discussed by Litynski[4] and Leedale[5]. Large solar furnaces have been built utilizing arrays of individually flat or spherical mirrors focused to a given point [6,7]. A recent note[8] describes the use of small glass "ribs" mounted on a stationary concave aluminum base for focusing sunlight on a moveable collection tube. The solar tower concept with its large array of flat mirrors is conceptually related to the FSSRC and has recently received detailed attention[9]. It is noted that the literature contains relatively little as far as analytical models are concerned.

II. FRESNEL REFLECTOR CONCEPT

The Fresnel solar strip reflection concentrator consists basically of a large number of long, narrow, mirror-like reflector strips constructed or mounted in a flat plate arrangement. Individual mirror surfaces are oriented such that all incident parallel rays of light intercepted by the plate are reflected to a common focal point. A pictorial representation of a Fresnel-type reflector is given in Figure 1.

The optimum cross-sectional geometry of an individual mirror strip surface is that of a section of a parabola; such a shape assures that all parallel rays incident on an individual mirror strip are reflected to the same point. However, if the strips are made very narrow, flat reflector surfaces serve as acceptable approximations to the optimum shape. Flat reflector surfaces are highly preferred for manufacturing and maintenance simplicity and, hence, reduced costs. For the remainder of this report the FSSRC individual reflector surfaces will be assumed planar in shape.

Various geometrical factors affect the concentrating power of the FSSRC. The choice of a focal length determines the width of the central solar image in the focal plane. Decreasing the width of the reflector strips improves the focusing characteristics. Minimization of shaded areas over the width of the FSSRC due to width and positioning of reflector strips optimizes the concentrator efficiency. In addition, accuracy of reflector surface angles and degree of planarity of reflector surfaces obviously help determine the degree of concentration.

III. OPTIMUM PERFORMANCE ANALYSIS

A. Model Assumptions

The optimum concentration characteristics of the FSSRC may be determined by analyzing an ideal concentrator. For proper assembly, one necessarily must know the reflector surface angle (rsa) as a function of strip position along the width dimension of the concentrator for any given focal length. Knowledge of the intensity distribution of the concentrated solar energy in the focal plane of the concentrator as a function of focal length and total concentrator width is of primary concern in the design of any system utilizing an FSSRC. Important quantities associated with this intensity distribution are the total range in the focal plane over which there is nonzero intensity, the width and intensity in the central solar image, the full width at half-maximum of the distribution, and the fraction of the concentrated energy intercepted by a target of given width placed in the focal plane.

For an "ideal" FSSRC, we shall assume the following:

1. The widths of the reflecting strips are infinitesimal.

2. No shading of one reflecting strip by adjacent strips occurs.

3. The focal length is long compared to dimensions describing the cross-sectional geometry of individual reflector strips.

4. No shading occurs due to the presence of a target in the concentrator focal plane.

5. The reflector sun tracking system is perfect.

6. The reflectivity is independent of wavelength over the solar spectrum received.

7. The reflectivity is independent of angle of incidence.

8. The intensity of solar radiation received is constant over the solar disk.

The first two assumptions are the most severe and obviously cannot represent a real system. Assumption (3) would be expected to apply well to a real Fresnel reflector of the type analyzed. The effects of target shading of the reflector and sun-tracking inaccuracies depend on target size and magnitude of the tracking error but are expected to be of relatively minor importance in real systems. While the reflectivity of some metals varies significantly with angle of incidence and wavelength, candidates for the reflector surface such as aluminum and silver show little variation in reflectivity over the expected ranges of incidence angles and over the received solar spectrum[10].

An analysis based on the above assumptions can produce only ideal results. However, conclusions may be drawn concerning performance limitations of a real system. Also such an analysis points out important overall or gross characteristics present in real systems. Later analyses or models may more closely describe real systems by treating finite reflector strip widths, shading, etc., as perturbations on the ideal case.

B. Reflector Surface Angles

A ray diagram for the reflection of incident solar radiation by the nth reflector strip is depicted in Figure 2 (cross-sectional view). From the diagram it is evident that the reflector surface angle (rsa) for the nth strip is given by

$$\theta_n = \frac{1}{2} \text{ Arctan} \left(\frac{y_n}{f - x_n} \right) \quad . \tag{1}$$

Applying assumption (3),

$$\theta_n = \frac{1}{2} \text{ Arctan} \left(\frac{y_n}{f} \right) \quad . \tag{2}$$

Graphs of the rsa as a function of reflector surface position and for various focal lengths are presented in Figure 3.

C. Solar Image Widths and Range of Nonzero Intensity in the Focal Plane

As shown in Figure 2, a cone of solar radiation reflected from the nth mirror strip intersects the focal or target plane over a width L_n, where

$$L_n = Y_l^n + Y_r^n \tag{3}$$

For the geometry present, the intensity in the focal plane will not be a function of distance along the length axis of the FSSRC. The problem therefore reduces to finding the characteristics of the intensity distribution with respect to the focal plane variable Y. Referring to the ray diagram and applying simple laws of trigonometry, we find

$$Y_r^n = \frac{\left\{ y_n^2 + (f - x_n)^2 \right\}^{1/2} \sin \alpha}{\cos(2\theta_n + \alpha)} \tag{4}$$

$$Y_l^n = \frac{\left\{ y_n^2 + (f - x_n)^2 \right\}^{1/2} \sin \alpha}{\cos(2\theta_n - \alpha)}$$

From equations (4) we note that, to a very good approximation,

$$Y_r^n = Y_l^n \tag{5}$$

Recognizing the fact that α is very small and using equation (2), we obtain for the focal plane spread width of the beam from the nth reflector strip

$$L_n \simeq 2 \alpha f \left(1 + \frac{y_n^2}{f^2} \right) \tag{6}$$

We note that L_n reduces to $2 \alpha f$ when $y_n = 0$, as expected. As illustrated in Figure 4, L_n increases parabolically with y_n for a given focal length. The maximum L_n occurs for y_n equal to $W/2$ where W is the concentrator width. Thus, the maximum beam spread in the focal plane is

$$L = 2 \alpha f \left(1 + \frac{W^2}{4f^2} \right) \qquad . \tag{7}$$

Given a concentrator width, L goes through a minimum with respect to focal length, as shown in Figure 5. Differentiating equation (7) and equating to zero, we find the minimum L occurs when

$$f = \frac{W}{2} \qquad ; \qquad (\text{minimum } L) \quad . \tag{8}$$

Further,

$$L_{min} = 2 \alpha W \qquad . \tag{9}$$

D.   Intensity Distribution in the Focal Plane

The results in the previous section indicate the nonzero intensity distribution width for an ideal concentrator of given dimensions and focal length. Of greater interest, however, is the shape of the intensity distribution curve within this width. To determine such a distribution, we assume that all the solar radiation striking the reflector strip of infinitesimal width Δy_n (normal to solar incidence direction) is reflected in the beam illustrated in the ray diagram of Figure 2. This energy is then distributed over the width L_n. The focal plane intensity contribution from the nth reflector strip is then

$$\Delta I_n = \frac{\gamma q_s \Delta y_n}{L_n} \qquad ; \qquad -\frac{L_n}{2} < Y < +\frac{L_n}{2} \qquad , \tag{10}$$

where γ is the reflectivity, q_s the incident solar flux, and Y the focal plane variable.

Over the solar image width ($2 \alpha f$) obtained for the central mirror strip, reflections from all strips contribute. The total intensity over this width is

$$I_o = 2 \sum_n I_n = \frac{\gamma q_s}{\alpha f} \sum_n \frac{\Delta y_n}{1 + \dfrac{y_n^2}{f^2}} \quad ; \quad -\alpha f < Y < +\alpha f \quad . \tag{11}$$

Taking the limit as Δy_n becomes very small, we have

$$I_o = \frac{\gamma q_s}{\alpha f} \int_0^{W/2} \frac{dy}{\left(1 + \dfrac{y^2}{f^2}\right)} \quad . \tag{12}$$

Performing the integration yields

$$I_o = \frac{\gamma q_s}{\alpha} \operatorname{Arctan}\left(\frac{W}{2f}\right) \quad ; \quad -\alpha f < Y < +\alpha f \quad . \tag{13}$$

The number of reflection strips contributing to the focal plane intensity progressively diminishes as we move outward from the edge of the central solar image, beginning, of course, with the loss of a contribution from the central mirror surface. Thus, for zone p in the focal plane region beyond the central solar image (see sketch),
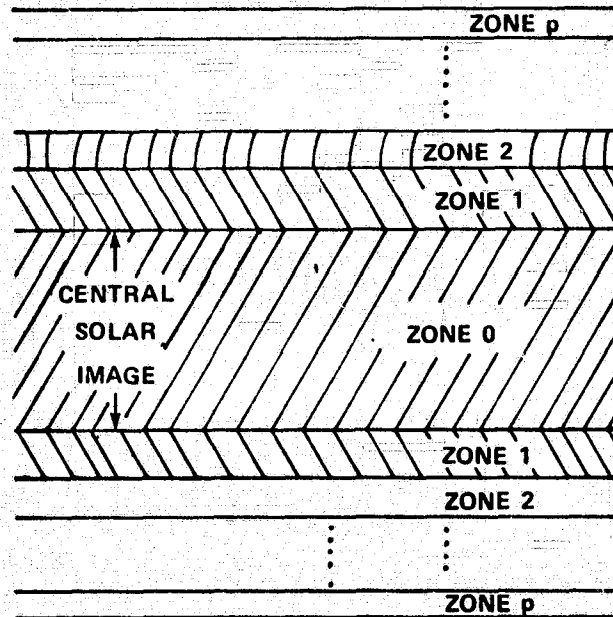
$$I_p = I_o - \frac{\gamma q_s}{\alpha f} \sum_{n=0}^{(p-1)} \frac{\Delta y_n}{1 + \frac{y_n^2}{f^2}} \quad ; \quad \text{for} \quad \begin{cases} -\frac{L_p}{2} < Y < -\alpha f \\ \\ +\alpha f < Y < +\frac{L_p}{2} \end{cases}$$

(14)

Again, taking the limit,

$$I(Y) = I_o - \frac{\gamma q_s}{\alpha f} \int_0^Z \frac{dy}{\left(1 + \frac{y^2}{f^2}\right)} \quad ,$$

(15)

where the upper limit of integration is given by

$$Z = f \left(\frac{Y}{\alpha f} - 1\right)^{1/2} \quad .$$

(16)

Integrating,

$$I(Y) = I_o - \frac{\gamma q_s}{\alpha} \text{Arctan} \left\{ \left(\frac{Y}{\alpha f} - 1\right)^{1/2} \right\} \quad ; \quad |Y| > \alpha f \quad ,$$

(17)

or we may write

$$I(Y) = I_o \left\{ 1 - \frac{\text{Arctan} \left[\left(\frac{Y}{\alpha f} - 1\right)^{1/2} \right]}{\text{Arctan} \left[\frac{W}{2f} \right]} \right\} \quad ; \quad |Y| > \alpha f \quad .$$

(18)

For a given concentrator width and focal length, equations (13) and (18) fully describe the intensity variations in the focal plane. In Figures 6, 7, and 8, intensity curves "normalized" to the reflected fraction of incident solar radiation intensity are drawn for concentrator widths 2, 6, and 10 feet with various focal lengths.

Characterization of such curves requires specification of the maximum intensity I_o, the central solar image width ($2 \alpha f$), and a quantity which measures the rate at which the intensity is spatially decreasing beyond the central image. The latter requirement is satisfied by determining the full width at half-maximum, i.e., the distance between positions on either side of the focal line where the intensity falls to one-half of the central image intensity. Setting I/I_o equal to one-half in equation (18), we find the full width at half-maximum:

$$\Delta Y = 4 \alpha f \left(1 + \frac{4f^2}{W^2} \right) - \frac{8 \alpha f^2}{W} \left(1 + \frac{4f^2}{W^2} \right)^{1/2} \quad . \tag{19}$$

The variation of ΔY with focal length is illustrated in Figure 9 for a number of concentrator widths.

E. Target Intercept Fraction

A quantity useful in the design of target absorbers is the fraction F of the total concentrated flux intercepted by a target of given width Y_t centrally located in the focal plane:

$$F = \frac{\displaystyle\int_{-Y_{t/2}}^{+Y_{t/2}} I(Y) \, dY}{\gamma q_s W} \tag{20}$$

Using equation (13) for the case of a target width less than the central solar image width, F reduces to

$$F = \frac{Y_t}{\alpha W} \text{Arctan} \left(\frac{W}{2f} \right) \quad ; \quad Y_t < 2 \alpha f \quad . \tag{21}$$

For a wider target, equations (13), (18), and (20) yield

$$F = \left(\frac{Y_t}{\alpha W} \right) \left\{ \text{Arctan} \left(\frac{W}{2f} \right) - \text{Arctan} \left[\left(\frac{Y_t}{2 \alpha f} - 1 \right)^{1/2} \right] \right\} + \frac{2f}{W} \left(\frac{Y_t}{2 \alpha f} - 1 \right)^{1/2} \quad . \tag{22}$$

Figures 10, 11, and 12 detail the variation of the intercepted fraction with target width for various concentrator widths and focal lengths. We also note that the quantity $\epsilon = \gamma F$ represents the fraction of the total energy incident on the concentrator that is received by the absorber. ϵ may be referred to as the concentration efficiency.

The concentration ratio for the FSSRC system may be defined as the ratio of the average incident radiation intensity over the absorber to the solar flux incident on the concentrator:

$$C \equiv \frac{\dfrac{1}{Y_t} \displaystyle\int_{-Y_{t/2}}^{+Y_{t/2}} I(Y)\,dY}{q_s} . \tag{23}$$

Using equation (20),

$$C = \frac{\gamma\, WF}{Y_t} . \tag{24}$$

Using equation (24) and equation (21) or (22), the concentration ratio for a given concentrator-target system may be determined.

IV. RESULTS AND DISCUSSION

From equation (2) and Figure 3, we see that for a given point on the concentrator, the larger the focal length the smaller is the reflection surface angle. Further, the rate of increase of the rsa with distance from the concentrator center decreases with increasing focal length. The design of a real concentrator may be restricted by the requirements on the rsa. For example, if a 10 foot wide, 5 foot focal length FSSRC is constructed of 1 inch wide strip mirrors, the maximum rsa is less than 23 degrees and the difference in rsa's of the last two strips is approximately 0.2 degree. This imposes rather stringent strip orientation requirements on the assembly of the concentrator if one is to gain by having such narrow mirror strips.

From the analysis of the intensity distribution in the focal plane (Section III.D), we find that a high local concentration ratio ($I/\gamma\, q_s$) in the central solar image is incompatible with the desired small area confinement of the concentrated energy flux. An optimum intensity confinement situation is found to exist when the concentrator focal

length is equal to the concentrator half-width (Figures 6, 7, 8). From these results, and from those of Section III.E, we conclude the optimum concentrator-target system to be one where the concentrator focal length is half the concentrator width and where the concentrator and target widths are chosen compatible with the energy requirements and heat transfer constraints of the end use and collection systems. We note also that the target width may be chosen such that the intensity is nearly uniform over the target area, avoiding local "hot spots" and minimizing possible heat transfer difficulties.

The concentration ratio defined by equation (23) gives the "flux multiplication" factor for the concentrator-target system and is important only in applications where intensity is of dominant interest. For solar power plants it is the total energy collected by the target that is of primary importance. In this case the concentration ratio is relatively unimportant when compared to the target intercept fraction. For example, a high concentration ratio may occur when the target width is smaller than the central solar image, while at the same time, the target intercept fraction or total energy collected may be very small.

V. SUMMARY AND CONCLUSIONS

The concentration characteristics of an ideal Fresnel solar strip reflection concentrator were analyzed in detail. The required reflection surface angles were calculated as a function of position and focal length. The intensity profiles of the concentrated solar radiation in the focal plane of concentrators with various widths and focal lengths were examined and characterized by a maximum intensity, a central solar image width, a full width at half-maximum, and a maximum beam spread. The fraction of the total concentrated flux intercepted by a target placed at the focal plane was determined as a function of target width. Again the analytical expression was used to examine this fraction for various concentrator widths and focal lengths. A concentration ratio and concentration efficiency were defined.

From the results of this study we conclude:

1. The optimum focal length for an ideal FSSRC is half the concentrator width.

2. The relationship of primary importance to the concentrator-target system is the target intercept fraction-target width relation.

3. Evaluation of the effects of shading, finite width of reflector strips, and other characteristics of real systems may be treated as perturbations on the model of an ideal FSSRC.

Several aspects of the FSSRC require additional analysis. Future studies should consider:

1. The effects of shading of one reflector strip by another and reflector designs to minimize shading.

2. The smearing of the solar image due to finite reflector strip widths.

3. Target shading of the reflector.

4. The effects of small tracking inaccuracies.

5. The distribution of radiation over the sun's disk.

6. The properties of actual reflective materials including reflectivity, durability in outdoor environments, and costs.

7. Substrate materials, manufacturing costs, and modular designs for the FSSRC.

8. Collector configurations including support base and tracking mechanism.

9. Comparison of cost-performance aspects of the FSSRC with other concentrators such as the cylindrical parabolic reflector.

VI. REFERENCES

1.   See, e.g., "Comparative Systems Analysis," Task 1 Report ATR-73(7283-01)-1, The Aerospace Corporation, November 15, 1972; and "Research Applied to Solar-Thermal Power Systems," Report NSF/RANN/SE/GJ-34871/PR/7214, University of Minnesota and Honeywell, Incorporated, December, 1972.

2.   K.E. Hassan and M.F. El-Fefaie, Solar Energy 15, 219 (1973).

3.   R.D. Tyler and R.B. McClure, "Materials and Construction Techniques for Space Solar Reflectors" in Power Systems for Space Flight, Ed. M.A. Zipkin and R.N. Edwards, Vol. II, 713(1962).

4.   Z. Lhynski, "Direct Energy Conversion in the USSR-Soviet Solar Concentrators," ATD Report 66-138, Surveys of Foreign Scientific and Technical Literature, Library of Congress, 84(1966).

5.   E. Leedale, "A Review of the Solar Furnace as a High Intensity Heat Source," Technical Note No. 1: Mech. Eng. 322, Royal Aircraft Establishment, Ministry of Aviation, London, 5 (1960).

6.   F. Trombe and A. LePhat Vinh, Solar Energy 15, 57 (1973); Solar Energy 15, 63 (1973).

7.   G. Francia, Solar Energy 12, 51 (1968).

8.   "Concentrating Research on Solar Energy" in Industrial Research, 21 (May, 1974).

9.   "Solar Thermal Power Systems Based on Optical Transmission," Report NSF/RANN/SE/GI-39456/PR/73/4, University of Houston and McDonnell Douglas Astronautics West, February, 1974.

10.   See, e.g., F.A. Jenkins and H.E. White, Fundamentals of Optics, McGraw-Hill, 1957, p. 520.

TYPICAL CROSS-SECTIONAL VIEW
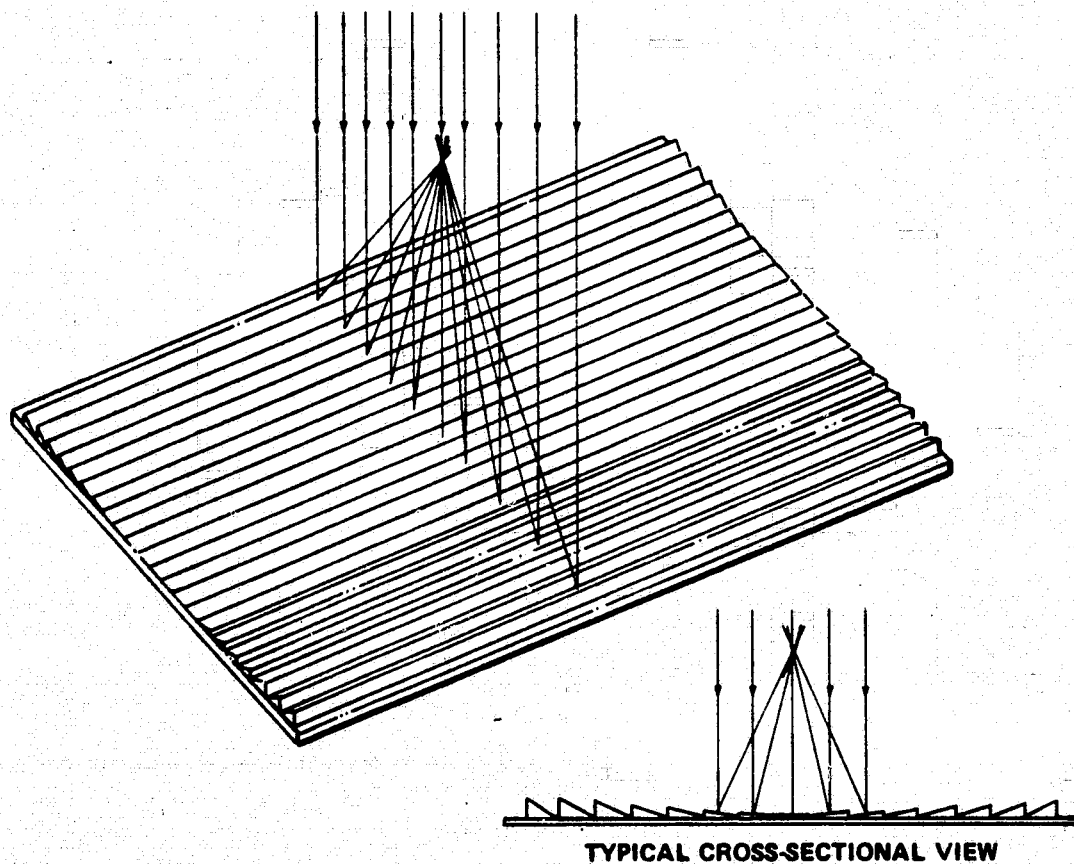
Figure 1. A Fresnel Solar Strip Reflection Concentrator.
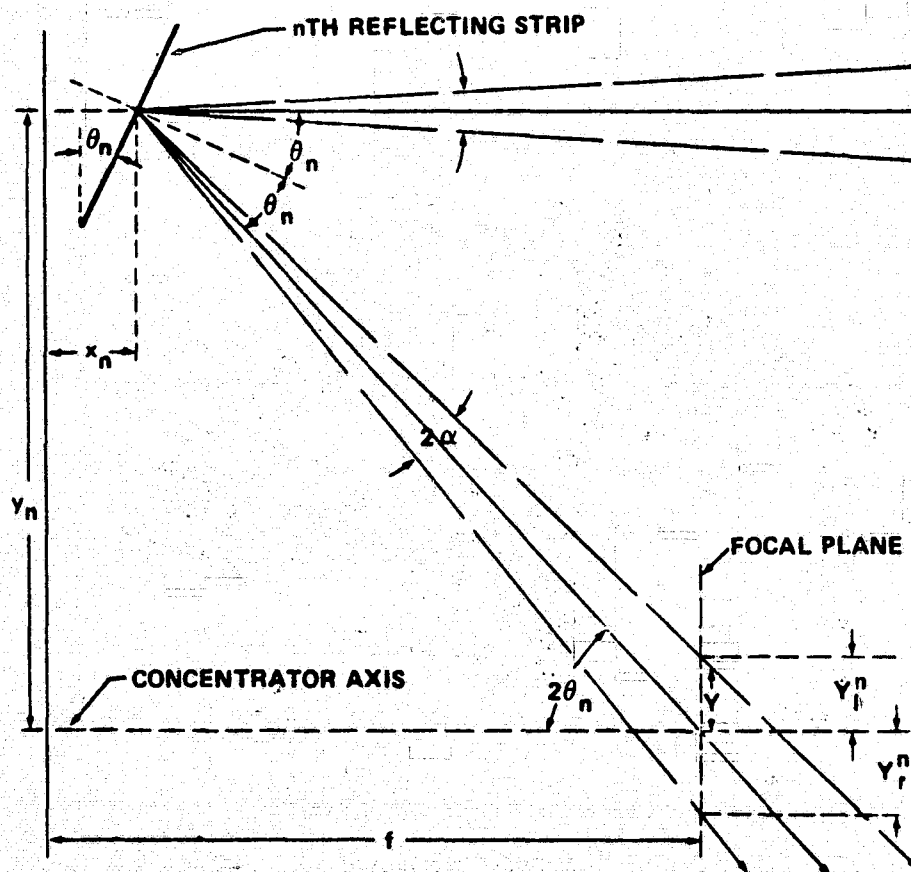
Figure 2. Ray Diagram for the Reflection of a Beam of Sunlight to the Focal Plane.
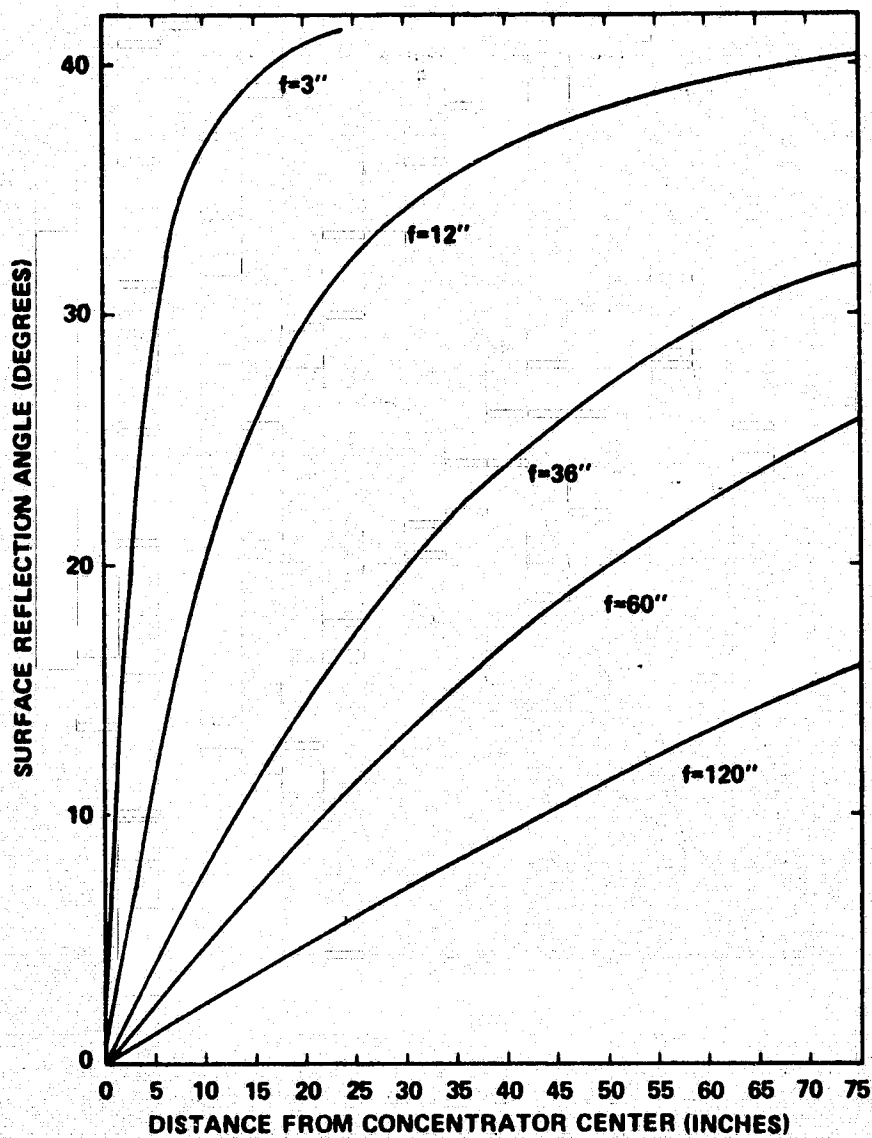
Figure 3. Variation of Surface Reflector Angle with Position Relative to the
Concentrator Axis for Various Focal Lengths.
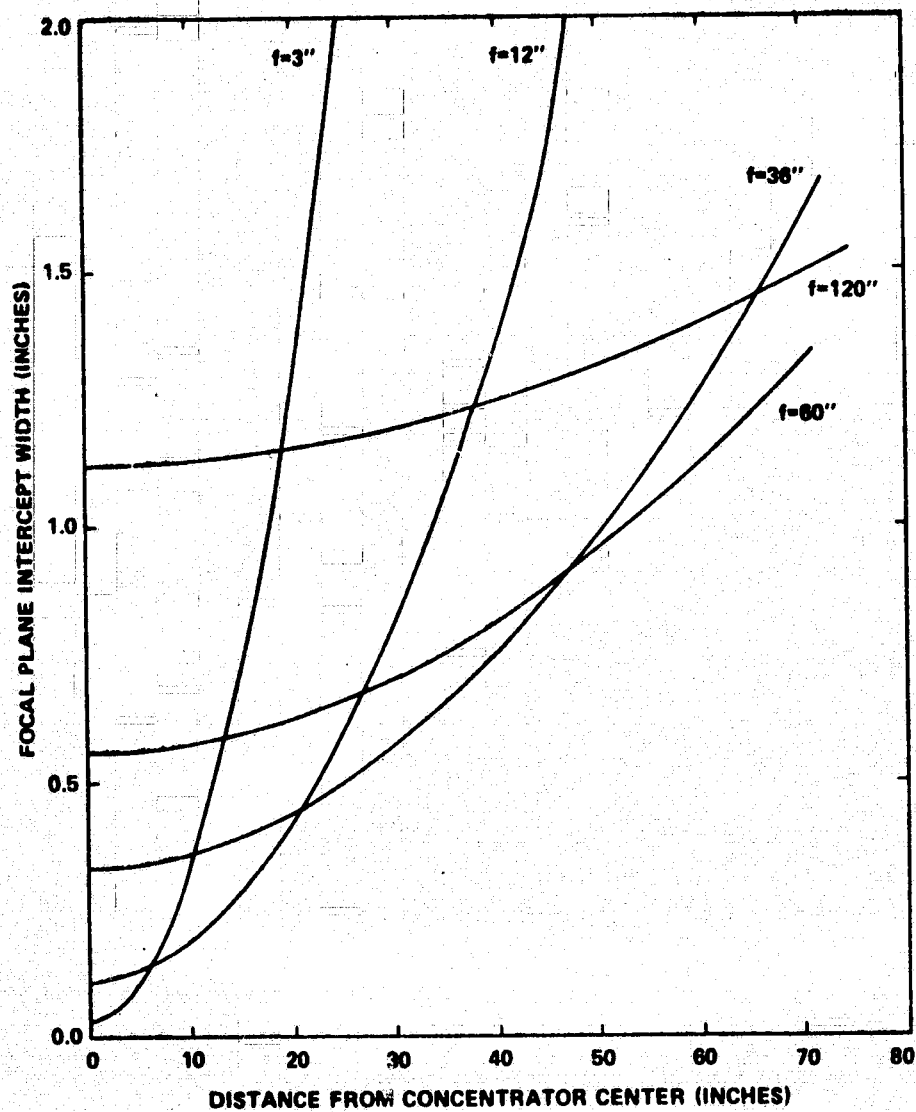
Figure 4. Variation of the Focal Plane Intercept Width with Surface Reflector Position for Various Focal Lengths.
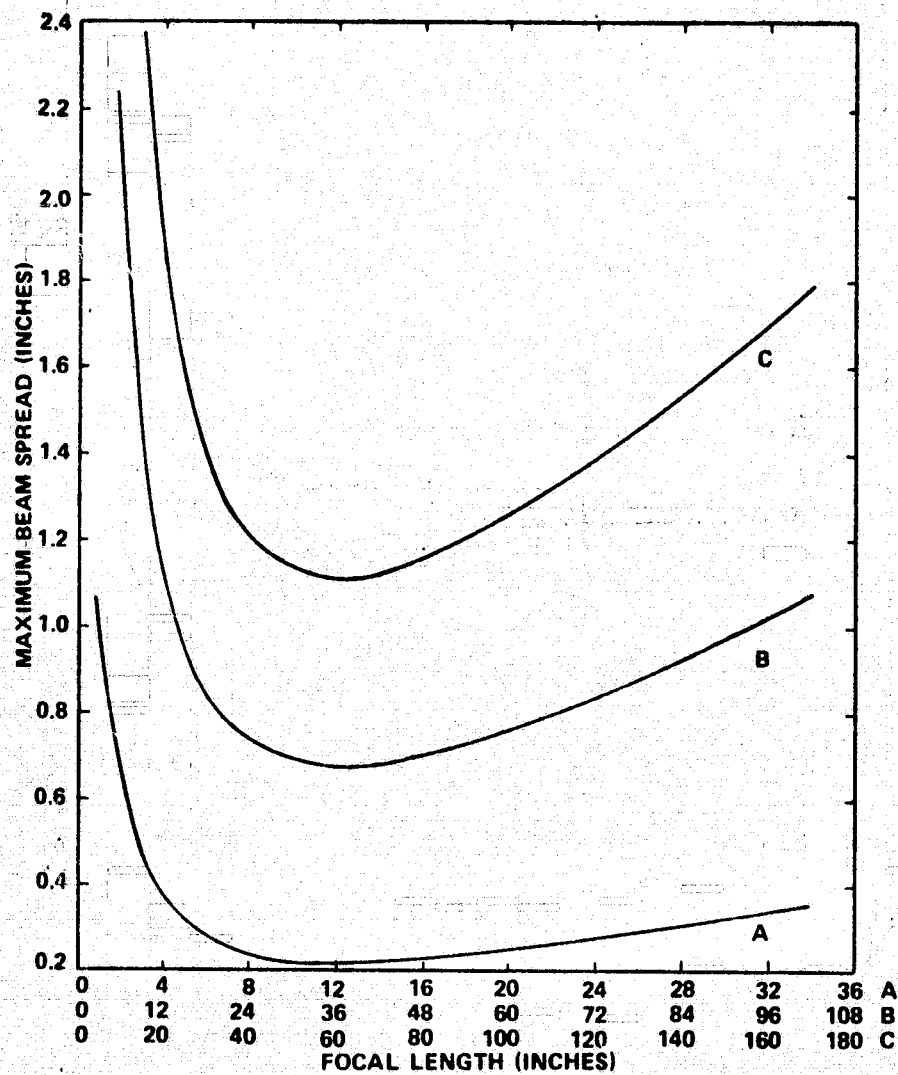
Figure 5. Dependence of the Maximum Beam Spread on Focal Length for
Concentrator Widths: A-24 in., B-72 in., C-120 in.
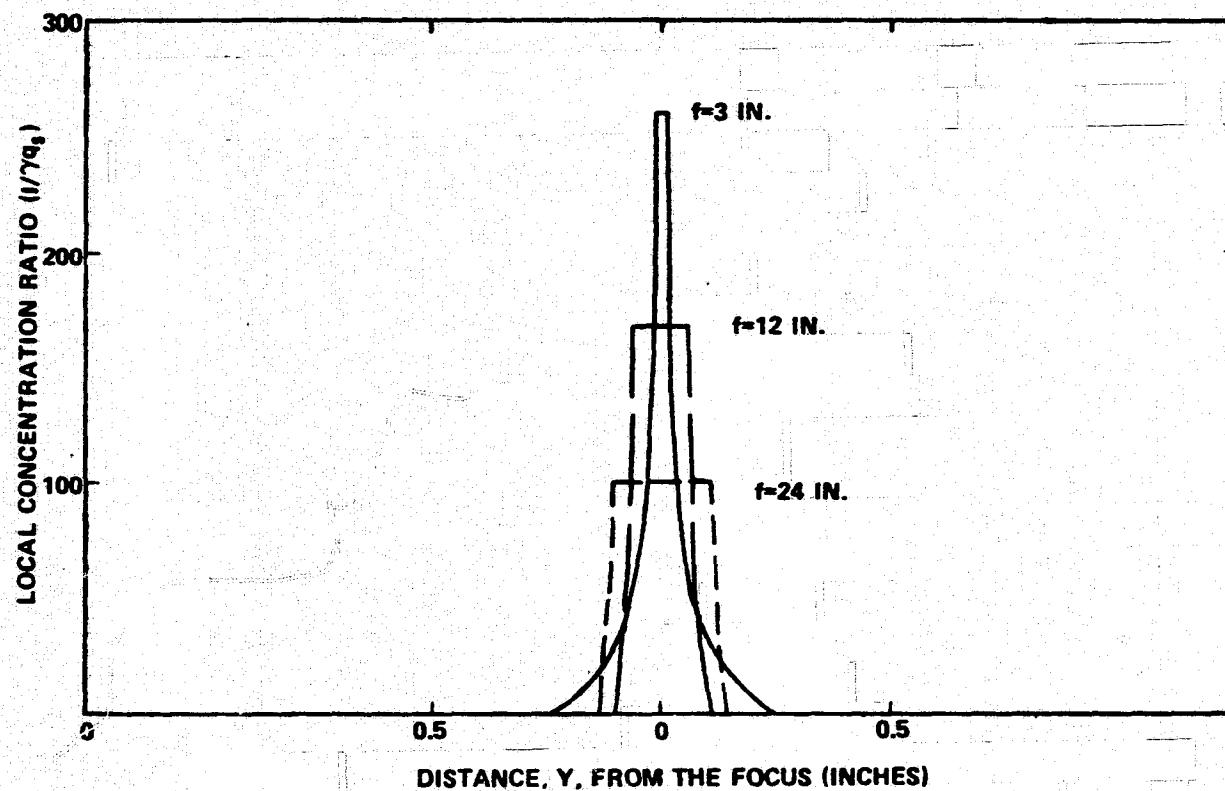
Figure 6. Variations of Local Concentration Ratio (Normalized Intensity) with Focal
Plane Position for a Concentrator Width W = 2 ft.
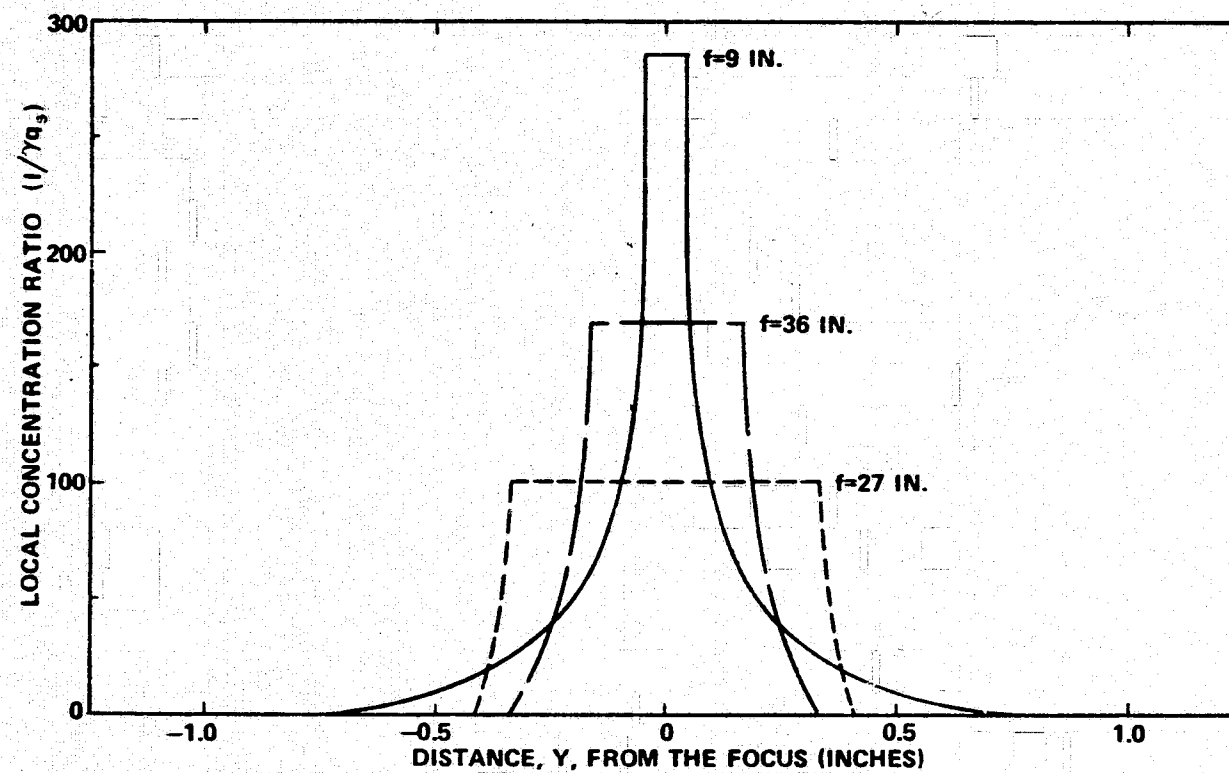
Figure 7. Variation of Local Concentration Ratio (Normalized Intensity) with Focal Plane Position for a Concentrator Width W = 6 ft.
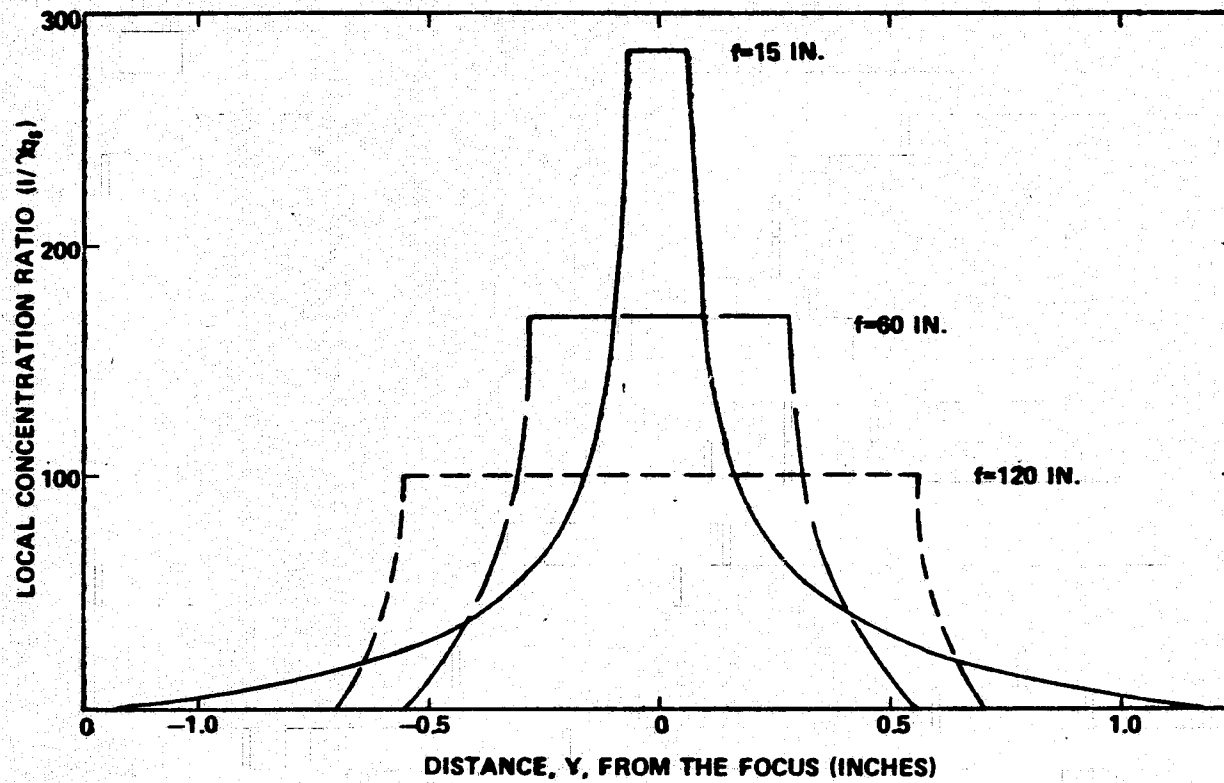
Figure 8. Variation of Local Concentration Ratio (Normalized Intensity) with Focal
Plane Position for a Concentrator Width W = 10 ft.
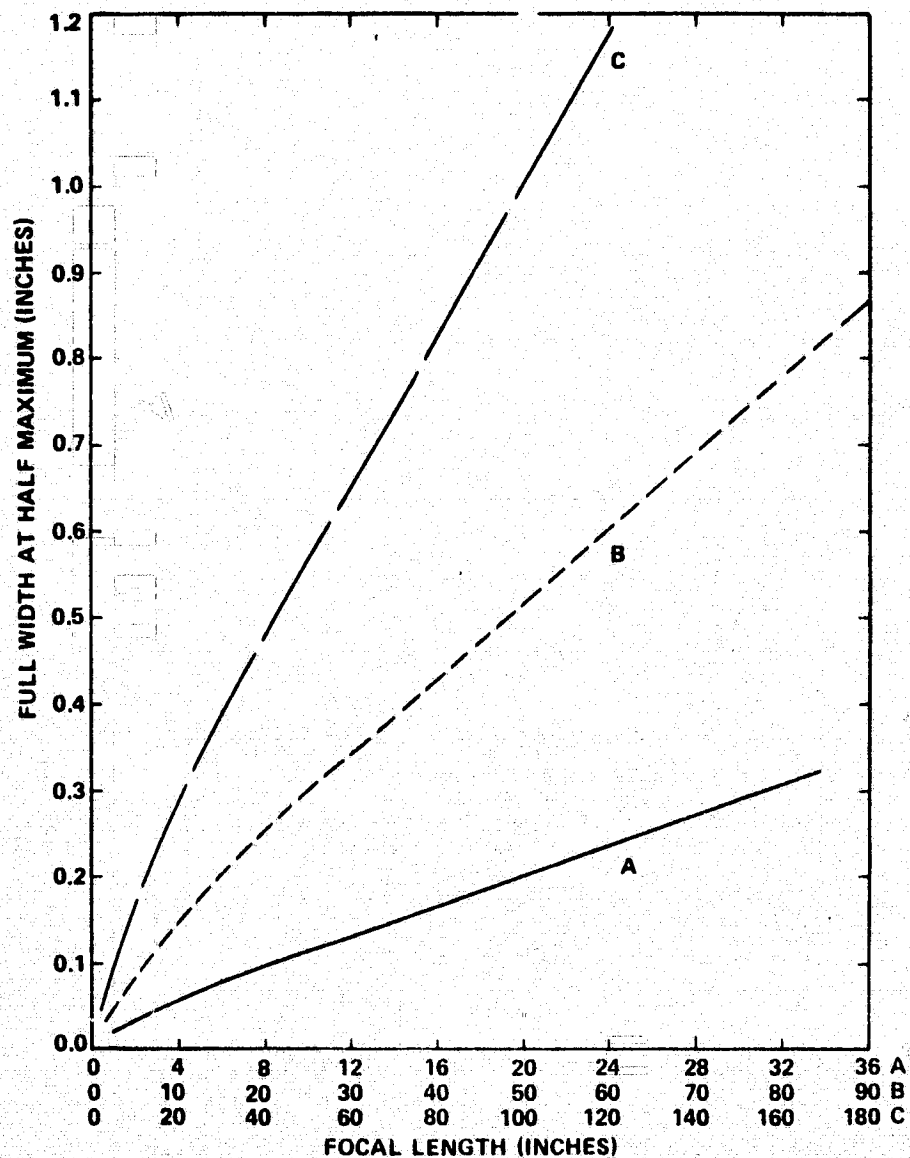
Figure 9. Dependence of Full Width at Half-Maximum of the Focal Plane Intensity Distribution Curve on Concentrator Focal Length for Concentrator Widths: A-2 ft, B-6 ft, C-10 ft.
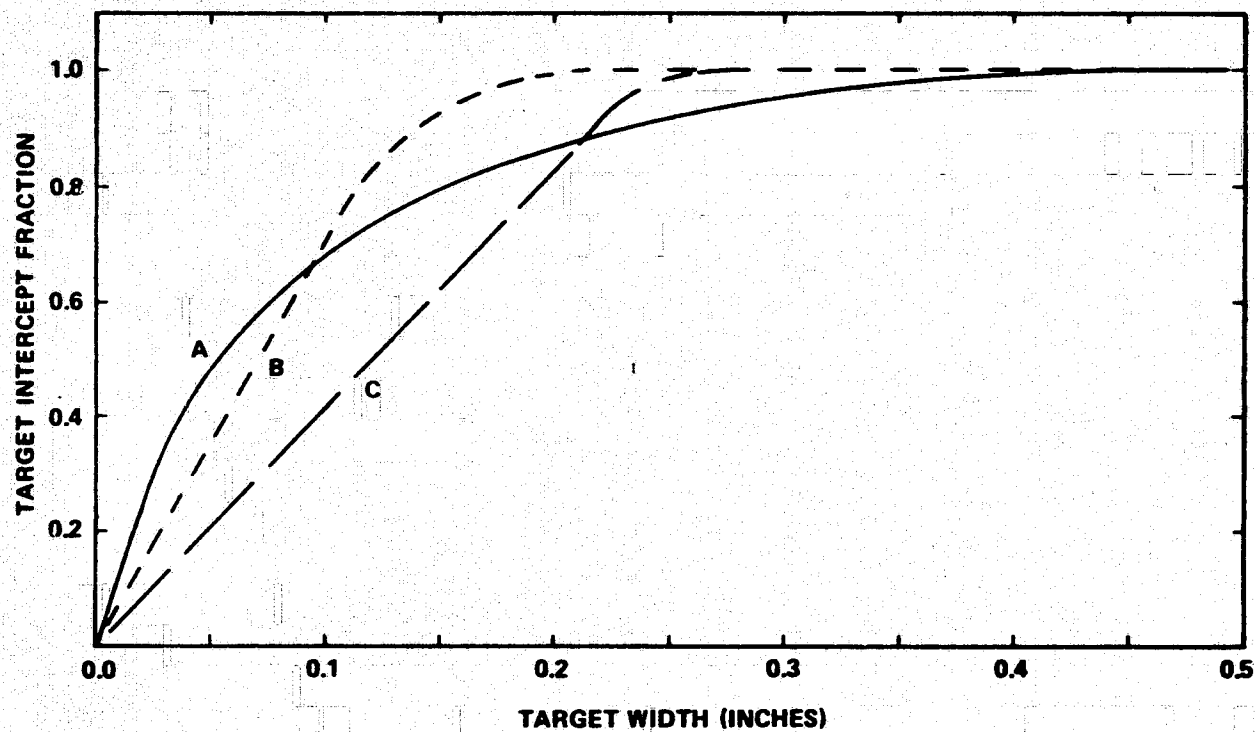
Figure 10. Variation of Target Intercept Fraction with Target Width for a Concentrator of Width W = 2 ft and for Focal Lengths: A-3 in., B-12 in., C-24 in.
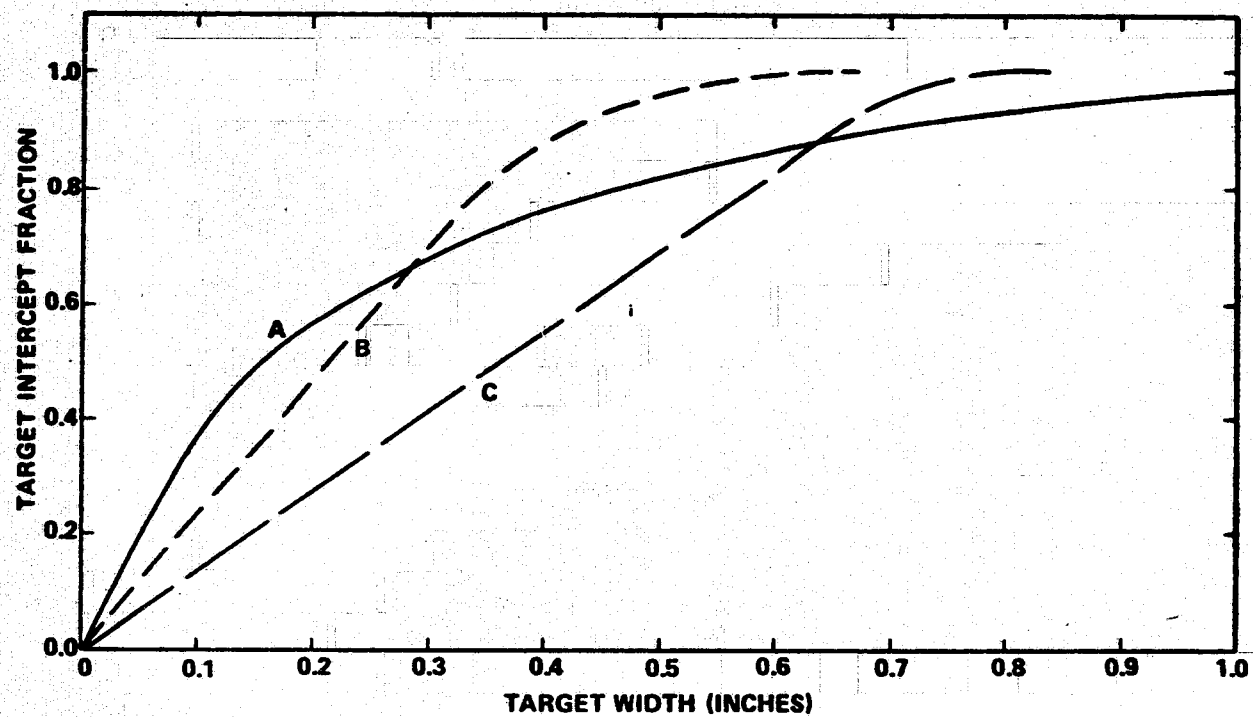
Figure 11. Variation of Target Intercept Fraction with Target Width for a Concentrator of Width W = 6 ft and for Focal Lengths: A-9 in., B-36 in., C-72 in.
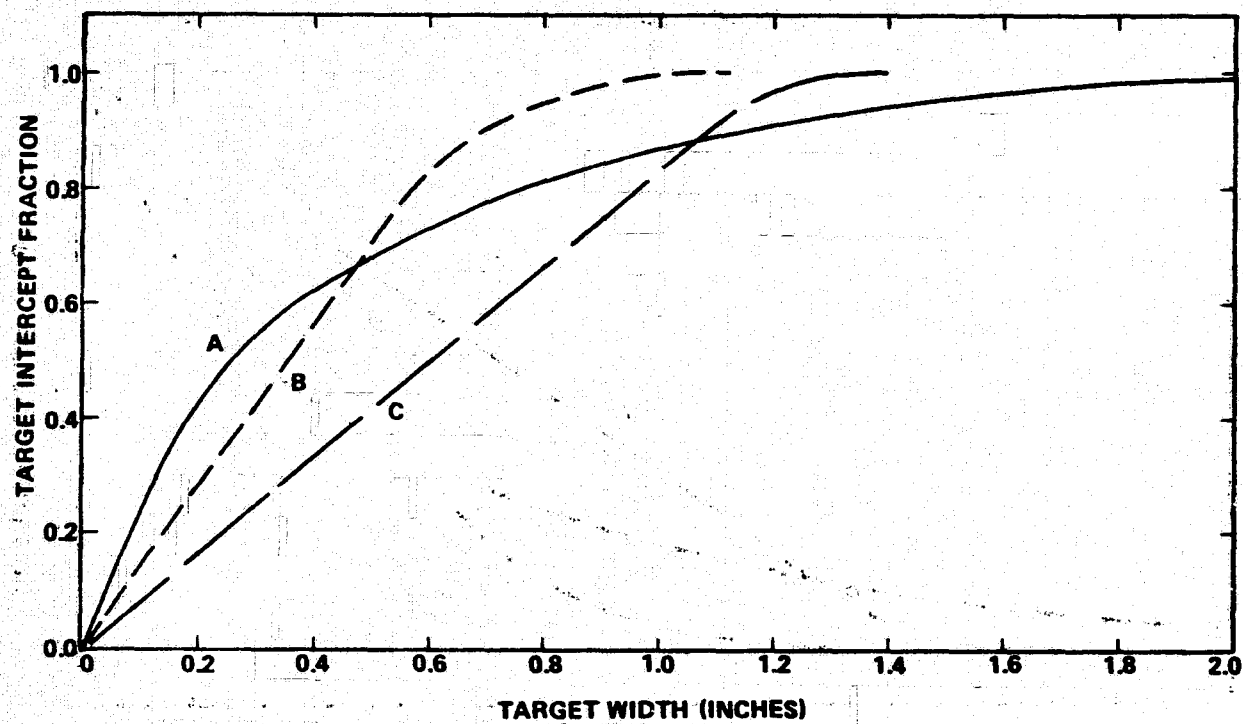
Figure 12. Variation of Target Intercept Fraction with Target Width for a Concentrator of Width W = 10 ft and for Focal Lengths: A-15 in., B-60 in., C-120 in.

1974

ASEE - NASA SUMMER FACULTY FELLOWSHIP PROGRAM

MARSHALL SPACE FLIGHT CENTER

(AUBURN UNIVERSITY - UNIVERSITY OF ALABAMA)

OPTICAL PROPERTIES OF THE II-VI

COMPOUND SEMICONDUCTOR ZnTe

IN THE VACUUM ULTRAVIOLET

Prepared by: Merrell E. Crandell, PhD.

Academic Rank: Associate Professor

Department and University: Department of Physics
                                      Muskingum College

NASA/MSFC Assignment:
     (Laboratory)   Space Sciences Laboratory
     (Division)   Physics & Instrumentation
     (Branch)   Surface Sciences

NASA Research Colleague: Roger C. Linton

Date: August 9, 1974

Contract No.:   NGT-01-003-045

OPTICAL PROPERTIES OF THE II-VI
COMPOUND SEMICONDUCTOR ZnTe
IN THE VACUUM ULTRAVIOLET

by

Merrell E. Crandell

ABSTRACT

The optical constants of a thin film of the II-VI compound semi-
conductor ZnTe have been determined in the vacuum ultraviolet from
3.5 to 21.5 eV. The normal incidence reflectivity has been compared
with that of a quasi-single crystal. It has been found that the
general structure of both samples is very similar to that found in
previous measurements on a pure single crystal. It was found that
the transitions at 10.4 and 13.6 eV, which were previously attributed
to transitions from the d-bands of Zn, were probably plasma resonances,
and the d-band transitions really occurred at 8.3 and 12 eV.

Evidence was also found that the true energies could have been
modified due to the buildup of electric charges on the surface of
the samples caused by photoemission from the sample.

INTRODUCTION

In the search for new materials for use in optical coatings or as photodetectors, interest has been shown in some of the compound semiconductors. One of the major difficulties with these materials is the inability to form large single crystals which are usually used in photodetectors. It is possible however to prepare quasi-single crystals (aggregates of small single crystals) or thin films. In this study the optical properties of both a quasi-single crystal and a thin film of the II-VI compound semiconductor ZnTe have been determined for the vacuum ultraviolet.

Previous optical reflectance studies on ZnTe in this range (2,11) have been limited to cleaved single crystals, and due to uncertainties in the magnitude of the reflectance, could only be used for finding the transition energies between electron bands within the crystal. These studies indicate that most of the structure occurs between 2.5 and 7.5 eV, with two other reflection peaks near 10.6 and 14.6 eV which were attributed to transitions from d-bands in Zn.

Preliminary studies on thin films of ZnTe (4) indicate that the transition near 10.6 eV could be due to a collective electron oscillation (plasma resonance). In order to verify the nature of this transition, and also to look at the transition near 14.6 eV, this study was extended to 22.5 eV, and a quasi-single crystal was included for comparison with the thin film.

The preliminary study also indicated that the only change in optical properties with film thickness was due to reflections from the substrate in the case of films of thickness between 10 and 50 nm. For this reason the only film included in this study was thick enough to ignore any substrate effects.

SAMPLE PREPARATION

Binary compounds in which both components evaporate at approximately the same rate can be evaporated in a straightforward manner from the bulk material (3). Since ZnTe is such a material, a 70 nm thick thin film was evaporated onto a fused silica substrate from 99.999 % pure ZnTe. The thickness was monitored with a quartz crystal monitor, and the resulting film was examined visually and found to be free of any noticeable imperfections.

The quasi-single crystal was a 1" diameter, 1/8" thick disc purchased commercially as a single crystal. One face of this was polished mechanically with various polishes down to .05 micron alumina. When examined with a metallurgical microscope, it was found to have a rather rough surface with many small pits which appeared to be caused by voids in the crystal structure. This led to the conclusion that this was really a quasi-single crystal.

APPARATUS

The reflectances were measured at incident angles of 20° and 70° by determining the intensity of both the incident and reflected beams and taking their ratio. Between 95 and 350 nm, the source was a Hinteregger hydrogen discharge lamp used in conjunction with a McPherson 225 vacuum monochrometer (4). Between 55 and 100 nm, the 240-MeV electron storage ring of the Physical Science Laboratory (PSL) of the University of Wisconsin[*] provided highly polarized synchrotron radiation (8). This was then sent through a normal incidence monochrometer designed by PSL to the reflectometer. Because of the low signal levels and possible stray radiation in this portion of the study, the incident light was chopped at 300 Hz and a Princeton Applied Research lock-in amplifier was used to detect the signal.

DATA ANALYSIS

The index of refraction, n, and the extinction coefficient, k, were determined from the reflectances by a two-angle iterative computer program (5), and from these the other optical constants of interest could be derived (6,7).

The complex dielectric constant $\epsilon = \epsilon_1 + \epsilon_2$,

where
$$\epsilon_1 = n^2 - k^2$$

$$\epsilon_2 = 2 n k ,$$

is useful in relating the spectra to the atomic band structure. It can be shown that ϵ_2 is proportional to the density of states, and therefore its behavior, especially maxima and steep slopes, can be related to transitions between filled and unfilled states.

The energy loss functions $Im(-1/\epsilon)$ and $Im(-1/(1+\epsilon))$,
where
$$Im(-1/\epsilon) = 2 n k/(n^2+k^2)^2$$

$$Im(-1/(1+\epsilon)) = 2 n k/((n^2-k^2 + 1)^2 + (2 n k)^2) ,$$

have peaks corresponding to characteristic absorption processes. These are particularly important in assigning a particular process such as an interband transition or plasma resonance to the absorption. The $Im(-1/\epsilon)$ term can usually be associated with volume processes, whereas the $Im(-1/(1+\epsilon))$ term usually involves surface processes.

Two other constants which can be used to distinguish between interband transitions and plasma resonances are the optical conductivity, σ, and the absorption coefficient, α,
where
$$\sigma = 4 \pi n k/\lambda$$

$$\alpha = 4 \pi k/\lambda$$

$(\lambda = \text{wavelength}).$

A computer program was used to determine all of these constants for the thin film, and they are shown along with n and k in figures 2 - 5.

RESULTS

The normal incidence reflectivities of the thin film and quasi-single crystal as a function of photon energy are shown in figure 1. As can be seen, the crystal has much sharper peaks than the thin film. (The discontinuity in the crystal reflectivity near 12.5 eV is probably due to surface roughness and slightly different geometries in the two measurement systems.) This is quite typical of amorphous semiconductors such as the thin film (9), and indicates that the electron band structure is broadened due to imperfections in the crystal structure. A comparison of the peaks in each of these samples and those measured for a single crystal (2) is given in Table I.

TABLE I - Energy of Reflectance Peaks (eV)

Transition (2)	single crystal (2)	quasi-single crystal	thin film
$\Gamma_{15} - \Gamma_1$	$\begin{cases} 2.35 \\ 3.26 \end{cases}$	- - - -	- - - -
$\Lambda_3 - \Lambda_1$	$\begin{cases} 3.58 \\ 4.14 \end{cases}$	- - 4.13	- - 4.27
$L_3 - L_1$	$\begin{cases} 3.41 \\ 3.96 \end{cases}$	- - - -	- - - -
$X_5 - X_1$	5.41	5.51	5.45
$L_3 - L_3$	$\begin{cases} 6.90 \\ 7.49 \end{cases}$	6.95 7.51	6.89 7.29
d_1	10.6	10.4	10.4
d_2	14.6	13.8	13.6

As can be seen, almost all the peaks found in the single crystal were found in both the quasi-single crystal and the thin film. The only one that appears to be missing is the L_3-L_1 peak at 3.96 eV. (The other missing peaks are outside the range studied.) On the curves, it appears that this peak could be masked by the peak at 4.13 eV, so this is not thought to be significant. There are, however, some additional peaks that do appear in the quasi-single crystal and thin film that do not

appear in the single crystal. In order to interpret these peaks, it is necessary to look at the optical quantities derived from the reflectivities. These are shown in figures 2-5 for the thin film. Due to surface roughness and therefore inaccuracies in the absolute values of reflectivity for the quasi-single crystal, these quantities are not available for the crystal.

The most interesting peaks in both the thin film and the crystal reflectivities are the two at 8.3 and 9.5 eV. For the thin film, these points correspond with peaks in the energy loss function $Im(-1/\epsilon)$ (figure 4) and the absorption coefficient, a, and optical conductivity, σ, (figure 5). These are very close to the transition energy of 9 eV found for Zn 3d electrons in ZnTe by photoemission studies (10). This same study reported a second transition at 12.4 eV, or about 3.3-3.4 eV above the first. This is due to a splitting of the d-band caused by spin-orbit coupling. In examining the results in the present study, it is seen that there is a slight peak in $Im(-1/\epsilon)$, σ and a around 12 eV. This peak is masked somewhat by the peak at 13.6 eV.

If the d-band transitions are assigned to the peaks at 9 and 12 eV, (the splitting of the peak at 9 eV would then have to be due to imperfections in the crystal structure or a shift in energy due to charge buildup on the surface (10)) the question then arises as to the significance of the peaks at 10.4 and 13.6 eV. Looking at the energy loss functions in figure 5, it is seen that the peak at 10.4 eV results in a large peak in the surface function $Im(-1/(\epsilon +1))$. This is indicative of a surface plasma resonance. This is further confirmed by the fact that σ decreases at this point, which means that the conductivity decreases because the electrons are involved in a plasma resonance at this point. At 14.2 eV there is a small peak in the volume loss function $Im(-1/\epsilon)$ which would be indicative of a volume plasma resonance. The fact that the peak in the volume function is much smaller than that of the surface function, and that there is a displacement of the volume function from the theoretical (1) value of $\sqrt{2}$ times the surface energy is further evidence for the hypothesis that there may be some electric charge buildup on the surface. The additional peaks at 17.7 eV in the thin film and 21 eV in the crystal are probably due to transitions from lower levels and would also affect the position of the plasma resonances.

CONCLUSIONS AND RECOMMENDATIONS

The previous (2) determination of transition energies from the d-bands of Zn in ZnTe at 10.6 and 14.6 eV is apparently incorrect as applied to thin films of ZnTe. These energies are closer to photo-emission results (10) and occur at 8.3 and 12 eV, while transitions at 10.4 and 14.2 eV are in reality plasma resonances.

The accuracies of the energies determined in this study were hampered by possible charge buildup on the surface of the samples. This would seem to indicate that if optical properties of semiconductors are to be determined in the vacuum ultraviolet modifications should be made to the present system that would prevent charge buildup. One possible solution to this problem would be to arrange for some external electric field that could sweep away any charges caused by photoemission from the sample.

If semiconductor surfaces are to be used for optical coatings in space, where electric charges cannot be easily removed, then further studies should be done on the precise effect of charge buildup on optical properties. In fact, this could also be used to test the possibility that optical contamination of metallic surfaces is influenced by charging of the nearby gas molecules due to photoemission from the metallic surface.

ACKNOWLEDGEMENTS

REFERENCES

1. Braundmeir, A. J.:"Experimental Investigations of Surface Plasmon Radiation from Aluminum", Oak Ridge National Laboratory Report, ORNL-TM-2612 (1969)

2. Cardona, M. and Greenaway, D.L.:"Fundamental Reflectivity and Band Structure of ZnTe, CdTe, and HgTe", Phys. Rev. B, 1, 98-103 (1970)

3. Cardona, M. and Harbeke, G.:"Absorption Spectrum of Germanium and Zinc-blend-type Materials at Energies Higher Than the Fundamental Absorption Edge", J. Appl. Phys., 34, 813-818 (1963)

4. Crandell, M.E.:"Optical Properties of ZnTe Thin Films in the Vacuum Ultraviolet", 1973 ASEE-NASA Summer Faculty Fellowship Program, Marshall Space Flight Center, Contract No. NGT-01-002-080

5. Crandell, M.E. and Linton, R.C.:"Computer Analysis of 2 Angle Optical Reflectance Data", Appl. Opt., (submitted for publication)

6. Ehrenreich, H.:"Electromagnetic Transport in Solids: Optical Properties and Plasma Effects", Optical Properties of Solids, Course XXXIV, Enrico Fermi International School of Physics, J. Tauc, ed., Academic Press, New York (1966)

7. Linton, R.C.:"The Optical Properties of Platinum and Gold in the Vacuum Ultraviolet", NASA Technical Note, NASA TN D-7061 (1972)

8. Synchrotron Radiation Facility Users Handbook, Physical Science Laboratory, University of Wisconsin, Madison, Wisconsin

9. Tauc, J.:"Optical Properties of Semiconductors", Optical Properties of Solids, Course XXXIV, Enrico Fermi International School of Physics, J. Tauc, ed., Academic Press, New York (1966)

10. Vesely, C.J., Hengehold, R.L. and Langer, D.W.:"uv Photoemission Measurements of the Upper d Levels in the IIB-VIA Copounds", Phys. Rev. B, 5, 2296-2301 (1972)

11. Walter, J.P., Cowan, M.L., Petroff, Y. and Balkanski, M.: "Calculated and Measured Reflectivity of ZnTe and ZnSe", Phys. Rev. B, 1, 2661-2667 (1970)

LIST OF FIGURES

FIGURE 1. Normal Incidence Reflectivity of ZnTe
Thin Film and Quasi-Single Crystal.
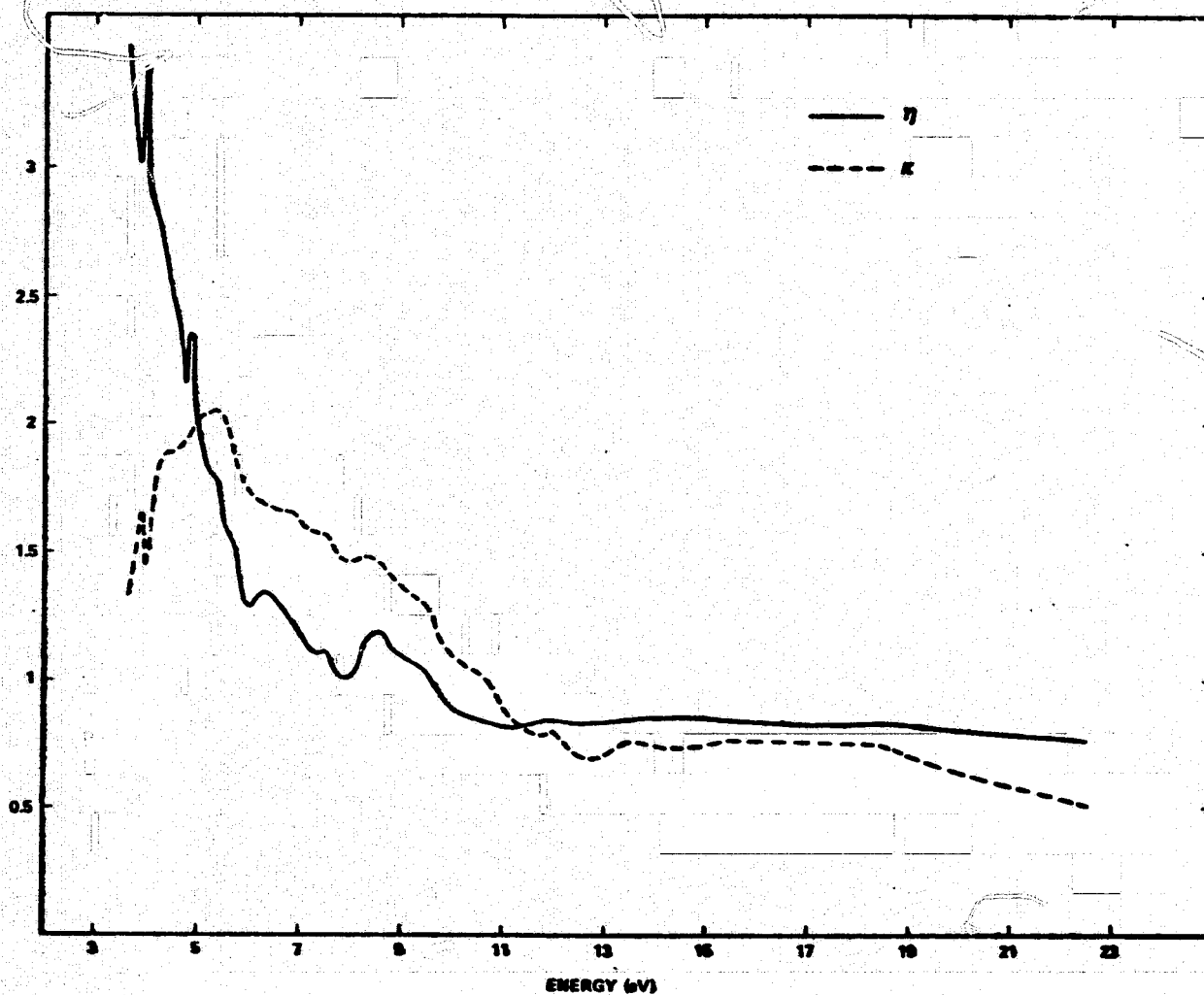
FIGURE 2. The Optical Constants n and k of ZnTe
Thin Film.
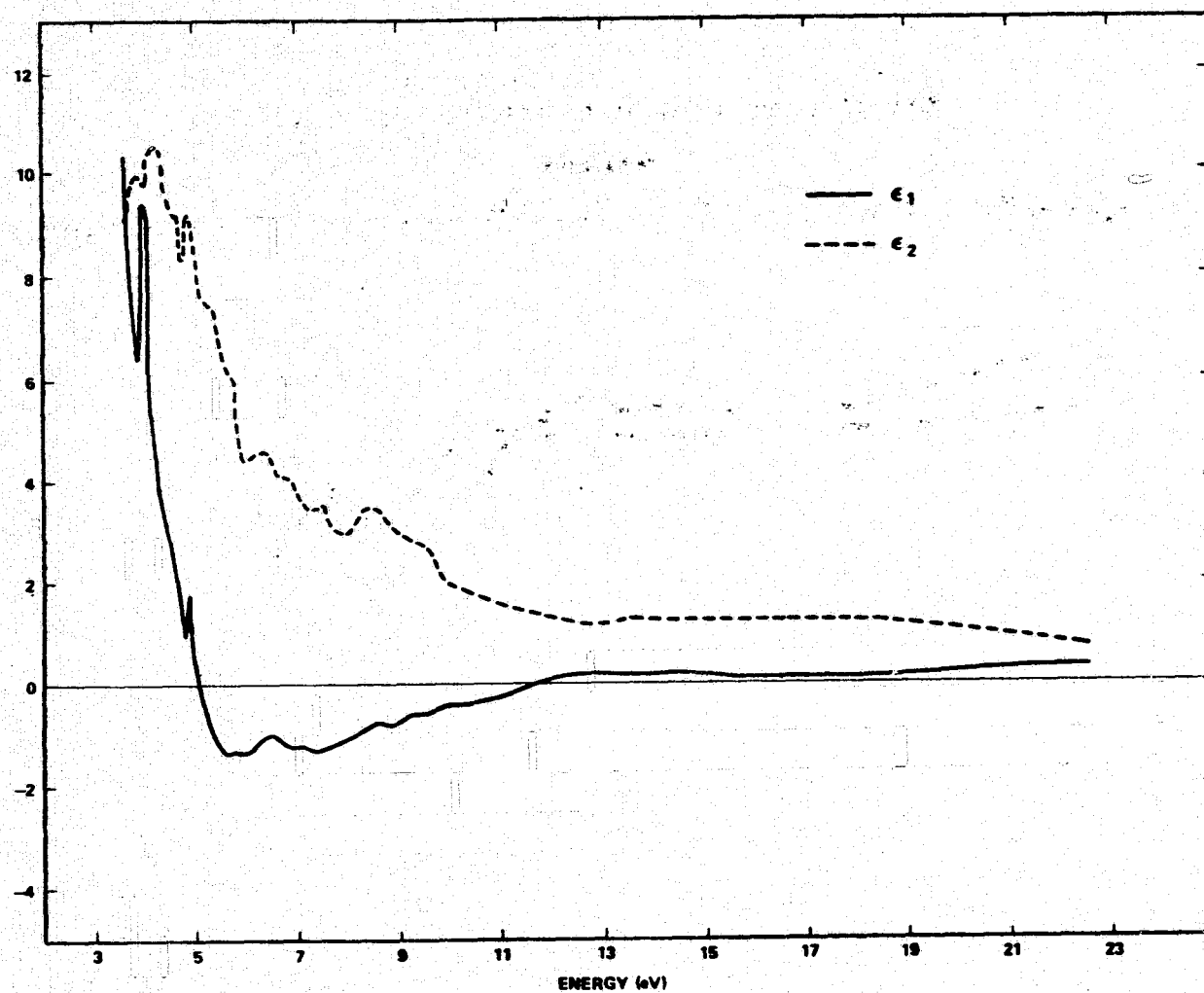
FIGURE 3. The Dielectric Constants ε_1 and ε_2 of ZnTe Thin Film.
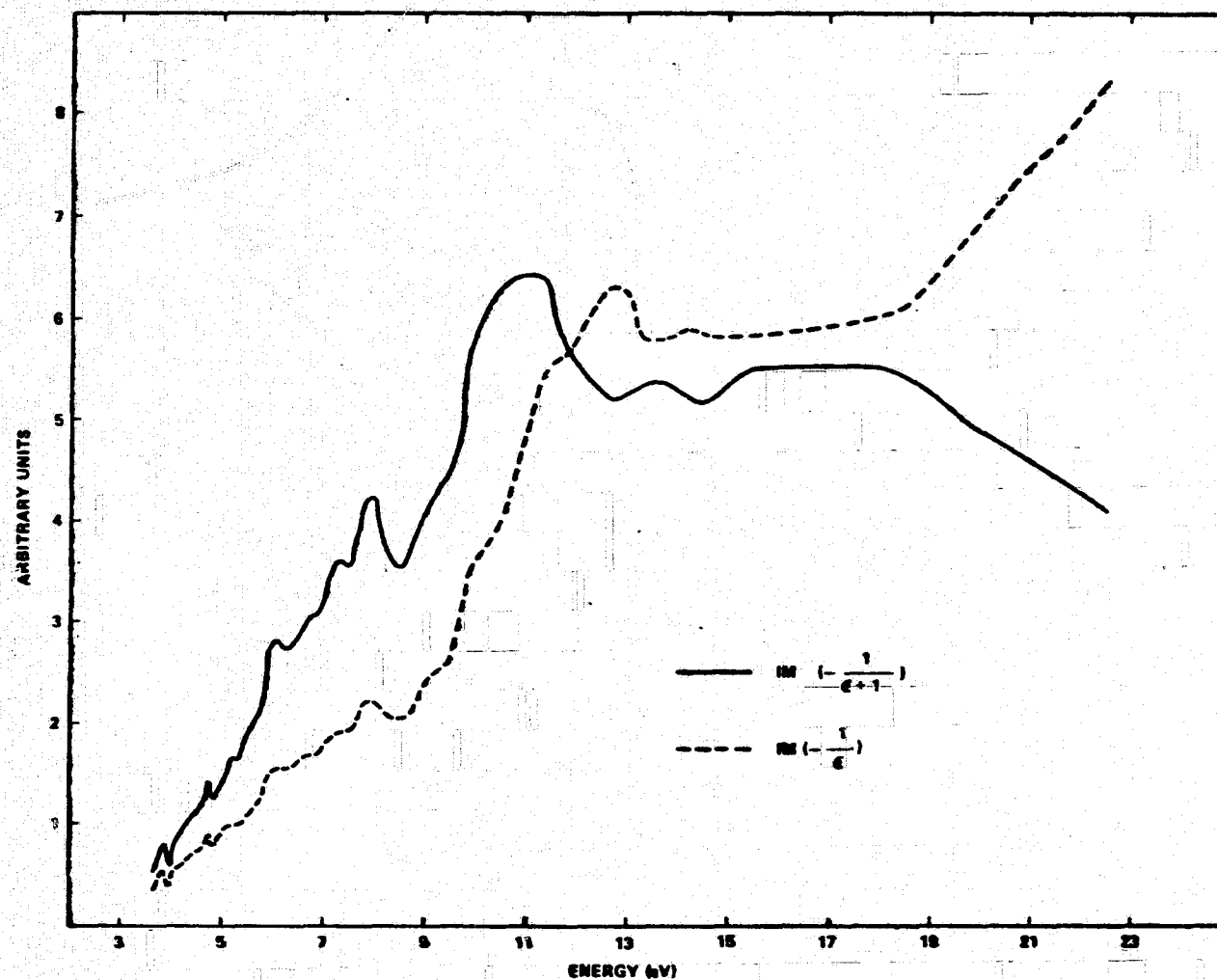
FIGURE 4. The Energy Loss Functions Im(-1/ε) and
Im(-1/(ε+1)) of ZnTe Thin Film.
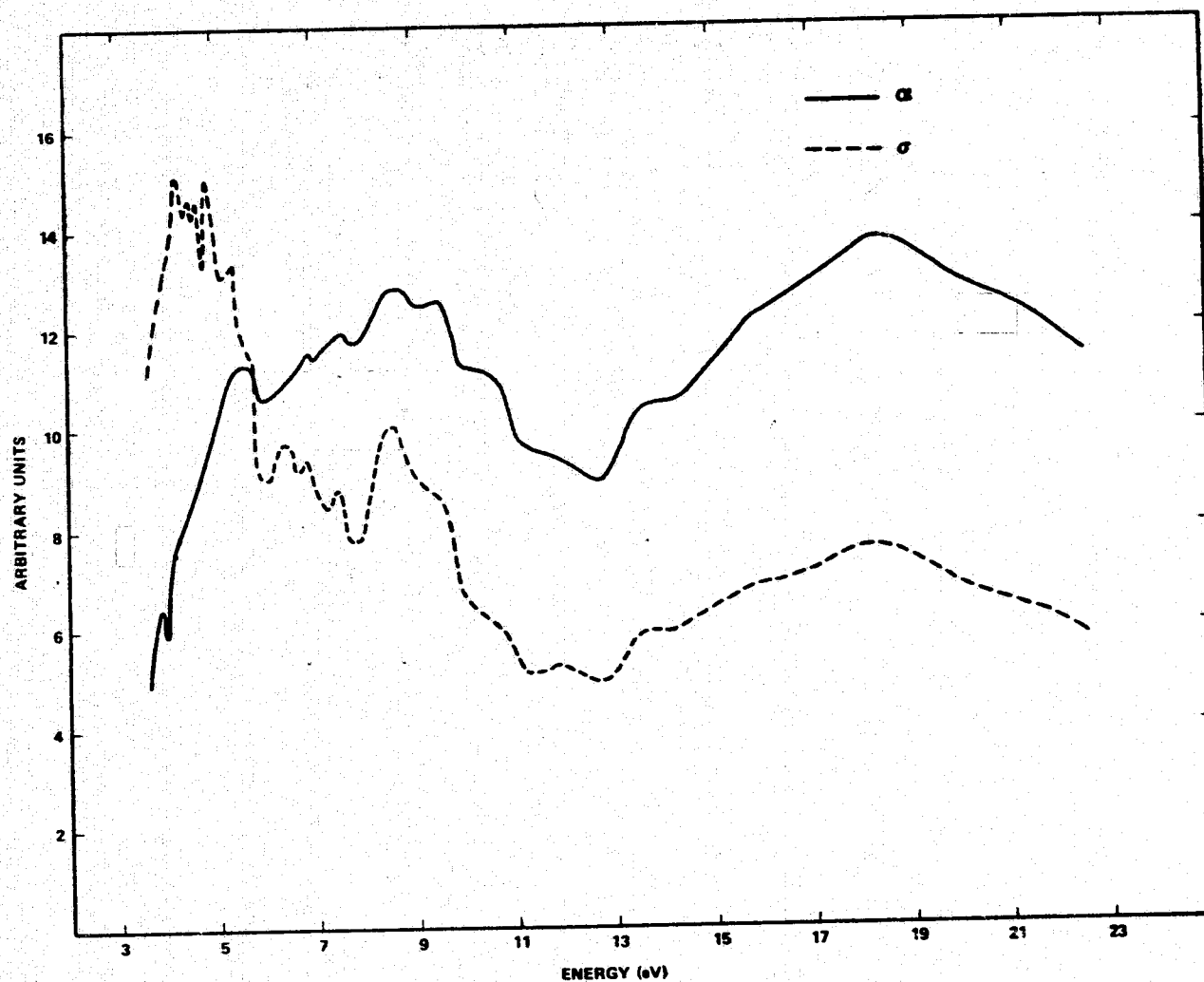
FIGURE 5. The Absorption Coefficient α and Optical
Conductivity σ of ZnTe Thin Film.

1974

ASEE - NASA SUMMER FACULTY FELLOWSHIP PROGRAM

MARSHALL SPACE FLIGHT CENTER

(AUBURN UNIVERSITY - UNIVERSITY OF ALABAMA)

CALIBRATION AND REDUCTION

OF VIDEO CAMERA DATA

Prepared by: Theodore D. Fay, Jr.

Academic Rank: Visiting Assistant Professor

Department and University: Department of Physics and Astronomy
                                      Louisiana State University

NASA/MSFC Assignment:
      (Laboratory)   Space Sciences
      (Division)   Physics, Electromagnetic
      (Branch)   Astronomy

NASA Research Colleagues: Edgar R. Miller
                                      Billy J. Duncan

Date: August 9, 1974

Contract No.:   NGT-01-003-045

CALIBRATION AND REDUCTION
OF VIDEO CAMERA DATA

By

Theodore D. Fay, Jr.

ABSTRACT

This report is divided into several parts. We consider first the effect of atmospheric scattered light on the reduction of video camera observations of solar magnetic fields. We derive equations that enable us to correct for the effect of atmospheric and instrumental scattered light during magnetograph data reduction at MSFC.

We outline two procedures for calibrating and reducing spectra recorded at 4A resolution with a video camera. We found it difficult to obtain a sufficient number of strong and unblended comparison lines for a wavelength calibration (from 4300-8600A) across the entire horizontal TV frame line. We overcame this difficulty by using a noble gas (Ne, Ar and Kr) lamp covered by glass (density 1.6) and Aluminum coated (density 1.5) filters. We calibrated our TV camera at 5.75 and 2.00 kilovolts with and without preparation of the SEC target of the camera. We constructed a microscopically reduced rule to affect a calibration between the vertical distance on the slit and the vertical lines on the TV frame. We have written (and had accepted) a proposal to Kitt Peak National Observatory to use our video camera to map the variations of the ammonia and methane bands across the disk of Jupiter and to monitor the time variations of the optical spectra of newly discovered X-ray sources.

ACKNOWLEDGEMENTS

LIST OF FIGURES

LIST OF TABLES

NOMENCLATURE

C_λ - The observed intensity difference between the circularly polarized components of the 5250A iron absorption line at any given position on the sun.

d - radial angular distance from the sun's center to position of scattered light measurement

θ - azimuth angle on the solar disk measured counterclockwise from north to the d vector.

I_λ - total unscattered light intensity at any (d, θ) position on the sun.

S - light intensity of the solar aureole at position d

C_s - fraction of polarized scattered light

$P_V(OBS)$ = fraction of circular polarization observed

$P_V(CORR)$ = fraction of circular polarization corrected for scattered light

ρ - radial distance from disk center

$\emptyset$ - position angle of the radius vector joining the disk center to point d relative to that joining the disk center to point ρ

r - is defined so that $r^2 = d^2 + \rho^2 - 2\rho d \cos \emptyset$

ψ - spread function of solar scattered light

B, C, D, G and b - spread function constants

α_i - limb darkening constants

r_{max} - angular field of view of magnetograph monitor along a radial vector from disk center that passes through the pixel with the

S_{max} - angular field of view in a direction perpendicular to the radial line

U - pixel number on the r_{max} direction

NOMENCLATURE (cont.)

V -   pixel number on the S_{max} direction

R -   angular radius of sun at time of observation

d_ℓ -   smallest value of d of any pixel on the r_{max} line

d_p -   value of d for any U, V pixel

$\phi_\vdash$ -   angle between u axis of monitor screen and radial vector from the sun's center

L_{max}, L_{min} -   maximum and minimum wavelengths of Jupiter spectral band

$I(L_p)$ -   intensity in Jupiter spectral band as a function of wavelength, L, and pixel number, p

INTRODUCTION

Television cameras (low light level vidicons) may be used to re-
cord many picture elements (pixels) of information simultaneously.
The information can be read from these cameras at very high rates
(five or more megabits per second) creating the need for sophisticated
schemes to calibrate and reduce this information. A short discussion
of video camera reduction procedures and a guide to the literature
may be found in Ref 1.

The purpose of this report is to consider several different
calibration and reduction problems of video camera data that are of
interest to the astronomy group at Marshall Space Flight Center. The
first of these is to outline a procedure to correct solar magneto-
graph observations for instrumental and atmospheric scattered light
by slightly modifying a technique developed for unpolarized continuum
light by Ref 2.

We also wish to consider procedures for calibrating and reducing
astronomical spectra recorded at 4A resolution with a video camera.
We outline our choice of wavelength standards to calibrate the hori-
zontal lines of the TV frame. The vertical calibration between
distances along the slit and the vertical TV frame lines was attempted
using a microscopic rule placed on the slit jaws. We also discuss
measurements of the light transfer function of our SEC video camera
at different voltages and target preparations. This data enables us
to convert signals from the SEC target directly to light intensity.

We also describe our Kitt Peak National Observatory proposal to
use our video camera to map variations in ammonia and methane bands
across the disk of Jupiter. Our observations will be coordinated
with photographic observations of the Lunar and Planetary Laboratory.
We also present finder charts of newly discovered X-ray sources that
will be observed at Kitt Peak and with the 0.4 meter telescope at
Marshall Space Flight Center.

MAGNETOGRAPHS AND ATMOSPHERIC SCATTERING

Let the observed intensity difference between the circularly polarized components of the 5250A line be $C_\lambda(d, \theta)$. The value of $C_\lambda(d, \theta)$ is observed to vary from place to place on the solar disk and with time. The angular distance, d, is measured from disk center to the point C (d = 1.0 for the solar limb) and θ is the azimuth angle measured counterclockwise from north to the d vector. The total un-scattered light for a (d, θ) position on the disk is $I_\lambda(d, \theta)$.

The earth's atmosphere and the observing instrument scatter sunlight over and off the disk of the sun, forming an aureole at $d > 1.0$. The intensity of this aureole, S(d) decreases with increasing d, and is usually assumed independent of θ. We assume that this scattered light is unpolarized, $C_S(d) = 0$, because: (1) the general magnetic field of the sun is less than one gauss and has no preferred polarity when averaged over the disk. (2) The polarization of skylight is small at small angles to the sun's direction (see Ref. 3). Of course $C_S(d)$ could be measured for $d > 1.0$ and corrections made for this effect. The observed fraction of circular polarization P(OBS) can be corrected by P_V(CORR).

$$P_V(OBS) = (C_\lambda(d, \theta) + C_S(d))/(I_\lambda(d, \theta) + S(d)) = C_\lambda(d, \theta)/(I_\lambda(d, \theta) + S(d))$$

$$P_V(CORR) = C_\lambda(d, \theta)/I_\lambda(d, \theta) = P_V(OBS) (1 + S(d)/I_\lambda(d, \theta))$$

The computation of P_V(CORR) proceeds as follows: first we observe $I_\lambda(d, \theta)$, the aureole function, S(d), for $d > 1.0$ and P_V(OBS). One may compute P_V(CORR) using these tabulated observations, and the above equation. To actually compute P_V(CORR), however, one must of course evaluate S(d) for $d < 1.0$. The form of S(d) is given by (see Ref. 4)

$$S(d) = \int_0^{2\pi}\int_0^1 I_\lambda(\rho) \, \psi(r) \, \rho \, d\rho \, d\phi$$

in this case $r^2 = d^2 + \rho^2 + (2\rho \cos \phi)d$. We assume that S(d) is independent of θ, and in practice the aureole is measured at a number of θ values of equal d and an average is taken. The limb darkening function $I_\lambda(\rho)$ is conveniently tabulated (see Ref. 4) in terms of $\alpha_{i\lambda}$ constants defined by:

$$I_\lambda(\rho) = 1 - \sum_{i=1}^m \alpha_{i\lambda} \rho^{2i}$$

Our preliminary measurements of S(d) for the MSFC magnetograph suggest an aureole not unlike that observed by Mattig (see Ref. 4), i.e. $S(d = 1.06) = 0.01$ and $S(d = 2.0) = 0.003$. Mullen (Ref. 4) shows that Mattig's aureole can be described by a gaussian-lorentz spread function, $\psi(r)$ as given by

$$\psi(r) = \frac{1}{B^2 + r^2} + \frac{C}{D^2 + r^2} + G \, (\exp -r^2/b^2)$$

where $B = 8 \times 10^{-3}$, $c = 9.0$, $D = 1.2$, $G = 157.3$ and $b = 0.0173$. Unfortunately the value of B has only a small effect on S(d) if $d > 1.0$ but is the dominant term in S(d) when $d < 1.0$. Mullen has, however, put lower limits on B (hence upper limits on $S(d < 1.0)$) from Mattig's observations of Mercury's transit.

Let us estimate the importance of the scattered light correction to the amount of circular polarization observed. A typical dark spot umbra should have $I(d, \theta) = 0.1$ at 5250A (see Ref. 5). For simplicity we assume the spot is located at disk center $(d = 0, \theta$ undefined). We find an upper limit of $S(d = 0)$ of 0.08 from (Ref. 4) if $S(d = 1.06)$ is about 0.01. We then compute

$$P_V(\text{CORR})/P_V(\text{OBS}) \lesssim 1 + \frac{0.08}{0.1} \lesssim 1.8$$

The corrections to P(OBS) may be almost a factor of 2, even blue sky days, so we conclude that quantitative measurements of P(OBS) should not be attempted on hazy days $(S(d = 1.06R) > 0.05$, $S(d) = 0.4$ and $P(\text{CORR})/P_V(\text{OBS}) \gtrsim 5.0)$. Our lack of knowledge of the value of the spread function constant B prevents us from deriving an accurate value of $S(d)/I(d, \theta)$ and this severely limits the accurary of $P_V(\text{OBS})/P_V(\text{CORR})$ if the correction is five times the observed value.

Finally we mention the possibility of circularly polarized penumbral light being partially scattered into the umbra. This effect would be due to atmospheric seeing and will definitely degrade the resolution of the magnetograph. It will also contract the apparent size of the umbra. The observations of Fay, Wyller and Yun (Ref. 5) indicate, however, that the umbral central regions of spot Rome Number 5759 are contaminated by the general aureole rather than penumbral detail near the umbral boundary. The spot Rome Number 5759 developed a penumbral light bridge that divided the spot umbra into two parts. The observed umbral to photosphere intensity ratios were unchanged by the large change in penumbral structure. If the umbral corrections for penumbral scattered light were important, one would expect the value of the correction to depend on penumbral structure.

We will conclude this section with a brief outline of how the value of d might be determined for each pixel on the monitor screen. Suppose the monitor is turned off the disk of the sun. Let the d value of the closest pixel to the limb be d_c. Define a (U, V) coordinate system along and perpendicular to the line between the d_c pixel and the sun's center. The value of d_c may be determined by timing the movement of the telescope drive from d_c to the closest limb relative to the drive time between limbs. The relation between the (U, V) coordinate system and that on the monitor screen (U', V') may be related by a simple rotation:

$$U = U' \cos \phi_r + V' \sin \phi_r$$

$$V = U' \sin \phi_r + V' \cos \phi_r$$

The angle ϕ_r is determined by measuring the angle between the tangent to the sun's limb and the V' axis on the monitor.

If r_{max} and S_{max} are the *half* angular sizes of the U', V axes on the screen and R is the angular radius of the sun at the time of observation then the value of d for ano U, V pixel, d_p, is given by

$$d_p(U) = d_c(1 + (U\ r_{max}/128R))$$

$$d_p(V) = (R + \sqrt{(d_p(U)\ V\ S_{max}/128R)^2 - (d_p(U)R)^2}\ )/R$$

$$d_p^2 = d_p(U)^2 + d_p(V)^2$$

Finally, Mattig (Ref. 2) has emphasized that penumbral light makes an important contribution to the aureole. For those spots where penumbral scattered light is important (i.e. those spots having penumbrae larger than 5 arc sec and high penumbral fields) we must revise the equation for $P_V(CORR)$ as follows:

$$P_{CORR} = P_{OBS}(1+S(d)/I_\lambda(d,\ \theta)) - (C_S(d)/I_\lambda(d,\ \theta)) \times \left(\begin{smallmatrix} FRACTION\ OF\ S(d) \\ FROM\ PENUMBRA \end{smallmatrix} \right)$$

A first approximation to $C_S(d)$ would be the observed value of the penumbral polarization. This correction applies only to that part of the aureole that is scattered from the penumbra, and is small unless the penumbral field is such that

$$C_S(d)/I_\lambda(d,\ \theta) > 0.2 \text{ (or 20\% polarization).}$$

## CALIBRATION AND REDUCTION OF VIDEO CAMERA SPECTRA

The spectrograph of the astronomy group at the MSFC Space Sciences Lab is a Boro Spotz instrument and gives a reciprocal dispersion of 80A/mm in second order. This spectrograph has been equipped with a Westinghouse SEC vidicon camera (WX-30791NC, S-20 photocathode) that responds to light from 4000-8500A. The camera has a commercial TV field of 256 horizontal lines that are read each 1/60 sec. Each alternate horizontal line field is displaced by one-half line to achieve 512 lines horizontal resolution. The SEC photocathode size is 25mm so that the corresponding number of lines/mm is 512/25 or about 20/mm. Therefore, our spectral resolution is about (80A/mm)/20mm = 4A.

The slit of the spectrograph is about 25mm long and the focal ratio of camera lens to collimator lens on the spectrograph is about 6. There are 256 vertical lines on the 25mm photocathode (or 10 lines/mm). Hence, there are only 40 horizontal lines of spectral information recorded on each frame, because only about 25mm/6 or 4mm of the photocathode can be illuminated by light from the slit.

In order to record a spectrum of the light entering the slit on the TV monitor as shown in Figure 1, we must prepare the SEC target by a series of readings of the target and series of light flashes of the photocathode. After target preparation, the photocathode is exposed to the spectrum until it is fully charged. The target is then read, and the analog signal is stored on a Data Disk, Inc. Model 6236 Recording System. The output of the disk can be fed to a Colorado Video, Inc. Model 260, Bandwidth Compressor that converts the analog signal into digitized spectra (about 40 horizontal spectra and 64 grey levels of intensity at each wavelength) onto magnetic tape. See Ref. 6 for the detailed description of this system.

We placed a submillimeter rule on the slit to make a calibration between the slit and the recorded spectra of each horizontal line. Marks on the microscopic rule were made at intervals of 25mm/40 (or about 0.6mm) apart to establish a relation between each TV line number and position on the slit. Later we found that we could monitor the slit with a Panasonic commercial TV camera and monitor as shown in Figure 1. The resultant magnification of the monitor image allows calibration of the slit with a millimeter rule. The Panasonic camera has only 10 grey levels, however, so that the rule on the slit may be needed where high contrast is required, i.e., planetary spectroscopy.

In addition to the slit calibration, we must calibrate position on the horizontal line versus wavelength. We chose to do this with a
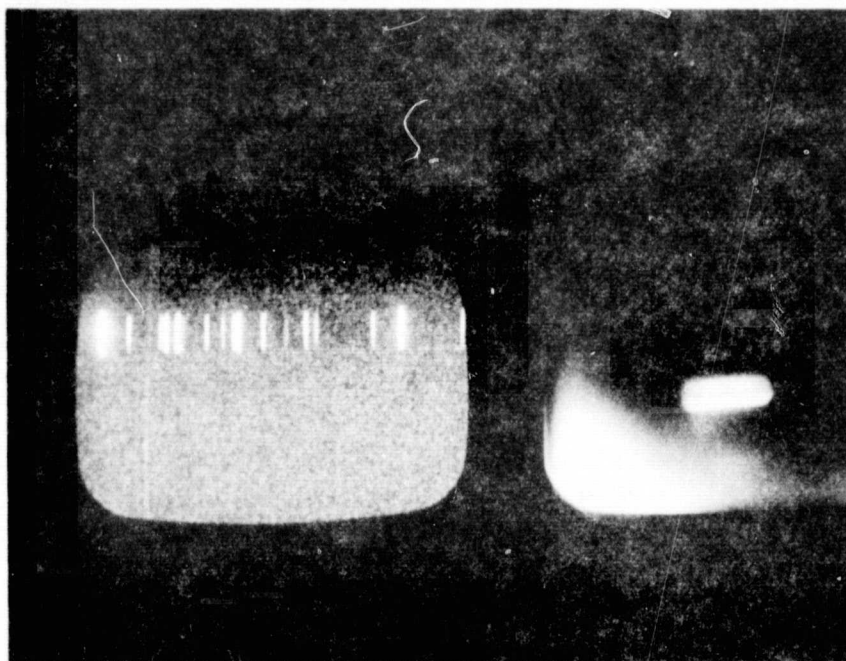
5800A   7245A   Panasonic camera
NE30 LAMP SPECTRUM   view of spectrograph
slit

Figure 1.

General Electric NE 30 noble gas lamp. This lamp provides numerous unblended Ne, Ar and Kr lines at 4A resolution from 4000-8500A. We show a 5700-8500A spectrum of this lamp on Figure 2 of TV frame line 140. The exposure time is 1/30 sec. The 64 grey levels of intensity (SEC Signal) are shown on the vertical axis. We must also calibrate the intensity of this signal . with light intensity on the photocathode.

We use a series of filters placed before the slit to aid in the wavelength and intensity calibration of the noble gas lamp. Sample spectra are shown on Figure 3a to 3d, with wavelengths indicated. These spectra are polaroid photographs of the waveform monitor. The spectra from 4300-5800A were made with a Density 1.5 Aluminum filter and the 5800-8500A spectra were made with a density 1.5 Al filter, plus a density 1.6 glass filter. The glass filter has an infrared leak allowing us to record the 7500A and longer wavelengths at the same signal as 6000A wavelengths, despite the drop in camera sensitivity. Table 1 gives data on the noble gas spectra and Table 2 lists the wavelengths. Unblended lines are listed with an asterisk, and these lines should make the best wavelength standards, as listed in Ref. 7.

A calibration between wavelength and pixel number is established with a peak picker computer program that finds the pixel numbers closest to the emission peaks. A polynomial least squares program then establishes a relation between the peak pixel numbers and the comparison line wavelengths.

The final calibration is to convert signal from the target to light intensity. We calibrated the target by exposing the spectrograph to the NE30 noble gas lamp from periods of 4, 8, 16, 32 and 64 sec. We have plotted exposure versus signal on Figures 4 and 5. We find a flattening of the light transfer function if we prepare (flash) the target, i.e.

log (INTENSITY) = 1.64 log (SIGNAL)

This was done by flashing the target 5 times, reading 10 times and repeating this cycle 12 times. The prepared target curves are shown on Figure 4 (red lines) and Figure 5 (5400A lines) by solid lines. The Figure 5 data were taken from spectra shown on Figure 6. The dashed curve is the light transfer function of an unprepared target. There is a linear relation between signal and exposure if the target is not flashed:

log (INTENSITY) = 1.00 log (SIGNAL)

TABLE 1

JOURNAL OF NOBLE GAS SPECTRA

Figure Number	Grating Position	Order Wavelength	Density of Filter	Camera Exposure	6000A Filter
3a,b	2.45	5100 (2nd)	1.5 Al	32 sec	no
3c,d	1.00	6500 (2nd)	1.5 Al+1.6 glass	16 sec	no
3e	3.15	7700 (1st)	"	8 sec	no
3f	2.60	8400 (1st)	"	64 sec	yes
3g	2.45	8600 (1st)	1.5 Al	512 sec	yes
3h	2.45	4300 (2nd)	1.5 Al	32 sec	no
6a	2.45	4800 (2nd)	1.5 Al	4 sec	no
6b	"	"	"	8 sec	no
6c	"	"	"	16 sec	no
6d	"	"	"	32 sec	no
6e	"	"	"	64 sec	no

6a-e done with target preparation (5 flashes, 10 reads) x 12 repetitions

6f-e done without target flashing otherwise identical to 6a-e

TABLE 2

NOBLE GAS EMISSION LINES AT 4A RESOLUTION

Density 1.5 Aluminum Filter

Element of Line	Peak Wavelength Angstrom	Line Sec Signal (110 Full Scale)	Strength Handbook of Physics
Kr	4318.55	110	5.66
	4319.57		
Ar	4333.56*	90	3.32
Ar	4345.17	20	2.91
Kr	4362.64*	110	4.96
Kr	4376.12*	110	5.21
Kr	4453.92	80	5.25
Kr	4463.69	110	5.03
Kr	4502.35*	110	5.12
Ar	4510.73	15	3.12
Ne	5037.75*	45	4.27
Ne	5080.38	22	4.04
Ne	5116.50*	40	4.27
Ne	5144.94	12	3.91
Ne	5188.61	12	3.81
Ne	5330.78	90	4.55
Ne	5341.09	110	4.54
Ne	5400.56*	110	4.73
Ar	5495.87	15	2.72
Ar	5558.28	-	2.84
Kr	5570.28*	96	5.94
Ne	5656.66*	30	4.20
Ne	5689.81	10	4.17
Ne	5748.30	15	4.4
Ne	5764.42*	90	5.08
Ne	5820.16	20	4.87

INSERT DENSITY 1.6 GLASS FILTER TO RECORD 5850A to 8000A LINES
AT EQUAL SIGNAL STRENGTH

Ne	5852.48	110	5.90
Ne	5881.89	18	5.23

TABLE 2 (cont.)

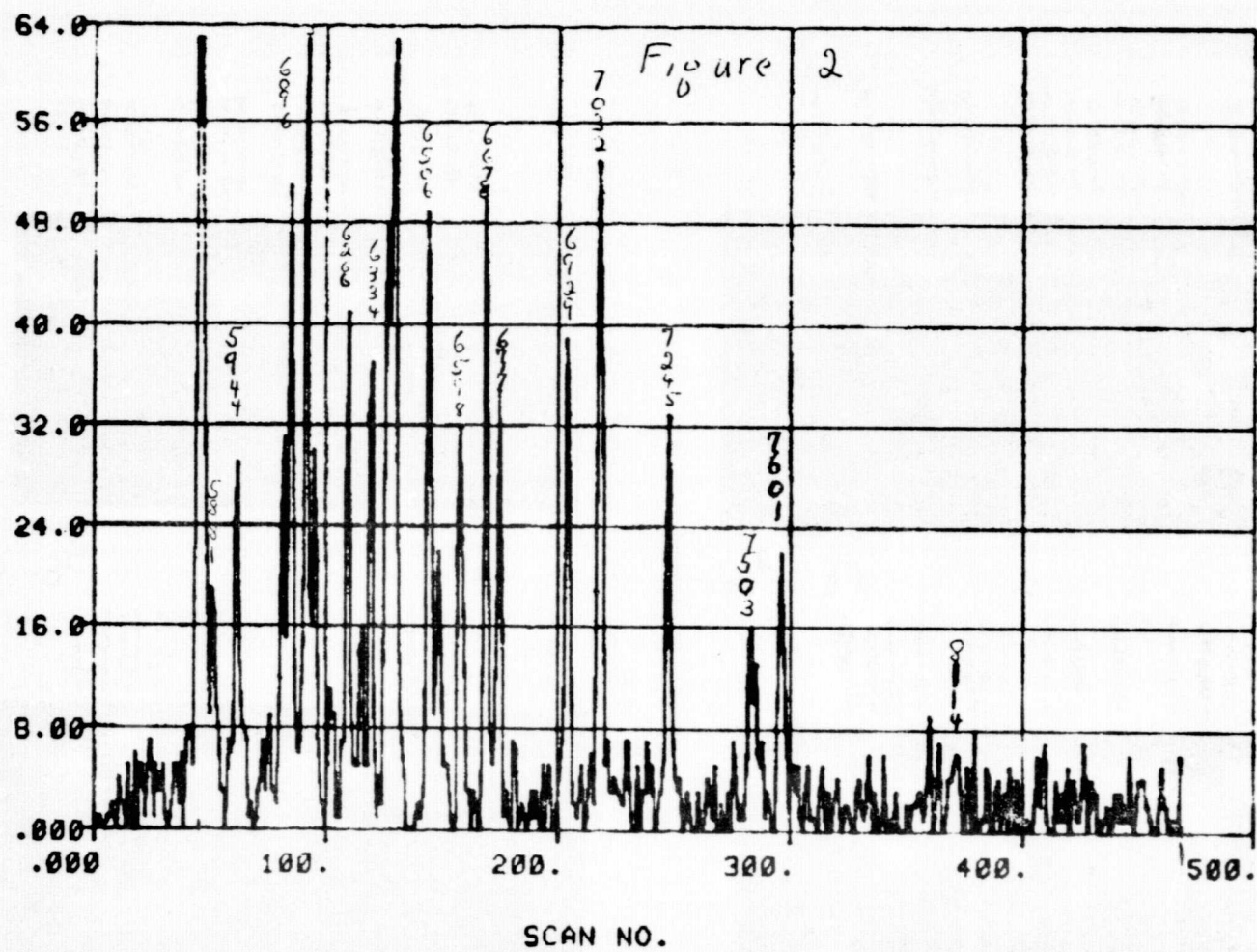| Element of Line	Peak Wavelength Angstrom	Line Sec Signal (110 Full Scale)	Strength Handbook of Physics
Ne	5944.83*	22	5.36
Ne	6074.33*	38	5.41
Ne	6096.16*	38	5.42
Ne	6143.06*	55	5.48
Ne	6163.59	18	5.23
Ne	6266.49	33	5.34
Ne	6304.78	17	5.42
Ne	6334.42	28	5.57
Ne	6382.99	45	5.50
Ne	6402.24*	70	5.93
Ne	6506.52*	52	5.63
Ne	6532.88	22	5.38
Ne	6598.95	30	5.74
Ne	6678.27*	70	5.84
Ne	6717.04*	55	5.76
Ne	6929.47*	90	5.96
Ne	7032.41*	110	5.73
Ne	7059.10	20	4.9
Ne	7173.94	30	5.79
Ne	7245.16*	110	5.75
Ar	7383.97*	15	5.02
Ne	7438.89*	70	5.51
Ne	7488.87	80	5.39
Ar	7503.86*	90	5.35
Ne	7535.77	70	5.35
Ne	7544.04	80	4.96
Kr	7587.41	75	6.36
Kr	7601.55	100	6.91
Ar	7635.11*	100	5.53
Kr	7685.24*	55	6.37
Ar	7723.75*	40	5.44
Kr	7854.82*	30	6.45
Ar	7948.17	20	5.13
Ar	8014.78*	20	5.30
Kr	8059.50*	30	6.42

TABLE 2 (cont.)

Element of Line	Peak Wavelength Angstrom	Line Sec Signal (110 Full Scale)	Strength Handbook of Physics
Kr	8104.36*	110	6.81
Ar	8103.69	wk	5.30
Ar	8115.31	100	5.58
Kr	8112.90	100	6.99
Kr	8190.06*	20	6.68
Kr	8263.24*	30	6.76
Kr	8298.11*	20	6.86
Ne	8377.61*	25	5.96
Ar	8408.21	1	5.36
Kr	8508.87	1	6.54
Kr	8776.75	1	6.94

Figure 2

LINE NUMBER 140

Fig 3a

Fig. 3b

Fig 3c

Fig 3d

Fig. 3e.

Fig. 3f. 8114A at left edge,
light short of 6000A blocked

```
↑ ↑ ↑↑↑   ↑↑ ↑↑↑↑↑↑↑ ↑↑
7 7 777   77 7788888 88
1 2 34    67 890011234
7 4 83    82 541519670
3 5 39    53 484940388
```

```
↑↑↑↑↑↑↑ ↑ ↑
8888888 8 8
1223456 6 7
1697005 5
0388884 4 6
```
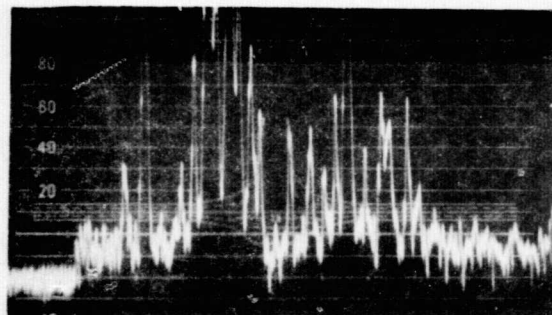
Fig. 3g. 8508A off left edge
light short of 6000A blocked
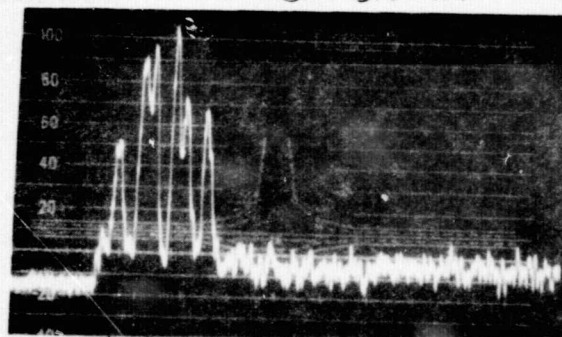
Fig. 3h, same as Fig 3g
-6 spectrum, but 6000A and shorter
wavelengths permitted from 2ND ORDER

```
↑ ↑ ↑↑↑
8 8 888
5 6 789
0 5 752
8 4 638
```

```
↑↑ ↑ ↑↑ ↑
44 4 44 4
33 3 74 5
33 7 70 0
93 6 73 2
```

Figure 4

Figure 5

LOG SIGNAL

LOG EXPOSURE

● TARGET FLASHED
X TARGET UNFLASHED

7-23

Figure 6

SEC TARGET NOT FLASHED   SEC TARGET FLASHED
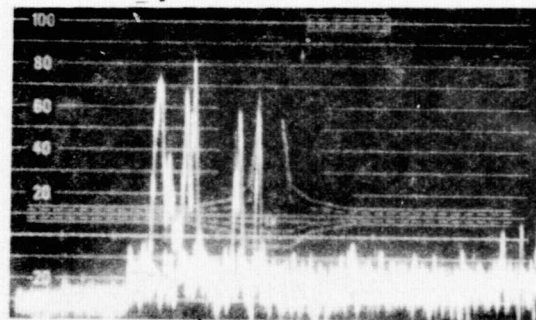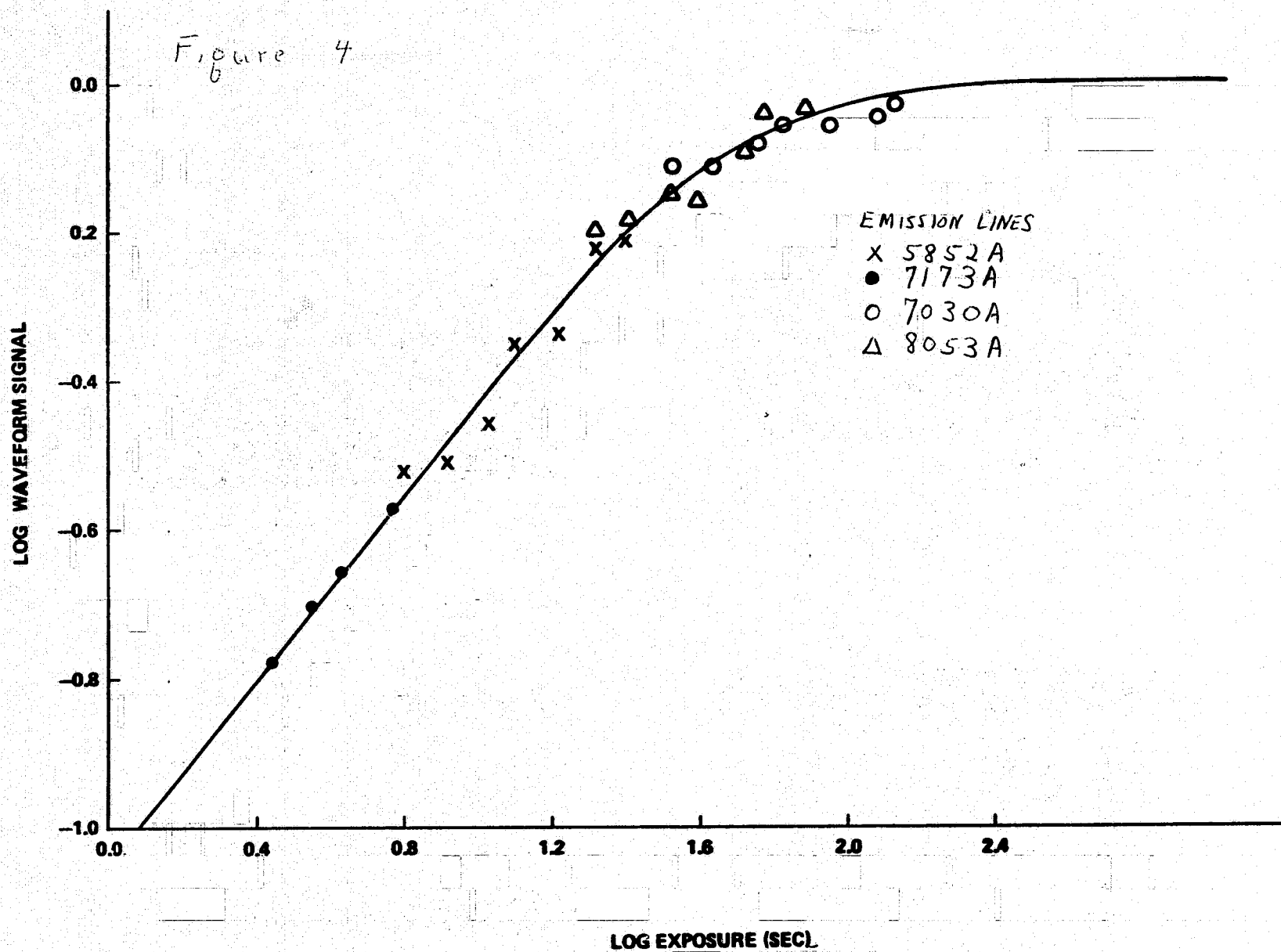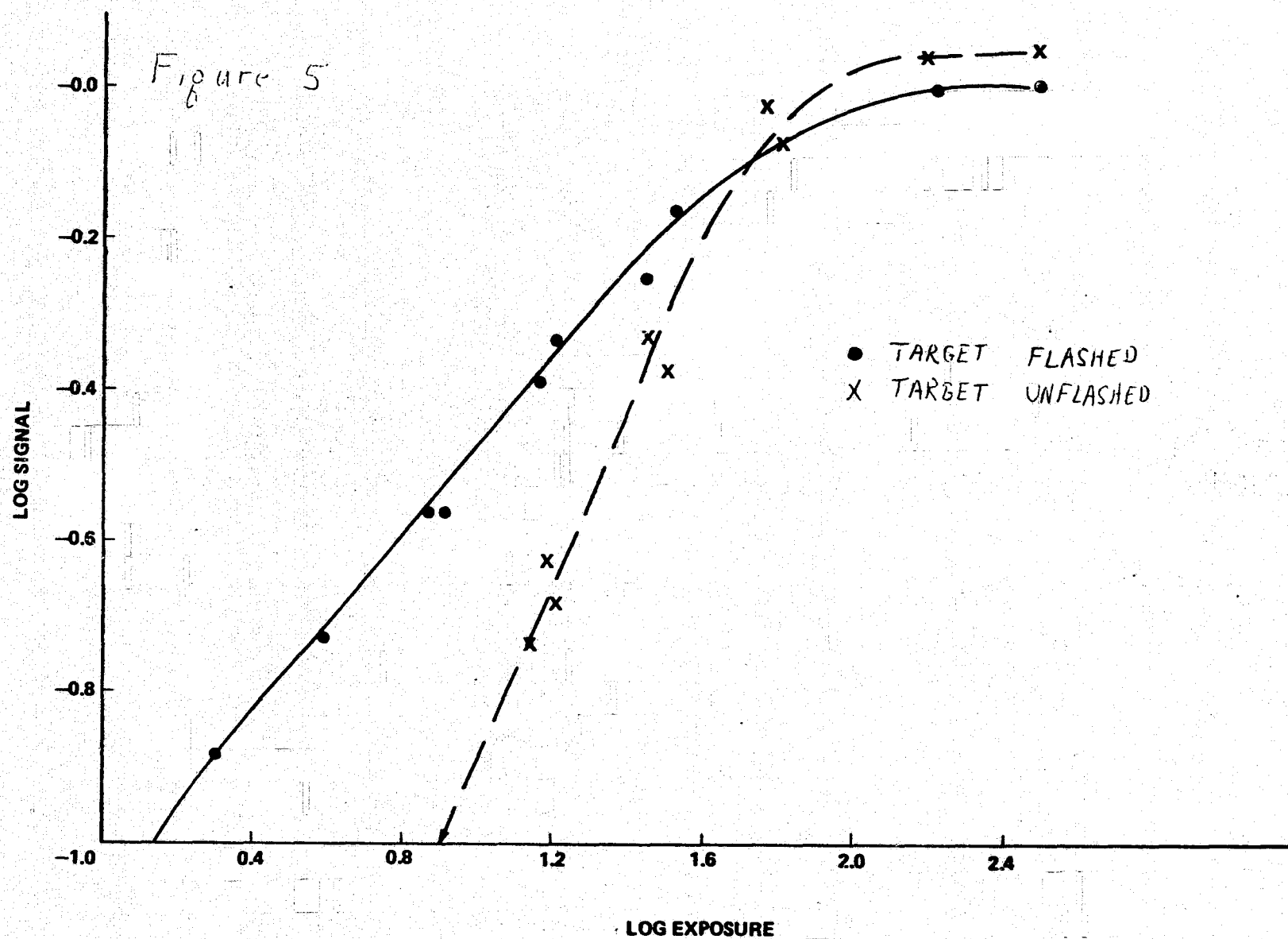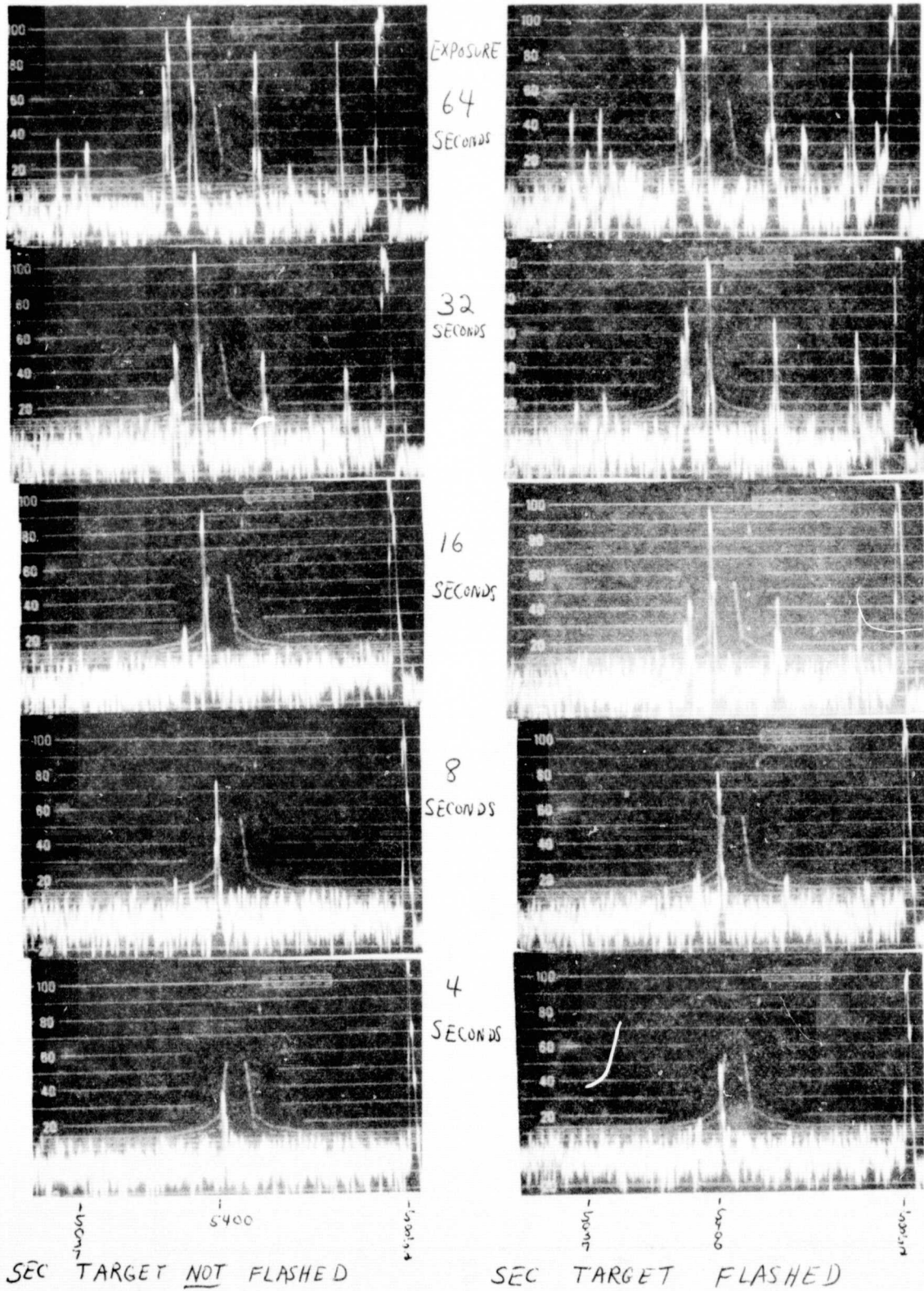
There appears to be an optimum gain in signal of a factor of about two if the target is prepared for exposures that are a factor of ten below saturation levels. The signal gain in preparing the target is dependent on the number of flashes per read. We empirically determined that 12 cycles of 5 flashes per 10 reads is optimum. More repetitions do not significantly increase signal and simply waste time in preparing the target. We emphasize that the calibration of the target is critically dependent on the number of target flashes per read, and must be recalibrated when this setting is changed. We also found that the voltage on the photocathode must be about 5.75 kilovolts, and not near 2.00 kilovolts, so that signal will not be sensitive to small voltage changes, and photocathode gain will be optimum. A final note about the reduction of these spectra concerns suppression of the high frequency pre-amp noise seen on the waveform monitor photographs in Figure 3a - 3d. We suggest that the data be treated with a running gaussian whose width is half that of the spectral lines. This procedure will suppress high frequency noise. A thorough treatment of noise suppression by modulation transfer function and fourier transform techniques may be found in Ref. 8.

METHANE AND AMMONIA MAPPING OF JUPITER

The importance of an extensive program to map the time and spatial variations of CH_4, NH_3 and continuum bands across the disk of Jupiter has been demonstrated in Ref. 9 and 10. These Jovian observations are essential if a realistic model of density and temperature variations of the gas above the cloud top layer is to be made. Dr. Willem Wamsteker and the author have submitted and had approved a Kitt Peak National Observatory proposal to use the MSFC video system coupled to the 1.5 meter McMath solar telescope for the purpose of mapping the NH_3 and CH_4 bands on Jupiter's disk between 5800A and 8000A.

The wavelength ranges of the features we propose to map are shown in Table 3. We will define CH_4, NH_3 and continuum indexes for each part of Jupiter's disk by integrating the calibrated intensities from each pixel, p, between the upper and lower wavelength limits, L_{max} and L_{min}, for each range.

$$\text{Band Index} = \int_{L_{min}}^{L_{max}} I(Lp)dLp$$

It is our hope that this averaging procedure will produce band indexes accurate to 2%, because we will average over 100A/4 = 25 pixels and have a signal/noise of 12 per pixel. Four CH_4 bands of different strengths were chosen to construct CH_4 curves of growth.

TABLE 3

BAND INDEXES FOR JUPITER MAPPING

Wavelengths

L_{min} Angstrom	L_{max} Angstrom	Feature Definition
1. 6010	6130	Continuum
2. 6130	6262	CH_4 (strong)
3. 6310	6370	Continuum
4. 6420	6546	NH_3
5. 6570	6700	CH_4 (weak)
6. 6700	6800	Continuum
7. 6870	6930	Continuum
8. 6930	7090	CH_4 (very weak)
9. 7150	7445	CH_4 (very strong)
10. 7445	7610	Continuum

A LIST OF RAPIDLY VARYING STARS

Our video system is especially suited to recording the spectral variations of all types of rapid variables. One group of these variables, (those with X-ray counterparts) are important enough to be discussed separately in this report. In this section we list an example (Table 5) of the brightest star in each of the other rapid variable star groups. Finder charts for these objects are enclosed in Figure 7.

TABLE 4

RAPID VARIABLE STARS

Star Name	BD Number	1970 R.A.	Coordinates Dec.	Spectral Type	Visual Mag	Variable Group
T Tauri	$10^{\circ}706$	04:19.1	19:27	G5	10-13	T Tau
RW Aur	$30^{\circ}792$	05:06.2	30:21	G5	10-13	RW Aur
AI Vel	CPD-$44^{\circ}2376$	08:13.1	-44:04	A2-F2	6.4-7.1	Cepheid
VZ Cnc	$10^{\circ}1848$	08:39.3	+9.55	A7-F2	7.2-7.9	Cepheid
Z Cam	-	08:21	+73:13	Pec	10-14	U Gem
AG Peg	$11^{\circ}4673$	21:49.6	12:29	Pec	7-9	Symbiotic
Z And	$48^{\circ}4093$	00:01	48:36	Pec	8-12	Symbiotic

OPTICAL SPECTRA OF HIGH ENERGY TARGETS

Ostriker and Davidsen (Ref. 11,12) have shown that optical and infrared observations of the time variations of X-ray sources can help in building models of these sources. We therefore think it worthwhile to monitor these sources with the video data system recently constructed at the MSFC Space Sciences Lab. These sources show rapid (as fast as 100msec) changes in X-ray intensity (Ref. 13, 16) as well as rapid variations in hydrogen line emission at optical wavelengths (Ref. 14).

The time resolution of our video system is limited by the time required to charge the SEC target for each spectrum. Estimates of this time (based on past observations) are about 1 min for a V=6.0 magnitude star and about 16 min if V=9.0. We assume the use of a 0.4 meter telescope and a 4A resolution spectrograph. Our video system allows us to record up to 40 successive spectra per TV frame.

Each frame will therefore display wavelength on the x-axis (4000-8000A) and time change on the y-axis. Our data are then digitized and read onto magnetic tape for further reduction.

The X-ray sources selected for study with our video system are shown in Table 5. A literature search was made for the X-ray sources with the brightest optical counterparts (see Ref. 23). These bright sources will allow the highest time resolution for a given sized telescope and spectral resolution. Only three sources (0900-40, 1700-37, and 1956+35) have firmly established correlations between optical and X-ray time variations. The other X-ray sources are co-incident with variable stars to within 2 arc min. Figure 7 gives finding charts for these X-ray sources.

INDIVIDUAL SOURCES

I. Possible Collapsars

Recent optical observations of the 06 star 1700-37 are given in Ref. 14, 16, 17, 22 and 24. There are no observations of this star at wavelengths longer than 5000A, except Ref. 24. A recent discussion of the 5000-7000A spectra of 0 stars is given in Ref. 25. Additional optical observations of the 09.5I star 1956+35 could distinguish between the collapsar models and those involving a triple star system (see Ref. 27). The time variations near 6500A have been described by Ref. 26, but the authors request additional observations. An object related to 1700-37 and 1956+35 is 0900-40.

II. Supernovae Remnants

The Cygnus loop is of interest because of a possible X-ray pulsar at the center of the loop (period = 63msec). This pulsar may be coincident with an H II region. Spectrophotometry of the loop center (done as described in Ref. 21) would be of interest. The crab nebula central regions should be scanned for comparison.

III. U Geminorum Stars

Possible X-ray emission has been reported for SS Cygni in Ref. 28.

IV. Unclassified Sources

We need additional spectral classification for stars within 2 arc min of sources 1758-25 and 2030+40. The U-B of source 1758-25, GX5-1, No. 3 is -0.4 in Ref. 19 and +0.12 in Ref. 15. The spectral

Cygnus X 1 Fig. 7a   Fig. 7b   Figure 7
HDE 226868   3U 2030+40
3U 1956+35   V=8.9   BD+40 4218   V=9.1
              O9.5
NORTH   NORTH
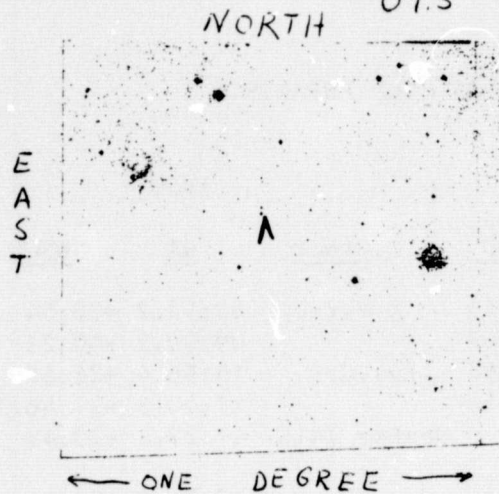
EAST   WEST

← ONE DEGREE →   ← ONE DEGREE →
   1975   1975
α = 19:57.5   α = 20:31.3
δ = +35:08   δ = 40:52

Fig. 7c   Fig. 7d
  SS Cygni   3U 1901+03   V=9.2
3U 2142+43   V=8-12   BD+2°3771   BO

NORTH   NORTH

EAST   WEST

← ONE DEGREE →   ← ONE DEGREE →
   1975   1975
α 21:43.0   α 19:03.0
δ 43.27   δ +3:03

7-29
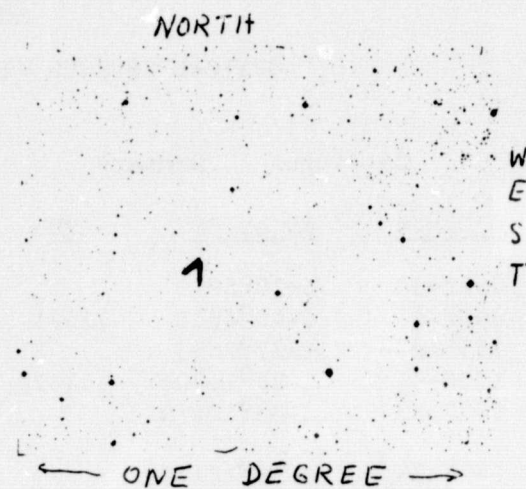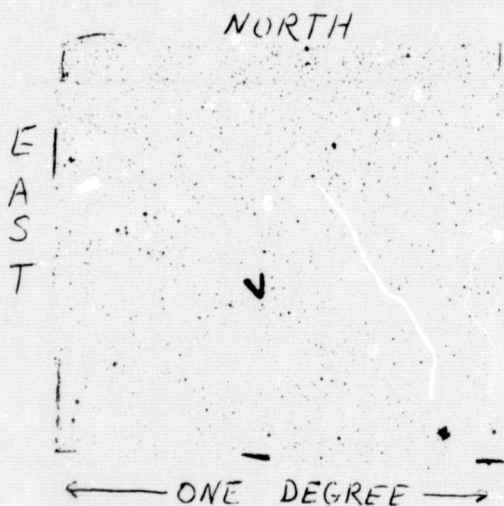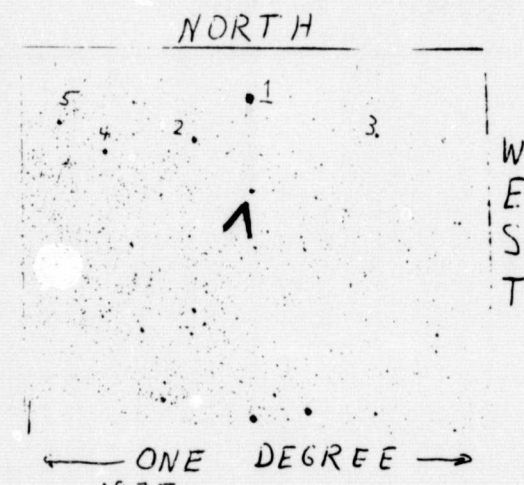
type of Henize 1416 is listed as Be in Ref. 18 and A1I in Ref. 15. The optical identification of 1727-33 could be SAO 20881 or Henize 1416.

TABLE 5

OPTICAL SOURCES WITH X-RAY COUNTERPARTS

Catalogue	Numbers				1950	
3 Uhuru	CD or BD	HD	SAO	Other	RA	DEC
0352+30	B+30°591		056815	X Persei	03:52.2	+30:54
0900-40	C-40°4838	77581	220767		09:00.2	-40:21
1555+27	B+27°2558		084098	Eps.Crb.	15:56.4	+26:58
1700-37	C-37°11206	153919	208356		17:00.5	-37:46.5
1727-33	C-33°12119			Henize 1416	17:27.1	-33:43
1727-33	C-33°12117		20881		17:26.8	-33:41
1735-28	C-28°13401			Henize 1450	17:36.4	-28:34
1755-33	C-33°12697		209568		17:56.6	-33:53
1758-25				GX5-1	17:58.0	-25:04
1901+03	B+2°3771		124218		19:01.7	+03:01
1915-05	B-5°4936		143286	26 Aql.	19:18.0	-05:31
1956+35	B+34°3815	226868	069181	Cygnus X-1	19:56.5	+35:04
2030+40	B+40°4218		049756		20:30.3	+40.47
2050+30				Cygnus Loop	20:49.7	+30.43
2142+43	B+42°4186			SS Cygnus	21:41.6	+43.21

TABLE 5

ADDITIONAL INFORMATION ON SOURCES

3 Uhuru	RA	1975 DEC	Visual Mag	Color B-V	Spectral Type	GEN. REM.
0352+30	03:53.7	+30:59	6.0-6.6		B0p, Ope	
0900-40	09:01.2	-40:27	6.9	0.48	B0.5Ib	collapsar?
1555+27	15:57.4	+26:58	4.2,12.6	Ref. 20	KIII+?	sep=2"
1700-37	17:02.2	-37:48	6.6	0.27	06.5f	Ref. 6
1727-33	17:27.7	-33:44	10.0	2.09	Ale, Be?	Ref. 5
1727-33	17:27.4	-33:42	6.7	0.14	B0III	"
1735-28	17:37.0	-28:41	11.1	1.01	Be	"
1755-33	17:58.1	-33:53	8.3	0.20	B1Ib	"
1758-25	17:59.5	-25:04	11.8	0.20	?	?
1901+03	19:03.0	03:03	9.2	0.63	B0III	
1915-05	19:19.2	-05:29	5.1	Ref. 20	G8III	binary
1956+35	19:57.5	+35:08	8.9	0.85	09.5I	collapsar?
2030+40	20:31.3	+40:52	9.1	?	?	Ref. 23
2050+30	20:50.7	+30:48	17	supernova remnant		
2142+43	21:43.0	+43:27	8-12		A1+dGep	U. Gem.

CONCLUSIONS

We conclude that correction of solar magnetograph observations for scattered light is important and that the correction formulae considered in this report should be applied to the magnetograph data on a routine basis.

We have outlined a procedure for the calibration and reduction of video camera observations with a spectrograph at 4A resolution. The wavelength calibration has been aided by the use of glass and Aluminum filters to achieve approximately equal signal from emission lines between 4300-8500A. The vertical calibration of the slit has been aided by mounting a TV camera to view the slit and by the use of a microscopic rule placed on the slit. We have also established that the light transfer function of our target is sensitive to target preparation. The relation between signal and exposure is linear if the target is not flashed and flashing the target can increase signals that are near 10% of saturation by a factor of two or more.

We have submitted and had approved a proposal for the use of the 1.5 meter McMath solar telescope at Kitt Peak National Observatory to map CH_4 and NH_3 bands across the disk of Jupiter and to monitor the variations of X-ray sources with bright optical counterparts. We have six nights on the telescope from Sept. 1 to 10, 1974, and look forward to being able to interpret these observations using our video system.

REFERENCES

1. Morton and Chevalier, <u>Astrophysical Journal</u>, Vol. 174, Page 489, Jun. 1972.

2. Mattig, W., <u>Solar Physics</u>, Vol. 18, Page 434, July 1971.

3. Jenkins, F. A. and White, H. E., <u>Fundamentals of Optics</u>, (McGraw-Hill, New York), Page 498, Jan. 1957.

4. Mullen, D. J., <u>Solar Physics</u>, Vol. 32, Page 65, July 1973.

5. Fay, T. D., Wyller, A. A. and Yun, H. S., <u>Solar Physics</u>, Vol. 23, Page 58, Sept. 1972.

6. Honeycutt, R. K., Report, ASEE-NASA Summer Faculty Fellowship Program, Marshall Space Flight Center (University of Alabama-Auburn University), August 1973.

7. Crosswhite, H.M. and Dieke, G. H., <u>Handbook of Physics</u>, 3rd <u>Edition</u>, American Institute of Physics, New York, Jan. 1968.

8. Brault, J. W. and White, O. R., <u>Astronomy and Astrophysics</u>, Vol. 13, Page 169, Jan. 1971.

9. Avery, R. W., Michalsky, J. J. Jr., and Stokes, R. A., <u>Icarus</u>, Vol. 21, Page 47, January 1974.

10. Michalsky, J. J., Stokes, R. A. Avery, R. W. and De Marcus, W. C., <u>Icarus</u>, Vol. 21, Page 55, January 1974.

11. Davidsen, K. and Ostriker, J. P., <u>Astrophysical Journal</u>, Vol. 79, Page 585, Jan. 1973.

12. Ibid, <u>Astrophysical Journal</u>, Vol. 189, Page 331, April 1974.

13. Hoover, R. B., Thomas, R. J. and Underwood, J. H., <u>Adv. Space Sci.</u> and <u>Tech.</u>, Vol. 11, Page 118, 1972.

14. Bopp, B. W., Grupsmith, G. and Vander Bout, P. A., <u>Bull. A. A. S.</u>, Vol. 6, Page 276, March 1974.

15. Jones, C. A., Chetin, T. and Liller, W., <u>Astrophysical Journal (Letters)</u>, Vol. 190, Page L1, May 1974.

16. Jones, C. A., et. al., <u>Astrophysical Journal (Letters)</u>, Vol. 181, Page L43, April 1973.

REFERENCES (cont.)

17. Wolff, S. C. and Morrison, N. D., <u>Astrophysical Journal</u>, Vol. 187, Page 69, Jan. 1974.

18. Wackerling, L. R., <u>Royal Astronomical Society Memoirs</u>, Vol. 73, Page 153, Jan. 1970.

19. Kunkel, W., et. al., <u>Astrophysical Journal (Letters)</u>, Vol. 161, Page L169, Sept. 1970.

20. Giacconni, R., et. al., <u>Astrophysical Journal</u>, Suppl., No. 237, Vol. 27, Page 37, Feb. 1974.

21. Miller, J. S., <u>Astrophysical Journal</u>, Vol. 189, Page 239, April 1974.

22. Perry, M. E. and Peterson, B. A., <u>Astronomical Journal</u>, Vol. 79, Page 1, Jan. 1974.

23. Gursky, H., <u>Astrophysical Journal (Letters)</u>, Vol. 175, Page L141, Aug. 1972.

24. Bessell, M. S., et. al., <u>Astrophysical Journal</u>, Vol. 187, Page 355, Jan. 1974.

25. Conti, P. S., <u>Astrophysical Journal</u>, Vol. 187, Page 539, Feb. 1974.

26. Brucato, R. J. and Zappala, R. R., <u>Astrophysical Journal (Letters)</u>, Vol. 189, Page L71, April 1974.

27. Bacall, J. N., et. al., <u>Astrophysical Journal (Letters)</u>, Vol. 189, Page L17, April 1974.

28. Rappaport, S., et. al., <u>Astrophysical Journal (Letters)</u>, Vol. 187, Page L5, Jan. 1974.

1974

ASEE - NASA SUMMER FACULTY FELLOWSHIP PROGRAM

MARSHALL SPACE FLIGHT CENTER

(UNIVERSITY OF ALABAMA - AUBURN UNIVERSITY)

FRACTURE MECHANICS OF

CER-VIT C-101 GLASS-CERAMIC

Prepared by:	William B. Hall, PhD
Academic Rank:	Associate Professor
University:	Mississippi State University
NASA/MSFC Assignment:	Materials & Processes Lab Non-Metallic Mat'l Division
Research Counterpart:	Harry M. King
Date:	August 10, 1974
Contract No:	NGT-01-003-045

FRACTURE MECHANICS OF CER-VIT C-101 GLASS CERAMIC

By

WILLIAM B. HALL

ABSTRACT

Cer-Vit C-101 is a glass-ceramic material being considered for the three-meter reflecting mirror of the Large Space Telescope. One desired property characterization of Cer-Vit C-101 is its fracture mechanics.

Fracture mechanics properties were determined by crack propagation studies made utilizing the constant load technique on double cantilever beam specimens. Data was taken in ambient atmospheres of dry nitrogen, water, and air with varying relative humidities. The crack velocity data is presented in graphical form, and the data is consistent with the Charles-Hillig stress corrosion theory.

Recommendations for continuing the work are made.

INTRODUCTION

The objective of this study was to measure the fracture mechanics behavior of Cer-Vit C-101, a glass-ceramic material manufactured by Owens-Illinois of Toledo, Ohio. Cer-Vit C-101 has essentially a zero thermal expansion coefficient and because of this, it is one of the leading candidates for the three-meter reflecting mirror for the Large Space Telescope.

Certain mechanical properties of Cer-Vit C-101 have already been determined by Owens-Illinois. They are as follows:[1]

Density, gm/cc	2.50
Modulus of Rupture, Abraded Cane, psi	8,300
Knoop Hardness (200 gm loading)	540
Young's Modulus, psi	13.37×10^6
Shear Modulus, psi	5.34×10^6
Bulk Modulus, psi	8.97×10^6
Poisson's Ratio	0.252

With this data available, one property of interest was the delayed failure characteristics of Cer-Vit C-101. Delayed failure is caused by subcritical crack growth, which results in the material having a time dependent strength. Because delayed failure can occur without warning weeks or months after the application of a load, this phenomenon needs to be understood to prevent structural failure.

Fracture mechanics is the study of subcritical crack growth so that the mechanisms may be understood and design criteria be established to prevent delayed failures. It was, therefore, decided to study the crack growth of Cer-Vit C-101 utilizing the constant load technique on double cantilever beam specimens. The ambient atmosphere surrounding the specimens would simulate handling and use environments of the reflecting mirror. The critical stress intensity factor would also be determined for the material using three-point bending of edge-cracked specimens.

OBJECTIVES

The objectives of the program are:

1. Obtain crack velocity versus stress entensity factor data in various ambient environments for Cer-Vit C-101.

2. Obtain the critical stress intensity factor for Cer-Vit C-101.

3. Characterize the fracture mechanics behavior of Cer-Vit C-101 utilizing the data from 1 and 2 above.

TECHNICAL DISCUSSION

Glass and ceramic materials have excellent strength when one restricts the testing to compressive loading. However, when testing the same materials in tension, the strength values decrease in order of magnitude with a huge increase in the variance of the data. The most popular method of testing these materials in tension is the three point bond test, giving a breaking stress or modulus of rupture. The breaking stresses of brittle ceramics vary from 1,000 psi to 300,000 psi. This difference in strength is related to flaws in the brittle material, usually surface flaws. For example, commercial flint glass rods typically have modulus of rupture values in the range of 20,000 psi, while these same rods, when etched properly in dilute hydrofluoric acid, can have strengths in the range of 300,000 psi. Griffith was first to publish on this subject, and he developed a failure criterion based on an energy inventory at the tip of a crack. He stated that a crack will propagate in a material provided[1]

$$\frac{\partial E}{\partial c} \left[-\frac{\pi \sigma^2 c^2}{E} (1 - \gamma^2) + 4 c \alpha \right] \qquad (1)$$

where c = crack length, J = applied stress, E = Young's modulus, = Poisson's ratio, and = energy per unit area of surface created by fracture propagation. When the above equation is solved for , the Griffith stress is obtained:

$$\sigma \geq \sqrt{\frac{2 \alpha E}{\pi c (1 - \gamma^2)}} = \sigma^* \qquad (2)$$

The applied stress σ must equal or exceed the Griffith stress σ^* for the crack to propagate and rupture occur.

Glass and ceramics are noted for their inertness to most corrosive atmospheres, but they are susceptible to stress corrosion caused by

water in the environment.[2] This phenomenon is known as stress corrosion, static fatigue, or delayed failure. Griffith did not take this property into consideration in his determination of σ^*, the Griffith stress, in equation 2, above. It is currently believed that static fatigue results from the growth of small surface cracks until the crack length, c in equation 2, causes the stress σ to exceed σ^*, at which point catastrophic failure occurs.

The susceptibility of ceramics and glass materials to stress corrosion was first obsreved by Grenet [2] who observed time dependent failure and strength values that were dependent upon loading rate. One method for studying stress corrosion is to measure the velocity of macroscopic cracks as a function of selected variables such as load and environment. These experimental determinations are generally called fracture mechanics studies. Fracture mechanics is important in characterizing subcritical crack growth because the crack tip stresses that cause crack growth are directly proportional to the stress intensity factor.[3]

The angular (θ) and spatial (r) distribution of normal stresses at the tip of a crack, σ_n, for plane strain crack displacements can be given by:[4]

$$\sigma_n = \frac{K_I f(\theta)}{\sqrt{2\pi r}} \tag{3}$$

where K_I referred to the stress intensity factor. A simple dimensional analysis of a body containing a crack of length 2l subjected to an applied stress, σ_l, indicates that the stress intensification at the crack must be related to σ_l and l by:[4]

$$K_I = \sigma_l Y \sqrt{l} \tag{4}$$

where Y is a dimensionless constant wh ch must depend on the variables of shape and size of specimens and the crack shape. Brittle materials will then rupture when the stress at the crack tip exceeds the bond strength. There is a stress intensity factor corresponding to this condition and this should be a material parameter.[4] Measurements of K_I for fast fracture verifies this material parameter, and it is known as K_{IC}, the critical stress intensity factor.

Two theories on delayed fracture have been published, that of Charles and Hillig along with that of Hasselman.[1] Charles and Hillig state that delayed fracture is due to a stress enhanced chemical reaction, with the parameters being stress intensity factor,

environment of crack tip (moisture content), and the character of the material itself. Wiederhorn's and other's [5-13] stress corrosion studies have done much to confirm the Charles-Hillig theory. Hasselman states that the microcracks grow by the stress enhanced, thermally activated formation of vacancies at the crack tip. This theory agrees with data taken on a typical industrial glass.

EXPERIMENTAL PROCEDURE

Fracture mechanics data on the Cer-Vit C-101 material was obtained on double cantilever beam specimens for K_I, the stress intensity factor, and the experimental geometry is shown in Figure 1. The essential experimental parameters are crack length, 1; thickness, b; width, 2d; and applied load, P. The purpose of the slot was to restrict the crack propagation to the midplane. The specimens were loaded by means of a string through the notches shown in Figure 1, and crack propagation was observed through a X14 microscope attached to a cathometer. The crack was illuminated by direct or reflected light, dependent on which method produced a more defined crack tip. A constant load was maintained through the use of a spring between the load and the specimen. The crack length, 1, was mechanically introduced into the slot by scratching the slot with a SiC tipped pick, and gently tapping the specimen until the crack appeared. This was not the most desirable method as there was no control on the crack length. Some were too short and some cracked the entire length of the slot.

Two boxes were constructed of 1/4" plexiglass to control the environment of the specimen during testing. A small box 3/4" x 3 1/2" x 4 1/2" was used for atmospheres of dry nitrogen, water, 100% R.H. air, and 50% R.H. air. A larger box 13" x 18" x 22" was used for atmospheres of 20% R.H. air and 36% R.H. air, the larger size being required to hold the containers of saturated salts required to maintain the desired relative humidity. A saturated aqueous solution in contact with an excess of a solid phase at a given temperature will maintain a constant humidity in a closed space. Table I [1] presents data for selected solutions at 30°C.

TABLE I

Reagents for Humidity Control at 20°C

Aqueous Solutions, Std.	Relative Humidity, %	Dew Point, °K
1. $ZnCl_2 \cdot 1\tfrac{1}{2}H_2O$	10	260.4
2. $KC_2H_3O_2$	20	269.5
3. $CaCl_2 \cdot 6H_2O$	32	276.0
4. $Zn(NO_3)_2 \cdot 6H_2O$	42	280.0
5. $Na_2Cr_2O_7 \cdot 2H_2O$	52	282.9
6. $NaHSO_4 \cdot H_2O$	52	282.9
7. $NaNO_2$	66	286.5
8. $NaClO_3$	75	288.5
9. $(NH_4)_2SO_4$	81	289.7
10. $KCrO_4$	88	291.0
11. $Na_2SO_3 \cdot 7H_2O$	95	292.2
12. $Na_2HPO_4 \cdot 12H_1 1)$	95	292.2

For this experimental geometry, the stress intensity factor, K_I, is given by:[3]

$$K_I = \left(\frac{Pl\, b^{\frac{1}{2}}\, d^{3/2}}{w^{1/2}}\right) \left(3.467 + 2.315\frac{d}{l}\right) \qquad (5)$$

The critical stress intensity factor was determined by three point bending of an edge cracked bar, a modified modulus of rupture test. This method is intended for the determination of K_{IC}, not for the velocity of crack propagation. The experimental geometry of this test is shown in Figure 2. The essential experimental parameters are crack length, 1; thickness, b; height, h; load, p; and Span, S. The load was applied on a Instron universal testing machine. The critical stress intensity factor, K_{IC}, is given by:[9]

$$K_{IC} = \frac{PSl^{1/2}}{Bw^2}\left[2.93 - 4.36\frac{l}{w} + 21.15\left(\frac{l}{w}\right)^2 - 36.83\left(\frac{l}{w}\right)^3 + 38.27\left(\frac{l}{w}\right)^4\right]$$

RESULTS

The fracture behavior of Cer-Vit C-101 is shown in Figure 3; different relative humidities do not seem to have an effect on the rate of crack propagation, while the gas from dewar LN_2 does have. The LN_2 curve is similar to one obtained by Wiederhorn[3] who tested soda lime glass in dry nitrogen The curve is explained as follows: The bottom straight line portion of the curve is a function of the stress intensity as there is sufficient water vapor present for stress corrosion to occur as rapid as crack propagation. The plateau section of the curve is not dependent upon stress intensity, but is dependent upon the diffusion rate of the water vapor. The stress intensity factor is not high enough to rupture bonds without the help of stress corrosion. The top straight line portion of the curve is again a function of the stress intensity factor. Bonds are broken without the help of stress corrosion.

The curve for the various relative humidities may have a plateau of higher crack propagation velocities, but it would not be of engineering interest as the crack is growing at such a rate that catastrophic failure is imminent.

Both curves of Cer-Vit C-101 glass ceramic indicate its fracture properties are superior to the various glasses reported by Wiederhorn.

The critical stress intensity factor, K_{IC}, was determined by breaking twenty-three (23) prenotched bars   The notch length was measured on both sides of the bar, and a maximum and minimum K_{IC} calculated   These values were 870 psi$\sqrt{in}$ and 742 psi$\sqrt{in}$ respectively.

RECOMMENDATIONS FOR CONTINUING THE PROGRAM

The following recommendations are made for continuing the program:

1. Crack propagation studies should be made in a vacuum environment. If stress corrosion theory holds, no slow crack growth should be observed i.e., only the top portion of the curve in Figure 3 for dry nitrogen.

2. The data gathered to date should be statistically analyzed to determine the significance of the different sets of data.

3. A procedure to control the initiating of cracks into the test specimens should receive a portion of the effort.

4. Very slow crack growth velocities should be studied to determine if there is a "threshhold" stress intensity factor below which no crack growth is observed. This would be very time consumming, and would not be suitable for the 10-weeks summer program.

8-8
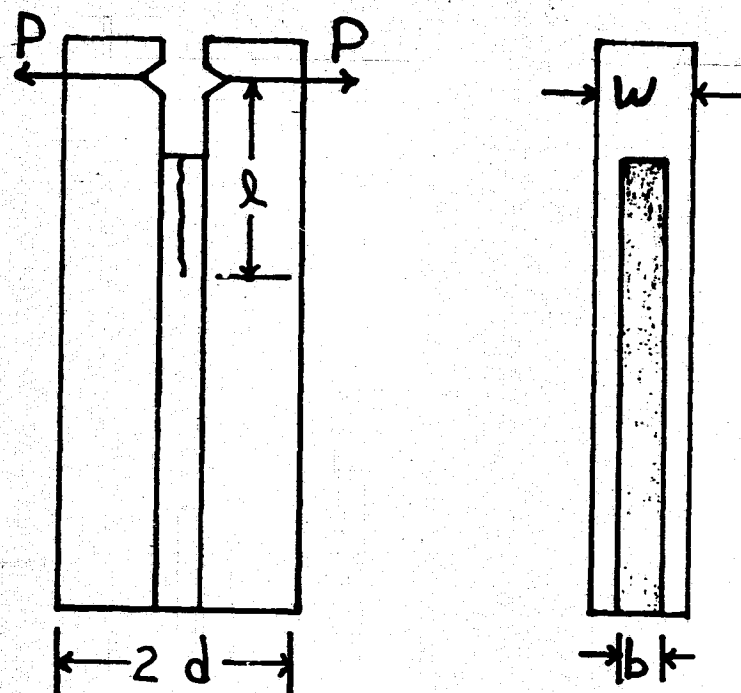
FIGURE 1: Double Cantilever Beam Specimens for Determination of K_I
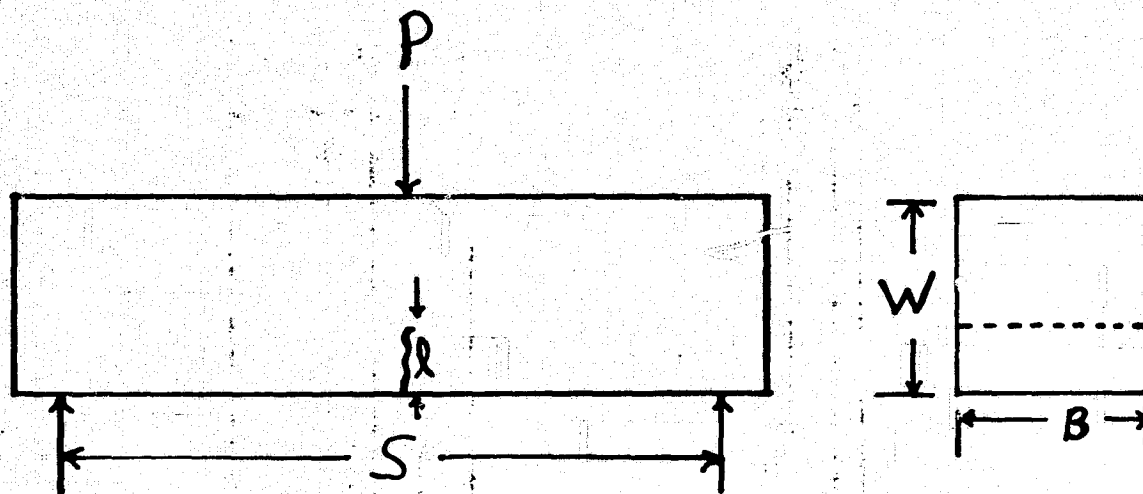
FIGURE 2:   Edge Cracked, Three Point Bend Specimens for
            Determination of K_{IC}
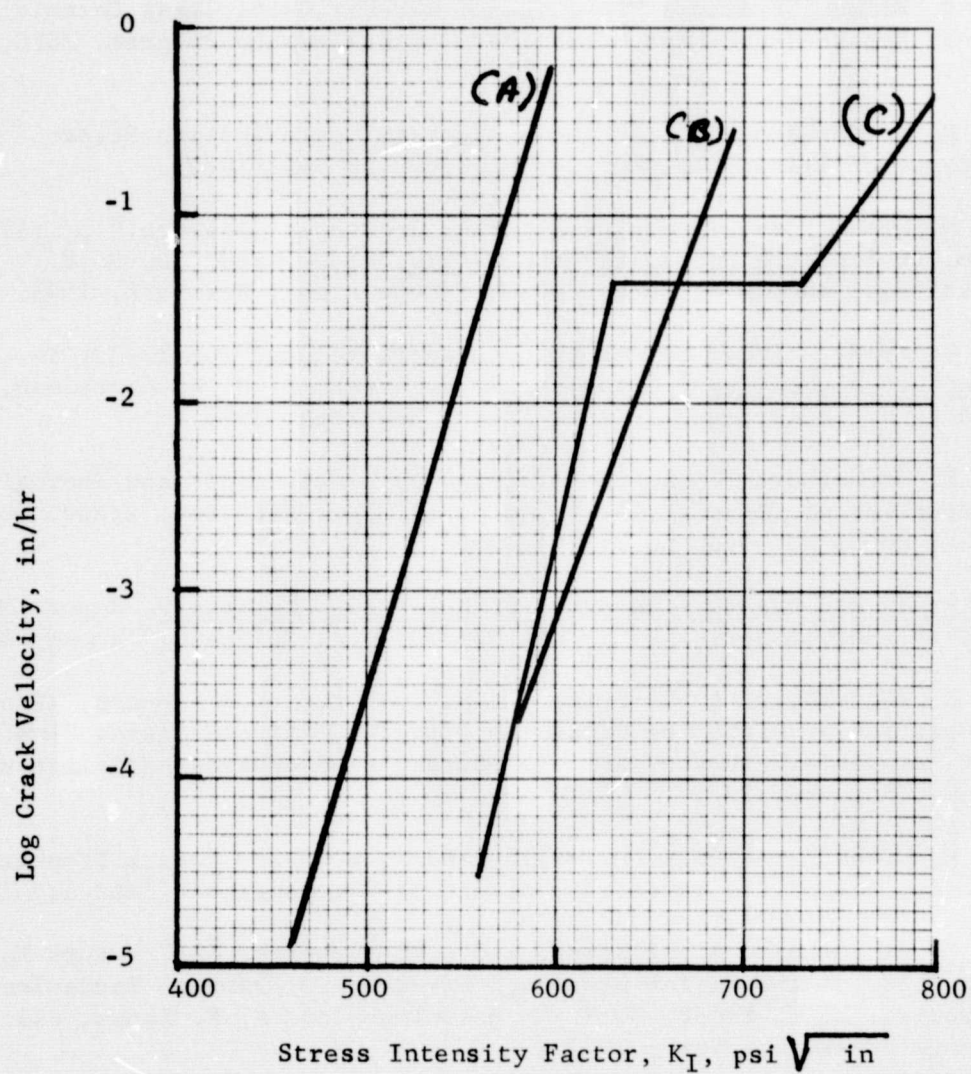
FIGURE 3: Crack Propagation of Cer-Vit C-101
Curve A - Commerical Cer-Vit in Water, 100% R.H. 50% R.H.
Curve B - Premium Cer-Vit in 20% R.H., 36% R.H. 50% R.H.
Curve C - Commercial Cer-Vit in Dry Nitrogen

8-11

REFERENCES

1. S. D. Brown, "Fracture Mechanics of Cer-Vit C-101 Glass Ceramic," Final Report, ASEE-NASA Summer Faculty Fellowship Program, MSFC, 1973

2. S. M. Wiederhorn and L. H. Bolz, "Stress Corrosion and Static Fatigue of Glass," _J. Am. Ceram. Soc._, 53 543 (1970).

3. S. M. Wiederhorn, "Subcritical Crack Growth in Ceramics," pp 613-646, in _Fracture Mechanics of Ceramics_, R. C. Bredt, D. P. H. Hasselman, and F. F. Lange, eds., Plenum Press, New York, 1973

4. A. G. Evans, "Fracture Mechanics Determinations," pp 17-37, in _Fracture Mechanics of Ceramics_, R. C. Bredt, D. P. H. Hasselman, and F. F. Lange, eds., Plenum Press, New York, 1973

5. S. M. Wiederhorn, "Fracture of Ceramics," Mechanical and Thermal Properties of Ceramics, J. B. Wachtmon, ed., Nat. Bur. Stand. (U.S.) Spec. Publ. No. 303, pp 217-41, 1969

6. _Strength and Fracture Behavior of MDA Window Materials_, Report MCR--73-27, Martin Marietta Corporation, Denver, Colorado, January 1973

7. S. M. Wiederhorn, A. G. Evans, E. R. Fuller, and H. Jonson, "Fracture Properties of Ultra Low Expansion Titanium Silicate Glass, "Institute for Materials Research, National Bureau of Standards, Washington, D. C., November 1973.

8. S. M. Wiederhorn, D. R. Mulville, and P. W. Mast, "Crack Propagation Studies in Brittle Materials, Report of NRL Progress, February 1972.

9. S. M. Wiederhorn, A. G. Evans, and D. E. Roberts, "A Fracture Mechanics Study of the Skylab Windows," 829-841, in Fracture Mechanics of Ceramics, R. C. Bredt, D. P. H. Hasselman, and F. F. Lange, eds., Plenum Press, New York, 1973.

10. J. E. Ritter, Jr., and C. L. Sherburns, "Dynamics and Static Fatigue of Silicate Glasses," _J. Am. Ceram. Soc._ 54, 601 (1971).

11. E. B. Shand, "Strength of Glass -- The Griffith Method Revised," _J. Am. Ceram. Soc._ 48, 43 (1965).

12. (a) S. M. Wiederhorn, "Influence of Water Vapor on Crack Propagation in Soda-Lime Glass." J. Am. Ceram. Soc., 50, 407 (1967).

13. S. W. Freiman, D. R. Mulville, and P. W. Mast, "Crack Propagation Studies in Brittle Materials" Report, Naval Research Laboratory, Washington, D. C. (April, 1973), 22 pp.

1974

ASEE - NASA SUMMER FACULTY FELLOWSHIP PROGRAM

MARSHALL SPACE FLIGHT CENTER

(AUBURN UNIVERSITY - UNIVERSITY OF ALABAMA)

SPACE SHUTTLE EXTERNAL PROPELLANT
TANK PRELAUNCH HEAT TRANSFER

Prepared by: LeRoy A. Holmes

Academic Rank: Engineering Instructor

Department and University: Department of Engineering and
                                    Physical Sciences
                                    Modesto Junior College

NASA/MSFC Assignment:
     (Laboratory)   Structures and Propulsion
     (Division)   Engineering Analysis
     (Branch)   Thermal Engineering

NASA Research Colleague: F. Huneidi

Date: August 9, 1974

Contract No.:   NGT-01-003-045

SPACE SHUTTLE EXTERNAL PROPELLANT
TANK PRELAUNCH HEAT TRANSFER

By

LeRoy A. Holmes

ABSTRACT

Analysis is developed for predicting surface temperatures of large
cryogenic tanks insulated with spray-on-foam insulations. The analyti-
cal model consists of a cooled vertical cylinder subjected to moist air
crossflow. Conduction, convection, condensation and radiation heat
transfer are included in computer programs to: (1) determine insula-
tion thickness requirements to prevent ice/frost formation and (2)
evaluate system performance under various environmental conditions.
The computed results are presented and compared with available experi-
mental results.

NOMENCLATURE

C_p	= specific heat (BTU/lb-$^\circ$F)
D	= tank diameter (ft)
g	= acceleration due to gravity (32.2 ft/sec^2)
Gr	= Grashof Number ($g\beta L^3 \{T_A - T_W\} / \nu^2$)
h	= convection film coefficient (BTU/hr-ft^2-$^\circ$F)
h_c	= condensation film coefficient (BTU/hr-ft^2-$^\circ$F)
h_{fg}	= latent heat of vaporization (BTU/lb)
k	= thermal conductivity (BTU/hr-ft-$^\circ$F)
L	= tank sidewall length (ft)
Nu_D or Nu_L	= Nusselt Number (hD/k or hL/k)
Pr	= Prandtl Number ($\mu C_p/k$)
q	= heat transfer rate (BTU/hr-ft^2)
Ra_L	= Rayleigh Number ($g\beta\rho^2 C_p L^3 \{T_A - T_W\} / \mu k$)
Re_D	= Reynolds Number (VD/ν)
S	= specific humidity (lb moisture/lb dry air)
T	= temperature ($^\circ$F)
V	= velocity (ft/sec)
X	= insulation thickness (ft)
β	= coefficient of thermal expansion (1/$^\circ$F)
ϵ	= emissivity
μ	= dynamic viscosity (lb/ft-sec)
ν	= kinematic viscosity (ft^2/sec)
ρ	= density (lb/ft^3)

Subscripts

A	= ambient
C	= wall (internal, propellant)
R	= radiation source (sink)
W	= wall (external, SOFI)

INTRODUCTION

With past designs of large cryogenic propellant tanks, ice and/or frost formations have been common during prelaunch operations. For the Space Shuttle, the External Propellant Tank (ET), which is required to carry liquid hydrogen and liquid oxygen for boost of the Shuttle vehicle Orbiter, may also have a tendency to form ice/frost. The configuration and design of the Shuttle vehicle, however, precludes ice/frost buildup on the ET surfaces since falling ice may structurally damage the Orbiter's thermal protection system. Consequently, it has been proposed that the ET be insulated with additional spray-on-foam-insulation (SOFI) to eliminate ice/frost formations.

In order to establish the feasibility of maintaining a frost free surface on the ET, to provide design guidelines for the insulation analysis, and to provide a capability that would allow rapid reaction to design changes and proposed changes, a study was initiated with the objective of developing convenient thermal design tools that would provide accurate thermal predictions for the ET during prelaunch. To satisfy the objective of the study, two computer codes were written in the BASIC language for the PDP8-E time sharing computer. These two codes provide the necessary thermal analysis capability. One code may be used to determine the insulation thickness required as a function of the prevailing environmental conditions. The other code is formulated to evaluate the performance of a specific insulation system (i.e., one with a fixed insulation thickness) when subjected to off-design environments.

The thermal analysis assumes the ET is a cooled, 27 foot diameter cylinder 154 feet tall, that stands vertically in a humid air environment. Heat transfer by conduction through the SOFI, by condensation of water vapor from the air onto the insulation surface, by either free or forced convection to the cylinder, and by radiative energy exchange with the surroundings is included in the model. Predicted results using the thermal model developed compare favorably to recent MSFC tests of a SOFI insulated cryogenic tank.

THE THERMAL MODEL AND HEAT TRANSFER CORRELATIONS

The thermal model for the ET is shown schematically in Figure 1. The model is basically a cooled vertical cylinder subjected to humid air crossflow. Thermal energy is transferred to the surface of the cylinder by convection (forced or free), condensation and radiation. This energy is then conducted through the insulation to the propellant. The thermal resistance of the tank structure and the propellant is assumed to be small allowing the interior surface of the SOFI to be taken equal to the temperature of the stored propellant. The energy
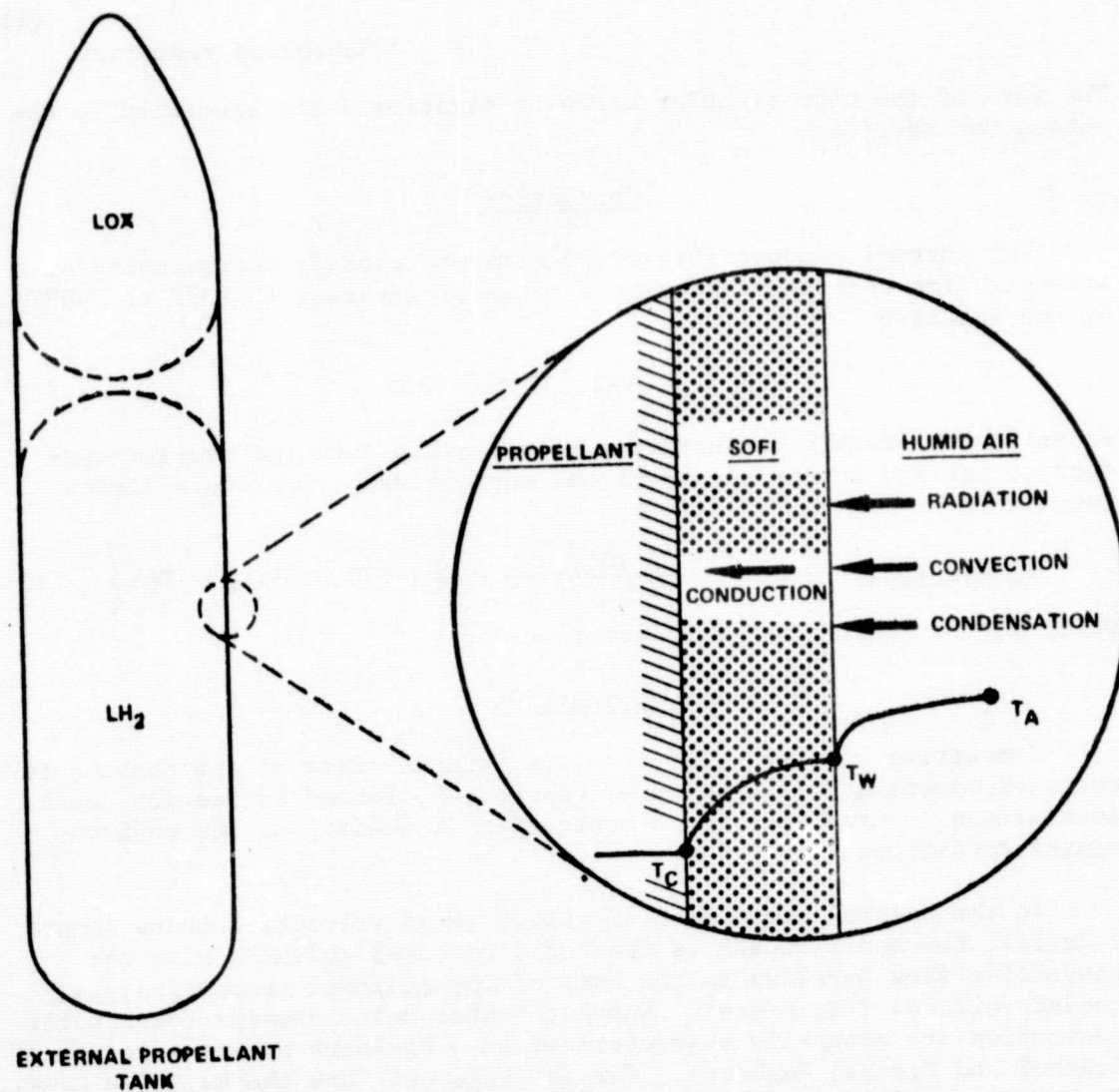
Figure 1   External Tank Thermal Model

balance at the outer surface of the insulation may be written as

$$q_{conduction} + q_{emitted \ radiation} = q_{convection} + q_{condensation}$$
$$+ \ q_{absorbed \ radiation}. \tag{1}$$

The form of the heat transfer terms in equation 1 are specified in the subsequent sections.

Conduction

The thermal conductivity of SOFI may be closely approximated by a straight line over the temperature range of interest (-423°F to 200°F) by the equation

$$k = 3.59 \times 10^{-5} T + 0.0155 . \tag{2}$$

Substitution of this conductivity relationship into the fourier conduction law and integration over the appropriate temperature limits results in

$$q_{conduction} = \frac{1}{X} \left\{ \frac{3.59 \times 10^{-5}}{2} (T_W^2 - T_C^2) + 0.0155(T_W - T_C) \right\} , \tag{3}$$

which may be substituted into equation 1.

Convection

Convective heat transfer from the External Tank of the Shuttle to the environment can be by natural convection, forced convection, or a combination natural and forced convection, depending on the environmental conditions.

In the natural convection situation (wind velocities below about 2 knots), the model chosen is that of a vertical cylinder with the convective flow parallel to the axis of the cylinder (essentially a cooled vertical flat plate). Nusselt Number relationships for natural convection are generally characterized by a Rayleigh Number (product of Grashof and Prandtl Numbers). For the External Tank the Rayleigh Number range of interest is from 10^{10} to 10^{14} and the flow, therefore, is turbulent (The transition from laminar to turbulent flow occurs at a Rayleigh Number of approximately 10^9). For turbulent flow on vertical cylinders or flat plates, two Nusselt Number relationships are generally recognized as being acceptable correlations of data over the External Tank Rayleigh Number range. The first is

$$Nu_L = 0.10 \ (Ra_L)^{1/3} \tag{4}$$

and represents the correlation of Bayley (Reference 1). The second is

$$Nu_L = 0.0210 \ (Ra_L)^{2/5} \tag{5}$$

and represents the analytical derivations of Eckert and Jackson
(Reference 2). In reviewing these two correlations, one finds small
differences in predicted Nusselt Numbers, however, recent work has
correlated more closely with the correlation of Bayley (References 3
and 4). Therefore, equation 4 is suggested as the most appropriate
for natural convection.

For forced convection, the External Tank can be modeled by a
cylinder with forced flow perpendicular to the cylinder axis (i.e.,
transverse flow); the flow being provided by the prevailing wind
conditions. For forced convection in air the Nusselt Number is a
function of the Reynolds Number. Wind velocities from 2 to 15 knots
on the External Tank will result in a Reynolds Number range of 5×10^5
to 3.9×10^6. Experimental correlations for transverse air flow on
cylinders have considered data with a Reynolds Number up to 4×10^5
(higher Reynolds Number data is apparently not available). Douglas
and Churchill (Reference 5) correlated data for Reynolds Numbers
from 100 to 400,000 using the following equation

$$Nu_D = 0.46 \ (Re_D)^{1/2} + 0.00128 Re_D \ . \tag{6}$$

It is felt that this correlation is superior to the one of McAdams
(Reference 6)

$$Nu_D = 0.0239 \ (Re_D)^{0.805} , \tag{7}$$

in that Douglas and Churchill have pointed out an error in McAdams
analysis. Equation 6 is suggested for forced flow. It must be noted
that a transition from laminar to turbulent flow occurs for cylinders
at a Reynold's Number of approximately 500,000 and extrapolating this
equation to the high Reynold's Number conditions of the External Tank
may lead to erroneous predictions. It is anticipated, however,
that the film coefficients computed from equation 6 will be lower
than actual since turbulent flow conditions normally enhance the heat
transfer as compared to laminar flow. Thus, for ice/frost prevention,
the results will be conservative.

A number of investigators have attempted to define the transition
from the natural to the combined natural/forced regime and from the
combined natural/forced to the forced regime, and the appropriate heat
transfer relationships in the combined regime for flow over cylinders
(References 7, 8, and 9). The data available for combined heat
transfer to a vertical cylinder in transverse air flow is sparse and
has been taken at Reynolds and Rayleigh Numbers well below the region
of interest. Consequently, it is suggested that convective heat
fluxes be computed by assuming that heat transfer occurs either
wholly by natural convection or wholly by forced convection (whichever
gives the larger heat flux). It is reasonable to assume that in the

combined regime both natural and forced convection contribute to the heat transfer. Consequently, the suggested approach will provide heat flux predictions that are lower than actual and will, in the present study, yield conservative results.

The convective heat transfer may be computed using

$$q_{convection} = h(T_A - T_W) ,$$ (8)

where the film coefficient is chosen as the larger value computed from equations 4 and 6.

Condensation

Since the surface of the External Tank will be lower than ambient, the possibility of condensation of water vapor in the air must be considered in order to provide accurate heat transfer predictions. As both the natural and forced convection conditions are turbulent it is reasonable to assume that the Lewis relation holds for the condensation film coefficient (Reference 10). That is,

$$h_c = \frac{h}{C_p} .$$ (9)

Experimental evidence (Reference 11) substantiates this assumption for turbulent flow.

Using the Lewis relationship, the heat transfer due to condensing may be approximated by

$$q_{condensation} = \frac{h}{C_p}(S_A - S_W) h_{fg}$$ (10)

for film condensation when the thermal resistance of the film is neglected. The film coefficient used in equation 10 is the same as the film coefficient used in equation 8. As long as the wall temperature is below the dew point the specific humidity difference, $S_A - S_W$, is found by subtracting the value of the specific humidity for the prevailing ambient conditions from the specific humidity of saturated air at the wall temperature. If the wall temperature is above the dew point, condensation does not take place and the specific humidity difference is equal to zero.

Radiation

Radiation heat transfer may be computed without significant error by assuming grey body exchange between the ET surface and a radiation source (sink) at a temperature, T_R.

$$q_{absorbed} - q_{emitted} = 0.174 \epsilon \left\{ \left(\frac{T_R + 460}{100} \right)^4 - \left(\frac{T_W + 460}{100} \right)^4 \right\}$$ (11)

Although only one radiation source (sink) temperature is indicated, several may be accommodated by simply defining the appropriate shape factors and specifying the other source(sink) temperatures.

Heat Transfer Balance

Substitution of equations 3, 8, 10, and 11 into equation 1 yields an equation for the heat transfer balance at the surface of the SOFI as

$$\frac{1}{X} \left\{ \frac{3.59 \times 10^{-5}}{2} (T_W^2 - T_C^2) + 0.0155 (T_W - T_C) \right\} =$$

$$h(T_A - T_W) + \frac{h}{C_p} (S_A - S_W) h_{fg} + 0.174\epsilon \left\{ \left(\frac{T_R + 460}{100}\right)^4 - \left(\frac{T_W + 460}{100}\right)^4 \right\} \tag{12}$$

In the design of the External Tank, the insulation thickness is normally desired as a function of the environmental parameters and equation 12 may be solved directly for the insulation thickness. To determine the insulation surface temperature for various environmental parameters once the insulation thickness has been specified, requires that equation 12 be solved by an iterative procedure.

Fluid Property Values

Many of the property values used in the heat transfer relations vary significantly with temperature. In order to provide accurate heat transfer computations, the property terms were least square curve fitted and included in the computer programs as functions of temperature. The polynomial equations used for each property and the accuracy of the polynomial are shown in Appendix A. In the computations, the properties used in the Reynold's Number, the Nusselt Number and the Rayleigh Number were evaluated at the mean of the wall and the ambient temperatures. The specific humidity difference, $S_A - S_W$, in the condensation equation was determined by subtracting the specific humidity of saturated air at the wall temperature from the prevailing ambient specific humidity. The latent heat of vaporization was evaluated at the wall temperature.

COMPUTER PROGRAMS

As noted, two computer codes were developed for the thermal analyses of the SOFI insulated External Tank. The program developed to determine the SOFI thickness required to produce a prescribed minimum surface temperature for a given set of prevailing ambient conditions has been designated as the INSuLation DEsign Program (INSLDE). The other program, designated the INSuLation PErformance Program (INSLPE), was developed to determine the ET surface temperature with the SOFI thickness and the ambient environment specified.

The input information required for both programs is similar. For the INSLDE Program, the input required, in the order requested, is:

1. AMBIENT TEMPERATURE, T_A ($^\circ$F)

2. RELATIVE HUMIDITY (%)

3. RADIATION ENVIRONMENT TEMPERATURE, T_R (°F)

4. MINIMUM WALL SURFACE TEMPERATURE DESIRED (°F)

5. TANK INTERNAL TEMPERATURE, T_C (°F)

6. TANK DIAMETER (FT)

7. WIND VELOCITY (KNOTS)

8. TANK WALL EMISSIVITY

The input information required for the INSLPE Program is identical except for item 4. In place of the minimum surface temperature, the insulation thickness (inches) is requested.

At first glance, one may conclude that the tank sidewall length has been erroneously omitted as an input parameter. The specification of the sidewall length appears to be required prior to calculating the free convection heat transfer rates. However, it may be seen that the sidewall length used to compute the Rayleigh Number is cancelled by the sidewall length in the Nusselt Number and consequently, the free convection film coefficient is independent of the sidewall length.

The complete listings of the INSLDE and INSLPE computer codes, including sample runs, are contained in Appendix B.

Comparison with Experiment

To verify the thermal model used in the computer codes a comparison of computed predictions was made with experimental results obtained at MSFC. During January and February, 1974, several tests were conducted on a 6 foot diameter SOFI insulated tank containing liquid hydrogen. The test parameters and data are contained in Table 1 along with surface temperatures computed using the INSLPE Program. As may be noted, the computed and measured surface temperatures compare favorably and indicate that the thermal model used is satisfactory.

INSLDE Parametric Study

Sample results obtained from the INSLDE Program are shown in Figures 2, 3, and 4. Figure 2 indicates the minimum SOFI thickness required to prevent frost formation as a function of wind velocity for several ambient temperature conditions. One may note the significant increase in insulation required as the ambient temperature is reduced. The breaks in the curves are caused by the computational scheme and indicate the transition from free to forced convection.

TABLE 1. COMPARISON OF MSFC EXPERIMENTAL SURFACE TEMPERATURE MEASUREMENTS WITH PREDICTED VALUES USING THE INSULATION PERFORMANCE COMPUTER CODE

TEST NO.	DATE	TEST TIME	WIND SPEED (KNOTS)	RELATIVE HUMIDITY (%)	AMBIENT TEMPERATURE ($^\circ$F)	MEASURED SURFACE TEMPERATURE ($^\circ$F)	COMPUTED SURFACE TEMPERATURE ($^\circ$F)
30-03	Jan. 31, 1974	13:15-14:30	4-5	20-22	68-71	49-56	51.0
30-04	Feb. 4, 1974	10:55-12:20	9-12	60	38-42	24-30	Below 32°F
30-05	Feb. 14, 1974	13:00-14:12	2	96-98	58-59	36-38	40.7
30-06	Feb. 19, 1974	12:43-14:15	7	70	47-50	36-37	36.7
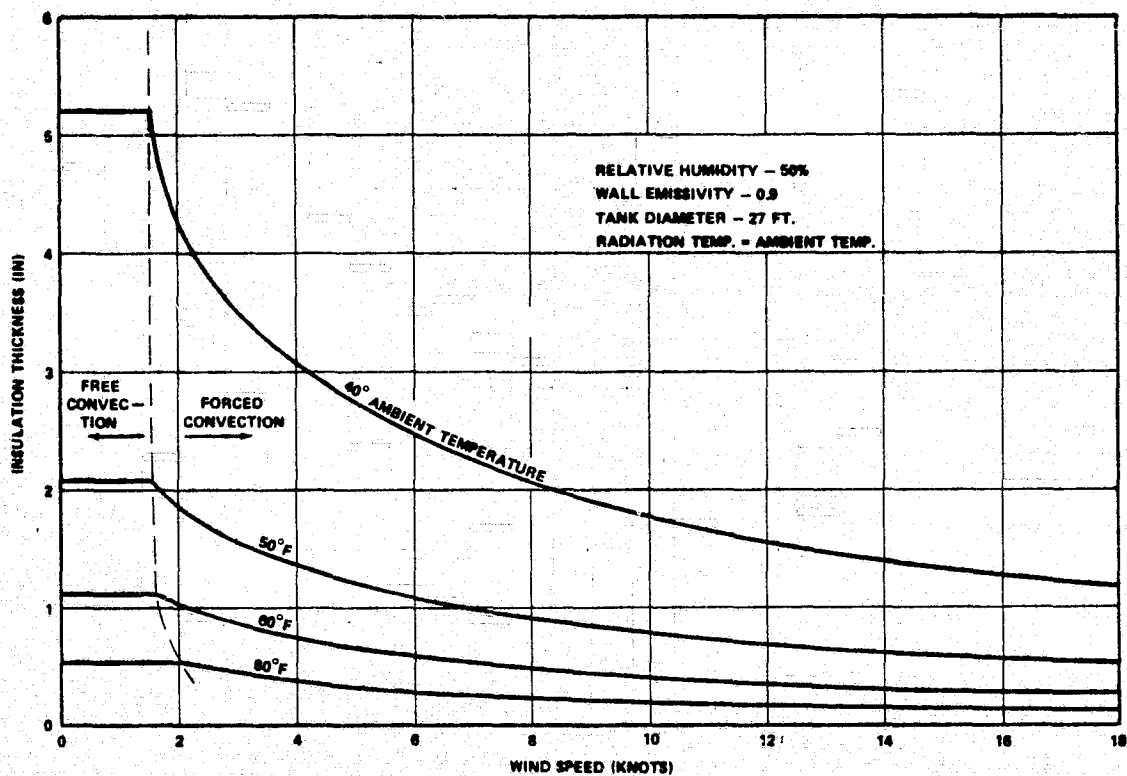
Figure 2   LH$_2$ Tank Spray-on-Foam Insulation Thickness Requirements To
Maintain a 32°F Surface Temperature versus Wind Speed for
Different Ambient Temperatures
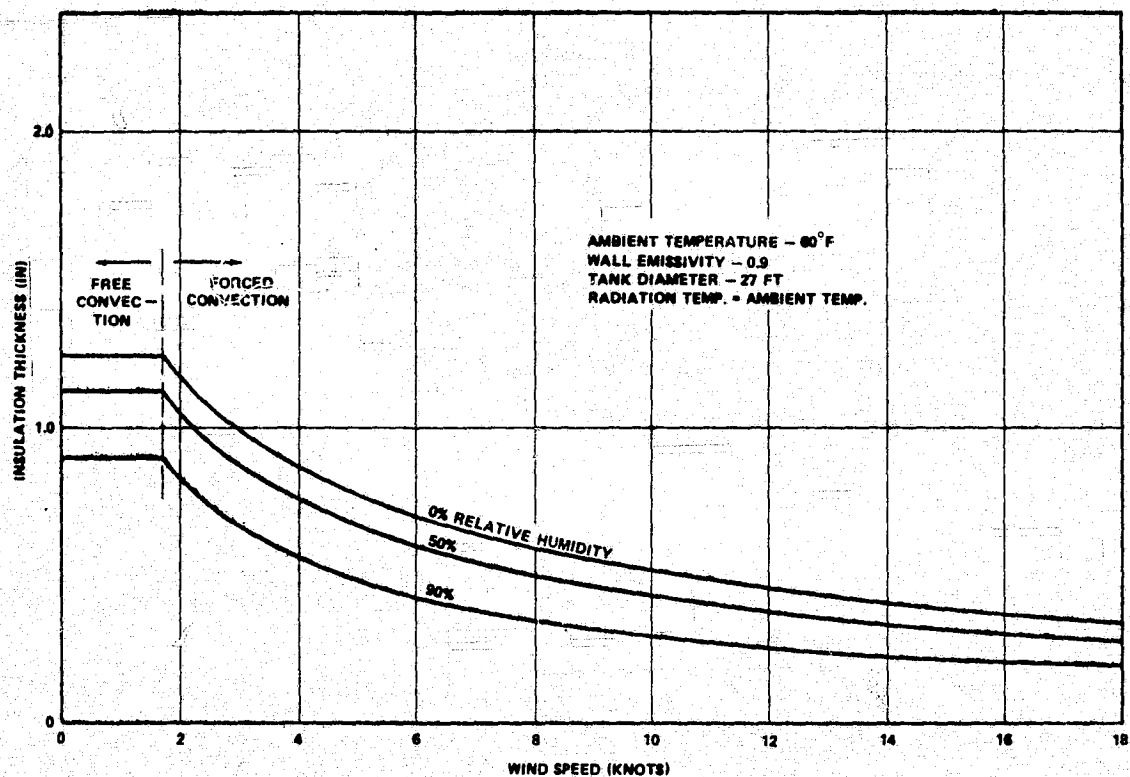
Figure 3   LH$_2$ Tank Spray-on-Foam Insulation Thickness Requirements to
Maintain a 32°F Surface Temperature versus Wind Speed for
Several Relative Humidity Values
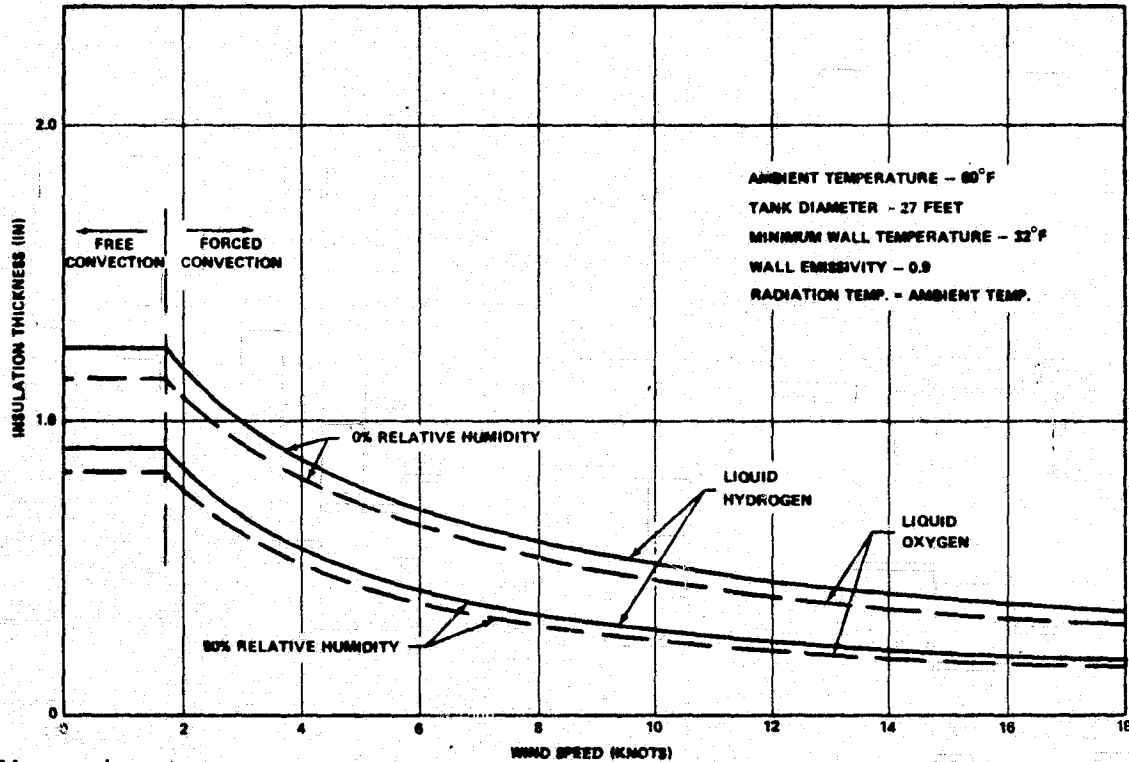
Figure 4 A Comparison of the Spray-on-Foam Insulation Requirements for the LH$_2$ and LOX Tanks to Maintain a 32°F Surface Temperature

The shift of the break to the right as the ambient temperature increases is due primarily to the fact that the natural convection film coefficient is proportional to the third root of the temperature difference (which increases with an increase in temperature) while the forced convection film coefficient is independent of temperature (except for property variations). The results presented in Figure 3 indicate the effect of relative humidity on the insulation thickness requirements versus wind velocity.

Figure 4 compares the insulation thickness requirements for the LH$_2$ and the LOX tanks. The small difference in the requirements, even though the LH$_2$ tank has a substantially greater temperature difference, may be attributed to the decreased thermal conductivity of the SOFI at LH$_2$ temperatures. From the standpoint of design, it appears that the LH$_2$ and the LOX tanks will have essentially the same insulation requirements.

It may be concluded from these results that the most severe combination of environmental conditions (giving the thickest insulation) is a very cold, low relative humidity, low wind speed day. On such days, it may be wise to provide active means by which to augment the cross winds, provide heating and/or increase the relative humidity so that the design insulation thickness may be held to a reasonable value.

INSLPE Parametric Study

Results from the INSLPE computer program are shown in Figures 5 through 9. These figures attempt to give an indication of the significance of the various environmental parameters on the SOFI performance. The results shown in each of the figures are for a 27 foot diameter tank containing liquid hydrogen insulated with 1.0 inch of SOFI.

Figure 5 shows the effect of the transverse wind velocity on the insulation surface temperature for various relative humidity conditions. The 0% relative humidity line represents conditions where condensation does not occur. Condensation can occur only when the insulation surface temperature is below the dew point. For 70°F air at 50% relative humidity the dew point is 50°F, and is illustrated on this figure by the intersection of the 50% relative humidity line and the 0% relative humidity line. As may be seen, for wind velocities above approximately 6.5 knots, the 0% relative humidity and the 50% relative humidity curves are the same. For 70% relative humidity and 70°F air, the dew point is approximately 59.5°F; the apparent intersection of the 70% relative humidity and the 0% relative humidity lines. Again, the breaks in the curves occur at the transition from free to forced convection and are a result of the computational scheme rather than an indication of actual occurrences.
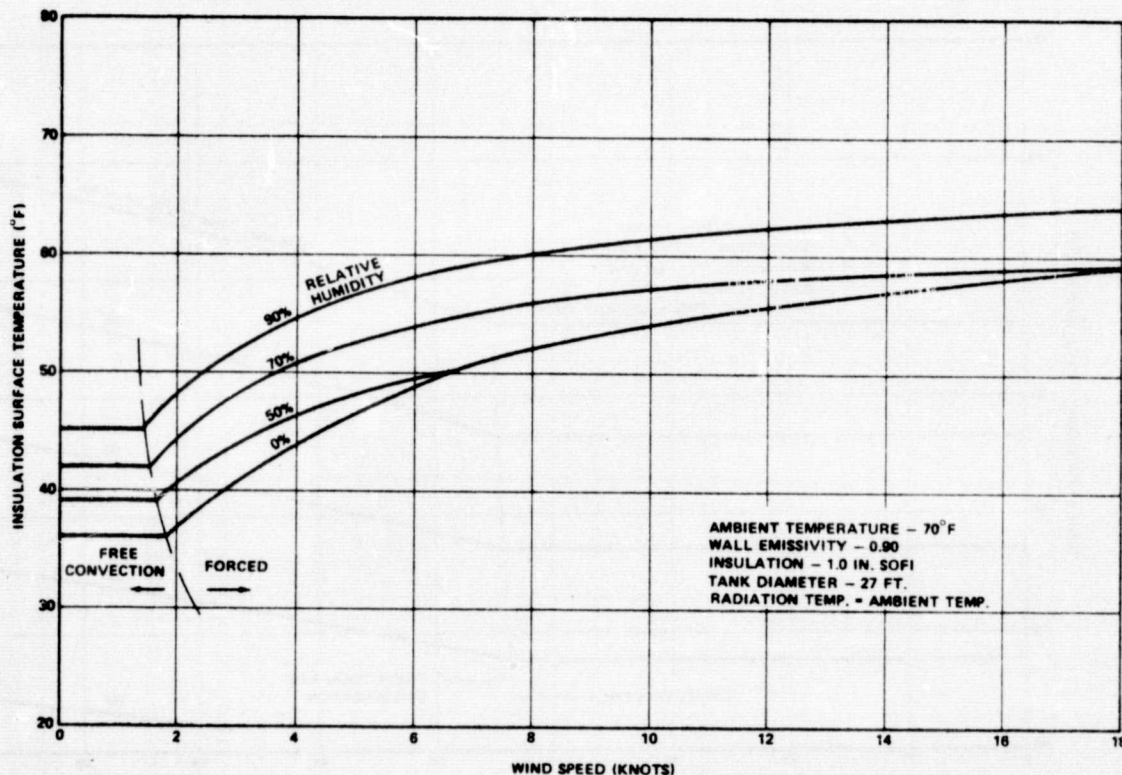
Figure 5   LH$_2$ Tank Surface Temperature versus Wind Speed for Different Relative Humidity Values when Insulated with 1.0 Inch of Spray-on-Foam Insulation

The influence of the relative humidity on the insulation surface temperature for various ambient temperature and wind conditions is shown in Figures 6 and 7. The definite breaks in these curves represent the separation of the convection and the convection plus condensation regimes. One may note the significant increase in surface temperature with an increase in ambient temperature. The significantly increased surface temperature when condensation occurs may also be noted.

The effect of the insulation thickness on the insulation exterior surface temperature is shown in Figure 8 for a 5 knot wind condition and 50% relative humidity. For the particular conditions presented, it may be noted that for a $50^{\circ}F$ ambient temperature, the minimum insulation thickness to prevent frost formation is approximately 1.25 inches. For $70^{\circ}F$ the minimum is slightly less than 0.50 inches and for $90^{\circ}F$ it is only about 0.25 inches. These results agree with those obtained using the Insulation Design Program, INSLDE (see Figure 2).

Figure 9 illustrates the effect of day and night launches and the value of the surface emissivity on the insulation exterior temperature. For the day launch computations, the surface exchanged radiant energy with surroundings at a temperature equal to the ambient
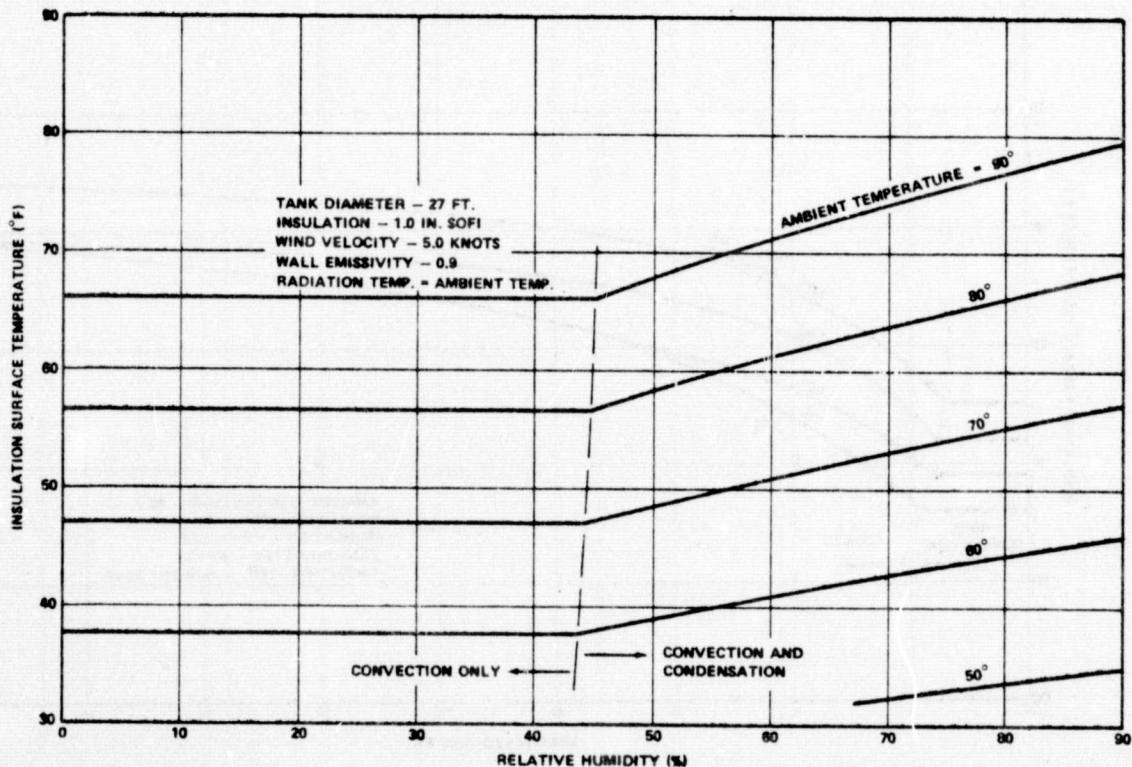
Figure 6   LH$_2$ Tank Surface Temperature versus Relative Humidity for Different Ambient Temperatures when Insulated with 1.0 Inch of Spray-on-Foam Insulation
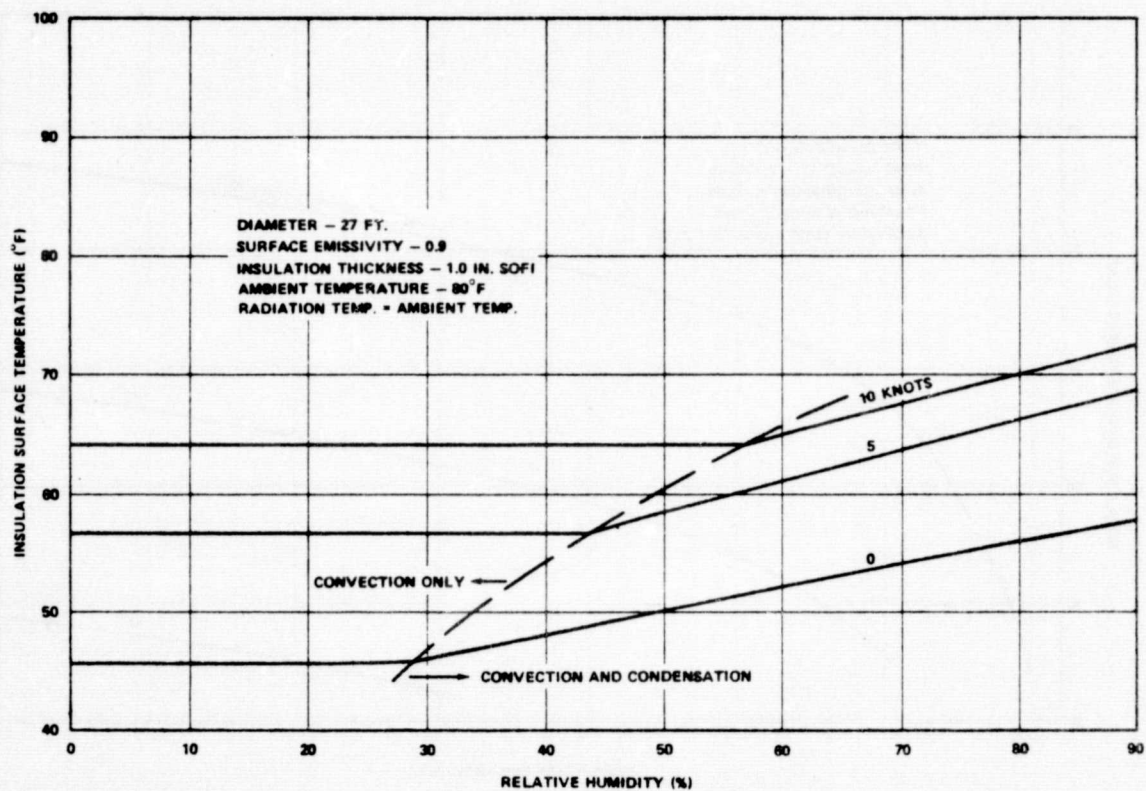
Figure 7   LH$_2$ Tank Surface Temperature versus Relative Humidity for Different Wind Speeds when Insulated with 1.0 Inch of Spray-on-Foam Insulation
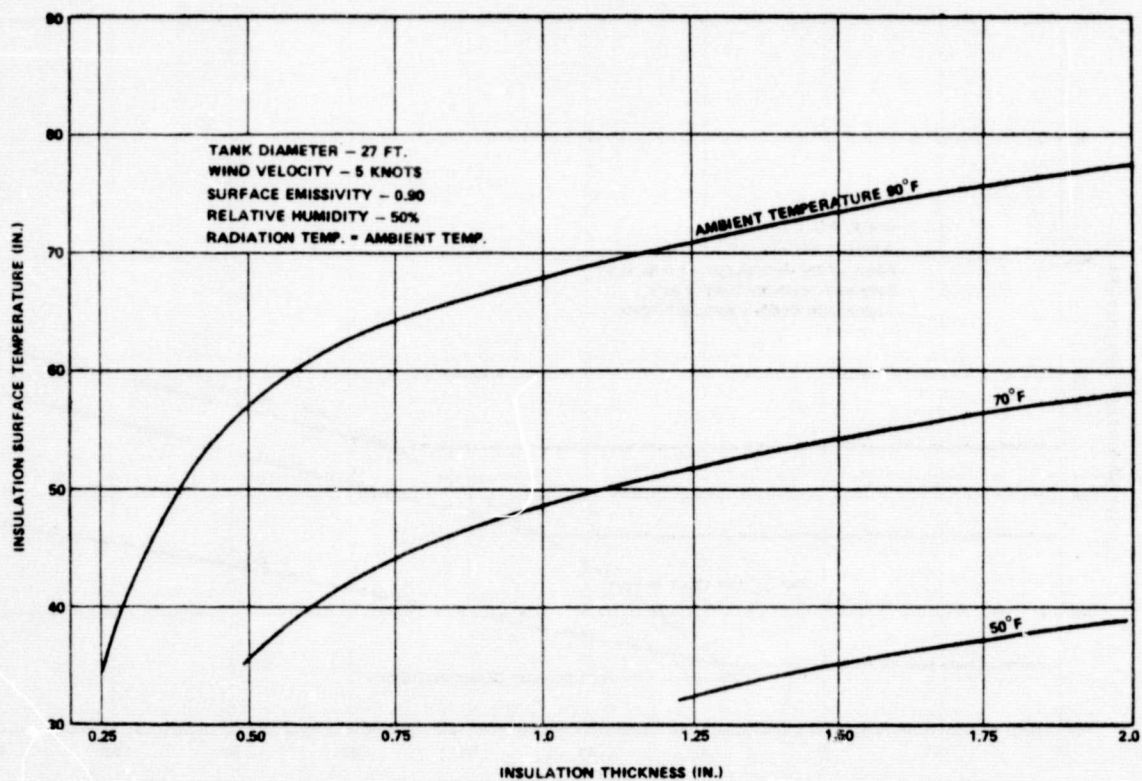
Figure 8   LH$_2$ Tank Surface Temperature versus Insulation Thickness for
Different Ambient Temperatures

Figure 9   The Influence of Surface Emissivity on the LH$_2$ Tank Surface
Temperature for Day and Night Launches

temperature. Direct solar radiation was not included because cloudiness, fog and the time of day will significantly alter the magnitude of the solar flux on the vehicle. By omitting the solar radiation, conservative results will be obtained for the ice/frost problem. For day launches, the value of the insulation emissivity does not appear to be too important. A change in emissivity from 0.5 to 0.9 changes the predicted wall temperature by only 3°F. Night launches were simulated by establishing the surroundings at 5°F (sky radiation temperature). This radiation temperature may be somewhat low in that cloudy conditions, nearby structures and other objects would tend to establish the night launch radiation environment closer to ambient temperatures. The results of a 5°F radiation environment, however, do show that a significant decrease in insulation surface temperatures may occur as compared to a day launch. A 15°F difference exists between the predicted insulation surface temperatures for day and night launches with an emissivity of 0.9. Table II is included to demonstrate that the indicated surface temperature differences in day and night launches is not simply peculiar to the conditions used in Figure 9. This table shows significant surface temperature differences between day and night launches for other SOFI thickness values and relative humidity conditions. These results indicate that night launches may necessitate the use of radiation shields, heaters, or some other devices to maintain the insulation above 32°F.

Figure 9   The Influence of Surface Emissivity on the LH_2 Tank Surface
Temperature for Day and Night Launches

temperature. Direct solar radiation was not included because cloudi-
ness, fog and the time of day will significantly alter the magnitude
of the solar flux on the vehicle. By omitting the solar radiation,
conservative results will be obtained for the ice/frost problem. For
day launches, the value of the insulation emissivity does not appear
to be too important. A change in emissivity from 0.5 to 0.9 changes
the predicted wall temperature by only $3^{\circ}F$. Night launches were
simulated by establishing the surroundings at $5^{\circ}F$ (sky radiation
temperature). This radiation temperature may be somewhat low in that
cloudy conditions, nearby structures and other objects would tend to
establish the night launch radiation environment closer to ambient
temperatures. The results of a $5^{\circ}F$ radiation environment, however,
do show that a significant decrease in insulation surface tempera-
tures may occur as compared to a day launch. A $15^{\circ}F$ difference exists
between the predicted insulation surface temperatures for day and night
launches with an emissivity of 0.9. Table II is included to demonstrate
that the indicated surface temperature differences in day and night
launches is not simply peculiar to the conditions used in Figure 9.
This table shows significant surface temperature differences between
day and night launches for other SOFI thickness values and relative
humidity conditions. These results indicate that night launches may
necessitate the use of radiation shields, heaters, or some other
devices to maintain the insulation above $32^{\circ}F$.

TABLE II.   A COMPARISON OF SOFI SURFACE TEMPERATURES FOR DAY
AND NIGHT LAUNCHES (80°F AMBIENT TEMPERATURE)

LAUNCH CONDITION	SOFI EXTERNAL SURFACE TEMPERATURE (°F)			
	1.0 INCH SOFI 50% REL. HUM.	1.0 INCH SOFI 90% REL. HUM.	0.5 INCH SOFI 50% REL. HUM.	0.5 INCH SOFI 90% REL. HUM.
Day ($\epsilon = 0.9$)	58.3	68.5	46.5	58.0
Night ($\epsilon = 0.9$)	43.6	56.2	Below 32	44.2

CONCLUSIONS AND RECOMMENDATIONS

The programs developed on this study to aid in the Space Shuttle
External Tank thermal analysis appear to give reasonable, accurate
predictions. The ease with which the programs may be used allows an
extremely rapid response (on the order of one hour) to design changes.
Although the programs were designed specifically for the ET, they may
be used on any large cylindrical cryogenic tank insulated with SOFI
where the flow is turbulent.

It is recommended that the programs be further verified for
accuracy when the results of the MSFC tests of cryogenic tanks insulated
with SOFI become available.

REFERENCES

1. Bayley, F. J., "An Analysis of Turbulent Free-Convection Heat Transfer," Proceedings of the Institution of Mechanical Engineers, Vol. 169, No. 20, 1955, p. 361.

2. Eckert, E.R.G., and T. W. Jackson, "Analysis of Turbulent Free-Convection Boundary Layer on Flat Plate," NACA TN 2207, 1950.

3. Cheesewright, R., "Turbulent Natural Convection From a Vertical Plane Surface," Journal of Heat Transfer, February 1968.

4. Warner, C. Y., "Turbulent Natural Convection in Air Along a Vertical Flat Plate," PhD Thesis, University of Michigan, Ann Arbor, Michigan, December 1966.

5. Douglas, W.J.M., and S. W. Churchill, "Recorrelation of Data for Convective Heat Transfer Between Gases and Single Cylinders with Large Temperature Differences," AICHE Chemical Engineering Symposium Series, No. 18, Vol. 52, 1956, p. 23.

6. McAdams, W. H., Heat Transmission, 3rd Edition, McGraw-Hill Book Company, Inc., N. Y., 1954.

7. Sharma, G. K., and S. P. Sukhatme, "Combined Free and Forced Convection Heat Transfer From a Heated Tube to a Transverse Air Stream," Journal of Heat Transfer, August 1969, p. 457.

8. Rapp, G. M., "Convective Heat Transfer and Convective Coefficients of Nude Man, Cylinders and Spheres at Low Air Velocities," Transactions ASHRAE, 1973, p. 75.

9. Hatton, A. P., D. D. James, and H. W. Swire, "Combined Forced and Natural Convection with Low-Speed Air Flow Over Horizontal Cylinders," Journal of Fluid Mechanics, Vol. 42, Part One, 1970, p. 17.

10. Eckert, E.R.G., and R. M. Drake, Heat and Mass Transfer, McGraw-Hill Book Company, Inc., New York, 1959, p. 477.

11. Trammell, G. J., J. Canterbury, and E. M. Killgore, "Heat Transfer From Humid Air to a Horizontal Flat Plate Held at Sub Freezing Temperatures," Transactions ASHRAE, 1967, p. IV.3.1.

APPENDIX A - POLYNOMIAL PROPERTY CURVES

Polynomial curve fits were made for the property terms used in the computer codes using a least squares technique. The degree of polynomial selected for use was based on the accuracy of the computed property values. The following sections give details of the equations used.

Rayleigh Number

The Rayleigh Number (product of the Grashof and Prandtl Numbers) is defined as:

$$Ra = GrPr = \left[\frac{g\ \beta\ \rho^2\ Cp}{\mu\ k} \right] L^3\ \Delta T$$

As may be noted the bracketed term is dependent only on the properties of the fluid of interest. In order to avoid curve fitting each of the properties, the entire term was fitted. An acceptable polynomial for this term over temperature range of $10^\circ F$ to $206^\circ F$ was found to be:

$$\left[\frac{g\ \beta\ \rho^2\ Cp}{\mu\ k} \right] = (3.24 - 3.80 \times 10^{-2}T + 2.86 \times 10^{-4}T^2 - 1.28 \times 10^{-6}\ T^3 + 2.35 \times 10^{-9}\ T^4) \times 10^6$$

Temperature is measured in degrees Fahrenheit and the polynomial has units of $(^\circ F)^{-1}\ (ft)^{-3}$. A comparison of the input values to the computed values is shown below.

TEMPERATURE ($^\circ F$)	$\left[\frac{g\ \beta\ \rho^2 C_P}{k} \times 10^{-6} \right]$ ACTUAL ($^\circ F^{-1}\ FT^{-3}$)	$\left[\frac{g\ \beta\ \rho^2 C_P}{k} \times 10^{-6} \right]$ COMPUTED ($^\circ F^{-1}\ FT^{-3}$)
10	2.90	2.88
25	2.42	2.44
43	2.03	2.03
62	1.73	1.70
80	1.48	1.46
97	1.27	1.27
115	1.10	1.10
133	0.95	0.95
152	0.82	0.82
170	0.72	0.70
206	0.57	0.57

Reynolds Number

The Reynolds Number (VD/ν) contains only the kinematic viscosity as a property term. The kinematic viscosity was fitted over a temperature range of $0^\circ F$ to $300^\circ F$ by the polynomial:

$$\nu = 0.130 \times 10^{-3} + 4.57 \times 10^{-7}T + 4.28 \times 10^{-10}T^2$$

Temperature is measured in degrees and ν has the units of square feet per second. A comparison of the input values and the computed values is shown below.

TEMPERATURE ($^\circ F$)	($\nu \times 10^3$) ACTUAL (FT^2/SEC)	($\nu \times 10^3$) COMPUTED (FT^2/SEC)
0	.130	.130
30	.145	.144
100	.180	.180
200	.239	.238
300	.306	.306

Nusselt Number

The Nusselt Number (hL/k or hD/k) contains the thermal conductivity as a property term which must be curve fitted. The thermal conductivity was curve fitted over a temperature range of $0^\circ F$ to $300^\circ F$ by the polynomial:

$$k = 0.01333 + 1.99 \times 10^{-5}T$$

where temperature is measured in degrees Fahrenheit and the conductivity is measured in BTU/HR-FT-$^\circ F$. A comparison of the input values with the computed values is shown below.

TEMPERATURE ($^\circ F$)	k_{ACTUAL} BTU/HR-FT-$^\circ F$	$k_{COMPUTED}$ BTU/HR-FT-$^\circ F$
0	.0133	.0133
30	.0140	.0139
100	.0154	.0153
200	.0174	.0173
300	.0193	.0193

Condensation Heat Transfer

In order to compute the condensation heat transfer it was necessary to curve fit the latent heat of vaporization (h_{fg}) for water and the specific humidity of saturated air, W.

The latent heat of vaporization was fitted over a temperature range 32°F to 120°F by the polynomial:

$$h_{fg} = 1093 - 0.5555T - 7.330 \times 10^{-5} T^2$$

where temperature is measured in degrees Fahrenheit and the latent heat of vaporization is measured in BTU's per pound. A comparison of the input values to computed values is shown below.

TEMPERATURE (°F)	h_{fg} ACTUAL (BTU/LB)	h_{fg} COMPUTED (BTU/LB)
32	1075.16	1075.14
40	1070.64	1070.66
60	1059.43	1059.40
80	1048.07	1048.08
100	1036.72	1036.71
120	1025.28	1025.28

The specific humidity of saturated air, W, was fitted over a temperature range of 32°F to 120°F by the polynomial:

$$W = (-0.136 + 0.139T - 2.39 \times 10^{-3} T^2 + 7.23 \times 10^{-5} T^3 - 5.86 \times 10^{-7} T^4$$
$$+ 5.86 \times 10^{-9} T^5 - 3.03 \times 10^{-11} T^6 + 1.13 \times 10^{-13} T^7) \times 10^{-3}$$

where temperature is measured in degrees Fahrenheit and the specific humidity is measured in pounds of water per pound of dry air. A comparison of the input values to computed values is shown below.

TEMPERATURE (°F)	$(W \times 10^3)$ ACTUAL (LB_{H_2O}/LB_{AIR})	$(W \times 10^3)$ COMPUTED (LB_{H_2O}/LB_{AIR})
32	3.788	3.785
40	5.213	5.218
50	7.658	7.656
60	11.08	11.07
70	15.82	15.82
80	22.33	22.32
90	31.18	31.18
100	43.19	43.18
110	59.44	59.44
120	81.49	81.48

APPENDIX B - COMPUTER PROGRAMS

Program Variable Notation

A	Property factor for Rayleigh Number $(g\beta\rho^2 C_p/\mu\,k)$ $(^\circ F^{-1}\;FT^{-3})$
A1	Dummy variable used in condensation coefficient computation
A7	Reynold Number
D	Tank diameter (FT)
E1	Tank wall emissivity
H	Latent heat of vaporization (BTU/LB)
H1	Free convection film coefficient $(BTU/HR\text{-}FT^2\text{-}^\circ F)$
H2	Forced convection film coefficient $(BTU/HR\text{-}FT^2\text{-}^\circ F)$
H3	Dummy film coefficient (maximum of H1 and H2)
H3	Condensation film coefficient $(BTU/HR\text{-}FT^2\text{-}^\circ F)$
K	Thermal conductivity of air $(BTU/HR\text{-}FT\text{-}^\circ F)$
L	Length of tank sidewall (FT)
Q	Total heat transfer into tank, Q1+Q2+Q3, $(BTU/HR\text{-}FT^2)$
Q1	Heat transfer to tank by radiation $(BTU/HR\text{-}FT^2)$
Q2	Heat transfer to tank by convection $(BTU/HR\text{-}FT^2)$
Q3	Heat transfer by condensation $(BTU/HR\text{-}FT^2)$
Q4	Conductive heat transfer $(BTU/HR\text{-}FT^2)$
R	Relative humidity (%)
T	Mean temperature used for evaluating properties, (T2 + T3)/2, $(^\circ F)$
T1	Tank internal temperature $(^\circ F)$

APPENDIX B - COMPUTER PROGRAMS

Program Variable Notation

T2	Insulation exterior surface temperature ($^{\circ}$F)
T3	Ambient temperature ($^{\circ}$F)
T4	Radiation sink temperature ($^{\circ}$F)
T7	Dummy temperature variable
T9	Insulation thickness (inches)
V	Wind velocity (knots)
V1	Kinematic viscosity of air (FT^2/SEC)

INSuLation DEsign Program (INSLDE) Listing

```
1 PRINT "
2 PRINT " THIS PROGRAM DETERMINES THE SPRAY ON FOAM REQUIRED"
3 PRINT " TO PREVENT FROST FORMATION ON CYLINDRICAL TANKS"
4 PRINT " SUBJECT TO FORCED CONVECTION, FREE CONVECTION,"
5 PRINT " RADIATION AND CONDENSATION"
6 PRINT "
7 PRINT "*****************************************************"
8 PRINT
9 PRINT
10 PRINT "AMBIENT TEMPERATURE (F) = ",
20 INPUT T3
40 PRINT "RELATIVE HUMIDITY(%) = ",
50 INPUT R
60 PRINT "RADIATION ENVIRONMENT TEMPERATURE (F) = ";
70 INPUT T4
80 PRINT "MINIMUM WALL SURFACE TEMPERATURE (F) DESIRED ( MUST BE"
82 PRINT "GREATER THAN 32 F) = ";
85 INPUT T2
86 PRINT "TANK INTERNAL TEMPERATURE (F) = ";
87 INPUT T1
90 PRINT "DIAMETER OF TANK (FT) = ";
100 INPUT D
130 PRINT "WIND VELOCITY (KNOTS) = ";
140 INPUT V
150 PRINT "WALL EMISSIVITY = ";
160 INPUT E1
170 DEF FNA(X)=-.13566+.1389*X-2.39/10^3*X^2+7.231/10^5*X^3
175 DEF FNB(Y)=-5.865/10^7*Y^4+5.862/10^9*V^5-3.027/10^11*V^6+1.132/10^13*V^7
200 Q1 = .174*E1*((((T4+460)/100)^4-((T2+460)/100)^4)
210 T = (T2+T3)/2
220 A= 323800-38000*T+285.9*T^2-1.28*T^3+.002346*T^4
230 V1 =( .1303 +4.573/10^4*T+4.277/10^7*T^2)/1000
240 K = .01337 +1.992/10^5*T
250 H1 = .1*K*A^.33*(T3-T2)^.33
262 A7 = 1.69*V*D/V1
264 H2 = K/D*( .46*A7^.5+.00128*A7)
266 IF H1<H2 GOTO 269
267 H3 =H1
268 GOTO 270
269 H3 =H2
270 H=1093.002 -.5555*T2-7.3296/10^5*T2^2
280 A1 = H3/.24/(T3-T2)*H
290 H4 = A1*(R/100*(FNA(T3)+FNB(T3))-(FNA(T2)+FNB(T2)))/1000
295 IF H4<0 GOTO 297
296 GOTO 300
297 H4 =0
300 Q3 = H4*(T3-T2)
305 Q2 = H3*(T3-T2)
310 Q =Q1+Q2+Q3
320 T9 = (3.59/10^5*(T1^2-T2^2)/2 + .0155*(T1-T2))/Q*12
321 PRINT
322 PRINT
323 PRINT
324 T9 =-T9
330 PRINT "INSULATION THICKNESS (IN) = ", T9
331 PRINT
340 PRINT " FORCED CONVECTION COEF = ", H2,"BTU/HR-FT-FT-F"
341 PRINT
350 PRINT " FREE CONVECTION COEF = ", H1,"BTU/HR-FT-FT-F"
351 PRINT
360 PRINT " CONDENSATION COEF = ", H4,"BTU/HR-FT-FT-F"
361 PRINT
362 PRINT "*****************************************************"
363 PRINT
364 PRINT " CASE NUMBER ",
365 INPUT M
366 PRINT
367 PRINT
370 IF M>0 GOTO 7
380 END
```

INSuLation PErformance Program (INSLPE) Listing

```
1 PRINT "THIS PROGRAM DETERMINES THE INSULATION SURFACE TEMPERATURE"
2 PRINT "FOR SOFI ON CYLINDRICAL TANKS SUBJECT TO FORCED CONVECTION,"
3 PRINT "FREE CONVECTION, RADIATION AND CONDENSATION."
4 PRINT " ..........................................................."
5 PRINT "*********************************************************"
7 PRINT
8 PRINT
10 PRINT "AMBIENT TEMPERATURE (F) = ";
20 INPUT T3
40 PRINT "RELATIVE HUMIDITY(%) = ";
50 INPUT R
60 PRINT "RADIATION ENVIRONMENT TEMPERATURE (F) = ";
70 INPUT T4
80 PRINT "INSULATION THICKNESS (IN) = ";
81 INPUT T9
86 PRINT "TANK INTERNAL TEMPERATURE (F) = ";
87 INPUT T1
90 PRINT "DIAMETER OF TANK (FT) = ";
100 INPUT D
130 PRINT "WIND VELOCITY (KNOTS) = ";
140 INPUT V
150 PRINT "WALL EMISSIVITY = ";
160 INPUT E1
170 DEF FNA(X)=-.13566+.1709*X-2.39/10^3*X^2+7.231/10^5*X^3
175 DEF FNB(Y)=-5.865/10^7*Y^4+5.862/10^9*Y^5-3.027/10^11*Y^6+1.132/10^13*Y^7
176 Y=0
177 Z=1
178 T2=T3-1
180 GOTO 200
181 T7=T2
182 T2=T2-10/Z
200 Q1 = .174*E1*(((T4+460)/100)^4-((T2+460)/100)^4)
210 T = (T2+T3)/2
220 A= 3230000-30000*T+205.9*T^2-1.28*T^3+.002346*T^4
230 V1 =(.1383+4.573/10^4*T+4.277/10^7*T^2)/1000
240 K = .01337 +1.992/10^5*T
250 H1 = .1*K*A^.33*(T3-T2)^.33
262 A7 = 1.69*V*D/V1
264 H2 = K/D*(.46*A7^.5+.00128*A7)
266 IF H1<H2 GOTO 269
267 H3 =H1
268 GOTO 270
269 H3 =H2
270 H=1093.002 -.5555*T2-7.3296/10^5*T2^2
280 A1 = H3/.24/(T3-T2)*H
290 H4 = A1*(R/100*(FNA(T3)+FNB(T3))-(FNA(T2)+FNB(T2)))/1000
295 IF H4<0 GOTO 297
296 GOTO 300
297 H4 =0
300 Q3 = H4*(T3-T2)
305 Q2 = H3*(T3-T2)
310 Q4 =1/T9*12*(3.59/10^5/2*(T2^2-T1^2) +.0155*(T2-T1))
312 X = Q4-Q1-Q2-Q3
314 IF Y/X<0 GOTO 320
316 Y=X
318 GOTO 181
320 IF (T7-T2)<.01 GOTO 329
321 PRINT
322 Z = 10*Z
323 PRINT
324 X=Y
326 T2 =T7
328 GOTO 182
329 PRINT
330 IF T2<32 GOTO 332
331 GOTO 333
332 PRINT " COMPUTED TEMPERATURE IS BELOW 32 F.. RESULTS MAY BE INVALID"
333 PRINT
335 PRINT "INSULATION SURFACE TEMPERATURE(F) =",T2
336 PRINT
337 PRINT
340 PRINT " FORCED CONVECTION COEF = ",H2,"BTU/HR-FT-FT-F"
341 PRINT
350 PRINT " FREE CONVECTION COEF = ",H1,"BTU/HR-FT-FT-F"
351 PRINT
360 PRINT " CONDENSATION COEF = ",H4,"BTU/HR-FT-FT-F"
361 PRINT
362 PRINT "*********************************************************"
363 PRINT
364 PRINT " CASE NUMBER ";
365 INPUT M
366 PRINT
367 PRINT
370 IF M>0 GOTO 10
380 END
```

INSLDE Sample Runs

THIS PROGRAM DETERMINES THE SPRAY ON FOAM REQUIRED
TO PREVENT FROST FORMATION ON CYLINDRICAL TANKS
SUBJECT TO FORCED CONVECTION, FREE CONVECTION,
RADIATION AND CONDENSATION.

****

AMBIENT TEMPERATURE (F) = ? 60
RELATIVE HUMIDITY(%) = ? 90
RADIATION ENVIRONMENT TEMPERATURE (F) = ? 60
MINIMUM WALL SURFACE TEMPERATURE (F) DESIRED (MUST BE
GREATER THAN 32 F) = ? 32
TANK INTERNAL TEMPERATURE (F) = ? -423
DIAMETER OF TANK (FT) = ? 27
WIND VELOCITY (KNOTS) = ? 3
WALL EMISSIVITY = ? .9

INSULATION THICKNESS (IN) = .666165

 FORCED CONVECTION COEF =   .8397853   BTU/HR-FT-FT-F

 FREE CONVECTION COEF =   5133879   BTU/HR-FT-FT-F

 CONDENSATION COEF =   8307876   BTU/HR-FT-FT-F

****

CASE NUMBER ? 2

****

AMBIENT TEMPERATURE (F) = ? 60
RELATIVE HUMIDITY(%) = ? 0
RADIATION ENVIRONMENT TEMPERATURE (F) = ? 60
MINIMUM WALL SURFACE TEMPERATURE (F) DESIRED (MUST BE
GREATER THAN 32 F) = ? 32
TANK INTERNAL TEMPERATURE (F) = ? -423
DIAMETER OF TANK (FT) = ? 27
WIND VELOCITY (KNOTS) = ? 3
WALL EMISSIVITY = ? 9

INSULATION THICKNESS (IN) = 1.001191

 FORCED CONVECTION COEF =   .8397853   BTU/HR-FT-FT-F

 FREE CONVECTION COEF =   .5133879   BTU/HR-FT-FT-F

 CONDENSATION COEF =   0   BTU/HR-FT-FT-F

****

INSLPE Sample Runs

THIS PROGRAM DETERMINES THE INSULATION SURFACE TEMPERATURE
FOR SOFI ON CYLINDRICAL TANKS SUBJECT TO FORCED CONVECTION,
FREE CONVECTION, RADIATION AND CONDENSATION.

****

AMBIENT TEMPERATURE (F) = ? 60
RELATIVE HUMIDITY(%) = ? 0
RADIATION ENVIRONMENT TEMPERATURE (F) = ? 60
INSULATION THICKNESS (IN) = ? 1
TANK INTERNAL TEMPERATURE (F) = ? -423
DIAMETER OF TANK (FT) = ? 27
WIND VELOCITY (KNOTS) = ? 0
WALL EMISSIVITY = ? .9

 COMPUTED TEMPERATURE IS BELOW 32 F .. RESULTS MAY BE INVALID

INSULATION SURFACE TEMPERATURE(F) =   26.43

 FORCED CONVECTION COEF =   0   BTU/HR-FT-FT-F

 FREE CONVECTION COEF =   5477662   BTU/HR-FT-FT-F

 CONDENSATION COEF =   0   BTU/HR-FT-FT-F

****

CASE NUMBER ? 2

AMBIENT TEMPERATURE (F) = ? 90
RELATIVE HUMIDITY(%) = ? 50
RADIATION ENVIRONMENT TEMPERATURE (F) = ? 90
INSULATION THICKNESS (IN) = ? 1
TANK INTERNAL TEMPERATURE (F) = ? -423
DIAMETER OF TANK (FT) = ? 27
WIND VELOCITY (KNOTS) = ? 1
WALL EMISSIVITY = ? .9

INSULATION SURFACE TEMPERATURE(F) =   60.64

 FORCED CONVECTION COEF =   .3247857   BTU/HR-FT-FT-F

 FREE CONVECTION COEF =   .4988656   BTU/HR-FT-FT-F

 CONDENSATION COEF =   .3185926   BTU/HR-FT-FT-F

****

1974

ASEE-NASA SUMMER FACULTY FELLOWSHIP

MARSHALL SPACE FLIGHT CENTER

(AUBURN UNIVERSITY - UNIVERSITY OF ALABAMA)

ANALYSIS OF FINE GUIDANCE POINTING

STABILITY FOR SPACECRAFT

Prepared by: Walter G. Hopkins, III, Ph.D.

Academic Rank: Associate Professor

Department and University: Department of Engineering Technology
                                      Alabama A. & M. University

NASA/MSFC Assignment:
     (Office)   Preliminary Design
     (Division)   Subsystems Design
     (Branch)   Navigation and Control

NASA Research Colleague: Onis C. Green

Date: August 9, 1974

Contract No. :   NGT-01-003-045

ANALYSIS OF FINE GUIDANCE POINTING STABILITY

FOR SPACECRAFT

BY

Walter G. Hopkins, III

ABSTRACT

The purpose of this project was to perform research and theoretical invest-igations to determine the capability for fine pointing stability considering the effects of noise propagation and perturbation effects. It was also desired to develop analytic models and simulations for the fine pointing control system that were capable of assessing the effects of sensor noise, both position and rate, as well as actuator characteristics.

This study was begun by assuming a certain configuration of gyroscopic mount for a remote sensing platform (RSP) to be mounted on the Atmospheric, Magnetospheric, and Plasma in Space (AMPS) payload intended for shuttle. A deterministic model was developed and a suitable control law for pointing towards targets which are specified in earth based coordinates has been implemented. A stochastic representation was then developed and the theory of optimal estimation was reviewed to determine applicable concepts. Two alternatives are presented, one traditional Kalman filter and the other a "moving horizon" optimizer. It is suggested that these concepts be applied to payloads such as AMPS for maximum pointing accuracy due to optimum estimation of pointing related state variables.

I. INTRODUCTION

The objective of this study is to investigate the accuracy of a fine pointing control system in the presence of random disturbances such as man motion, external torque such as reaction jet firing and corrupted measurements such as those due to sensor noise. The approach taken is to model the system under consideration and to investigate classical Kalman filter techniques and also to investigate other techniques which may seem more applicable to this particular physical configuration. In order to illustrate the results, a proposed shuttle mission carrying the Atmospheric, Magnetospheric, and Plasmas in Space (AMPS) Sortie Payload was chosen to analyze. The purpose of this Sortie Mission is to observe and artificially perturb the near space environment (magnetosphere). The current mission model identifies 34 Sortie flights of the AMPS payload.

One of the experiment requirements of the AMPS payload is that a group of experiments be precisely pointed at targets specified in a rotating earth coordinate system. For example, it may be necessary to point at the horizon or to a point at a specified altitude above a prescribed location on the Earth's surface.

These experiments are to be packaged on a gimballed platform designated as the Remote Sensing Platform (RSP). It is necessary, then, to examine the control strategy required to point this RSP in the correct direction with adequate stability and to examine the pointing accuracy which can therefrom be expected.

II. AMPS FINE POINTING CONTROL

A. REMOTE SENSING PLATFORM

A candidate Remote Sensing Platform (RSP) is shown in Figure 1. The gimbal arrangement is such that pointing is normally implemented by using only two rotations (so called elevation over azimuth). A third degree of freedom, orthogonal to the other two, is available with a few degrees maximum capability in order to avoid singular conditions. This study does not consider the singularity problem, and all maneuvers in pointing are made using only the two main rotation capabilities. Although full coverage is possible by allowing only $\pm 90^{\circ}$ rotation in the outer degree of freedom, $\pm 180^{\circ}$ capability is assumed since this will not increase the package size and will probably preclude some discontinuous conditions in tracking.
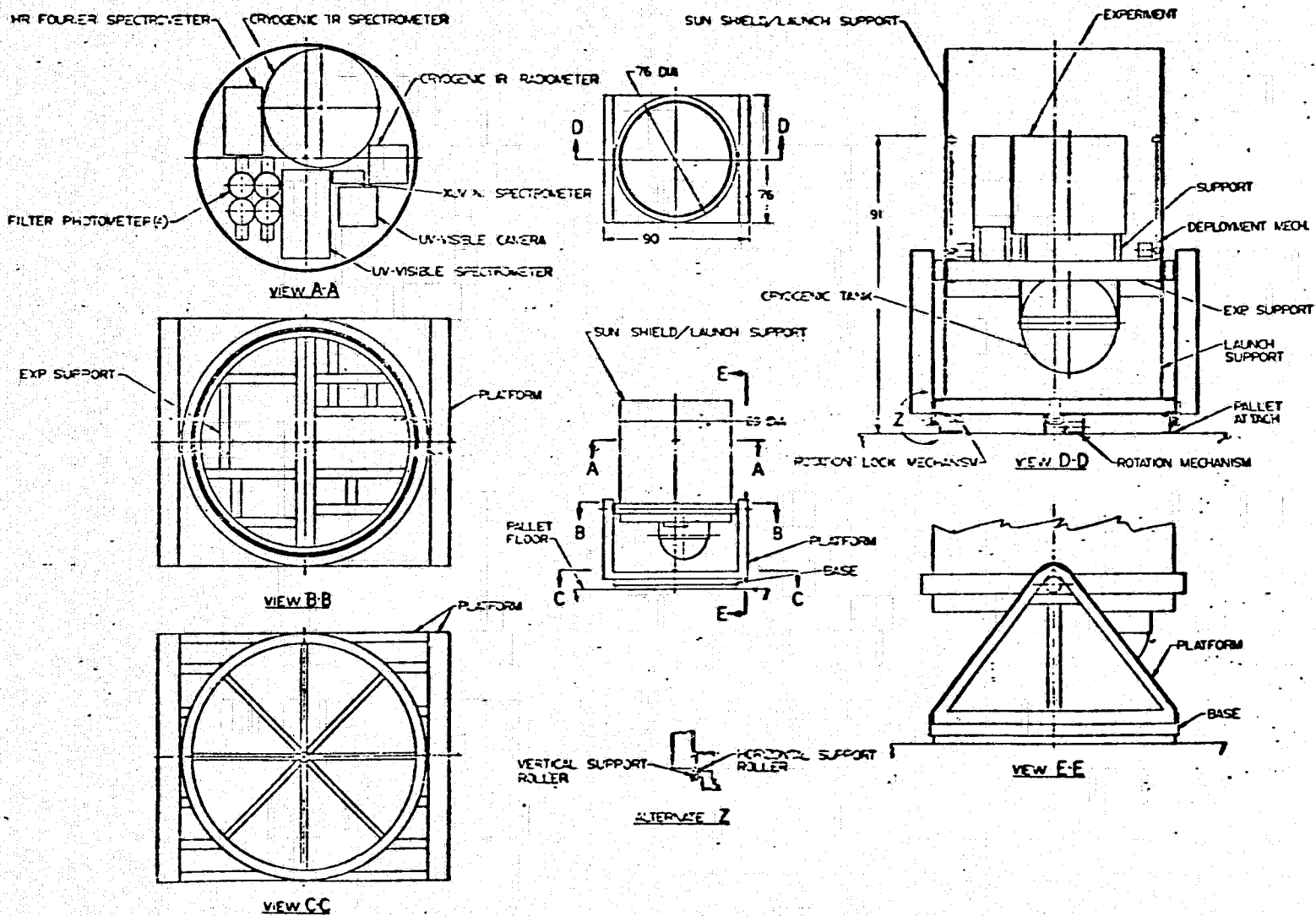
FIGURE 1. AMPS REMOTE SENSING PLATFORM

B. COORDINATE SYSTEMS

In order to develop control equations, it is first necessary to establish a set of coordinate systems to be used. Figure 2 illustrates two sets of coordinate systems. The RSP system associated with the platform is such that the Z axis is in the pointing direction, the Y axis is the axis of rotation of the inner gimbal, and the X axis forms a right-hand system. At zero deflection on both gimbals, the X axis in the RSP system is parallel to the X axis in the body coordinate system (R system), which is pointed toward the tail of the orbiter. The Z axis in the R system points up and the Y axis **forms** a right hand set. Figure 3 shows several more coordinate systems, the G, E, O, and P reference frames. All are right handed coordinate systems.

The geocentric inertial coordinate system (G) is defined so that the X and Y axes are in the equatorial plane, X pointing to Aries and the Z axis pointing north. The earth equatorial coordinate system (E) can be formed by rotating the G system about its Z axis until the X axis is aligned with the ascending line of nodes. This angle,Ω, is called the precession angle of the line of nodes. An orbit reference frame (O) can be established by a rotation about the X_E axis equal to the orbit inclination angle, i. Hence, the orbit X-Y axis lies in the orbit plane with the X **axis** along the intersection of the orbit and equatorial planes. A local vertical reference frame (P) can be established by rotating about Z_0 the angle Θ_0 which defines the Shuttle orbital position relative to the line of nodes.

In addition to the above coordinate frames, an earth-fixed frame (L) is required for locating targets. The L frame is defined such that X_L is the earth radial through the Greenwichmeridian and the equator, Y_L is in the equatorial plane and Z_L points north. The L frame is located with respect to the G inertial frame via a rotation Θ_G, about the Z_G, Z_L axis, where

$$\Theta_G = \Omega_0 (t - t_0)$$

and Ω_0 is the earth rotation rate and t_0 is a reference time.

Coordinate transformation matrices have been derived and are shown in Figure 4. The complete transformation from RSP to R coordinates is shown, but in subsequent discussion, γ is always assumed as 0^0.

C. TARGET POINTING
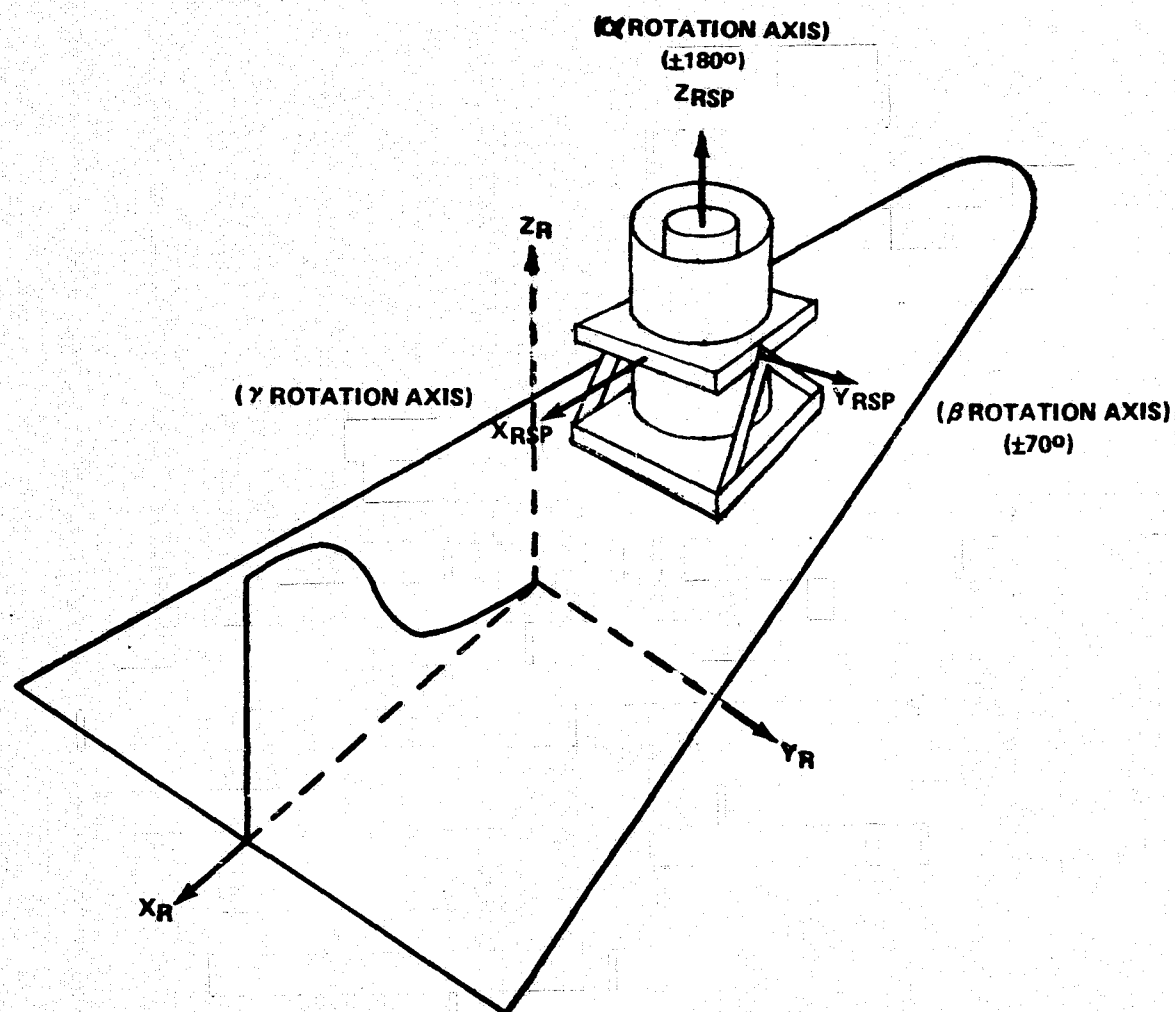
FIGURE 2. RSP MOUNTED ON ORBITER SHOWING R AND RSP COORDINATE SYSTEMS
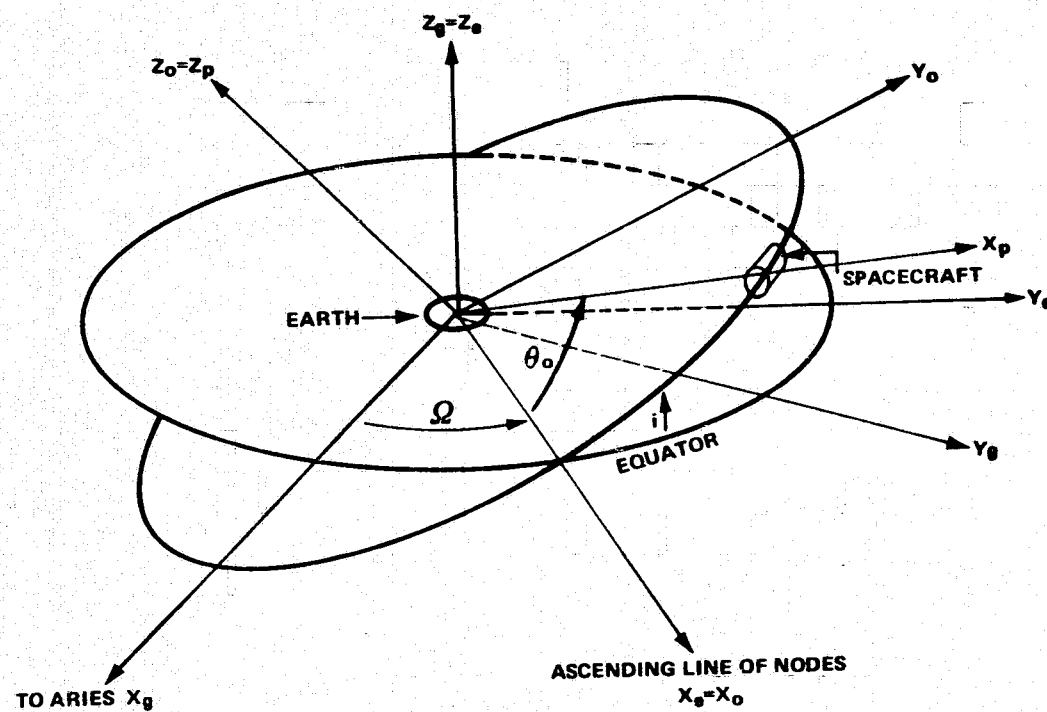
FIGURE 3. COORDINATE SYSTEMS

$$A_{EG} = \begin{bmatrix} \cos\Omega & \sin\Omega & 0 \\ -\sin\Omega & \cos\Omega & 0 \\ 0 & 0 & 1 \end{bmatrix} ; A_{DE} = \begin{bmatrix} 1 & 0 & 0 \\ 0 & \cos i & \sin i \\ 0 & -\sin i & \cos i \end{bmatrix}$$

$$A_{RSP,R} = \begin{bmatrix} C\alpha C\beta & S\alpha C\beta & -S\beta \\ C\alpha S\beta S\gamma - S\alpha C\gamma & C\alpha C\gamma + S\alpha S\beta S\gamma & C\beta S\gamma \\ S\alpha S\gamma + C\alpha S\beta C\gamma & S\alpha S\beta C\gamma - C\alpha S\gamma & C\beta C\gamma \end{bmatrix}$$

$$A_{LG} = \begin{bmatrix} \cos\theta_G & \sin\theta_G & 0 \\ -\sin\theta_G & \cos\theta_G & 0 \\ 0 & 0 & 1 \end{bmatrix} ; A_{PD} = \begin{bmatrix} \cos\theta_0 & \sin\theta_0 & 0 \\ -\sin\theta_0 & \cos\theta_0 & 0 \\ 0 & 0 & 1 \end{bmatrix}$$

FIGURE 4. TRANSFORMATION MATRICES

It is assumed that the target is initially specified in L (earth fixed) co-
ordinates. This can easily be obtained from latitude, longitude, and altitude,
as indicated in Figure 5. The current location of the Shuttle may be deter-
mined in either local vertical (P) coordinates or directly in inertial (G)
coordinates. There are two basic methods for obtaining this data. In the
first method, ground radar measurements are input to a ground based orbit
determination computation in which a convenient set of orbital elements are
derived. These elements could be orbit inclination angle, i, line of nodes
precession angle, Ω, , and geometric and timing data necessary to recon-
struct a precise orbit equation. With this data, the radius vector, in local
vertical (P) coordinates, can be reconstructed. Knowledge of Θ_0, i, and
permits transformation of this position vector to the G frame. The
second technique for obtaining Shuttle position is to obtain it directly from
the Shuttle nav computer. In this case, the data would probably be in
inertial coordinates. Very brief investigation indicates, at this point, that
both methods are of equal accuracy since the Shuttle derived data is updated
via the ground based measurements.

The tracking problem is illustrated in Figure 6. Here, it is assumed
that Shuttle position, r_R, is first in P coordinates and the target, r_T, is
specified in L coordinates. They are both transformed to G coordinates by
the indicated transformations (Figure 4). Next, a command vector, **r** point,
is obtained by

$$\{r \text{ point}\}_G = \{r_T\}_G - \{r_R\}_G$$

This command vector can be transformed to RSP coordinates by the
relation:

$$\{r \text{ point}\}_{RSP} = [A_{RSP, G}] \{r \text{ point}\}_G = \begin{Bmatrix} r_{c_1} \\ r_{c_2} \\ r_{c_3} \end{Bmatrix}$$

Figure 7 shows the relationship between these coordinates and the pointing
direction. Since it is desired that the $\{r \text{ point}\}$ RSP vector be (in normalized
form) equal to $[0 \ 0 \ 1]^T$, the components of $\{r \text{ point}\}$ RSP can be used to
provide error detection. The desired pointing direction can be obtained by
nulling r_{c_1} and r_{c_2}. The derivation of an error signal to do this is facilitated
by referring to Figure 7 and assuming that the required correction angles
are fairly small (so that small angle approximations are valid). It is assumed

$$-180° \leq \theta \text{LONG} \leq 180°$$
$$-90° \leq \theta \text{LAT} \leq 90°$$

$$X_L = H_O \cos \theta \text{LONG} \cos \theta \text{LAT}$$
$$Y_L = H_O \sin \theta \text{LONG} \cos \theta \text{LAT}$$
$$Z_L = H_O \sin \theta \text{LAT}$$
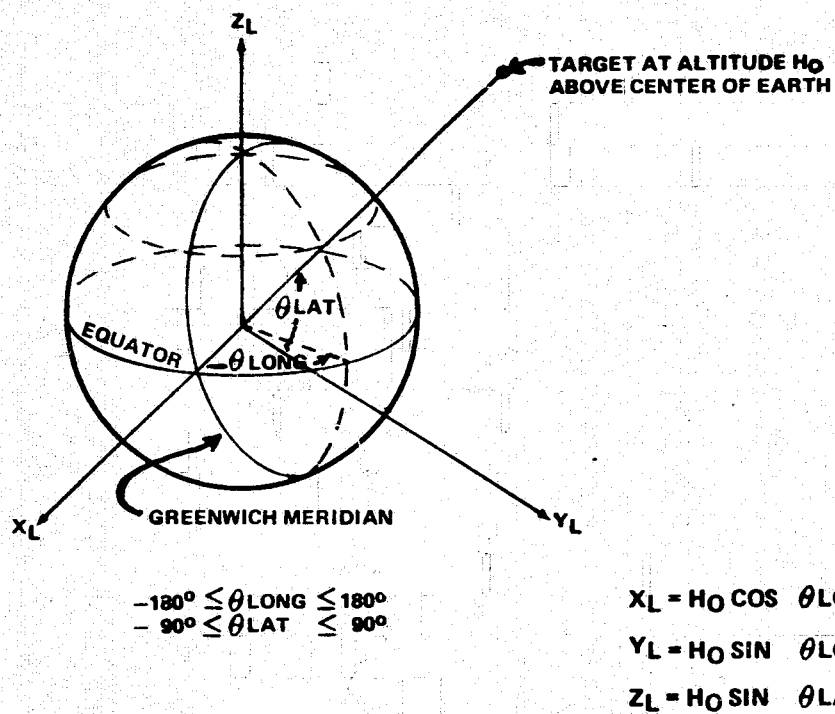
FIGURE 5. EARTH FIXED COORDINATE SYSTEMS SHOWING
RELATIONSHIP TO LATITUDE, LONGITUDE, AND ALTITUDE
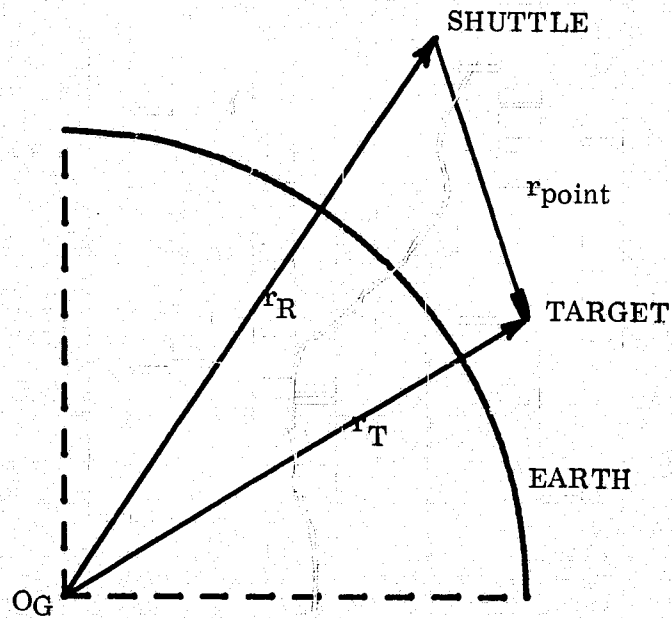
FIGURE 6. POINTING COMMAND GEOMETRY
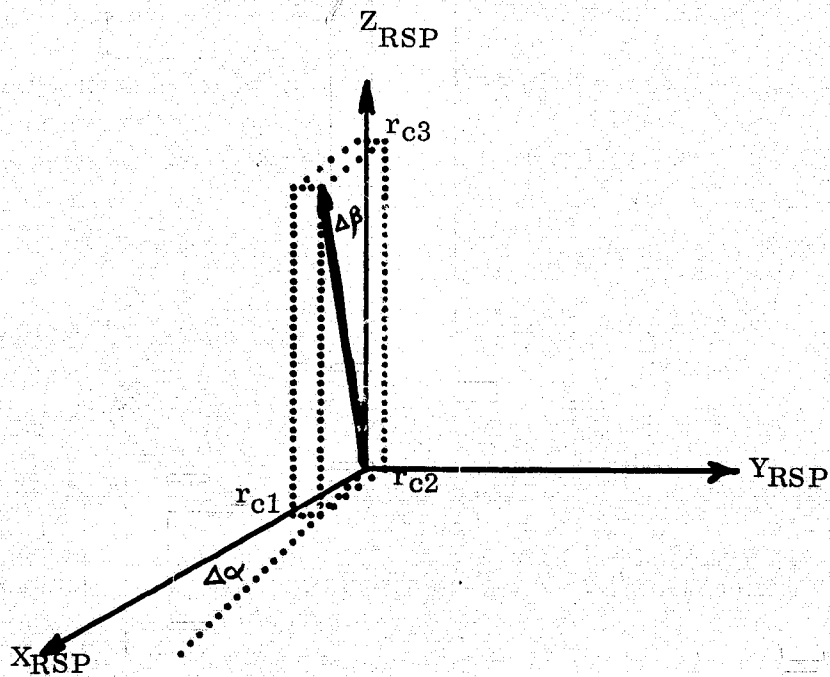
FIGURE 7. NULLING THE POINTING COMPONENTS

that the center of the RSP system and the center of the R system are coincident, even though this is not usually true. The error introduced is less than 1 sec under the mission profile studied.

$$r_{c1} = -|r \text{ point}| \cos \Delta\alpha \sin \Delta\beta$$

$$r_{c2} = |r \text{ point}| \sin \Delta\alpha \sin \Delta\beta$$

$$r_{c3} = -|r \text{ point}| \cos \Delta\beta$$

So that for small errors,

$$\Delta\alpha \approx -r_{c2}/r_{c3}$$

$$\Delta\beta \approx r_{c1}/r_{c3}$$

are the commands that the gimbals must be given to bring the RSP pointing axis (Z_{RSP}) in line with the desired pointing direction. The above calculations must be performed repeatedly to maintain the pointing direction while both the target and shuttle are moving. An illustration of this pointing law applied to an example problem is shown in Figure 8. In this figure, ideal actuator characteristics are assumed, but fairly large initial offset angles are used and the scheme still converges even though the small angle approximations are known to be inapplicable. Further experimentation would be necessary to see whether this fortunate situation would apply in a global sense. During this study, no conflicting case was found, however.

III. OPTIMAL LINEAR FILTERING

The problem of optimal linear filtering in the continuous case, using state space formulation, was first solved by Kalman and Bucy in their classic paper [1]. This filter is well known as the Kalman-Bucy filter [2, 3]. The extension to include the cross correlation was also done by Kalman [4]. More recently, an optimal filter whose implementation is more straight forward than that of Kalman has been presented [5].

This filter requires a-priori knowledge of a limited number of coefficients which can be determined by physical arguments. The stationary version of this filter has a gain given by the solution of a linear Lyapunov equation. In order to illustrate both methods, a simple example is worked from each standpoint and the resulting filters are compared.
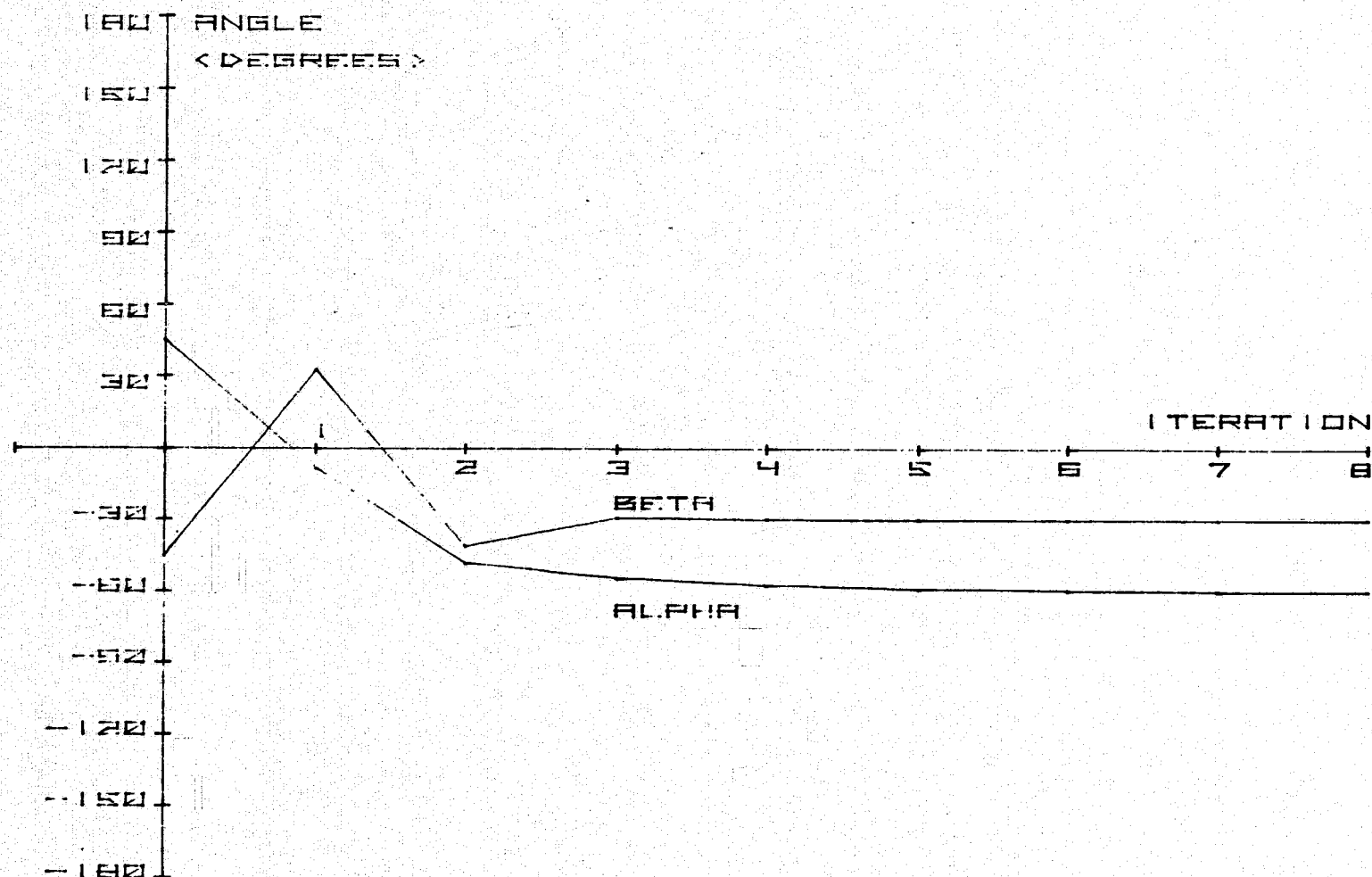
FIGURE 8. CONTROL STRATEGY APPLIED IN WHICH $\alpha_o = 45^o$, $\beta_o = -45^o$, $\alpha_f = -60^o$, $\beta_f = -30^o$

A. KALMAN FILTER

Consider the system represented in Figure 9. The equations are

$$\dot{X}(t) = F(T) X(t) + G(t) W(t) + B(t) U(t), \quad t \in [t_o, T]$$

$$X(t_o) = Xo$$

$$Z(t) = Y(t) + V(t) = H(t) X(t) + V(t)$$

where X(t) represents the true state (an n-vector), F(t) is the system dynamics matrix (n X n), G(t) is an input distribution matrix (n X k), W(t) is a white noise input (a k-vector), B(t) is the control distribution matrix (nxm), U(t) is the control (an m-vector), Xo is the initial state vector, Z(t) is the observation (a p-vector), Y(t) is the system output (a p-vector), V(t) is the output noise (a p-vector), and H(t) is the observation matrix (p X n). In addition, we define e(t), the optimal estimation error (an n-vector); P(t), the covariance of e(t) represented cov $[e(t), e(t)]$; Q(t), a k X k symmetric nonnegative definite matrix associated with W(t); R(t), a p X p symmetric positive definite matrix associated with the covariance of V(t); and S(t), a k Xp matrix associated with the cross covariance of W(t) and V(t). The optimal linear filter in this case has been shown to be, as represented in Figure 10, characterized by the solution to a matrix Ricatti equation

$$\dot{P}(t) = F(t)P(t) + P(t)F^T(t) + G(t)Q(t) G^T(t)$$
$$+ \left[P(t) H^T(t) + G(t)S(t) \right] R^{-1}(t) \left[P(t) H^T(t) + G(t)S(t) \right]^T$$

$$P(t_o) = P_o$$

where Po is the initial state covariance matrix and a superscript T represents transposition. From the solution to this equation, the optimal gain matrix is obtained as

$$K(t) = \left[P(t) H^T(t) + G(t) S(t) \right] R^{-1}(t).$$

An analytic solution is not feasible for the multivariate case, but a simple one dimensional example illustrates the technique.

1. A Scalar Example

Consider the system described by
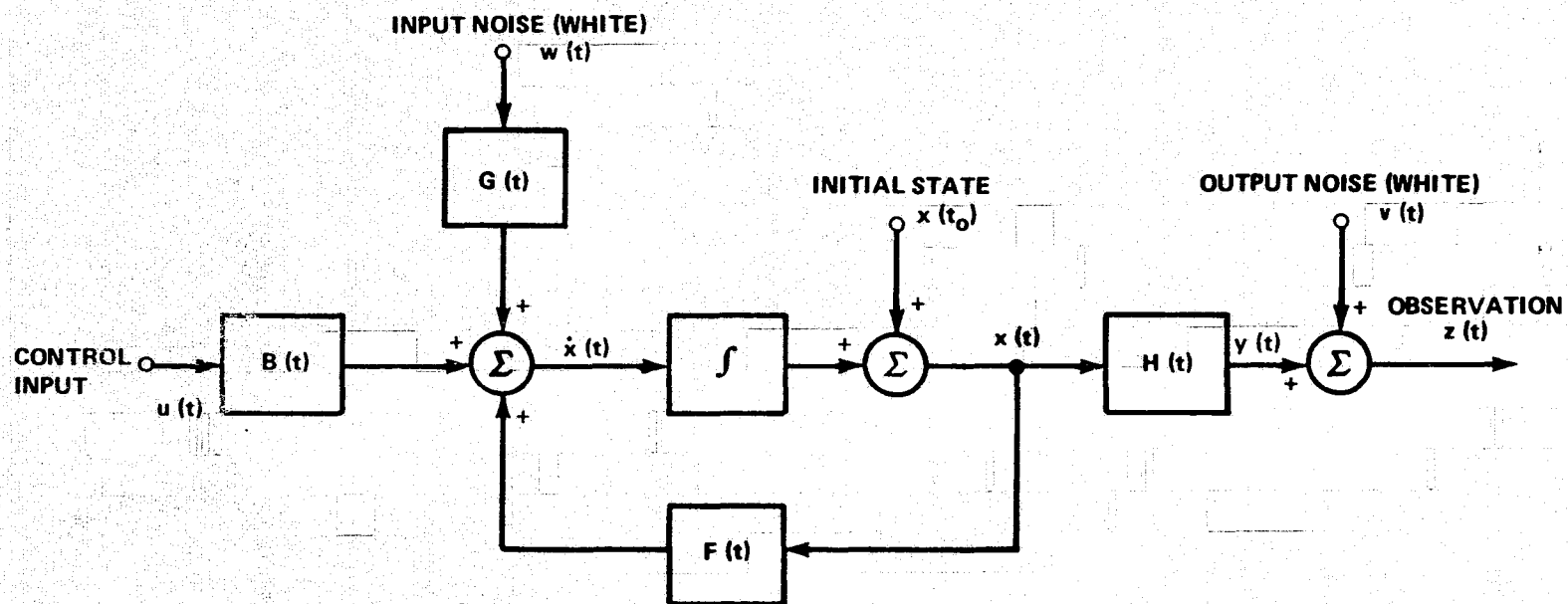
FIGURE 9. BLOCK DIAGRAM OF THE SYSTEM
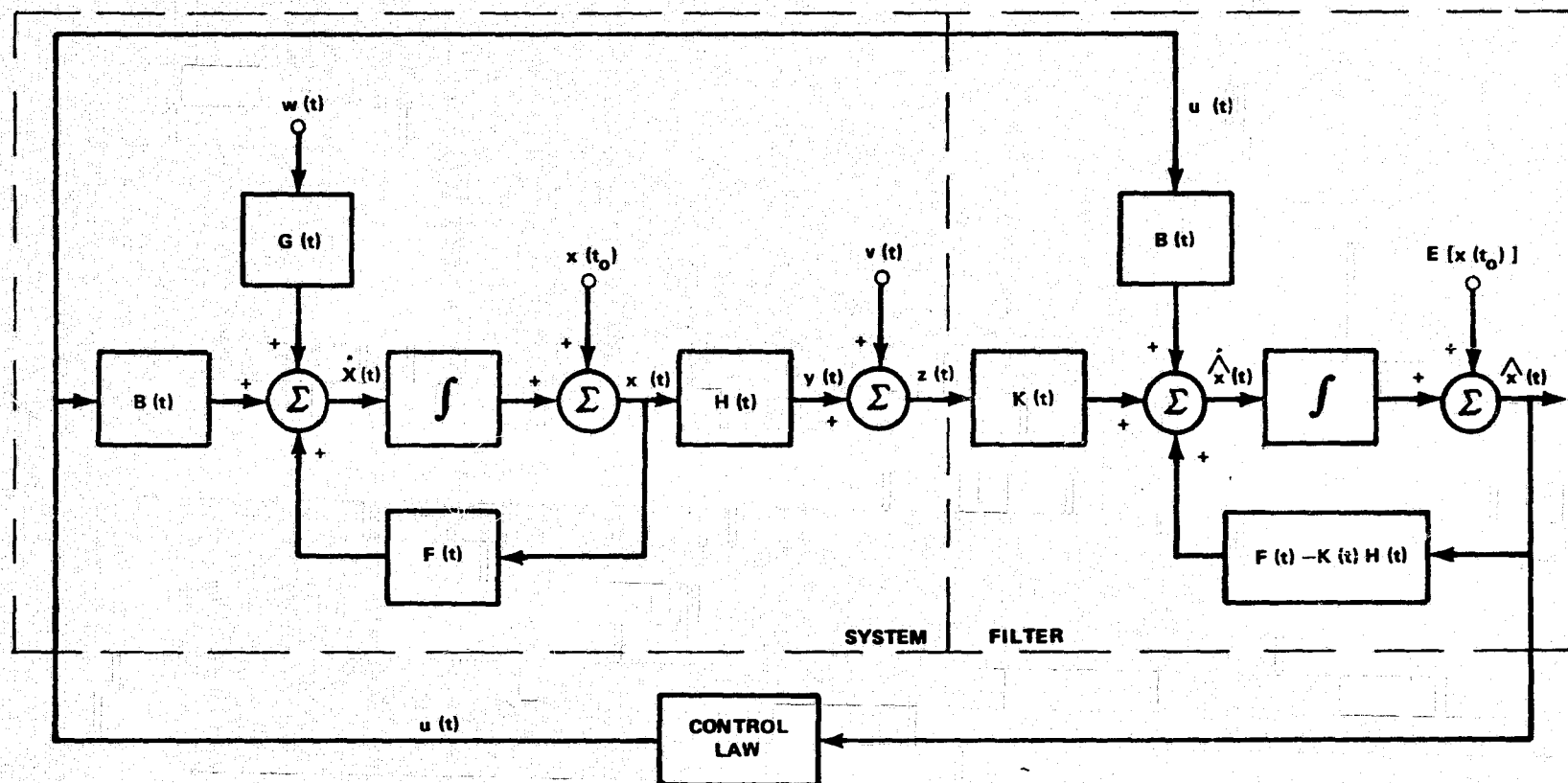
FIGURE 10. BLOCK DIAGRAM OF A SYSTEM AND ASSOCIATED OPTIMAL LINEAR FILTER

$\dot{X}(t) = -X(t) + W(t) + U(t)$

$X(o) = Xo$

$Z(t) = X(t) + V(t);$ $V(t) = 1/2 W(t).$

In the usual notation $F = [-1]$, $G = [1]$, $B = [1]$, $H = [1]$, $Q = [4]$, $R = [1]$, $S = [2]$. The solution for P is now a scalar solution to $\dot{P}(t) = -P -P + 4 + (P+2)^2$. Separation of variables and integration can be used to solve this differential equation. The result is

$$P(t) = \frac{6 P_o e^{-6t}}{6 + Po(1 - e^{-6t})}.$$

The optimal gain equation is therefore

$$K(t) = \frac{6 P_o e^{-6t}}{6 + Po(1 - e^{-6t})} + 2$$

It is of interest to consider the steady state solution for K(t) obtained when $\dot{P}(t) = O$. This could easily have been obtained directly by solving for the nonnegative solution of

$$O = -P - P + 4 + (P + 2)^2$$

and can be obtained also by taking

$$\lim_{t \to \infty} K(t) = 2.$$

2. A Vector Example:

In the second order case, a steady state solution is the only analytic one which is feasible to consider. Take the following second order example.

$\dot{X}_1 = X_2;$ $X_1(O) = 1$

$\dot{X}_2 = -3X_1 - 4X_2 + U;$ $X_2(O) = O$

$Z = [1 \quad 0] X + V$

So that $F(t) = \begin{bmatrix} O & 1 \\ -3 & -4 \end{bmatrix}$, $G(t) = \begin{bmatrix} O \\ O \end{bmatrix}$, $B(t) = \begin{bmatrix} O \\ 1 \end{bmatrix}$, $Xo = \begin{bmatrix} 1 \\ O \end{bmatrix}$, $H(t) = [1 \quad O]$, $R = [1/2]$, $Q = [O]$, $S = [O]$.

The steady state solution is obtained by solving for for P in the following ($\dot{P}$ set equal to $\begin{bmatrix} 0 & 0 \\ 0 & 0 \end{bmatrix}$).

$$\begin{bmatrix} 0 & 0 \\ 0 & 0 \end{bmatrix} = \begin{bmatrix} 0 & 1 \\ -3 & -4 \end{bmatrix} P + P \begin{bmatrix} 0 & -3 \\ 1 & -4 \end{bmatrix} -P \begin{bmatrix} 1 \\ 0 \end{bmatrix} [2][1 \ 0] P$$

A numerical method yields the following steady state solution (chosen to be the nonnegative definite solution).

$$P_{ss} = \begin{bmatrix} 10.01 & 100.24 \\ 100.24 & 2436.83 \end{bmatrix}$$

So that K (t) in steady state is

$$K_{ss} = \begin{bmatrix} 20.02 \\ 200.48 \end{bmatrix}.$$

Figure 11 shows the implementation of this filter in block diagram form where $\widehat{X}_1$ (t) and $\widehat{X}_2$ (t) are the optimal estimates of X_1 and X_2.

B. ALTERNATE OPTIMAL FILTER

Consider a system of the same form as before (Figure 9). In addition, let

$$Z \ (t) = D \ x \ (t)$$

where D is an m x n matrix (unknown) which associates a measurement at time t with the state of the system, X (t). Now define Z (τ, C) as the value of Z (t) when X (t) is equal to some arbitrary value, C. Then the difference between the process output and the model output can be written as ε (τ, C), i.e.

$$\varepsilon \ (\tau, \ C) = Y \ (\tau) - Z \ (\tau, \ C) = Y \ (\tau) - D \ X \ (\tau).$$

If there exists a C such that ε (τ, C) vanishes on $[t_o, \ t]$, it is of necessity the true state of the system. Generally there is no such C because of disturbances, measurement errors, and differences between the true equations of the process and those of the model.

In order to optimize our estimation, it is necessary to have a criterion of goodness. Consider
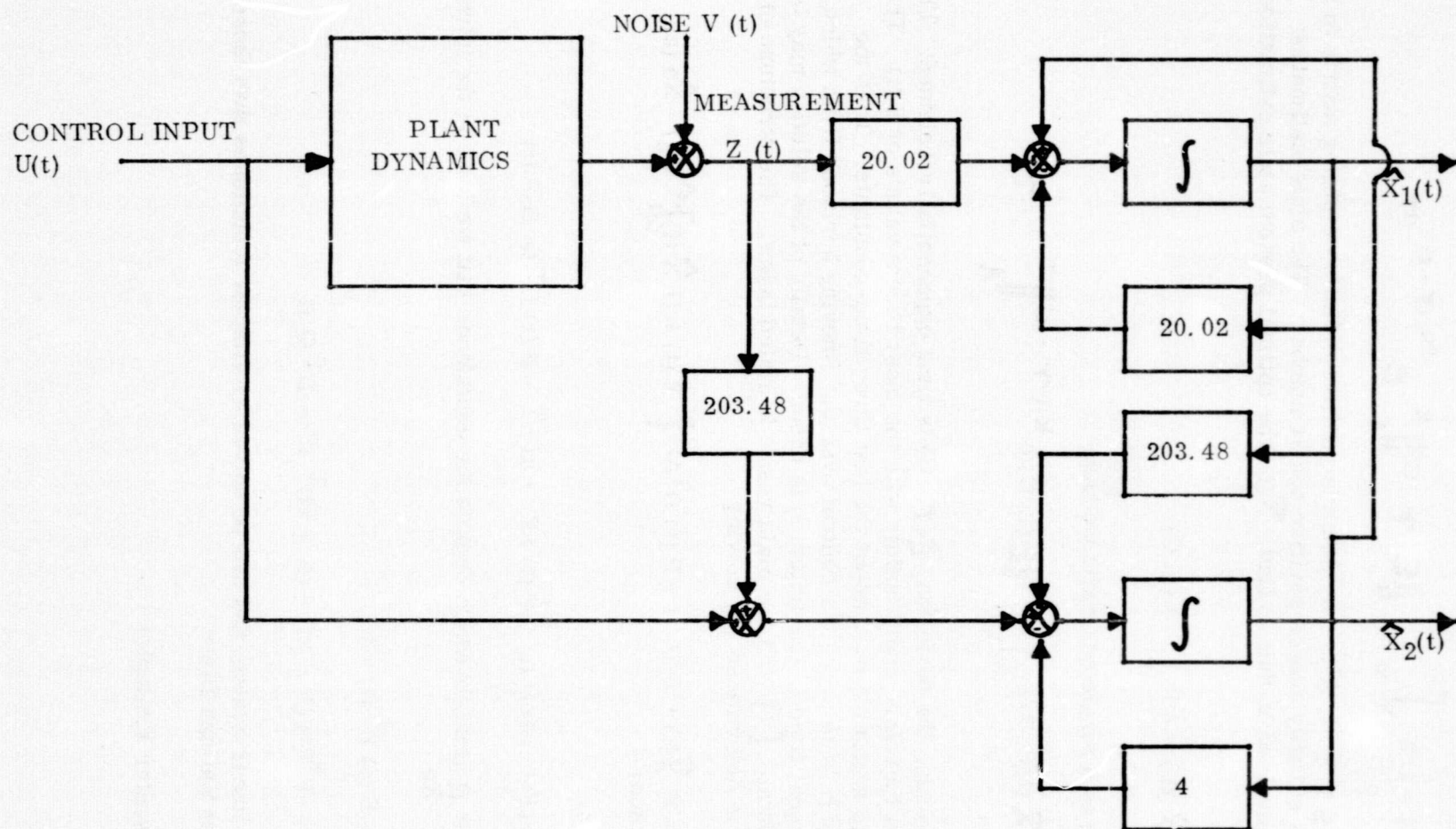
FIGURE 11. KALMAN FILTER FOR SECOND ORDER EXAMPLE

$$J(t, C) = 1/2 \int_{t_o}^{t} \| \mathcal{E}(\gamma, C) \|_A^2 \, e^{2k(\gamma - t)} \, d\gamma$$

where $t_o \leq \gamma \leq t$, A is a symmetric positive definite weighting matrix (n x n) and K is a suitably chosen positive scalar number. The state-estimation problem involved is then to find $\hat{X}(t)$ (the optimal present state estimation) such that

$$J(t, \hat{X}(t)) = \min_{C} \, J(t, C).$$

Rewriting as a single quadratic we have

$$J(t, \hat{X}(t)) = 1/2 \int_{t_o}^{t} \| \mathcal{E}(t, C) e^{k(\gamma - t)} \|_A^2 \, d\gamma \; .$$

In other words, the deviation $\mathcal{E}(\gamma, C)$ is time exponentially weighted. The estimation therefore deals mainly with the most recent values of Y (t). The effect is to minimize over about the last three time-constants. Thus the function of K is to provide a control over the "moving horizon" from which, to the present time t, the criterion is based. Details of the solution may be found in detail [5], but the main result is stated below. The structure of the filter is determined, by solving

$$\dot{\hat{X}}(t) = F \hat{X}(t) + B U(t) + P(t) D^T A \left[Y(t) - D \hat{X}(t) \right]; \hat{X}(t_o) = \hat{X}o \text{ (an}$$
initial choice)

and

$$\dot{P}(t) = (F + kI) P(t) + P(t)(F + kI)^T - P(t) D^T Q D P(t)$$

$P(t_o) \approx \Lambda$ (matrix which depicts the confidence that we have in the initial choice Xo.

or setting $P(t) P^*(t) = I$

$$\dot{P}^*(t) = -P^*(t)(F + kI) - (F + kI)^T P^* + D^T Q D$$

This is a linear system and can be solved by simpler techniques than those used in the Kalman filter.

1. A scalar Example:

The same system examined earlier is used to compare the results with a Kalman filter. Recall

$$\dot{X}(t) = -X(t) + W(t) + U(t)$$

$$X(0) = 0$$

$$Z(t) = X(t) + V(t); \quad V(t) = 1/2 \, W(t)$$

In this case, we must solve $(A = \begin{bmatrix} 4 \end{bmatrix}, \quad D = \begin{bmatrix} 1 \end{bmatrix})$ $P^* = -P^*(-1 + k) - (-1 + k) P^* + 4 = -(k - 1)^2 P^* + 4.$

The solution is

$$P^*(t) = (Po + 4)e^{-(k - 1)^2 t}$$

and therefore

$$P(t) = \frac{1}{Po + 4} e^{(k - 1)^2 t}$$

from which **k** is chosen less than one so that

$$\lim_{t \to \infty} P(t) = O.$$

The filter equations are now

$$\dot{\hat{X}}(t) = -\hat{X}(t) + U(t) + \frac{4}{Po + 4} e^{(k - 1)^2 t} \begin{bmatrix} Z(t) - \hat{X}(t) \end{bmatrix}$$

$$\hat{X}(t_o) = E\begin{bmatrix} X(t_o) \end{bmatrix}$$

and the realization approaches a Kalman filter as $t \to \infty$.

IV. APPLICATION OF OPTIMAL ESTIMATION TO AMPS

The application of the theory discussed in the previous section is applied in this section to a system such as the AMPS pointing control system. For simplicity, only one gimbal servo system is analyzed numerically, however only complexity of presentation and computation precludes application to all gimbals including cross coupling if desired.

A. RSP GIMBAL DYNAMICS

Assume that the state equations of the gimbal servo loops is available in the form

$$\dot{X}(t) = F(t) x(t) + G(t) W(t) + B(t) U(t)$$

$$X(t_o) = X_o$$

$$Z(t) = H(t) x(t) + V(t)$$

Where $V(t)$ represents measurement noise (all contributions lumped) and $W(t)$ represents perturbation to the system dynamics (again lumped together and resulting primarily from man motion and thruster firings). Then the solution for the Kalman filter is simply that shown in figure 10 with $K(t)$ obtained in the manner outlined in the previous section. The total implemen - tation would be similar to that shown in Figure 12.

B. NUMERICAL EXAMPLE

Assume that one of the gimbals is adequately described by the transfer function $\dfrac{40}{s^2(s+1)}$. Then define the angle of that gimbal to be θ.

Let $\quad X_1 = \theta$

$$X_2 = \dot{\theta} = \dot{X}_1$$

$$X_3 = \ddot{\theta} = \dot{X}_2$$

Or

$$\dot{X}_1 = X_2$$

$$\dot{X}_2 = X_3$$

$$\dot{X}_3 = -X_3 + 40\ U$$

Adding noise processes, we obtain

$$\dot{X}(t) = F(t) x(t) + G(t) W(t) + B(t) U(t)$$

$$X(t_o) = X_o$$

$$Z(t) = H(t) x(t) + V(t)$$
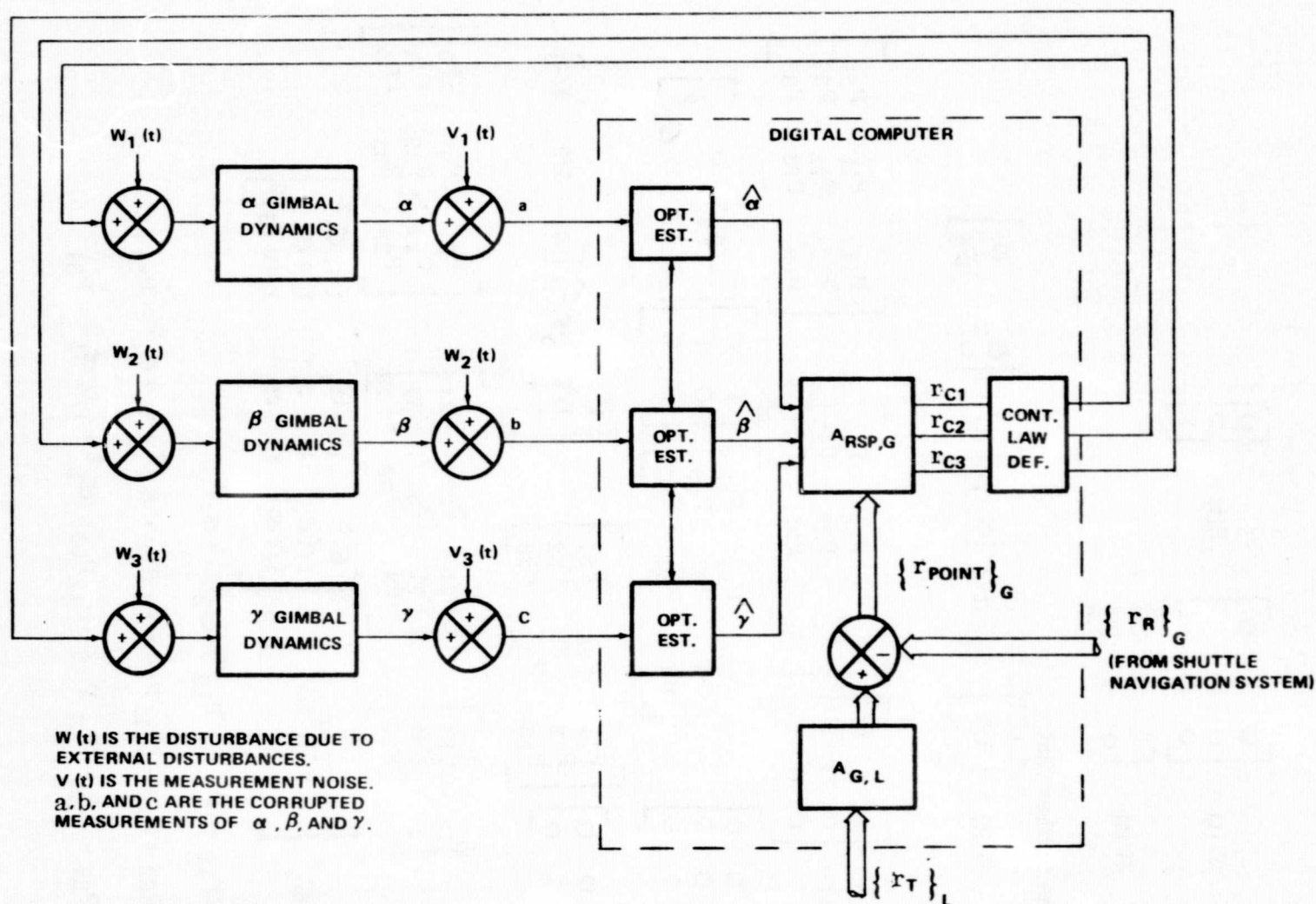
FIGURE 12. IMPLEMENTATION OF AN AMPS CONTROL SCHEME
SHOWING THE LOCATION OF OPTIMAL ESTIMATION FILTERS

10-23

Where

$$F(t) = \begin{bmatrix} O & 1 & O \\ O & O & 1 \\ O & O & -1 \end{bmatrix} \qquad B(t) = \begin{bmatrix} O \\ O \\ 1 \end{bmatrix}$$

$$H(t) = \begin{bmatrix} 1 & O & O \\ O & 1 & O \end{bmatrix}$$

Assume further that

$$G(t) = \begin{bmatrix} 1 \\ 1/2 \\ 1/4 \end{bmatrix} \; ; \; Q(t) = \begin{bmatrix} \sigma_1^2 \end{bmatrix}; \; R(t) = \begin{bmatrix} \sigma_2^2 & O \\ O & \sigma_2^2 \end{bmatrix}$$

Then

$$\dot{P}(t) = \begin{bmatrix} O & 1 & O \\ O & O & 1 \\ O & O & -1 \end{bmatrix} \begin{bmatrix} P_{11} & P_{12} & P_{13} \\ P_{21} & P_{22} & P_{23} \\ P_{31} & P_{32} & P_{33} \end{bmatrix} + \begin{bmatrix} P_{11} & P_{21} & P_{31} \\ P_{12} & P_{22} & P_{32} \\ P_{13} & P_{23} & P_{33} \end{bmatrix}$$

$$\begin{bmatrix} O & O & O \\ 1 & O & O \\ O & 1 & -1 \end{bmatrix} - \begin{bmatrix} P_{11} & P_{12} & P_{13} \\ P_{21} & P_{22} & P_{23} \\ P_{31} & P_{32} & P_{33} \end{bmatrix} \begin{bmatrix} 1 & O \\ O & 1 \\ O & O \end{bmatrix} \begin{bmatrix} 1/\sigma_2^2 & O \\ O & 1/\sigma_2^2 \end{bmatrix}$$

$$\begin{bmatrix} 1 & O & O \\ O & 1 & O \end{bmatrix} \begin{bmatrix} P_{11} & P_{21} & P_{31} \\ P_{12} & P_{22} & P_{32} \\ P_{13} & P_{23} & P_{33} \end{bmatrix} + \begin{bmatrix} 1 \\ 1/2 \\ 1/4 \end{bmatrix} \begin{bmatrix} \sigma_1^2 \end{bmatrix} \begin{bmatrix} 1 & 1/2 & 1/4 \end{bmatrix}$$

$$\begin{bmatrix} \dot{P}_{11} & \dot{P}_{12} & \dot{P}_{13} \\ \dot{P}_{21} & \dot{P}_{27} & \dot{P}_{23} \\ \dot{P}_{31} & \dot{P}_{32} & \dot{P}_{33} \end{bmatrix} = \begin{bmatrix} P_{21} & P_{22} & P_{23} \\ P_{31} & P_{32} & P_{33} \\ -P_{31} & -P_{32} & -P_{33} \end{bmatrix} + \begin{bmatrix} P_{21} & P_{31} & -P_{31} \\ P_{22} & P_{32} & -P_{32} \\ P_{23} & P_{33} & -P_{33} \end{bmatrix}$$

$$- 1/\sigma_2^2 \begin{bmatrix} P^T H^T H P \end{bmatrix} + \begin{bmatrix} \sigma_1^2 & 1/2\,\sigma_1^2 & 1/4\,\sigma_1^2 \\ 1/2\sigma_1^2 & 1/4\,\sigma_1^2 & 1/8\,\sigma_1^2 \\ 1/4\sigma_1^2 & 1/8\,\sigma_1^2 & 1/16\,\sigma_1^2 \end{bmatrix}$$

$$\dot{P}_{11} = 2P_{12} - (P_{11}^2 + P_{12}^2)/\sigma_2^2 + \sigma_1^2$$

$$\dot{P}_{12} = P_{22} + P_{13} - (P_{11}P_{12} + P_{12}P_{22})/\sigma_2^2 + 1/2\,\sigma_1^2 = \dot{P}_{21}$$

$$\dot{P}_{13} = P_{23} - P_{13} - (P_{11}P_{13} + P_{12}P_{23})/\sigma_2^2 + 1/4\,\sigma_1^2 = \dot{P}_{31}$$

$$\dot{P}_{22} = 2P_{23} - (P_{12}^2 + P_{22}^2) / \sigma_2^2 + 1/4 \, \sigma_1^2$$

$$\dot{P}_{23} = P_{33} - P_{23} - (P_{12} P_{13} + P_{22} P_{23}) / \sigma_2^2 + 1/8 \, \sigma_1^2 = \dot{P}_{32}$$

$$\dot{P}_{33} = -2P_{33} - (P_{13}^2 + P_{23}^2) / \sigma_2^2 + 1/16 \, \sigma_1^2$$

For $\sigma_1^2 = .5$, $\sigma_2^2 = .2$, numerical results are

$$P_{SS} = \begin{bmatrix} .372621 & .166039 & .045086 \\ .166039 & .083996 & .024061 \\ .045086 & .024061 & .009096 \end{bmatrix}$$

and

$$K_{SS} = \begin{bmatrix} .372621 & .166039 \\ .166039 & .083996 \\ .045086 & .024061 \end{bmatrix} \begin{bmatrix} 5 & 0 \\ 0 & 5 \end{bmatrix}$$

$$= \begin{bmatrix} 1.863105 & .830195 \\ .830195 & .419980 \\ .225430 & .120305 \end{bmatrix}$$

V. RESULTS AND SUGGESTIONS

Either of the two optimal estimation schemes described in the previous section should be applicable to AMPS. Due to the late stage in the research that the paper [5] was obtained. the results presented therein have not been completely digested in order to know the full possibilities as applied to a vehicle such as AMPS. The Kalman filter as presented in the previous section is, however, completely applicable. The only drawback is the difficulty of solving multiple variable non-liner equations. a drawback eliminated in the altemate scheme. For this reason it is suggested that further work be done to completely evaluate the contribution made in this recent study [5] .

Either method of estimation could then be simulated and the effect on noisy measurements be evaluated. For this purpose an analog simulation would be useful but lacks the capability to simulate an on board computer in the feedback loop. For this overall evaluation, a hybrid computation would be desirable.

Contributions to pointing error such as misalignment of the gimbal systems with the shuttle itself and flexible members in the control loops are not accounted for in this type of formulation. These are two more problems which should be attacked in any final study of the AMPS pointing problem.

REFERENCES

1. Kalman, R. E., and R. S. Bucy, "New Results in Linear Filtering and Predicting Theory," _Transactions of the ASME, Journal of Basic Engineering,_ 83D, March 1961, pp. 95-108.

2. Kalman, R. E., "Linear Stochastic Filtering Theory-Reappraisal and Outlook," _Proc. Symp.on System Theory_ (Polytechnic Institute of Brooklyn, New York, April 1965), pp. 197-205.

3. Athans, M. and E. Tse, "A Direct Derivation of Optimal Linear Filters Using the Maximum Principle," _IEEE Trans. on Automatic Control,_ Vol. AC-12, No. 6, December 1967, pp. 690-698.

4. Kalman, R. E.,"New Methods in Wiener Filtering Theory," _Proc. First Symp. on Engineering Applications of Random Function Theory and Probability._ New York: John Wiley and Sons, Inc., 1963, pp. 270-388.

5. de Larminat, P., D. Sarlat, and Y. Thomas, "Invariant Imbedding and Filtering: A Moving Horizon Criterion," _Proceedings of the 1974 Joint Automatic Control Conference,_ (Austin, Texas, June 1974), pp. 609-614.

6. Dwivedi, N. P., _Filtering and Optimization of Linear Stochastic Systems with Cross-Correlated Noise: An Application to Fine Pointing Control System,_ Ph.D. Dissertation, Auburn University, Auburn, Alabama, 1969.

1974

ASEE-NASA SUMMER FACULTY FELLOWSHIP PROGRAM

MARSHALL SPACE FLIGHT CENTER

(AUBURN UNIVERSITY - UNIVERSITY OF ALABAMA)

ON THE MEANING OF THE
HOLOGRAPHIC INTERFEROMETRIC FRINGES

Prepared by: Hua-Kuang Liu, Ph. D.

Academic Rank: Associate Professor

Department and University: Department of Electrical Engineering
                                          The University of Alabama

NASA/MSFC Assignment: Space Sciences Laboratory
                                          Physics & Instrumentation Division
                                          Optics & Electro-Optics Branch

NASA Research Colleague: Robert L. Kurtz, Ph. D.

Date: August 9, 1974

Contract No.:   NGT-01-003-045

ON THE MEANING OF THE
HOLOGRAPHIC INTERFEROMETRIC FRINGES

By

Hua-Kuang Liu

ABSTRACT

A brief review of the principles of a holographic nondestructive test system (HNDT) and the theory of small surface displacement has been carried out. The theory of Haines and Hildebrand and Sollid was extended to interpret the relationship between the holographic interferometric fringes and the surface variations. Experiment on small surface displacement due to the object's lateral translations of less than $10 \mu m$ was performed in the HNDT system. Data revealed excellent agreement with the theoretical predictions. Applications of the findings to the holographic nondestructive test system are discussed.

TABLE OF CONTENTS

LIST OF FIGURES

I. INTRODUCTION

Recently, laser holographic nondestructive testing (HNDT) technique has been proved to be very sensitive and effective in the detection of debonds in ceramic-epoxy-fiberglass composite structures [1]. The debonds would appear as surface deformation after the structure was loaded by an appropriate external stress. Either double-exposure or real-time interference fringe patterns would be able to reveal the existence of any surface deformation on the order of a quarter of the radiation wavelength of the laser. Small displacements on the surface would cause nonuniformity or irregularity in the interference patterns [2].

To understand the experimental results, it is important to interpret the fringe patterns. Haines and Hildebrand have presented a detailed theory for the interpretation of the interference phenomenon. Sollid [3] has discussed how either a single hologram or multiple holograms could be used in the measurement of small static displacements on a diffusely reflecting surface. However, in any practical situation these theories are found to be difficult, if not impossible, to apply.

Very lately, Bellani and Sona [4] have reported the method of scanning a double-exposure hologram and counting the number of fringes on the real image of the object. The method worked well with simple motions of the object, but it was not applied to any complex displacements.

All the above work is based on the principle of the small displacement of the object from one point to another only, but no explicit explanation between fringe contrast and the displacement of the object was given. Many workers have attempted to use the term "fringe localization" in the consideration of the relationship between fringes and object displacement. The application of the concept of fringe localization is in practice often very confusing since interference is a three-dimensional phenomenon; and, therefore, it is extremely difficult, if not impossible, to catch the localized position of the fringes.

The purpose of the present report is to show that the theory of Haines and Hildebrand can be extended such that a direct interpretation of the relationship between the fringe contrast and surface displacement can be accomplished. The results interpret experimental findings due to simple translation of the object quite satisfactorily. It can be seen that this kind of interpretation gives good insight into the fringe variations when a more complicated object such as a shuttle engine is under test in a holographic nondestructive test system. The HNDT system and the research results of Haines and Hildebrand and Sollid are briefly described in Section II. The extension of this theory is given in Section

III. Section IV presents the experimental data and their interpretation by the application of the present theorem. And, finally, Section V provides the conclusion.

II. THEORETICAL REVIEW

The Composite Mobile HNDT System

The composite mobile HNDT system is a variable sensitivity system. The main advantage of this kind of system is that all methods of HNDT can be accommodated with basically the same holographic arrangement. The system can be illustrated by Figure 1. Configuration No. 1 of Figure 1 may be described below. Laser light is incident on the field mirror assembly which contains a spatial filter and a beam splitter. This assembly or unit is translatable to the left along the path Sb. The reflected portion of the radiation is made incident on the micrometer translatable object in such a direction as to make an angle $\theta = 0$ with the perpendicular bisector of this object. This radiation is then turned antiparallel to itself where it passes onto the film recorder. The film recorder is itself translatable to the right along the path Δf. The radiation transmitted through the field mirror assembly is incident on mirror M, which is itself translatable to the right along path Δm. From here it is turned to be incident on the film recorder and interferes with the object beam.

Configuration No. 2 may be traced in a similar fashion, except that the object beam makes some angle $\theta > 0$ with the perpendicular bisector of the object.

The system is composite because one needs to only slightly manipulate three components (field mirror assembly, mirror M, and film recorder) to change from one method of HNDT to another. It is not necessary to establish a new geometry in order to perform the various HNDT methods. The system is mobile because all of the optical components are mounted on a precalibrated rigid table and may be locked in any position along their translatable paths. The system has variable sensitivity (which affords the composite structure) by virtue of the control over the angle θ which the object beam makes with the perpendicular bisector of the object.

The principle of the double-exposure technique has shown that zeros indicating the presence of fringes occur for the movement of the object for a distance

CONFIGURATION #1
$\theta_i = 0$

MICROMETER
TRANSLATABLE
OBJECT

$\theta_1 = \theta_2 = 0$

FIELD
MIRROR
ASSEMBLY

Δm

LASER

M

ΔSb

FILM

Δf

CONFIGURATION #2
$\theta_i > 0$

FIELD MIRROR ASSEMBLY

$\theta_1 | \theta_2$

$\theta_1 = \theta_2 > 0$

MICROMETER
TRANSLATABLE
OBJECT

ΔM

LASER

M

ΔSb

Δf
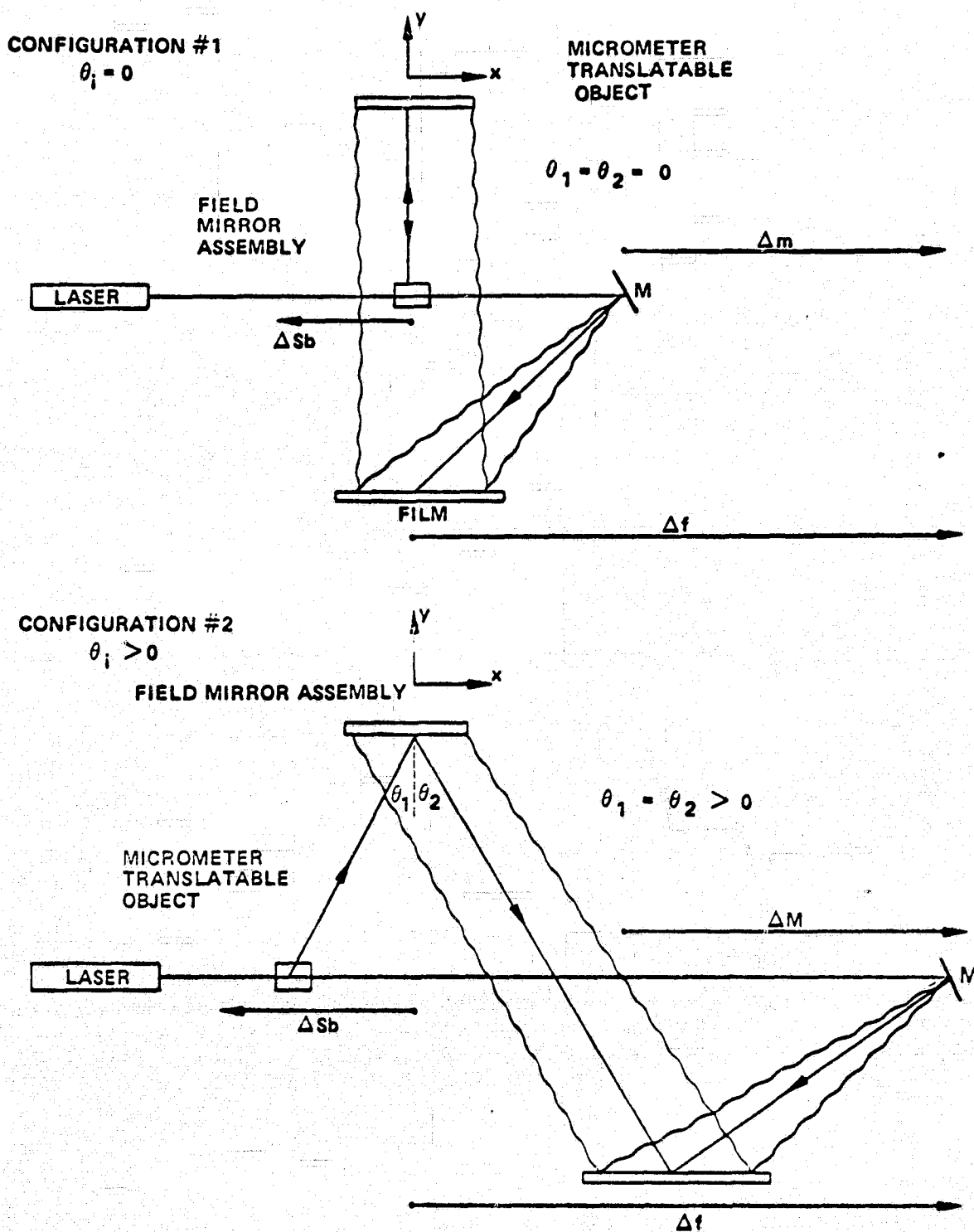
FIGURE 1. COMPOSITE MOBILE HOLOGRAPHIC NONDESTRUCTIVE
TEST SYSTEM.

$$m = \frac{(2n - 1)\lambda}{2(\cos \theta_i + \cos \theta_s)} \tag{1}$$

where n is the number of fringes.

Consider the case of $\theta_1 = \theta_2 = 0$, and $\lambda = 6328 \,\overset{\circ}{A}$ for a He-Ne laser; then Equation (1) becomes

$$m = (2n - 1)\frac{\lambda}{4} = (2n - 1) \frac{6328 \overset{\circ}{A}}{4} = (2n - 1) 0.1582 \mu m \ ,$$

which says that in order to obtain one fringe on the object, the movement of the object (in the same direction) must be as great as $0.6112 \mu m$. While both of these movements are small, their relative values differ by about one-half order of magnitude. This provides an indication of the variation of sensitivity of this system by the minute adjustment of three single components on a precalibrated mobile table. The table is precalibrated in terms of the desired sensitivity.

Fringe Formation in the HNDT System

In the application of holography to the field of nondestructive testing, it is generally agreed that there are three kinds of techniques: real-time, double-exposure, and time-averaged. Nevertheless, the basic principle with regard to the interference fringe formation is the same for all three techniques. This principle can be illustrated by the real-time testing case as discussed below. The application of this principle to the other two cases will follow.

As mentioned in the last section, the present holographic nondestructive testing system is based on the principle that extremely small displacements on the surface of an object, on the order of .15 μm (if a He-Ne laser is used), can be detected by the difference of the interference fringe patterns as viewed through the hologram on a real-time basis. The fringe patterns will vary according to the small displacement on the surface because there is a phase difference between the two path lengths, one is the light from a point of the virtual image of the object and the other is from the same corresponding point on the real displaced object. The phase difference can be simply analyzed with the help of Figure 2 [2, 3].

Where in Figure 2, S represents the laser light source, p and p' represent, respectively, the same spot on the virtual image of the object and the displaced object. H is a point on the hologram. It can be easily seen that the path length L_1 and L_2 may be written in terms of the various distance vectors as follows:
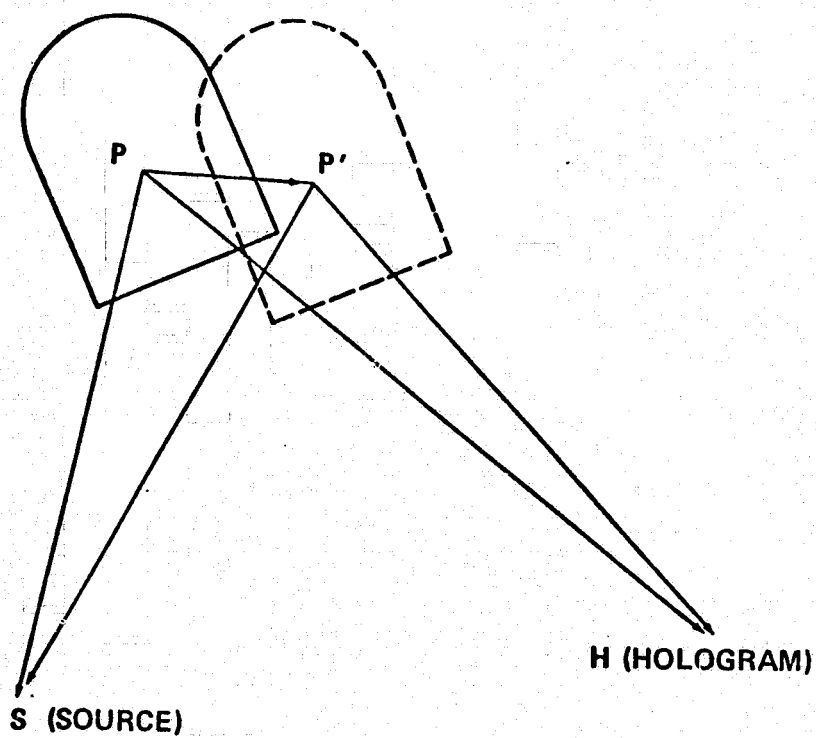
FIGURE 2. CREATION OF THE PHASE DIFFERENCE $\Delta \theta$

$$L_1 = \left|\vec{pS}\right| + \left|\vec{pH}\right|$$

$$= (\vec{pS} \cdot \vec{pS})^{\frac{1}{2}} + (\vec{pH} \cdot \vec{pH})^{\frac{1}{2}} \tag{2}$$

and

$$L_2 = (\vec{p'S} \cdot \vec{p'S})^{\frac{1}{2}} + (\vec{p'H} \cdot \vec{p'H})^{\frac{1}{2}} . \tag{3}$$

The phase difference θ is defined as

$$\theta = (2\pi/\lambda) \times (L_1 - L_2) , \tag{4}$$

where λ is the wavelength of the light.

Through some arithmetic manipulations and an assumption that the displacement $\vec{pp'}$ is always much smaller than either $\vec{pS}$ or $\vec{pH}$, we obtain a simplified expression [2] for $\Delta\theta$:

$$\Delta\theta = (2\pi/\lambda) \times [\vec{pS}/(\vec{pS} \cdot \vec{pS})^{\frac{1}{2}} + \vec{pH}/(\vec{pH} \cdot \vec{pH})^{\frac{1}{2}}] \cdot \vec{pp'} . \tag{5}$$

The above equation represents a general and basic relation necessary for the analysis of the small displacements in any holographic interferogram of a diffusely reflecting surface.

In the application of this principle to explain the double-exposure technique, all we have to do is to consider the interference between two virtual images displaced from each other.

If we apply Equation (5) to the three-dimensional case just as in our nondestructive testing system where we have no a priori knowledge of the displacement vector, theoretically speaking, two methods are available for the determination of the displacement vector $\vec{pp'}$ based on the observed fringe patterns. If zeroth-order fringes are identifiable, a multiple hologram method [3] may be used. If, on the other hand, the zeroth-order fringes cannot be localized, a single hologram technique must be employed. Very recently, Bellani and Sona [4] reported that they have applied a new scanning method which was able to count the number of fringes from the real image of a double-exposure hologram. The method was not tested for the case of any complicated motion of the object or any object with irregular or curved surfaces as in realistic testing situations.

III. THEORY

The present theory is based on the result of Equation (5) in the last section; and, therefore, all the assumptions in the derivation of Equation (5) will still be valid. For simplicity, we shall use $\vec{k}_1$, $\vec{k}_2$ and $\vec{d}$ to represent, respectively, the unit vectors along $\vec{pS}$, $\vec{Hp}$ and the displacement vector $\vec{pp'}$. Equation (5) then can be rewritten as

$$\Delta\theta = (2\pi/\lambda) \times (\vec{k}_1 - \vec{k}_2) \cdot \vec{d} \quad . \tag{6}$$

If a point P_1 translates to a new position Q_1 through a displacement vector $\vec{d}_1$ and another point P_2 translates to a new position Q_2 through a displacement vector $\vec{d}_2$, the fringe contrast as viewed from the hologram position H is controlled by the difference of the phase differences $\Delta\theta_1$ of P_1 and $\Delta\theta_2$ of P_2, which will be denoted as $\Delta\delta$. That is,

$$\Delta\delta = \Delta\theta_1 - \Delta\theta_2 \quad . \tag{7}$$

In the above equation

$$\Delta\theta_1 = (2\pi/\lambda)(\vec{k}_{11} - \vec{k}_{12}) \cdot \vec{d} \tag{8}$$

and

$$\Delta\theta_2 = (2\pi/\lambda)(\vec{k}_{21} - \vec{k}_{22}) \cdot \vec{d} \quad , \tag{9}$$

where the k vectors in Equations (8) and (9) are defined in a similar fashion as those in Equation (6).

When $\Delta\delta = \pi$, the contrast between the two points, P_1 and P_2, should be the greatest. With this interpretation of the fringes in mind, it is clear that we do not have to localize the fringes in the process of their interpretation with regard to surface displacement. For the purpose of the illustration of the principle just derived, a simple experiment is discussed below.

IV. EXPERIMENTAL DATA AND THEIR INTERPRETATION

The double-exposure holographic technique was applied to a flat object of approximately 8.6 cm × 8.6 cm in the HNDT system. Small displacement was controlled by a micrometer with an accuracy of 2.54 μm for the finest scale. Between the two exposures, a translation of the object along the direction parallel to the surface was made. Representative results are shown in Figure 3. These photographs are taken from the real images of the double-exposure holograms. Figure 3(a) has had a lateral displacement of (4.5 ± 0.5) μm and Figure 3(b) has had a (16.5 ± 0.5) μm translation between the two exposures, respectively. The errors recorded are attributed to either the mechanical inaccuracies of the micrometer or to the human error in the reading of the micrometer dial.

The above results can be interpreted by the application of Equation (7) with the assistance of Figure 4 as follows. In Figure 4, ABCD and A'B'C'D' represent, respectively, the original and displaced flat surfaces of an object. The displacement vector is denoted by $\vec{d}$. If the surface is rigid, then the four representative points on the surface, P_{11}, P_{12}, P_{21} and P_{22}, will translate to Q_{11}, Q_{12}, Q_{21} and Q_{22} by the same amount, $\vec{d}$. Notice that P_{11} and P_{12} were chosen on one vertical line, and P_{21} and P_{22} were chosen on another vertical line for the purpose of the present consideration.

According to Equations (8) and (9), the phase differences of the four points are

$$\Delta\theta_{11} = (2\pi/\lambda)\,\vec{d}\cdot(\vec{k}_{111} - \vec{k}_{112}) \ , \tag{10}$$

$$\Delta\theta_{21} = (2\pi/\lambda)\,\vec{d}\cdot(\vec{k}_{211} - \vec{k}_{212}) \ , \tag{11}$$

$$\Delta\theta_{12} = (2\pi/\lambda)\,\vec{d}\cdot(\vec{k}_{121} - \vec{k}_{122}) \ , \tag{12}$$

$$\Delta\theta_{22} = (2\pi/\lambda)\,\vec{d}\cdot(\vec{k}_{221} - \vec{k}_{222}) \ , \tag{13}$$

where the k vectors are illustrated in Figure 4. From Equation (7), the fringe contrast between P_{11} and P_{21} and P_{12} and P_{22} is then determined by $\Delta\delta_{1121}$ and $\Delta\delta_{1222}$, respectively, as defined below:
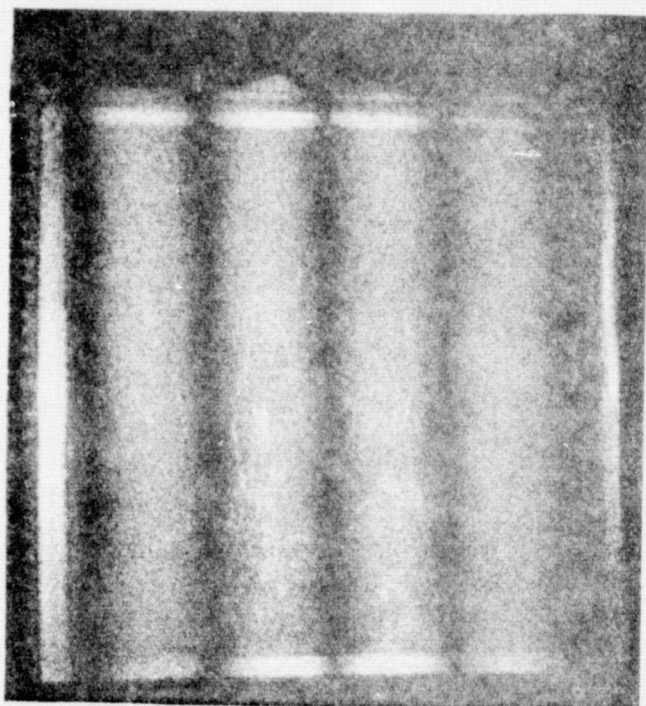
(a) Translation to the right,
   d = (4.5 ± 0.5) μm
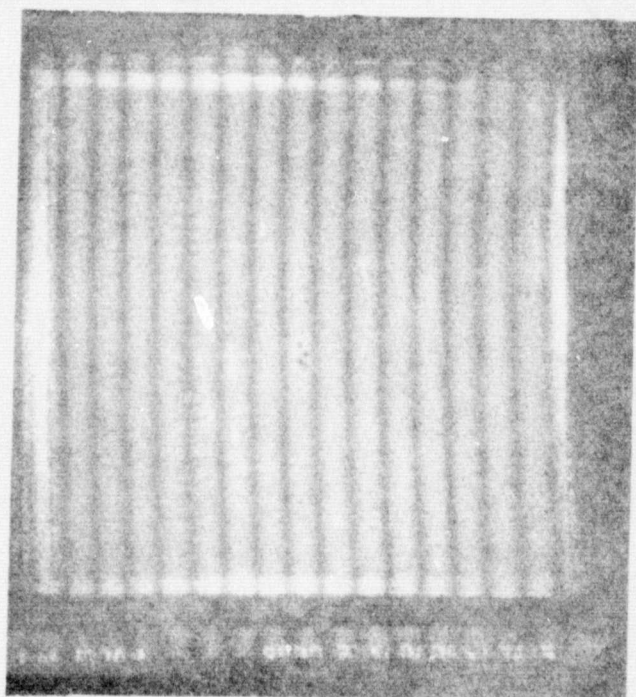
(b) Translation to the right,
   d = (16.5 ± 0.5) μm

FIGURE 3. IMAGES OF DOUBLE-EXPOSURE HOLOGRAMS
SHOWING TRANSLATIONS.
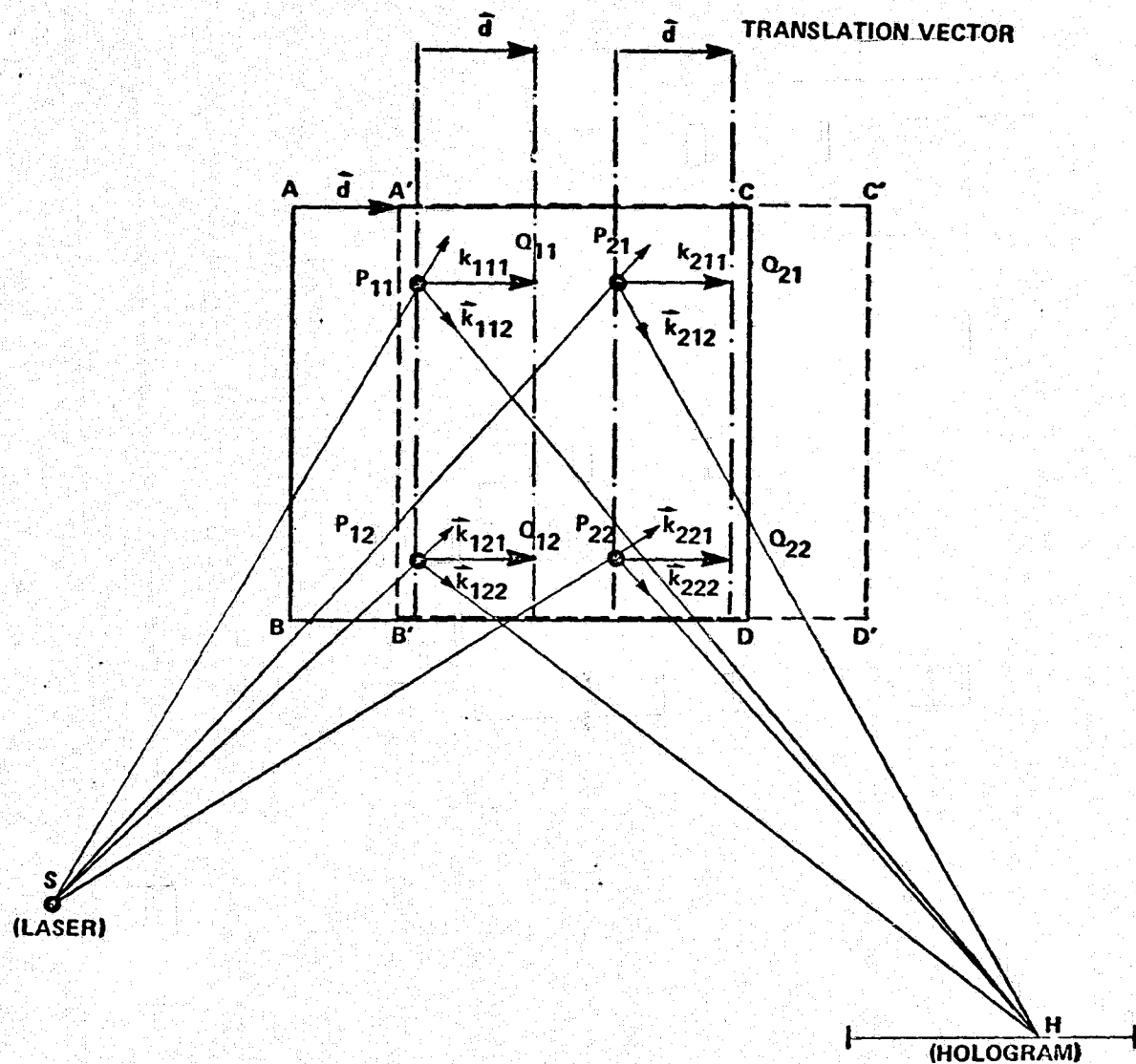
FIGURE 4. TRANSLATION OF A RIGID SURFACE ABCD TO A'B'C'D' ALONG A VECTOR $\vec{d}$ PARALLEL TO THE HOLOGRAM PLANE. S IS A POINT SOURCE FROM THE LASER.

$$\Delta \delta_{1121} = \Delta \theta_{11} - \Delta \theta_{21} \tag{14}$$

and

$$\Delta \delta_{1222} = \Delta \theta_{12} - \Delta \theta_{22} \tag{15}$$

The fringe intensity at P_1 is the same as that at P_2; this is because of the fact that

$$\Delta \theta_{11} - \Delta \theta_{12} = (2\pi/\lambda) \vec{d} \cdot [(\vec{k}_{111} - \vec{k}_{112}) - (\vec{k}_{121} - \vec{k}_{122})]$$

$$= (2\pi/\lambda) \vec{d} \cdot [(\vec{k}_{111} - \vec{k}_{121}) - (\vec{k}_{112} - \vec{k}_{122})] \tag{16}$$

$$= 0$$

Equation (16) is true because of the geometrical consideration that each individual k vector involved has no component along the $\vec{d}$ direction whatsoever. Therefore, we conclude that the line $P_{11}P_{12}$ will have the same fringe intensity. Similarly, the line $P_{21}P_{22}$ will also have a uniform fringe intensity. Hence, all the lines perpendicular to $\vec{d}$ should have the same intensity, and the phenomenon that the fringes are parallel to the direction of motion as shown in Figure 3 is expected.

Next we shall quantitatively explain the spacings between the fringes. We shall let $\hat{i}$, $\hat{j}$, and $\hat{k}$ be three orthonormal vectors. Then we may write

$$\vec{d} = d\,\hat{i} \tag{17}$$

Consider the case shown in Figure 3(a). Choose a point on the object in the center of one dark fringe and another point in the center of the next dark fringe such that their $\hat{j}$ components are zero with respect to the origin. The origin is set at the point of observation on the hologram. The $\hat{k}$ vectors for this point are then measured in the HNDT system, and a calculation shows that

$$\vec{k}_{111} = 0.9886\,\hat{k} + 0.1544\,\hat{i}$$

$$\vec{k}_{211} = 0.9806\,\hat{k} + 0.1959\,\hat{i}$$

$$\vec{k}_{112} = -0.9429\,\hat{k} + 0.3331\,\hat{i}$$

$$\vec{k}_{212} = -0.9603\,\hat{k} + 0.2791\,\hat{i}$$

The $\hat{k}$ component as well as the $\hat{j}$ component, if any, is immaterial in this case, since $\hat{i} \cdot \hat{k} = 0$ and $\hat{i} \cdot \hat{j} = 0$ in the calculation of the phase differences. Substitute these $\hat{k}$ vectors into Equation (14); we have

$$\Delta\delta_{1121} = (2\pi/\lambda)\,d\hat{i} \cdot (\vec{k}_{111} - \vec{k}_{112} - \vec{k}_{211} - \vec{k}_{212})$$

$$= 2\pi\,(d/\lambda)\,(0.1543 - 0.3331 - 0.1959 + 0.2791) \qquad (18)$$

$$= 2\pi(d/\lambda)\,(-0.956)$$

The hologram of Figure 3(a) was taken with an Argon laser which has a wavelength $\lambda = 0.5145\,\mu m$. The magnitude of the distance $d = (4.5 \pm 0.5)\,\mu m$. Upon substitution of these values into Equation (18), we have $\Delta\delta_{1121} = 2\pi\,(0.8361 \pm 0.0929)$. This result is within 20 percent of the expected value of $\Delta\delta = 2\pi$ for such a fringe separation.

The result of Figure 3(b) can likewise be explained, or we may just simply examine the ratio of d and the ratio of fringe spacings (or, equivalently speaking, the number of dark fringes across the surface of the object). The calculations are shown below:

$$\frac{d \text{ of Fig. 3(a)}}{d \text{ of Fig. 3(b)}} = \frac{(4.5 \pm 0.5)\,\mu m}{(16.5 \pm 0.5)\,\mu m} \qquad (19)$$

$$\simeq 0.27$$

$$\frac{\text{No. of dark fringes in Fig. 3(a)}}{\text{No. of dark fringes in Fig. 3(b)}} = \frac{5}{16} \qquad (20)$$

$$= 0.31$$

Consider the possible error in Equation (19); the result of Equation (18) is really extremely close to the result of Equation (19). Double-exposure holograms of other displacement vectors of magnitudes 2.5 μm and 9 μm have been taken; fringe separations proportional to those shown in Figure 3 resulted.

V. CONCLUSION

It has been demonstrated that the theory proposed in the present work interprets the relationship between fringe contrast and small surface displacement rather well in the case of translational experiment. The viewpoint suggested here has given an insight for a more realistic HNDT result. Quantitative explanation of such a result is under way. The work here may be used as a cornerstone for the future effort on fringe interpretation.

VI. REFERENCES

1. Kurtz, R. L., and Liu, H. K., Holographic Nondestructive Tests Performed on Composite Samples of Ceramic-Epoxy-Fiberglass Sandwich Structure, NASA TR R-430, June 1974.

2. Haines, K. A., and Hildebrand, B. P., "Surface-Deformation Measurement Using the Wavefront Reconstruction Technique," Applied Optics 5, pp. 595-602, April 1966.

3. Sollid, Jon E., "Holographic Interferometry Applied to Measurements of Small Static Displacements of Diffusively Reflecting Surfaces," Applied Optics, 8, pp. 1587-1595, August 1969.

4. Bellani, V. Fossati, and Sona, A., "Measurement of Three-Dimensional Displacements by Scanning a Double-Exposure Hologram," Applied Optics, 13, pp. 1337-1341, June 1974.

1974

ASEE - NASA SUMMER FACULTY FELLOWSHIP PROGRAM

MARSHALL SPACE FLIGHT CENTER

(AUBURN UNIVERSITY - UNIVERSITY OF ALABAMA)

ATMOSPHERIC WIND AND STRESS PROFILES

IN A TWO-DIMENSIONAL INTERNAL BOUNDARY LAYER

Prepared by: Earl Logan, Jr.

Academic Rank: Professor

Department and University: Mechanical Engineering Department
                                    Arizona State University

NASA/MSFC Assignment:
      (Laboratory)   Space Sciences
      (Division)   Aerospace Environment
      (Branch)   Environmental Dynamics

NASA Research Colleague: Dr. George H. Fichtl

Date: August 9, 1974

Contract No.:   NGT-01-003-045

ATMOSPHERIC WIND AND STRESS PROFILES
IN A TWO-DIMENSIONAL INTERNAL BOUNDARY LAYER

by

Earl Logan, Jr.

ABSTRACT

Aeronautical systems and aeronautical-like space vehicles are buffeted by random forces produced by atmospheric motion. Adequate prediction of fluid motion close to the surface of the earth, particularly in the vicinity of landing strips, is important to the safe operation and design of such vehicles.

The purpose of this research is to develop a model for low-level atmospheric flow over terrains of abruptly changing roughness, such as those occurring near the windward end of a landing strip, and to use the model to derive functions which define the extent of the region affected by the roughness change and allow adequate prediction of wind and shear stress profiles at all points within the region.

A model consisting of two bounding logarithmic layers and an intermediate velocity defect layer is assumed, and dimensionless velocity and stress distribution functions which meet all boundary and matching conditions are hypothesized. The functions are used in an asymptotic form of the equation of motion to derive a relation which governs the growth of the internal boundary layer. The growth relation is used to predict variation of surface shear stress.

Adequate prediction of wind and stress profiles was achieved for that portion of the internal boundary layer inside the logarithmic portion of the undisturbed Ekman layer.

ACKNOWLEDGEMENTS

LIST OF FIGURES

NOMENCLATURE

b	=	dimensionless ratio λ/δ_0
c	=	dimensionless constant
erf	=	error function
$\vec{f}$	=	fluctuating component of force vector
F	=	velocity defect function for IBL
F_X	=	velocity defect function for outer Ekman layer
G	=	shear stress difference function
h	=	height of Ekman layer
IBL	=	internal boundary layer
k	=	von Karman constant = 0.4
M	=	logarithm of ratio z_{01}/z_0
r	=	dimensionless ratio δ_i/z_0
T	=	matrix of transfer functions
$\vec{u}$	=	fluctuating component of wind vector
u	=	horizontal component of mean wind
u_g	=	horizontal component of geostrophic wind
u_o	=	mean wind velocity at $z = \delta_0$
u_i	=	mean wind velocity at $z = \delta_i$
u_b	=	mean wind velocity at $z = \lambda$
u_{*01}	=	surface friction velocity upwind of discontinuity
u_{*0}	=	surface friction velocity downwind of discontinuity
X	=	horizontal coordinate, X = 0 at discontinuity
z	=	vertical coordinate, z = 0 at surface of earth

z_{o1} = roughness length upwind of discontinuity

z_o = roughness length downwind of discontinuity

β = dimensionless ratio δ_i / δ_o

δ_i = thickness of IBL

δ_o = thickness of outer layer of IBL

η = dimensionless ratio z / δ_o

λ = thickness of sublayer of IBL

Λ = dimensionless coefficient

ξ = argument of error function

τ = shear stress

τ_{o1} = surface shear stress upwind of discontinuity

τ_o = surface shear stress downwind of discontinuity

INTRODUCTION

Aeronautical systems and aeronautical-like space vehicles, i.e., Space Shuttle, are buffeted by random external forces occurring on the various surfaces during the vehicle's operation in ascent, descent, or horizontal flight. These forces are random functions of time dependent on pressure fluctuations in the enveloping fluid. Because fluid pressure is related to fluid velocity through the governing momentum equations, force fluctuations, represented by a vector $\vec{f}$, may be written in equation form as a function of the velocity fluctuations, represented by the vector $\vec{u}$, in the following way

$$\vec{f} = T\vec{u} \tag{1}$$

where T is a matrix of transfer functions and is defined by the vehicle's configuration and the governing equations of fluid motion.

To provide the required knowledge of average wind profiles and velocity fluctuations occurring in the atmosphere in the vehicle's flight path one must first find suitable physical models of the various layers of the atmosphere pertinent to low-level flight operation. The physical model should characterize the flow field in a manner which provides reasonable agreement with prior experimental observation. A model so defined can be described mathematically in terms of boundary conditions at the earth's surface and at the upper extent of the Ekman layer (about 1 kilometer), as well as in terms of matching conditions in regions intermediate between the various layers of the model.

The mathematical conditions required by the assumed model are used to test candidate functions employed to specify the steady-state distributions of mean velocity (wind) and Reynolds shear stress. Functions which satisfy boundary and matching conditions can be utilized to predict distributions of turbulent energy, spectra and scale.

OBJECTIVES

The purpose of this research is to develop a model of a low-level atmospheric flow for use in the simulation of random external forces experienced by aerospace and aeronautical vehicles operating at altitudes below 1 km in the vicinity of landing strips. The study treats the atmospheric flow field over a terrain of changing height of surface protrusions, i.e., changing roughness length. Specifically, the flow is found at the windward end of a landing strip as the wind blows onto the relatively smooth surface of the strip from the relatively rough surface of the surrounding terrain. The objective of the work is to develop a model for this flow and to use the model to derive functions which define

the extent of the region and allow the calculation of wind and shear stress profiles at all points within the region.

The technique of asymptotic matching in conjunction with assumed scaling laws shall be used to extract as much information as possible from the equations of motions about the flow of concern. The motivation for this is to avoid lengthy and complicated numerical solution methods which tend to mask the physics of the problems. The technique of asymptotic matching permits one to capture the physics of the problem, extract basic needed information, and avoids the negative aspects of numerical methods noted above.

BASIC IDEALIZATIONS

This investigation deals with the transition region occurring in a turbulent Ekman layer downwind of an abrupt change in surface roughness, the line of the discontinuity being normal to the direction of the wind. It is assumed that the surfaces are covered with uniformly distributed roughness elements, i.e., small obstacles or protrusions, the height of which may be characterized by the scale z_o known as roughness length. The flow is assumed to be steady, two-dimensional, and incompressible with neutral hydrostatic stability prevailing throughout the entire Ekman layer.

PREVIOUS INVESTIGATIONS

Elliott [Ref. 1] was one of the first to study the change of terrain problem. He predicted that the thickness δ_i of the region affected by the change in roughness length increases with the 4/5 - power of distance X from the discontinuity, i.e., with fetch. Elliott refers to the region of the flow disturbed by the discontinuity as the internal boundary layer (IBL). Other investigators have pursued the problem using various models for the internal boundary layer, e.g., Panofsky and Townsend [Ref. 2], Townsend [Ref. 3-5], Taylor [Ref. 6], Peterson [Ref. 7], and Rao, Wyngard, and Cote [Ref. 8]. Plate [Ref. 9] has reviewed work done prior to 1971 on the internal boundary layer problem. The most recent studies utilize computer methods to solve the governing equations together with a suitable turbulence closure model.

A few investigators have studied the problem experimentally in wind tunnels. The earliest experimenter was Jacobs [Ref. 10] and the latest was Antonia and Luxton [Ref. 11]. The latest field data was reported by Bradley [Ref. 12]. Fair agreement has been obtained between experimental data and theoretical predictions.

PROPOSED MODEL

It is proposed to attack the problem without the use of computer or of unnecessary assumptions about distributions of wind and shear stress

in the internal boundary layer. The approach is similar to that taken by Clauser [Ref. 13] in his study of the turbulent boundary layer and by Csanady [Ref. 14] and by Blackadar and Tennekes [Ref. 15] in their investigations of turbulent Ekman layers.

Blackadar and Tennekes [Ref. 15] have shown that the wind profile in the equilibrium surface layer (upwind of the discontinuity) is given by

$$\frac{u}{u_{*01}} = \frac{1}{k} \ln \frac{z}{z_{01}} \tag{2}$$

and that the outer Ekman layer is governed by a velocity defect law of the form

$$\frac{u - u_g}{u_*} = F_x\left(\frac{z}{h}\right) \tag{3}$$
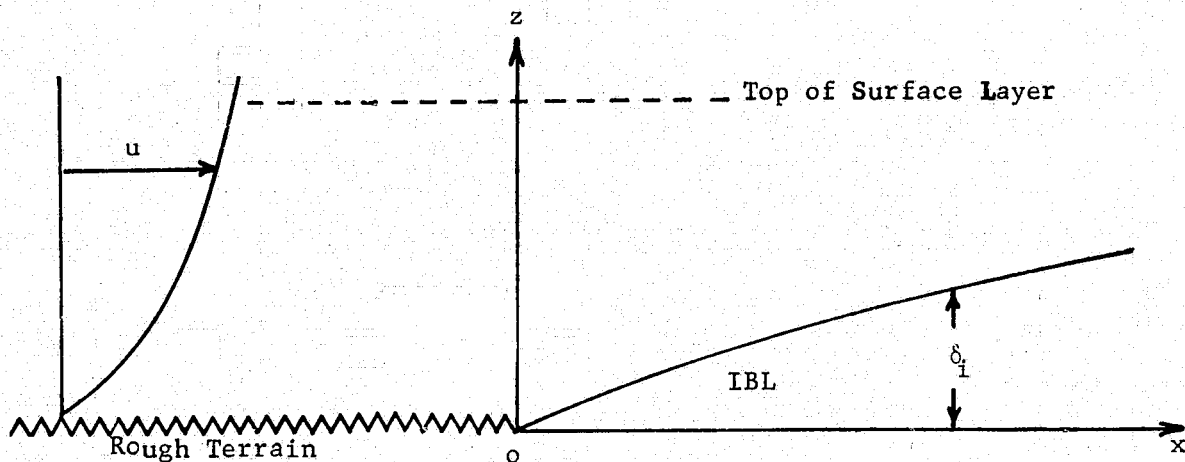
FIGURE 1. DEVELOPMENT OF AN INTERNAL BOUNDARY LAYER: ROUGH-TO-SMOOTH TRANSITION

This equilibrium wind profile is represented schematically in Fig. 1. Panofsky [Ref. 16] states that the thickness of this surface, or logarithmic, layer of the atmosphere is of the order of 30 meters and that the Coriolis forces may be neglected in this layer.

Previous investigators have assumed that an internal boundary layer is formed above the smooth surface (roughness length of z_0) and that it

grows with increasing distance from the discontinuity at X = 0. In,
Fig. 1 two regions are defined by a curve emanating from the origin,
i.e.,

$$z = \delta_i(x) \tag{4}$$

which forms a surface above which the wind profile is described by
equation (2) and below which the wind profile is defined by a non-
equilibrium profile which approaches a new equilibrium condition with a
logarithmic profile given by

$$\frac{u}{u_{*o}} = \frac{1}{k} \ln \frac{z}{z_o} \tag{5}$$

The fetch X corresponding to the achievement of this condition is repre-
sented mathematically as $X \to \infty$. At this fetch the wind profile of equation
(5) merges into that given by

$$\frac{u - u_g}{u_*} = F_x\left(\frac{z}{h}\right) \tag{6}$$

Equations (5) and (6) are of the same form as equations (2) and (3) and
differ only in length and velocity scales, z_o and u_{*o}, respectively.

It was assumed by early investigators that the entire internal
boundary layer for $0 < X < \infty$ is described by the logarithmic wind profile
equation (5) and that the surface stress experiences a step change from
τ_{01} to τ_0 and thus remains constant for $X > 0$. Experimental measurements
of surface stress (see Ref. 12) indicate that an undershooting of sur-
face stress occurs at the discontinuity and that τ_0 ($\tau_0 = u_{*_0}^2$) approaches
its higher equilibrium value asymptotically. However, measured wind
profiles do confirm the logarithmic nature of their distributions, i.e.,
equation (5) is the correct form for the profiles in the layer closest
to the smooth surface. The slopes of these profiles and the surface
friction velocities u_{*_0} inferred from them agree with direct measurement
of surface stress, again offering experimental confirmation of a definite
undershoot of u_{*_0} at the discontinuity.

A deficiency of the model of the flow as depicted in Fig. 1 is that
it does not provide for a gradual change of slope of the wind profile
across the surface $\delta_i(X)$. One can easily verify that the velocity grad-
ient $\frac{\partial u}{\partial z}$ obtained from differentiating equation (2) is not equal to that
obtained from differentiation of equation (5). Thus, although wind may
be specified as continuous at boundary of the two regions, viz.,

$$\frac{u_{*o1}}{k} \ln \frac{\delta_i}{z_{o1}} = \frac{u_{*o}}{k} \ln \frac{\delta_i}{z_o} \tag{7}$$

at $z = \delta_i$, the derivatives are not continuous across this boundary.

To circumvent this difficulty it is proposed that the IBL be modelled as before, but that an intermediate or matching region be inserted between the two logarithmic regions as indicated in Fig. 2. The layer denoted as region I is the logarithmic layer in contact with the smooth
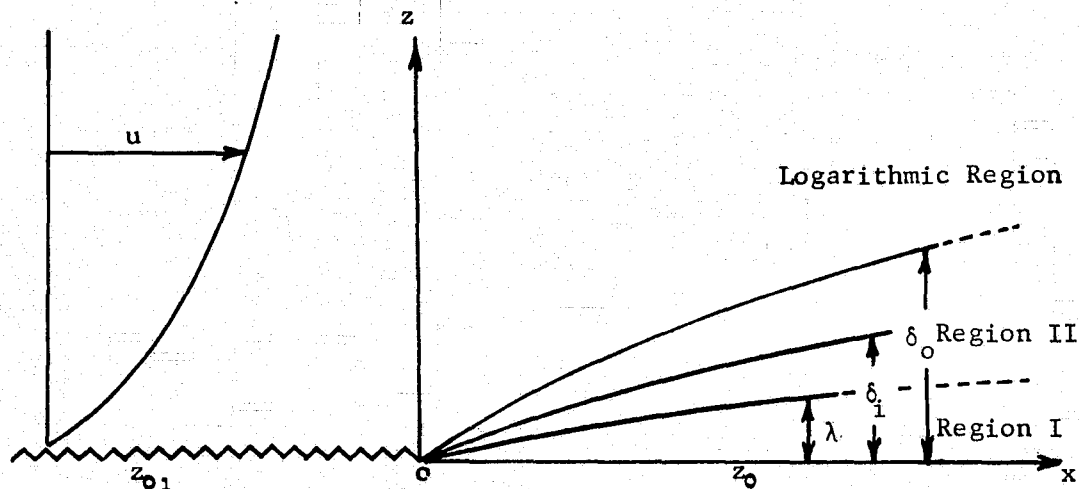
FIGURE 2.   SUBLAYERS OF THE INTERNAL BOUNDARY LAYER OF PROPOSED
            MODEL

surface. In region I the profile conforms to equation (5) with u_{*_o} a function of X. The thickness of this layer is denoted by λ with $\lambda < \delta_i$. Region II is the new intermediate layer of thickness $\delta_0 - \lambda$ in which a gradual transition from one logarithmic wind profile to the other is accomplished. A velocity defect law is hypothesized for this region defined by $\lambda < z < \delta_0$. Along the surface defined by $z = \delta_0$, it is assumed that complete matching to the external flow, governed by equation (2), has been accomplished, including wind, stress, and their derivatives.

The thickness δ_i of the internal boundary layer as previously defined and as depicted in Fig. 1 is intermediate between the outer layer defined by the surface $z = \delta_0$ (X) and the sublayer defined by the surface $z = \lambda$ (X). Along the surface the wind velocity u is given by

$$\frac{u_i}{u_{*o1}} = \frac{1}{k} \ln \frac{\delta_i}{z_{o1}} \tag{8}$$

This means that δ_i defines the surface below which the flow has accelerated relative to the original equilibrium profile given by equation (2). Continuity requires that the region defined by $\delta_i < z < \delta_0$ contain a flow which has decelerated relative to the original equilibrium profile.

Thus the proposed model includes three length scales, viz., λ, δ_i, and δ_o and three velocity scales, viz., u_{*_o}, u_{*}, and u_{*_o}. These scales will be utilized in the next section to develop suitable similarity functions for wind and shear stress.

PROPOSED SIMILARITY FUNCTIONS

Townsend [Ref. 3] found that similarity is possible in disturbed boundary layers, if the disturbed layer is thin compared with the thickness of the boundary layer and if the roughness length is small compared with the thickness of the disturbed layer. Similarity may be assumed in the present problem, if it is required that $\delta_i \ll h$ and $z_o \ll \delta_i$, which are the relationships one would expect in the practical problem as posed previously.

Two functions are defined: the velocity defect function $F(\eta)$, which applies only to the intermediate layer (region II in Fig. 2), and the shear stress function $G(\eta)$ which applies to the lower logarithmic layer (region I) as well as the intermediate layer. The velocity defect function is defined as

$$F(\eta) \equiv \frac{u - u_i}{u_*} \tag{9}$$

with the dimensionless height above the surface defined as

$$\eta \equiv \frac{z}{\delta_o} \tag{10}$$

The velocity u_i is the velocity on the surface defined by $z = \delta_i(X)$ and is calculated from equation (8). Friction velocity u_* in equation (9) is not the value at the surface but is a variable function of height z and fetch X. It is dependent on surface stress u_{*_o}, a function of fetch only, and the shear stress function $G(\eta)$, which is defined as

$$G(\eta) \equiv \frac{\tau - \tau_{oi}}{\tau_o - \tau_{oi}} \tag{11}$$

An alternative form of the definition of shear stress function is

$$G(\eta) \equiv \frac{u_*^2 - u_{*oi}^2}{u_{*o}^2 - u_{*oi}^2} \tag{12}$$

which clearly indicates the relationship between u_* and $G(\eta)$.

The nature of the similarity functions defined in equations (9) and (11) can be determined from a consideration of the boundary and matching conditions to which they must conform. The most obvious of these conditions are written first, viz., those for which the function is zero or unity.

The function $F(\eta)$ is zero when the velocity u equals the velocity u_i on the surface defined by $z = \delta_i(X)$. The height of this surface is expressed non-dimensionally as

$$\beta \equiv \frac{\delta_i}{\delta_o} \tag{13}$$

Thus the condition at this surface can be written as

$$F(\beta) = 0 \tag{14}$$

The function $G(\eta)$ is zero at the outer portion of region II where the shear stress must approach the upstream value τ_{o1} which is the value of shear stress found at all heights in the equilibrium layer upstream of the discontinuity. This condition occurs at the height $z = \delta_o$ and is written as

$$G(1) = 0 \tag{15}$$

The derivative of $G(\eta)$ with respect to η, i.e., $G'(\eta)$, also approaches zero at the outer portion of region II. This can be shown by differentiating τ with respect to height; using τ from equation (11) we obtain

$$\frac{\partial \tau}{\partial z} = (\tau_o - \tau_{o1}) G'(\eta) \frac{\partial \eta}{\partial z}$$

In the region above region II the shear stress is constant; therefore

$$\frac{\partial \tau}{\partial z} = 0 \qquad z > \delta_o$$

The resulting condition for the shear stress function is

$$G'(1) = 0 \tag{16}$$

In the lower part of the internal boundary layer a similar constant shear stress layer exists, so that in region I

$$\frac{\partial \tau}{\partial z} = 0 \qquad z < \lambda$$

The resulting condition for the function $G(\eta)$ is

$$G'(\eta) = 0 \qquad \eta \leq b \qquad (17)$$

where

$$b \equiv \frac{\lambda}{\delta_0} \qquad (18)$$

Conditions at the extremities of region I may be written as

$$G'(b) = 0 \qquad (19)$$

and

$$G'(0) = 0 \qquad (20)$$

In region I the stress function is unity since $\tau = \tau_0$ throughout the layer. Thus

$$G(\eta) = 1 \qquad \eta \leq b \qquad (21)$$

or, at two specific points of interest,

$$G(b) = 1 \qquad (22)$$

and

$$G(0) = 1 \qquad (23)$$

Thus, all the boundary and matching conditions on the stress function are included in equations (15) through (23). Additional conditions on the velocity defect function $F(\eta)$ will be sought next.

At the outer limit of region II where $\eta \to 1$ the following equations may be written:

$$F(1) = \frac{u_0 - u_i}{u_{*01}}$$

$$F(1) = \frac{1}{k} \ln \frac{\delta_0}{z_{01}} - \frac{1}{k} \ln \frac{\delta_i}{z_{01}}$$

Thus

$$F(1) = -\frac{1}{k} \ln \beta \qquad (24)$$

where β is defined in equation (13). The value of velocity substituted for u_i was obtained from equation (8) and that for u_0 from the following:

$$\frac{u_0}{u_{*01}} = \frac{1}{k} \ln \frac{\delta_0}{z_{01}} \tag{25}$$

In order that the flow be self-preserving, i.e., that the function $F(\eta)$ not depend on fetch X, it is required that

$$F(1) = \text{constant}$$

Equation (24) implies that

$$\beta = \text{constant} \tag{26}$$

The constant β will be determined later, permitting $F(1)$ to be equated to a numerical constant. A condition on the derivative $F'(1)$ may be obtained by matching derivatives at the juncture of region II and the upper logarithmic region. Two forms of velocity gradient at this interface are

$$\frac{\partial u}{\partial z} = \frac{u_{*01}}{k \delta_0} \tag{27}$$

which is the derivative as $z \to \delta_0$ from above the interface, and

$$\frac{\partial u}{\partial z} = u_{*01} F'(1) \frac{\partial \eta}{\partial z} + F(1) \frac{\partial u_*}{\partial z} \Big|_{z \to \delta_0} \tag{28}$$

which is the derivative as $z \to \delta_0$ from below the interface. Differentiation of equation (12) and substitution of equation (16) show that in the limit

$$\frac{\partial u_*}{\partial z} \Big|_{z \to \delta_0} = 0 \tag{29}$$

Since

$$\frac{\partial \eta}{\partial z} = \frac{1}{\delta_0(x)} \tag{30}$$

equating of (27) and (28) and using results (29) and (30) yields

$$F'(1) = \frac{1}{k} \tag{31}$$

Next the interfacial conditions as $z \to \lambda$ ($\eta \to b$) are considered. Again the derivatives are matched with the following result:

$$\frac{\partial u}{\partial z}\bigg|_{z \to \lambda} = u_{*o}\frac{F'(b)}{\delta_o} = \frac{u_{*o}}{k\lambda}$$

Thus the appropriate matching condition is

$$F'(b) = \frac{1}{kb} \tag{32}$$

Similarity requires that

$$b = \text{constant}$$

and the value of b is to be derived later.

At this point a tentative velocity defect function is constructed which satisfies all of the necessary conditions for matching at the upper and lower bounds of region II; these conditions were given previously as equations (14), (24), (31), and (32). A suitable function for the region of velocity defect is

$$F(\eta) = \frac{1}{k}\ln\frac{\eta}{\beta} \tag{33}$$

and this function can be utilized to determine velocity distribution in region II after the growth law governing δ_i and the constant β are determined.

Equation (33) may be utilized to derive a relationship between surface friction and internal boundary layer thickness. At the outer interface of region I equation (33) becomes

$$F(b) = \frac{1}{k}\ln\frac{b}{\beta} \tag{34}$$

From the definition of the defect function (equation 9)

$$F(b) = \frac{u_b - u_i}{u_{*o}} \tag{35}$$

where u_b is evaluated from equation (5) as

$$\frac{u_b}{u_{*o}} = \frac{1}{k}\ln\frac{\lambda}{z_o} \tag{36}$$

Equation (36) written in a modified form becomes

$$u_b = \frac{u_{*o}}{k}\left(\ln\frac{b}{\beta} + M + \ln\frac{\delta_i}{z_{o1}}\right) \tag{37}$$

12-16

where

$$M \equiv \ln \frac{z_{01}}{z_0} \tag{38}$$

Substitution of equations (8), (34), and (37) into (35) yields

$$\ln \frac{\delta_i}{z_{01}} = \frac{M}{\frac{u_{*01}}{u_{*0}} - 1} \tag{39}$$

which provides a useful relationship. Equation (39) was used to calculate surface friction as a function of fetch, and the results are discussed later in this report.
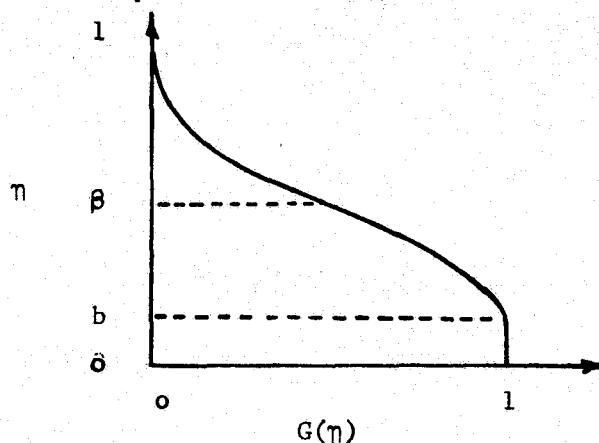
FIGURE 3. STRESS FUNCTION

The required stress function must satisfy the matching conditions given by equations (15), (16), (19), (20), (22), and (23). Figure 3 depicts the shape of the required function as determined from the conditions listed above. An error function satisfies all matching conditions and is used to construct the stress function as is described below. The general form of the function is taken to be

$$G(\eta) = \Lambda \, erf \, \xi + C \tag{40}$$

where the argument ξ is a function of η.

Let $\eta = \beta$ be chosen to be the point of inflection, i.e., the maximum absolute value of slope $G'(\eta)$. This choice follows from a consideration of the terms of the equation of motion which governs flow in region II, i.e.,

$$u \frac{\partial u}{\partial x} + w \frac{\partial u}{\partial z} = \frac{\partial \tau}{\partial z} \tag{41}$$

12-17

As was shown previously the stress gradient is proportional to $G'(\eta)$. Equation (41) shows a direct dependence of stress gradient upon convective acceleration. Since the surface $z = \delta_i(X)$ separates regions of net positive and negative acceleration, it is plausible that fluid in the vicinity of that surface experiences the largest accelerations, and hence the largest stress gradients. Since maximum stress gradient implies maximum absolute value of $G'(\eta)$, then $\eta = \beta$ corresponds to the maximum value of the derivative of the error function, i.e., $\xi = 0$ at $\eta = \beta$. Substitution into equation (40) yields

$$G(\beta) = C \tag{42}$$

To construct the argument ξ cognizance is taken of the requirements stated in equations (16) and (19). The derivative of the error function is approximately zero when $|\xi| > 2$, where the error function itself is approximately unity. Choosing $|\xi| = 4$ for $\eta = b$ and $\eta = 1$, the following equations can be written:

$$G(b) = 1 = \Lambda \, erf \, 4 + G(\beta) \tag{43}$$

$$G(1) = 0 = \Lambda \, erf(-4) + G(\beta) \tag{44}$$

Simultaneous solution of equations (43) and (44) yields

$$G(\beta) = \frac{1}{2} \tag{45}$$

$$\Lambda = \frac{1}{2} \tag{46}$$

To satisfy the conditions $\xi = 4$ at $\eta = b$ and $\xi = 0$ at $\eta = \beta$ the argument

$$\xi = \frac{4(\beta - \eta)}{\beta - b} \tag{47}$$

is selected. Substituting $\xi = -4$ at $\eta = 1$ into equation (47) gives the relation between β and b, viz.,

$$\beta = \frac{1}{2}(b + 1) \tag{48}$$

Substituting equations (42), (45), (46), (47), and (48) into (40) results in the following expression for the shear stress function:

$$G(\eta) = \frac{1}{2} \operatorname{erf}\left[\frac{4(1+b-2\eta)}{1-b}\right] + \frac{1}{2} \tag{49}$$

The constant b remains undetermined and experimental data must be utilized in the determination of this constant. Only one point of data is required as will be demonstrated in the next section.

PREDICTED GROWTH OF THE INTERNAL BOUNDARY LAYER

In this section a relationship between the thickness δ_i of the IBL and the fetch X, i.e., the IBL growth law, is derived. This is obtained by integrating an asymptotic form of equation (41), the equation of motion. The terms are simplified by letting $\eta = \beta$ and $X \to 0$. This results in an easily integrated differential equation, since $F(\beta)$, $F'(\beta)$ and u_* are known for these limits. The value of $F(\beta)$ is zero as was stated in equation (14). The derivative is obtained from equation (33) by differentiation; thus

$$F'(\beta) = \frac{1}{k\beta} \tag{50}$$

The surface friction velocity approaches zero in the limit as $X \to 0$, which is consistent with equation (39). In view of this it is plausible that u_* at $\eta = \beta$ will approach zero as the discontinuity is approached; however, equation (12) indicates a minimum value of u_* but does not predict a zero value. In reducing the equation of motion it is assumed that $u_* \to 0$ as $X \to 0$. A physical justification for this assumption is that the velocity gradient given by

$$\frac{\partial u}{\partial z} = \frac{u_* F'(\beta)}{\delta_0} = \frac{u_*}{k \delta_i} \tag{51}$$

is expected to be small in the vicinity of $\eta = \beta$, i.e., in the vicinity of the juncture of the new and old velocity profiles. This is expected because of the acceleration of the fluid inside the IBL relative to that above the IBL. It is further expected that the velocity gradient would increase with distance from the discontinuity until the equilibrium condition is achieved.

Other variables appearing in equation (41) reduce to the following for the assumptions set forth above:

$$u = u_i = \frac{u_{*oi}}{k} \ln \frac{\delta_i}{z_{oi}} \tag{52}$$

$$\frac{\partial u}{\partial x} = \frac{u_{*01} \delta_i'}{k \delta_i} \tag{53}$$

and

$$\frac{\partial \tau}{\partial z} = - \frac{u_{*01}^2 G'(\beta)}{\delta_0} \tag{54}$$

Substitution of equations (52), (53), and (54) into equation (41) yields the differential equation

$$ln \frac{\delta_i}{z_{01}} \delta_i' = - k^2 \beta G'(\beta) \tag{55}$$

Integration of equation (55) results in the growth law,

$$r\left[\ln r - (1+M) \right] = - \frac{k^2 \beta G'(\beta) x}{z_0} \tag{56}$$

where

$$r \equiv \frac{\delta_i}{z_0} \tag{57}$$

Equation (56) can be used to predict the growth of the internal boundary layer if the constant $\beta G'(\beta)$ is determined from experimental data. From Bradley's data (Ref. 12) as plotted in Fig. 12 of Ref. 8 the following data are taken:

$$\delta_i \cong 11 \, cm \quad at \quad x = 1 \, m.$$
$$z_0 = 0.002 \, cm \, , \quad z_{01} = 0.25 \, cm.$$

Noting that $M = 4.83$ is obtained from equation (38) and substituting the above data into equation (56)

$$\beta G'(\beta) = - 1.918 \tag{58}$$

is obtained.

The resulting value from equation (58) may be used with equation (56) to predict internal boundary layer thicknesses at other fetches. A curve showing the results of this calculation is shown in Fig. 4 with Bradley's data for M = 4.83. The agreement is reasonably good.
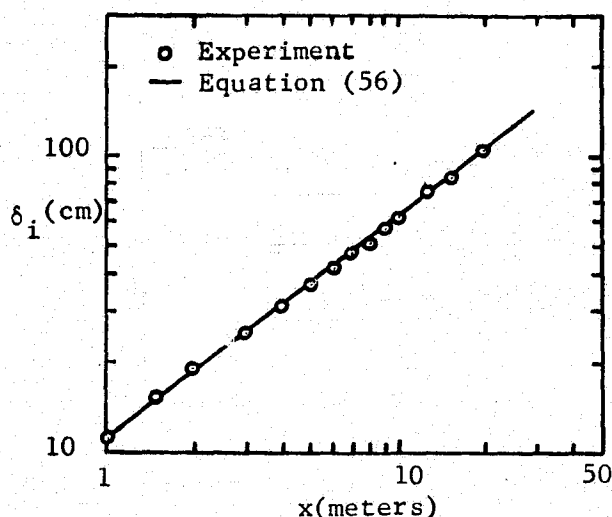
FIGURE 4. GROWTH OF IBL THICKNESS WITH FETCH

Equation (58) can be used to determine the constant b by differentiating equation (40) with respect to η and evaluating at $\eta = \beta$. Thus

$$\beta G'(\beta) = \beta \wedge \left[\frac{d e^{-\beta \xi}}{d \xi} \frac{d \xi}{d \eta} \right]_{\xi=0, \eta=\beta} \tag{59}$$

Substituting from equations (47), (48), and (58) yields the result

$$-1.918 = \div 1.128 \left(\frac{1+b}{1-b} \right) \tag{60}$$

from which

$$b \cong \frac{1}{4} \tag{61}$$

Equation (48) allows evaluation of β as

$$\beta = \frac{5}{8} \tag{62}$$

Substitution of equation (61) into (49) results in the final form of the shear stress similarity function, viz.,

$$G(\eta) = \frac{1}{2} erf\left[\frac{4(5-8\eta)}{3}\right] + \frac{1}{2} \qquad (63)$$

The same substitution in equation (33) results in the final form for
the velocity defect similarity function, viz.,

$$F(\eta) = 2.5 \ln\left(\frac{8\eta}{5}\right) \qquad (64)$$

Finally, the values of δ calculated from equation (56) can be utilized
with equation (39) to determine surface stress as a function of fetch.
The curve shown in Fig. 5 shows the comparison of predicted surface
stresses with experimental data from Ref. 12 and numerical predictions
from Ref. 8. The agreement is reasonably good.
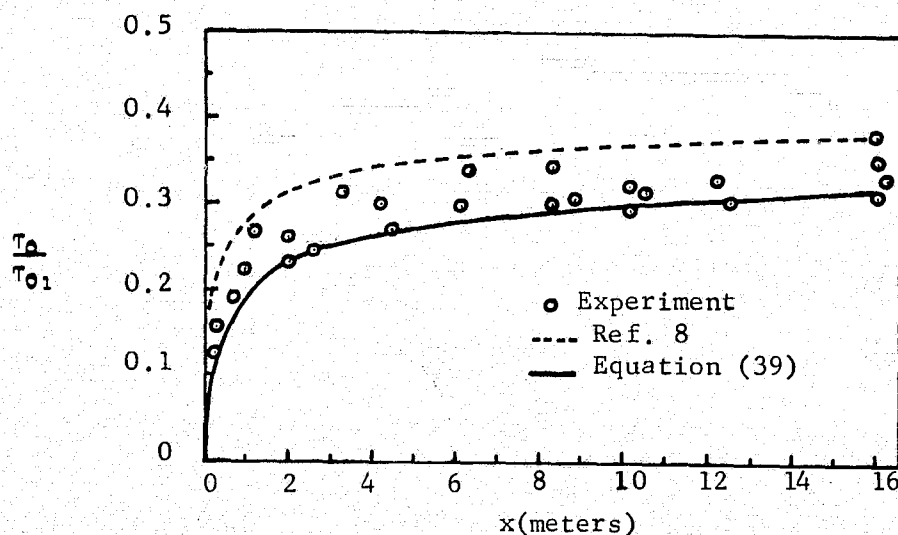
FIGURE 5.   SURFACE SHEAR STRESS VARIATION WITH FETCH

The equations derived above will be applied to the prediction of
wind and stress profiles in the next section.

PREDICTED WIND AND SHEAR STRESS PROFILES

The prediction of wind and shear profiles in the internal boundary
layer following a discontinuity in surface roughness can be achieved
through the use of the equations developed in previous sections. To
illustrate the use of these equations the wind profile at $X = 6.1m$ will
be predicted in this section using Bradley's starting profile [Ref. 12]
and roughness lengths. One pair of coordinates of the starting profile
is needed to start the calculation. This information is extracted from

Fig. 9 of Ref. 12 and is used to calculate $u_{*_{01}}^{+}$ by means of equation (2) where the plus (+) superscript indicates that the friction velocity is non-dimensionalized with the reference wind velocity $u_{112.5}$ observed at $z = 112.5$ cm. The result is $u_{*_{01}}^{+} = 0.0656$. Other needed data are $z_{01} = 0.25$ cm, $z_0 = 0.002$ cm and $M = 4.83$.

The next step in the procedure is to calculate δ_i from equation (56). This results in $\delta_i \approx 45$ cm for $X = 6.1$ m. Equation (39) is then utilized to determine $u_{*_0}^{+}$; the resulting value is $u_{*_0}^{+} = 0.034$. In addition δ_i may be used to calculate u_i from equation (52); this value is $u_i^{+} = 0.852$. Finally, equations (13) and (18) are used to determine δ_0 and λ; these are 72 cm and 18 cm, respectively.

With all of the values calculated as indicated above, a set of values is calculated at each height z; for region II this procedure is carried out as follows: i) η is calculated from equation (10); ii) $G(\eta)$ is calculated from equation (63); iii) u_*^2 ($u_*^2 = \tau$) is calculated from equation (12); iv) $F(\eta)$ is calculated from equation (64); v) u is calculated from equation (9). This completes the method of calculating wind and shear stress profiles in region II, i.e., $u - z$ and $\tau - z$ profiles, respectively. Outside of region II the wind profile is determined from equation (2) for $z > \delta_0$ and from equation (5) for $z < \lambda$. The results of this calculation are shown graphically in Fig. 6 and are compared with the experimental data of Bradley [Ref. 12]. The profile predicted by the above method agrees reasonably well with the profile measured by Bradley.

It is evident from the preceding example that the calculation method based on the proposed model is capable of producing reasonable predictions of wind profiles in that part of the internal boundary layer having a thickness less than that of the logarithmic part of the Ekman layer, i.e., the surface layer. Since the calculation of wind profile requires use of the shear stress profile, the model is assumed to be valid for stress prediction as well.

CONCLUSIONS AND RECOMMENDATIONS

The proposed model for the internal boundary layer formed over a smoother surface in an Ekman layer initially at equilibrium with a rougher surface is suitable for prediction of wind and shear stress profiles, IBL thickness as a function of X and surface stress as a function of X in that portion of the IBL inside of the undisturbed logarithmic layer.

Further work is required to extend this analysis to include that portion of the IBL bounded by the surface of the earth beneath and the undistrubed velocity defect layer above. The required functions for this region of the IBL must match the asymptotic form developed in this
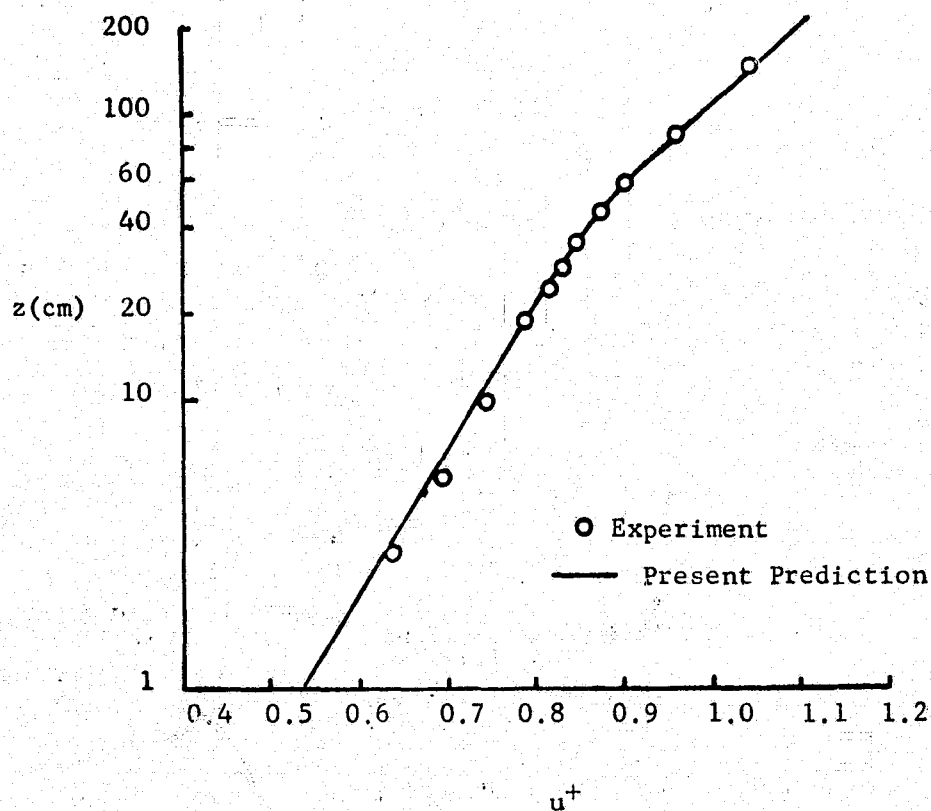
FIGURE 6. WIND PROFILE AT x = 6.1 METERS

report (X→0) and the equilibrium form (X→∞) far downwind. Prediction of profiles in Ekman layer, i.e., above the logarithmic layer will require inclusion of the Coriolis force term in the equation of motion.

Since actual practice involves variable terrain roughness, oblique wind direction, and heated (solar) landing strips, these effects should also be considered.

REFERENCES

1. Elliott, W. P., 1958: The growth of the atmospheric internal boundary layer. _Trans. Amer. Geophys. Union_, 39, 1048-1054.

2. Panofsky, H. A. and A. A. Townsend, 1964: Change of terrain roughness and the wind profile. _Quart. J. Roy. Meteor. Soc._, 90, 147-155.

3. Townsend, A. A., 1965: Self-preserving flow inside a turbulent boundary layer. _J. Fluid Mech._, 22, 773-797.

4. Townsend, A. A., 1965: The response of a turbulent boundary layer to abrupt changes in surface conditions. _J. Fluid Mech._, 22, 799-822.

5. Townsend, A. A., 1966: The flow in a turbulent boundary layer after a change in surface roughness. _J. Fluid Mech._, 26, 255-266.

6. Taylor, P. A., 1969: The planetary boundary layer above a change in surface roughness. _J. Atmos. Sci._, 26, 432-440.

7. Peterson, E. W., 1969: Modification of mean flow and turbulent energy by a change in surface roughness under conditions of neutral stability. _Quart. J. Roy. Meteor. Soc._, 95, 561-575.

8. Rao, K. S., J. C. Wyngaard and O. R. Cote, 1974: The structure of the two-dimensional internal boundary layer over a sudden change of surface roughness. _J. Atmos. Sci._, 31, 738-746.

9. Plate, E. J., 1971: _Aerodynamic Characteristics of Atmospheric Boundary Layers._ U. S. Atomic Energy Commission, TID-25465, 190 pp.

10. Jacobs, W., 1939: Transformation of turbulent velocity profiles. _Z. Angew. Math. Mech._, 19, 87-100. (NACA-TM951).

11. Antonia, R. A. and R. E. Luxton, 1972: The response of a turbulent boundary layer to a step change in surface roughness. Part 2. Rough-to-smooth. _J. Fluid Mech._, 53, 737-757.

12. Bradley, E. F., 1968: A micrometeorological study of velocity profiles and surface drag in the region modified by a change in surface roughness. _Quart. J. Roy. Meteor. Soc._, 94, 361-379.

13. Clauser, F. H., 1956: The turbulent boundary layer. _Adv. Appl. Mech._, 4, 1-51.

14. Csanady, G. T., 1967: On the resistance law of a turbulent Ekman layer. _J. Atmos. Sci._, 24, 467-471.

REFERENCES (continued)

15. Blackadar, A. K. and H. Tennekes, 1968: Asymptotic similarity in neutral barotropic planetary boundary layers. J. Atmos. Sci., 25, 1015-1020.

16. Panofsky, H. A., 1974: The atmospheric boundary layer below 150 meters. Annual Rev. Fluid Mech., 6, 147-177.

1974

ASEE - NASA SUMMER FACULTY FELLOWSHIP PROGRAM

MARSHALL SPACE FLIGHT CENTER

(AUBURN UNIVERSITY - UNIVERSITY OF ALABAMA)

HOLOGRAPHIC NONDESTRUCTIVE TESTING

Prepared by: Ashley M. Martin, III. Ph. D.

Academic Rank: Associate Professor & Chairman

Department and University: Department of Physics
                                    Athens College

NASA/MSFC Assignment:
  (Laboratory)   Space Sciences
  (Division)   Physics and Instrumentation
  (Branch)   Electro-Optics
NASA Research Colleague: Robert L. Kurtz

Date: August 9, 1974

Contract No.:   NGT-01-003-045

HOLOGRAPHIC NONDESTRUCTIVE TESTING

By

Ashley M. Martin, III

ABSTRACT

Holographic interferomatric techniques have been applied to shuttle engine components to test the feasibility of this method for detecting weaknesses or defects in these materials. A one tenth thrust model of the shuttle engine has been tested and the results presented. Also tests were applied to a flat sample of the same construction as the shuttle engine body and the results are presented. Tentative conclusions are drawn as a result of these tests.

LIST OF FIGURES

INTRODUCTION

Nondestructive testing of all types of mechanical structures is of great practical interest. Although the quantitative interpretations of the results from the holographic techniques, developed for this purpose, have not been established conclusively, the results have given very favorable indications of successful performance during feasibility tests [1].

A hologram is a photographic recording of the interference pattern created in the photographic emulsion by two beams of light, one of which is a reference beam and the other is reflected from a given subject. When a hologram storing a pair of such interference patterns is illuminated with coherent light, the reconstructed wave fronts interfere with each other. This multiple wave front comparison is called holographic interferometry, and one application is called holographic nondestructive testing (HNDT). HNDT is concerned with the formation and interpretation of the fringe patterns which appear when a wave front generated at some earlier time and stored in a hologram is later reconstructed and caused to interfere with a comparison wave. It is this storage or time delay aspect which gives the holographic method a unique advantage over conventional optical interferometry. Holography permits diffusely reflecting or scattering surfaces which are subjected to stress to be interferometrically compared with their non-stressed state.

The purpose of this report is to describe the application of HNDT techniques to Shuttle engine samples.* Possible loading techniques include heating, cooling, positive pressure, negative pressure and vibration; but only positive pressure shall be considered in this report.

THEORY

Holograms are made by using coherent monochromatic electro-magnetic radiation sources. The best sources presently available are lasers. The basic holographic image recording (construction) and

---

* A description of these samples is given in Section III.

13-4

retrieving (reconstruction) processes are illustrated in Figure 1. If the amplitude of the reference beam is R and the scene beam is S, then

$$R(x, y, z, t) = r(x, y, z) e^{j\omega t}$$

and

$$S(x, y, z, t) = s(x, y, z) e^{j\omega t} \quad .$$

During the recording process the photographic emulsion responds to the intensity of light reaching it from all sources where

$$I = |R + S|^2$$

$$= rr^* + ss^* + rs^* + r^*s \quad .$$

Since this is not a function of time but of position, only the energy density received by the plate is the product of $I \times t_o$ where t_o is the exposure time.

As shown in Figure 1, the image is reconstructed by illuminating the developed film with light from a laser at approximately the same angle as that made by the reference beam with the hologram during the recording phase. The fraction of light transmitted through the hologram is given by

$$T = T_o - kE$$

where T_o is the transmittance of the unexposed plate. It is the spatially varying portion of this term which is of interest here. If we multiply that term of the transmittance by the amplitude of the reconstructing (reference) wave, we have

$$R k E = e^{j\omega t} k(rrr^* + rss^* + rrs^* + rr^*s) \quad .$$

This last term can be identified as the amplitude of the reconstructed image whose intensity is given by [2]

$$I_o = k^2 r^4 s^2 \quad .$$
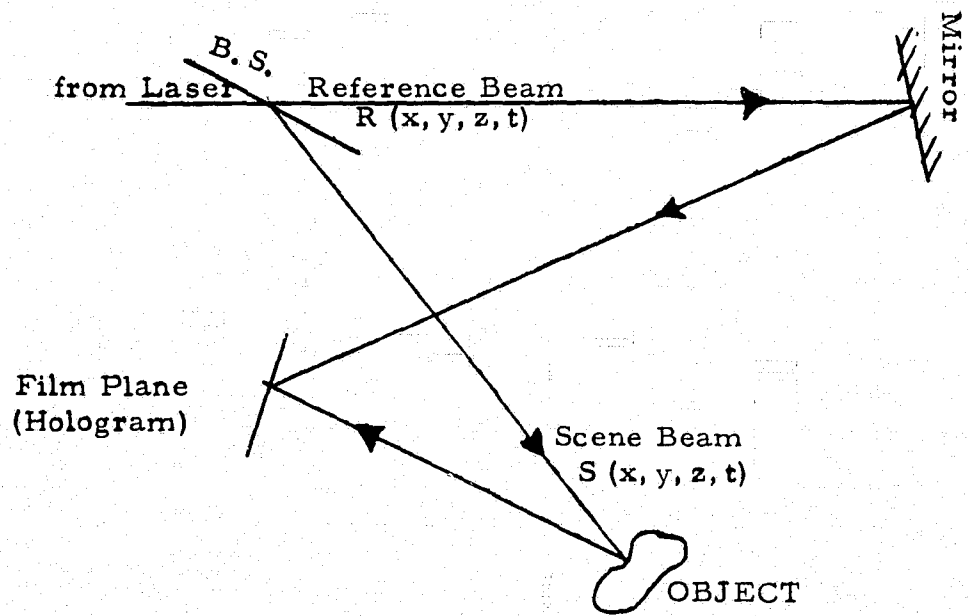
HOLOGRAPHIC RECORDING SYSTEM

In the recording system: from Laser, B.S., Reference Beam R (x, y, z, t), Mirror, Film Plane (Hologram), Scene Beam S (x, y, z, t), OBJECT

In the reconstruction system: from Laser, Reference Beam R (x, y, z, t), Mirror, OBSERVER, HOLOGRAM, HOLOGRAPHIC RECONSTRUCTION, VIRTUAL IMAGE OF OBJECT
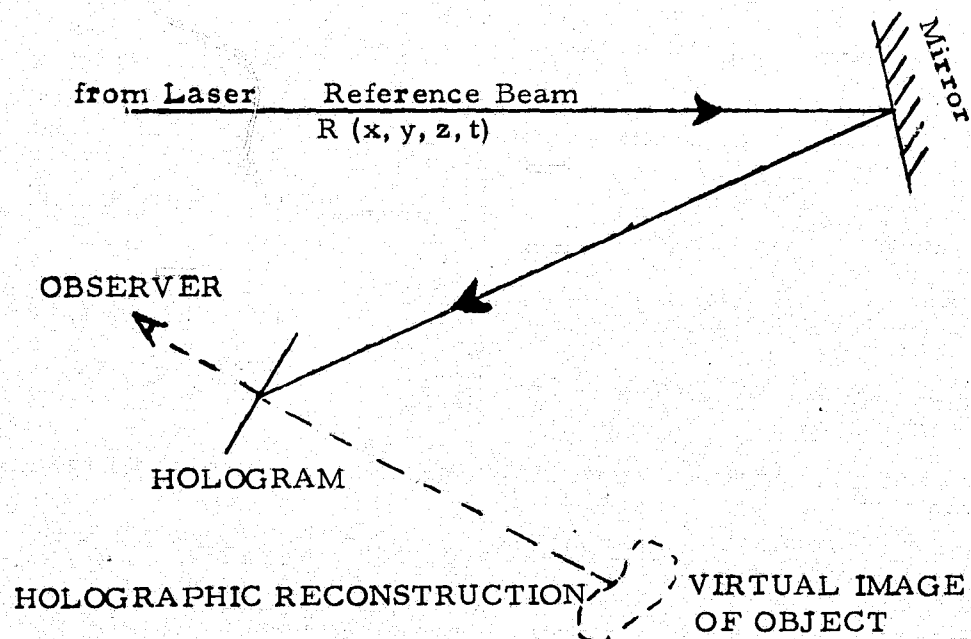
Figure 1. HOLOGRAPHIC RECORDING AND RECONSTRUCTION

There are three basic types of HNDT; namely, time-average, real-time, and double-exposure interferometry. Each of these will be described briefly and the double-exposure process will be discussed in detail.

1. Time-average interferometry. When a hologram is made of an object that is moving during an exposure time, light will be reflected from the object in each position it assumed. If the motion is nearly simple harmonic, the strongest images will correspond to the object at the extremities of its harmonic motion and the resulting interference pattern is called time-average interferometry.

2. Real-time interferometry. Real-time interferometry uses a hologram to store an image of an object and then the image is reconstructed and compared with the object under stress or some form of loading. The interference pattern resulting from the comparison is called real-time interferometry. Extreme care must be taken to replace the hologram in its precise original location.

3. Double-exposure interferometry. After one holographic exposure is made, the object is displaced a small distance and another exposure taken. The two scene beams interfere with one another just as the object beam interfered with the image beam in real-time interferometry. The resulting hologram will exhibit interference patterns which are called double-exposure interferometry.

Illumination of the doubly exposed hologram not only effects the simultaneous reconstruction of two waves which had been scattered from the subject at different times but causes them to interfere under ideal conditions. The waves can share the diffraction efficiency of the hologram equally. Thus, their intensities are equal and the interference fringes they produce have high contrast. For purposes of analysis, the two virtual images of the subject surface generated by the reconstructed waves may be considered to be slightly different physical surfaces. One can imagine these initial state and final state surfaces to be simultaneously illuminated with the coherent light originally illuminating the subject.

Suppose a hologram were made of an object having a scene beam amplitude S_1. If the object is strained and a second exposure made with corresponding scene beam amplitude S_2 on the same hologram, upon

reconstruction, two virtual images will be seen when viewing through the hologram. Their composite amplitude is given by

$$A = -krr^* (s_1 + s_2) \quad .$$

Where these two scene beams interfere constructively, bright regions appear; and where they interfere destructively, dark areas (fringes) appear.

In order to understand the occurrence of these fringes, consider the following general derivation (see Figure 2). Light with propagation vector $\vec{k}$ is incident on a point P located by position vector $\vec{r}$ from an arbitrary origin O (located at the pinhole of the spatial filter illuminating the object). The light is scattered with propagation vector k_2 and detected at S, which is located by $\vec{R}$. The point P translates to point P'. In its new location light with propagation vector $\vec{k}_3$ is incident and is scattered into $\vec{k}_4$, which is also detected at S. Because the path length OPS is different from OP'S, these two waves have a phase difference given by $2\pi/\lambda$ multiplied by the path length differences. Let OP'S - OPS = ΔL; if $\Delta L = n\lambda/2$ (n = 1, 3, 5, . . .), we get destructive interference (dark bands), and if $\Delta L = n\lambda/2$ (n = 0, 2, 4, . . .), we get constructive interference (white bands). The expression for the change in phase for a given displacement is [3]

$$\frac{2\pi}{\lambda} \Delta L = (\vec{k}_1 - \vec{k}_2) \cdot (\vec{r}_1 - \vec{r}_3) \quad .$$

This is the basic relation necessary for the analysis of the static displacements involved in HNDT.

EXPERIMENT

The first sample investigated is a one-tenth thrust model of one of the Shuttle engines. A picture of the sample is found in Figure 3a. Only a part of the sample was investigated holographically because of its large size. The illuminated region included the throat up to and including part of the cylindrical surface and down to and including part of the conical surface. Thus all the different shapes of surfaces were investigated; and it is logical to assume that, given a sufficiently powerful object beam, illumination of the entire object can be accomplished.
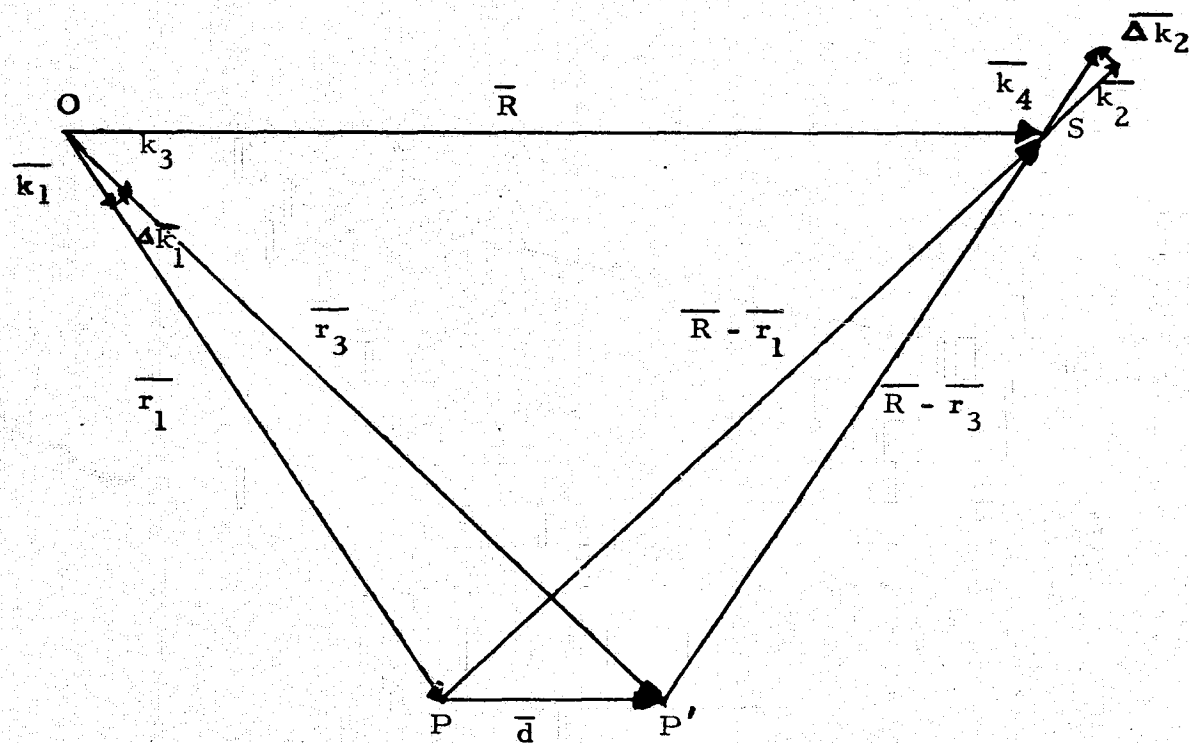
Figure 2.   PROPAGATION VECTORS FOR SCATTERED LIGHT.
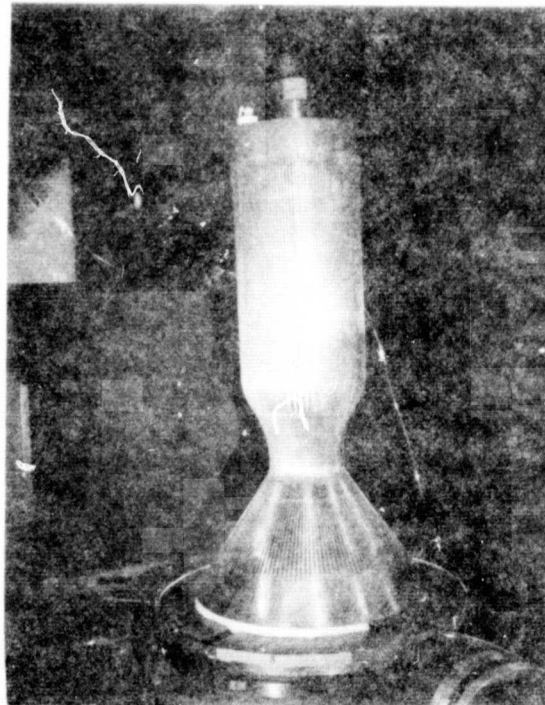
(a)
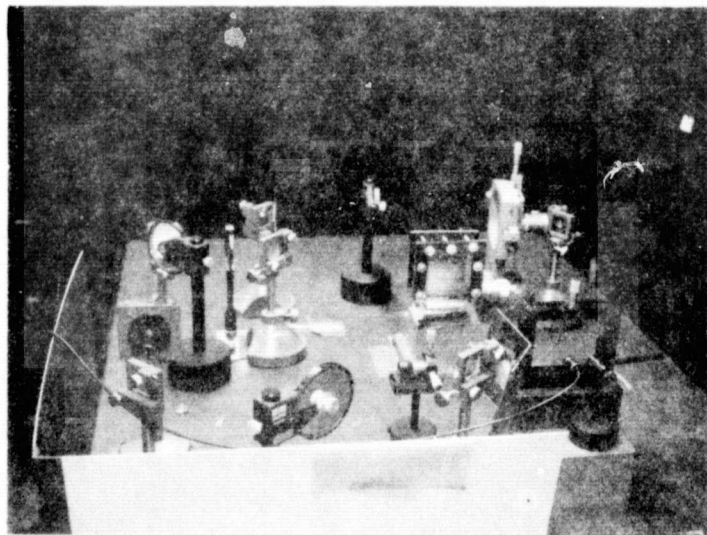
(b)

Figure 3. Holographic Systems Test Samples.

13-10

One of the most effective and easily accomplished loading techniques is positive pressure loading, which was applied to this sample. The first few real-time interferograms revealed a system vibration manifesting itself in a vibration of the real-time fringes. This oscillation appeared to be of the order of $\lambda/8$, which is not large enough to prevent obtaining a hologram; but, nevertheless, it seemed desirable to eliminate this vibration. The source of the vibration was manyfold, and for all practical purposes it was eliminated.

It was known from the beginning of the testing that the sample had a pressure leak that was larger than desirable. The leaking was initiated by an improper setting in the machining process which inadvertently cut all the way through the sample. In repairing this with solder, further complications were introduced and will be discussed later.

As can be seen in Figure 3a, the sample was placed on a milling head to accomplish rotating it. The first series of double exposures was taken to investigate how much of an angular range was useful in a given hologram. As the setting of the milling head was varied between 315 deg and 36 deg a number of double exposures were taken. A few of these are shown in Figures 4 and 5. (These are photographic recordings of the projected real images from the double-exposure holograms.) From these pictures it was determined that the useful portion covers an angular range of approximately 90 deg. This useful range begins not too far from the edge of the illumination on the left and extends not as near the edge of illumination on the right where a large surface area of the sample is crowded onto a small area on the photograph. As a consequence of these investigations, double exposures were taken at 45-deg intervals in order to give a reasonable overlap from one exposure to the next.

The next question to be answered was "Can the fringe pattern be tracked or followed with these rotations?" Referring again to Figures 4 and 5, this question can be answered affirmatively. At this point, however, it is useful to point out that the fringe patterns are highly complex and rather lacking in symmetry. This complexity of fringes will most probably make searching for a flaw to be programmed on later most difficult if not impossible.

Another question to be answered was "Do we get the same fringe patterns for a given ΔP at different reference pressures?" This question is answered by referring to Figure 6. Both of the photographs

$$\theta = 315^\circ \qquad\qquad\qquad\qquad \theta = 346^\circ$$

Figure 4.   Double exposures with $\Delta P = 7$ psi.

$\theta = 26^{\circ}$ $\theta = 36^{\circ}$

Figure 5.   FURTHER DOUBLE EXPOSURES WITH ΔP = 7.0 PSI.
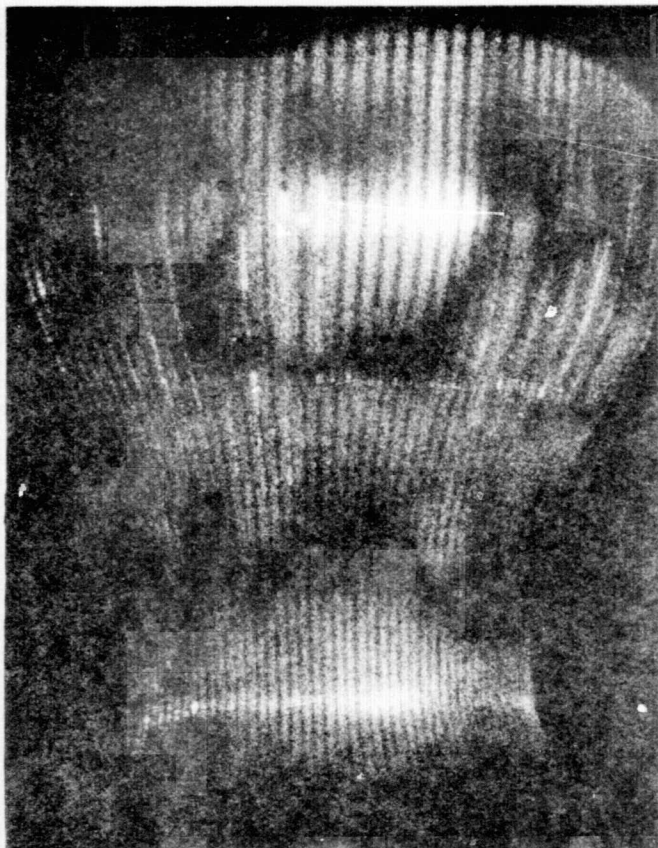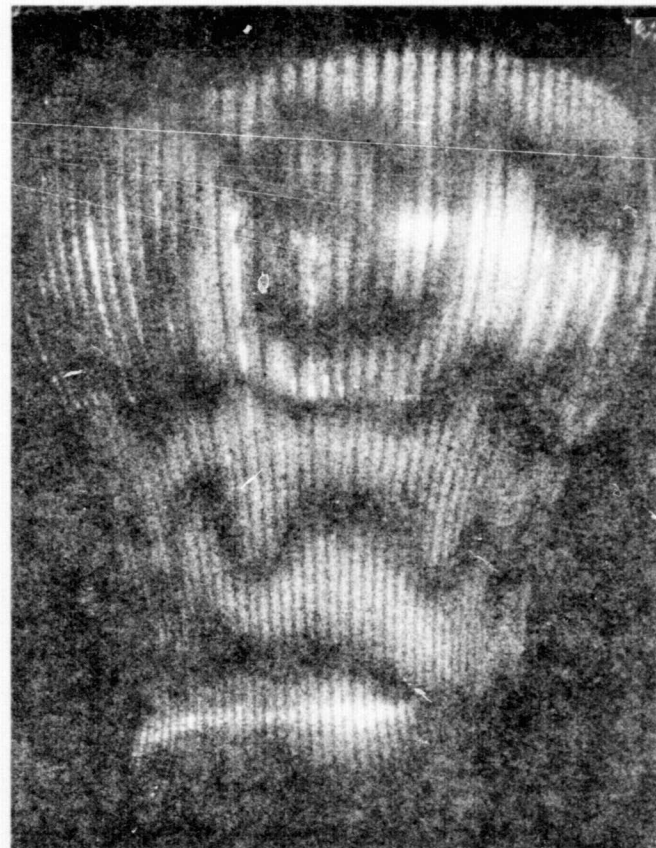
Ref. P = 0.0 psi.   Ref. P = 9.0 psi.

Figure 6.   Double exposures with ΔP = 3 psi at different reference pressures.

are from double exposures with ΔP = 3 psi (the one on the left was taken at a reference pressure of 0 psi, while the one on the right was taken at a reference of 9 psi). These are but two of many such double exposures taken, all of which indicate an increasing degree of complexity as the reference pressure was increased. This is contrary to previous experience [1]. The conclusion drawn from this is that the repairing of the aforementioned leaks had fatigued the sample in such a way as to cause portions of the surface to be more stiff than others.

The second sample tested is pictured together with its associated holographic system in Figure 3b. The sample was to be representative in structure of the body of the previously described Shuttle engine. The sample, however, was a flat copper plate with grooves cut on it similar to the grooves cut in the Shuttle engine for cooling purposes. In order to form again a closed system, the plate was bonded to a solid copper block through which a tube was inserted to pressurize the sample. This entire sample was placed in a holder to more rigidly confine its outer extremities so that the plate bowed out as it was pressurized. The holographic system is a variable sensitivity system designed by Robert L. Kurtz [4].

This sample was supposedly a replica of one tested earlier in this laboratory, and it was desired to reproduce the earlier results and to add a few new tests. Unfortunately, the first few double exposures taken revealed a fringe pattern which was not characteristic of the previous sample. The fringe pattern as shown in Figure 7 exhibited a double center formation. These fringes, being phase contours, seem to indicate the shape of the surface is like a pair of mountains with the two centers representing the peaks of these mountains, and a valley falling in between these. Figure 8 shows the practically circular single center fringe pattern that was characteristic of the earlier tests [1].

Numerous tests were performed in an attempt to determine the origin of this strange double center fringe pattern. The tests at least indicated for certain that the orientation of the double center was fixed with respect to the plate and did not depend on how the plate was oriented in the holder nor how tight the screws were tightened. The most believable explanation, presently, is that the sample has been fatigued and that there is a stiff region located between the two centers at approximately the lateral geometric center of the plate. It is quite conceivable that the sample was pressure tested beyond its elastic limit by the machinist. The group responsible for the machining is unable to
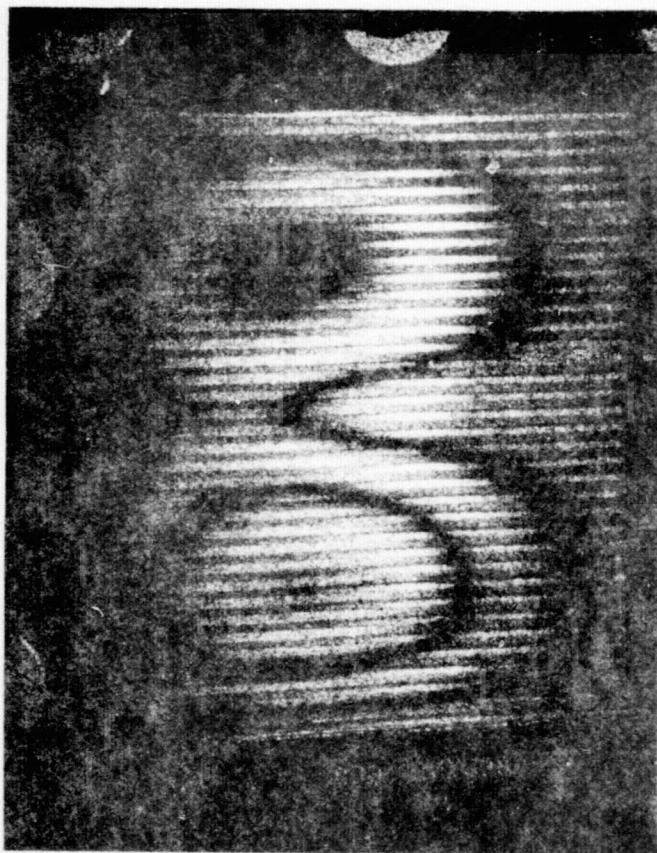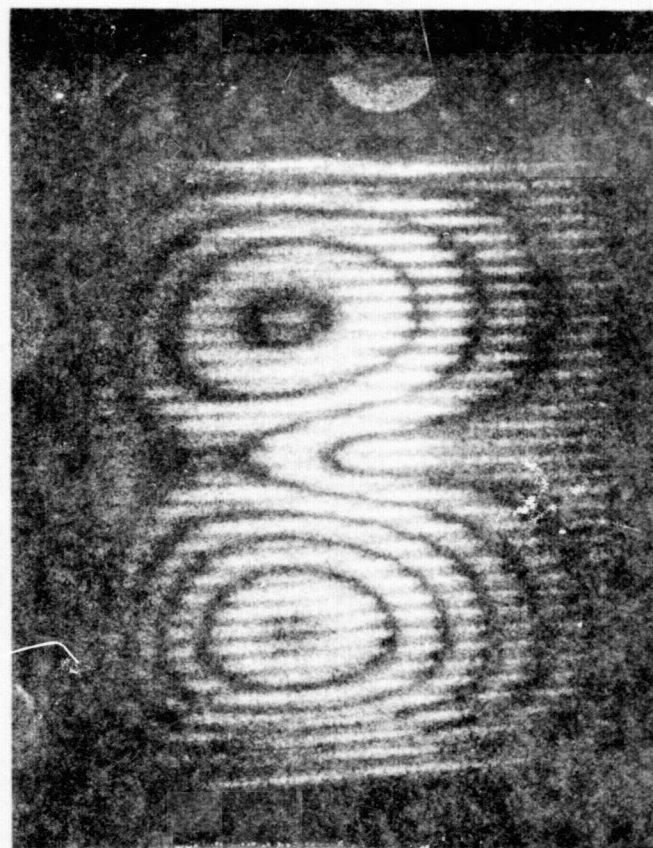
ΔP = .1 PSI ΔP = .25 PSI

Figure 7. DOUBLE EXPOSURES WITH DIFFERENT ΔP.
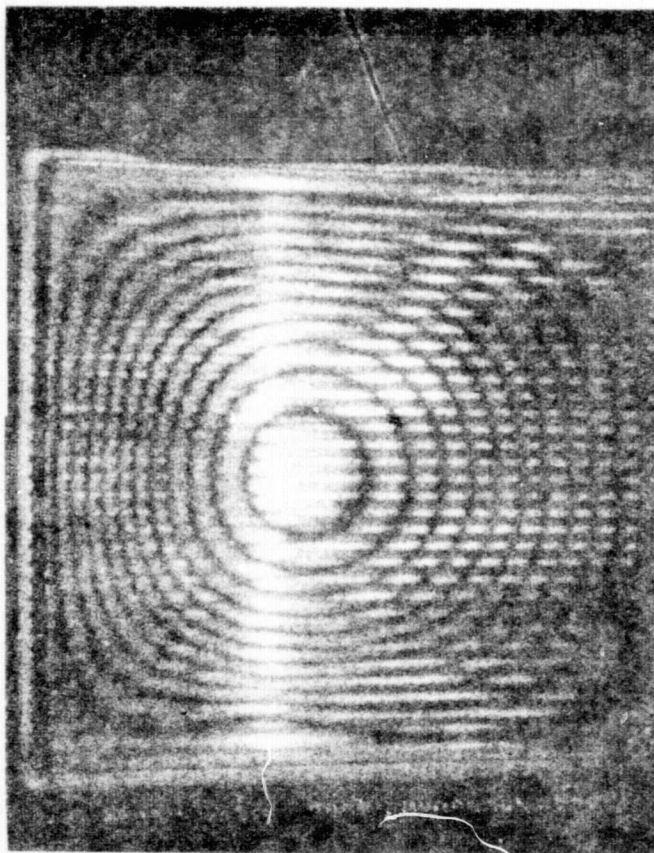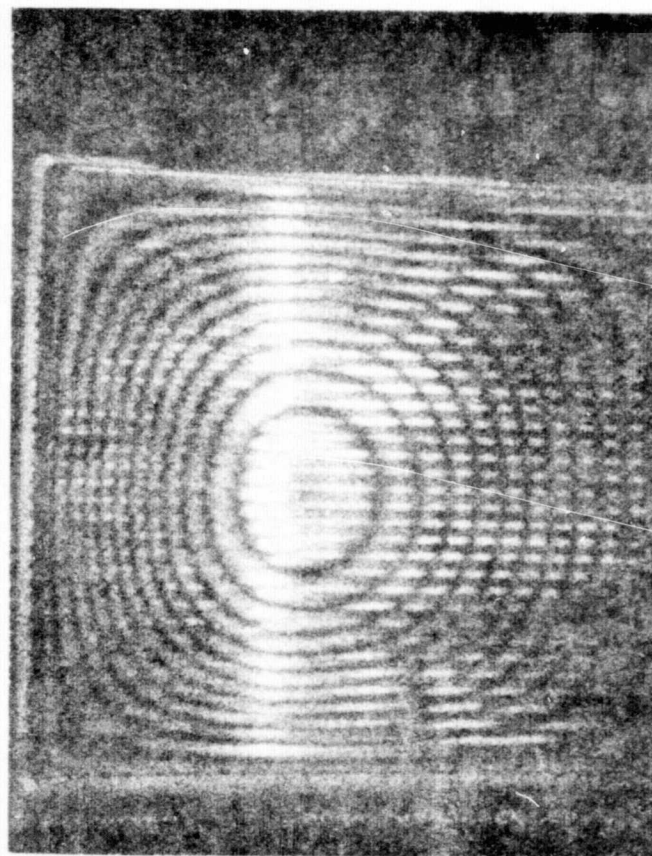
Ref. P = 1.00 PSI   Ref. P = 15.00 PSI

FIGURE 8.   DOUBLE EXPOSURES WITH SAME ΔP.

confirm or deny the performance of a pressure check. It was also learned that in the process of cutting the grooves the samples curled up from the heat and/or mechanical stress and had to be flattened out again. This, again, is further evidence of the existence of fatigue in the sample. Because this problem did not result in much more complex fringe patterns, it is believed that the sample is still useful for flaw probing by HNDT. With this in mind, further tests were run on the sample.

In this feasibility test for HNDT it was first necessary to learn what ΔP will produce a desirable fringe density (i.e., fringe density is a direct function of ΔP). Figure 7 indicates that a $\Delta P = 0.1$ psi does not produce a dense enough fringe pattern and $\Delta P = 0.25$ psi is just about the right fringe density. Consequently, a complete series of double exposures was taken from reference pressure 1.0 to 20.0 psi and with $\Delta P = 0.25$ psi. This investigation revealed a transition period from double center pattern to single center oval pattern at about 7.75 psi. This is illustrated in Figure 9. It appears that at the transition point the rigid line between the centers gave way to the higher reference pressure. Figure 10 shows the same sample without the holder and, as demonstrated, the oval, noncircular pattern is characteristic of its fringe patterns. As had been discovered earlier, the holder tends to emphasize the weakness, which is highly desirable for discovering unknown flaws.

Briefly, loading techniques of heating and cooling were tried. The results of the tests as shown in Figure 11 indicate, among other things, a need for a technique of heating and cooling more uniformly. The technique applied for cooling was placing a chunk of dry ice on the sample between exposures. The technique of heating was done with a heat gun.

CONCLUSION

In summary, it was the intent of the work here to obtain good "clean" reference fringes on the unperturbed samples and to compare later HNDT results after certain types of flaws were programmed on the samples. What was accomplished for both samples, however, was more than this. The perturbations already applied to the samples inadvertently are definitely exposed in these double-exposure interferograms.
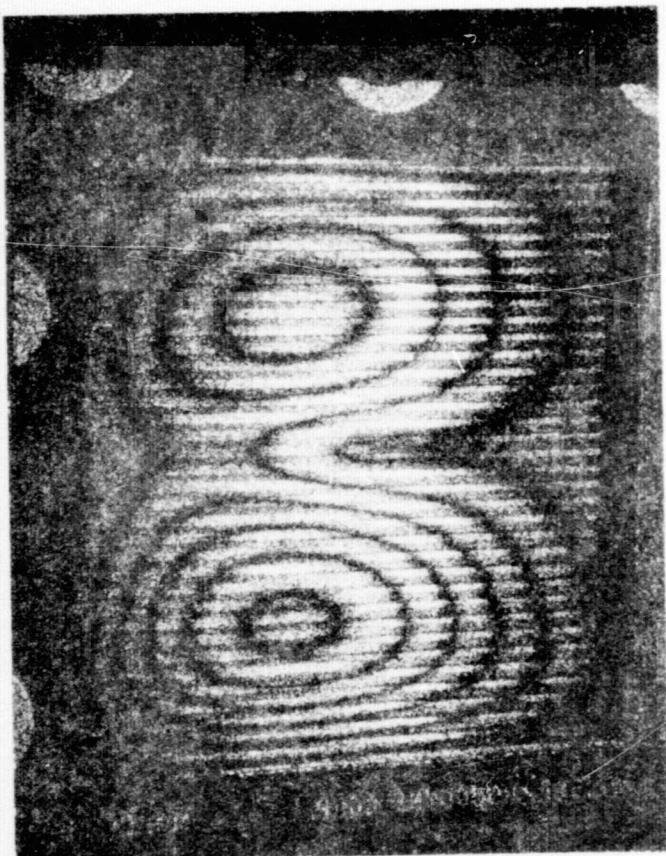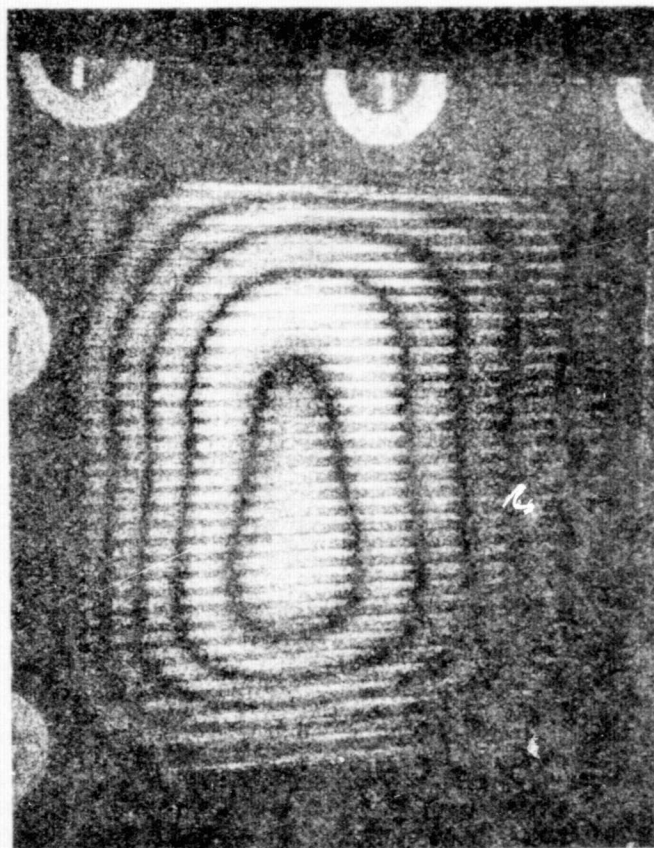
P = 7.00 - 7.25 psi   P = 7.75 - 8.00 psi

Figure 9. DOUBLE EXPOSURES INDICATING TRANSITION REGION.
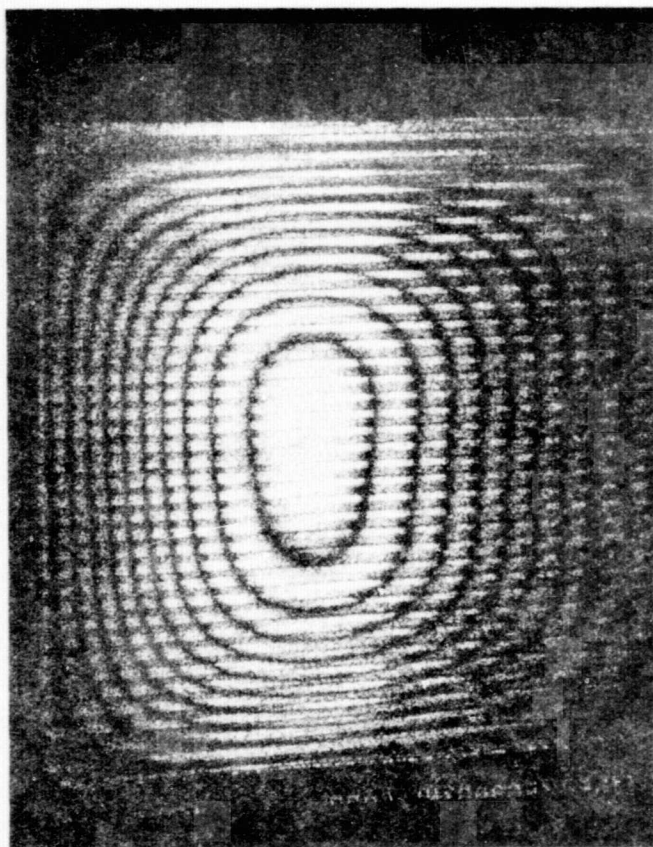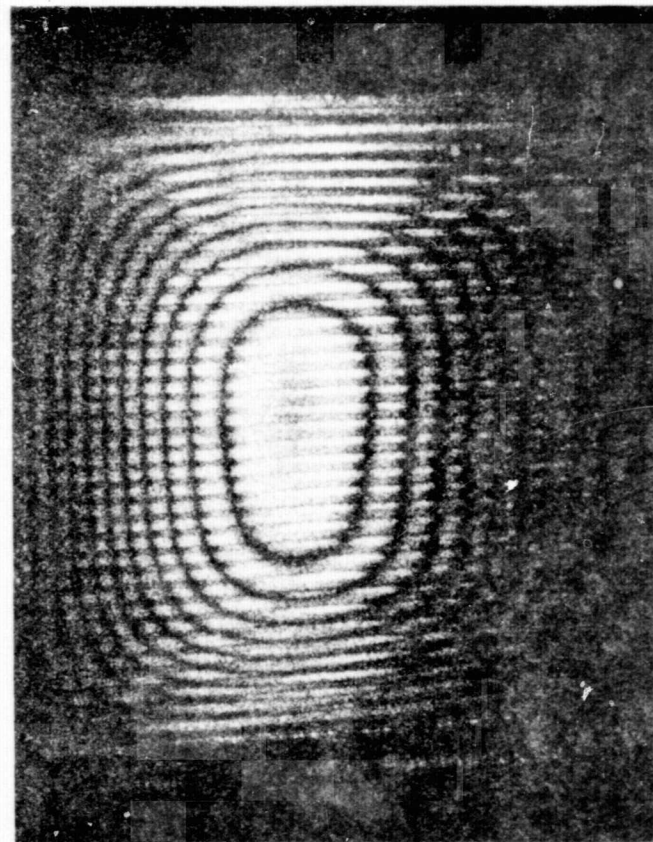
P = 4.00 - 4.25 psi   P = 16.00 - 16.25

FIGURE 10.   DOUBLE EXPOSURES WITHOUT HOLDER.
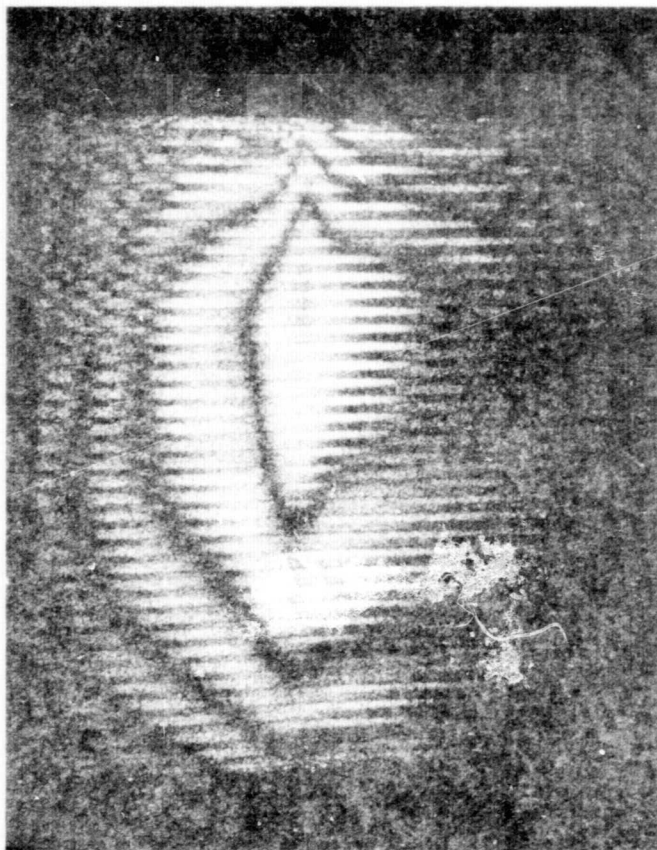
COOLING WITH DRY ICE   HEATING WITH HEAT GUN

Figure 11.   HEATING AND COOLING DOUBLE EXPOSURES.

In the case of the engine model, the tremendous amount of soldering and repairing done has apparently caused so much stress that it will be necessary to begin again on a better engine model. For the flat sample the process of programming flaws on the sample is being done, and it is believed that the fatigue in this sample is not severe enough to prohibit detection of the planned flaws.

REFERENCES

1.   Kurtz, Robert L., Private communication.

2.   Schliekmann, R. J., Holographic Interference as a Means for
      Quality Determination of Adhesive Bonded Metal Joints. Inter-
      national Council of the Aeronautical Sciences, 8th Congress,
      Amsterdam, Netherlands, August 28-September 2, 1972.

3.   Sollid, Jon E., Holographic Interferometry Applied to Measure-
      ments of Small Static Displacements of Diffusely Reflecting
      Surfaces. Applied Optics, Vol. 8, No. 8, August 1969, pp.
      1587-1595.

4.   Kurtz, Robert L., and Liu, H. K., Holographic Nondestructive
      Tests Performed on Composite Samples of Ceramic-Epoxy-
      Fiberglass Sandwich Structures. NASA TR R-430, June 1974.

1974

ASEE - NASA SUMMER FACULTY FELLOWSHIP PROGRAM

MARSHALL SPACE FLIGHT CENTER

(AUBURN UNIVERSITY - UNIVERSITY OF ALABAMA)

TEMPERATURE REQUIREMENTS FOR THE FLOATING ZONE CRYSTAL

GROWING TECHNIQUE IN A SPACE ENVIRONMENT

Prepared by: John R. McDonald

Academic Rank: Assistant Professor

Department and University: Department of Mechanical Engineering
                            South Dakota School of Mines
                            and Technology

NASA/MSFC Assignment: Space Science Laboratory

NASA Research Colleague: Mirt Davidson

Date: August 9, 1974

Contract No.:   NGT-01-003-045

TEMPERATURE REQUIREMENTS FOR THE FLOATING ZONE CRYSTAL GROWING TECHNIQUE IN A SPACE ENVIRONMENT

by

John R. McDonald

ABSTRACT

A numerical solution to the two-dimensional heat conduction equation will be presented suitable for determining the temperature variation in a finite cylindrical rod through which a floating liquid zone is being passed. The two-dimensional transient analysis result will be determined by specifying boundary conditions which are valid within a space environment and applying them to the heat conduction equation in cylindrical coordinates, with the angular coordinate constant. Since the crystals are to be grown in a space environment, the convective mixing terms in the liquid can be neglected with seem to be a valid assumption based on preliminary Skylab results from growing crystals in a zero gravity environment.

A finite difference technique will be applied to the governing differential equation with latent heat effects considered across the solid-liquid interface. The resulting temperatures within a material can then be determined by solving the simultaneous, finite-difference equations, with particular interest being the shape of the isotherm located at the solid-liquid interface.

ACKNOWLEDGEMENT

INTRODUCTION

Material processing in a space environment offers an opportunity
for growing single crystals in the absence of gravity, which has many
uses in the semiconductor field. Industry has expressed interest in
single crystals of large diameters. Techniques of zone melting with-
out a container have been devised to handle certain materials, when
melted, are so reactive or effective as solvents that they cannot be
zone-refined to high purity in any known container. These techniques
have limitations, however, they have resulted in some of the purest
materials ever produced.

Most commonly used is the floating-zone technique where a molten
zone is held in place by its own surface tension between two vertical
colinear solid rods. Much research has been conducted to determine
possible sizes and shapes of molted zones under the influences of
surface tension and gravity, induction and electron-beam heating
techniques, which are the two most widely used, solar heating, and
other heating techniques.

The stability of molten zones has been analyzed mathematically
and the results have received experimental verification. Heywang and
Ziegler,[6] and later Heywang,[5] showed, for round rods, that the max-
imum length(height) of zone that can be supported by its own surface
tension increases linearly with rod radius for small radii and ap-
proaches a limit at large radii. Carruthers and Grasso[1] questions
that the generally accepted Heywang criterion for the stability of

14-4

cylindrical liquid zones, and feel it is no longer valid under reduced
gravitational conditions. The maximum stable length of a vertically
suspended liquid zone depends on the quantity $\left(\sigma/\rho g\right)^{1/2}$, where σ is
the surface tension, ρ the liquid density, and g is the gravitational
acceleration. Therefore, materials with low σ and high ρ are difficult
to grow with a floating zone. Another difficulty arises with larger
diameters and low thermal conductivities because of the adverse
solid-liquid interface curvatures. In order to melt a zone completely
through, the external molten zone length can easily exceed the limit
where surface tension will contain it.

Additional flexibility in floating-zone crystal growth is
provided by the pedestal technique where the solid end members are
unequal in diameter. Greater control of the radial temperature
gradients is possible with this geometry. Also, liquid column heights
in excess of that allowed by the smaller diameter alone are allowed.

Fowle and Haggerty[4] has conducted work to maximize the potential
benefits of creating pure, stress-free silicon crystals in the space
environment by the float-zone process. By incorporating relative
rotation of the crystal and feed stock one induces forced convective
currents in the melt which may possibly result in a more desireable
radial distribution of heat flux at the freezing interface referred
to above is one that leads to no radial temperature gradient and,
hence, essentially stress-free crystal growth at the freezing inter-
face.

They consider reducing thermal gradients in the melt zone by virtue of the forced secondary flow circulation to be of primary interest. However, forced circulation is of real value only if it reduces the thermal gradients by a significant amount relative to the case of no circulation. The author is not convinced that forced circulation is necessary, and it is hoped the results of this study will verify this opinion.

The problem facing crystal growers in the past is a lack of knowledge concerning the shape of the solid-liquid interface, or more specifically the curvature of the isotherm at this interface. It is the desire of the author to write the governing differential equations applicable to the heat flow process in a crystal growing specimen. The solution to these differential equations will be presented in the form of finite difference equations which can be solved by the use of computers.

In this paper, attention is focused on the use of solar energy as the most attractive heat source for a space process because of its avilability and its system size, weight and life characteristics are considered to be superior. As a first approximation to the solution of this problem the only requirements of the heating system will be a capability to provide energy such that the incident light rays are normal to the centerline of the specimen and maintain a constant magnitude around the circumference of the specimen. The type of heating system should be able to satisfy such requirements

whether it be a solar furnace or resistance heater. This require-
ment forces radial heat flow and allows removal of the circular
dimension enabling a two-dimensional approach to the problem.

Much work has been conducted in the interest of crystal
growing, however, the state of the art is at the present relatively
untouched. In order to control the growth rate and diameter of the
single crystal, the isotherm located at the solid-liquid interface
must be perpendicular to the centerline of the cylindrical rod
through which the thermal gradient is being passed. Many investigators
have devoted much effort into designing a solar furnace to transmit
a particular energy profile to the circumferencial surface of the
crystal growing specimen. It is the opinion of the author that
first one should ask the question, what are the energy requirements
necessary to produce a planar solid-liquid interface at the melting
end of the molten zone? Some satisfy this requirement by rotating
each end of the specimen, either in the same direction or counter-
rotation which induces the non-existant convective mixing of the
zero gravity environment. From the results of Skylab, it is
clearly seen that no convective mixing in the liquid took place and
this is why the convective terms in the energy equation was not
considered in this report.

The approach to this problem seems evident, what must be the
shape of the thermal gradient at the surface of the cylindrical
specimen in order to ensure a flat isotherm at the melting boundary

of the floating zone? The author attempts to offer an insight to
this problem by solving the transient heat conduction equation
subject to the boundary conditions one would expect when conducting
the float zone crystal growing process in a zero gravity environment.

The problem at hand is among a most important group of problems
in which a substance has a transformation point at which it changes
from one phase to another with emission or absorption of heat. The
first published discussion of such problems seems to be that by
Stefan in a study of the thickness of polar ice, and for this reason
the problem of freezing is frequently referred to as the "problem
of Stefan".

Before considering a specific solution, it is desirable to
indicate what exact solutions have been obtained and the methods
available. The most important exact solution is that of Neumann
for the semi-infinite region $x > 0$ initially at a constant temperature.
There are no closed solutions for other important boundary conditions
at $x = 0$ such as constant flux or radiation, though there are some
for various perscribed values of the surface temperature which are
of no great physical importance. An approximation which is frequently
made consists of neglecting the heat capacity of the material between
$x = 0$ and the surface of separation, that is, of assuming that the
flow through this region is of steady type.

Exact solutions are also available for a number of problems
on the infinite region in which $x < 0$ is initially solid at constant

temperature and $x>0$ is initially liquid at constant temperature. These solutions can also be generalized to the case of several transformation temperatures and to the case of a melting range in place of a fixed melting point.

No exact solutions are available of other regions such as the slab $-a<x<a$ with its surface maintained at zero, or for the region $-a<x<a$ initially liquid and $|x|>a$ initially solid.

For problems on radial flow in cylindrical or spherical co-ordinates the position is even worse. The only simple exact solution in cylindrical coordinates corresponds to addition or removal of heat by a continuous line source. For the region bounded internally or externally by a circular cylinder with constant surface temperature, only an approximate solution is available.

Apart from the few exact solutions, all problems have to be attacked by numerical methods: digital methods, the differential analyser, and an electrical analogue method called the thermal analyser have all been used. The exact solutions mentioned above are frequently useful as starting solutions in these cases. The systematic use of numerical methods has the advantage that the variation in the thermal properties with temperature, which is usually considerable over the ranges of temperature involved in problems on melting and solidification, can be taken into account.

STATEMENT OF PROBLEM

The transient solution to the heat conduction equation in cylindrical coordinates will be presented in terms of finite difference equations in order to calculate the temperature of a given point at some future time in terms of its existing temperature driven by prescribed boundary conditions. The difference equations will be written for a semi-infinite cylindrical rod in which a constant temperature heat source is being impressed on a portion on its circumference, as shown in Figure 1.

a = diameter of specimen
d = distance between specimen and inside diameter of quartz tube
h = length of heat source
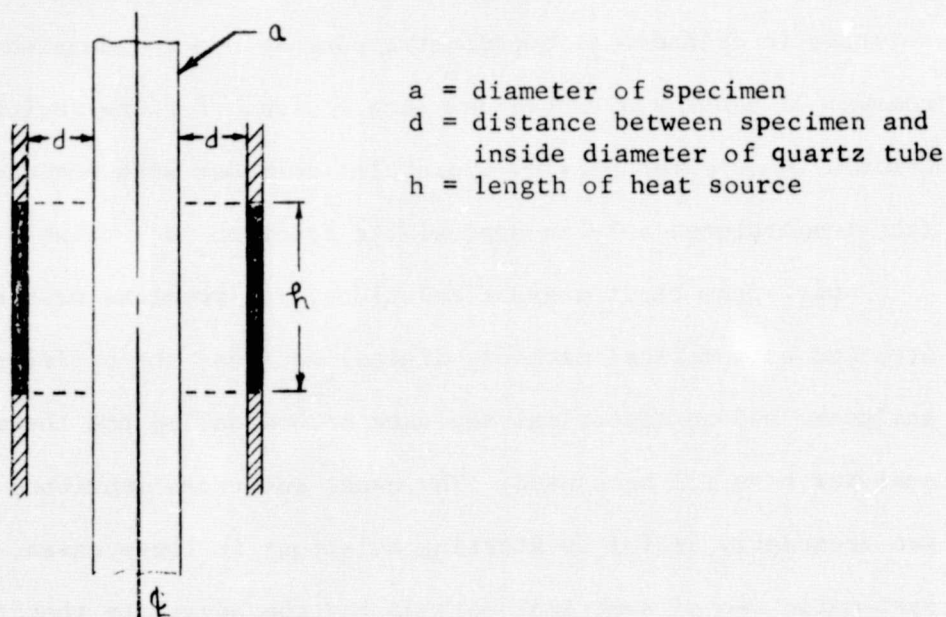
Figure 1. Float Zone Technique for Growing Crystals.

It is proposed the specimen will be a cylinder of diameter a and length L which is placed inside a quartz tube of inside diameter a + 2d and length L such that their centerlines coincide. This alignment is critical, but is expected to be incorporated in the basic design.

In a sense, the quartz tube will provide a window for allowing energy from an external source to reach the specimen. The inside surface, excluding the windows, will be coated with a thin film possessing the properties of a perfect reflector, that is its absorptivity and transmissivity is negligible compared to its reflectivity, such that any incident energy is reflected back to the specimen. This allows a finite difference approach to the problem where the nodes along the circumference of the specimen are subjected to a radiation boundary condition.

General assumptions pertinent to this problem is that of constant thermal properties which is consistent with the idea of considering the phases separately. No internal heat generation terms will be considered as the latent heat terms will be entered as boundary conditions across the solid-liquid interface.

From the first law of thermodynamics, the general two-dimensional heat conduction equation in cylindrical coordinates with radial symmetry becomes:

$$\frac{\partial^2 T}{\partial r^2} + \frac{1}{r}\frac{\partial T}{\partial r} + \frac{\partial^2 T}{\partial z^2} = \frac{1}{\alpha}\frac{\partial T}{\partial t} \tag{1}$$

Considering the two phases independently the governing equations can be written for each phase as follows:

$$\frac{\partial^2 T^1}{\partial r^2} + \frac{1}{r}\frac{\partial T^1}{\partial r} + \frac{\partial^2 T^1}{\partial z^2} = \frac{1}{\alpha_1}\frac{\partial T^1}{\partial t} \tag{2}$$

$$\frac{\partial^2 T^2}{\partial r^2} + \frac{1}{r}\frac{\partial T^2}{\partial r} + \frac{\partial^2 T^2}{\partial z^2} = \frac{1}{\alpha_2}\frac{\partial T^2}{\partial t} \tag{3}$$

where, $T_2^1 = T(r,z,t)$ = temperature in the melt
$T^2 = T(r,z,t)$ = temperature in the solid
α_1, α_2 = thermal diffusivities in the melt and solid, respectively.

Initially the entire solid is at some $T = T_o$, for $t < 0$,

$$T^2(r,z,-t) = T_o$$
$T^1(r,z,-t)$ does not exist(no melt present)

At $t = 0$, a constant line heat flux is applied along the outside circumference of the solid cylindrical rod. $\Psi(r)$ is the magnitude of the heat source.

In order to write finite difference equations, the cylindrical rod must first be subdivided. The simple and obvious method for subdividing the system is in equal increments of the radius, this will be used here, and the accuracy is quite satisfactory. There are two other possibilities for subdividing the system. Subdivision in equal increments of the logarithm of the radius, which is not applicable to the present case of a solid cylinder. It has some advantages for a hollow cylinder, especially if the interest is in the thermal gradients near the inner surface. A subdivision in equal increments of cross-sectional area is applicable to solid or hollow cylinders and is useful for a close subdivision near the surface.

The system is laid out as in Figure 2. For convenience an arc of 1 radian is used, since the θ coordinate is constant, and the depth in the axial direction is taken as Δz, which is made equal to Δx the radial increment.
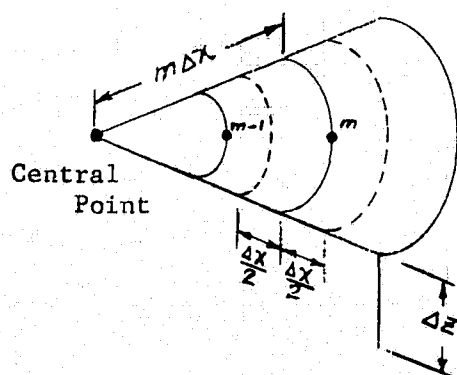
Figure 2. Subdivision of System

The system is divided as shown in Figure 2, with the radial

increment Δx, the axial increment Δz, and a constant angular

arc of 1 radian. For a particular volume, the nodal points m,m - 1,

are located in the center of that volume on a radial line at equal

radial increments, where Δr = $\angle$x.

The area to be used in the heat conduction equation for heat

flow in the radial direction between the nodal points m and m - 1

is taken to be the area of the surface located at the mid point

between the two nodal points. This area changes for each node,

and must be calculated at each node.

The finite difference equations are written interms of the

thermal conductance, which is defined as the thermal conductivity

multiplied by the area divided by length of heat flow path. So,

it becomes necessary to write an equation for the central point

(located at the centerline of the rod), for heat flow in the radial direction for points m and m - 1, and m and m + 1, and a node located on the outside surface.

For validity, the finite difference equation will be written for a general intermediate point, and shown that in the limit results in the general heat conduction equation in cylindrical coordinates. Nodal points are numbered m in the radial direction and n in the axial direction.

General Intermediate Point

Thermal Conductance between points m and m - 1.

$$\frac{k(2m-1)\Delta z}{2}$$

Thermal Conductance between points m and m + 1.

$$\frac{k(2m+1)\Delta z}{2}$$

Thermal Conductance in the axial direction.

$$\frac{k m \overline{\Delta x}^2}{\Delta z}$$

Finite Difference Equation.

$$\frac{k(2m-1)\Delta z}{2}\left(T_{m-1,n} - T_{m,n}\right) + \frac{k(2m+1)\Delta z}{2}\left(T_{m+1,n} - T_{m,n}\right) +$$

$$\frac{k m \overline{\Delta x}^2}{\Delta z}\left(T_{m,n+1} - T_{m,n}\right) + \frac{k m \overline{\Delta x}^2}{\Delta z}\left(T_{m,n-1} - T_{m,n}\right) =$$

$$\frac{m \overline{\Delta x}^2 \Delta z}{\Delta t} \rho c \left(T'_{m,n} - T_{m,n}\right) \qquad (4)$$
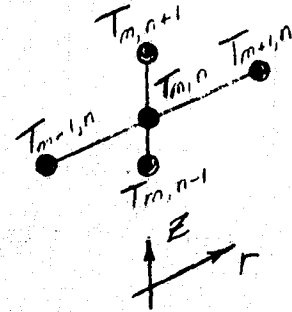
rearranging,

$$\frac{\left(\frac{T_{m-1,n}-T_{m,n}}{\Delta x}\right)-\left(\frac{T_{m,n}-T_{m+1,n}}{\Delta x}\right)}{\Delta x} + \frac{1}{m\Delta x}\left(\frac{T_{m+1,n}-T_{m-1,n}}{2\Delta x}\right) +$$

$$\frac{\left(\frac{T_{m,n+1}-T_{m,n}}{\Delta z}\right)-\left(\frac{T_{m,n}-T_{m,n+1}}{\Delta z}\right)}{\Delta z} = \frac{1}{\alpha}\left(\frac{T'_{m,n}-T_{m,n}}{\Delta t}\right) \qquad (5)$$

taking the limit as

$$x \longrightarrow 0$$
$$z \longrightarrow 0$$
$$t \longrightarrow 0$$

$$\frac{\partial^2 T}{\partial r^2} + \frac{1}{r}\frac{\partial T}{\partial r} + \frac{\partial^2 T}{\partial z^2} = \frac{1}{\alpha}\frac{\partial T}{\partial t} \qquad (6)$$

The finite difference equation for a general intermediate point results in the form of the differential equation in cylindrical coordinates for the case of radial symmetry. This minimizes the descrepancy of the numerical solution.

The finite difference equation for a general intermediate point will be the same as equation (4). This equation will be solved for the nodal temperature at a future time in terms of the existing temperature. Therefore,

$$T'_{m,n} = \left(\frac{2m-1}{2mM}\right)T_{m-1,n} + \left(\frac{2m+1}{2mM}\right)T_{m+1,n} + \left(\frac{1}{M}\right)T_{m,n+1} +$$

$$\left(\frac{1}{M}\right)T_{m,n-1} + \left(\frac{M-4}{M}\right)T_{m,n} \qquad (7)$$

where the prime denotes time at $t + \Delta t$.

$$M = \frac{\overline{\Delta x}^2}{\alpha \Delta t}$$

Finite Difference Equation for a Point on the Center Line

For convenience the nodal points will be numbered such that the node located on the center line is designated by m - 2 in the axial direction.

Radial Thermal Conductance.

$$\frac{k \Delta Z}{2}$$

Axial Thermal Conductance.

$$\frac{k \overline{\Delta x}^2}{8 \Delta Z}$$

Finite Difference Equation.

$$\frac{k \Delta z}{2}\left(T_{m-1,n} - T_{m-2,n}\right) + \frac{k \overline{\Delta x}^2}{8 \Delta z}\left(T_{m-2,n-1} - T_{m-2,n}\right) +$$

$$\frac{k \overline{\Delta x}^2}{8 \Delta z}\left(T_{m-2,n+1} - T_{m-2,n}\right) = \frac{c\rho \overline{\Delta x}^2 \Delta z}{8 \Delta t}\left(T'_{m-2,n} - T_{m-2,n}\right)$$

Solving for the temperature at $t + \Delta t$,

$$T'_{m-2,n} = \frac{1}{M}\left(T_{m-2,n-1} - T_{m-2,n+1}\right) + \frac{4}{M} T_{m-1,n} + \left(\frac{M-6}{M}\right) T_{m-2,n} \quad (8)$$

Finite Difference Equation for a Point Located on the Surface of the Cylinder

Again for convenience, the nodal points will be numbered such that the node located on the outside surface is designated by m + r in the radial direction.

Radial Thermal Conductance.

$$k\left[2(m+r)-1\right] \Delta Z$$

Axial Thermal Conductance.

$$\frac{k\left[4(m+r)-1\right]}{\Delta Z} \frac{\overline{\Delta x}^2}{8}$$

Finite Difference Equation.

$$\mathcal{k}\big[2(m-r)-1\big]\Delta z\big(T_{m+r-1,n} - T_{m+r,n}\big) + \frac{\mathcal{k}\big[4(m+r)-1\big]\overline{\Delta x}^2}{8\Delta z}\big(T_{m+r,n+1} - T_{m+r,n}\big) +$$

$$\frac{\mathcal{k}\big[4(m+r)-1\big]\overline{\Delta x}^2}{8\Delta z}\big(T_{m+r,n-1} - T_{m+r,n}\big) + \psi(r) =$$

$$\frac{\rho c\big[4(m+r)-1\big]\overline{\Delta x}^2\Delta z}{8\Delta t}\big(T'_{m+r,n} - T_{m+r,n}\big)$$

Rearranging and defining two new terms,

$$\overline{M} = \frac{8\big[2(m+r)-1\big]}{M\big[4(m+r)-1\big]} \qquad A(r) = \frac{8\,\psi(r)}{\mathcal{k}\Delta z\,M\big[4(m+r)-1\big]}$$

$$T'_{m+r,n} = \overline{M}\,T_{m+r-1,n} + \frac{1}{M}\big(T_{m+r,n+1} + T_{m+r,n-1}\big) + A(r) +$$

$$\big(1 - \overline{M} - \frac{2}{M}\big)\,T_{m+r,n} \tag{9}$$

Finite Difference Equation for Calculating the Temperatures Located Adjacent to the Solid-Liquid Interface

In order to write the finite difference equation for a point located adjacent to the solid-liquid interface, a heat balance must first be made. If L is the latent heat of fusion of the specimen and T_m is its melting point, and if the surface of separation between the solid and liquid phases is at X(t), one boundary condition to be satisfied at this surface is

$$T^1 = T^2 = T_m \qquad \text{when } x = X(t) \tag{10}$$

A second boundary condition concerns the absorption or liberation of latent heat at this surface. Suppose that the region $x > X(t)$ contains liquid at temperature $T^1(r,z,t)$, and that $x < X(t)$ contains solid at temperature $T^2(r,z,t)$. Then, when the surface of separation moves a distance dX, a quantity of heat $L\rho dX$ per unit area

14-17

is liberated and must be removed by conduction. This requires

$$k_{11} \frac{\partial T'}{\partial r} + k_1 \frac{\partial T'}{\partial z} - k_2 \frac{\partial T^2}{\partial r} - k_2 \frac{\partial T^2}{\partial z} = \rho L \frac{dX}{dt} \tag{11}$$

Equation (11) may be put into an alternative form by considering the curves of constant temperature $T^1(r,z,t) = T_m = T^2(r,z,t)$.

$$\frac{\partial T'}{\partial r} dr + \frac{\partial T'}{\partial z} dz + \frac{\partial T'}{\partial t} dt = 0 = \frac{\partial T^2}{\partial r} dr + \frac{\partial T^2}{\partial z} dz + \frac{\partial T^2}{\partial t} dt$$

Letting $dr = dz = dX$,

$$\frac{dX}{dt} = \frac{-\frac{\partial T'}{\partial t}}{\frac{\partial T'}{\partial r} + \frac{\partial T'}{\partial z}} \tag{12}$$

Using this definition, the finite difference equation becomes:

$$\frac{-k_2 \left(T_M - T_{m+r-1,n}^{2'} \right)}{\Delta X} - \frac{k_2 \left(T_M - T_{m+r+1,n}^{2'} \right)}{\Delta X} - $$

$$\frac{k_1 \left(T_M - T_{m+r,n-1}^{'} \right)}{\Delta z} - \frac{k_1 \left(T_M - T_{m+r,n+1}^{'} \right)}{\Delta z} = $$

$$\frac{-\rho L \left(\frac{T_M - T_{m+r,n}^{'}}{\Delta t} \right)}{\left(\frac{T_M - T_{m+r-1,n}^{'}}{\Delta r} \right) + \left(\frac{T_M - T_{m+r,n+1}^{'}}{\Delta z} \right)} \tag{13}$$

When applying this equation care must be taken to choose the approiate distances each time when writting the heat balance. Since the position of the solid-liquid interface is unknown, the distances in equation (13) is the distance from the interface to the nearest nodal point, and care nust be taken when program-ming these equations. For example, Δr and Δz should be taken as the distance from a point $m + r,n$ to the melt front in the r and z direction.

In order to investigate the expected error between the analytical solution of the heat conduction equation and numerical solution, one must look at what the author defines as the stability criterion. Stability is determined by equating to zero the coefficient of the existing node temperature in the finite difference equation written for that node and solved for the temperature at some future time.

For any intermediate point, the coefficient is from eq. (7),

$$\frac{M-4}{4} = 0$$

or M = 4.

For any point located on the centerline of the cylinder, the coefficient which must be zero is from eq. (8).

$$\frac{M-6}{6} = 0$$

therefore M = 6 defines the stability criterion, or

$$M = 6 = \frac{\overline{\Delta x}^2}{\alpha \Delta t}$$

This means the dimensional increment is not independent of the time increment.

CONCLUSIONS AND RECOMMENDATIONS

A set of finite difference equations has been written which will allow one to determine the temperature history for a float-zone crystal growing process in a zero-gravity environment. It was shown that these equations result to the general heat conduction equation in cylindrical coordinates with radial symmetry. To further this work the algebratic equations should be solved by use of

computers. It is believed this work will offer some insight to

the complicated thermal process which takes place in a crystal

growing apparatus.

REFERENCES

1. Carruthers, J.R., and Grasso, M., "Studies of Floating Liquid Zones in Simulated Zero Gravity," Journal of Applied Physics, Vol. 43, No. 2, February 1972.

2. Carslaw, H.S., and Jaeger, J.C., Conduction of Heat in Solids, 1959, Oxford University Press.

3. Dusinberre, M.G., Heat Transfer Calculations by Finite Differences, 1961, International Textbook Company.

4. "Float-Zone Processing in a Weightless Environment," Bi-Monthly Progress Report, March 1974.

5. Heywang, W., Z. Naturforsch., 11a, 238(1956).

6. Heywang, W., and Ziegler, G., Z. Naturforsch., 9a, 561(1954).

1974

ASEE-NASA SUMMER FACULTY FELLOWSHIP PROGRAM

MARSHALL SPACE FLIGHT CENTER

(AUBURN UNIVERSITY - UNIVERSITY OF ALABAMA)

NATURAL NEUTRALIZATION OF A
CHARGED SPACECRAFT IN THE IONOSPHERE

Prepared by:	W. Barlow Newbolt, Ph.D.
Academic Rank:	Professor of Physics
Department and University:	Department of Physics Washington and Lee University
NASA Assignment:	Program Development, Payload Studies Office, Space Physics Group
NASA Colleague:	James O. Ballance
Date:	August 9, 1974
Contract No.:	NGT-01-003-045

NATURAL NEUTRALIZATION OF A
CHARGED SPACECRAFT IN THE IONOSPHERE

By

W. Barlow Newbolt

ABSTRACT

As a part of the AMPS program there are plans to fly an accelerator and an ion ejector on a spacelab pallet, for magnetospheric and plasma physics experiments.

In this paper a simple model is proposed for the neutralization of a spacecraft which emits a pulse of ion or electron current from an on-board accelerator.

From these calculations it appears that any spacecraft which can present a large area ($800m^2$) normal to the magnetic field direction can be neutralized naturally by the electron currents which exist in the ionosphere.

ACKNOWLEDGEMENTS

The author wishes to thank the staff of the NASA/ASEE Summer

Program for providing this summer opportunity for research in the

space program. In particular, thanks are due to Fred O'Brien and

Charles Jones.

The author has enjoyed his summer in the Space Physics Group

where he joined in stimulating discussions of everything from politics

to the space program.

Finally, the author would like to thank Mr. Jim Ballance who

served as his research counterpart in spite of a heavy schedule of

other duties, and Mrs. Smartt who typed this paper.

Whatever errors persist in this paper are the author's.

SYMBOLS AND CONSTANTS

In these calculations I have used the following constants.

Electron charge = $e = 1.6 \times 10^{-19}$ coul

Electron mass = $m = 9.1 \times 10^{-31}$ kg.

Plank's constant = $h = 6.6 \times 10^{-34}$ j-sec.

Boltzmann's Constant = $k = 1.38 \times 10^{-23}$ j/°K

Electron Density = $N_o = 1.0 \times 10^{4}$ electrons/m³

$$\frac{1}{4\pi\epsilon_o} = 9 \times 10^{9} \text{ MKS units}$$

INTRODUCTION

If a spacecraft with an on-board electron or ion accelerator existed in a complete vacuum, and emitted a beam on the order of an ampere, the potential of the spacecraft would become so great that the beam would be cut off in a time which is short in comparison with the proposed length for beam pulses.

Fortunately, the spacecraft does not exist in a vacuum, but is in the ionosphere. Because of the charge carriers in this medium, a current will flow in the region around the spacecraft and this current will help to neutralize the craft. The ionosphere is a complex medium made up of free electrons, positive ions, negative ions, and neutral atoms and molecules. Each of the charged particles has a trajectory which is determined by its thermal velocity and the local electric and magnetic fields.

The simplest interesting question one can ask about this situation is: If our spacecraft emits pulses of electron current of about 1.0 amperes for a time of about 10 milliseconds, will the current which flows to the spacecraft be sufficient to neutralize it? If the current to the spacecraft is not sufficient to neutralize it, it may be necessary to

attach some sort of collector to the spacecraft but these are expensive, cumbersome, and may be quite unnecessary.

I. Spacecraft in a Vacuum

It is easy to show that neutralization of the spacecraft is necessary for the success of the experiment. A spherical craft made of conducting material has a capacitance of $4\pi\varepsilon_0 R_p$ in a vacuum. If we use a spherical craft with a radius of 3 meters we have a capacitance

$$C = 4\pi\varepsilon_0 (3m) = 1.1 \times 10^{-10} \text{ farad}$$

The current from the accelerator will continue to flow for a time equal to the time required for the charge on the spacecraft to reach the accelerator potential. If the electron beam has an average current of 1.0 ampere it will raise the potential of the spacecraft to 15 kilovolts (the design potential for the electron accelerator) in a time, t, given by

$$t = \frac{CV}{I} = \frac{(1.1 \times 10^{-10} \text{ f})(15 \times 10^3 \text{ volts})}{1.0 \text{ amperes}}$$

$$= 1.7 \times 10^{-6} \text{ sec} = 1.7 \text{ microsec}$$

It is necessary to multiply this time by more than five thousand before a reasonable pulse time is attained (10 milliseconds). It is clear that the spacecraft must be neutralized before the experiment will be successful.

II. Neutralization of Spacecraft Due to Thermal Current

Now we return to the question posed in the Introduction: What natural neutralization current will flow to a spacecraft in the ionosphere which emits an electron current of 1.0 ampere ?

Consider a spacecraft in an isotropic distribution of plasma . We shall assume here that the electrons and ions are in thermal equilibrium at 2500°K. (Reference 2) We shall further assume that the neutralization current is entirely due to the electrons because the ions have much smaller thermal velocities. Collection of electrons near the surface will be aided by electric fields in the plasma sheath. It will be assumed that all the electrons which reach the surface are collected.

The average speed of a Maxwell-Boltzmann distribution of electrons is easy to calculate. (Reference 4)

$$\bar{v} = \frac{\int_0^\infty e^{-\frac{mv^2}{2kT}} v^3 \, dv}{\int_0^\infty e^{-\frac{mv^2}{2kT}} v^2 \, dv}$$

$$\bar{v} = \sqrt{\frac{8kT}{\pi m}}$$

This results in an average speed of approximately 3×10^5 m/sec. Since the typical spacecraft velocities are only 3% of the average

thermal velocity of the electrons, it seems safe to neglect the space-craft's orbital motion as a first approximation. For this part of the calculation the effects of the earth's magnetic field will be neglected.

Consider an element of the plasma at a distance, R, from the spacecraft. If N_o is the electron density, and Rp the radius of the spacecraft, $d\varphi$ is the amount of charge in a spherical shell of charge centered on the spacecraft.

$$d\varphi = e \, N_o \, 4\pi R^2 \, dR$$

We shall assume that all the electrons have the average speed calculated above, and that collisions are infrequent enough to be neglected. The solid angle subtended by the craft, $d\Omega$, is just the ratio of its area to the total area of a sphere of radius R. Now, the total charge, dq, collected by the craft from the element of charge at a distance R is

$$dq = d\varphi \, d\Omega = e \, N_o \, 4\pi R^2 \, dR \cdot \frac{\pi R_p^2}{4\pi R^2}$$

$$dq = e \, N_o \, \pi R_p^2 \, dR$$

If we are to determine the currents it will be necessary to realize that the radial distance of the charge element from the spacecraft is related to the time at which it arrives by the equation:

$$R = (3 \times 10^5 \, m/sec) \, t$$

$$dR = (3 \times 10^5 \, m/sec) \, dt$$

If we substitute this value for dR into the expression for the charge delivered to the spacecraft, we get

$$d q = e \, N_\infty \, \pi \, R_p^2 \, (3 \times 10^5 \, m/sec) \, dt$$

and the current collected by the spacecraft is

$$I = \frac{dq}{dt} = e \, N_\infty \pi \, R_p^2 \, (3 \times 10^5 \, m/sec)$$

If thermal motion of the electrons is the only source of neutralization current, we can calculate the effective radius of the spacecraft which is necessary to neutralize it with thermal electrons.

$$R_p = \sqrt{\frac{I}{e \, N_\infty \pi \, (3 \times 10^5 \, m/sec)}}$$

The result is:

$$R_p = 8.4 \, meters$$

for the effective radius of the craft. What is really important, however, is not the radius, Rp, but the collection area. These conclusions would apply to any simple shape with an area of:

$$A = \pi R_p^2 = 220 \text{ m}^2$$

It is important to note that this current does not violate the neutrality of the plasma. Because we are removing electrons at one point (the surface of the spacecraft) they will flow in toward the surface from the surrounding plasma. Violation of neutrality would require large fields and large amounts of energy.

III. Influence of Electrostatic Field Near the Spacecraft on the Neutralization Current

It appears that, in the case of a spacecraft with a collector area of 220 m² or larger, the emission of an ampere of electron current would not build up an appreciable potential on the spacecraft. If, however, the craft has a smaller area than this, a potential will build up on it.

We might suppose that the electric fields set up by this charging would be an important factor in increasing the neutralization current, but this does not seem to be the case. The reason is not hard to find. The ionosphere is a tenuous medium and we have to depend on current

from a large volume for neutralization. Throughout most of this

volume the electric fields are not influential because the plasma

sheath forms an electrostatic shield around the spacecraft. Electro-

static effects of the craft are shielded out in one DeBye length. The

DeBye scattering length is one of the quantities which determines the

properties of a plasma. It is given by:

$$\lambda_D = \sqrt{\frac{kT\,(4\pi\epsilon_o)}{e^2\,N_\infty\,4\pi}}$$

For a plasma in thermal equilibrium at 2500°K we find that:

$$\lambda_D = 1.1 \text{ cm}$$

The only charges collected by the charged spacecraft which would

not be collected if the craft were not charged, are those whose thermal

velocity would carry them within one centimeter of its surface. This

small change in the effective area of the spacecraft makes a negligible

change in the thermal current.

IV. Neutralization of a Spacecraft During Emission of an Ion Beam

If our spacecraft emits a positive beam natural neutralization due

to the motion of the ions will not be possible. An estimate of the

current due to thermal motion and the current due to the orbital motion

of the spacecraft yields only .04 amperes. Basically, this is because

of the lower mobility of the massive ions. (Reference 2)

It appears that this will not eliminate the possibility of thermal

neutralization because the photoelectric effect can provide conduction

electrons at the surface of the craft. If the surface of the craft is a

metal with a reasonable work function (4 electron volts) we can

estimate that all solar electrons with a frequency above 1.0×10^{15} hz

can produce photoelectrons, and if one-third of the total solar radiation

is absorbed at altitudes above our spacecraft, we are left with

1.0×10^3 watts/m^2 (Reference 6) of radiation on the spacecraft.

Approximately one-third of this is above the photoelectric threshold

so 3.3×10^2 watts/m^2 may produce photoelectrons. Assume that

the average frequency of the active radiation be 5×10^{15} hz and that

the photoelectric yield is 10^{-3} (Reference 6).

The current produced by an area of 220 m^2 may be calculated

with the formula:

$$I = \frac{(10^{-3})e \; (3.3 \times 10^2 \; watts/m^2)A}{h \; (5 \times 10^{15} \; hz)}$$

The result is: I = 3.5 amperes. This is a sufficient supply of charge

carriers for neutralization.

V.   Neutralization in the Earth's Magnetic Field

Let us consider a spacecraft in the earth's magnetic field. If the field does not vary greatly over the dimensions of the collection sphere, we may calculate the electron current to a positively charged craft in a manner similar to that of Part II.

What is important for this case is not the total speed of the electron but the component along the magnetic field line. If we use the Maxwell-Boltzmann distribution and let $\overline{v_{z_+}}$ represent the average of the velocities along the positive z- axis

$$\overline{v_{z_+}} = \frac{\int_0^\infty e^{-\frac{m v_z^2}{2kT}} v_z \, dv_z}{\int_{-\infty}^\infty e^{-\frac{m v_z^2}{2kT}} dv_z}$$

$$= \sqrt{\frac{kT}{2\pi m}} = 7.5 \times 10^4 \, m/sec$$

In a similar way we can calculate the average along the negative axis and obtain

$$v_{z_-} = -\sqrt{\frac{kT}{2\pi m}} = -7.5 \times 10^4 \, m/sec$$

The reason the component of the speed along the magnetic field is the important one is that the spacecraft will now collect electrons that spiral along the magnetic field lines toward the craft from the z- direction and the negative z-direction. The z-axis is chosen

to be along the direction of the field. Mobility of electrons normal to

the field is greatly reduced.

Now, we can calculate the charge dq transferred to the craft due

to elements of charge from the positive $\hat{z}$-direction and the negative

$\hat{z}$ - direction.

$$dq = e \, N_\infty \, A \, (7.5 \times 10^4 \, m/sec) \, dt$$

If the current, dq/dt, is to be an ampere, then we calculate an area

of 830m^2. Now there is a further requirement - only the component

of area normal to the field collects current. A rough approximation

indicates that when the Shuttle orbiter is oriented to have its largest

collecting area normal to the field, its area is about 500m^2 on the top

and 500m^2 on the bottom for a total area of 1000m^2 which is clearly

sufficient to collect a neutralization current. In other orientations

with respect to the field the collection area might be insufficient.

CONCLUSION

This is a rough calculation, but it does seem fair to conclude

that in the most favorable orientation the Shuttle will collect enough

current to neutralize itself when an on-board accelerator emits a

1.0 ampere beam of electrons or positive ions. In the case of the

positive ions a key role is played by the photoelectrons emitted by the orbiter. In other cases it may be necessary to deploy a collector normal to the field lines to increase the effective collection area.

At present a further study of this problem is beginning. It will be a numerical calculation of the neutralization and will include the effects of collisions and the detailed orbits of particles in the geo-magnetic field.

REFERENCES

1. Bernstein and Rabinowitz, Physics of Fluids, 2, 112 (1959).

2. Lui, Space Science Reviews, 9, 423 (1969).

3. Clemmow and Dougherty, Electrodynamics of Particles and Plasmas, Addison-Wesley, (1969).

4. Glasstone, Theoretical Chemistry, Van Nostrand (1944).

5. Jackson, Classical Electrodynamics, Wiley, (1966).

6. Condon and Odishaw, Handbook of Physics, McGraw-Hill, (1958).

1974

ASEE - NASA SUMMER FACULTY FELLOWSHIP PROGRAM

MARSHALL SPACE FLIGHT CENTER

(AUBURN UNIVERSITY - UNIVERSITY OF ALABAMA)

COMPUTER PROGRAM FOR
PRELIMINARY DESIGN OF CRYOGENIC PROPELLANT
PRESSURIZATION SYSTEMS FOR SPACE VEHICLES

Prepared by: James O. Nichols

Academic Rank: Associate Professor

Department and University: Department of Aerospace Engineering
                                    Auburn University

NASA/MSFC Assignment:
    (Laboratory)   Preliminary Design Office
    (Division)   Subsystems Design Division
    (Branch)   Propulsion Systems Branch

NASA Research Colleaque: James L. Sanders

Date: August 9, 1974

Contract No. :   NGT-01-003-045

COMPUTER PROGRAM FOR

PRELIMINARY DESIGN OF CRYOGENIC PROPELLANT

PRESSURIZATION SYSTEMS FOR SPACE VEHICLES

BY

James O. Nichols

ABSTRACT

A procedure has been devised for the preliminary design of pressurization systems for space vehicles using cryogenic propellants on multiburn missions. The method is not expected to yield final design requirements but to provide a method for rapid evaluation of proposed systems and for feasibility studies.

Transient conditions are not considered. It is assumed that each coast phase of the mission will be of sufficient duration that equilibrium saturation conditions will be established. Each engine burn period will be short compared to the total mission time, and the pressurant required for expulsion is determined by a semiempirical equation developed by Epstein and Anderson. Stratification of the propellant is neglected because of the absence of gravitational effects during coast periods and the short duration of burn periods.

The design procedure allows pressurization with propellant vapor or by some inert gas such as helium or nitrogen.

A computer program has been written in basic FORTRAN language which greatly facilitates the design procedure. A small digital computer (SDS 930) has sufficient capability to perform the necessary computations. Equations for thermodynamic properties are formulated for saturated liquids and vapors and for gases. These equations are used in subroutines of the program.

ACKNOWLEDGEMENTS

I want to take this opportunity to express my appreciation to NASA and ASEE for providing this Summer Faculty Research Program and for having selected me as a participant.

I also wish to say that it has been a pleasure to have been associated with the people of the Propulsion Systems Branch of the Preliminary Design Office at Marshall Space Flight Center. A special thanks to my NASA colleague Jim Sanders.

I am also indebted to Charles Haupt, a co-op student from Purdue University, for his help in running the computer, punching cards, finding thermodynamic property data, and curve fitting. Thanks also to Linda Moffett and Jennifer Stewart for typing this report.

LIST OF FIGURES

LIST OF TABLES

NOMENCLARTURE

Computer Code Symbol — **Definition**

Symbol	Definition
A, B	Functions of tank pressure used to calculate density in SUBROUTINE PRESS.
AC	Acceleration of vehicle (ft/sec^2).
AL	Length of propellant line (ft).
ALAM	Heat of vaporization (Btu/lbm).
A1, B1	Functions of tank pressure used to calculate thermal conductivity in SUBROUTINE PRESS.
BARMP	Molecular weight.
BETA	Coefficient of thermal expansion (1/^{o}R).
C, S, Q, DENOM	Factors in equation for pressurant mass ratio.
CP	Specific heat at constant pressure (Btu/lbm-^{o}R).
CPG	Specific heat at constant pressure based on mean temperature TM (Btu/lbm-^{o}R).
D	Diameter of propellant lines (ft).
DELM	Propellant mass evaporated (lbm).
DELPA	Pressure increase due to acceleration (psi).
DELPF	Pressure drop due to line friction (psi).
DELPV	Change in vapor pressure (psi).
DELVU	Change in ullage volume (ft^3).
DT	Equivalent cylindrical tank diameter (ft).
ETL	Equivalent length to diameter ratio of propellant line.
F	Engine thrust (lb).
FR	Friction factor.
GAMMA	Ratio of specific heats.
GK	Thermal conductivity (Btu/sec-ft-^{o}R).
HC	Heat transfer coefficient (Btu/sec-ft^2-^{o}R).
HI	Distance from liquid-gas interface to engine pump inlet (ft).
I	Integer used to indicate type of propellant. (1=oxygen, 2=hydrogen, 4=nitrogen, 5=fluorine.)
IPRS	Integer used to indicate type of pressurant. (1=oxygen, 2=hydrogen, 3=helium, 4=nitrogen, 5=fluorine.)
K, M, N	Integers used as counters.
MT	Integer used to indicate type of propellant tank material.
P	Partial pressure of propellant vapor (psia).
PG	Partial pressure of pressurant gas (psia).
PT	Tank pressure required for expulsion (psia).

PTC	Tank pressure after pressurant collapse (psia).
PTI	Tank pressure after coast period (psia).
PTIN	Initial tank pressure (psia).
PV	Saturated vapor pressure (psia).
PV1	Saturated vapor pressure at TS=TS+.1 (psia).
PVENT	Vent pressure (psia).
QDOT	Heat flux into propellant tank (Btu/ft^2-hr).
QT	Heat transferred from pressurant to propellant (Btu).
Q1	Heat input from surroundings (Btu).
Q2	Heat absorbed by propellant (Btu).
RATIO	Ratio of pressurant mass required for expulsion to ideal pressurant mass required.
RHO	Density of saturated liquid propellant (lbm/ft^3).
RHOC	Product of propellant tank density and specific heat at inlet temperature (Btu/ft^3-^oR)
RHOG	Density of pressurant gas at mean temperature TM (lbm/ft^3).
RHOP	Density of pressurant gas (lbm/ft^3).
RHO1	Density of pressurant gas used as a reference (lbm/ft^3).
RN	Reynolds number
R1, R2, R3	Factors in equation for pressurant mass ratio.
SUMBO	Mass of propellant lost due to boiloff (lbm).
SUMDM	Mass of propellant vaporized (lbm).
SUMZM	Mass of pressurant required (lbm).
TC	Coast phase duration (hr).
TF	Engine burn duration (sec).
TI	Inlet pressurant temperature (^oR).
TS	Saturation temperature of propellant (^oR).
TW	Thickness of propellant tank wall (ft).
U	Internal energy of liquid propellant (Btu/lbm).
UP	Internal energy of pressurant gas (Btu/lbm).
U1	Internal energy of liquid propellant used as a reference (Btu/lbm).
U2	Internal energy of pressurant gas used as a reference (Btu/lbm).
VLP	Velocity of liquid propellant in line (ft/sec).
VMASS	Total mass of vehicle (lbm).
VT	Volume of propellant tank (ft^3).
VU	Propellant tank ullage volume in fraction of total tank volume.

W	Mass of propellant used during engine burn (lbm).
WD	Oxidizer or fuel flow rate (lbm/sec).
WI	Mass of propellant in tank (lbm).
WDOT	Propellant flow rate (lbm/sec).
XISP	Specific impulse (sec).
XM	Oxidizer to fuel ratio.
XMU	Propellant viscosity (lbm/ft-sec).
XMUG	Pressurant gas viscosity (lbm/ft-sec).
XNPSP	Net position suction pressure (psia).
YMI	Mass of pressurant required for each prepress (lbm).
ZMI	Ideal mass of pressurant required for expulsion (lbm).
ZM	Mass of pressurant required for expulsion (lbm).
ZP	Pressurant compressibility factor.

INTRODUCTION

A procedure has been devised for the preliminary design of pressurization systems for space vehicles using cryogenic propellants on multi-burn missions (Ref. 1). The procedure, which allows pressurization with propellant vapor or by some inert gas such as helium or nitrogen, is not expected to yield final design requirements but to provide a method for rapid evaluation of proposed systems and for feasibility studies.

Because of numerous iterations use of a digital computer is required to reduce the computation time. A computer program has been written in basic FORTRAN language which greatly facilitates the design procedure. A small digital computer such as the one used in the development of this program, the SDS 930, has sufficient capability to perform the necessary computations. Equations for thermodynamic properties of saturated liquids and vapors and for gases have been formulated by curve fit of graphical and tabulated data where formulae were not available.

Transient conditions are not considered in the analysis. It is assumed that each coast period of the mission will be of sufficient duration that equilibrium saturation conditions will be established. Stratification of the propellant is also neglected because of the absence of gravitational effects during coast periods and because of short duration of burn periods.

The procedure in general applies to any cryogenic propellant; however, the expulsion equation (Ref. 2) was obtained by a curve fit of over 125 points calculated using a generalized pressurization computer program (Ref. 3). The pressurants and propellants for which the equation is valid are listed in Table 1. The range of variables used in the calculations are listed in Table 2.

Caution should be exercised when using the procedure for conditions other than those listed in Tables 1 and 2.

TABLE 1
APPLICABLE FLUIDS

Pressurant	Propellant
H_2, H_e	H_2
O_2, N_2, H_e	O_2
N_2, H_e	H_2
F_2, H_e	F_2

TABLE 2
RANGE OF VARIABLES

Variable	Range
Spherical Tank Diameter	5-30 ft
Ellipsoidal Tank Diameter	5-30 ft
Cylindrical Tank Diameter	4-35 ft
Wall Thickness	0.1-1 in.
Ratio of Pressurant Inlet Temperature to Propellant Saturation Temperature	2-15
Total Outflow Time	200-500 sec.
Ambient Heat Flow	0-10,000 Btu/ft^2-Hr.

PROGRAM DESCRIPTION

The main computer program contains all the necessary computations to determine the mass of pressurant required for prepress and expulsion of the propellant. The amount of propellant vaporized or condensed during coast periods and the amount of propellant boiled off due to heat addition are also calculated. The term "boiloff" is used herein to refer to propellant vented overboard. Vaporized propellant remains in the tanks. It is assumed that when venting takes place only propellant vapor is vented. No pressurant nor liquid propellant is lost. This tends to overestimate the loss of propellant, if some means can be provided to prevent loss of liquid propellant, since some pressurant would be included in the vent gas.

All thermodynamic properties, heat transfer coefficients, and transport properties are computed in subroutines. This facilitates updating the program to include additional fluids and improving the equations as new data becomes available. A typical subroutine flow chart is shown in Figure 2. At present only oxygen, hydrogen and helium properties have been programmed. Properties of nitrogen and fluorine will be added later.

The main program can be broken down into seven principal divisions. Output is provided at the end of each division 2 through 7. A detailed discussion of each division follows and the flow chart is shown in Figure 1.

1. Input Data.
   Input data is grouped into four catagories:
   a. Vehicle data which contains pertinent dimensions such as tank diameter, tank wall thickness, etc.
   b. Propellant and pressurant data.
   c. Engine data such as thrust, specific impulse, etc.
   d. Mission data such as burn time, heat input, and coast time.

Table 3 describes the input data in detail.
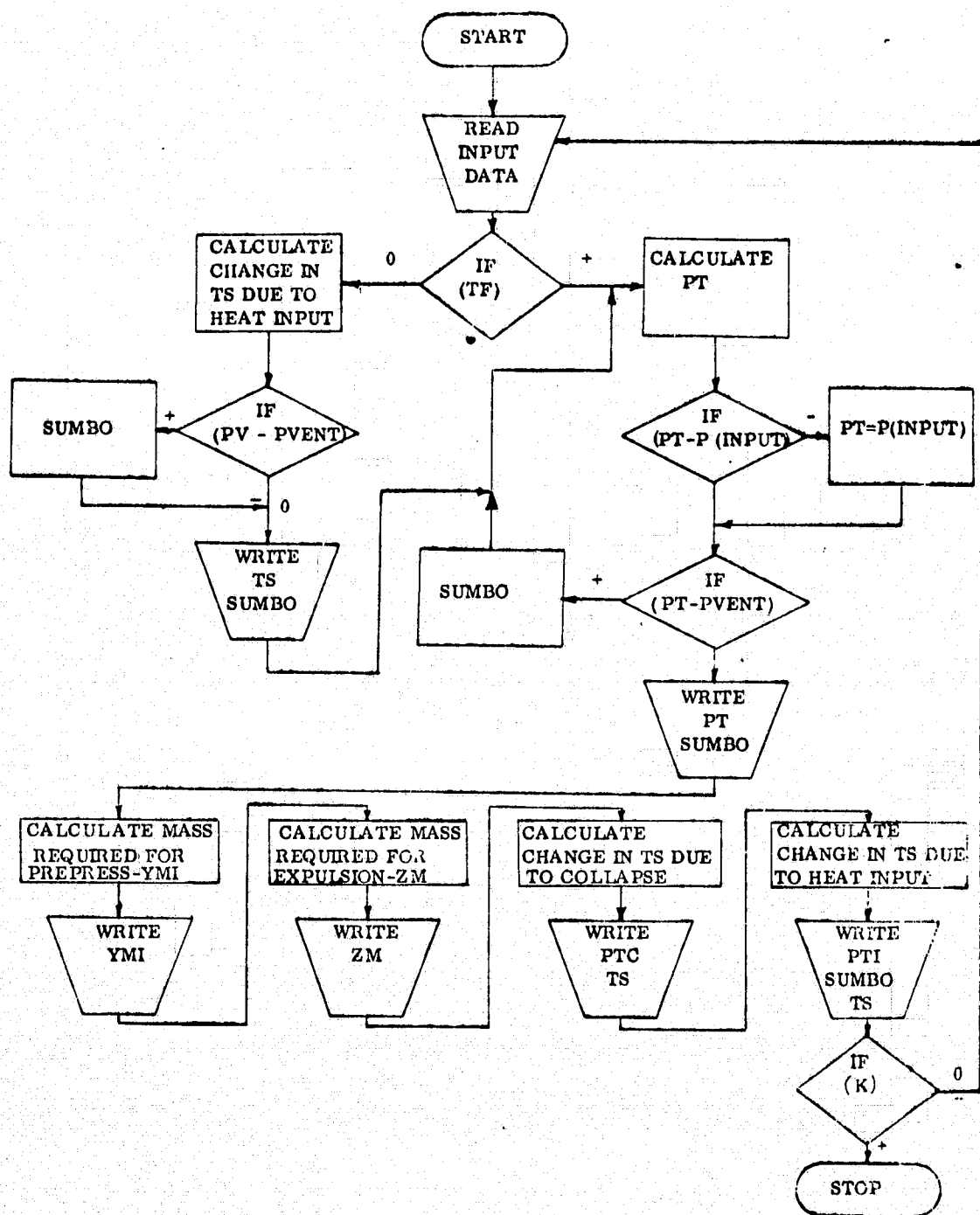
FIGURE 1. MAIN PROGRAM FLOW CHART
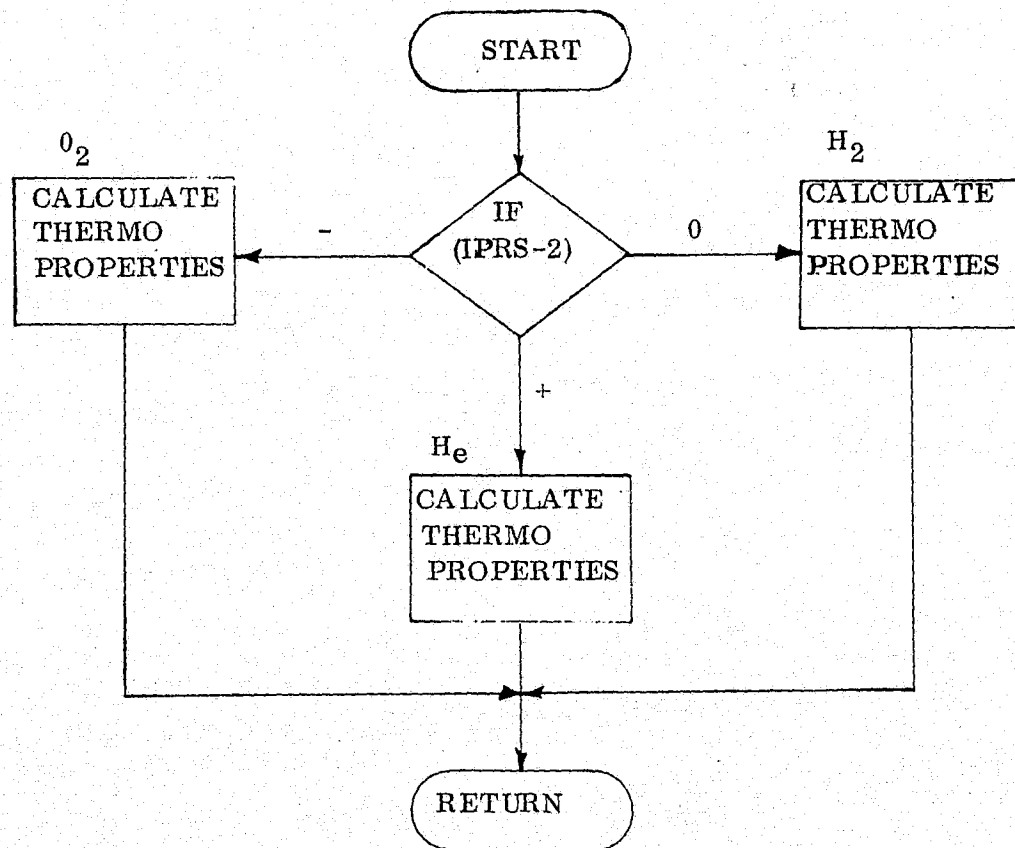
FIGURE 2. TYPICAL SUBROUTINE FLOW CHART

2. Initial Coast.

During an initial coast period heat input to the propellant tanks will cause an increase in saturation temperature and a corresponding rise in vapor pressure. If the vapor pressure exceeds the vent pressure propellant will boil off. This part of the program assumes that the heat input is absorbed in vaporizing part of the propellant and by increasing the internal energy of the liquid propellant. If the vapor pressure reaches vent pressure before all of the heat is absorbed the remaining heat boils off propellant at a constant pressure and at constant saturation conditions.

3. Tank Pressure Required for Expulsion.

The tank pressure required for expulsion is calculated. It is a function of NPSP, vapor pressure, acceleration head and pipe friction losses. There is also the option to specify tank pressure and/or vent pressure in the input data. If the calculated tank pressure is less than the specified tank pressure, the pressure used for expulsion will be the specified tank pressure. If the calculated pressure exceeds the vent pressure boil off of the propellant will occur to reduce the saturation conditions to the point that the calculated pressure will be below the vent pressure.

4. Prepress Pressurant Required.

If the initial pressure in the propellant tank is less than the pressure used for expulsion, pressurant will be used to raise the pressure. This calculation is based on an adiabatic compression of the pressurant gas and then corrected by emperical constants based on experimental data (Ref. 4). For ullage volumes less than 20 percent the pressurant mass requirement was increased by 50 percent, for volumes less than 40 percent but greater than 20 percent the pressurant increase was 20 percent, and 10 percent increase for ullage volumes over 40 percent.

5. Expulsion Pressurant Required.

The equation used to calculate the mass of pressurant required for expulsion has already been discussed in the Introduction.

6. Pressurant Collapse After Engine Cut-Off.

At engine cut-off the propellant tanks will be closed with a mass of high temperature pressurant gas above a cold propellant. As heat flows from the gas to the propellant the pressure will drop; however, since the propellant is at its saturation condition, the heat flow into the propellant will vaporize some of the propellant, tending to increase the pressure. As the vapor pressure increases the saturation temperature increases allowing the propellant to absorb some of the heat. An iteration scheme is used which

allows the difference in the heat given up by the gas and that absorbed by the propellant to be used in evaporating part of the propellant. The pressure is calculated and compared with the vapor pressure corresponding to the temperature. The iteration is continued until the pressure agrees with the vapor pressure. Since a gas other than the propellant vapor may be used as the pressurant, the partial pressure of the propellant vapor is the pressure calculated and required to match the vapor pressure. Condensation of propellant vapor may occur in order to establish equilibrium saturation conditions.

7. <u>Pressure Rise Due to Heat Addition During Coast</u>.
Even though the pressurant collapse and pressure rise due to heat addition are occuring at the same time they are separated here in order to keep the computations tractable.

The procedure is the same as for the initial coast period except that partial pressures are used to account for pressurant gases other than propellant vapor. This computation also sets the initial pressure to be used in steps 3 and 4. If the tank pressure rises above the vent pressure boil off will occur.

TABLE 3
INPUT DATA CARDS

Computer
Symbol   Definition

                                Vehicle, propellant, and pressurant data.

                                Card 1

HI (1)   Distance from liquid-gas interface of oxidizer to engine
                                pump inlet (ft). May be entered as 0.0 if not known.
                                This will cause acceleration pressure to be zero.

D (1)   Diameter of oxidizer line (ft). May be entered as 0.0
                                if not known. This will cause pressure drop due to
                                friction to be zero.

AL (1)   Length of oxidizer line (ft). May be entered as 0.0 if
                                D (1) = 0.0.

16-14

TABLE 3 (CONTINUED)

Computer Symbol	Definition
ETL (1)	Equivalent length to diameter ratio of oxidizer line for losses due to bends (=10.) , valves (=2.5), and disconnects (=20.). May be entered as 0.0 if D (1) = 0.0.
TW (1)	Thickness of oxidizer tank wall (ft).
DT (1)	Diameter of equivalent cylindrical oxidizer tank (ft). DT is equal to 2/3 the actual diameter for a spherical tank.
MT (1)	Control to designate type of oxidizer tank material. Use 1 for steel or 2 for aluminum. Use 0 for other material and input RHOC.

Card 2

I (1)	Control to designate type of oxidizer. Use 1 for oxygen, 5 for fluorine.
IPRS (1)	Control to designate type of pressurant. Use 1 for oxygen, 3 for helium, 4 for nitrogen, 5 for fluorine.
TS (1)	Saturation temperature of liquid oxidizer (^{O}R).
VU (1)	Oxidizer tank ullage volume in fraction of total tank volume.
TI (1)	Oxidizer tank inlet pressurant temperature (^{O}R).
VT (1)	Oxidizer tank volume (ft^3).
WI (1)	Mass of oxidizer in tank (lbm).
PT (1)	Oxidizer tank pressure required for expulsion (psia). Enter as 0.0 if tank pressure is to be determined.
RHOC (1)	Product of oxidizer tank density and specific heat at inlet temperature TI (Btu/ft^3-^{O}R).

TABLE 3 (CONTINUED)

Computer Symbol	Definition

Card 3

PVENT (1)   Oxidizer tank vent pressure (psia). Enter a high value if no venting is to occur or if PT is to be determined. Use a value slightly higher than PT if PT is specified.

Card 4, 5, and 6

Cards 4, 5, and 6 contain the same variables as cards 1, 2, and 3, respectively. Only the subscript changes; a 2 is used to indicate reference to the fuel system where a 1 indicated the oxidizer system on cards 1, 2, and 3.

Engine and Mission Data

Card 7

XNPSP (1)   Net positive suction pressure required at the engine pump oxidizer inlet (psia).

XNPSP (2)   Net positive suction pressure required at the engine pump fuel inlet (psia).

F   Engine thrust (lb).

XISP   Specific impulse (sec).

XM   Oxidizer to fuel mixture ratio.

VMASS   Total mass of vehicle (lbm).

Card 8, 9, etc.

TF   Engine burn duration (sec). Enter 0. 0 if there is an initial coast period.

QDOT (1)   Heat flux into oxidizer (Btu/ft^2-hr).

TABLE 3 (CONTINUED)

Computer Symbol	Definition
TC	Coast phase duration (hr).
K	(Control to indicate end of data. Enter 0 except on last data card, enter 1 on it.

PROGRAM LIMITATIONS

Some limitations on the design procedure have been mentioned and are listed in Tables 1 and 2. Further limitations on the computer program are brought about by the method in which thermodynamic properties are calculated in the subroutines .

Five subroutines have been used because different properties are needed in different segments of the program. Calculating only those properties needed at a particular point in the program reduces the computational time. Two of the subroutines, PROP and PROP 1, are for calculating properties of the saturated liquid propellant. Two, PRESS and PRESS 1, are for calculating properties of the pressurant gas at inlet temperature, and one, PRESS 2, calculates properties of the pressurant gas at the saturation temperature of the propellant.

Both oxygen and hydrogen vapor are considered to be real gases with the compressibility factor of the saturated vapor being calculated in subroutine PRESS 2. Helium, however, is not used near its saturation temperature and is assumed to be a perfect gas. This introduces an error of less than 5 percent in calculating pressurant density except near the hydrogen saturated vapor temperature (40° - 60°R) where the error is about 7 percent based on data from Reference 5.

The properties of oxygen were obtained from Reference 6 and were the ones most completely documented. The properties of hydrogen and helium were obtained from several sources (Refs. 7, 8, 9, 10 and 11) and were generally presented in graphical form which has less accuracy than the tabulated data of Reference 6 for oxygen. The internal energy of hydrogen and helium were not found in any of the references; however, the enthalpy of hydrogen (Ref. 8) was used to calculate its internal energy. The internal energy of helium was calculated by multiplying the specific heat at constant volume (Ref. 9) by the temperature.

Equations for the properties of saturated liquids and vapors were obtained by a nonlinear curve fit program based on Article 169 of Reference 12. The properties were expressed as functions of saturation temperature. For gases the properties are functions of both pressure and temperature. In some cases the dependence on pressure is very weak such as the viscosity of oxygen. In these cases the pressure dependence is neglected and a curve fit at a pressure of 30 psia was used. The pressure range over which the equations are valid is generally 14.7 to 50 psia.

For cases where the pressure dependence could not be neglected the isobaric curves were assumed to be linear on a log-log plot. This lead to an expression of the form

$$P = \left(\frac{A}{T}\right)^B$$

where P represents a fluid property, A and B are functions of pressure, and T is absolute temperature. A and B are assumed to be linear functions of pressure. B is the slope of log P vs log T. Once B is measured, A can be determined for given P and T. A plot of B vs pressure and A vs pressure can be fitted by a straight line giving A and B as linear functions of pressure.

Table 4 is a summary of the equations that were obtained by using the nonlinear curve fit program. Included in the Table are the data source reference, root mean square deviation, maximum percentage error, the subroutine in which the equation is used, and the range of pressure and temperature for which the equation is used, and the range of pressure and temperature for which the equation is valid. Table 5 presents the same information, except for the root mean square deviation, for the equations which were based on the linear assumption.

Equations for the volumetric heat capacity of stainless steel and aluminum tanks were also obtained by the nonlinear curve fit program with data from Reference 13. The ratio of specific heats, GAMMA, was consided constant for all gases. Equations for the coefficient of thermal expansion, β (BETA), were derived for gaseous hydrogen and helium based on the defintion

$$\beta = \frac{1}{\rho} \left(\frac{\partial \rho}{\partial T}\right)_P$$

where ρ is the gas density, T is temperature and sub P indicates the derivative is taken at constant pressure.

Equations were found which were valid between the triple point and critical point for the following:

1) Heat of vaporization for hydrogen (Ref. 9)
2) Vapor pressure for hydrogen (Ref. 10)
3) Density of saturated liquid hydrogen (Ref. 10)
4) Vapor pressure for oxygen (Ref. 6).

TABLE 4

SUMMARY OF EQUATIONS OBTAINED BY USING THE
NONLINEAR CURVE FIT PROGRAM

Equation	Reference	Root Mean Square Deviation	% Error	Subroutine	Pressure Range - psi	Temperature Range - ^{O}R
1. Saturated Liquid H_2 Viscosity-XMU	7	.238 E-02	9%	PROP	Saturated Vapor Pressure	25° to 60°
2. Saturated LOX Viscosity-LOX	6	.778 E-03	.01%	PROP	10 to 50	156° to 187°
3. Saturated LOX Density-RHO	6	.1429 E-02	.004%	PROP	10 to 50	156° to 187°
4. Saturated LOX Internal Energy-U	6	.14824 E-02	.02%	PROP 1	10 to 50	156° to 187°
5. Gaseous O_2 Coefficient of Thermal Expansion - Beta	6	.1916 E-04	.6%	PRESS	30 *	175° to 600°
6. Gaseous O_2 Thermal Conductivity - GK	6	.2004 E-03	3.5%	PRESS	30 *	175° to 600°
7. Gaseous H_2 Coefficients to the Thermal Conductivity - GK	7	A1:.549797 E-06 B1:.36014 E-10	0% 0%	PRESS	Both: 14.7 to 60	Both: 50° to 100°
8. Gaseous O_2 Internal Energy-UP	6	.5555	1.6%	PRESS 1	30 *	175° to 600°
9. Saturated Vapor H_2 Density-RHOP	9	.24699E-01		PRESS 2	Saturated Vapor Pressure	20° to 60°
10. Saturated Vapor O_2 Internal Energy-UP	6	.3801 E-03	.001%	PRESS 2	10 to 50	155° to 190°

TABLE 4 (Continued)

Equation	Reference	Root Mean Square Deviation	% Error	Subroutine	Pressure Range - psi	Temperature Range - $^{\circ}$R
11. Saturated Vapor O_2 Internal Energy-UP	6	.38401 E-03	.001%	PRESS 2	10 to 50	155° to 190°
12. Saturated Vapor O_2 Compressibility Factor - ZP	6	.46731 E-10	0%	PRESS 2	Saturated Vapor Pressure	180° to 270°
13. Saturated Vapor H_2 Internal Energy-UP	8	.3756 E-06	0%	PRESS 2	14.7 to 130	35° to 55°
14. Helium Thermal Conductivity-GK	9	.2522E-03	.9%	PRESS	14.7 *	0° to 500°
15. Helium Viscosity-XMUG	9	.26126 E-01	1.3%	PRESS	14.7 *	0° to 500°
16. Stainless Steel Volumetric Heat Capacity - RHOC	13	.48 (T$\leq$200°) .81 (T >200°)	8% 4%			T $\leq$ 200° T > 200°
17. Aluminum Volumetric Heat Capacity - RHOC	13	.2 (T$\leq$200°) .46 (T>200°)	7% 2.6%			T $\leq$ 200° T > 200°
18. Saturated LOX Heat or Vaporization - ALAM	6	.9482	4%	PROP 1	Saturation Vapor Pressure	160° to 275°
19. Gaseous O_2 Viscosity - XMUG	6	.3645 E-3	.07%	PRESS	30 *	175° to 600°
20. Saturated Vapor H_2 Compr. Factor - ZP	11	.35078E-02	.8%	PRESS 2	Saturated Vapor Pressure	28.8° to 54°

*Weak Function of Pressure

TABLE 5.

SUMMARY OF EQUATIONS USING LINEAR LOG-LOG CURVE

FIT PROCEDURE

Equation	Reference	Temperature Range-^{O}R	Pressure Range psi	Max Percent Error	Subroutine	Remarks
Saturated Liquid H_2 Internal Energy-U	8	36.5^O to 45°	14.7 - 45		PROP 1	Linear with TS
Gaseous O_2 Density-RHOP	6	Saturation to 500°	14.7 - 50	-4.2 %	PRESS	
Gaseous O_2 Specific Heat at Const. Press - CP	6	Saturation to 600°	14.7 - 50	1.7%	PRESS	
Gaseous H_2 Density- RHOP	7	Saturation to 100°	14.7 - 60	7%	PRESS	
Gaseous H_2 Specific Heat at Const. Press - CP	7	Saturation to 100°	14.7 - 60	8.5%	PRESS	
Gaseous H_2 Viscosity - XMUG	7	Saturation to 100°	14.7 - 60	-2.8%	PRESS	

TABLE 5 (Continued)

Equation	Reference	Temperature Range-^{O}R	Pressure Range psi	Max Percent Error	Subroutine	Remarks
Gaseous H_2 Thermal Conductivity - GK	7	Saturation to 100°	14.7 - 60	3.4	PRESS	In this case coefficients were assumed non-linear. See Table 4
Gaseous H_2 Internal Energy-UP	8	Saturation to 70°	20 - 60		PRESS 1	Derived from Enthalpy

CONCLUSIONS AND RECOMMENDATIONS

The program is still in the process of being checked out or debugged. Preliminary results are favorable and support the general concepts. A complete mission profile will be run and compared with estimates from other sources. At present no flight data is available with which to compare the results.

The accuracy of the program can be improved by obtaining more accurate data for hydrogen and helium. The range of temperatures and pressures could also be extended in some cases. The ranges were picked arbitrarily assuming that a mission would start at sea level conditions and a minimum tank pressure would be used.

Extension of the program to include nitrogen and fluorine can also be accomplished by simple changes in the appropriate subroutines.

REFERENCES

1. Nichols, J. O., Preliminary Design of Cryogenic Propellant Pressurization Systems for Space Vehicles, Final Report, ASEE-NASA Summer Faculty Fellowship Program, Marshall Space Flight Center, August 1973.

2. Epstein, M. and R. E. Anderson, An Equation for the Prediction of Cryogenic Pressurant Requirements for Axisymmetric Propellant Tanks, Advances in Cryogenic Eng., Vol. 13, Plenum Press, 1968.

3. Epstein, M., H. K. Georgius, and R. E. Anderson, A Generalized Propellant Tank-Pressurization Analysis, Advances in Cryogenic Eng., Vol. 10, Plenum Press, 1965.

4. Stochl, R. J., P. A. Masters, R. L. DeWitt, and J. E. Maloy, Gaseous-Hydrogen Pressurant Requirements for the Discharge of Liquid Hydrogen from a 3.96-Meter- (13-Ft.) Diameter Spherical Tank, NASA, Lewis Research Center, TN D-5387, August 1969.

5. Sanders, W. T., J. J. Hartl, and J. H. Dubkins, Space Shuttle Pressurization System Parametric Design Study, Brown Engineering, SMSD-PD-1112, March 1970.

6. Roder, H. M. and L. A. Weber, Editors, ASRDI Oxygen Technology Survey Volume I: Thermophysical Properties, Cryogenics Division, Institute for Basic Standards, National Bureau of Standards, Boulder, Colorado, for Aerospace Safety Research and Data Institute, NASA Lewis Research Center, NASA SP-3071, 1972.

7. Seader, J. D., W. S. Miller, and L. A. Kalvinska, Boiling Heat Transfer for Cryogenics, NASA CR-243, 1965.

8. Properties of Principal Cryogenics, Aerojet- General Corporation, Sacramento, Calif., October 1966.

9. Johnson, V. J., General Editor, A Compendium of the Properties of Materials at Low Temperature (Phase I) Part 1. Properties of Fluids, National Bureau of Standards, Cryogenic Engineering Laboratory for Wright Air Development Division, WADD Technical Report 60-56, July 1960.

10. Shaffer, A., and J. Rousseau, <u>Thermodynamic Properties of 20.4°k-Equilibrium Hydrogen,</u> AiResearch Manufacturing Company for Aeronautical Systems Division, Air Force Systems Command, Wright-Patterson Air Force Base, Ohio, ASD Technical Report 61-360, October 1961.

11. Kunkle, J. S., S. D. Wilson, and R. A. Cota, Editors, <u>Compressed Gas Handbook,</u> NASA SP-3045, 1969.

12. Scarborough, J. B., <u>Numerical Mathematical Analysis,</u> 5th Edition, The John Hopkins Press, Baltimore, Maryland, 1962.

13. <u>Pressurization Systems Design Guide, Volume I-Systems Analysis and Selection,</u> Aerojet General Corporation, Report No. 2736, Revised July 1966.

1974

ASEE-NASA SUMMER FACULTY FELLOWSHIP PROGRAM

MARSHALL SPACE FLIGHT CENTER

(AUBURN UNIVERSITY-UNIVERSITY OF ALABAMA)

HOLOGRAPHIC TECHNIQUES FOR CLOUD

CHAMBER STUDIES

Prepared by:	Ralph E. Oberly
Academic Rank:	Assistant Professor, Chairman
Department and University:	Department of Physics and Physical Science Marshall University

NASA/MSFC Assignment:
    (Laboratory)
    (Division)
    (Branch)
	Space Sciences
	Physics and Instrumentation
	Optics and Electro-optics

NASA Research Colleague:	R. L. Kurtz
Date:	August 9, 1974
Contract No:	NGT-01-003-045

HOLOGRAPHIC TECHNIQUES FOR CLOUD CHAMBER STUDIES

by

Ralph E. Oberly

Abstract

An on-board holographic system has been proposed for the Space Shuttle/Spacelab program that will be used in cloud microphysical research under zero-g conditions. The holographic system is to be used to record particle size and particle position as droplets form in a cloud chamber. This report describes work done toward mating a holographic system to a cloud chamber as an anticipatory step toward the on-board system. Holograms have been recorded and viewed for a static particle field inside a cloud chamber in order to determine the effect of the chamber windows on the quality of the holographic image. The real images from the hologram are viewed on a video monitor after being magnified by a lens system. The overall system magnification is determined to be about 350. Recommendations are included for further investigations of the one-g laboratory system using dynamic object fields.

LIST OF FIGURES

INTRODUCTION

Holography has recently received a great deal of attention in terms of its application to physical measurement problems. Three primary characteristics of this technique make it ideally suited for physical measurements. The holographic technique uses coherent light to record and reconstruct a three-dimensional image of an object field. The three-dimensional nature of the recorded images allows the investigator to record information over an extended depth of field that would be lost using conventional optical image processing. The image formation technique is extremely sensitive to motion in the object field. Object motion on the order of a few tenths of a wavelength for the light used can be easily detected in double-exposure holographic images. Using visible radiation, the technique can detect object motions of a few ten-millions of a meter. In addition, holography is a nondestructive testing technique. For moderate light power levels, the object field is undisturbed during the image formation state. The investigator then has the freedom to perform a series of tests on a given object field, or to perform a single test and record a sequence of images that show how the object field changes with time.

In view of the above characteristics, it has been proposed [1] that the holographic technique be used to investigate particle size distribution in an atmospheric simulation cloud chamber. Specifically, it is desirable to study the particle growth rate within the cloud chamber. A sequence of holographic images can nondestructively record the growth rate for a particle field of extended depth and simultaneously record the particle motion. The information stored in this sequence of images allows the investigator to measure particle size, particle size distribution, particle growth rate, particle trajectories, particle deformation, and particle velocity distribution.

The cloud chamber and holographic system are proposed for onboard use in the Space Shuttle/Spacelab program. Particle growth can then be observed under zero-g conditions. This will eliminate the net vertical force component on the particles and the motion resulting from this force. The reduced motion will allow longer observation times for individual particles. Given a sufficiently long observation time, experiments involving collisions, changes of state, and diffusional growth can be performed with individual droplets. Ultimately, the information derived from these experiments should help meteorologists to better understand atmospheric cloud formation.

The purpose of this work is to perform investigations concerning the mating of a holographic system to a cloud chamber and to record particle data with this combination. The mating operation is an anticipatory step to predict what problems could arise with the onboard flight system. The holograms recorded in this work are to demonstrate the capability of the system to detect and measure the size of test particles.

DESCRIPTION OF HOLOGRAPHIC PROCESS

Holography is basically a two-step process in which a three-dimensional object field can be recorded. In the recording step of the process two coherent wave fronts are superimposed in the same region of space and the resulting interference pattern is recorded on a suitable medium such as a photographic plate. The recorded interference pattern contains sufficient phase and amplitude information for a complete three-dimensional description of the original wave fronts, within a limited perspective determined by the size and position of the recording medium.

Figure 1 shows the recording arrangement for an in-line hologram of an object field. For this case a single collimated beam passes through the object field. If the particle density in the object field is not too dense, a portion of the incident beam traverses the object field without scattering or attenuation and travels on to the photographic plate. This part of the incident beam is called the reference beam and, in the example shown, has a planar wave front. Some of the incident beam is scattered by points in the object field, as Figure 1 shows for a single point object. The light scattered by the point object is called the object beam and approaches the photographic plate as a spherical wave front. For a more complex object field, each point that scatters light generates its own set of spherical wave fronts. The resultant object beam is then the superposition of the spherical wave fronts arising from all scattering points.

The theoretical treatment of the holographic process is well developed in the literature [1-4]; consequently, only a very brief summary will be given here. As a convenient frame of reference, consider the holographic plate to be in the x-y plane of a coordinate system. The two beams of light approaching the holographic plate can be described by their electric field components E as
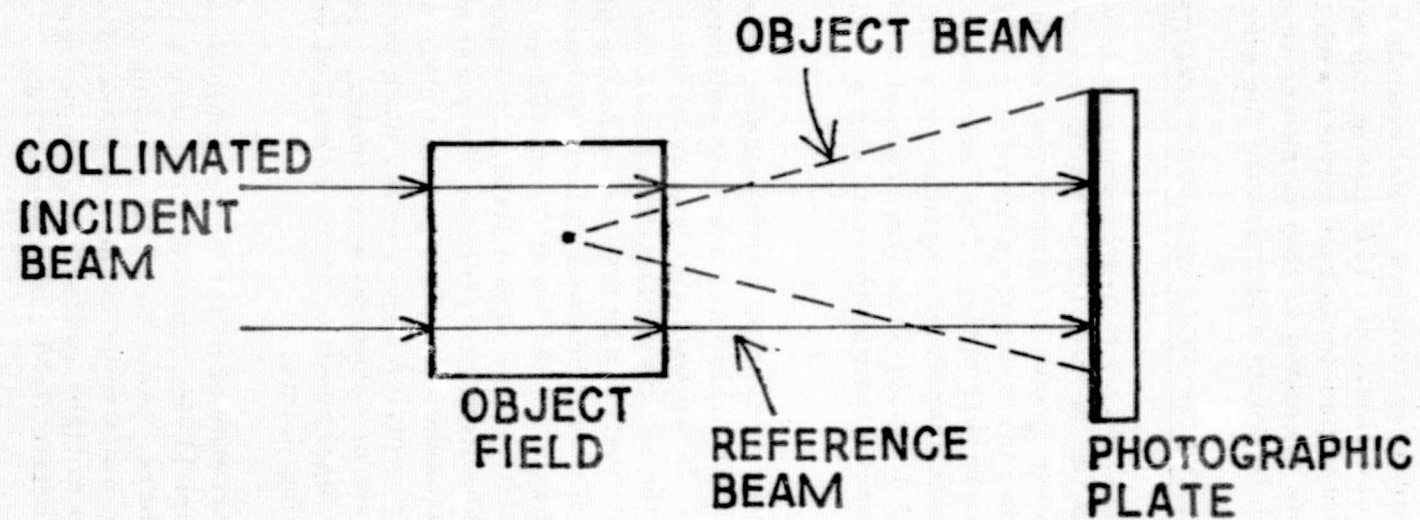
Figure 1. In-line geometry for recording a hologram.

$$E_r = a(x, y) e^{i[\alpha(x, y) - \omega t]} \tag{1}$$

$$E_o = b(x, y) e^{i[\beta(x, y) - \omega t]} \tag{2}$$

where $a(x, y)$ and $b(x, y)$ are position-dependent amplitude functions, $\alpha(x, y)$ and $\beta(x, y)$ are position-dependent phase functions, ω is the angular frequency of the light source, and t is the time. r and o refer to the reference and object beams, respectively. At each point on the holographic plate the two vectors above would be superimposed, giving a resultant amplitude equal to their vector sum. The intensity I in the x-y plane is proportional to the square of the resultant amplitude

$$I = m(E_r + E_o)(E_r^* + E_o^*) \tag{3}$$

where m is the proportionality constant and the asterisk denotes a complex conjugate operation. Upon expansion and substitution, the intensity can be shown to have the form

$$I = m\left[(b^2 + a^2) + abe^{i(\beta - \alpha)} + abe^{-i(\beta - \alpha)}\right] \tag{4}$$

where a, b, α, and β are assumed to be real functions of x and y. The photographic plate is exposed to this position-dependent intensity for a time τ, giving an exposure

$$\mathcal{E} = \int_0^\tau I dt = I\tau \ . \tag{5}$$

The exposure is assumed to be in the linear region of the density versus log (exposure) curve for the film.

Retrieval of the holographic image constitutes the useful and interesting step of the process. The exposed plate is developed by standard photographic procedures and replaced in the light path with the object field removed. The intensity and distribution of the light transmitted by the developed photographic plate is needed for the interpretation of the holographic images. Reference 1 gives an expression for the transmitted light when the reference beam during construction is virtually identical to the reconstruction beam. The result is

$$E_t = \left[ka\,(a^2 + b^2) \right] \left\{ e^{i(\alpha - \omega t)} + \frac{ab}{a^2 + b^2} \left[e^{i(\beta - \omega t)} \right. \right.$$

$$\left. \left. + e^{-i(\beta - 2\alpha + \omega t)} \right] + \text{terms of} \atop \text{higher order} \right\}$$

(6)

where E_t is the transmitted light amplitude and k is a constant. In this expression the term

$$ka\,(a^2 + b^2)\, e^{i(\alpha - \omega t)} \tag{7}$$

represents a wave front with the same geometry and direction as the reconstruction beam. However, it is attenuated by the $k(a^2 + b^2)$ factor.

The next term

$$k\,a^2\, be^{i(\beta - \omega t)} \tag{8}$$

represents a wave front having the same geometry and direction as the original object wave. It arises from selective scattering of the reconstruction beam by the interference pattern on the photographic plate. If an observer looks along the negative direction of propagation for this wave front, he sees a virtual image of the original object field attenuated by a ka^2 factor.

The third term in equation (6) is

$$k\,a^2\, be^{i(\beta - \omega t)}\, e^{2i(\alpha - \beta)} \tag{9}$$

which again resembles the original object wave. However, this term represents a converging rather than a diverging wave front, and it gives rise to an aberrated real attenuated image of the original object field. This image is located as a reflection across the plane of the holographic plate from the virtual image. The real image is used in the analysis of the cloud chamber holograms.

Figure 2 illustrates the side band geometry for recording the holograms. The reference and object beams are separated before the object field and travel along different paths before recombination to form the interference pattern at the plate. In principle the holographic image is recorded and reconstructed as in the in-line geometry. The side band geometry has the advantage of a cleaner reference beam which would be easier to reproduce during the reconstruction step. In addition, the side band geometry permits individual control over the reference and object beam intensities, which is important for good contrast holographic images. However, the image resolution is generally worse for the side band geometry because the object field is often located farther from the holographic plate. The resolution is further degraded by large angles between the reference and object beams as they approach the plate. This effect results from the limited ability of the photographic emulsion to resolve interference fringes of high spatial frequency. It is desirable to maintain a minimum angle between the two beams during the construction step.

Two additional theoretical concepts need to be mentioned, although reference is again made to the literature. First, the droplets suspended in a cloud chamber will experience some motion even in a zero-g environment. Fortunately, the velocities for large droplets are very small compared to those for atomic and molecular particles composing the atmosphere of the chamber. Also, for small particle sizes it will be necessary to magnify the particles during recording and/or reconstructing the holographic image. This can be done with holographic techniques, conventional optical techniques, or a combination of the two techniques.

Object motion considerations have been reported in references 5 and 6. The primary concern in a cloud chamber study is that the interference pattern at the holographic plate not change significantly during the exposure time τ. The interference pattern is determined for each point on the plate by the difference in optical path lengths for the reference and object beams. If this difference is zero or a whole number of wavelengths maximum intensity occurs at the point. If the difference is an odd integer multiple of a half wavelength minimum intensity occurs. If these conditions change during the exposure time the emulsion will effectively record the average intensity. A small change in optical path difference would result in a slight blurring of the holographic image. This blurring increases as the change increases until the change becomes a half wavelength for all points on the plate. Then, a uniformly exposed plate will result with no recorded information and no holographic image. Consequently, it is desirable to
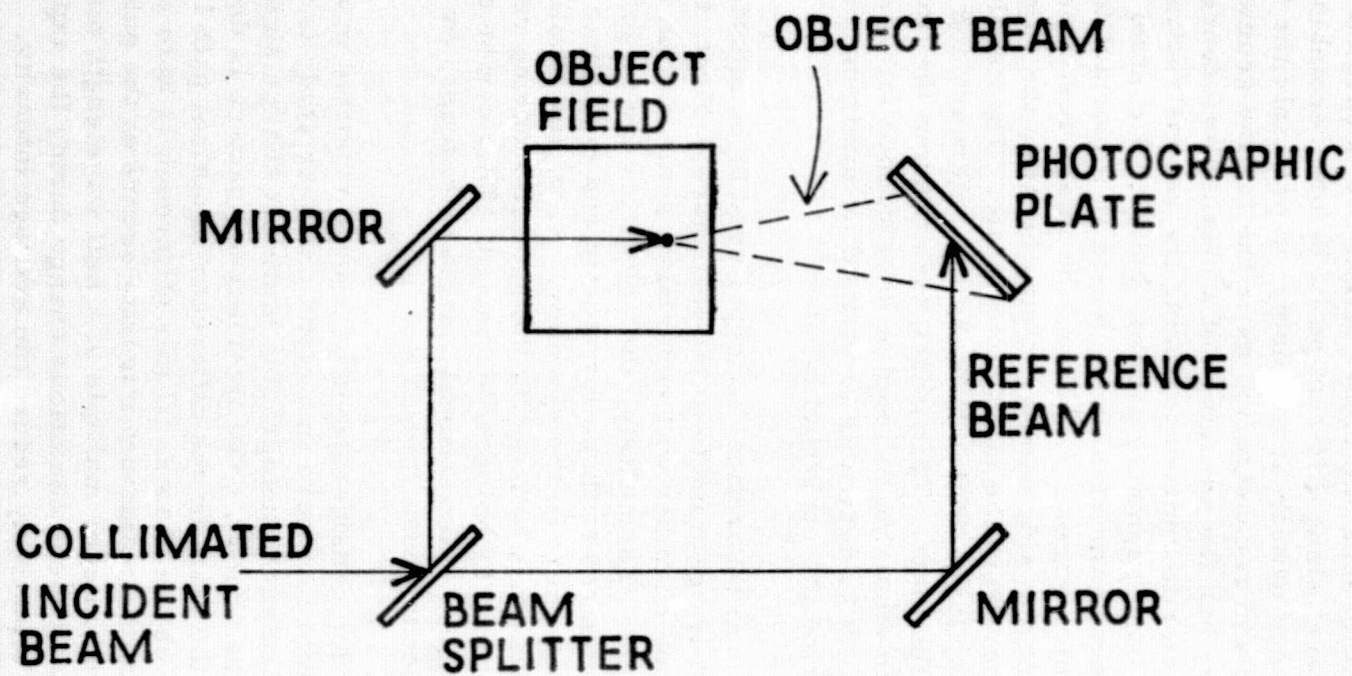
Figure 2. Side band geometry for recording a hologram.

choose the exposure time so that the maximum change in optical path difference for all emulsion points is much less than a half wavelength. If this change results from a droplet moving a distance d with speed v, the condition for selecting the exposure time becomes

$$d = v \tau << \lambda/2 \qquad (10)$$

Therefore, a light source is needed that will properly expose the photographic emulsion in a time τ obtained from equation (10).

Holographic microscopy considerations have been reported in references 3, 7, and 8. The holographic magnification has been reported as [Ref. 3, eq. (4-20)]

$$M = \left[\frac{R_1}{R_1 + z_1} - \frac{\lambda_1 z_1}{\lambda_2 R_2} \right]^{-1} \qquad (11)$$

where R_1 and λ_1 are the wave front radius and wavelength for the reference beam, R_2 and λ_2 are the corresponding values for the reconstruction beam, and z_1 is the object plane to hologram plane distance. The simplest case is for reference and reconstruction beams both having planar wave fronts. For this case, the radii go to infinite values and the limiting value of equation (11) is unity, regardless of the values for the wavelengths and z_1. Planar wave fronts are used in this study as no recording magnification is necessary for the results reported here.

SYSTEM DESCRIPTION

The cloud chamber used in this study, shown in figure 3, is a cylinder of height 1.1 cm and diameter 7.5 cm. Two rectangular windows are located across from each other so that a collimated light beam can enter the chamber, pass through the droplets along a diameter, and exit on the other side. The windows are 0.6 cm high and 1.3 cm wide. The cloud chamber was positioned at the object field location when holograms were recorded.

As this study was to investigate the problem of mating the cloud chamber to the holographic system a static particle field was established as a control situation. The static particle field consisted of wires erected in a roughly vertical orientation. The wires had a known precision diameter of 63.5 microns (0.0025 inches). Holograms

17-11
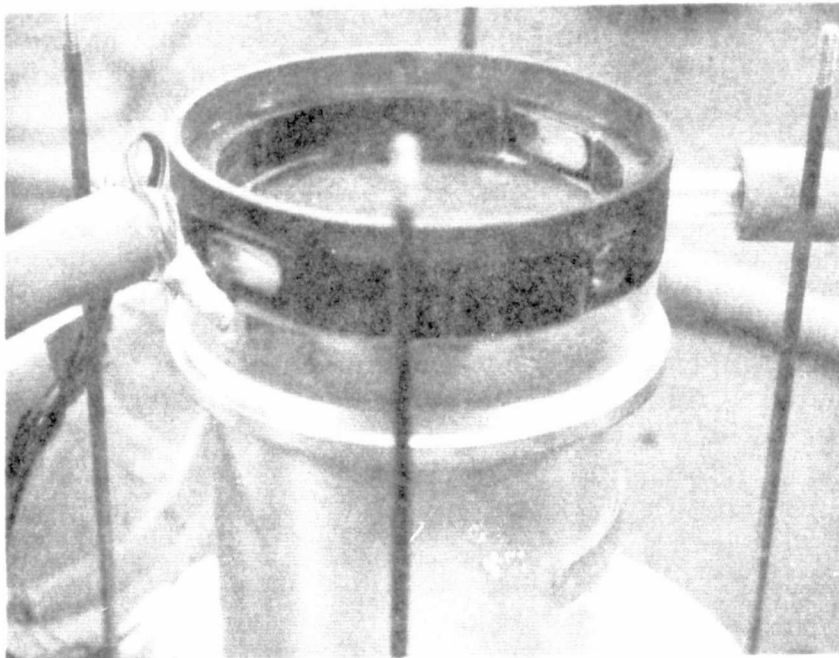
A
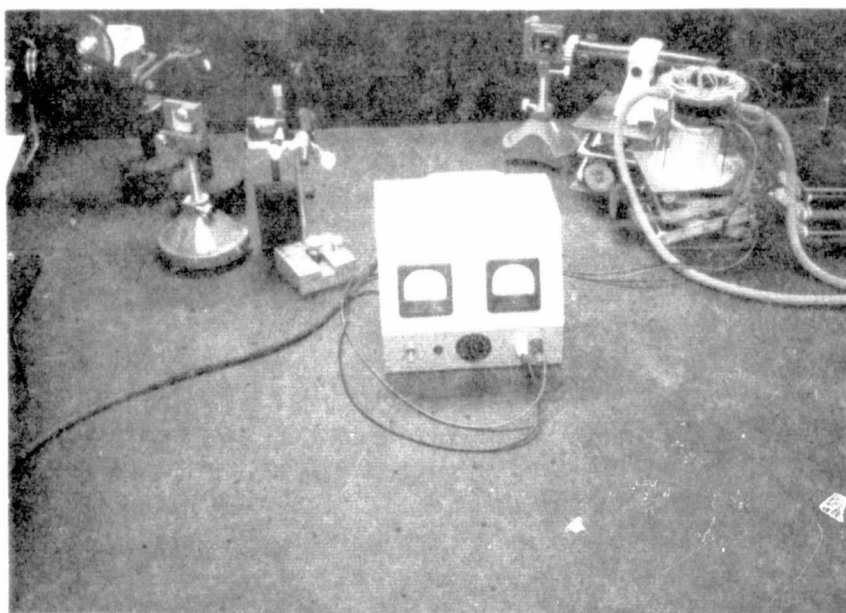
B

Figure 3. A. Photograph of cloud chamber with top removed.
B. Photograph of cloud chamber and holographic system.

were recorded with the wires on a rigid stand without the cloud chamber, and inside the chamber to demonstrate the effect of the chamber windows and the restricted object beam size.

The holographic images are displayed on a video monitor as shown schematically in figure 4. The hologram is mounted vertically on an optical bench so that it can be rotated about a vertical axis. In order to observe the real image from the hologram the reconstruction beam direction is reversed relative to the reference beam direction during the recording step. In this study collimated reference and reconstructionbeams are used to provide unity magnification for the holographic image. The lens L is used to form a magnified real image of the real holographic image. The second real image (formed by the lens rather than directly from the hologram) is projected onto the face of a lensless vidicon tube which feeds the resulting signal to a video monitor.

The two reconstruction beam directions are to accomodate both in-line and side band holograms. Rotation of the holographic plate about a vertical axis allows for selection of the proper angle between the reconstruction beam and the plane of the hologram. This angle is of extreme importance if optimum display of microscopic particles is to be achieved (See ref. 9).

The holographic image is displayed with only a single thin slice of the image field appearing in focus on the video monitor. The lens to vidicon tube distance is fixed for the formation of the second real image. Therefore, only one thin plane through the first image field is in focus through the magnifying lens L. The total holographic image field can be scanned by sliding the holographic plate along the optical bench, thus positioning different slices of the first image field at the correct object point for the lens.

In order to accomodate a large depth of field in the video display system for the side band geometry it is necessary to construct a mounting system for a mirror to be attached to the carriage holding the hologram. As the hologram travels along the optical bench this mirror must maintain a constant angle between the recontruction beam and the plane of the hologram, and it must direct the beam onto a single fixed point on the plate. Figure 5 shows the optical arrangement for this mirror. The double-headed arrows indicate the directions of travel for the mirror and bracket that allow this device
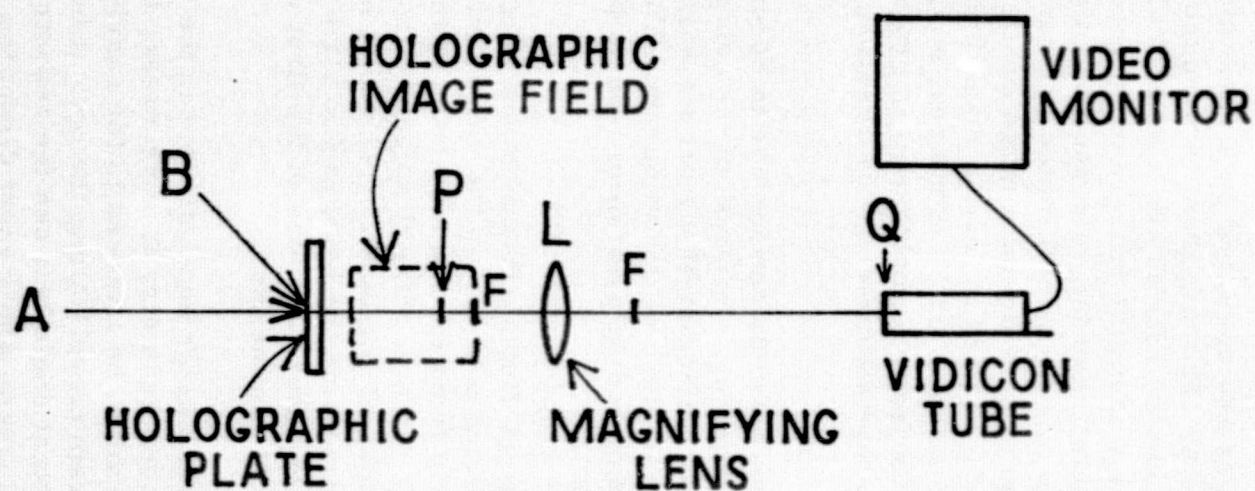
Figure 4. Schematic diagram of the video display system. A - in-line reconstruction beam direction, B - side band reconstruction beam direction, P - plane of image field satisfying condition for lens L to form a sharp focused image on the vidicon tube face Q, F - focal points of lens L.
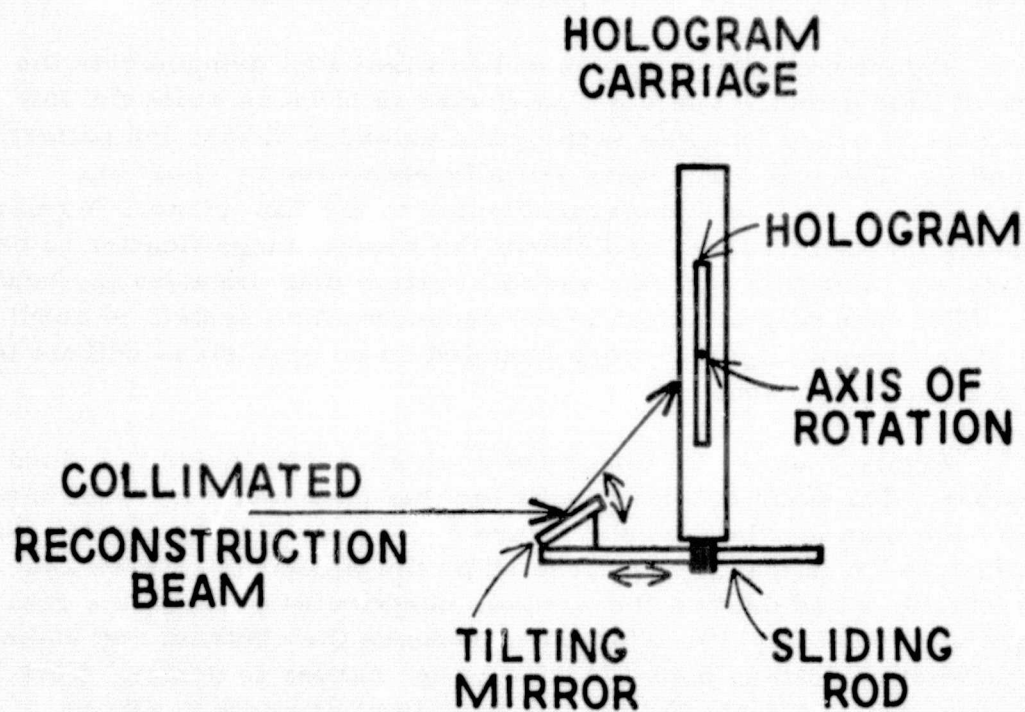
Figure 5. Optical arrangement for directing side band reconstruction beam onto hologram.

to accomodate different incident angles for the reconstruction beam.
The hologram travels along the optical bench in a direction that is
parallel to the light beam approaching the mirror.

DISCUSSION

The work completed is an initial investigation of the holographic
recording and display systems needed for the cloud chamber studies.
Figures 6 and 7 show holographic images of static 63.5 micron
diameter wires that are displayed on the video monitor.

Figure 6 contains images of two wires that demonstrate the
depth of field effect. The right hand wire is in focus while the left
hand wire is out of focus as seen by the extended diffraction pattern
around it. The two wires were initially separated by about one
centimeter in the direction perpendicular to the film plane. A ruler
overlays the video screen and allows the system magnification to be
calculated. For this case the overall system magnification is about
350. (The lens magnification in the reconstruction system is about
15.) The wires in figure 6 were mounted on an open stand without the
cloud chamber present.

Figure 7 shows an image for a wire located inside the cloud
chamber. The point of sharp focus for this case was somewhat harder
to achieve than for the wires in figure 6. A possible explanation for
this difference is that light diffracted by the window apertures and
imperfections and dust on the windows contributes noise to the real
image wavefront (eq. 9). This noise reduces the contrast and makes
the diffraction pattern near the wire image harder to detect. This
indicates that in the cloud chamber studies of droplets it will be
necessary to maintain the exit window in the cleanest possible condition
without condensation on its inner surface.

Figure 8 illustrates another noise component that degrades
image quality. This component arises during image reconstruction
and is especially prominent for in-line holograms. When a wave
front of coherent light enters the thin glass plate on the front of the
vidicon tube multiple reflections can occur within the glass plate.
The multiple reflections establish an interference pattern that is
displayed on the video screen. In this case the wave front is nearly
planar and the interference pattern consists of a set of concentric
rings. This noise component can be reduced by placing a "dc-stop",
or small opaque dot, at the secondary focal point of the magnifying
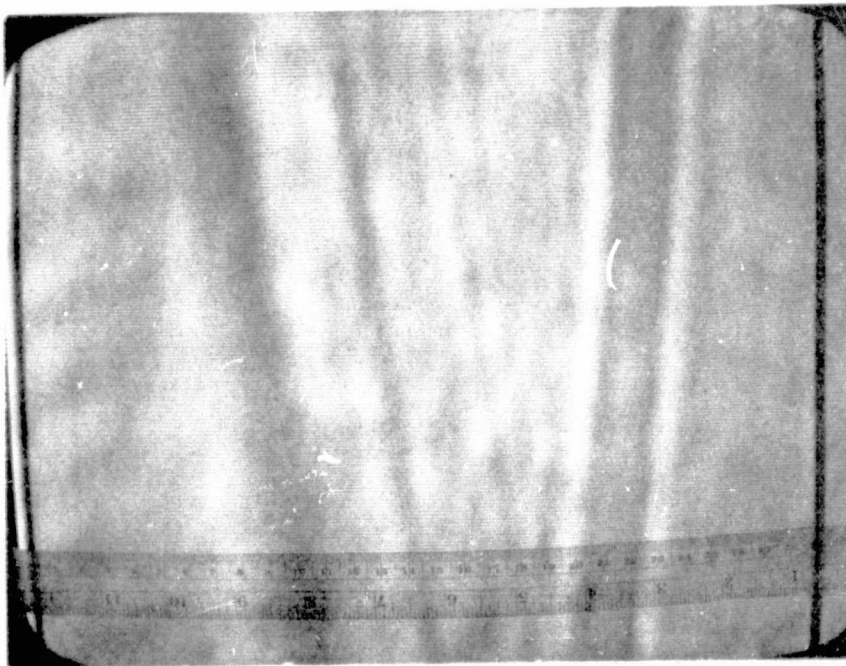
Figure 6.   Video display of holographic images of two wires.
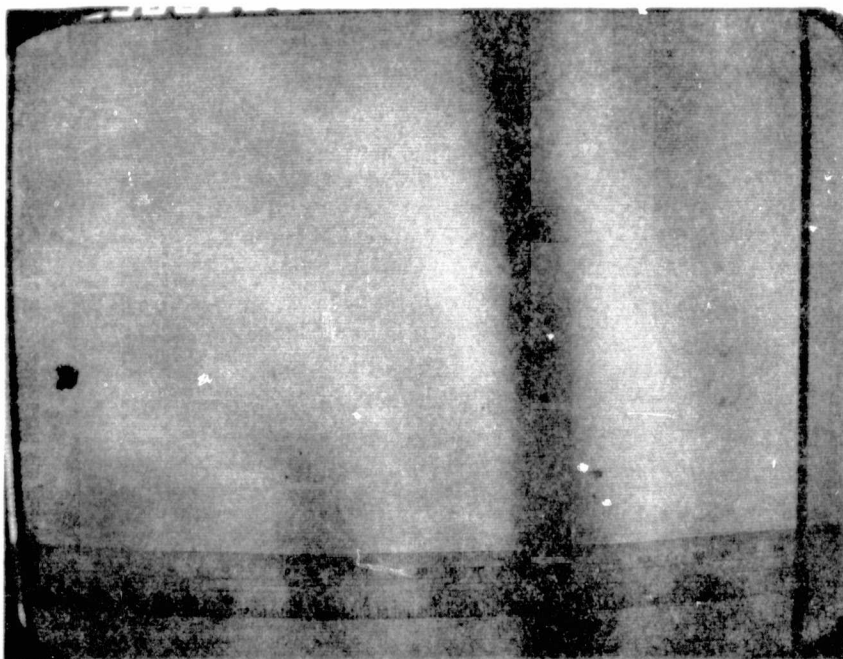
Figure 7. Video display of holographic image of a wire inside the cloud chamber.
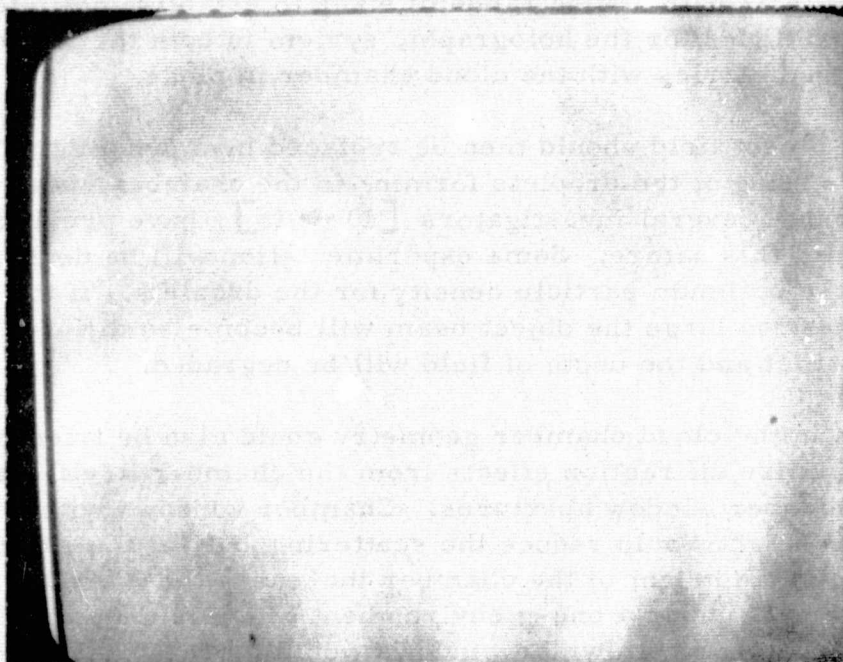
Figure 8. Video display of thin film interference fringes formed
on the face of the vidicon tube.

lens. The function of the dc-stop is to absorb the strong reconstruction wave front (eq. 8) while allowing the real image wave front to reach the vidicon tube. The size of the dc-stop is chosen with regard to the wavelength of light and the focusing properties of the magnifying lens.

This work has been a first step toward the development of a flight system for cloud microphysical research. This first step has focused attention on several steps that should follow.

The static object field used in this study was located from 12 to 15 centimeters from the holographic plate. This distance should be varied using objects with a wide range of sizes to establish definite resolution capabilities for the holographic system in both the in-line and side band geometries with the cloud chamber in place.

The static object field should then be replaced by a dynamic particle field consisting of the droplets forming in the chamber under one-g conditions. Several investigators [10 → 15] have previously reported work of this nature. Some experimentation will be necessary to determine the optimum particle density for the droplets. If the density becomes too large the object beam will become so diffuse that the image contrast and the depth of field will be degraded.

Variations in the cloud chamber geometry could also be tried in an attempt to minimize diffraction effects from the chamber itself, especially the chamber window apertures. Chamber windows with a larger vertical height would reduce the scattering, but, at the same time, increasing the height of the chamber increases the internal convection currents under a one-g environment which is undesirable. A rectangular chamber with wider windows would increase the angle over which viewing could take place. In any chamber the exit window should be of good optical quality and free from condensation and other foreign matter. The best compromise between low diffraction losses and a wide angle of viewing at one extreme, and minimum convection currents at the other must be determined.

The maximum useful depth of field for the object field is highly desirable. This should be studied as the object field to hologram plane distance is varied, and as the object field density is varied. The coherence length of the light source also needs to be considered. The results of these studies need to be fedback for design considerations on the cloud chamber size.

The particle size range of interest to meterologists is from 0.01 micron to 1 centimeter. The lower end of this range has not been resolved with purely holographic techniques. A combination of holographic magnification (eq. 11) and conventional optical magnification needs to be studied for the recording step of the holographic process to possibly extend the range of particle sizes that can be measured. Again, the depth of field will be reduced by the introduction of conventional optical elements so another compromise is necessary.

The particle growth rate is of extreme importance to meterologists. Therefore, when the best compromise among resolution, depth of field, particle density, chamber size, chamber window size, and recording magnification is made, the system should be used with a film transport so that a sequence of exposures can be made for the same collection of droplets. This sequence will show in real time the progress of the cloud formation.

Finally, this information must be applied to an on-board system for the Space Shuttle/Spacelab program.

References

1. R. L. Kurtz, Optical Holography Applications for the Zero-G Atmospheric Cloud Physics Laboratory, NASA Technical Report, NASA TR R-424, May 1974.

2. R. J. Collier, C. B. Burckhardt, and L. H. Lin, Optical Holography (Academic Press, New York, 1971).

3. J. B. De Velis and G. O. Reynolds, Theory and Applications of Holography (Addison-Wesley Publishing Co., Reading, Mass., 1967).

4. H. M. Smith, Principles of Holography (Wiley-Interscience, New York, 1969).

5. D. B. Neumann, "Holography of Moving Scenes", J. Opt. Soc. Am. 58, 447 (1968).

6. R. L. Kurtz and H. Y. Loh, A Holographic System that Records Front-Surface Detail of a Scene Moving at High Velocity, NASA Technical Report, NASA TR R-380, January 1972.

7. E. N. Leith, J. Upatnieks, K. A. Haines, "Microscopy by Wave-front Reconstruction", J. Opt. Soc. Am. 55, 981 (1965).

8. R. L. Kurtz, The Techniques of Holographic Particle Sizing, NASA Technical Report, NASA TR R-404, March 1973.

9. E. B. Champagne and N. G. Massey, "Resolution in Holography", Appl. Opt. 8 1879 (1969).

10. B. J. Thompson, J. H. Ward, and W. R. Zinky, "Applications of Hologram Techniques for Particle Size Analysis", Appl. Opt. 6, 519 (1967).

11. J. D. Trolinger, R. A. Belz, and W. M. Farmer "Holographic Techniques for the Study of Dynamic Particle Fields", Appl. Opt. 8 957 (1969).

12. B. A. Silverman, B. J. Thompson, and J. H. Ward, "A Laser Fog Disdrometer", J. Appl. Meteorol. 3, 792 (1964).

13. B. J. Thompson, G. B. Parrent, J. H. Ward, and B. Justh, "A Readout Technique for the Laser Fog Disdrometer", J. Appl. Meteorol. $\underline{5}$, 343 (1966).

14. M. E. Fourney, J. H. Matkin, and A. P. Waggoner, "Aerosol Size and Velocity Determination via Holography", Rev. Sci. Inst. $\underline{40}$, 205 (1969).

15. J. Politch and B. Schmutter, "Measurements on Images Retrieved from Holograms", Appl. Opt. $\underline{13}$, 140 (1974).

1974

ASEE - NASA SUMMER FACULTY FELLOWSHIP PROGRAM

MARSHALL SPACE FLIGHT CENTER

AUBURN UNIVERSITY - UNIVERSITY OF ALABAMA

THEORETICAL ANALYSIS OF CONTINUOUS AND
INTERMITTENT LITHIUM-BROMIDE-WATER
ABSORPTION REFRIGERATION CYCLES

Prepared by: Edward H. Perry

Academic Rank: Assistant Professor

Department and University: Mechanical Engineering Department
                                      Memphis State University

NASA/MSFC Assignment:
  (Laboratory)   Structures and Propulsion
  (Division)   Engineering Analysis
  (Branch)   Life Support and Environmental

NASA Research Counterpart: J. C. Cody

Date: August 9, 1974

Contract No.:   NGT-01-003-045

THEORETICAL ANALYSIS OF CONTINUOUS AND INTERMITTENT LITHIUM-BROMIDE-WATER ABSORPTION REFRIGERATION CYCLES

By

Edward H. Perry

ABSTRACT

A theoretical analysis of continuous and intermittent absorption refrigeration cycles using lithium bromide and water was performed to determine their suitability for solar cooling systems. The effects of operating temperatures on the cycle performance characteristics were examined in detail. The results obtained indicate that low condenser and absorber temperatures and high evaporator temperatures result in a significant decrease in the size of the solar collector employed. Furthermore, the continuous cycle offers a higher coefficient of performance in general while the intermittent cycle offers a lower average generator temperature.

INTRODUCTION

The lithium bromide-water absorption refrigeration cycle has long been viewed as a promising means of providing cooling from solar energy [1-3]. It is well known that this absorbent and refrigerant combination offers the advantages of a low absorbent volatility, which eliminates the need for a rectifier, and a high refrigerant enthalpy of vaporization, which reduces the amount of refrigerant required to produce a given amount of cooling. In addition, this cycle offers the important advantage for solar cooling applications of being able to operate efficiently from the low-temperature thermal energy provided by a flat-plate solar collector. Attendant with this advantage, however, is the disadvantage of low absorber and condenser temperatures, which usually necessitates the use of a cooling tower.

Because of its appeal as a solar cooling cycle and because of a lack of published information on its performance characteristics, the lithium bromide-water absorption process was investigated theoretically. Both continuous and intermittent cycles were examined and will be discussed separately. The primary concern was to determine the effects of operating temperatures on the cycle performance. Also, in the case of the continuous cycle, the effects of introducing heat exchangers into the basic cycle were investigated. It was intended that the results obtained would permit a determination of the optimum operating conditions for the lithium bromide-water refrigeration process as a solar cooling cycle.

ANALYSIS OF THE CONTINUOUS ABSORPTION CYCLE

The continuous absorption system considered is shown in figure 1 and includes the usual basic components of absorber, generator, condenser, evaporator, pump, throttling valves, and associated piping. In addition to these were included a liquid heat exchanger and a refrigerant precooler.

During operation of the system, a lithium bromide-water mixture rich in water content is pumped from the absorber to the generator where water vapor is driven off by heat, which for a solar cooling cycle is provided by a flat-plate solar collector. This vapor is subsequently condensed and expanded through a throttling valve, resulting in a decrease in the pressure and temperature. In the evaporator the condensed liquid vaporizes by absorbing heat from the surroundings and, thereby, produces the desired refrigerating effect. Meanwhile the liquid left behind in the generator returns to the absorber and reabsorbs the water vapor coming from the evaporator. The liquid heat exchanger and refrigerant precooler are not essential to the operation of the system but, as will be seen, improve its performance.
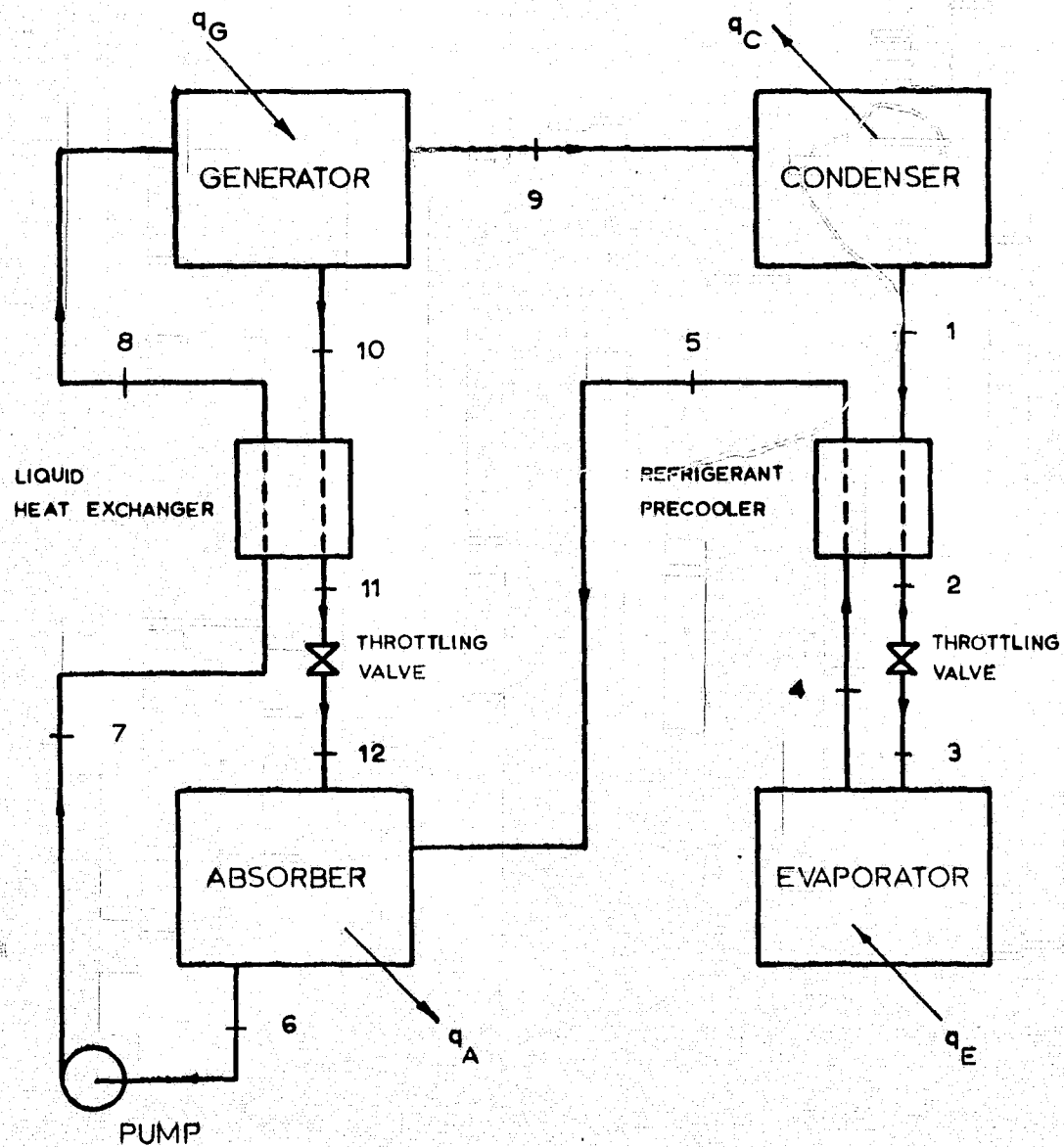
Figure 1. Continuous Absorption System Configuration

To simplify the analysis, it was assumed that the pump power is negligible, that no heat transfer and pressure losses occur in the interconnecting piping, and that thermodynamic equilibrium is maintained whenever two phases coexist. The energy and mass balance equations appropriate for the thermodynamic analysis have been discussed elsewhere [4, 5], but will be repeated here for the sake of completeness. Applying the First Law to a control volume surrounding each component of the system and assuming steady-state steady-flow conditions with a refrigerant mass flow rate of unity, the following equations result, where the numerical subscripts refer to the state locations shown in figure 1:

$$q_E = h_3 - h_4 \tag{1}$$

$$q_A = m_p h_6 - h_5 - (m_p - 1) h_{12} \tag{2}$$

$$q_G = h_9 + (m_p - 1) h_{10} - m_p h_8 \tag{3}$$

$$q_C = h_1 - h_9 \tag{4}$$

$$h_2 = h_3 \tag{5}$$

$$h_{11} = h_{12} \tag{6}$$

$$h_2 - h_1 = h_4 - h_5 \tag{7}$$

$$(m_p - 1)(h_{11} - h_{10}) = m_p (h_7 - h_8) \tag{8}$$

Similarly, a mass balance requires the following:

$$m_p = \frac{X_{10}}{X_8 - X_{10}} \tag{9}$$

Finally, using the usual definition for heat exchanger effectiveness, the following equations result:

$$\epsilon_{PC} = \frac{T_5 - T_E}{T_C - T_E} \tag{10}$$

$$\epsilon_{HE} = \frac{T_G - T_{11}}{T_G - T_A} \tag{11}$$

It should be noted that equations (10) and (11) were formulated assuming the heat capacity flow rates of the streams leaving the absorber and condenser are greater than those leaving the generator and evaporator, respectively.

From the above equations, a complete thermodynamic analysis can be obtained for a given set of operating temperatures and heat exchanger efficiencies, provided the required enthalpy and concentration values are available. For hand calculations such values have been provided by Ellington et al. [4] and Keenan et al. [6]. However, to avoid the time consuming process inherent in such calculations, the present thermodynamic analyses were performed using a digital computer supplied with polynomials fitted to the thermodynamic data mentioned above along with that provided by Pennington [7].

EFFECTS OF OPERATING TEMPERATURES

As discussed earlier, one of the primary purposes of the analysis was to determine the effects of varying the absorber, generator, condenser, and evaporator temperatures. A typical set of results is shown in figure 2 where the coefficient of performance, or more simply the C.O.P., defined as q_E/q_G, is given as a function of generator temperature for an evaporator temperature of 40°F., an absorber temperature of 90°F., and condenser temperatures ranging from 80°F to 110°F. For each case the effectiveness of the liquid heat exchanger
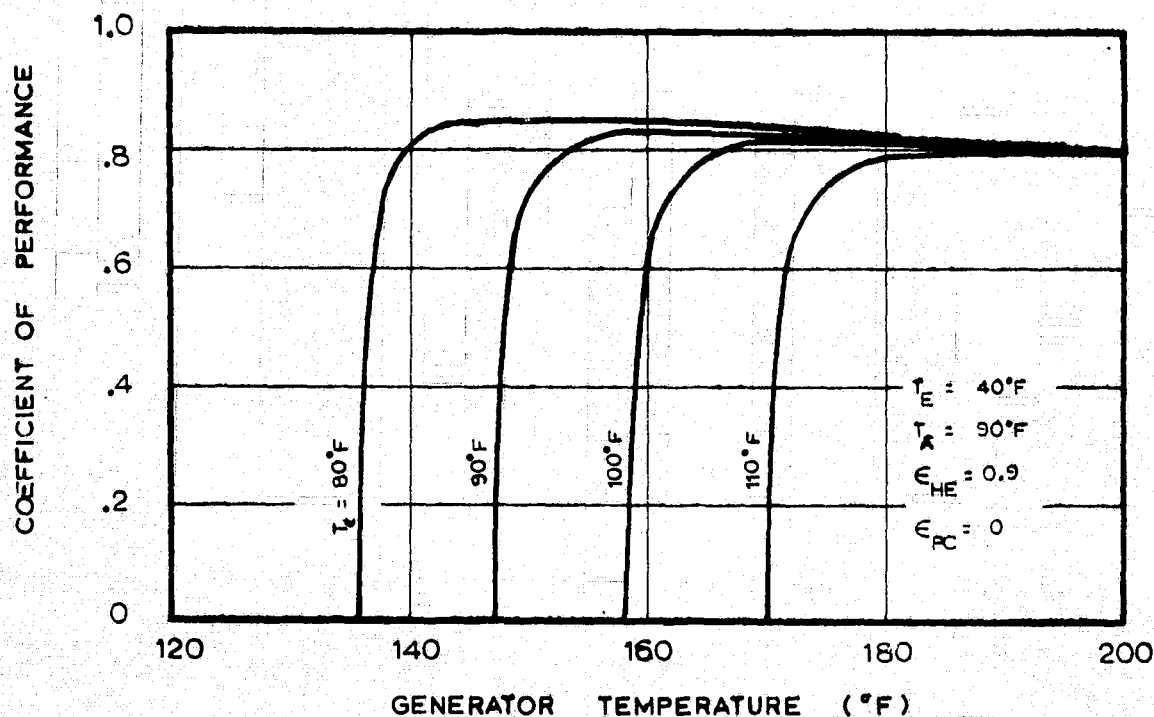
Figure 2. Effects of Generator and Condenser Temperatures on the Coefficient of Performance

was 0.9 and that of the refrigerant precooler was taken to be zero, which is equivalent to having no precooler present.

Several important characteristics of the cycle are apparent in figure 2. First, for given absorber, condenser, and evaporator temperatures no refrigeration occurs unless the generator is operated above some "cut-off" temperature. However, for generator temperatures above that value, the coefficient of performance rapidly increases to a maximum value and then slowly decreases with increasing generator temperature. Physically, the cut-off temperature corresponds to the saturation temperature of the mixture entering the generator. Unless the generator temperature is above this value, no refrigerant vapor is driven from the solution and, thus, no refrigeration can occur.

A second characteristic observed is that the cut-off temperature increases with increasing condenser temperature. This is easily explained when it is recalled that the saturation temperature of the solution entering the generator depends on the concentration of the solution and the vapor pressure above it. Since the latter is determined by the condenser temperature, the higher this value the higher the cut-off temperature. An interesting feature of the variation of the cut-off temperature with condenser temperature is the fact that the variation is almost linear with a given change in the condenser temperature resulting in an almost identical change in the cut-off temperature.

A third characteristic apparent from figure 2 is that the higher the condenser temperature the lower the coefficient of performance for a particular generator temperature. This effect is presumably due to the fact that the greater the temperature difference between the condenser and evaporator, the greater the energy required to "pump" heat from the region surrounding the evaporator to that surrounding the condenser.

These three characteristics are not unique to the lithium bromide-water continuous absorption cycle for a nearly identical behavior has been reported for the water-ammonia continuous absorption cycle [8, 9].

Similar results are shown in figure 3 for absorber temperatures ranging from 70°F. to 100°F. An increase in the absorber temperature is seen to result in an increase in the generator cut-off temperature and a decrease in the coefficient of performance. The first effect occurs because as the absorber temperature rises, so does the concentration of the solution entering the generator and the saturation temperature of that solution. The second effect is best explained by viewing the absorption cycle as a heat engine driving a compression
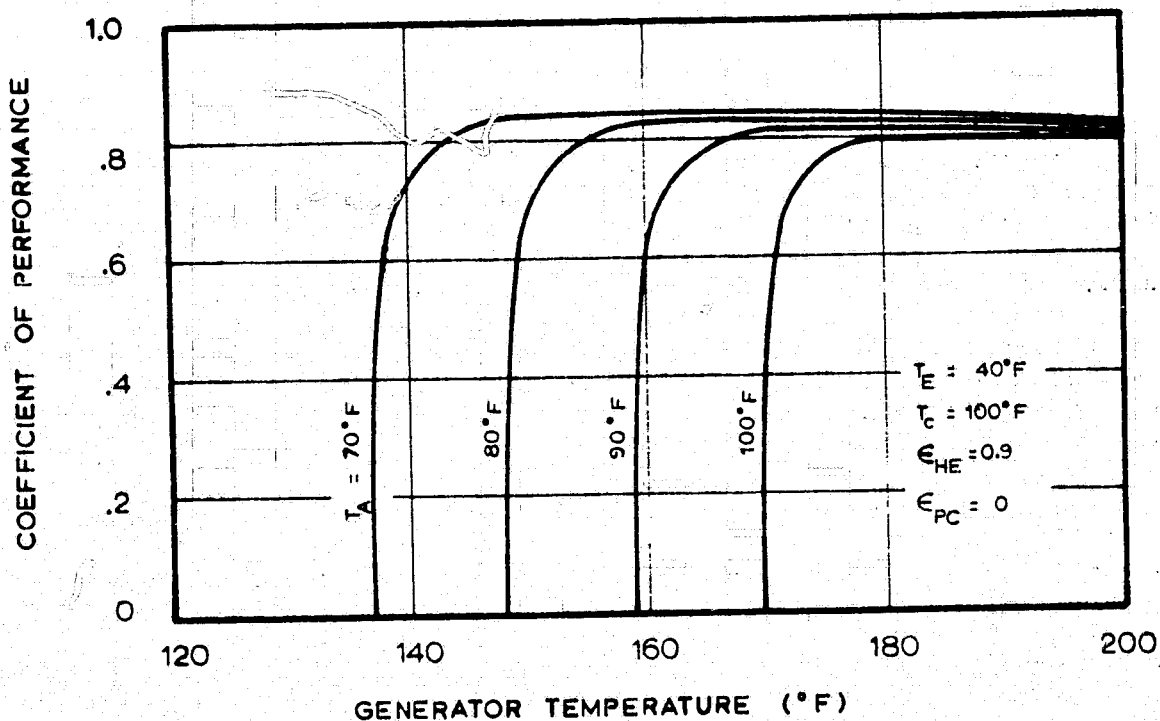
Figure 3. Effects of Generator and Absorber Temperatures
on the Coefficient of Performance

refrigerator as discussed by Ellington et al. [4]. In such a
representation the absorber temperature is the temperature at which
the heat engine rejects energy. Thus, the higher the absorber
temperature, the lower the efficiency of the engine and the lower
the coefficient of performance of the cycle as a whole.

Finally, from figure 4 we find that an increase in the evaporator
temperature results in a decrease in the cut-off temperature and an
increase in the coefficient of performance. The first effect is
due to the fact that a low evaporator temperature produces a low vapor
pressure above the solution in the absorber which, in turn, requires
a low concentration of lithium bromide to maintain equilibrium. The
second effect occurs for the same reason as the condenser temperature's
effect on the performance.

EFFECTS OF HEAT EXCHANGER AND PRECOOLER EFFICIENCIES

Within the liquid heat exchanger there is a concurrent heating of
the stream entering the generator and cooling of that entering the
absorber. Consequently, the addition of a liquid heat exchanger to the
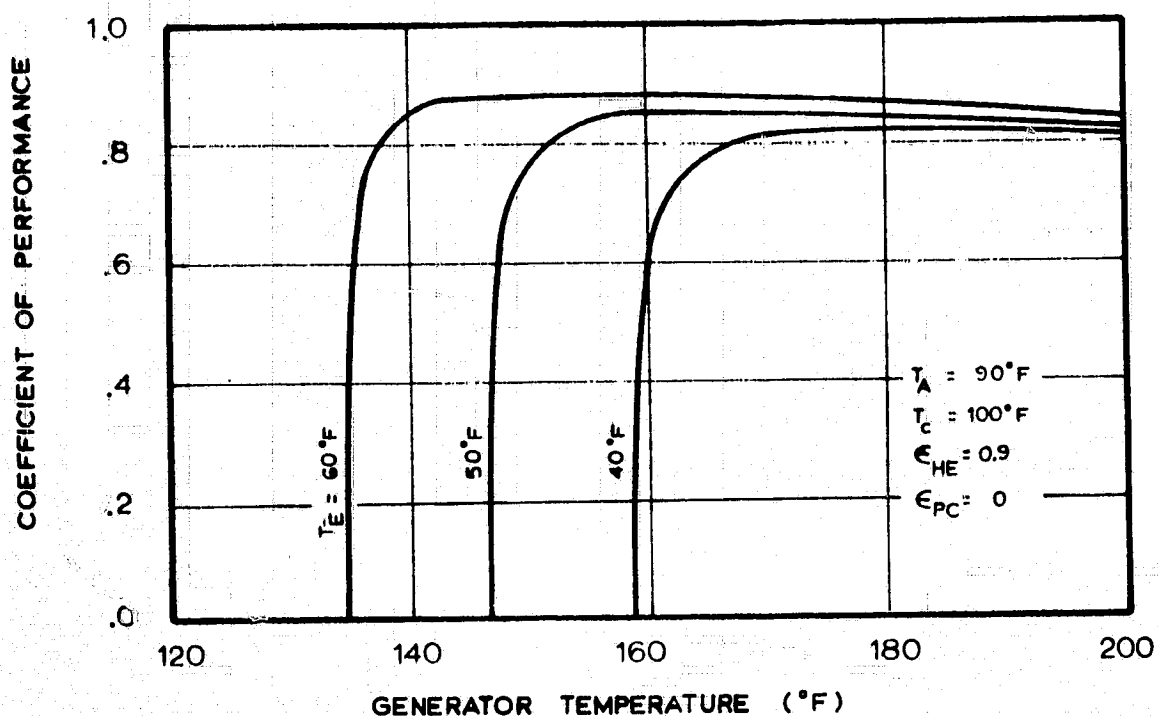
Figure 4. Effects of Generator and Evaporator Temperatures on the Coefficient of Performance

basic cycle reduces the heat required by the generator and that which must be removed from the absorber. Both effects are beneficial, but the former is of prime concern since it implies an increase in the coefficient of performance.

The influence of the liquid heat exchanger is shown in figure 5 where the coefficient of performance is plotted as a function of generator temperature for effectiveness values ranging from zero to unity, corresponding to no heat exchanger whatsoever and an ideal exchanger, respectively. Three effects are immediately evident from the figure. First, the higher the effectiveness the higher the coefficient of performance. This is to be expected since it is the very reason for including the heat exchanger. Second, the generator cut-off temperature is independent of the heat exchanger effectiveness. This, too, is to be expected since the cut-off temperature depends only on the concentration of the solution entering the generator and the vapor pressure above that solution, and neither of these factors depends on the heat exchanger. Third, the more effective the heat exchanger, the faster the coefficient of performance rises to its maximum value. Stated another way, the more effective the heat
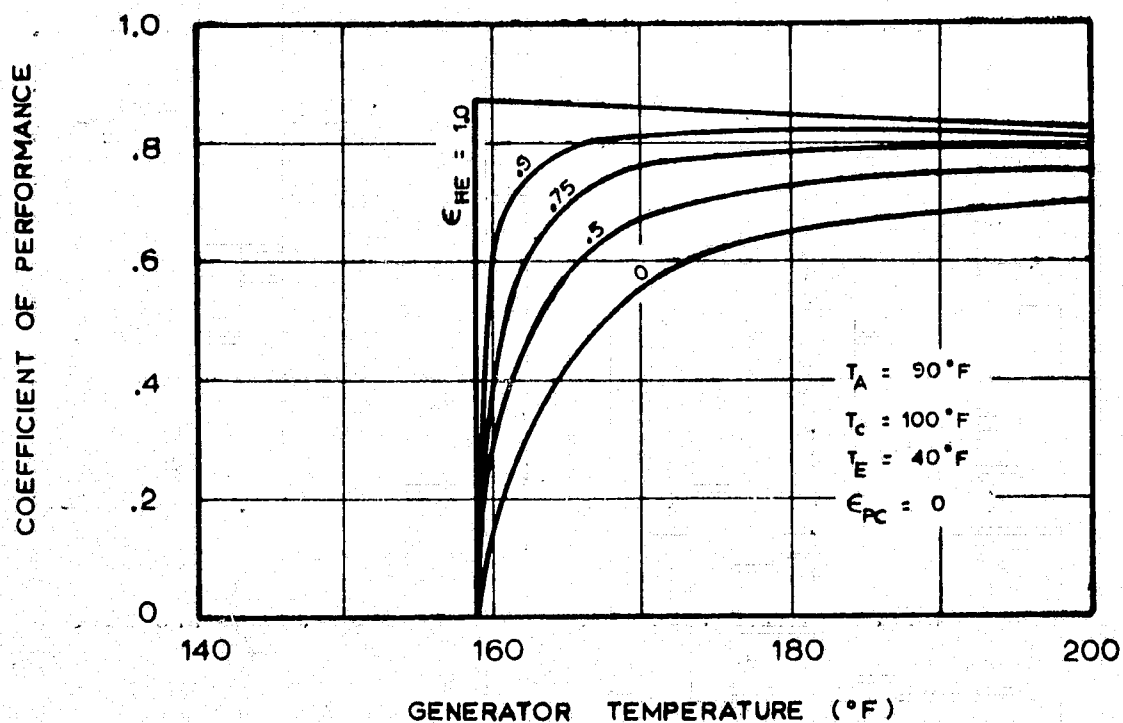
Figure 5. Effects of Generator Temperature and Liquid Heat Exchanger Effectiveness on the Coefficient of Performance

exchanger the closer the generator can operate to its cut-off temperature and still maintain satisfactory cycle performance.

Within the precooler the warm liquid refrigerant leaving the condenser is cooled by the vapor leaving the evaporator. Consequently, less refrigerant must evaporate adiabatically to cool the remaining liquid to the evaporator temperature. This, in turn, implies that more liquid refrigerant is available to absorb heat from the surroundings. However, since only a small fraction of the refrigerant "flashes" upon expanding through the throttling value in any case, the addition of a precooler should not result in a dramatic increase in the coefficient of performance. That such an increase does not indeed occur is shown in figure 6 where two extreme cases for the precooler are considered. The upper curve represents an ideal precooler, while the lower curve represents a cycle with no precooler present. There is clearly so little difference between the two that it is doubtful whether a precooler could ever be justified economically even for a solar cooling system where every improvement in the coefficient of performance means a reduction in the size of the relatively expensive solar collector.
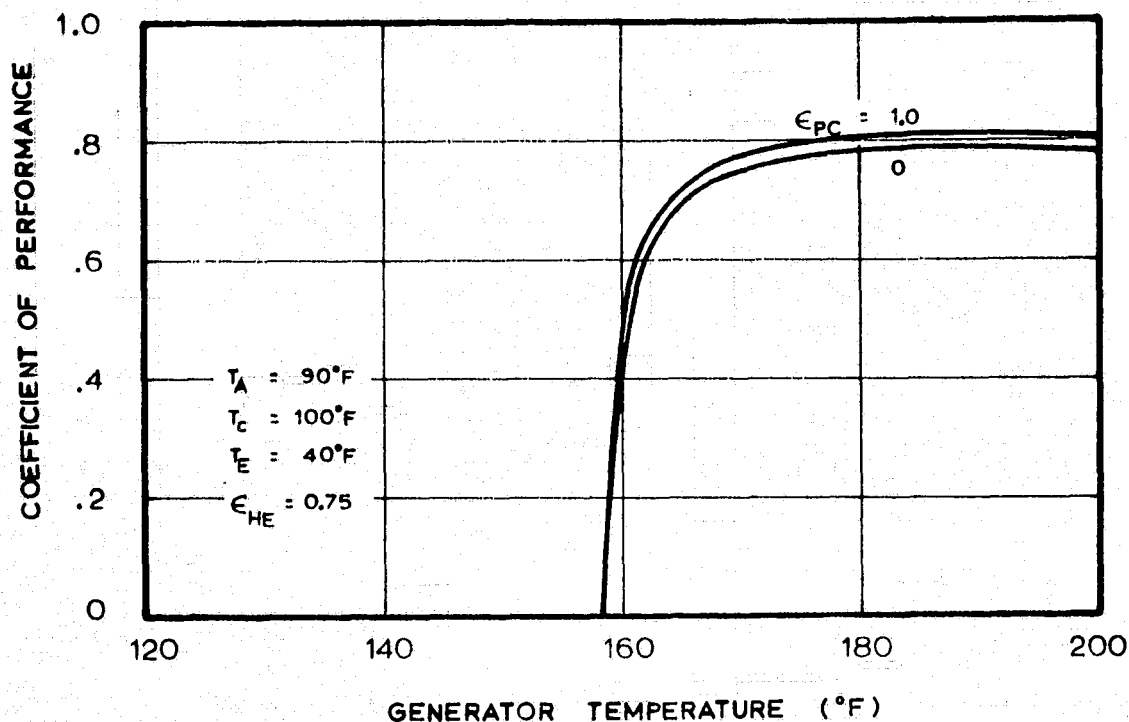
Figure 6. Effects of Generator Temperature and Refrigerant Precooler Effectiveness on the Coefficient of Performance

COMBINED EFFECTS

Certainly more important than any of the individual effects discussed above are the combined effects of low absorber and condenser temperatures, high evaporator temperature, and a highly effective heat exchanger. An example of these combined effects is provided by figure 7 where two sets of operating conditions are represented. The advantages of the case represented by the upper curve are at least threefold for solar cooling applications. First, the maximum coefficient of performance is over 10 percent higher. Second, the solar collector supplying the energy to the generator could operate approximately 50 degrees cooler, resulting in an improvement on the order of 20 percent in its collection efficiency. Third, by operating at this lower temperature, the collector could supply useful energy for a longer period each day. Combined, these effects could result in a significant decrease in the size of the collector and hence in the overall cost of the solar cooling system.
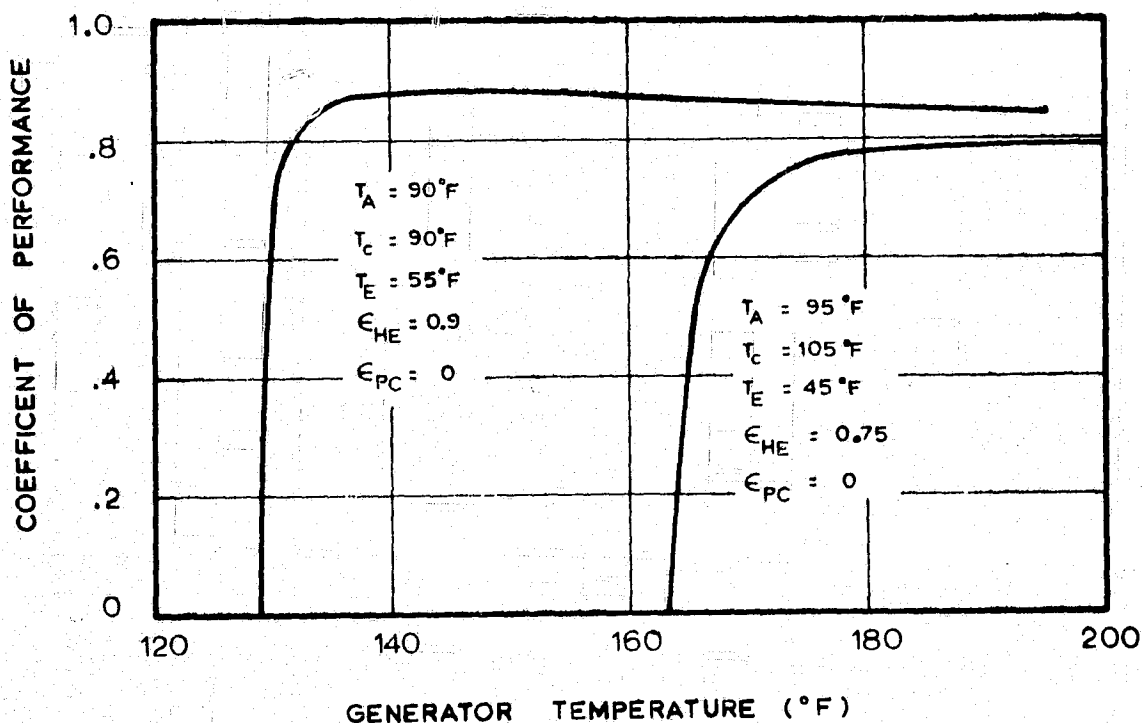
Figure 7. Comparison of Performance Characteristics For Two Sets of Operating Conditions

DESCRIPTION OF THE INTERMITTENT ABSORPTION CYCLE

Because of the intermittent nature of solar energy, intermittent absorption cycles have long been considered as logical approaches to solar cooling systems [10 - 15]. In figure 8, the two phases of an intermittent absorption cycle are shown. During regeneration heat added to the absorbent-refrigerant solution contained in the generator.drives off refrigerant vapor which is subsequently condensed in the condenser. During the refrigeration phase, the condenser becomes an evaporator, and the condensate vaporizes by absorbing heat from the region to be cooled and is reabsorbed by the original solution in the generator, which becomes the absorber.

Absorbent-refrigerant combinations which have been examined for solar cooling applications include water-ammonia 10 - 14 , glycol ether-Freon 21 [11, 12], lithium nitrate-ammonia [13], and sodium thiocyanate-ammonia [15]. The combination of lithium bromide and water, although used extensively for continuous absorption cycles, appears to have been ignored as an intermittent cycle possibility.

GENERATOR

CONDENSER

Q_G

Q_C

REGENERATION

ABSORBER

EVAPORATOR

Q_A

Q_E
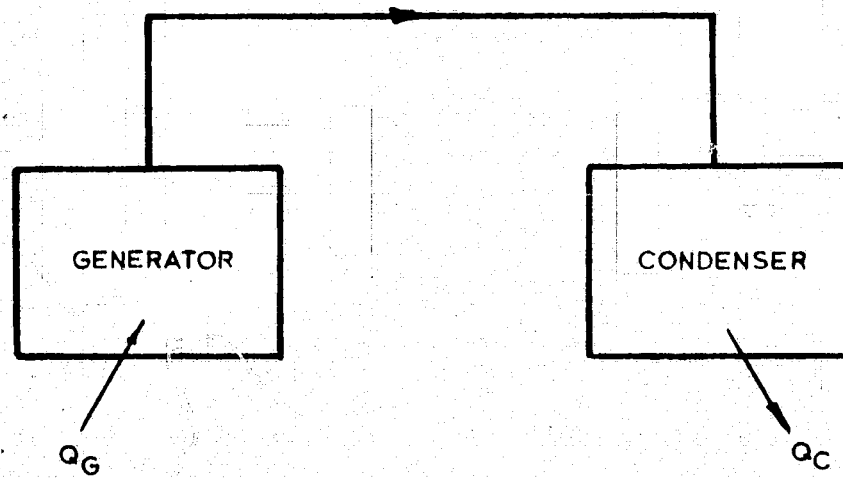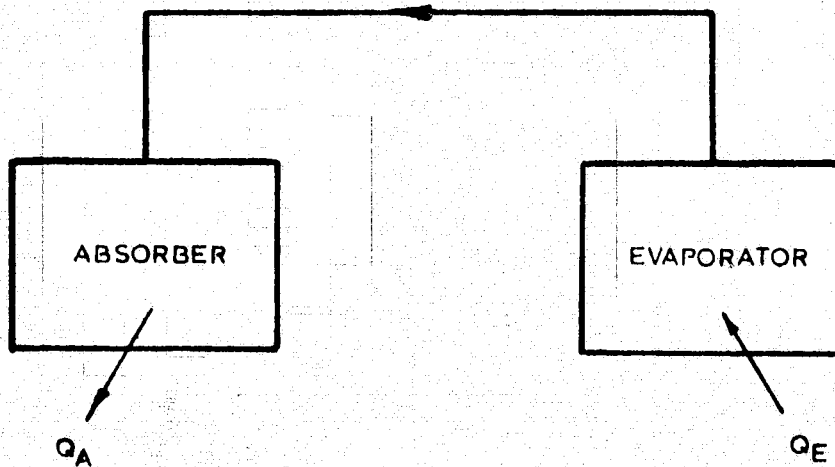
REFRIGERATION

Figure 8. Stages of Operation for the Intermittent Absorption Cycle

INTERMITTENT CYCLE ANALYSIS

The thermodynamic cycle considered is represented by the solid line in figure 9 where the generator temperature is plotted versus the lithium bromide weight percent. Regeneration begins at 1 as heat is added to the generator contents. At 2, sufficient heating has occurred to make the vapor pressure of the solution equal to the saturation pressure of water at the condenser temperature. Consequently, water vapor begins leaving the generator and continues to do so until the heating stops at 3. The generator, which now becomes the absorber, begins to cool, thereby initiating the refrigeration phase. A small portion of the condensate vaporizes by absorbing heat from the remaining water which cools the latter to the desired evaporation temperature. The absorber contents, now at 4, continue to cool while the water in the evaporator vaporizes and is reabsorbed. As the last of the condensate disappears, the evaporator temperature rises to the initial condenser temperature and the solution in the generator-absorber returns to 1 to begin the cycle anew. From figure 9 we see that if the generator temperature gets too high, crystal formation will occur during the cooling from 3 to 4. This condition is, of course, undesirable.

The coefficient of performance for the intermittent cycle is defined as the ratio of the energy absorbed from the surroundings by the refrigerant during refrigeration to that absorbed by the generator contents during regeneration. Sargent and Beckman [15] have shown that this ratio is approximately given by

$$C.O.P. = W_4 h_{fg} / (m_3 h_3 - m_1 h_1 + \int_1^3 h_g \, dm_g) \qquad (12)$$

where the numerical subscripts refer to the states designated in figure 9. In terms of solution concentration, this may be rewritten as

$$C.O.P. = \frac{(1 - x_1/x_4) \, h_{fg}}{\dfrac{x_1}{x_3} h_3 - h_1 - m_1 \int_1^3 h_g \dfrac{dx}{x^2}} \qquad (13)$$

Equation (13) was evaluated for a number of operating temperatures using a digital computer and the polynomial approximations discussed earlier for the thermodynamic properties.

EFFECTS OF OPERATING TEMPERATURES

The effects of operating temperatures are shown in figures 10 - 12 where the coefficient of performance is plotted as a function of the
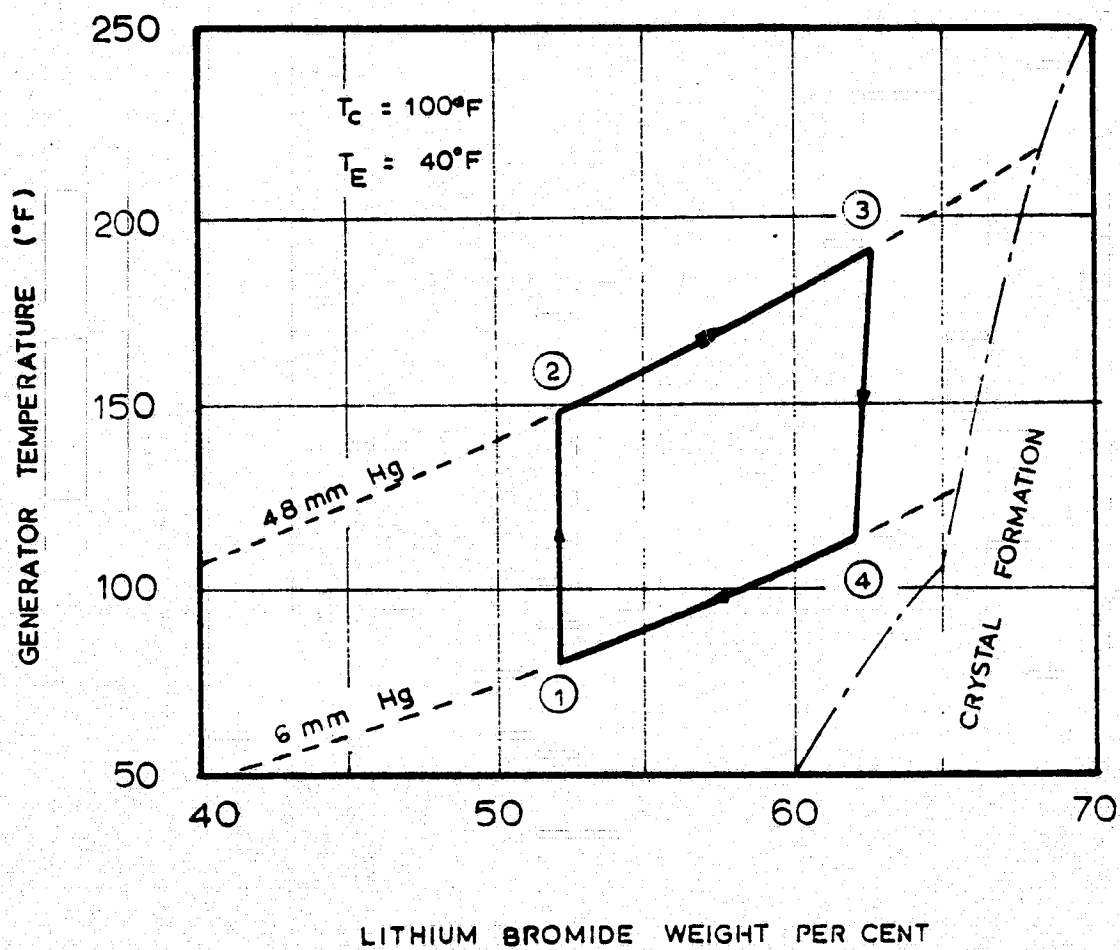
Figure 9. Thermodynamic Cycle for a Typical Absorption Cycle
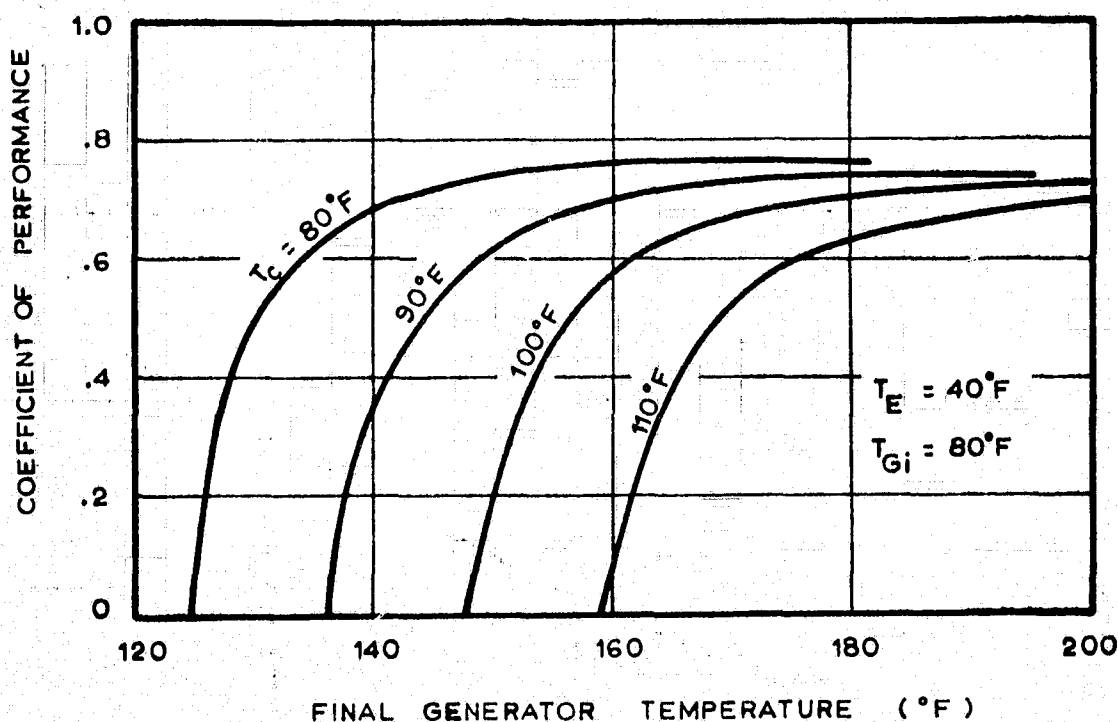
Figure 10. Effects of Final Generator Temperature and Condenser Temperature on the Coefficient of Performance

final, or highest, generator temperature for various condenser, evaporator, and initial generator temperatures, respectively. The curves obviously show strong resemblances to those discussed earlier for the continuous cycle. This, of course, should not be surprising since the physical processes occurring in the continuous and intermittent cycles are identical.

The most obvious feature in figures 10 - 12 is that for given condenser, evaporator, and initial generator temperatures there is a minimum final generator temperature which results in some cooling. Physically, this temperature is the temperature at which the vapor pressure of the original solution equals the saturation pressure of water at the condenser temperature. Thus, unless the final generator temperature exceeds this value, no vapor is driven from the solution and no refrigeration occurs.

Also, from figures 10 - 12 we find that increases in the condenser and initial generator temperatures and decreases in the evaporator temperature lead to increases in this minimum final generator temperature and to decreases in the coefficient of performance. Thus, for
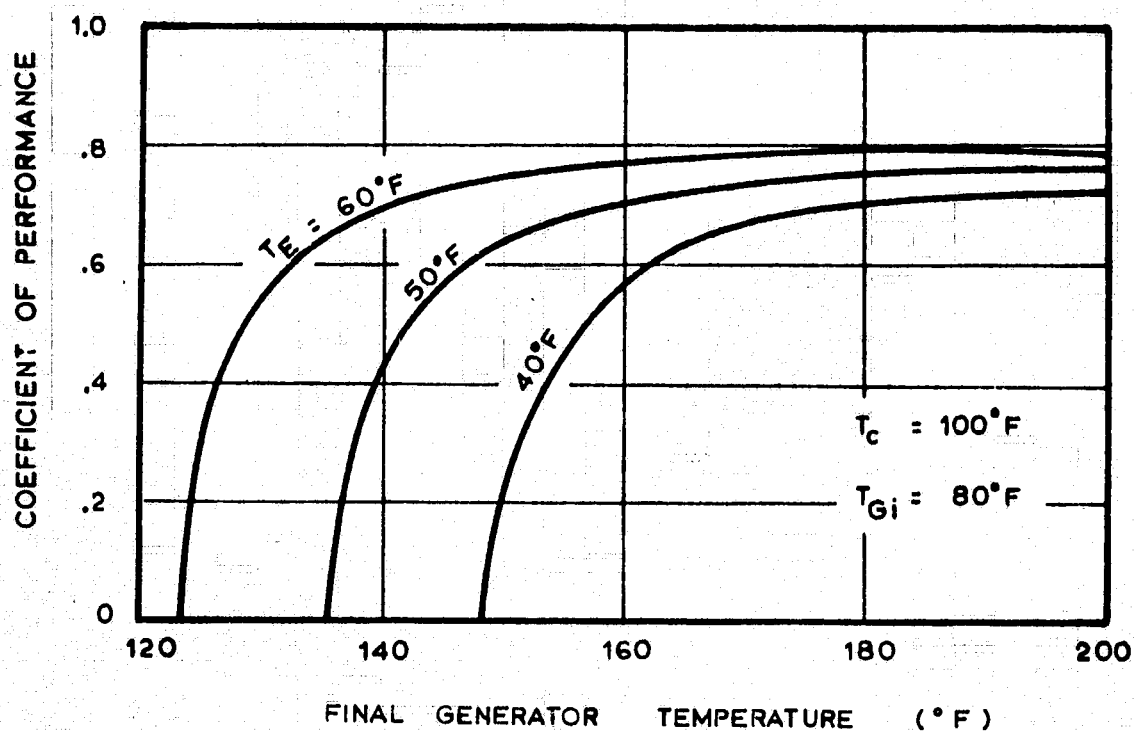
Figure 11. Effects of Final Generator Temperature and Evaporator Temperature on the Coefficient of Performance
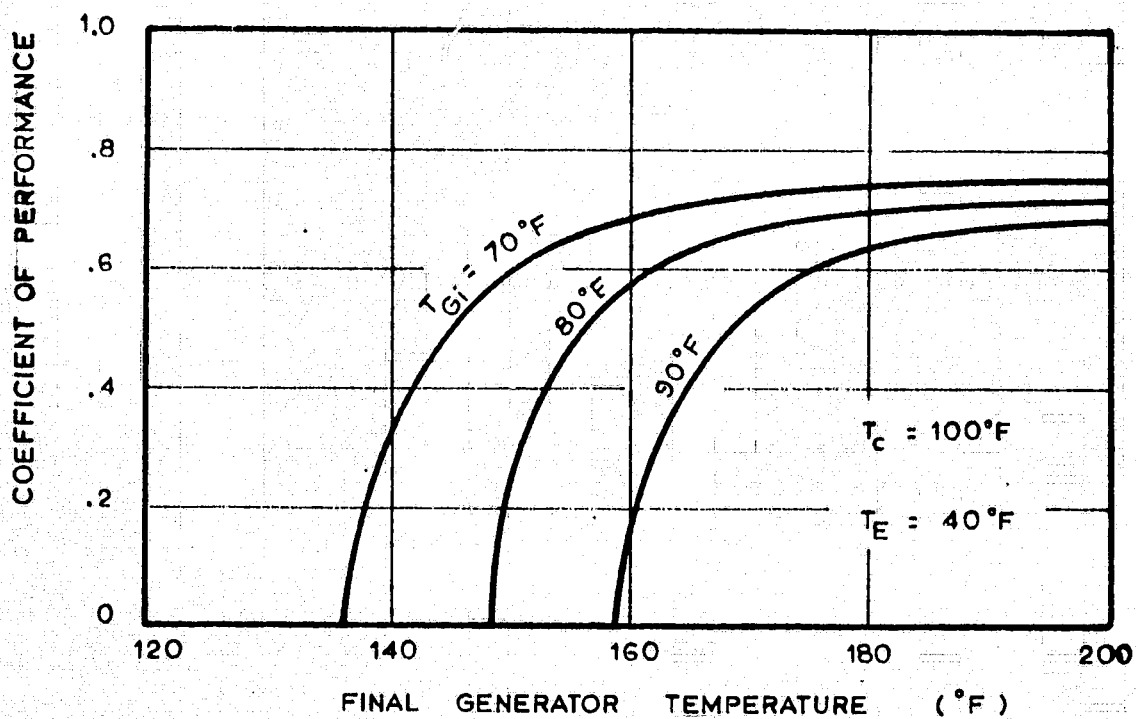
Figure 12. Effects of Final and Initial Generator Temperature on the Coefficient of Performance

18-17

solar cooling applications desirable features include low condenser and initial generator temperatures and a high evaporator temperature. The advantages of such operating temperatures are the same as those discussed for the continuous cycle.

CONCLUSIONS AND RECOMMENDATIONS

Both the continuous and the intermittent lithium bromide-water absorption refrigeration cycles appear well suited for solar cooling systems. For both cycles the coefficient of performance is higher and the generator temperature lower than for other absorbent-refrigerant combinations considered in the past for solar applications.

Operating temperatures have a strong effect on the size of the solar collector required for either cycle. The lower the condenser, absorber, and initial generator temperatures and the higher the evaporator temperature, the smaller the collector area.

For the continuous cycle, a liquid heat exchanger can enhance the performance considerably, but little is to be gained by including a refrigerant precooler.

Comparing the two cycles one finds that the continuous cycle offers a higher coefficient of performance in general while the intermittent cycle offers a lower average generator temperature. Thus, for solar applications it is not immediately apparent which of the two offers the greater cooling capacity for a given solar collector area. For this reason, it is recommended that an analysis be performed for an entire solar cooling system to determine the relative merits of the continuous and intermittent cycles. In addition to the refrigeration cycle, the analysis should include the solar collector and possibly energy storage devices.

Finally, experiments should be undertaken to determine the validity of the theoretical analyses performed in the present study.

NOMENCLATURE

h = enthalpy

h_{fg} = enthalpy of vaporization of refrigerant

m_g = mass of saturated refrigerant vapor leaving generator during regeneration

m_p = ratio of pump mass flow rate to evaporator mass flow rate

q = heat transfer per unit mass of refrigerant

Q = total heat transfer

T = temperature

W = refrigerant mass

x = weight fraction of lithium bromide

ϵ = effectiveness

Subscripts:

A = absorber

C = condenser

E = evaporator

g = saturated vapor

G = generator

Gi = initial generator condition

HE = liquid heat exchanger

PC = refrigerant precooler

REFERENCES

1. H. Tabor, "Use of Solar Energy for Cooling Purposes," U.N. Conf. on New Sources of Energy, Paper GR/18, Rome, 1961.

2. J. A. Duffie, R. Chung, and G. O. G. Löf, "A Study of a Solar Air Conditioner," Mechanical Engineering, p. 31, Aug. 1963.

3. N. R. Sheridan, "Performance of the Brisbane Solar House," Solar Energy, Vol. 13, p. 395, 1972.

4. R. T. Ellington, G. Kunst, R. E. Peck, and J. F. Reed, The Absorption Cooling Process, IGT Research Bulletin 14, Chicago, 1957.

5. ASHRAE Handbook of Fundamentals, ASHRAE, New York, 1967.

6. J. H. Keenan, F. G. Keyes, P. G. Hill, and J. G. Moore, Steam Tables, John Wiley and Sons, New York, 1969.

7. W. Pennington, "How to Find Accurate Vapor Pressures of LiBr Water Solutions," Refrigng. Engng., Vol. 63, p. 57, May 1955.

8. N. G. Ashar and A. R. Reti, "Engineering and Economic Study of the Use of Solar Energy for Space Cooling in India and Pakistan," U. N. Conf. on New Sources of Energy, Paper S/37, Rome, 1961.

9. W. F. Stoecker and L. D. Reed, "Effect of Operating Temperatures on the Coefficient of Performance of Aqua-Ammonia Refrigerating Systems," ASHRAE Transactions, Vol. 77, Part I, p. 163, 1971.

10. F. Trombe and M. Foex, "The Production of Cold by Means of Solar Radiation," Solar Energy, Vol. 1, p. 51, 1957.

11. D. A. Williams, R. Chung, G. O. G. Löf, D. A. Fester, and J. A. Duffie, "Cooling Systems Based on Solar Regeneration," Refrigng. Engng., Vol. 66, p. 33, 1958.

12. R. Chung and J. A. Duffie, "Cooling with Solar Energy," U.N. Conf. on New Sources of Energy, Paper S/82, Rome, 1961.

13. J. C. V. Chinnappa, "Experimental Study of the Intermittent Vapour Absorption Refrigeration Cycle Employing the Refrigerant-Absorbent Systems of Ammonia Water and Ammonia Lithium Nitrate," Solar Energy, Vol. 5, p. 1, 1961.

REFERENCES

14. J. C. V. Chinnappa, "Performance of an Intermittent Refrigerator Operated by a Flat-Plate Collector," _Solar Energy_, Vol. 6, p. 143, 1962.

15. S. L. Sargent and W. A. Beckman, "Theoretical Performance of an Ammonia Sodium Thiocyanate Intermittent Absorption Refrigeration Cycle," _Solar Energy_, Vol. 12, p. 137, 1968.

1974

ASEE - NASA SUMMER FACULTY FELLOWSHIP PROGRAM

MARSHALL SPACE FLIGHT CENTER

(AUBURN UNIVERSITY - UNIVERSITY OF ALABAMA)

NUMERICAL ANALYSIS OF A TWO-DIMENSIONAL
THERMAL CAPACITOR ELEMENT

Prepared by:	Donald R. Pitts, Ph.D.
Academic Rank:	Professor
Department and University:	Department of Mechanical Engineering Tennessee Technological University

NASA/MSFC Assignment:
  (Laboratory)
  (Division)
  (Branch)
	Structures and Propulsion
	Engineering Analysis
	Life Support and Environmental

NASA Research Colleague:	William R. Humphries
Date:	August 9, 1974
Contract No.:	NGT-01-003-045

ABSTRACT

NUMERICAL ANALYSIS OF A TWO-DIMENSIONAL
THERMAL CAPACITOR ELEMENT

by

D. R. Pitts

The present study is a continuation of a parametric numerical study
of the transient thermal response of a single cell of a phase change
material (PCM) - type thermal capacitor. The model for the basic
study consists of a base plate, two vertical walls, and a cap plate
forming a two-dimensional cavity filled with phase change material.
Approximately 300 different combinations of capacitor cell physical
dimensions and heat fluxes are included in the two-dimensional study.
Major results of this numerical investigation include: (1) the
transient overall temperature difference required to maintain a con-
stant heat flux, and (2) the value of this temperature difference at
the point in time when all phase change material has just melted.
Several other factors of interest, including the melt fraction as a
function of time and the transient location of the phase change
front, are readily obtainable with the computer program used.

A significant contribution of the current effort is the comparison
of a one-dimensional model, with properties modified to simulate a
two-dimensional design, with the results of the two-dimensional study.

NOMENCLATURE

A	area perpendicular to heat flux
C	nodal thermal capacitance, dimensionless
$\bar{C}$	nodal thermal capacitance, dimensional
c_p	specific heat
$\bar{G}$	thermal conductance, dimensional
GH	horizontal conductance, dimensionless
$\overline{GH}$	horizontal conductance, dimensional
GV	vertical conductance, dimensionless
H	cell PCM or fin height
h_f	latent heat of fusion
h_{TR}	latent heat of solid-to-solid transition
I	nodal designation integer, Figure 4
J	nodal designation integer, Figure 4
k	thermal conductivity of metal
k_w	thermal conductivity of phase change material
M	number of horizontal nodes of PCM, Figure 4
N	number of vertical nodes of PCM, Figure 4
PCM	phase change material
R_1 , R_2 , R_3	dimensionless ratios defined in text
R_4 , R_5 , R_6	dimensionless ratios defined in text
R_7 , R_8	dimensionless ratios defined in text
S_1	base plate thickenss, top plate thickness
S_2	fin thickness

T	temperature
T'	future temperature (after time step)
T1	present temperature
T2	future temperature (after time step)
t	time
W	cell PCM half-width
x	spatial coordinate
y	spatial coordinate
α	thermal diffusivity of metal
α_w	thermal diffusivity of PCM
ρ	density of metal
ρ_w	density of PCM

Subscripts

a, b, c, d, e	nodal designations, Figure 3
n	denotes a general node
w	denotes PCM (or wax) property

INTRODUCTION

The ability of a phase change material to absorb or liberate a large quantity of thermal energy without significant temperature change is a very important principle in the design of thermal control and protection devices for spacecraft. The study of devices and systems utilizing the phase change phenomenon has been ongoing at Marshall Space Flight Center for several years, originating with the need for passive thermal control and protection of several devices associated with the Apollo program. The need for design knowledge was further accentuated by the usage of a large number of phase change material (PCM) capacitors on Skylab.

Successful applications of PCM capacitors on the Apollo program included the use of paraffin-type units for the wheel drive control electronics (DCE) and the navigational signal processing unit (SPU) of the Lunar Roving Vehicle (LRV) of Apollo flights 15, 16, and 17. These capacitors were used to absorb waste energy and thereby keep temperature excursions below allowable maximum levels during LRV sorties. Following each sortie, thermal radiators were deployed to allow dissipation of the thermal energy in the capacitors and consequent resolidification of the paraffin material. This, of course, readied the capacitor for the next sortie.

Sixteen PCM thermal capacitors were included in various systems aboard Skylab I. Five of these were incorporated in the two environmental control cooling systems and were intended for thermal control of liquid temperatures. The remainder of the units aboard Skylab I were directly mounted to metallic trays which were used to store samples of human waste while being transported back to earth.

A cross-sectional view of a typical thermal capacitor used in manned space flight vehicles is shown in figure 1. This consists of a metallic container filled with a phase change material. Most suitable PCM's have very low thermal conductivity, and hence, it is usually necessary to provide a "filler" to enhance the heat transfer rate into the capacitor. Common designs include straight parallel metallic fins and honeycomb material. The case of parallel fins results in a transient two-dimensional thermal analysis problem, whereas the honeycomb design requires a three-dimensional analysis. (This latter design could perhaps be modeled, although not exactly, by a two-dimensional, cylindrical cell approximation.)

The overall design problem for a given PCM application involves

  (i)   selection of suitable material(s) for the container and
         filler

  (ii) selection of an appropriate PCM
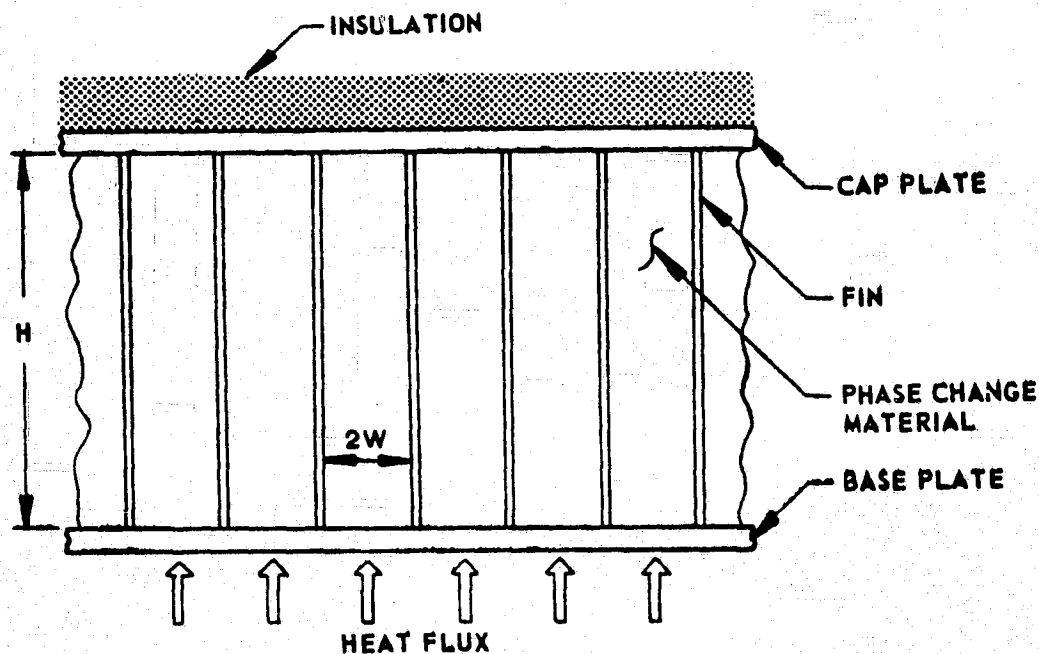
Figure 1. Cross—Section of a Typical PCM Thermal Capacitor

       (iii)   determination of the filler material (fin, honeycomb, etc.) design, and

       (iv)   sizing the device to accomplish its intended purpose.

Hale, et al., [1] , and Humphries [2] , consider the first two of the above, with emphasis upon properties of the phase change material. Reference 1 considers the use of aluminum, titanium, and stainless steel for the container and filler material. Reference 2 summarizes the properties of approximately twenty paraffins that could be used in thermal capacitors for space applications. References 1 and 6 consider the problem of volume change accompanying phase change; the latter of these references considers the resulting stress problem. The overall size of a capacitor is easily determined for a specific service following completion of items (i), (ii), and (iii).

    The most difficult part of the design is item (iii). With reference to figure 1, it is quite obvious that the rate of energy absorption, for example, is closely related to fin spacing, fin thickness, etc., for a given temperature potential for heat transfer. The fin (or filler material) design can only be based upon an accurate transient thermal analysis, or experimental data.

OBJECTIVES

The present study is a continuation of a long range effort to provide parametric results using numerical analyses which, in turn, will permit expeditious filler element design of two-dimensional PCM-type capacitors. To accomplish this, the primary objective was to obtain results for 300 specific cases; these were defined prior to the beginning of the present summer program by the NASA research counterpart.

A secondary objective was to investigate the suitability of a one-dimensional analysis for predicting the performance of a two-dimensional capacitor element.

LITERATURE REVIEW

Efforts directed toward analysis of phase change thermal control devices include, among others, the general study by Hale, Hoover, and O'Neill [1] , the extensive work of Humphries [2] , the numerical studies pertaining to a single cell by Griggs [3] and Pitts [4] , the further experimental and numerical investigation of Griggs [5] , the continuing analytical efforts of Bailey and his co-workers [6] , and the experimental and numerical investigation of Abhat and Groll [7]. The analysis of reference 1 assumes a linear temperature gradient and a one-dimensional model within the capacitor to carry out a parametric study resulting in estimates of fin thickness-to-PCM material thickness, etc., for application purposes. The two-dimensional analysis of reference 2 utilizes experimental fin temperature gradients, as does that of reference 3. The numerical study of reference 5 includes determination of the fin temperature distribution as a part of a two-dimensional analysis, while reference 4 outlines the non-dimensionalization of the two-dimensional cell and begins the parametric study. Reference 6 reports an analytical technique for predicting outlet fluid temperatures for a coolant-PCM thermal capacitor heat exchanger. Reference 7 employs the Chrysler-Sinda lumped capacity network and a semi-one-dimensional approach in a numerical study which predicts the thermal performance of a PCM device. In this last work, results were obtained for three configurations, i.e., no filler, aluminum fins, and aluminum honeycomb; and these are compared with experimental results.

The present study is part of an effort to furnish a wide range of parametric results for a two-dimensional capacitor utilizing straight rectangular aluminum fins extending from the base plate to the top or cap plate. This design was chosen for geometric simplicity and because it represents some of the designs used in NASA programs. A secondary objective of the current work is the

determination of the range of applicability of a modified one-dimensional approach which could be used for two-dimensional (fins) or three-dimensional (honeycomb) filler material designs.

ANALYSIS

The following presentation is similar to that part of reference 4 which pertains to an implicit formulation, and this is given here in slightly improved form for the sake of completeness.

The straight fin filler design with uniform fin spacing results in a number of similar cells as shown in figure 2. For space applications,
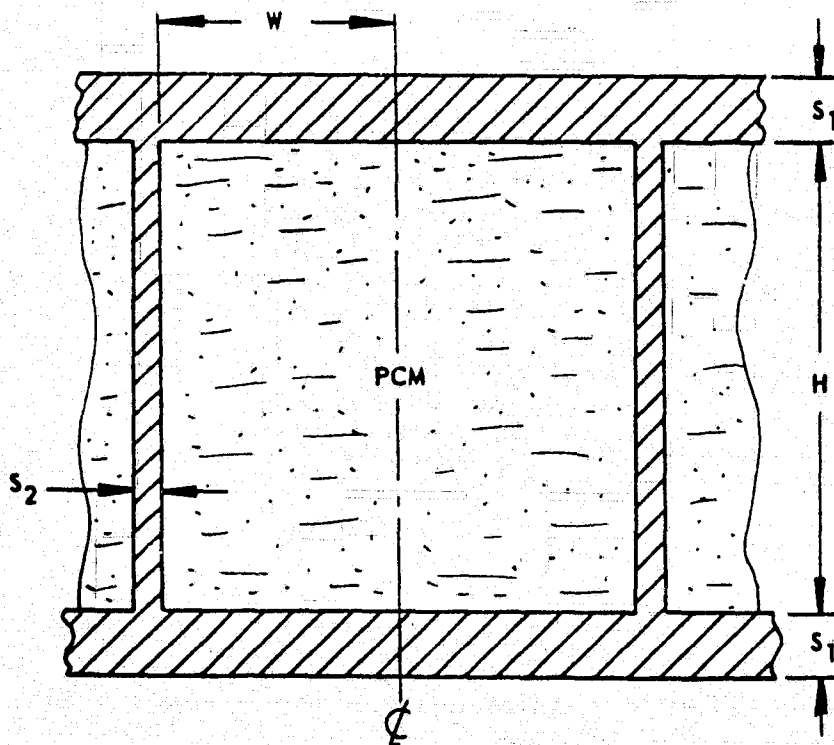
Figure 2. Typical Capacitor Cell

the dominant heat transfer mode within the cell is pure conduction.
The appropriate differential equations and their non-dimensionalization
are presented in reference 4. For the class of problem with a constant
heat transfer rate into the capacitor, the dimensionless ratios
obtained are

Geometric: $R_1 = H/W$

$R_2 = H/S_1$

$R_3 = W/S_2$

Material Properties: $R_4 = k/k_w$

$R_5 = \alpha/\alpha_w$

$R_6 = h_f/c_{pw}T_{melt}$

$R_7 = h_f/h_{TR}$

Thermal Loading: $R_8 = q''H/k_w T_{melt}$

Here the ratio R_7 is included since some paraffin materials undergo
transition prior to regular fusion or melting. An example is n-eicosane.

Finite Difference Formulation

The transient, two-dimensional conduction equation appropriate
for the present problem is

$$k\left(\frac{\partial^2 T}{\partial x^2} - \frac{\partial^2 T}{\partial y^2}\right) = \rho c_p \frac{\partial T}{\partial t} \tag{1}$$

The numerical formulation is obtained by replacing the derivatives in
equation (1) with finite-difference approximations. In the present
work, the implicit (backward) representation of the time derivative
is used. For the general nodal model of figure 3, a Taylor's series
expansion approach to obtain finite difference expressions for each
derivative in equation (1) results in (see, for example, Chapman [8])

$$\frac{k}{(\Delta x)^2}\left(T_b' - 2T_a' + T_c'\right) - \frac{k}{(\Delta y)^2}\left(T_d' - 2T_a' + T_e'\right)$$

$$= \frac{\rho c_p}{\Delta t}\left(T_a' - T_a\right) \tag{2}$$
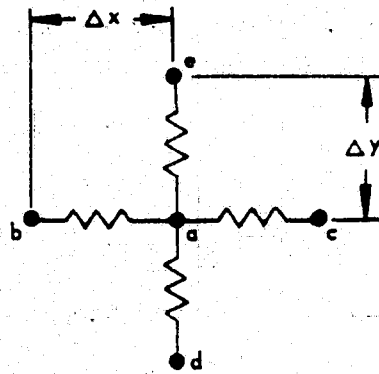
Figure 3. General Node

This expression relates the _future_ temperature at point a, T_a', to the present temperature at point a, T_a, and the _future_ temperatures of the four surrounding nodal points. Since the future temperatures of the surrounding nodal points are unknown at the start of a time step, it is necessary to perform a simultaneous solution of a set of equations, containing one like equation (2) for each nodal point in the temperature field, for each time step. Common mathematical methods for accomplishing this are matrix inversion or Gaussian elimination. The latter is usually preferable for thermal analyses according to Bayley, et al., [9], and is the method employed herein.

Grid Designation

The numerical analyses require an appropriate sub-division of the region of interest into a clearly defined grid network embodying nodal point identification. The scheme for nodal designation used in the present work is presented in figure 4. Since the accuracy of any numerical analysis depends somewhat upon the grid size, the present scheme was selected to permit flexibility for increasing or decreasing the number of nodes in accordance with the dictates of shape. Briefly summarizing, there are M x N PCM nodes; all J = 1 nodes are in the base plate, all J = N +2 nodes are in the cap plate, and all I = 1 nodes, for J greater than 1 and less than N + 2, are in the fin. The numbers of nodes in the base, cap, and fin are directly related to the PCM sub-division.
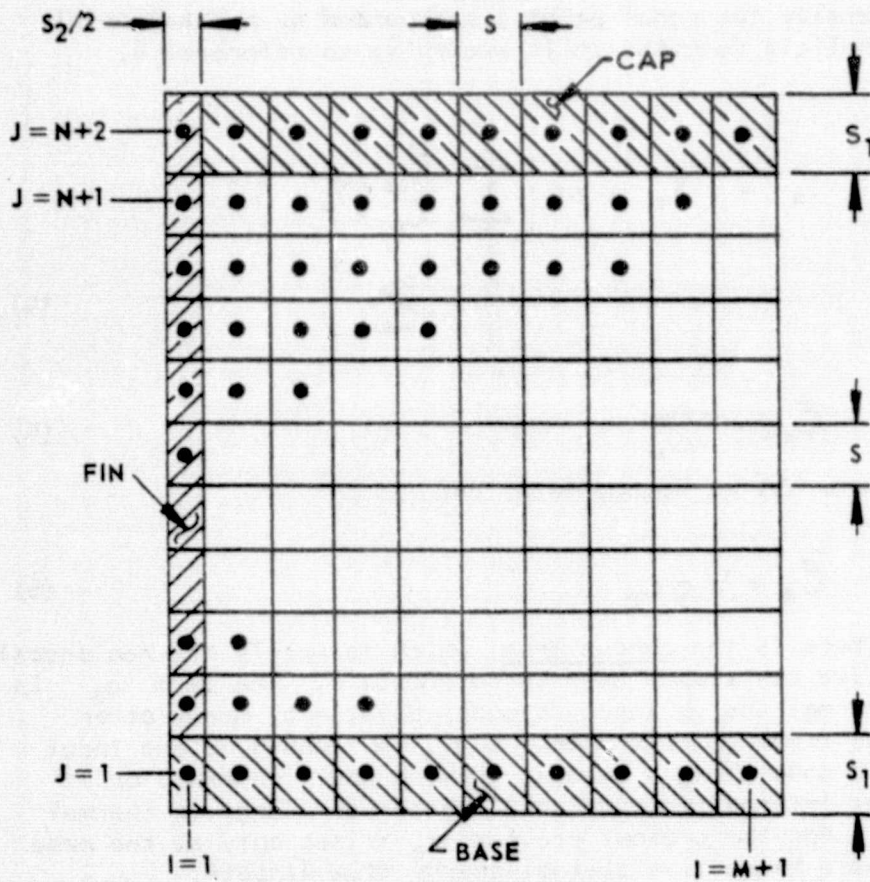
Figure 4. Nodal Grid Designation Scheme

Returning to equation (2), this can be rewritten as

$$\frac{kA_{ab}}{\Delta x}\left(T_b' - T_a'\right) + \frac{kA_{ac}}{\Delta x}\left(T_c' - T_a'\right) + \frac{kA_{ad}}{\Delta y}\left(T_d' - T_a'\right)$$

$$+ \frac{kA_{ae}}{\Delta y}\left(T_e' - T_a'\right) = \overline{C}_a\left(\frac{T_a' - T_a}{\Delta t}\right) \tag{3}$$

where, for example, A_{ab} is the area for conduction normal to a line connecting nodes a and b; thus, $A_{ab} = \Delta y(1)$ for unit depth. C_a is the product of mass associated with node a and its specific heat, so $\overline{C}_a = \Delta x \Delta y(1)(\rho)(c_p)$.

19-11

More generally for nodal point a surrounded by n other nodal points, the implicit formulation is according to reference 8.

$$T_a' = T_a + \Delta t \left[\sum_n \frac{\bar{G}_{an}}{\bar{C}_a} (T_n' - T_a') \right.$$
$$\left. + \frac{q_a}{\bar{C}_a} \right] \qquad (4)$$

where
$$\bar{G}_{an} = \frac{k A_{an}}{\Delta_{an}} \qquad (5)$$

Δ_{an} being Δx or Δy as appropriate, and

$$\bar{C}_a = V \rho c_p \qquad (6)$$

The $\bar{G}_{an}$ used here is the <u>conductance</u>, which is merely the reciprocal of the conductive resistance used in reference 8. The term q_a is the rate of thermal energy input to nodal point a by means other than conduction from adjacent nodes, e.g., this could be the input heat flux for a node along a boundary having heat transfer, or it could represent internal conversion of matter or energy to thermal energy (heat). For the present problem, q_a arises only at the base plate nodes where there is a thermal energy flux (input).

To implement a parametric study, it is convenient to formulate the set of nodal equations in non-dimensional form. Consequently, equation (4) is written in non-dimensional form for each nodal point of figure 4. To effect this, all temperatures are non-dimensionalized by dividing by the PCM melt temperature, T_{melt}. The time increment is non-dimensionalized by multiplying by H^2/α, the conductances are formulated in terms of the previously listed dimensionless ratios, and the capacitances are non-dimensionalized by division by the capacitance of a PCM node. In this manner, a typical nodal equation becomes

$$T2(I,J) = T1(I,J) - \frac{DT}{C(I,J)} \left\{ GH(I,J)\left[T2(I-1,J) - T2(I,J)\right] \right.$$
$$+ GH(I+1,J)\left[T2(I+1,J) - T2(I,J)\right] \qquad (7)$$
$$+ GV(I,J)\left[T2(I,J-1) - T2(I,J)\right]$$
$$\left. + GV(I,J+1)\left[T2(I,J+1) - T2(I,J)\right] \right\}$$

where q_a has been omitted since it is zero for all but
the base plate nodes. (This is, of course, included in the base
plate nodal equations used in the numerical program.) Here

$T2(I,J)$ = future dimensionless temperature of node (I,J)

$T1(I,J)$ = present dimensionless temperature of node (I,J)

DT   = dimensionless time increment, $(\Delta t)H^2/\alpha$

$GH(I,J)$ = dimensionless conductance between nodes
                $(I-1,J)$ and (I,J), see figure 5

$GV(I,J)$ = dimensionless conductance between nodes
                $(I,J-1)$ and (I,J), see figure 5
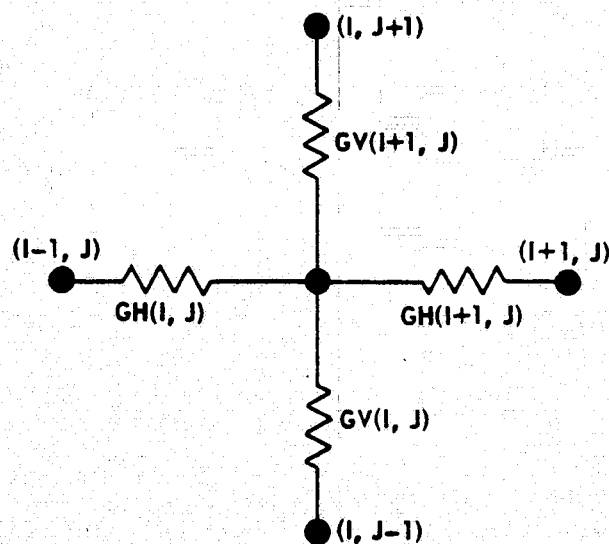
Figure 5. Conductance Designations

As a specific example of a dimensionless conductance, consider the horizontal conductance between the fin and the lower left hand corner PCM node. With reference to figures 4 and 5, application of Fourier's law yields a dimensional conductance

$$\overline{GH}(2,2) = \left[\frac{S_2}{4kBS} - \frac{1}{2K_wB} \right]^{-1} \tag{8}$$

where B is the depth (3rd dimension). Non-dimensionalizing by dividing by a wax node-to-wax node conductance, k_wBS/S, this can be expressed as

$$GH(2,2) = \frac{2}{1 + M/2R_3R_4} \tag{9}$$

Similarly, a typical vertical conductance, say that from a base plate node to an adjacent PCM node, is

$$GV(3,2) = \frac{2}{1 + R_1M/R_2R_4} \tag{10}$$

As an example of a capacitance, consider a base plate node for $I \geq 2$, say node (2,1). Then by use of the dimensionless ratios

$$\overline{C}(2,1) = \rho c_p V(2,1)$$
$$= \left(\rho_w c_{pw} S^2 B \right) \frac{MR_1R_4}{R_2R_5} \tag{11}$$

which after non-dimensionalization (i.e., division by a PCM nodal capacitance) is simply

$$C(2,1) = MR_1R_4/R_2R_5 \tag{12}$$

In like manner, all conductances and capacitances were formed and non-dimensionalized, and these are given in the computer program listing of Appendix A.

The computer program in simplified flow diagram form is shown in figure 6. The program constructs a square matrix of nodal equations, one for each node. The set of simultaneous, linear algebraic equations is then solved by the Gauss-Doolittle elimination technique using the BANSOL algorithm. For details of the method, see, for example, Segui [10].

PARAMETRIC STUDY

The numerical model is capable of considering a wide combination of materials and run conditions, so long as (i) the problem is two-dimensional and (ii) the energy input is a constant heat flux at the base. Under these two general conditions, one may employ a wide combination of geometric design ratios (R_1, R_2, and R_3) and various combinations of material property ratios (R_4, R_5, R_6, and R_7) for suitably selected values of thermal loading (R_8). Clearly, however, with this number of variables the total number of run condition combinations is extremely large. It was decided to consider only those conditions of possible future use in space flight applications. Further, the following conditions were to be employed for all runs:

- All runs begin at the melting temperature of the phase change material, but with latent energy of the PCM at zero.

- A typical aluminum material with
    $k = 93$ Btu/hr-ft-^{O}F.
    $\rho = 169$ lb$_m$/ft^3
    $C_p = 0.21$ Btu/lb$_m$-^{O}F.
  is used for the base and top plates, as well as for the fins.

- A typical paraffin material with
    $k_w = 0.087$ Btu/hr-ft-^{O}R
    $\rho_w = 50.0$ lb$_m$/ft^3
    $C_{p_w} = 0.50$ Btu/lb$_m$-^{O}R
    $h_f = 100$ Btu/lb$_m$
    $T_{melt} = 525^O$R
  is used as the PCM.

- As a consequence of beginning runs at T_{melt}, R_7 is not used in the program.

19-15
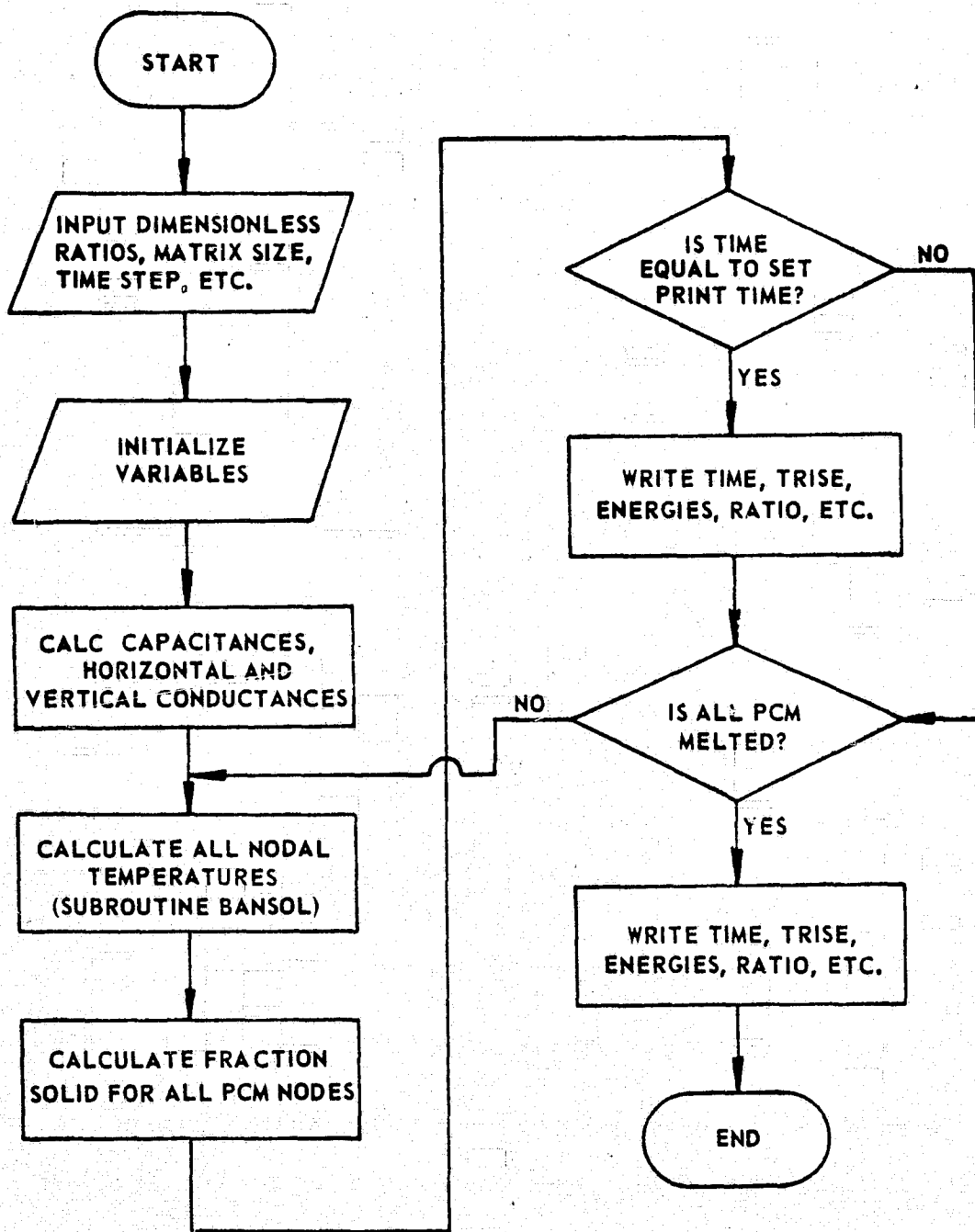
Figure 6. Computer Program Flow Diagram

This leaves the fin thickness, wax width, cell height, base and cap thicknesses, and heat flux at the base as variable run parameters. It was decided to fix the base thickness (one value) and to use five (5) wax widths, five (5) cell heights, three (3) fin thicknesses, and four (4) heat input rates.

The values used are

- base thickness, S_1 = 0.025 in.

- wax width, 2W = 0.1, 0.2, 0.4, 0.8, 1.6 in.

- cell height, H = 0.5, 1.0, 20., 4.0, 8.0 in.

- fin thickness S_2 = 0.005, 0.02, 0.05 in.

- heat flux rate, q'' = 100, 200, 400, 600 watt/ft^2

Run Matrix

The procedure followed was with the fin thickness S_2 fixed, the wax width 2W was varied over the five specified values. For each value of 2W,

- runs were made for each of five values of H

- for each combination of H and 2W, runs were made with each of the three values of S_2,

- for each combination of H, 2W, and S_2, runs were made for each of the four specified values of q''.

Thus, the total number of planned runs was

No. of runs = (5)(5)(3)(4) = 300

Of these, more than 200 have been completed at MSFC during the current summer NASA-ASEE Program. The remainder are being completed by co-workers at Tennessee Technological University, Cookeville, Tennessee. A sizeable number of overlapping runs have been undertaken here and at Tennessee Tech with excellent agreement between results.

RESULTS

Typical results obtained during the current program are presented in figures 7 and 8. In these, TRISE is the temperature of the base plate above the melting temperature of the wax non-dimensionalized by
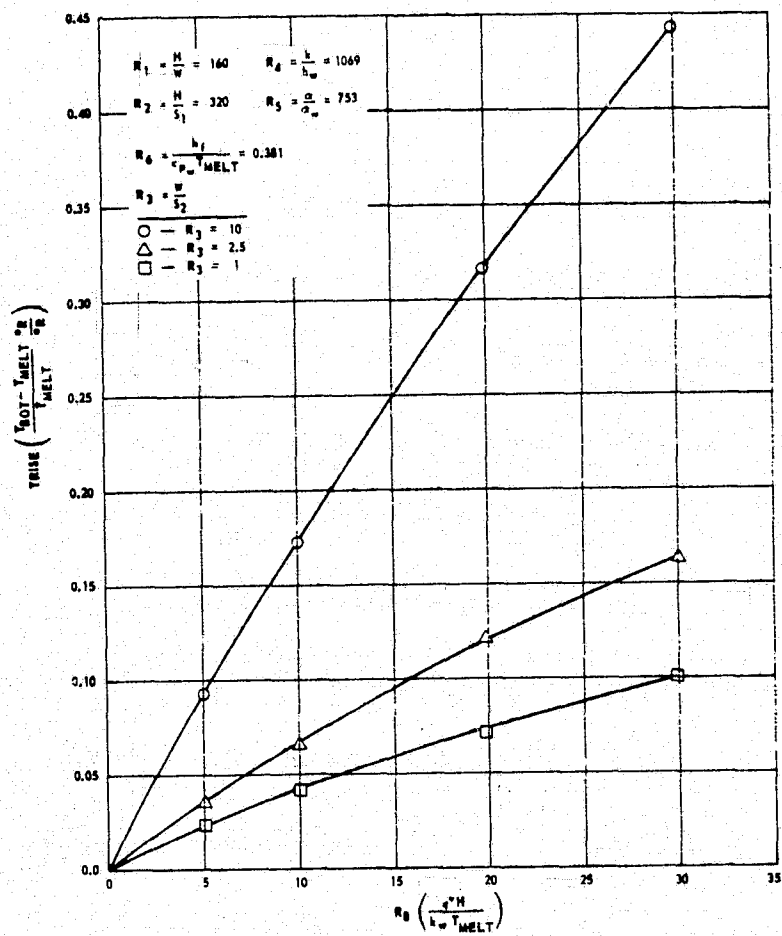
Figure 7. Typical TRISE vs. Thermal Load for a Tall Cell (Large R_1)
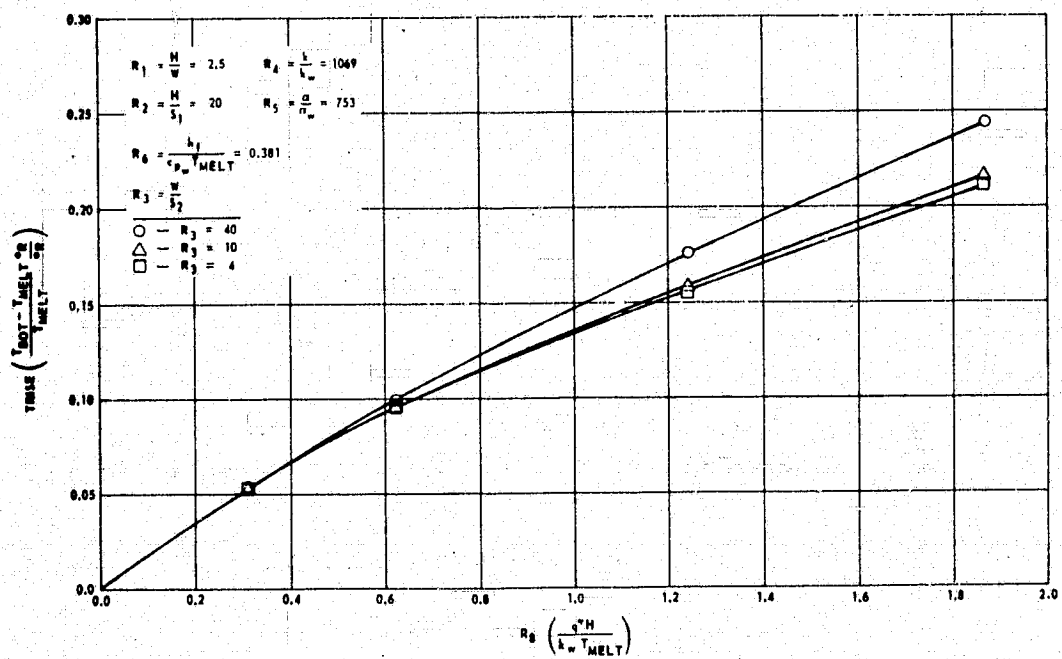
Figure 8. Typical TRISE vs. Thermal Load for a Short Cell (Small R_1)

$$TRISE = \frac{T_{Base} - T_{melt}}{T_{melt}} \tag{13}$$

where all temperatures are in absolute units. The values plotted in these figures are at the point in time when all wax has just finished melting. In effect, each of these figures presents the effects of varying R_3 (wax-to-fin base area ratio) and of varying R_8 (thermal loading), holding all other parameters fixed. These two figures were selected because they represent some noteworthy results.

In figure 7, the value of TRISE quickly becomes very large with increasing thermal loading. In fact, for $R_3 = 10$, it is evident that the higher R_8 values used in this stidy would result in some vaporization (boiling) within the cell - this condition certainly was not suspected prior to this study, although the investigators were somewhat concerned over the total range of conditions to be evaluated. In reality, TRISE values above approximately 0.1 to 0.2 are of questionable use, and it is also recognized that the use of constant thermal properties in the analysis is also questionable for large TRISE.

In figure 8, we have the rather unusual condition of R_3 not strongly influencing the overall performance, at least not in the range of TRISE of interest.

The complete results of this parametric study will be presented in a forthcoming report.

ONE-DIMENSIONAL MODEL

For several reasons, it appears to be desirable to evaluate the feasibility of using a one-dimensional model to represent a two- or three-dimensional capacitor. Clearly the computational time would be greatly reduced by the use of a one-dimensional model which would require division of the cell into a number of horizontal layer-type nodes. The resulting number of simultaneous algebraic equations would be considerably smaller for the same nodal dimension (vertically), and consequently, computer storage requirements and computational time would be reduced accordingly.

A second major reason is evident for the case of honeycomb-type filler materials. The resulting PCM cell in this case is clearly three-dimensional (which could be approximated reasonably well by a two-dimensional cylindrical model), and this could require even more computer storage and time than the two-dimensional model used for plate-type filler material in the present work.

Clearly, if a one-dimensional model is desired, a completely different formulation than that for the two-dimensional problem should be used. However, for the purpose of determining the suitability of a one-dimensional approach, a plausible attack is to simply compare one-dimensional results with those obtained with the two-dimensional model. This can be directly accomplished by modification of the two-dimensional computer program to render it one-dimensional; this is accomplished by the elimination of all heat transfer in the horizontal direction between adjacent nodes, i.e., by setting all $GH(I,J) = 0.0$. Also, appropriate modification of material properties is required. This approach permits direct comparison of the one-dimensional approximation with the more accurate two-dimensional approach under otherwise identical conditions.

With reference again to figure 2, it is clear that the two-dimensionality of the present model is a result of the filler material (fins) which are present only to enhance the energy transfer rate from the base into the phase change material. A logical approach to one-dimensionalization is then to consider the filler material as an "additive" which alters the thermal properties of the PCM. One such approach is to use volume-averaged thermal properties. But for a cell of constant height H and constant depth B, a volume-averaged property is the same as a base area-averaged property which is

$$\phi_{av} = \frac{2 R_3 \phi_w + \phi}{2 R_3 + 1} \tag{14}$$

where ϕ represents any thermal property. Here the unsubscripted value is that of the filler material (fin), while ϕ_w is that of the phase change material.

The computer program was modified to result in one dimensionality, and this involved the following:

1. Average values of thermal conductivity, density, specific heat, enthalpy of fusion, and thermal diffusivity are calculated.

2. R_4, R_5, R_6, and R_8 are modified to use average properties.

3. The dimensionless time step, (DT), is modified in agreement with the average thermal diffusivity.

4. All horizontal conductances are set equal to zero.

5. All capacitances in the base and cap are modified because of changes in R_4 and R_5.

6. All vertical conductances involving material in the base and cap are modified because of changes to R_4 and R_5.

7. In the "fraction solid" and temperature calculations, the "fin" nodes ($I = 1$) are allowed to melt in the same fashion as all PCM nodes.

8. The write statement and format were modified to include printout of an equivalent two-dimensional time, TIME2D.

A listing of the one-dimensional program is available from the author.

ONE-DIMENSIONAL RESULTS

A number of runs were undertaken with the one-dimensional model. Typical results are shown in figures 9, 10, and 11. Each of these figures contains the transient plots of T_{RISE} obtained under like conditions with both the two-dimensional and the one-dimensional models. The only difference between the three figures is the value of R_3, the ratio of phase change material base area to filler material base area. Figure 9 is for $R_3 = 80$, and the 1-D and 2-D models are in very good agreement. This agreement degenerates with decreasing R_3 as seen in figures 10 and 11 which were obtained with R_3 values of 20 and 8, respectively.

Efforts are continuing to evaluate the range of suitability of the one-dimensional model, but it is not expected to be appropriate for values of R_3 less than 20.

CONCLUSIONS AND RECOMMENDATIONS

As a result of the current study, the following conclusions were reached.

1. The total range of conditions used in the two-dimensional study results in sufficient parametric data to permit initial design of a thermal capacitor for most space mission applications.

2. A one-dimensional model can be used to predict the performance of a two-dimensional design so long as the ratio of phase change material volume to filler material volume is large, i.e., approximately 20 or greater.

It is recommended that the present parametric study be concluded with a presentation of the total set of results in graphical form, and that the range of applicability of the one-dimensional model be further investigated.
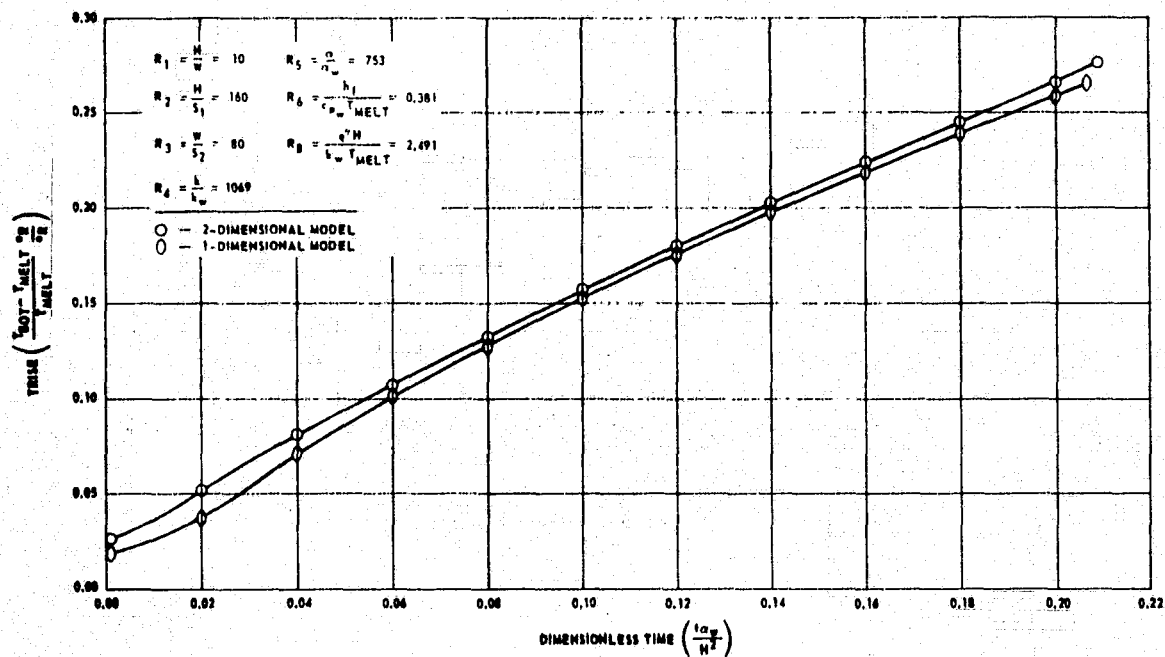
Figure 9. Transient TRISE for Run 55 -- Comparison of Two-Dimensional
and One-Dimensional Solutions
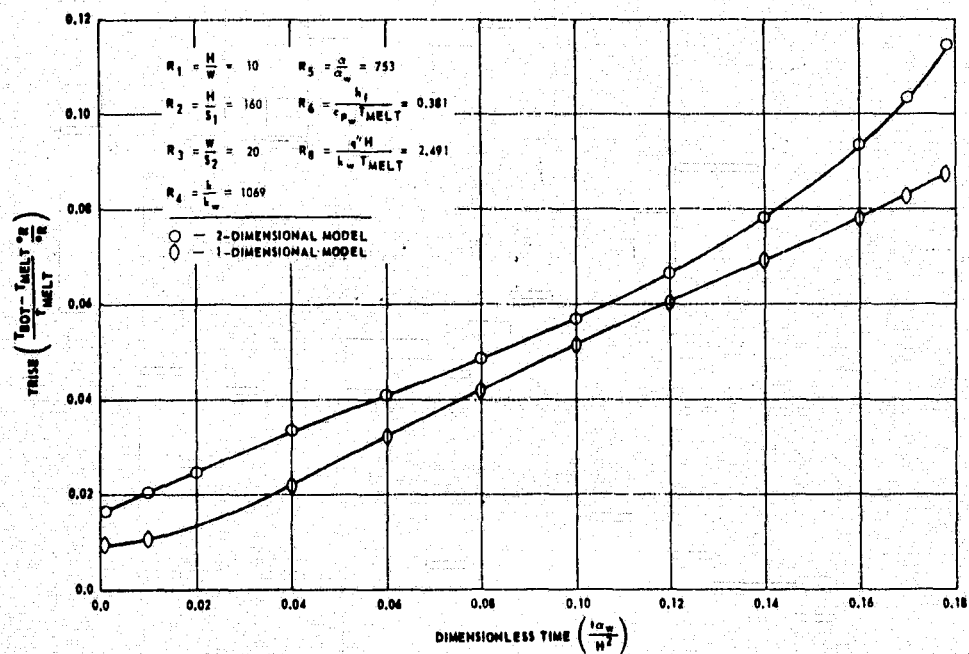
Figure 10. Transient TRISE for Run 56 -- Comparison of Two-Dimensional
and One-Dimensional Solutions
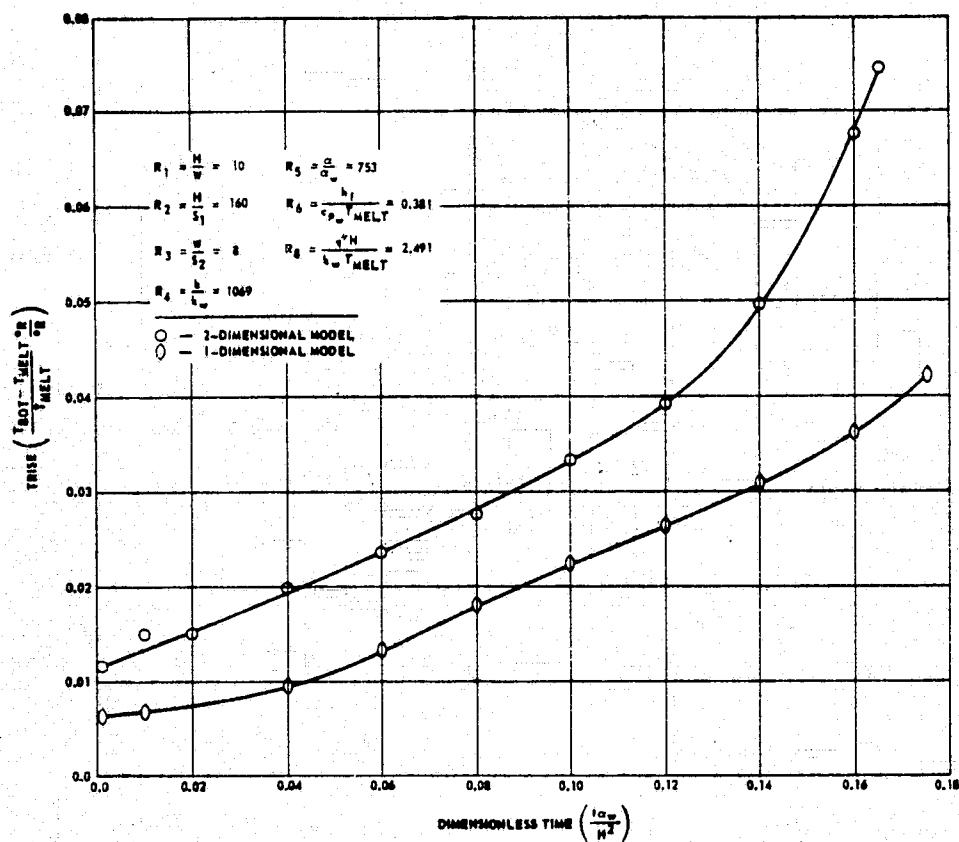
Figure 11. Transient TRISE for Run 57 -- Comparison of Two-Dimensional and One-Dimensional Solutions

19-24

REFERENCES

1.   Hale, D. V., M. J. Hoover, and M. J. O'Neill, "Phase Change Materials Handbook," NASA CR-61363, MSFC, Al., Sept., 1971.

2.   Humphries, W. R., Unpublished Doctoral Dissertation, University of Texas, Austin, Texas, 1974.

3.   Griggs, E. I., "Thermal Capacitor Study," Contract No. NGT-01-002-080, Univ. of Alabama--Auburn Univ. Res. Dept., 1971 NASA-ASEE Summer Faculty Fellowship Program, Sept., 1971.

4.   Pitts, D. R., "Parametric Study of the Transient Response of a Thermal Capacitor Cell," Univ. of Alabama Bureau of Engineering Research Dept. BER

5.   Griggs, E. I., "Investigation of Some Characteristics Related to PCM Thermal Capacitors," NASA CR-61396, Sept. 1972.

6.   Bailey, J. A., et al., "Thermal Capacitor Design Rationale," Interim Reports 1 through 7, dated May 1, 1972 through May 31, 1974, Dept. of Aerospace and Mech. Engineering, North Carolina State Univ., Raleigh, N. C.

7.   Abhat, A., and M. Groll, "Investigation of Phase Change Material (PCM) Devices for Thermal Control Purposes in Satellites," Paper 74-728 AIAA/ASME Thermophysics and Heat Transfer Confrence, Boston, Mass. July 15-17, 1974.

8.   Chapman, A. J., Heat Transfer, 2nd ed., The Macmillan Company, New York, 1967.

9.   Bayley, F. J., J. M. Owen, and A. B. Turner, Heat Transfer, Barnes and Noble, New York, 1972.

10. Segui, W. T., "Computer programs for the Solution of Systems of Linear Algebraic Equations," NASA CR-2173, Jan., 1973.

APPENDIX A

TWO-DIMENSIONAL COMPUTER PROGRAM

```
10         DIMENSION A( 63,19), T((9,  7), T2( 63), GH(10, 7), GV(9,  7),
20        1C(9,  7), F( 63), TEXC( 63), D( 63), MELT( 63)
30         IMPLICIT REAL*8(A-H,O-Z)
40   C ***  R1 = H/R | R2 = H/S| | R3 = H/S| | R4 = R/R* | ***************
50   C ***  R5 = (K/DEN*CP)/(KR/DEN*CPR) | R6 = HMELT/CP*TMELT ************
60   C ***  R7 = HMELT/HTR | R8 = U*H/R*TMELT *****************************
70         R4=1049.
80         R5=753.
90         R6=0.38|
100        DO 999 IR=1,12
110        READ(5,998) R1, R2, R3, R8, R9, ITT
120  C *** COMPUTATIONAL PARAMETERS ***
130        M = 8
140        N = 5
150        CR = 1.0
160        THELT = 1.0
170        DT=0.001
180        TCK = DT/2.0
190        ITIT = 1
200        TIN=1.0
210        SUS = 0.0
220        SUF = 0.0
230        SUB = 0.0
240        SUT=0.0
250        SUL = 0.0
260        QLAT = 0.0
270        ETUP = 0.0
280        EHOT=0.0
290        ITCB=0.0
300        MM = 0
310        TBOT = 0.0
320        TPHASE = R6
330        TIME = 0.0
340        AN = N
350        AM = M
360        QLATM = AM*AN
370        AMI = AM + 1.0
380        M1 = M + 1
390        M2 = M1 + 1
400        N1 = N + 1
410        N2=N+2
420        LL=N2*N1
430        L1 = 2*M1 + 1
440        L = M2
450        CD = (R1**2)*(AM**2)
460        DO 10 I = 1,LL
470        F(I) = 1.0
480        MELT(I)=G
490  10    TEXC(I) = 0.0
500        DO 20 J=1,N2
510        DO 20 I = 1,M1
520  20    T((I,J) = TIN
530  C ***** HORIZONTAL CONDUCTANCES,VERTICAL CONDUCTANCES,CAPACITANCES **
540  C ****  ARE CALCULATED *******
550        GV(1,1) = 0.0
560        DO 30 J=2,N1
570        DO 30 I=2,M1
580        GH(1,J) = 1.0
590        C(I,J) = 1.0
600  30    GV(I,J) = 1.0
610        DO 40 J = 2,N1
620        C(I,J) = (R8*AM1/(2.0*M6*R3)
630        GV(I,J) = (AM*R9)/(2.0*R3)
640        GH(2,J) = 2.0/(1.0 + AM/(2.0*R3*R4))
650        GH(M2,J)=0.0
660  40    GH(I,J) = 0.0
670        DO 50 I = 2,M1
680        C(I,1) = (AM*R1*R4)/(R2*R5)
690        C(I,N2)=C(I,1)
700        GV(I,2) = 2.0/(1.0 + (R1*AM/(R2*R4)))
710        GV(I,N2)=GV(I,2)
720        GV(I,1) = 0.0
730        GH(I,1) = R4*AM*K1/R2
740  50    GH(I,N2)=GH(I,1)
750        GH(I,1) = 0.0
760        GH(I,N2)=0.0
770        GH(M2,1)=0.0
780        GH(M2,N2)=0.0
790        GH(2,N2)=GH(2,1)
800        GV(I,2) = N9/(R3*(1.0/AM + K1/R3))
810        GH(2,1) = 2.0*N9/((R2/R1)*((1.0/(2.0*R3) + 1.0/AM))
820        GV(I,N2)=GV(I,2)
830        C(I,1) = (R1*N9*(AM**2))/(2.0*R2*R5*R8)
840        C(I,N2)=C(I,1)
850        DO 55 I=1,M1
860  55    TICR=TTCD*C(I,1)
870  C **** TEMPERATURES AT EACH NODE CALCULATED ***
880        WRITE(6,7500) R1, R2, R3, R4, R5, R8, R9, M, N, MM, ITT
890  60    TIME = TIME + DT
900        DO 70 I = 1,LL
910        DO 70 J = 1,L1
920  70    A(I,J) =0.0
930        DO 80 J=2,N1
940        DO 80 I = 1,M1
950        K = (J-1)*M1 + I
960        A(K,L-M1) = GV(I,J)
970        A(K,L*M1) = GV(I,J+1)
980        A(K,L) = -GH(I,J) - GV(I,J) - GV(I,J+1)-(C(I,J)/TOT+CD))-GH(I,J)
990        A(K,L+1) = GH(I,J)
```

19-26

```
1000        A(K,L+1) = GH(I+1,J)
1010     80 U(K) = -C(I,J)*T(I,J)/(CD*DT)
1020        DO 90 I=1,M1
1030        K=N(I)+I
1040        A(I,L) = -GH(I+1,1) - GH(I,1) - GV(I,2)  - C(I,1)/(DT*CD)
1050        A(I,L+1) = GH(I+1,1)
1060        A(I,L-1) = GH(I,1)
1070        A(I,L+M1) = GV(I,2)
1080        A(K,L) = -GH(I,N2) - GH(I+1,N2) - GV(I,N2) - C(I,N2)/(DT*CD)
1090        A(K,L-1) = GH(I,N2)
1100        A(K,L+1) = GH(I+1,N2)
1110     90 A(K,L-M1) = GV(I,N2)
1120        DO 110 I=1,M1
1130        K=N(I)+I
1140        U(I) = -C(I,1)*T(I,1)/(DT*CD) - RA/(M1*N1*DA)
1150    110 U(K) = -C(I,N2)*T(I,N2)/(DT*CD) - RA/(I2,8*N3*R1)
1160        U(I) = -C(I,1)*T(I,1)/(CD*DT) - RA/(I2,8*N3*R1)
1170        CALL BANSOL(A,LL,L,U,LL)
1180        DO 120 I=1,LL
1190    120 T2(I) = U(I)
1200  C  *** QUALITY CALCULATED ***
1210        DO 150 J=2,N1
1220        DO 150 I=2,M1
1230        K=(J-1)*M1 + I
1240        IF(MELT(K).GE.1) GO TO 150
1250        IF(T2(K).GT.TMELT)EXC(K) = EXC(K) + (T2(K) - TMELT)
1260        IF(T2(K).GE.TMELT)P(K) = 1.0 - TRA(K)/(RA0*TMELT)
1270        IF(T2(K).GT.TMELT) T2(K)=TMELT
1280        IF(EXC(K).GE.TPHASE)T2(K)=TMELT+EXC(K)-TPHASE
1290        IF(EXC(K).GE.TPHASE) P(K)=0.0
1300        IF(EXC(K).GE.TPHASE) MELT(K)=1
1310    150 CONTINUE
1320        DO 160 J = 1,N2
1330        DO 160 I = 1,M1
1340        K = (J-1)*M1 + I
1350    160 T(I,J) = T2(K)
1360        QLAT = 0.0
1370        DO 170 J= 2,N1
1380        DO 170 I = 2,M1
1390        K = (J-1)*M1 + I
1400    170 QLAT = QLAT + ( I*0 = P(K))
1410        IF(ABS(QLATH - QLAT).LT.0.0001) GO TO 180
1420        THIF = ABS(TIME - DT)
1430        IF(TU(IF.LT.TCK)ITT = ITT + 1
1440        IF(TU(IF.LT.TCK)GO TO 180
1450        IF(ITT.NE.(ITT)ITT = ITT + 1
1460        IF(ITT.NE.(ITT)GU TO 240
1470        ITT = 1
1480    180 DO 176 I=1,M1
1490        LTOP = LTOP + (C(I,N2)*(T(I,N2)-T(N))
1500    176 EBUT=EBUT+(C(I,1)*(T(I,1)-T(N))
1510        THUT=TIME+(EBUT/TIC8)
1520        TTOP = TIN + (LTUP/TIC8)
1530        LTUP = 0.0
1540        EBUT=0.0
1550        TRISE = TBOT - TMELT
1560        UCOEF = RA/(IQUT - TMELT)
1570        WRITE(6,8000)TIME,TRISE,UCOEF,TTOP
1580  C  *** ENERGY BALANCED ***
1590        DO 200 J = 2,N1
1600    200 SQF = SQF + (C(I,J)*(T(I,J) - TIN)/R6)
1610        DO 210 I = 1,M1
1620    210 SQT=SQT+(C(I,N2)*(T(I,N2)-TIN)/R6)
1630    210 SQB = SQB + (C(I,1)*(T(I,1) - TIN)/R6)
1640        DO 220 J = 2,N1
1650        DO 220 I = 2,M1
1660        K = (J-1)*M1 + I
1670        SQS=SQS+(C*(T2(K)-TIN)*P(K)/R6)
1680    220 SQL=SQL+(C*(T2(K)-TIN)*(1.0-P(K))/R6)
1690        QTOT = SQF + SQB + SQS + SQL + QLAT + SQT
1700        EIN = (AM*2*N1*N*N3)*(1.0 * 1)*U/(2.8*R1))*TIME
1710        RATIO = QTOT/EIN
1720        WRITE(6,1500)SQF,SQB,SQT,SQS,SQL,QLAT,QTOT,EIN,RATIO
1730        SQF = 0.0
1740        SQB = 0.0
1750        SQT=0.0
1760        SQS = 0.0
1770        SQL = 0.0
1780        THUT = 0.0
1790    240 IF(ABS(QLATH - QLAT).GT.0.0001) GO TO 60
1800    999 CONTINUE
1810   1500 FORMAT(1H ,'SQF =',F10.6,5X,'SQB =',F10.6,5X,'SQT =',F10.6,4X,
1820        1 'SQS =',F10.6,5X,'SQL=',F10.6,5X,'QLAT =',F10.6,5X,'QTOT =',F10.5,
1830        2 5X,'EIN =',F10.5,5X,'RATIO =',F10.4)
1840    998 FORMAT(4F10.6,2I5)
1850   2000 FORMAT(1H1)
1860   4000 FORMAT(1H ,T35,'HORIZONTAL CONDUCTANCE')
1870   5000 FORMAT(1H ,T35,'VERTICAL CONDUCTANCE')
1880   6000 FORMAT(1H ,T35,'THERMAL CAPACITANCE')
1890   7000 FORMAT(1H )
1900   7500 FORMAT(1H1,'K1=',F7.3,3X,'N2=',F6.1,3X,'R3=',F6.1,3X,'N4=',F7.1,3X
1910        1 'N5=',F5.1,3X,'N6=',F5.3,3X,'N8=',F6.3,3X,'M7=',I2,3X,'M9=',I3,3X,
1920        2'RUN NO. =',I3,4X,'ITT=',I2)
1930   8000 FORMAT(1H0,'TIME =',F7.5,6X,'TRISE =',F7.5,6X,'UCOEF =',F10.5,6X,
1940        1'TTOP =',F7.6)
1950        CALL EXIT
1960        END
```

END OF COMPILATION.   NO DIAGNOSTICS.

```
 1*        SUBROUTINE BANSOL(C,N,M,V,IV)
 2*        DIMENSION C(10,M),V(10)
 3*        IMPLICIT REAL*8(A-H,O-Z)
 4*        L = IMK/2
 5*        LI = L + 1
 6*        DO 2 IK = 1,LI
 7*        LK = L - IK
 8*        DO 2 I = 1,LK
 9*        DO 1 J = 2,M
10*      1 C(IK,J-1) = C(IK,J)
11*        MPI = N + 1 - IK
12*        MPI = M + 1 - I
13*        C(IMPI,MPI) = 0.0
14*      2 C(IK,M) = C(IMPI,MPI)
15*        MJ = M + 1
16*        DO 4 I = 1,MJ
17*        IPIV = I
18*        IMK = I + IMK
19*        DO 3 IK = IMK,L
20*        IF(ABS(C(IK,1)).LE.ABS(C(IPIV,1))) GO TO 3
21*        IPIV = IK
22*      3 CONTINUE
23*        IF(IPIV.EQ.I) GO TO 6
24*        T = V(I)
25*        V(I) = V(IPIV)
26*        V(IPIV) = T
27*        DO 4 J = 1,M
28*        T = C(I,J)
29*        C(I,J) = C(IPIV,J)
30*      4 C(IPIV,J) = T
31*      5 V(I) = V(I)/C(I,1)
32*        DO 6 J = 2,M
33*      6 C(I,J) = C(I,J)/C(I,1)
34*        DO 8 IK = IMK,L
35*        T = C(IK,1)
36*        V(IK) = V(IK) - T*V(I)
37*        DO 7 J = 2,M
38*      7 C(IK,J-1) = C(IK,J) - T*C(I,J)
39*      8 C(IK,M) = 0.0
40*        IF(I.LE.N) GO TO 9
41*        L = L + 1
42*      9 CONTINUE
43*        V(N) = V(N)/C(N,1)
44*        JM = 2
45*        DO 11 ICK = 1,N1
46*        IK = N - ICK
47*        DO 10 J = 2,JM
48*        IKM = IK - 1 + J
49*     10 V(IK) = V(IK) - C(IK,J)*V(IKM)
50*        IF(JM.EQ.M) GO TO 11
51*        JM = JM + 1
52*     11 CONTINUE
53*        RETURN
54*        END
```

1974

ASEE - NASA SUMMER FACULTY FELLOWSHIP PROGRAM

MARSHALL SPACE FLIGHT CENTER

(AUBURN UNIVERSITY - UNIVERSITY OF ALABAMA)

STRESS CONCENTRATION FACTORS

VIA THE FINITE ELEMENT METHOD

Prepared by:	Thomas R. Rogge, Ph.D.
Academic Rank:	Associate Professor
Department and University:	Department of Engineering Science and Mechanics Iowa State University
NASA/MSFC Assignment: (Laboratory) (Division) (Branch)	Structures and Propulsion Engineering Analysis Strength Analysis
NASA Research Colleague:	John E. Key
Date:	August 9, 1974
Contract No.:	NGT-01-003-045

STRESS CONCENTRATION FACTORS VIA THE FINITE ELEMENT METHOD

By

Thomas R. Rogge

ABSTRACT

Finite element analysis is used to study the stress distribution in the neighborhood of holes in plates under uniaxial tension. In particular, the stress concentration factor defined as $K = \sigma_{max}/\sigma_{nom}$ is computed and compared to both analytical and experimental results. Both isotropic and anisotropic materials are considered in this report.

In general, the finite element analysis gives a stress concentration factor smaller than the analytical or experimental results for isotropic materials.

ACKNOWLEDGEMENTS

NOMENCLATURE

K = stress concentration factor computed from maximum normal stress in y direction

K_p = stress concentration factor computed from maximum principal stress

k = stress intensity factor (psi $\sqrt{\text{in.}}$)

$\sigma_{xx} \; \sigma_{yy} \; \sigma_{xy}$ = Cartesian stresses (psi)

$u \quad v$ = displacements in the x, y direction

$T_x \; T_y$ = components of the stress vector in x, y direction

$E_1 \; E_2$ = modulus of elasticity in the two inplane principal material directions (psi)

G_{12} = shear modulus (psi)

ν_{ij} = Poisson's ratio giving strain in j-direction caused by a stress in i-direction (i, j = 1, 2)

INTRODUCTION

The introduction of defects into a material has long been recognized as a significant factor in reducing the useful life of the material. These defects in a material may be introduced during the production of the material, during the machining of the material, or during a fabrication process. Examples of the machining process are sharp notches left by milling machines or lathes while butt-welding can give rise to defects caused by fabrication. Depending on the design criteria adopted, the useful life of the material could be the fatigue life, the onset of plastic deformation, or fracture for brittle material. The defect contributes to a shortening of the useful life by increasing the magnitude of the stress distribution in a local neighborhood of the defect. Two different constants can be used to describe the effect of the defect in the material. One of the constants is a stress concentration factor while the other is the stress intensity factor. A stress concentration factor, K, is defined as $K = \sigma_{max}/\sigma_{nom}$ where σ_{max} is the stress at the tip of the defect and σ_{nom} is the nominal stress in the material away from the defect. Relations which exist between the stress concentration factor and the stress intensity factor, as shown in (1), allow calculation of one from knowledge of the other. In this paper, the stress concentration factor will be computed using the finite element method (FEM). These results will be compared to experimental results (2), (3) as well as analytic results (2).

The specific problem considered here is that of a plate in uniaxial tension with either a rectangular or elliptical shaped hole. Isotropic as well as certain anisotropic materials are considered. In all of the problems considered, the material is assumed to remain in the linear elastic range.

OBJECTIVES

The purpose of this work is to demonstrate the feasibility of using the finite element analysis method to calculate stress concentration factors. In many problems, the calculation presents massive analytic work or relatively difficult experiments. The FEM is relatively inexpensive and requires minimal analytic work.

PROBLEM DESCRIPTION

The problem to be considered here is that of a thin plate under uniaxial tension with a hole symmetrically located in the plate (figure 1). Physically the problem is considered to be one of plane stress. The shape of the hole is taken as either a rectangle or an ellipse and has one dimension which is small compared to the dimensions of the plate.

The size of the holes is changed while the width of the plate remains constant. This allows comparison of the finite element method results with both experimental and analytical results. As can be seen, the plate is symmetric so that only one-quarter of the plate needs to be used. Figure 2 shows a model of the plate that is used for the finite element method. The value of b was fixed and a and c were changed to examine different size holes. Also, the rectangular corner in a certain set of models was rounded to represent a fillet in the hole. With the inclusion of the fillet, one has an elliptical hole with a large major axis compared to its minor axis. The plate was subjected to a uniformly distributed axial load in the y direction and the maximum normal stress in the y direction as well as the maximum principal stress are used to compute the stress concentration factor. Because of the type of loading and geometry, the normal stress in the y direction and the maximum principal stress were close to each other in value. If the hole is considered small enough to behave like a crack, then it is possible to find the stress intensity factor from the stress concentration factor. The stress distribution about the crack tip can be computed using the stress intensity factor from the formulas given in (1).

Even though only centrally located holes are considered here, it can be easily seen that it is possible to consider holes in any arbitrary orientation and position and of any shape. Only two-dimensional problems are considered here, but three-dimensional problems can also be handled in a similar manner.

The finite element method is discussed extensively in (4) and many other books which will not be referenced here. The program used for these calculations is a modified version of the program found in (4). The elements used are either constant strain triangles or constant strain quadralaterals. A linear strain rectangle was also incorporated into the program and results from these runs are compared with the constant strain case.

To ensure a proper grid for the finite element model, the data were machine plotted and checked before the program was run. An example of a model is shown in figure 3. The finite element program is capable of handling isotropic as well as anisotropic materials, and stress concentration factors are given for examples of both types of materials.

The physical dimensions of the plate considered in the paper are 3.2-in. long and 2-in. wide with maximum hole length of 1.4 in. and maximum width of 0.2 in. For these dimensions, $L = 1.6$ in., $b = 1.0$ in., $0 < a \leq 0.7$ in., and $0 < c \leq 0.1$ in. In order to obtain good data near the hole, the dimensions of the elements need to be small. The smallest elements were 0.02 by 0.02 in. and had a ratio of element area to hole length square in the order of 10^{-4}. For convergence sake, (5) indicates this to be a reasonable size element near the hole so that the solutions should be close to the actual solutions.

The thickness of the plate was taken to be 0.07 in., and the load P was taken to be 70 lb. which corresponds to a uniaxial stress of 500 psi. The effect of the thickness was investigated and was seen not to influence the stress concentration factors. A problem in plane strain was also run, and again the results were not changed.

The boundary conditions for the quarter plate shown in figure 2 were as follows:

1. $x = 0$, $\sigma_{xx} = \sigma_{xy} = 0$

2. $y = 1.6$, $\sigma_{xy} = 0$, $\sigma_{yy} = 500$ psi

3. $x = 1.0$, $u = 0$, $\sigma_{xy} = 0$

4. $y = c$, $1-a < x \leq 1$, $\sigma_{xy} = \sigma_{yy} = 0$

5. $x = 1-a$, $0 \leq y < c$, $\sigma_{xx} = \sigma_{xy} = 0$

6. $y = 0$, $0 < x \leq 1-a$, $v = 0$, $\sigma_{xy} = 0$

Boundary conditions (3) and (6) arise from the symmetry conditions.

ANALYSIS OF RESULTS

Isotropic Materials

The finite element method produces a great amount of information regarding the solution to solid mechanics type problems. For each element, the displacements, strains, and stresses are known, which give the complete solution to an elastic problem. The important information needed for this particular problem is the maximum normal stress distribution in the y direction, the maximum principal stress, and the stress distribution sufficiently removed from the hole.

Table 1 is a list of different cases considered to obtain the behavior of the stress concentration factor as a function of hole size. To check the effect of thickness on the stress concentration factors, the thickness in cases 1 and 2 were changed. No difference in the results can be seen to two decimal places accuracy. It thus was concluded that the thickness factor needed in the finite element calculation does not enter in as far as the resulting value of the stress concentration factor is concerned. Obviously, for the analytic solution, the thickness is also not a factor in the two-dimensional problems.

To see whether results are influenced if the problem is considered one of plane strain rather than plane stress, case 6 was run under both conditions. Again, the results indicate no significant difference in the stress concentration factor.

Realizing that the stress gradient in the neighborhood of the defect is quite large, linear strain elements were used to see if the results were significantly different. Three cases, numbered 4LS, were considered, and, again, the stress concentration factor was not significantly changed. In the first case, only element 196, which is in the region of highest stress gradient, was taken to be a linear strain element. For the second case elements, 195, 196, 198, and 199 were taken as linear strain elements. For the last case, the elements on the top of the plate, 1 through 10, were taken as linear strain elements. This last case was considered to check the uniform stress distribution away from the hole. In all these cases, the stress was evaluated at the centroid of the rectangle. Figure 4 shows the stress distribution in the top two rows of elements for run number 4 for constant strain elements (top number) and for run number 4 for linear strain element (bottom number). It is seen that the distribution is nearly uniform in the first row, where the largest deviation is slightly less than 3 psi. The second row is not quite as uniform as the first row and has a deviation less than 15 psi. One notes that the difference between the constant strain elements and linear strain elements is again not significant.

In summary, information regarding stress concentration factors can be obtained for two-dimensional problems using either plane strain or plane stress finite element models with constant strain elements. The thickness of the model is not a significant factor in computing the stress concentration factor by this method.

The analytic solution for infinite plates with holes is given in (2). Even though we have finite plates, a comparison with these results gives an idea of the accuracy of the finite element method. In all the finite element models considered with a 90° corner, the maximum stress occurs in an element below the corner. The darkened element in figure 5 shows the location of the element with maximum σ_{yy} and maximum principal stress. The analytical solution (2) predicts the same location for the maximum stress. The experimental results in (3) also demonstrate a similar location for the maximum stresses. Comparison of the numerical values of the stress concentration factors from the analytic solutions and the finite element method indicates that agreement is not good. As as example, for $a/c = 4$ we have two values of K_p corresponding to two different values of a/b. These are $K_p = 4.58$ for $a/b = .4$ and $K_p = 3.46$ for $a/b = .2$. The corresponding values quoted in (2) are $K_p = 6.20$ for $a/c = 3.2$ and $K_p = 8.0$ for $a/c = 5$. In both cases, the analytical numerical values are high. Since the analytic solutions are for that of an infinite plate, the a/b ratio has no meaning, and, hence, the effects of the free edges of the plate play no role in the solution.

If the hole has a fillet, then the stress concentration factor for an ellipse or a circle can be used. Analytically, for a circular hole, K = 3.0, and for case 8, which is close to a circular hole, the FEM gives K = 3.25. The stress concentration factor for an ellipse with the ratio of semi-minor axis c to semi-major axis a of c/a = 2/3 is K_p = 4.0. Case 8 with a c/a ratio of .512 gives K_p = 3.25. Hence, numerically the prediction of K_p is in better agreement with analytic results for the hole without sharp corners.

The latest experimental evidence is given in (3) for narrow slits of width c = 0.004 in. The results of this analysis is given in table 1 for comparison sake. These results are given in (3) as a function of a/b, and no effect of the width of the hole is considered. As can be seen, the FEM predicts K_p's which are again low when compared to those in (3). The best correspondence again comes when the hole has the shape of an ellipse or approaches that of a circle.

One possible reason for the disagreement of the FEM results with the quoted results above is the fact that the stress gradient is quite steep around the hole, particularly near the 90° corners. To get an idea of the stress gradient, the stress concentration factor in the cross-hatched elements and the shaded element of maximum stress shown in figure 5 are plotted in figure 6. It can be seen that by extrapolating to the edge of the hole K= 9.37 and K_p = 9.93 which are in close agreement with (3). A plot of K and K_p for case la, 4, and 7 shown in figure 7 where the extrapolated values for both K and K_p are shown. The values shown in figure 7 are within the range of experimental scatter obtained in (3). For example, from an a/b = 7.2 the range of experimental values of K_p are 9.3 < K_p < 10.7. The maximum K_p for a/b = 7 is larger than the value quoted here and comes from the curve fitted to the experimental value.

An example of the stress gradient for a hole with a fillet such as case 6a is shown in figure 6. Here the two extrapolated values are K = 4.11 and K_p = 4.65. These are not much different than the calculated values given in table 1 and are within the range of scatter in the experimental data. It is noted that the stress gradient is not as steep for the case of the fillet as with the 90° corners. If the extrapolated values of the stress concentration factors from cases 3, 6a, and 8 are plotted on figure 7, the curve would be similar to those already on the graph. Hence, for clarities sake, this curve is left off.

The stress concentration factor for case 3 is seen to be high compared to other runs. Figure 8 shows the finite element model in the area of the fillet where the maximum stress occurs in the shaded triangular element. The stiffness of the triangular element gives a

stress higher than normally would be expected for the material in this region. As a comparison, case 5 used a triangular element and case 6a used a quadralateral in the region of highest stress as shown in figure 9. The value of K for these two cases is seen to differ by about 12 percent. Thus, to get a more realistic stress distribution, the quadralateral element should be used in areas of high stress.

Finally, one of the reasons for calculating the stress concentration factor is to compute the stress intensity factor from which the stress distribution in the neighborhood of a crack or a defect can be found.

For an elliptical shaped hole, the stress concentration is given by

$$K = 1 + 2\sqrt{a/\rho}$$

where a= half length of the hole and ρ = the root radius of the hole. In the limiting case where the hole approaches a crack, the stress intensity factor k is given by

$$k = \lim_{\rho \to 0} \frac{\sigma_{nom}}{2}(1 + 2\sqrt{a/\rho})\sqrt{\pi\rho} = \sigma_{nom}\sqrt{\pi a}$$

or in terms of the stress concentration factor

$$k = \lim_{\rho \to 0} \frac{\sigma_{nom}}{2} K \sqrt{\pi\rho}$$

As an approximation to the stress intensity factor for small values of ρ the above equation becomes

$$k \approx \frac{\sigma_{nom}}{2} K \sqrt{\pi\rho}$$

As an example, the stress intensity factor computed by both the above methods gives the following:

Case	$\frac{\sigma_{nom}}{2} K \sqrt{\pi\rho}$ psi $\sqrt{in}$	$\frac{\sigma_{nom}}{2}\sqrt{\pi a}$ psi $\sqrt{in.}$
6a	566	561
8	433	391
3	1038	741
5	648	560

where the σ_{nom} is taken as 500 psi.

As can be seen, the agreement in cases 6a and 8 is quite good, but cases 3 and 5 do not agree quite as well. Both 6a and 8 are more nearly a crack than 3 and 5 which can help explain the discrepancy.

Anisotropic Materials

The finite element method can easily be adapted to obtain the stress distribution in materials which are anisotropic. Again, a plate with a centrally located hole under uniaxial tension was chosen as the model to investigate. The material considered is fiberglass whose material properties are well known. In particular, a unipanel fiberglass plate and a crossply fiberglass plate were considered. The pertinent material properties of each material are given in table 2 in terms of the principal directions of the material tensor. For the computer runs, the principal material directions were taken parallel to the x, y axis shown in figure 2.

Tables 3 and 4 give the results of the finite element method for unipanel fiberglass where in table 3 the load is applied in the direction of the smallest value of the modulus, and in table 4 the load is applied in the direction of the largest value of the modulus. Tables 5 and 6 are the result for crossply fiberglass with the load applied as in tables 3 and 4.

The results of tables 3 - 6 show that when the load is along the direction of the largest modulus the stress concentration factor is largest. For the crossply, the values of the moduli are almost equal, and, hence, the difference in the stress concentration factors between the two different load conditions is small. This is not the situation for the unipanel fiberglass where there is a significant difference between the two moduli.

The above results indicate that the finite element method is capable of giving stress concentration factors as well as the complete stress distribution for anisotropic materials. The use of FEM to predict failure of such materials is beyond the scope of this report, but is a subject of interest particularly in regard to development of design criteria for composite materials.

CONCLUSION

The results of this investigation indicate that the finite element method can be used to calculate the stress distribution around defects or holes in isotropic or anisotropic materials. In particular, the stress concentration factors can be computed and are seen to agree reasonably well with the experimental and analytical results. In this analysis, the material was assumed to remain linearly elastic but techniques exist to extend the results into the plastic behavior of the material. Hence, it is possible to solve elasto-plastic problems.

Even though the loading condition considered here was that of uniaxial tension, it is possible to consider many other cases of loadings plus many different possible defect shapes.

Further effort should be directed toward analyzing with the FEM stress distribution in the neighborhood of defects with the following conditions being studied:

1. orientation of the defect with respect to the load
2. different types of loading conditions
3. effect of material properties
4. shapes of the defects
5. interrelation between the stress concentration factor, the stress intensity factor, and the failure criteria used for the material.
6. the inclusion of nonlinear elastic behavior
7. the dynamic propagation of cracks from the defects

REFERENCES

1. Paris, Paul C. and Sih, George C., "Stress Analysis of Cracks" Fracture Toughness Testing and its Applications, ASTM Special Technical Publication No. 381, June 1964.

2. Savin, G. N., "Stress Concentration Around Holes," Pergamon Press 1961.

3. Burger, C. P., Zachary, L., Tucker, L., Riley, W. F., "Application of Photoelasticity to a Weld Penetration Problem," (to be published in Experimental Stress Analysis).

4. Desai, C. S. and Abel, J. F., "Introduction to the Finite Element Method" Van Nostrand Reinhold Co., 1972.

5. Chan, S. K., Tuba, I. S., and Wilson, W. K., "On the Finite Element Method in Linear Fracture Mechanics" Eng. Fract. Mech., Vol. 2, 1970.

TABLE 1

COMPUTER RUNS ON PLATE WITH HOLES ISOTROPIC MATERIAL E = 30 × 10⁶psi $\nu = 1/3$

RUN NO.	a/b	a/c	TYPE OF PROBLEM	THICK-NESS	RADIUS OF FILLET	$K = \dfrac{max\ \sigma_{yy}}{500}$	$K_p = \dfrac{max\ \sigma_1}{500}$	REF 3. K_p
1a	0.7	7.0	Pl. Stress	.07		7.75	8.11	
1b	0.7	7.0	Pl. Stress	.25		7.75	8.11	
2	0.7	14.0	Pl. Stress	.07		8.61	8.98	11.1
	0.7	14.0	Pl. Stress	.10		8.61	8.98	
3	0.7	14.0	Pl. Stress	.07	0.05	10.48	11.75	
4	0.4	4.0	Pl. Stress	.07		4.35	4.58	
5	0.4	4.0	Pl. Stress	.07	.1	4.63	5.07	
6a	0.4	4.0	Pl. Stress	.07	.099	4.06	4.38	6.8
6b	0.4	4.0	Pl. Strain	.07	.099	4.06	4.36	
7	0.2	2.0	Pl. Stress	.07		2.93	3.05	4.7
8	~0.195	1.95	Pl. Stress	.07	.095	3.17	3.25	3.8
9	0.4	8.0	Pl. Stress	.07		4.91	5.13	6.8
10	0.2	4.0	Pl. Stress	.07		3.34	3.46	4.7

Linear Strain Elements

RUN NO.	a/b	a/c	TYPE OF PROBLEM	THICK-NESS	RADIUS OF FILLET	$K = \dfrac{max\ \sigma_{yy}}{500}$	$K_p = \dfrac{max\ \sigma_1}{500}$	REF 3. K_p
4LS	0.4	4.0	Pl. Stress (196)	.07		4.37	4.58	
4LS	0.4	4.0	Pl. Stress (195, 196, 198, 199)	.07		4.37	4.59	6.8
4LS	0.4	4.0	P. Stress (1 - 10)	.07		4.35	4.58	

TABLE 2

MATERIAL PROPERTIES

Orthotropic Plate	$E_1 \times 10^6$ psi	$E_2 \times 10^6$ psi	$G_{12} \times 10^6$ psi	ν_{12}	ν_{21}
Fiberglass (unipanel)	4.61	1.15	0.45	0.275	0.068
Fiberglass (crossply)	3.17	3.00	0.45	0.080	0.076

TABLE 3

FIBERGLASS (UNIPANEL) {x axis $\approx$ 1 axis, y axis $\approx$ 2 axis}
ORTHOTROPIC MATERIAL - PLANE STRESS   THICKNESS = 0.07 IN.
$E_x = 4.61 \times 10^7$ psi $E_y = 1.15 \times 10^6$ psi $G_{xy} = 4.5 \times 10^5$ psi
$\nu_{xy} = 0.275$ $\nu_{yx} = 0.068$

RUN NO.	a/b	a/c	RADIUS OF FILLET	$K = \frac{\max \sigma_{y'}}{\sigma_{nom}}$	$K_p = \frac{\max \sigma_{\flat}}{\sigma_{nom}}$
1	0.7	7.0		7.135	7.50
2	0.7	14.0		7.98	8.37
3	0.7	14.0	0.05	9.46	10.63
4	0.4	4.0		4.11	4.35
5	0.4	4.0	0.1	4.28	4.69
6	0.4	4.0	0.099	3.83	4.12
7	0.2	2.0		2.82	2.95
8	0.195	1.95	0.095	3.01	3.09
9	0.4	8.0		4.67	4.92

TABLE 4

FIBERGLASS (UNIPANEL) {x axis $\approx$ 2 axis, y axis $\approx$ 1 axis}
ORTHOTROPIC MATERIAL - PLANE STRESS THICKNESS = 0.07 IN.
E_x = 1.15 x 10^6 psi E_y = 4.61 x 10^6 psi
G_{xy} = 4.5 x 10^5 psi ν_{xy} = 0.068 ν_{yx} = 0.275

RUN NO.	a/b	a/c	RADIUS OF FILLET	$K = \dfrac{\max \sigma_{I'}}{\sigma_{nom}}$	$K_p = \dfrac{\max \sigma_I}{\sigma_{nom}}$
1	0.7	7.0		9.22	9.33
2	0.7	14.0		9.82	9.83
3	0.7	14.0	0.05	13.2	13.96
4	0.4	4.0		4.83	4.85
5	0.4	4.0	0.1	5.99	6.24
6	0.4	4.0	.099	4.75	5.02
7	0.2	2.0		3.38	3.42
8	0.195	1.95	0.095	4.23	4.27
9	0.4	8.0		6.10	6.16

TABLE 5

FIBERGLASS (CROSSPLY) {x axis ≈ 1 axis; y axis ≈ 2 axis}
ORTHOTROPIC MATERIAL - PLANE STRESS   THICKNESS 0.07 IN.
$E_x = 3.17 \times 10^6$ psi $E_y = 3.00 \times 10^6$ psi $G_{xy} = 4.5 \times 10^5$ psi
$\nu_{xy} = 0.076$ $\nu_{yx} = 0.08$

RUN NO.	a/b	a/c	RADIUS OF FILLET	$K = \dfrac{\max \sigma_{11}}{\sigma_{nom}}$	$K_p = \dfrac{\max \sigma_1}{\sigma_{nom}}$
1	0.7	7.0		8.00	8.16
2	0.7	14.0		9.00	9.15
3	0.7	14.0	0.05	11.22	12.07
4	0.4	4.0		4.74	4.84
5	0.4	4.0	0.1	5.16	5.46
6	0.4	4.0	0.099	4.34	4.62
7	0.2	2.0		3.13	3.19
8	0.195	1.95	0.095	3.71	3.76
9	0.4	8.0		5.38	5.48

TABLE 6

FIBERGLASS (CORSSPLY)   x axis   2 axis; y axis   1 axis
ORTHOTROPIC MATERIAL - PLANE STRESS   THICKNESS = 0.07 IN.
$E_x = 3.0 \times 10^6$ psi $E_y = 3.17 \times 10^6$ psi $G_{xy} = 4.5 \times 10^5$ psi
$\nu_{xy} = 0.08$ $\nu_{yx} \cong 0.076$

RUN NO.	a/b	a/c	RADIUS OF FILLET	$K = \dfrac{\max \sigma_{1'}}{\sigma_{nom}}$	$K_p = \dfrac{\max \sigma_{p}}{\sigma_{nom}}$
1	0.7	7.0		8.08	8.23
2	0.7	14.0		9.09	9.24
3	0.7	14.0	0.05	11.35	12.19
4	0.4	4.0		4.79	4.88
5	0.4	4.0	0.1	5.23	5.52
6	0.4	4.0	0.099	4.38	4.65
7	0.2	2.0		3.16	3.21
8	.195	1.95	0.095	3.76	3.82
9	0.4	8.0		5.44	5.53
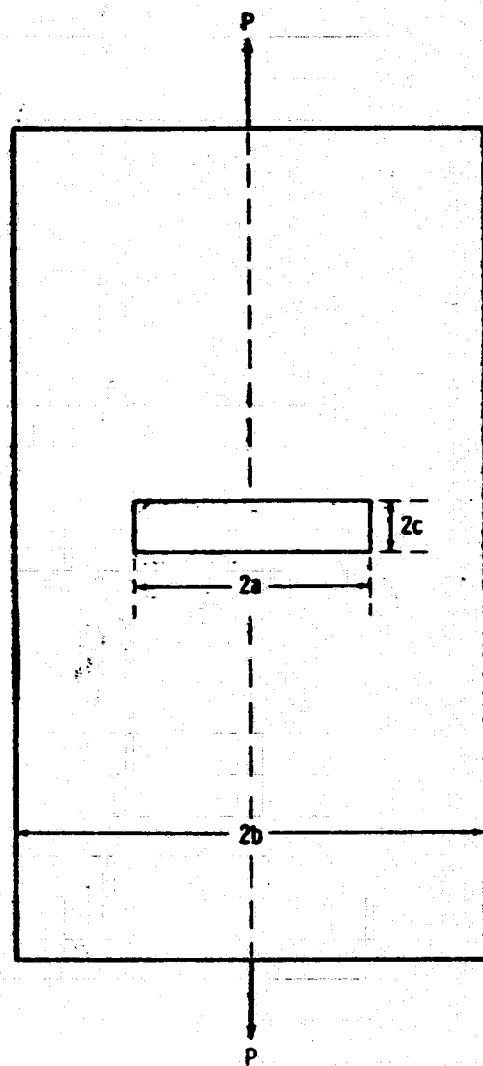
FIG. 1   REPRESENTATIVE PLATE GEOMETRY   FIG. 2   QUARTER OF PLATE FOR FINITE ELEMENT ANALYSIS
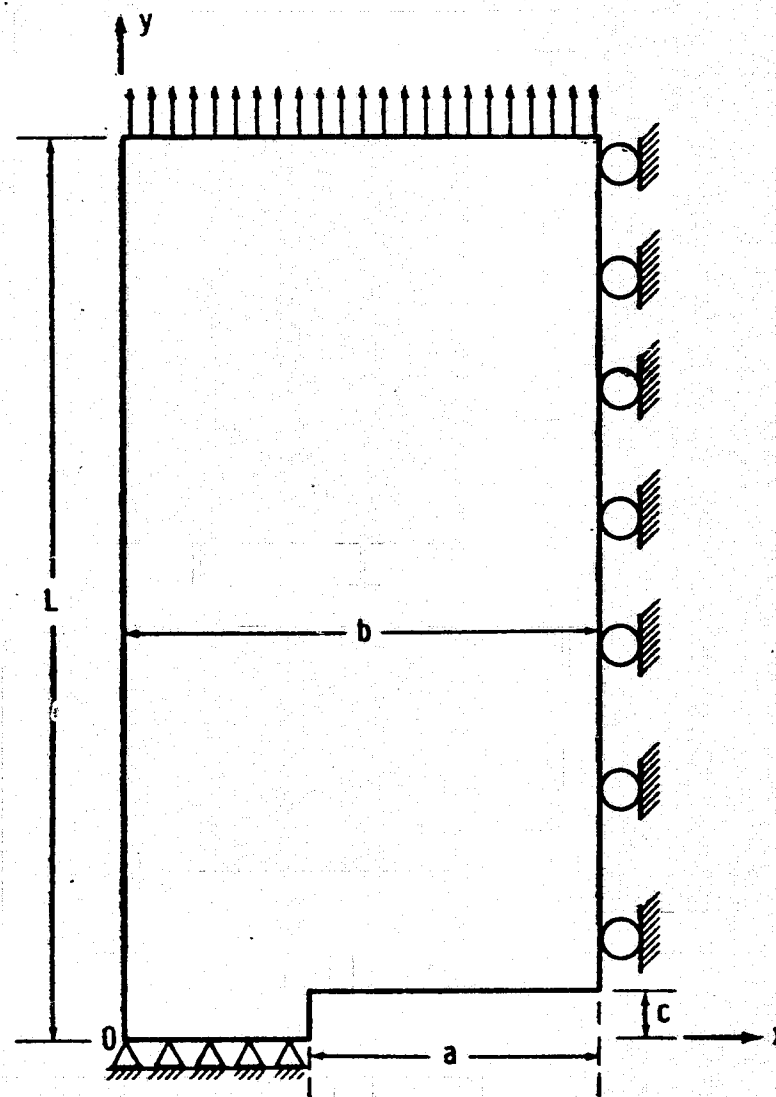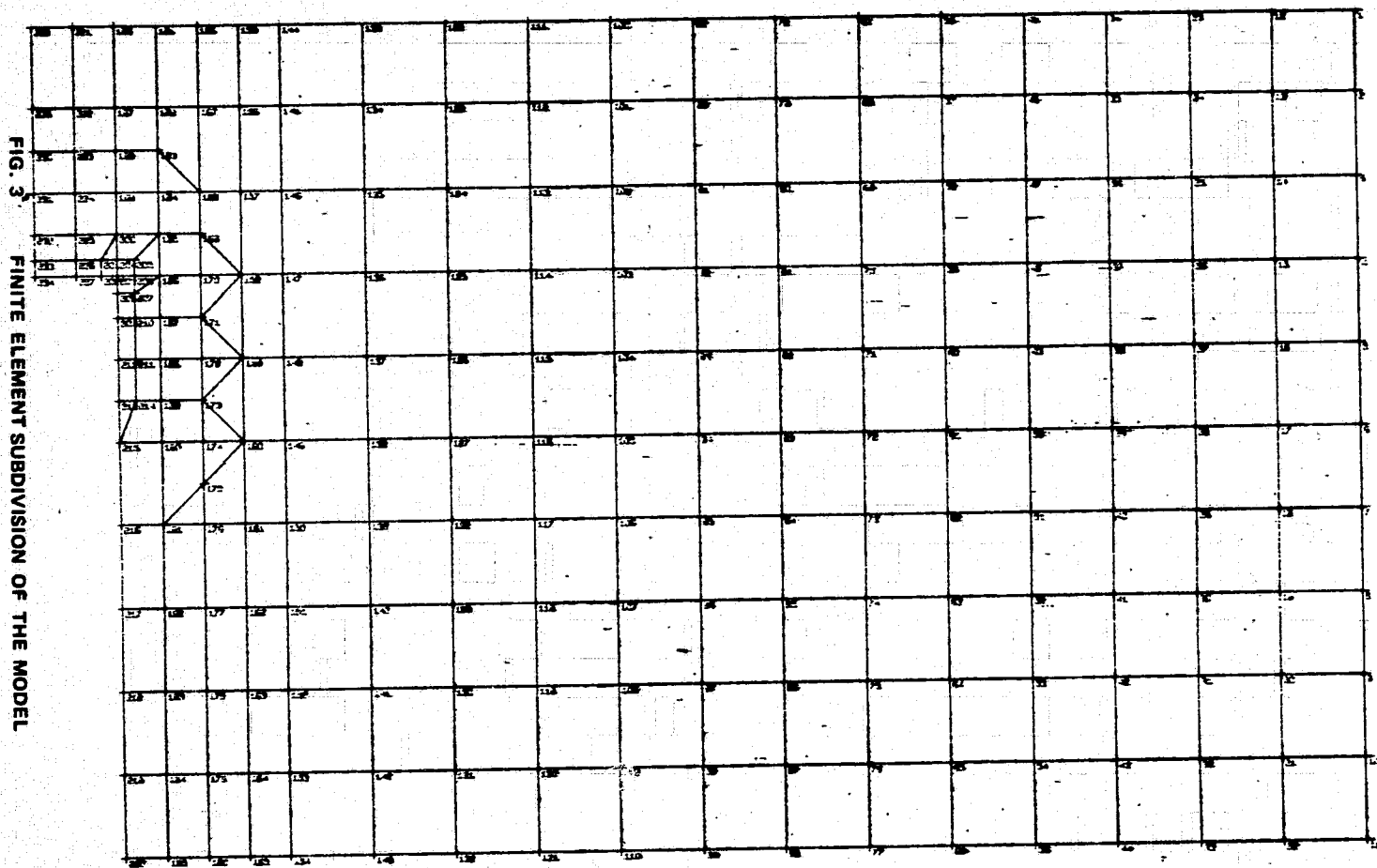
SCALE = 1 -/ 0.10
FINITE ELEMENT ANALYSIS OF A FINITE SLIT IN A PLATE

FIG. 3. FINITE ELEMENT SUBDIVISION OF THE MODEL

20-21

500.36	501.51	501.32	500.83	500.32	499.83	499.39	499.03	498.77	498.63
500.37	501.55	501.33	500.84	500.32	499.82	499.38	499.02	498.75	498.61
503.90	507.23	506.32	504.08	501.54	499.04	496.76	494.86	493.46	492.73
503.93	507.25	506.29	504.06	501.53	499.04	496.77	494.87	493.49	492.75

FIG. 4   STRESS DISTRIBUTION IN MODEL AWAY FROM THE HOLE
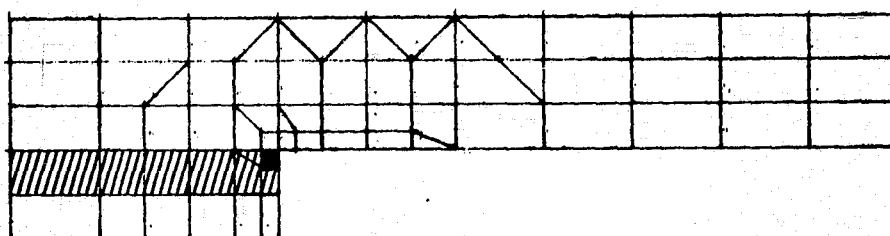
FIG. 5   AREA OF MAXIMUM STRESS AROUND HOLE
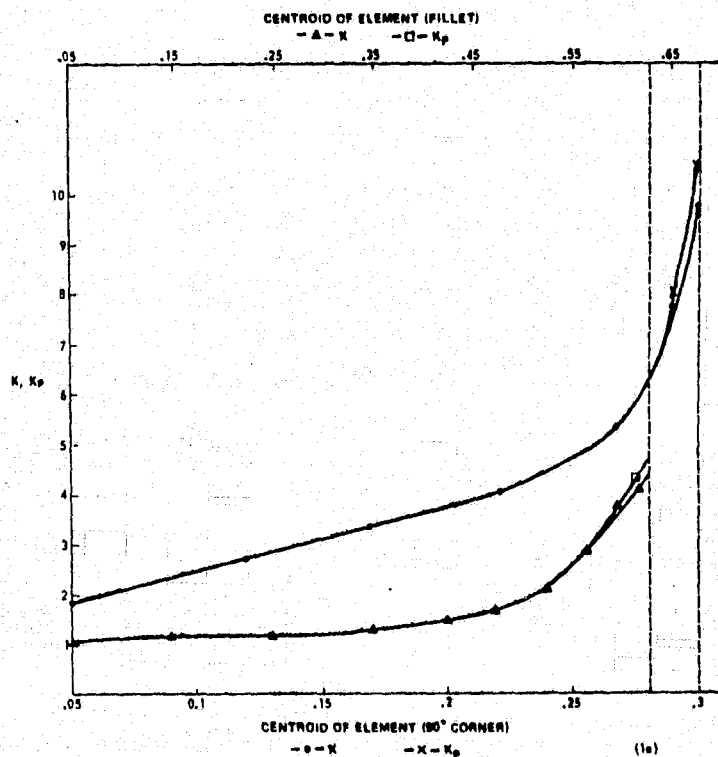
FIG. 6   STRESS CONCENTRATION FACTORS AS A FUNCTION OF POSITION RELATIVE TO THE HOLE
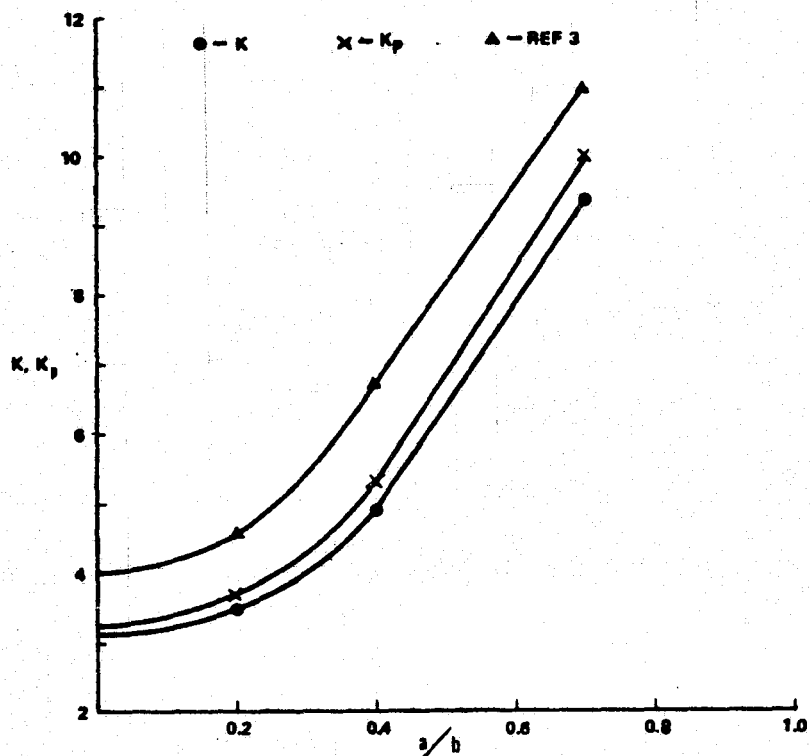
FIG. 7   STRESS CONCENTRATION FACTORS AS A FUNCTION OF HOLE LENGTH/PLATE WIDTH
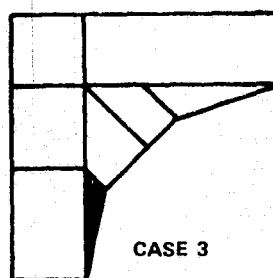
CASE 3

FIG. 8   FILLET MODEL FOR CASE 3

CASE 5   CASE 6a
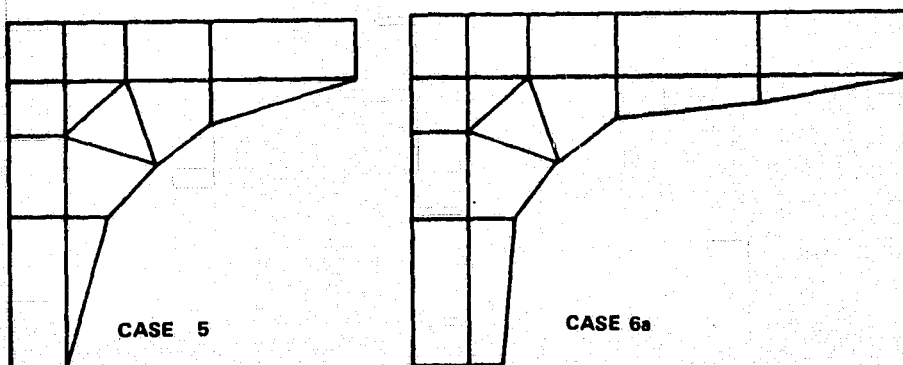
FIG. 9   FILLET MODEL FOR CASES 5 AND 6a.

1974

ASEE - NASA SUMMER FACULTY FELLOWSHIP PROGRAM

MARSHALL SPACE FLIGHT CENTER

(AUBURN UNIVERSITY - UNIVERSITY OF ALABAMA)

STABILITY AND DISPERSION OF

HIGH OHMIC VALUE THICK FILM

RESISTORS

Prepared by: Jerry E. Sergent, Ph. D.

Academic Rank: Assistant Professor

Department and   Department of Electrical Engineering
  University: University of South Florida

NASA/MSFC Assignment:
  (Laboratory)   Electronics and Controls
  (Division)   Electronics Development
  (Branch)   Electronics Packaging

NASA Research   S. V. Caruso
  Colleague:

Date: August 9, 1974

Contract No.:   NGT-01-003-045

STABILITY AND DISPERSION OF
HIGH OHMIC VALUE THICK FILM
RESISTORS

by

Jerry E. Sergent, Ph. D.

ABSTRACT

This report considers the short- and long-term stability and the dispersion of values of high ohmic value thick film resistors as a function of the design and fabrication procedure.

Thick film resistors of various geometries are fabricated under a wide range of the critical, firing parameters and statistically analyzed to determine the standard deviation. Certain of these resistors are then trimmed to a high ohmic value and all are subjected to electrical load and to temperature cycling to determine the effects of these factors on the nominal ohmic value, the temperature coefficient of resistance (TCR), and the noise factor.

From the results obtained, a procedure for the design and fabrication of high ohmic value resistors is determined.

I. INTRODUCTION

Thick film resistors of high ohmic value have been a major concern in the microelectronics industry since the very beginning of the hybrid industry. A number of resistors designed to be the same value are likely to have a very wide range of values resulting in increased cost due to rejections and excessive trimming time. Further, the resistors tend to increase in value with time, the nominal value tends to change permanently after a temperature cycle, the TCR may even change from positive to negative, and an applied voltage of sufficient magnitude may change the nominal value.

All the above mentioned properties of the resistors are strong functions of the processing steps. This program is a study of the degree to which each processing step affects the resistor properties and the establishment of an optimum design and fabrication procedure.

II. BACKGROUND THEORY

A thick film resistor consists of a metal or metal oxide powder mixed with a low melting point glass powder. An organic binder holds the two together during the pre-firing steps. This mixture is called a resistor "paste" or "ink". The paste is rated in ohms/square/mil, the rating being primarily determined by the percentage of metal or metal oxide powder in the mixture. The fundamental formula for resistance is

$$R = \frac{\rho L}{Wt} \tag{1}$$

where

R = resistance in ohms
ρ = resistivity in ohm-mils
L = length of resistor in mils
W = width of resistor in mils
t = thickness of resistor in mils

For a given material, the ratio, ρ/t is a constant and is called the $\Omega/\square/$mil rating. For L=W, or, where the resistor geometry is a square, the total resistance is equal to the $\rho/\square/$mil rating, no matter what the dimensions of the square. Frequently, the thickness of the resistor is assumed to be one mil and the rating is given simply as the

$\Omega/\square$rating. Thick film resistors are basically designed by manipulating squares in series and in parallel. The ratio of L to W is called the "aspect ratio" of the resistor and the ohmic value of the resistor is equal to the product of the $\Omega/\square$ rating and the aspect ratio, as shown in Figure 1.

The paste is placed on the ceramic substrate by forcing it through openings in a stainless steel screen which have been formed by photoresistive techniques. The resistors thus formed are dried to remove the more volatile organic materials and fired in a moving belt furnace. The purpose of firing is fourfold:

1. To remove the organic materials from the resistor materials.

2. To form a bond between the glass and the substrate for adherence.

3. To allow the metal or metal oxide materials to distribute themselves in the glass.

4. To allow chemical changes (if necessary) to take place.

It is apparent that both physical and chemical changes may take place, the physical changes being due to the migration of the metal or metal oxide particles in the glass matrix, and the chemical changes being due to the reaction of the components at high temperatures. Both the physical and chemical changes are both functions of temperature and time.

There are three significant variables under the control of the experimenter.

1. Total time of the firing cycle (controlled by the belt speed).

2. Peak temperature (controlled by the temperature control unit).

3. Time at peak temperature (controlled by the relative settings of the temperature control units).

The conduction mechanisms in a thick film resistor are not yet well understood. The glass is an insulator in large thicknesses and

Overlap

L/W = 2   R = 2 x Ω/□ rating
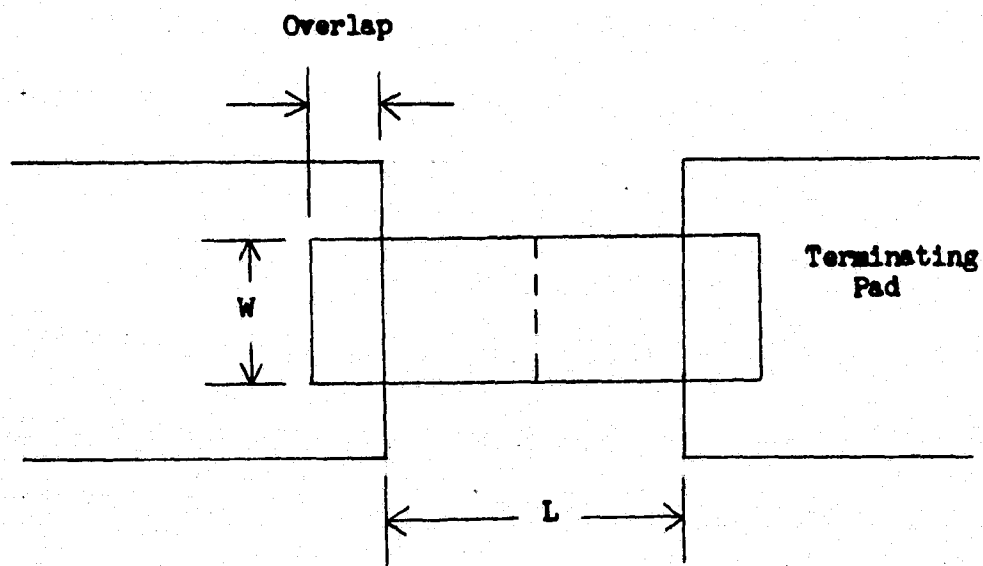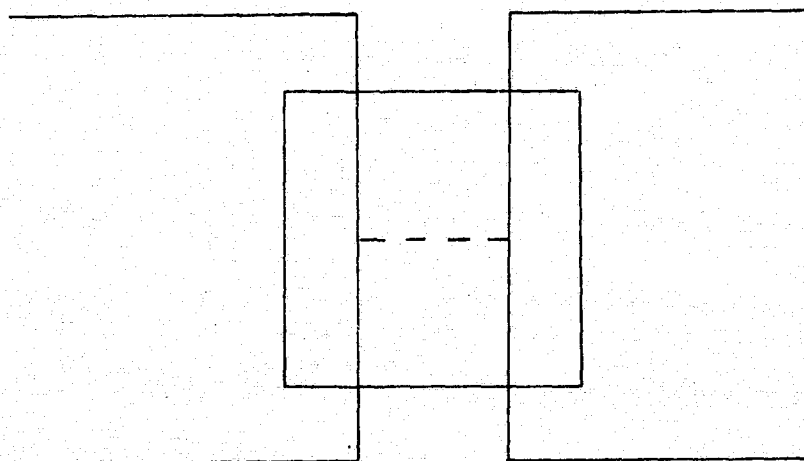
L/W = ½   R = ½ x Ω/□ rating

Figure 1. Design of Thick Film Resistors

a semiconductor in small thicknesses. Therefore, three basic modes of conduction are present.

Material	V-I Relationship	TCR
Metal	$I = K_1 V$	+
Semiconductor	$I = K_2 \epsilon \frac{qv}{kT}$	-
Insulator	$I = K_3 V^2$	0

In normal operation, the conduction process is a combination of all three, with the metal predominating in most thick film resistors.

In higher value resistors, the semiconductor and insulator mechanisms can be significant to the extent that the resistor has a negative TCR (temperature coefficient of resistance). Subsequent sections of this report characterize the effects of geometry and process variables on high value resistors.

III. EFFECT OF PEAK TEMPERATURE

The viscosity of the glass binder increases considerably with temperature consequently, the metal or metal oxide particles tend to migrate closer to each other and the resistor takes on metallic properties: the ohmic value of the resistor decreases, the TCR changes sign from negative to positive, and the VCR decreases.

For certain resistor materials, particularly those containing PdO, more drastic changes take place since PdO reduces to Pd and O_2 at higher temperatures. A plot of the normalized average $\Omega/\square$ value vs. normalized peak temperature is shown in Figure 2. The temperatures are normalized with respect to $850^{\circ}C$, the recommended firing temperature by the manufacturer and the resistance values are normalized to 818.4 K $\Omega/\square$, the value obtained when the resistor test pattern was fired at $850^{\circ}C$. It is apparent from Figure 2 that the rate of change decreases somewhat at higher temperatures, indicating that a limit point exists where the active particles cease to migrate.
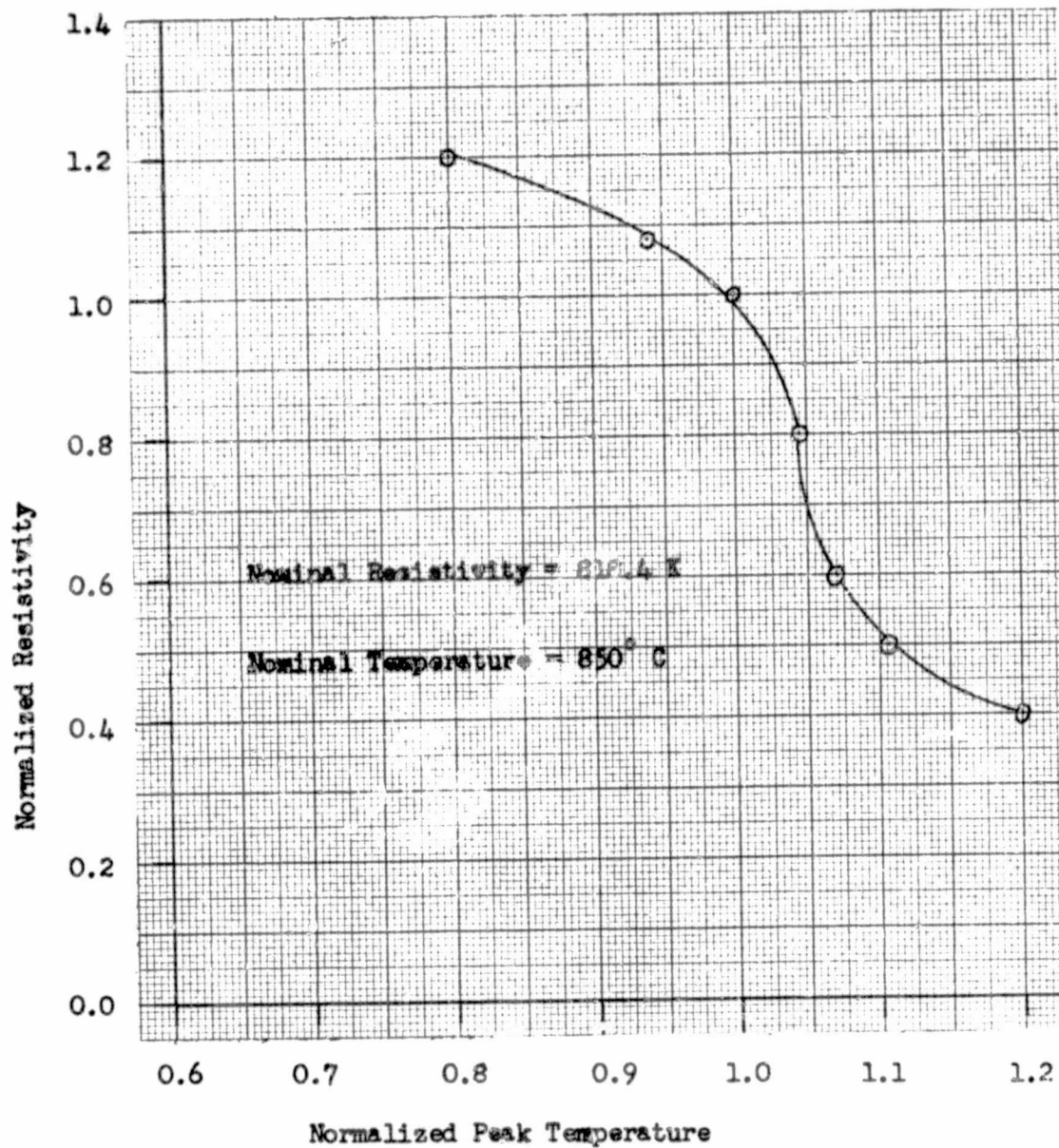
Figure 2.   Resistivity vs. Peak Temperature

IV. EFFECT OF TIME AT PEAK TEMPERATURE

When the resistor is subjected, to high temperatures for longer
periods of time, the particles have more time in which to migrate and
accumulate together. Hence, an effect similar to that of high tempera-
ture is observed. This effect is shown in Figure 3. The peak tempera-
ture is defined as T(max)- 2.0°C, and the time at peak temperature is
defined as the length of time during which the resistor is subjected to
a temperature of T(Peak) $\pm$ 2.0°C. The normalized values in Figure 3
are T(Peak) = 850°C, time = 12 min., and resistivity = 818.4 $\Omega/\square$.
The effect of time is, not surprisingly, linear, since it is to be ex-
pected that the number of particles which tend to accumulate in a glass
of constant viscosity would be linear.

V. EFFECT OF LENGTH OF FIRING CYCLE

This parameter has almost negligible effect on the resistivity.
The length of the firing cycle is significant at the beginning of the
cycle since all the organics must be burned out and is significant at
the end since stresses occur between the resistor and the substrate if
cooling occurs too rapidly. Beyond these points, the length of the cycle
is not significant if the time at peak temperature is held constant.

VI. EFFECT OF GEOMETRY

The value of a thick film resistor is not determined quite as readily
as depicted in Figure 1. The length and width of the resistor play
important parts for two reasons.

1. The thickness of the print is a function of resistor length due
to the nature of the screen printing process.

2. A number of the metal particles in the resistor termination
diffuse into the resistor during the firing process. This effect is felt
more in short resistors than in long resistors and manifests itself
even more in high ohmic value resistors due to the relative dearth of
particles ordinarily present. This effect is shown in Figure 4. The
wider resistor is clearly less affected by the aspect ratio.

VII. CONCLUSIONS

From the above data a set of design and processing steps may be
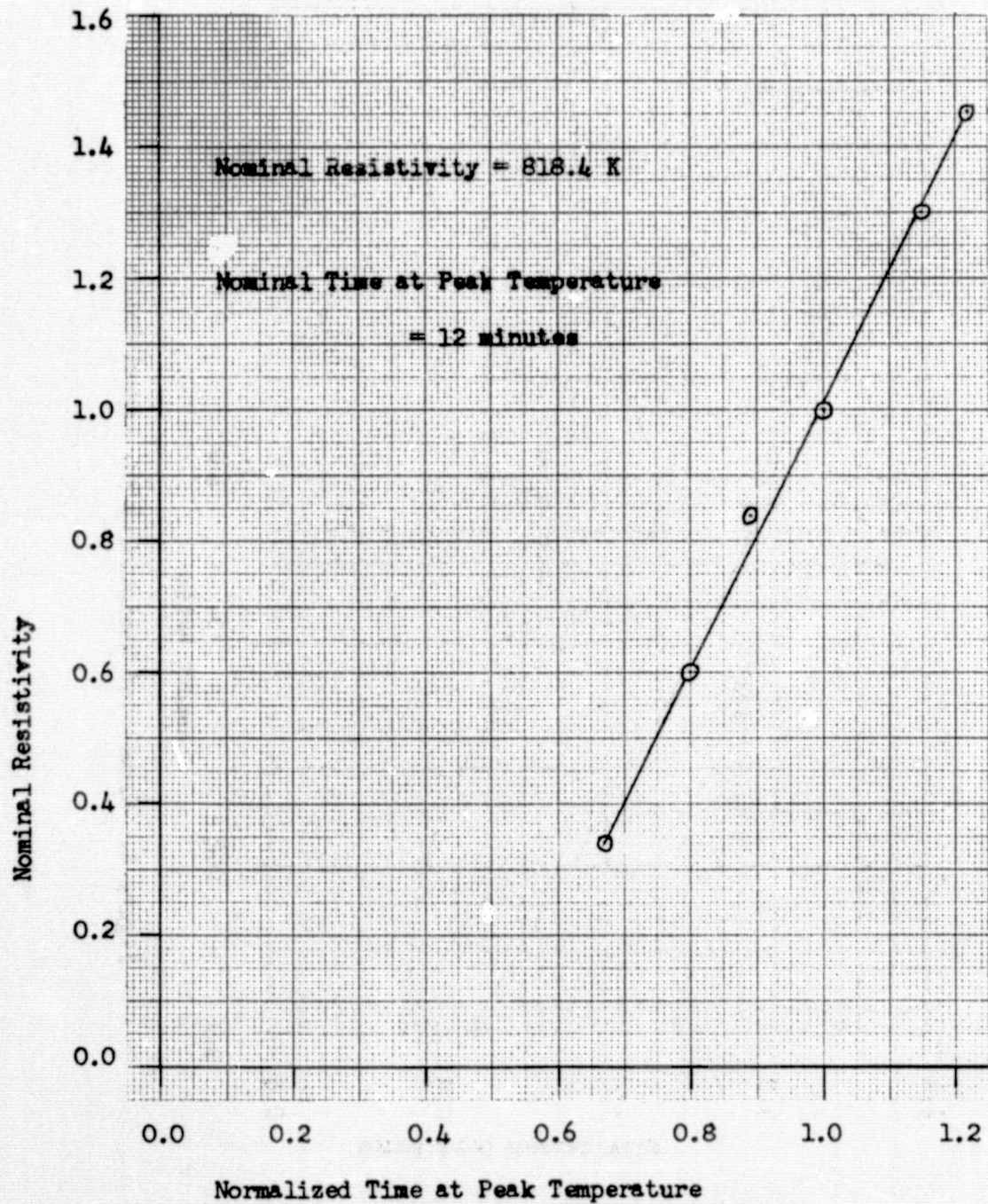
Figure 3. Resistivity vs. Time at Peak Temperature
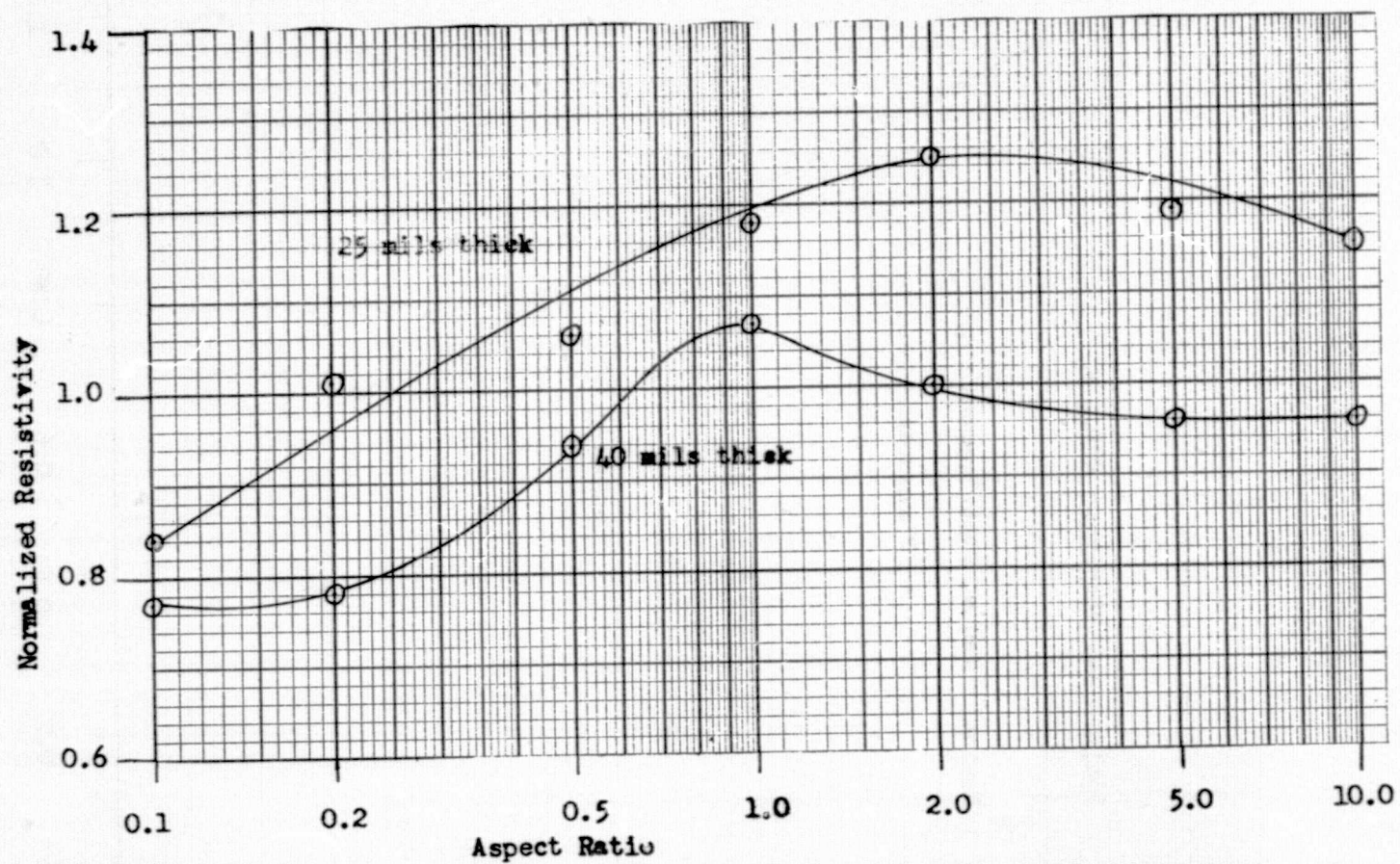
Figure 4. Normalized Resistivity vs. Aspect Ratio

determined which will yield resistors which are somewhat more predictable.

VII-A. GEOMETRY

It is recommended that the width of the resistor be at least 40 mils and that the aspect ratio be at least 1.0. From Figure 4, this will result in the smallest deviation.

VII-B. PEAK FIRING TEMPERATURE

It is recommended that the peak firing temperature be lowered to 825°C. As evidenced by Figure 4, the slope of the resistivity- vs.- peak temperature curve is somewhat less steep than at 850°C, the manufacturer's recommended value. This will make the resistors less sensitive to any random change in the ambient temperature.

VII-C. TIME AT PEAK TEMPERATURE

It is recommended that this parameter remain at the manufacturer's recommended value, 12 minutes. As noted from Figure 3, the resistivity- vs.-time curve is somewhat linear. This represents an excellent technique for varying the resistivity of the material to achieve the desired value.

VIII. SUGGESTIONS FOR FURTHER STUDY

This report represents approximately half of the author's effort. A number of areas were studied, some which show promise of fruition and some which do not. It is planned to continue the effort at the author's home institution with the immediate goal of obtaining accurate TCR, VCR (voltage coefficient of resistance) and noise measurements as a function of temperature. As a follow-on study, these results will be utilized to investigate the conduction mechanisms of thick film resistors, an area still not yet well-understood.

BIBLIOGRAPHY

1. The Thick Film Handbook, E.I. du Pont and Nemours Company, Wilmington, Delaware, 1973.

2. Hamer, D. and Biggers, J., The Fundamentals of Thick Film Hybrid Technology, State of the Art, Inc., State College, Pa.

1974

ASEE – NASA SUMMER FACULTY FELLOWSHIP PROGRAM

MARSHALL SPACE FLIGHT CENTER

(AUBURN UNIVERSITY – UNIVERSITY OF ALABAMA)

ELECTRICAL AND SUPERCONDUCTING PROPERTIES OF

LEAD-ZINC COMPOSITE MATERIALS

Prepared By: Jeffrey F. Trahan, Ph.D.

Academic Rank: Assistant Professor

Department and University: Physics Department
                                  Centenary College of Louisiana
                                  Shreveport, Louisiana

NASA/MSFC Assignment: Space Sciences Laboratory
                                  Radiation & Low Temperature Sciences
                                        Division
                                  Low Temperature & Gravitational
                                        Sciences Branch

NASA Research Colleague: Dr. Lewis L. Lacy

Date: August 9, 1974

Contract No.:   NGT-01-003-045

ELECTRICAL AND SUPERCONDUCTING PROPERTIES OF
LEAD-ZINC COMPOSITE MATERIALS

By

Jeffrey F. Trahan

ABSTRACT

The electrical and superconducting properties of lead-zinc com-
posite materials have been investigated. The resistivity of samples
prepared by quick freezing methods containing 50 weight percent lead
was measured as a function of temperature. At 2°K these samples are
thought to be superconducting although the lead was finely dispersed in
a zinc matrix. Extreme variability in the magnitudes of the resistiv-
ities and characteristics of the superconducting transition were
observed and found to be dependent on sample preparation techniques.

ACKNOWLEDGEMENTS

LIST OF FIGURES

INTRODUCTION

An experiment to process lead-zinc composite materials in a gravity-free environment during the Apollo/Soyuez Test Program (ASTP) in 1975 has been proposed. It is hoped that these materials will have interesting and unique properties. In order to anticipate the results of this experiment and to provide a basis on which the results of data taken on the space processed samples can be analyzed and compared, it is necessary to fully characterize ground processed samples. The purpose of this investigation is to determine the electrical properties of ground processed lead-zinc composite materials.

The phase diagram of the lead-zinc system[1] shows that lead and zinc are immiscible over most of the compositional range. One method of producing composite materials is to mix two immiscible liquids and freeze them. Two liquids are immiscible at a given temperature and pressure if they do not readily mix or react with each other to form compounds or solutions, a common example being oil and water. A fine dispersion of one immiscible liquid in another can be obtained by suitable mixing techniques. The dispersed liquid will form small globules in a matrix of the second liquid. If the densities of the two substances are different, the two liquids will separate quickly because of the buoyancy of one liquid in the other. This density segregation can be reduced by maintaining a small volume ratio of the dispersed phase to the matrix such that the average distance between dispersed particles will be very large. In addition, if the size of the dispersed particles is reduced to the submicron range, Brownian motion will prevent settling.

In the absence of gravity two immiscible liquids can remain mixed for very long periods of time, since the density differential in the two materials is now unimportant. A demonstration experiment (TV102) performed on the Skylab 4 mission illustrated the behavior of immiscible liquids in the absence of gravity. Krytox 143 AZ oil and water were finely dispersed by shaking. After 10 hrs, no detectable coalescence was observed, whereas ground control samples completely separated in 10 secs.[2]

It is expected that conductivity of very finely dispersed com - posite materials may be different than either of the component materials for the following reasons: If the radii of the dispersed particles are less than about 1 micron, then the dispersed phase might assume the properties of thin films; when the size of the dispersed particles is comparable to the mean free path of the electrons, the effects of particle size might be seen; effects of electron-interface scattering should be enhanced as the amount of surface area of the dispersant becomes large. It can be shown that the surface area of the dispersant is inversely proportional to the radius of the dispersed

particles[2], thus a small particle size implies a large electron interface scattering.

SAMPLE PREPARATION AND EXPERIMENTAL APPARATUS

Solid dispersions of two immiscible liquids can sometimes be obtained without mechanical mixing by taking advantage of the miscibility gap in the liquid state which occurs in many binary systems. In a system with a miscibility gap, at a given composition, there is a temperature range in which the two liquids are immiscible. Above this range, they mix; below this range, one or both substances solidify. The lead-zinc system has a miscibility gap. If the temperature of a lead-zinc mixture is raised to the temperature range in which they are miscible and then frozen in a zero-gravity environment, segregation of the two metals will not occur in the temperature range in which the metals are immiscible, and an extremely fine dispersion of one metal in the other can be made. A second method of making the solid dispersion is to quick freeze the mixture from the temperature at which miscibility occurs to the solid phase. If the freezing rate is great enough, segregation will not have time to occur.

Three lead-zinc composite samples were obtained[3] which had been processed by the quick freezing method. Two of the samples were prepared by heating the lead-zinc mixture to a temperature above the immiscibility gap after which the mixture was forced through a quartz capillary. These samples solidified while in flight. The samples, labeled Free Flight I and Free Flight II, were about 2 inches long and .010 inch in diameter. Free Flight I was beaded as if the liquid had begun to form drops before freezing, while Free Flight II was relatively uniform. The third sample was a ribbon, about .0006 inch thick, prepared by ejecting the liquid mixture on a rotating drum.[4] All three samples were of the same composition: 50 percent lead by weight. Photomicrographs of these specimens are shown in Figs. 1-5. The etchant used to enhance the contrast and clean the sample surface after polishing was made from 106 ml of water, 20 g CrO_3 and 1.5 g Na_2SO_4. In all cases zinc is the matrix and lead the dispersant; the dark spots being lead. The ribbon has an extremely fine submicron dispersal of lead in the zinc matrix. Filaments visible in the photomicrographs are also thought to be lead. Free Flight II also has a fine dispersion of lead in the zinc matrix, but it is apparently not as fine as in the ribbon. Resolution in the photomicrographs of these two samples is not sufficient to determine the particle sizes. The dispersion of lead in Free Flight I is composed of relatively large particles ranging in size from .5 to 15 μm.

Samples were also obtained which had been processed in the Marshall Space Flight Center (MSFC) drop tower.[5] These were solidified from a temperature above the immiscibility gap while falling in the earth's

gravitational field. This should be a good simulation of conditions which will be available aboard the Apollo/Soyuez flight. Photomicrographs of three samples processed in this manner show that dispersions of 1 μm or less were present in all samples.[7] In this case, the matrix was found to be lead and the dispersant, zinc. All samples were 50 percent atomic lead. The sample labeled #14 was chosen as the candidate for resistivity measurements because of the apparent uniformity and fine dispersion of zinc in the lead matrix. Microstructural differences in samples were attributed to different cooling rates.

The resistivity of Free Flight I, Free Flight II, and the ribbon was measured from 2 to 300°K. The drop tower sample was measured from 2 to 20°K. A conventional four-probe technique was employed with a constant current of 100 ma. Contacts were made of copper wire attached to the specimens with silver conductive paint. The sample temperature below 77°K was measured with a calibrated germanium resistance thermometer. Above this temperature, a calibrated platinum resistance thermometer was used.

RESULTS

The results of the resistivity measurements on Free Flight I, Free Flight II, and the ribbon are shown in Figs. 6 and 7. Data points in Fig. 7 have been omitted for clarity. The resistivities of pure lead and zinc are also shown in Fig. 6. Errors introduced by electronic equipment and measurements of sample dimensions were taken into account when calculating the magnitudes of the error bars at high temperatures.

The temperature dependence of the resistivity is that which would be expected of a classical metal, however, the variability of the resistivities of the samples is very large considering that all three samples are of the same composition. The resistivity of Free Flight I is very near that of zinc, but higher. This might be expected, since the lead particles seem to have congregated near the center of the sample leaving the volume near the surface predominantly zinc. Since zinc is a better conductor than lead at high temperatures, most of the current would be carried in the zinc sheath causing the resistivity to be similar to that of zinc.

It is not clearly understood why the resistivity of Free Flight II is very near that of lead. At high temperatures, the resistivity, $\rho(T)$, is linear in temperature and has a positive slope, characteristic of metals. This result is expected, because both lead and zinc have linear resistivities at high temperatures.

All samples exhibit a superconducting transition at about 7.2°K. This is the superconducting transition temperature of lead. At 2° all

three samples showed resistivities of less than 5×10^{-5} μΩcm which was the limit of the sensitivity of the equipment. The samples may be superconducting at this temperature. This is an unexpected result, because the photomicrographs do not show a continuous superconducting lead path in the samples and the residual resistivity of the zinc matrix should be seen. The breadth of the superconducting transition varies markedly in the three samples. The transition of Free Flight II is sharp, about .2°K wide, and that of Free Flight II very broad, on the order of 4.5°K. The ribbon initially has a very sharp transition which does not drop immediately to zero, but tapers off slowly over a range of 4°. Transition broadening might be due to the small lead particles exhibiting thin film characteristics, the transition temperature of the particles being a function of the particle radius. This explanation, however, does not explain why the transition of Free Flight II, which has a dispersion of very large particles, has a very broad transition. Broadening might also be due to strain in the samples.

TABLE I

CONSTANTS IN THE EQUATION $\rho = \rho_o + AT^n$ FOR THE LOW

TEMPERATURE RESISTIVITY OF THE QUICK-FROZEN LEAD-ZINC SAMPLES

	$A(\mu\Omega cm/°K)$	$\rho_o(\mu\Omega cm)$	n	Range(°K)
Free Flight I	.00057	.03570	3.52	7.2-24
Free Flight II	.011	.026	3.15	7.2-14
Ribbon	.034	.513	1.6	7.2-14

At low temperatures, but above the superconducting transition, the resistivity, $\rho(T)$, should follow Matthiessen's rule[6],

$$\rho(T) = \rho_o + AT^n ,$$

where ρ_o is the residual resistivity and T the absolute temperature. A and n are constants to be evaluated and are characteristic of a particular sample. For simple, classical metals like lead and zinc, n usually has a value of 5.[7] A fit of the low temperature data was made to this equation. Because of the superconducting transition, ρ_o could not be measured directly but was chosen by finding a value which gave the best straight line on a plot $\ln(\rho - \rho_o)$ vs lnT. The slope of this plot yields n while the intercept is A. The results of this fit are given in Table I. The column labeled "Range" indicates the

temperature range over which the plot is linear. Alexandrov[7] has shown that both purity and sample size will affect the nature and temperature dependence of the electrical resistance in metals. Low purity and small sample size will lower the measured values of n from a normal value of 5. In addition, he has shown that a decrease in metal purity will increase the magnitude of the coefficient A. The T^5 dependence at low temperatures is due to electron-phonon interactions and is present in these samples, but is apparently smothered by scattering of electrons from impurities and defects, which also have a temperature dependence, although it is small.[8] The ribbon has a very high residual resistivity, probably caused by the extremely high electron-interface scattering. In this sample, the surface area of the lead is extremely large due to the very small particle size. A low n and high A are consistent with a large impurity and defect scattering of electrons. Free Flight I would be expected to have a low residual resistivity, because it has relatively large lead particles. It is not understood why the residual resistivity of Free Flight II, which has a submicron dispersion of lead in the zinc matrix, should be lower than that of Free Flight I. The ribbon which has the finest dispersion, has the highest value of ρ_0 as expected.

Sample #14, prepared in the MSFC drop tower, had been cut into several pieces. The resistivity of two of these pieces was measured. The results of these measurements are shown in Fig. 8. No sharp superconducting transition was observed. This is an unusual result considering that the main bulk of the sample is lead. In one sample the resistivity drops to zero at 2°K, but in the other, a high residual resistivity is observed. This probably indicates that a portion of this sample is zinc which has not been bridged by lead. A superconducting transition has been observed in these samples utilizing inductance methods.[5] More work must be done on these samples before conclusive results can be drawn.

CONCLUSIONS

Lead-zinc composite materials are indeed interesting, and many aspects of the data are not understood: broadening of the superconducting transition cannot be explained on the basis of particle size of the dispersed lead; the large variability of the high temperature resistivity in different samples is not clearly understood; and finally the residual resistivities of Free Flights I and II and the ribbon at 2°K are extremely low, and the samples might be considered to be superconducting even though the matrix is zinc. To determine if the samples are actually superconducting, I propose that an experiment to measure the decay time of electrical currents in the samples be undertaken. In order to better characterize the dispersions of Free Flight II and the ribbon, a finer resolution is necessary than is available in photomicrographs. Some of the unusual effects seen in these samples might be attributed to structures not seen in the photomicrographs. For example, maybe there is some mixing of these two metals on an atomic scale, particularly in the samples with very fine dispersions. Perhaps quantum effects are being observed in the scattering of electrons from very small lead particles. Above all, it is evident that the properties of these samples are very sensitive to sample preparation techniques.
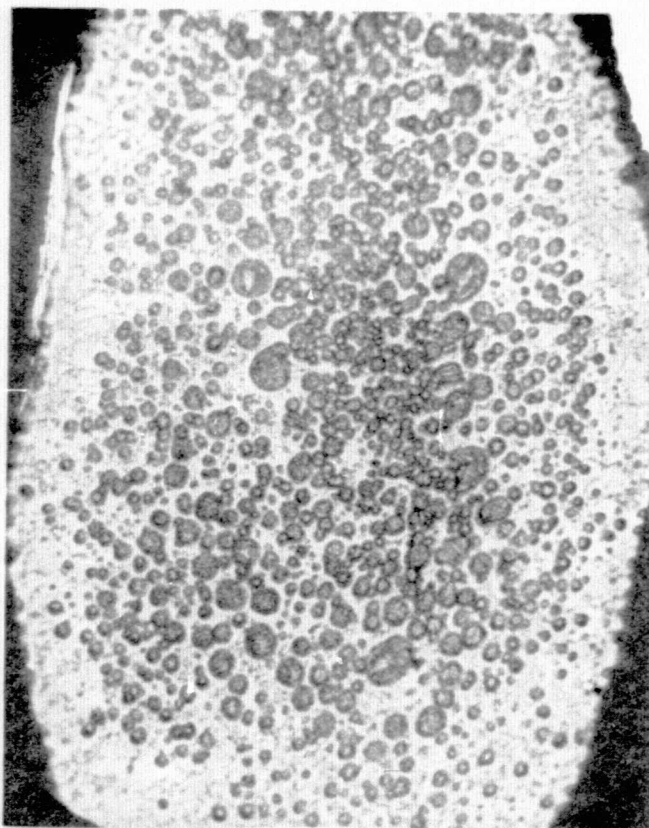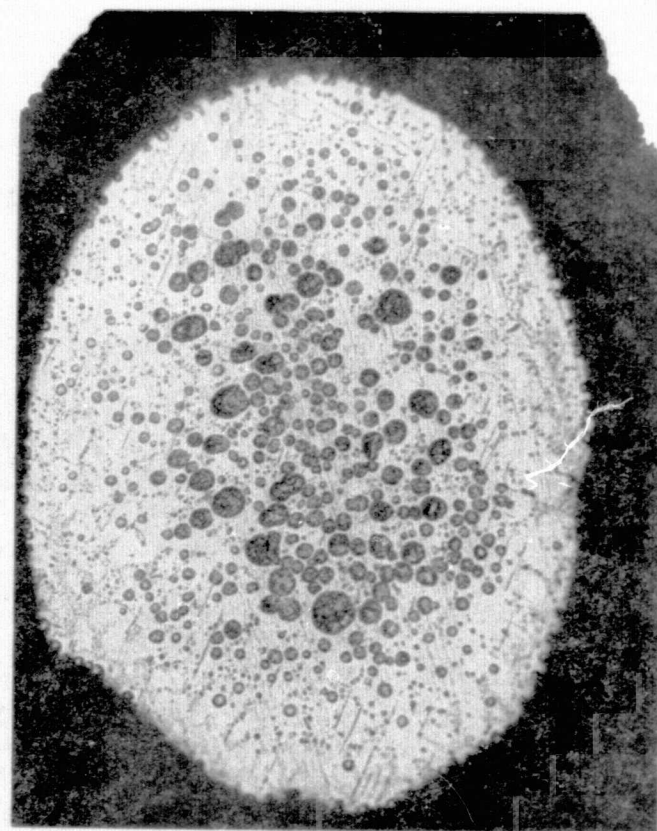
LONGITUDINAL CROSS SECTION   TRANSVERSE CROSS SECTION

FIGURE 1. FREE FLIGHT I   400X.
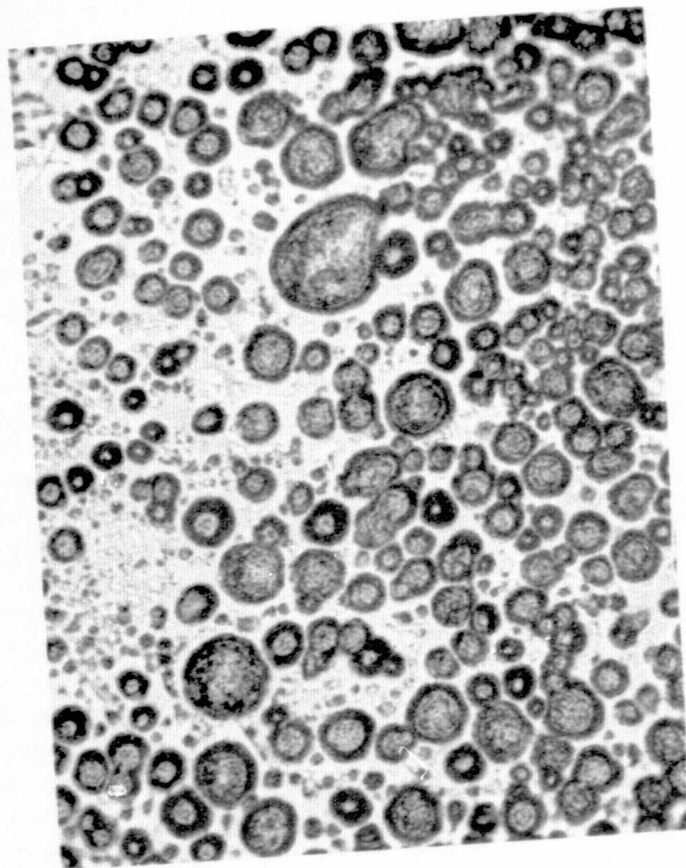
LONGITUDINAL CROSS SECTION
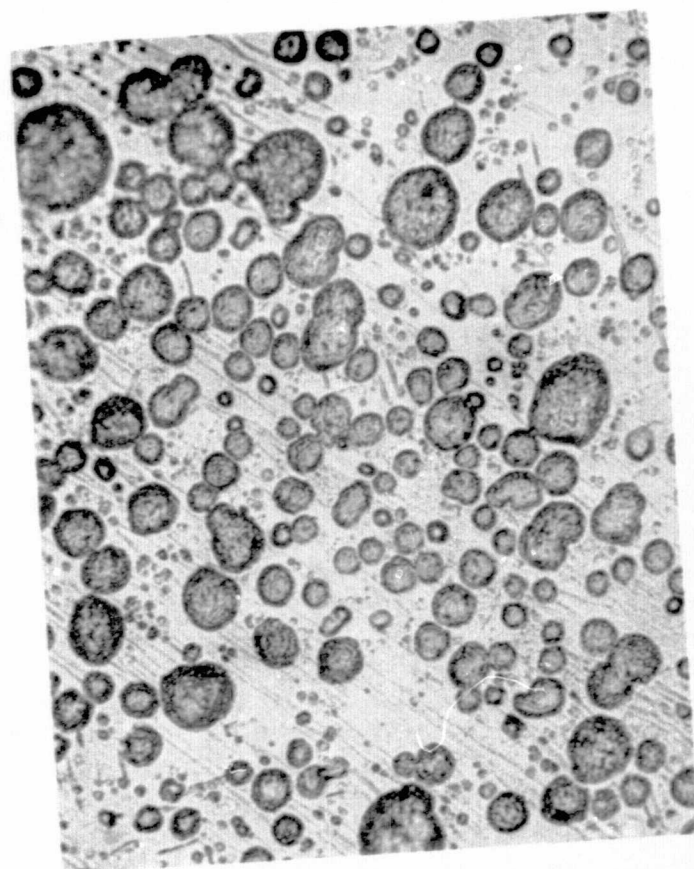
TRANSVERSE CROSS SECTION

FIGURE 2. FREE FLIGHT I 1000X.
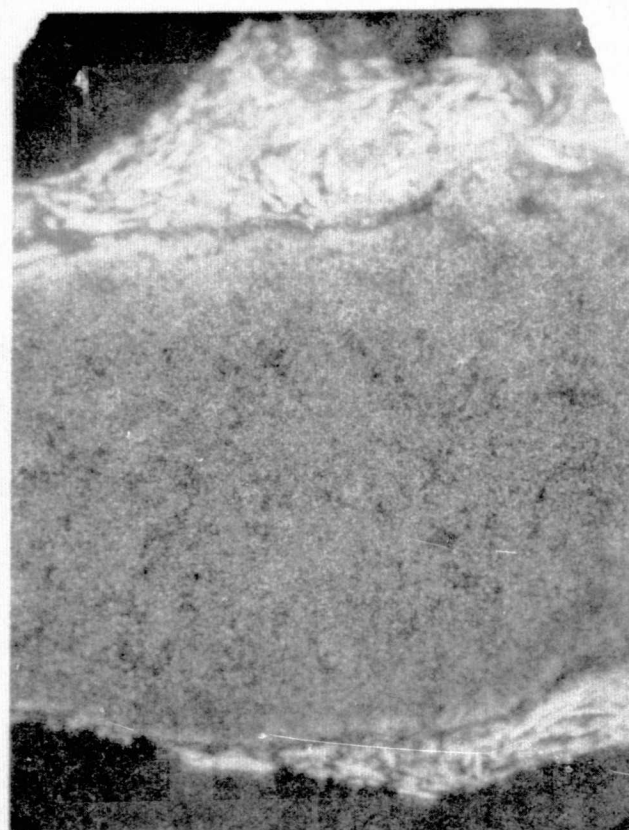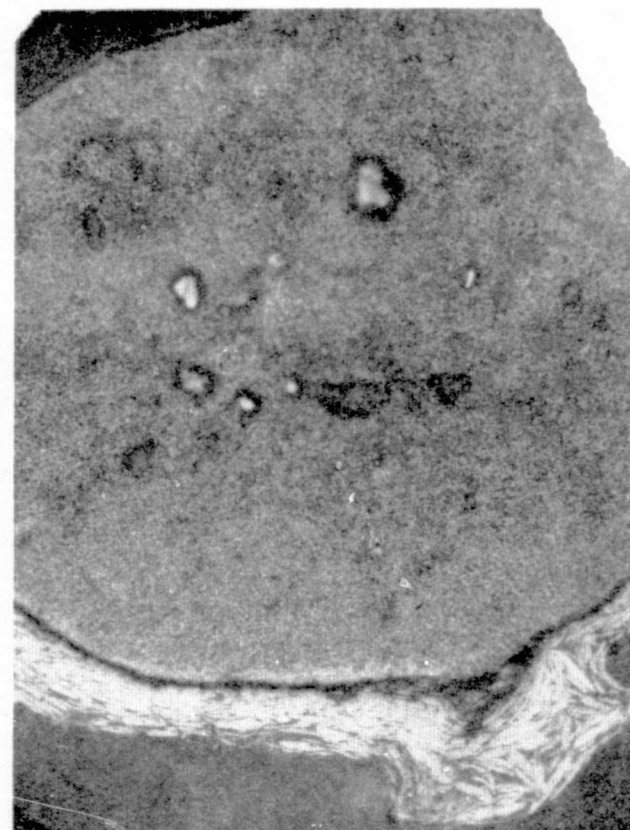
LONGITUDINAL CROSS SECTION   TRANSVERSE CROSS SECTION

FIGURE 3.   FREE FLIGHT II 400X.
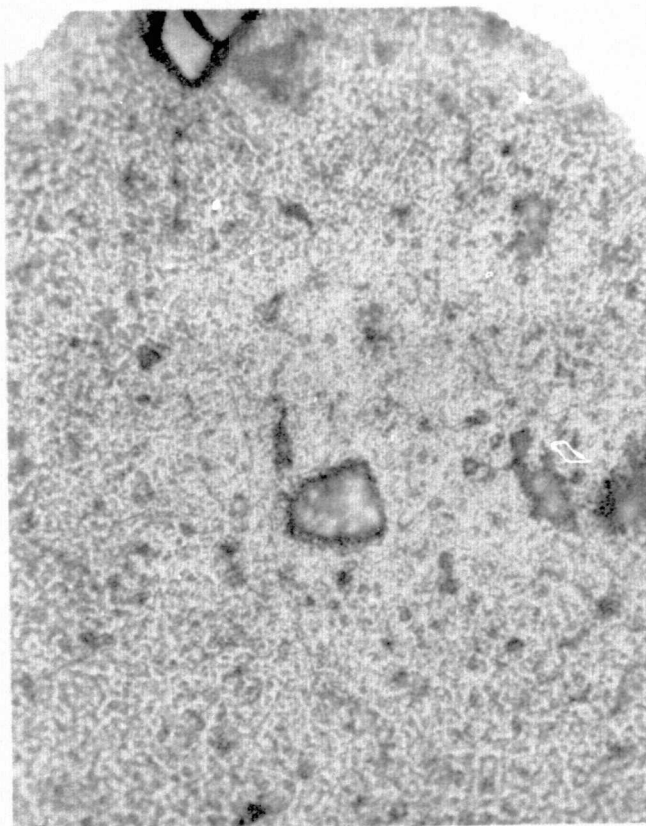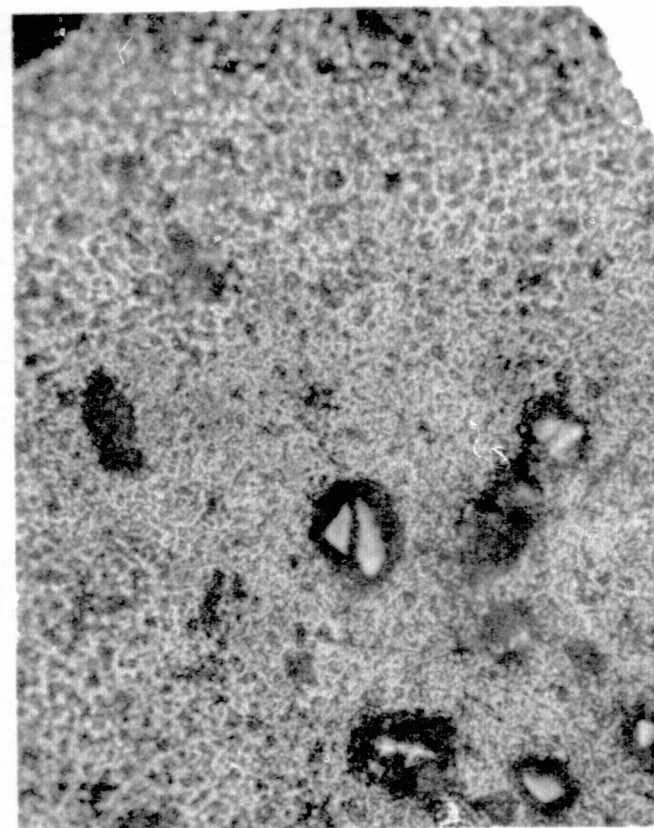
LONGITUDINAL CROSS SECTION   TRANSVERSE CROSS SECTION

FIGURE 4.   FREE FLIGHT II 1000X.
ONLY THE CENTERS OF THESE PHOTOGRAPHS ARE IN FOCUS.
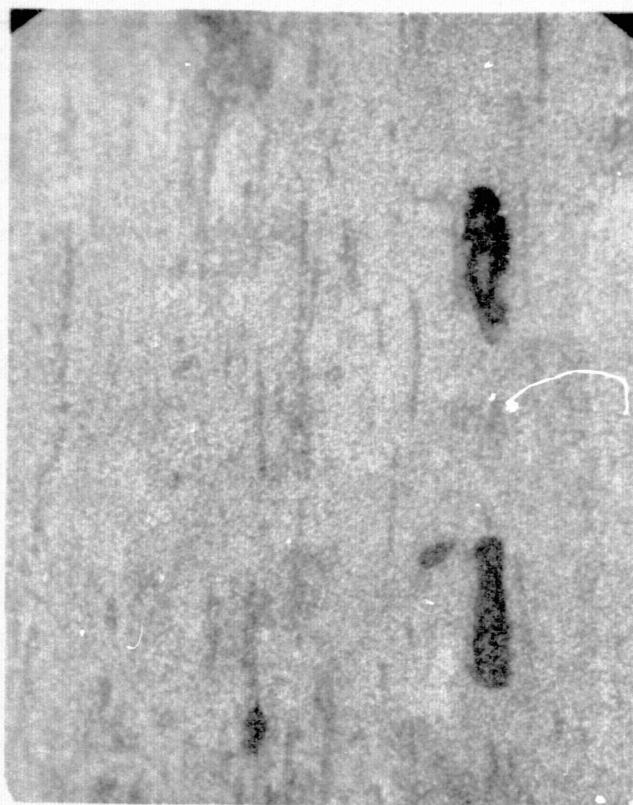
400X   1000X

FIGURE 5. RIBBON. ONLY THE CENTERS OF THESE PHOTOGRAPHS ARE IN FOCUS.
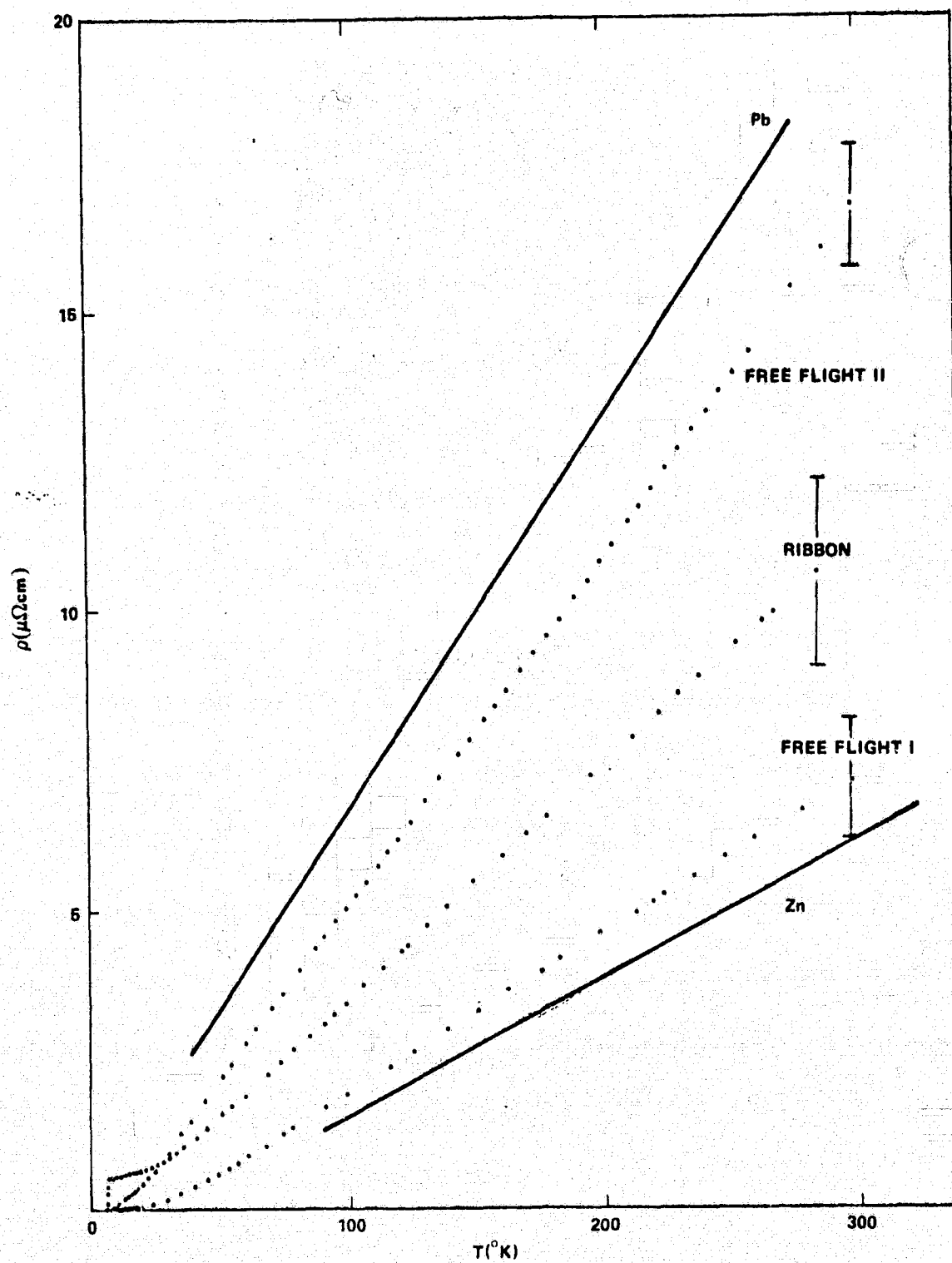
FIGURE 6. RESISTIVITY OF LEAD-ZINC SAMPLES FROM 2 TO 300°K.
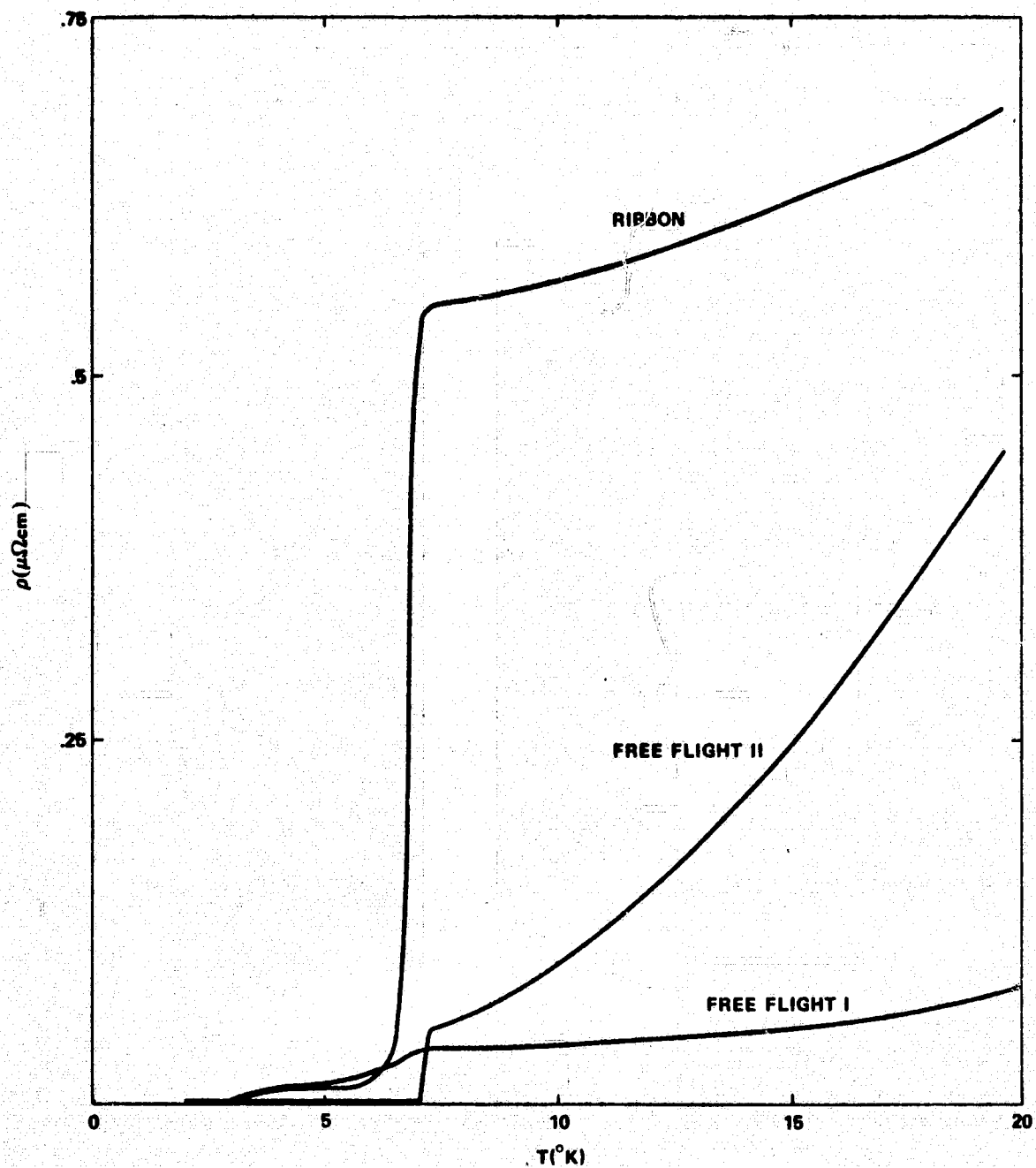
FIGURE 7. LOW TEMPERATURE RESISTIVITY OF LEAD-ZINC SAMPLES.
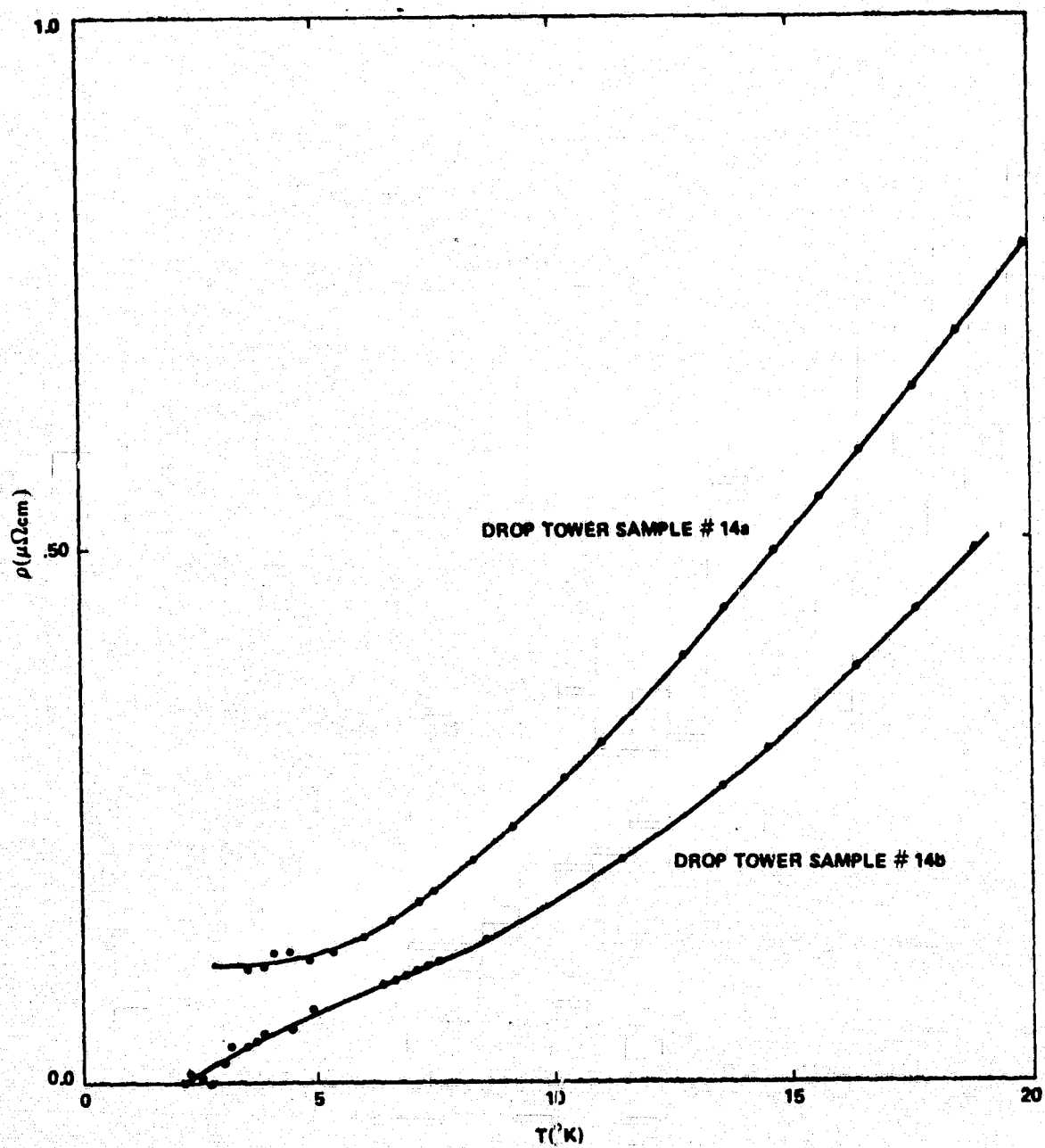
FIGURE 8. LOW TEMPERATURE RESISTIVITY OF THE MSFC DROP TOWER LEAD-ZINC
SAMPLES

REFERENCES

1. <u>Constitution of Binary Alloys</u>, 2nd ed., p. 1118, McGraw Hill Publishing Company (1965).

2. Otto, Guenther, Semi-Annual Progress Report on NASA Contract NAS8-27809 (Phase B) (June 1974).

3. These samples were obtained from Robert Pond of Johns Hopkins University.

4. Pond, R., Jr., Transactions of the Metallurgical Society of AIME, <u>245</u>, 2475 (1969).

5. Reger, J. L., Interim Report on NASA Contract NAS8-28267, TRW Systems Group Report No. 14725-6010-RU-00 (May 1973).

6. See for example: Wilson, A. H., <u>The Theory of Metals</u>, 2nd ed., Cambridge University Press, New York, NY (1965).

7. Alexandrov, B. and I. D'Yakov, Soviet Physics JETP <u>16</u>, 603 (1963).

8. See for example: Meaden, G., <u>Electrical Resistance of Metals</u>, p. 81, Plenum Press, New York, NY (1965).

1974

ASEE - NASA SUMMER FACULTY FELLOWSHIP PROGRAM

MARSHALL SPACE FLIGHT CENTER

(AUBURN UNIVERSITY - UNIVERSITY OF ALABAMA)

INVESTIGATION OF OPTIMAL PROJECT SCHEDULING

UNDER RESOURCE CONSTRAINTS WITH RESOURCE LEVELING

Prepared by: Alfred E. Traver, PhD.

Academic Rank: Associate Professor

Department and University: Department of Mechanical Engineering
                                    Tennessee Technological University

NASA/MSFC Assignment:
    Laboratory   Preliminary Design Office
    Division   Mission Operations & Integration Div.
    Branch   Mission Operations Branch

NASA Research Colleague: John W. Cole

Date: August 9, 1974

Contract No.:   NGT-01-003-045

INVESTIGATION OF OPTIMAL PROJECT SCHEDULING
UNDER RESOURCE CONSTRAINTS WITH RESOURCE LEVELING

By

Alfred E. Traver

ABSTRACT

An extensive survey of the existing literature was undertaken.
The current state of the art is that, while certain small and generally
well structured academic problems have been solved, no general
optimal solution technique exists in spite of a considerable expenditure
of effort in the attempt.

Constrained and unconstrained scheduling problems were formulated
using a zero-one programming approach. Computational experience with
a program based on the Balas algorighm indicated the solution of practical
scheduling problems was infeasible. Additional experience with a much
more efficient algorithm involving identification of the most severe com-
binations of constraints and their use early in the algorithm produced
dramatic reductions in the computation time. The computation time was
found to be extremely sensitive to the program formulation.

While small to medium-sized scheduling problems may be tractable
using the zero-one programming approach followed, large problems of
the kind to be encountered in the forthcoming Shuttle project will most
likely rely on approximate heuristic scheduling algorithms rather than
a true optimization algorithm. Experiments are now underway in the
development of such a heuristic program based on a stochastic assign-
ment of priorities to activities based on the inverse of their slack time.
An outline of the heuristic algorithm is presented.

INTRODUCTION

Techniques for the management of resources in project planning and scheduling are of obvious interest to NASA or any other organization faced with responsibility for carrying out a large-scale program involving the interdependence of many complex and long lead-time tasks. Early resource management techniques such as PERT and CPM have proven to be of less utility than had been generally believed at the time of their introduction. The purpose of this study was to examine the practicality of truly optimal scheduling of flights and ground support activities having constrained resources. There is a need for such an automatic scheduling routine capable of reflecting resource constraints, resource captial and incremental costs, task precedences, etc. The program could serve as a tool to minimize total project resource utilization, smooth the rate of resource use, and to establish minimum resource requirements.

There currently exist a number of automatic event scheduling programs which product good feasible schedules. These programs involve the use of some rule of thumb or heuristic procedure in determining priorities among jobs competing for available resources. These methods are in contrast to a second major group of procedures which aim at producing the best possible or optimal schedule. Such optimal procedures are often termed exact or analytical and generally involve the use of some form of analytical programming or other rigorous analytical procedure.

SUMMARY

The first action taken was a survey of the existing literature on this and related subjects. The survey was not very encouraging. While certain small, generally academic, problems have been solved, no general optimal solution technique exists for large problems though there has been a considerable expenditure of effort in the attempt.

To gain experience and explore some of the practical problems to be encountered, a zero-one formulation of several typical scheduling problems was made. The solution of any scheduling problem of practical interest will require machine computation. An algorithm developed by Balas to solve zero-one optimization problems was coded for experimentation. The Balas algorithm is based on an implicit enumeration of the feasible solutions among the 2^n combinations of all possible solutions for a problem of n variables. The computational experience suggested that the times required to solve realistic problems would be excessive.

An algorithm which places the most severe constraints, or some combination of them, early in the program so as to produce the maximum reduction in the number of feasible branches to be investigated would work much faster. Such an approach was adopted and produced a satisfactory solution of the test problems in a reasonable time. Unfortunately, modification of the objective function to achieve a multi-purpose objective increased the computer run time dramatically. This served to emphasize the sensitivity of computation time to program formulation.

Consideration of the size and complexity of the scheduling problems to be encountered in the forthcoming Space Shuttle program lead to the conclusion that both the computation time and the computer memory requirements will exceed practical limits if a true optimum solution is attempted.

The development of a heuristic scheduling program was undertaken. A heuristic algorithm will not necessarily produce an optimum schedule but, it will produce a "good" feasible schedule with a reasonable expenditure of computer time and a reasonable memory requirement.

LITERATURE REVIEW

The development of optimal procedures has progressed relatively slowly with most of the progress in the area occurring within the last ten years. Researchers in the area in the mid-1960's arrived at pessimistic conclusions and went on to develop heuristic procedures.

"In view of the difficulties involved there does not appear to be any direct (i.e., exact) approach to formulating and solving the resource loading problem." Kelly (1)

"Linear programming, dynamic programming, self-correcting and combinational approaches, were investigated and discarded because of the complexity of the problem." Anonymous - I. E. du Pont de Nemours and Co. (2)

"No formal mathematical model can be utilized at the present time for scheduling projects under limited resources. Rather, only heuristic methods can be employed." Brand, et. al. (3)

These pessimistic conclusions were due, at least in part, to the fact that at that time, the major alternatives to heuristic procedures were various ordinary linear programming formulations; an approach which, in general, has proven to be computationally impractical for even very

small problems. More recently research interest has focused on integer programming formulations and combinatorial solution methods such as implicit enumeration.

The first published integer programming formulation of the resource-constrained, duration-minimization, scheduling problem was presented by Wiest (4). Wiest made no attempt to implement his formulation and it is interesting primarily as a demonstration that integer programming can be applied to the problem. For even a small problem the number of variables and equations is prohibitive. A hypothetical project schedule involving 55 activities and 4 resources involved 1650 variables and 6870 constraints, although some are redundant.

Hadley (5) also presented an integer linear programming formulation with no implementation. The objective function used was total project cost including resource use at regular and overtime rates and the cost of changing resource levels. In evaluating his own formulation Hadley concluded, "For any realistic problem the number of constraints would be huge and the solution is at present quite impossible." A number of small problems were formulated and solved by various authors but the methods used were not extendable to larger practical sized problems, (6 through 10).

In 1969, Pritsker, Watters, and Wolf (11), developed a new integer linear programming approach to scheduling under multiple constraints. Their formulation reduces the redundancy inherent in the earlier zero-one programming formulations of the problem by Bowman (52). For example, a simple 3-project, 8-job problem involving 3 resource types, requiring 72 variables and 125 constraints using the Bowman zero-one formulation can be reduced to a problem requiring 33 variables and 37 constraints. The formulation uses binary, zero-one, variables to indicate, for select periods, whether or not a job is completed in those periods. This formulation is quite flexible and can accommodate a wide range of real-word situations. Like all of the mathematical programming techniques, it still requires a relatively large number of variables and constraints to formulate a practical sized problem, but at present this appears to be the most succinct and useful method being an extension of an earlier zero-one approach by Watters (12).

The most recent major work in the area seems to have been done by Fisher (13). Thus far, linear programming based optimal procedures have not developed to the point where they are capable of solving problems of the type and size easily handled by heuristic procedures. "They are today primarily an interesting research topic for academicians," Davis (14).

There are two principal approaches of current interest in finding optimal solutions to an integer programming problem. Several variants of each approach are available as the result of different researchers. No one algorithm is successful in all cases. The first principal category of techniques are the cutting plane algorithms most closely associated with the work of Gomory (15, 16, 17), Glover (18, 19), and others (20 through 24).

The second principal category of techniques are the various versions of the backtrack algorithms. The most useful variations are the so called branch and bound algorithms. Modifications of the branch and bound techniques are numerous. An excellent review of the development of these techniques was given by Lawler and Wood (25). The first application of these techniques to the constrained resource scheduling problem was by Mueller-Merbach (26), who concluded that branch and bound enumeration was not reliable for solving large problems but might be useful on portions of large networks. Johnson (27) developed a new branch and bound technique and carried out extensive computational experiments as a result of which he concluded that his method was not practical for scheduling single resource projects with more than 50 activities.

Davis (28) developed an algorithm he termed bounded enumeration. The computation time is reduced by beginning with a heuristically generated starting solution which is used as a reference in seeking improved solutions. A optimum solution was found in about 74 percent of his 65 experiments and an improved solution is the remainder of cases. Davis and Heidorn (29) eventually expanded the procedure until it was capable of handling projects of 220 duration units and up to 5 resource types.

A number of other recent developments have been subject to comparative study by Bennington and McGinnis (30). They concluded that relatively little progress has been made in the development of optimal scheduling techniques suitable for real practical sized problems.

Special mention is made to a class of implicit enumeration algorithms which are used only with zero-one problem formulations because they depend on the special structure of such a problem. The original algorithm due to Balas (31, 32) has been the subject of considerable experimental computation (33), and has been the starting point for improved techniques by other researchers, generally in combination with other programming methods (6, 12, 34, 35, 36, 37, 39).

While considerable progress has been made in recent years in the development of optimal procedures for small to medium sized problems, there is still no computationally feasible technique for handling the large complex projects which occur in practice, (38). Optimal schemes capable of handling 50 jobs having 1 resource or perhaps 20 jobs having 5 resource types seem to be about the state-of-the-art. Heuristic programs capable of handling several tens of thousand jobs and several hundred resource types have been developed.

Heuristic-based procedures for scheduling activities under multiple resource constraints were reported by Kelly (1) shortly after the general introduction of PERT and CPM techniques. More than 25 heuristic scheduling routines are known to have been developed in the United States alone. The details of these programs are not generally available as each is a computer program of some complexity representing a considerable development effort. Some of these programs are offered on a commercial basis. Unfortunately, there is little basis for meaningful comparison among these heuristic programs since in many cases not even the most general operating principles have been disclosed. Two descriptive comparisons were worked by Jenette (4), and Phillips (42). Several researchers have documented comparative computational experience such as Fendly (43), and Brand, et. al. (1).

Two particularly widely documented heuristics are RAMPS, described by Wiest (44), and the SPAR I, SPAR II, SPARTAN series developed by Wiest (4, 44, 46). A large number of other programs have been described very briefly by others, but not so completely that the development of a similar program is an unambiguous or trivial exercise; references (14, 38, and 47 through 51) contain such descriptions.

Over two-hundred likely bibliographic references were found and no doubt this list is far from complete. Limited time and limited library resources have made a comprehensive search of the related literature incomplete, but based on a limited sampling, certain conclusions can be safely made.

1. A great deal of research has been done in the area and a large body of literature exists in both the area of optimal scheduling and of heuristic scheduling under resource constraints with and without leveling.

2. The literature regarding optimal scheduling has, in general, attracted academic investigators whose findings have been openly reported.

    As a result, we can assume that the present state of optimal scheduling does not allow the generation of large schedules involving the required number of tasks and resources.

3. The literature regarding heuristic scheduling has been much more guarded. The objective often seems to have been to disclose the existence of a program and to "puff" its virtues while hiding its operation and rationale. The development of heuristic procedures is sufficiently advanced to allow the development of a program to do the scheduling of very large projects. All the automated scheduling of large projects is currently being done with heuristic programs.

4. No one heuristic program gives the best results in all cases. The effectiveness of a given scheme being highly problem specific. Experimentation and development is required to tailor existing well-known principles to a specific problem.

ZERO-ONE PROGRAMMING FORMULATION

It is common practice, in formulating large-scale models aimed toward planning decisions, to rely on integer programming. In particular situations requiring an "either-or" or a "go-no go" decision, are amenable to binary or zero-one programming which is a special case of the more general integer programming.

Of the integer programming techniques discussed in the literature, the approach of Pritsker, Watters and Wolfe (11), in formulating the multi-project, job shop scheduling problem, seemed to have the most potential for accommodation of the wide range of real world situations. Provisions can be made for including multiple-resource constraints, due dates, job splitting, resource substitutability, precedence, concurrancy or non-concurrancy of activity performance, etc. The method is also more succinct than other earlier formulations.

An efficient formulation of a scheduling problem will depend upon a judicious choice of definition for the variables. In this formulation zero-one variables are used to indicate, for select periods, whether or not an event has been scheduled to occur in that time period. The beginning, end, or some mid-point of an activity, such as a launch time, can be selected as the denotement. Define the variable X_{ij} to be one if event i occurs in time period j, making i an index of events or activities and j an index of time periods.

Activities or events are to be scheduled in a manner that optimizes some performance index or objective function. The choice of an appropriate performance criterion is dependent on the nature of the project. Two objective functions which might have some utility to NASA in the mission operations activity were considered, but they are by no means the only ones possible. In one case, hereafter called the constrained problem, it is assumed that a number of activities or events (jobs, flights, etc.) are to be performed so as to complete all of them by the earliest time subject to limitations or constraints placed upon the resources available at any given time. It is further assumed that certain of the activities must be performed before others can begin. An appropriate objective function might be,

$$\text{Minimize } J = \sum_i \sum_j j X_{ij} .$$

The second case considered is called the unconstrained problem.
In this case the resources are considered as being available in any
amount but, a capital cost is associated with each unit of resource
demand, i. e., each unit required to meet the peak requirement. Such
a formulation would result in a schedule that minimized the peak levels
of resource use and then working with these self generated constraints
minimize the time to complete all the required activities; that is, to
produce the earliest project completion time. Such a formulation would
be useful in sizing facilities or fleet sizing, etc., where the cost
associated with each additional demand unit of resource represents a
substantial cost increment. A natural extension of such a formulation
would be to define one of the resources as the operating expense
associated with the various resources and include it in the objective
function so as to achieve a minimization of the sum of the operating
and capital expenditures. The objective function for the unconstrained
case would be,

$$\text{Minimize} \quad f = \sum_{i=1}^{N} \sum_{j=1}^{T} j \, X_{ij} + \sum_{k=1}^{K} W_k \, \text{Max} \, (R_{kt})_k$$

Where k is the resource index or identifier, and R_{kt} is the amount of
resource k required during time period t. W_k is the weighing or cost
of a demand unit of resource k.

Note that for the constrained case, R_{kt} would be a predetermined limi-
tation on the amount of resource k being used on all jobs i during a time
period must be determined from,

$$R_{kt} = \max_{j} \sum_{i}^{N} r_{ik} \, X_{ij} \, ,$$

where r_{ik} is the amount of resource k used to perform job i.

Each problem involves sequencing constraints or precedences and
could involve requirements for concurrence or nonconcurrence of events.
For a case where event i = A must precede job i = B, these take the form,

$$\sum j \, X_{Aj} - \sum j \, X_{Bj} \leq d_i$$

where d_i is the duration (in time periods) required to perform
activity i.

The requirement that each job in the project be completed is easily formulated as,

$$- \sum_i \sum_j X_{ij} \leq N,$$

and

$$\sum_i (X_{ij})_i \leq 1,$$

where N is the number of jobs or activities to be performed in completing the project.

This formulation is directly adaptable to a multi-project situation by the use of an additional subscript and multi-project completion constraint similar to the project completion constraints above.

Resource constraints for the constrained case are specified as,

$$\sum_{i=1}^{N} \sum_{j=1}^{t} r_{ik} X_{ij} \leq R_{kt}.$$

The substitutability of resources, for example, the ability of a large facility to do a small job, can be handled by defining a set of mutually exclusive jobs, only one of which must be performed.

Noncurrency of two jobs, A and B, can be assured by the constraint,

$$\sum_i X_{Aj} + \sum_i X_{Bj} \leq 1.$$

While concurrency of two jobs, A and B, can be assured by specifing,

$$X_{Aj} = X_{Bj}, \quad \text{for all } j.$$

Job splitting can be allowed by considering each job as a number of subjobs with sequencing constraints. Concurrency and contiguous scheduling can also be required by use of one superjob replacing two or more jobs and the resources combined.

The unconstrained problem requires the use of the zero-one variables X_{ij} and constraints of the form just discussed. In addition, we also define a set of variables Y_{kl} which are zero if a demand unit of resource k is unused and one if the demand unit of resource k is used. The index l may be thought of as the serial number of the resource demand unit or facility being used. Naturally, the demand unit can be scaled where appropriate to reduce the number of variables involved at the expense of introducing some granularity into the problem. Alternately, the Y_{kl} variables could be defined as zero if resource k is used to a set level corresponding to index l.

As an example of the application of a zero-one formulation to a scheduling problem, consider a project consisting of nine events requiring three resources. Events 1 through 4 each require only resource S for two time periods, one period before and one after the event. Events 5 through 7 each require resource S for two time periods, also centered about the event, and resource T for three time periods, the one preceding the event, and the two periods following the event. Events 8 and 9 each require resource S for two time periods, the one preceding and the one following the event. Resource T is required for three time periods, the two preceding and the one following the event. Resource L is required for four time periods, the two preceding and the two following the event.

We will adopt as precedence constraints the requirements that event 1 must precede event 2, event 3 must precede event 4, event 5 must precede event 6, event 6 must precede event 7, and event 8 must precede event 9. The scheduling interval, or horizon, contains ten time periods. The resources available are two units of S, one unit of T and one unit of L for all time periods.

The problem formulation takes the form,

$$\text{Minimize} \quad \sum_j C_j X_j$$

subject to,

$$\sum_j A_{ij} X_j \quad B_i \text{ for } i = 1, 2, \dots, M$$

$$X_j = 0 \text{ or } 1 \qquad \text{for } j = 1, 2, \ldots, N$$

Here the variables X_j are the X_{ij} binary variables denoting the occurence of event i in time period j. The indices i and j now are redefined, changed so that the j index denotes the event-time variables and the i index numbers the constraints. For the unconstrained problem X_j also includes the resource use variables Y_{kl}.

The constrained version of the example problem requires ninety variables, one for each of the nine events in each of the time periods, and forty-five constraints, nine event constraints, the project completion constraint, five precedence constraints, and thirty resource constraints, one for each resource in each time period. The X_j vector contains ninety elements and a corresponding ninety coefficients C_j are required for the objective function. The constraint coefficient matrix A_{ij} contains forty-five rows and ninety columns or 4050 elements. The B_i vector requires forty-five elements. The values of these coefficients are presented in Table A for the constrained problem. Because the A_{ij} matrix is sparse and quite highly structured, a shorthand notation of the form UxV has been adopted to indicate that the value V is replicated U times in writing the elements of the i row.

Formulation of the unconstrained problem is similar, except that if up to two units of each resource are allowed for each of the three resources, the nine Y_{kl} resource variables are added to the ninety X_{ij} event-time variables to arrive at ninety-nine X_j variables in the minimization problem. Six additional constraints are required so the C_j array contains ninety-nine elements, the B_i array, fifty-one elements, and the A_{ij} array 5049 elements. These values are presented in Table B, using the same abbreviated notation used for the constrained case.

TABLE A. CONSTRAINED PROBLEM

Objective Function Coefficients

  $C_j = 9 \times (1, 2, 3, 4, 5, 6, 7, 8, 9, 10)$

Right-Hand Side of Constraints

  $B_i = 9 \times 1, -9, 2, 2, 3, 3, 4, 10 \times (2, 1, 1)$

Event Constraint Coefficients

  $A1_j = 10 \times 1, 80 \times 0$
  $A2_j = 10 \times 0, 10 \times 1, 70 \times 0$
  $A3_j = 20 \times 0, 10 \times 1, 60 \times 0$
  $A4_j = 30 \times 0, 10 \times 1, 50 \times 0$
  $A5_j = 40 \times 0, 10 \times 1, 40 \times 0$
  $A6_j = 50 \times 0, 10 \times 1, 30 \times 0$
  $A7_j = 60 \times 0, 10 \times 1, 20 \times 0$
  $A8_j = 70 \times 0, 10 \times 1, 10 \times 0$
  $A9_j = 80 \times 0, 10 \times 1$

Project Completion Constraint Coefficients

  $A10_j = 90 \times (-1)$

Sequence Constraint Coefficients

  $A11_j = -10, -9, -8, -7, -6, -5, -4, -3, -2, -1, 10, 9, 8, 7, 6, 5, 4, 3, 2, 1,$
      70×0
  $A12_j = 20 \times 0, -10, -9, -8, -7, -6, -5, -4, -3, -2, -1, 10, 9, 8, 7, 6, 5, 4,$
      $-3, -2, -1, 50 \times 0$
  $A13_j = 40 \times 0, -10, -9, -8, -7, -6, -5, -4, -3, -2, -1, 10, 9, 8, 7, 6, 5, 4,$
      $3, 2, 1, 30 \times 0$
  $A14_j = 50 \times 0, -10, -9, -8, -7, -6, -5, -4, -3, -2, -1, 10, 9, 8, 7, 6, 5, 4,$
      $3, 2, 1, 20 \times 0$
  $A15_j = 70 \times 0, -10, -9, -8, -7, -6, -5, -4, -3, -2, -1, 10, 9, 8, 7, 6, 5, 4,$
      $3, 2, 1$

Resource Constraint Coefficients

$A16j = 9 \times (2 \times 1, 8 \times 10)$
$A17j = 40 \times 0, 3 \times (2 \times 1, 8 \times 0), 20 \times 0$
$A18j = 70 \times 0, 2 \times (3 \times 1, 7 \times 0)$
$A19j = 9 \times (0, 2 \times 1, 7 \times 0)$
$A20j = 40 \times 0, 3 \times (3 \times 1, 7 \times 0), 20 \times 0$
$A21j = 70 \times 0, 2 \times (4 \times 1, 6 \times 0)$
$A22j = 9 \times (2 \times 0, 2 \times 1, 6 \times 0)$
$A23j = 40 \times 0, 3 \times (0, 3 \times 1, 6 \times 0), 20 \times 0$
$A24j = 70 \times 0, 2 \times (0, 4 \times 1, 5 \times 0)$
$A25j = 9 \times (3 \times 0, 2 \times 1, 5 \times 0)$
$A26j = 40 \times 0, 3 \times (2 \times 0, 3 \times 1, 5 \times 0) 20 \times 0$
$A27j = 70 \times 0, 2 \times (2 \times 0, 4 \times 1, 4 \times 0)$
$A28j = 9 \times (4 \times 0, 2 \times 1, 4 \times 0)$
$A29j = 40 \times 0, 3 \times (3 \times 0, 3 \times 1, 4 \times 0), 20 \times 0$
$A30j = 70 \times 0, 2 \times (3 \times 0, 4 \times 1, 3 \times 0)$
$A31j = 9 \times (5 \times 0, 2 \times 1, 3 \times 0)$
$A32j = 40 \times 0, (4 \times 0, 3 \times 1, 3 \times 0), 20 \times 0$
$A33j = 70 \times 0, 2 \times (4 \times 0, 4 \times 1, 2 \times 0)$
$A34j = 9 \times (6 \times 0, 2 \times 1, 2 \times 0)$
$A35j = 3 \times (5 \times 0, 3 \times 1, 2 \times 0)$
$A36j = 70 \times 0, 2 \times (5 \times 0, 4 \times 1, 0)$
$A37j = 9 \times (7 \times 0, 2 \times 1, 0)$
$A38j = 40 \times 0, 3 \times (6 \times 0, 3 \times 1, 0), 20 \times 0$
$A39j = 70 \times 0, 2 \times (6 \times 0, 4 \times 1)$
$A40j = 9 \times (8 \times 0, 2 \times 1)$
$A41j = 40 \times 0, 3 \times (7 \times 0, 3 \times 1), 20 \times 0$
$A42j = 70 \times 0, 2 \times (7 \times 0, 3 \times 1)$
$A43j = 9 \times (9 \times 0, 1)$
$A44j = 40 \times 0, 3 \times (8 \times 0, 2 \times 1), 20 \times 0$
$A45j = 70 \times 0, 2 \times (8 \times 0, 2 \times 1)$

$j = 1 \ldots \ldots 90$
$i = 1 \ldots \ldots 45$

TABLE B. UNCONSTRAINED PROBLEM

Objective Function Coefficients

$Cj = 9$ x $(1, 2, 3, 4, 5, 6, 7, 8, 9, 10)$, 3 x W_1, 3 x W_2, 3 x W_3

Right-Hand Side of Constraints

$Bi = 9$ x 1, -9, -2, -2, -3, -3, -4, 36 x 0

Event Constraint Coefficients

$A1j = 10$ x 1, 89 x 0
$A2j = 10$ x 0, 10 x 1, 79 x 0
$A3j = 20$ x 0, 10 x 1, 69 x 0
$A4j = 30$ x 0, 10 x 1, 59 x 0
$A4j = 40$ x 0, 10 x 1, 49 x 0
$A6j = 50$ x 0, 10 x 1, 39 x 0
$A7j = 60$ x 0, 10 x 1, 29 x 0
$A8j = 70$ x 0, 10 x 1, 19 x 0
$A9j = 80$ x 0, 10 x 1, 9 x 0

Project Completion Constraint Coefficients

$A10j = 90$ x 1, 9 x 0

Sequence Constraint Coefficients

$A11j = -10, -9, -8, -7, -6, -5, -4, -3, -2, -1, 10, 9, 8, 7, 6, 5, 4, 3, 2, 1,$
   79 x 0
$A12j = 20$ x 0, $-10, -9, -8, -7, -6, -5, -4, -3, -2, -1, 10, 9, 8, 7, 6, 5, 4,$
   $3, 2, 1$, 59 x 0
$A13j = 40$ x 0, $-10, -9, -8, -7, -6, -5, -4, -3, -2, -1, 10, 9, 8, 7, 6, 5, 4,$
   $3, 2, 1$, 39 x 0
$A14j = 50$ x 0, $-10, -9, -8, -7, -6, -5, -4, -3, -2, -1, 10, 9, 8, 7, 6, 5, 4,$
   $3, 2, 1$, 29 x 0
$A15j = 70$ x 0, $-10, -9, -8, -7, -6, -5, -4, -3, -2, -1, 10, 9, 8, 7, 6, 5, 4,$
   $3, 2, 1$, 9 x 0
$A16j = 9$ x $(2$ x 1, 8 x $0)$, 3x -1, 6 x 0
$A17j = 40$ x 0, 3 x $(2$ x 1, 8 x $0)$, 20 x 0, 3 x 0, 3x -1, 3 x 0
$A18j = 70$ x 0, 2 x $(3$ x 1, 7 x $0)$, 6 x 0, 3x -1
$A19j = 9$ x $(0$, 2 x 1, 7 x $0)$, 3x -1, 6 x 0
$A20j = 40$ x 0, 3 x $(3$ x 1, 7 x $0)$, 20 x 0, 3 x 0, 3x $- 1$, 3 x 0

23-16

Sequence Constraint Coefficients   (Continued)

$A21j = 70 \times 0, 2 \times (4 \times 1, 6 \times 0), 6 \times 0, 3x - 1$
$A22j = 9 \times (2 \times 0, 2 \times 1, 6 \times 0), 3 \times -1, 6 \times 0$
$A23j = 40 \times 0, 3 \times (0, 3 \times 1, 6 \times 0), 20 \times 0, 3 \times 0, 3 \times -1, 3 \times 0$
$A24j = 70 \times 0, 2 \times (0, 4 \times 1, 5 \times 0), 6 \times 0, 3 \times -1$
$A25j = 9 \times (3 \times 0, 2 \times 1, 5 \times 0), 3 \times -1, 6 \times 0$
$A26j = 40 \times 0, 3 \times (2 \times 0, 3 \times 1, 5 \times 0), 20 \times 0, 3 \times 0, 3 \times -1, 3 \times 0$
$A27j = 70 \times 0, 2 \times (2 \times 0, 4 \times 1, 4 \times 0), 6 \times 0, 3 \times -1$
$A28j = 9 \times (4 \times 0, 2 \times 1, 4 \times 0), 3 \times -1, 6 \times 0$
$A29j = 40 \times 0, 3 \times (3 \times 0, 3 \times 1, 4 \times 0), 20 \times 0, 3 \times 0, 3 \times -1, 3 \times 0$
$A30j = 70 \times 0, 2 \times (3 \times 0, 4 \times 1, 3 \times 0), 6 \times 0, 3 \times -1$
$A31j = 9 \times (5 \times 0, 2 \times 1, 3 \times 0), 3 \times -1, 6 \times 0$
$A32j = 40 \times 0, 3 \times (4 \times 0, 3 \times 1, 3 \times 0), 20 \times 0, 3 \times 0, 3 \times -1, 3 \times 0$
$A33j = 70 \times 0, 2 \times (4 \times 0, 4 \times 1, 2 \times 0), 6 \times 0, 3 \times -1$
$A34j = 9 \times (6 \times 0, 2 \times 1, 2 \times 0), 3 \times -1, 6 \times 0$
$A35j = 40 \times 0, 3 \times (5 \times 0, 3 \times 1, 2 \times 0), 3 \times 0, 3 \times -1, 3 \times 0$
$A36j = 70 \times 0, 2 \times (5 \times 0, 4 \times 1, 0), 6 \times 0, 3 \times -1$
$A37j = 9 \times (7 \times 0, 2 \times 1, 0), 3 \times -1, 6 \times 0$
$A38j = 40 \times 0, 3 \times (6 \times 0, 3 \times 1, 0), 20 \times 0, 3 \times 0, 3 \times -1, 3 \times 0$
$A39j = 70 \times 0, 2 \times (6 \times 0, 4 \times 1), 6 \times 0, 3 \times -1$
$A40j = 9 \times (8 \times 0, 2 \times 1), 3 \times -1, 6 \times 0$
$A41j = 40 \times 0, 3 \times (7 \times 0, 3 \times 1), 20 \times 0, 3 \times 0, 3 \times -1, 3 \times 0$
$A42j = 70 \times 0, 2 \times (7 \times 0, 3 \times 1), 6 \times 0, 3 \times -1$
$A43j = 9 \times (9 \times 0, 1), 3 \times -1, 6 \times 0$
$A44j = 40 \times 0, 3 \times (8 \times 0, 2 \times 1), 20 \times 0, 3 \times 0, 3 \times -1, 3 \times 0$
$A45j \quad 70 \times 0, 2 \times (8 \times 0, 2 \times 1), 6 \times 0, 3 \times -1$

Resource Level Constraint Coefficients

$A46j = 90 \times 0, -1, 1, 7 \times 0$
$A47j = 91 \times 0, -1, 1, 6 \times 0$
$A48j = 93 \times 0, -1, 1, 4 \times 0$
$A49j = 94 \times 0, -1, 1, 3 \times 0$
$A50j = 96 \times 0, -1, 1, 0$
$A51j = 97 \times 0, -1, 1$

$i = 51$
$j = 99$
$W_1 = 300$
$W_2 = 150$
$W_3 = 90$

SOLUTION OF THE ZERO-ONE FORMULATION

The number of possible solutions to the zero-one combination optimization is 2^n where n is the number of binary variables. Such problems are typically quite large, involving many variables and constraints. As we have seen, a relatively simple scheduling problem may involve on the order of a hundred variables and be a small problem. Yet $2^{100} = 1.27 \times 10^{30}$, obviously a very large number of possible solutions exist. A bit of reflection leads to the conclusion that an exhaustive search of the possible solutions is not a fruitful approach. Assuming a time of 10^{-6} seconds to evaluate one solution, the time required is on the order of 4×10^{16} years. It is apparent that any method or algorithm to be used in solving medium to large scale zero-one programming problems must avoid explicitly enumerating all the possibilities. What is needed are techniques for partially enumerating a manageable number of possibilities and implicitly enumerating all of the rest. The well-known simplex method for solving ordinary linear programming problems is such a system, it systematically examines only a small number of all the basic solutions. Dynamic programming recursions exploit Bellman's principle of optimality to circumvent enumerating all feasible solutions. At present, no general purpose technique exists which is satisfactory for the general integer programming problem in a manner analogous to the simplex method for solution of the general ordinary linear programming problem.

Currently, there are two principal approaches for finding a truly optimal solution to an integer programming problem. Several variants of each approach are available as the result of the work of various researchers, no one algorithm is successful in all cases.

The first principal category of approaches are the cutting-plane algorithms. In general, one starts with an optimal linear programming solution. At each iteration an additional linear constraint is added that is satisfied by any integer solution to the problem, but that rules out the current iteration's non-integer solution. Convergence is guaranteed in a finite, though sometimes very large, number of iterations. The speed of such methods is very sensitive to the specific way in which the problem is formulated, for example, the addition of redundant constraints will often substantially improve the convergence.

The second principal category of approaches are the various backtrack algorithms. The most useful variations are the so called branch and bound algorithms which, like the cutting-plane techniques, start with an optimal linear programming solution. A family of related but separate linear programming problems is solved, which bound the actual solution. This method works well for mixed as well as pure integer problems. Numerous modifications of the branch and bound techniques exist such as the methods of excluded subtours, designated routes, partial tours, etc.

If the number of variables is large, the general cutting-plane and branch and bound algorithms require an excessive number of iterations. As a consequence of the special structure of the scheduling problem formulated as a zero-one integer programming problem, one can use a partial enumeration algorithm such as the Balas algorithm. The classical zero-one integer programming problem can be characterized as,

$$\text{Maximize} \quad \sum_{j=1}^{n} C_j X_j$$

$$\sum_{j=1}^{n} A_{ij} X_j \leq Bi \quad \text{for } i = 1, 2, \ldots, M$$

$$X_j = 0 \text{ or } 1 \quad \text{for } j - 1, 2, \ldots N.$$

This is the dual of the minimization problem formulated for the scheduling problems.

Assume that each C_j is an integer, a condition that can be met by appropriate scaling.

The Balas additive algorithm exploits the zero-one conditions to limit the arithmetic to additions and subtractions. The usual integer programming methods require the solution of a sequence of ordinary linear programming problems which require multiplication and/or division. A digital computer normally performs addition in a fraction of the time required for multiplication, so this in itself will result in a significant saving in computation times if the number of computations is at all comprable.

Although there are 2^n possible assignments of the variables X_1, $X_2, \ldots X_n$, many of the assignments do not satisfy the constraints and relatively few will be optimal. A subset of the X_j is called a partial

solution and the X_j not included in the partial solution are free variables. Any particular assignment of values to free variables is called a completion of the related partial solution. A partial solution having s varibles has 2^{n-s} completions. The Balas algorithm involves a list of problems each one of which corresponds to a partial solution which may or may not be feasible and each of the associated partial solutions gives rise to a branch. The history of the algorithm's attempt at a solution can be displayed by means of a diagram resembling a tree. Once a feasible solution is found, the resultant value of the objective function becomes a lower bound. Given a partial solution no further branching is required if it can be shown that there is no feasible completion which yields a value of the objective function greater than the current lower bound. At this point the partial solution is said to be fathomed. When a partial solution of s variables is fathomed, 2^{n-s} possible assignments have been implicitly enumerated.

There is a close connection between the basis of this implicit enumeration and the Bellman's principle of optimality in dynamic programming. Given a partial solution, the remaining variables must be optimized in order for a completion to be optimal. If there are no values of the remaining variables that yield a feasible solution, or if the resultant optimal value of the objective function is better than a previously found solution, the set of optimal solutions does not contain the given partial solution.

At any iteration I designate the lower bound of the objective function as X_o^I. On the first iteration X_o^I can be the value of any feasible solution that is known, or if no feasible solution is known, X_o^I can be equal to $-\infty$. On the first iteration the list specifying the different partial solutions has two problems, which are found by selecting a particular variable X_j and letting one partial solution be $X_j = 1$, and the other $X_j = 0$. Given a partial solution, the linear constraints can be expressed as,

$$\sum_{\substack{\text{all free} \\ \text{variables}}} A_{ij} X_j \leq B_i - \sum_{\substack{\text{partial} \\ \text{solution variables}}} A_{ij} X_j \quad \text{for } i = 0, 1, 2, \ldots M$$

where each X_j in the partial solution has its assigned value in the summations on the right-hand side in the above equation and for $i = 0$, the coefficients are $A_{oj} = C_j$ and $B_o = -X_o^I - 1$. This implies that there is no feasible solution having an objective function value greater than the lower bound if ,

$$\sum_{\substack{\text{all free} \\ \text{variables}}} \text{Minimum (Aij, O)} > \text{Bi} - \sum_{\substack{\text{partial} \\ \text{solution variables}}} \text{Aij Xj for any i}.$$

The first summation is simply the sum of all the negative coefficients of the free variables. If this sum is larger than the second summation, then even if all the free variables have a value of 1 where Aij 0, it is not sufficient to satisfy the ith constraint in the previous equation.

Given a partial solution, a particular value must be assigned to a free variable for any feasible completion with an objective function value greater than the current lower bound. This suggests a computation similar to the preceeding, namely, if ,

$$\sum_{\substack{\text{all free} \\ \text{variables}}} \text{Minimum (Aij, O)} + |\text{Aij}| > B_i - \sum_{\substack{\text{partial} \\ \text{solution variables}}} \text{Aij Xj for any i},$$

then $X_j = 0$ if $Aij > 0$ and $Xj = 1$ if $Aij < 0$.

The implicit enumeration algorithm then becomes:

1. Terminate the computation if the problem list is empty. Otherwise, select a problem and remove it from the list.

2. If free variables can be found that must have a particular solution for any feasible completion with an objective function value greater than X_o^I, augment the chosen partial solution accordingly. It if is determined that there is no feasible completion having an objective value greater than X_o^I, then let $X_o^{I+1} = X_o^I$, and return to 1.

3. If the augmented partial solution is complete record it, let X_o^{I+1} be the associated value of the objective function, and return to 1.

4. Select any free variable Xj not in the augmented partial solution and add two problems to the problem list, one with Xj set equal to zero, the other with Xj set equal to one. Return to the step 1.

Termination occurs when the problem list is empty. If a feasible solution has been recorded, it is optimal though not necessarily unique. The method must terminate in a finite number of iterations.

A number of improvements and modifications of the basic Balas algorithm have been suggested in recent research papers. The Balas algorithm tests given can be applied not only to the formulated problem constraints, but also the composite constraints formed by adding positive combinations of the constraints.

$$\sum_j \left(\sum_i Y_i A_{ij} \right) X_j \leq \sum_i Y_i B_i ,$$

where $Y_i > 0$. Such additional constraints are called composite or surrogate constraints and can be useful in reducing the number of branches to be considered. A number of variations on the basic Balas algorithm were investigated and considerable research into various past investigations performed. The addition of an ordinary linear programming routine to generate the most severe possible surrogate constraints which are then used in an implicit enumeration algorithm to reduce the computation time seemed very promising.

COMPUTATIONAL EXPERIENCE

A program based on the simple Balas additive algorithm was unable to obtain a solution to either the constrained or the unconstrained problem in a reasonable length of time. The constrained problem which requires the search of fewer feasible solutions, ran for over 35,000 iterations without terminating. The time required was over ninety minutes on a CDC 3200 computer. The program was checked using several trivial problems involving nine variables and eight constraints and operated correctly. The conclusion was reached that a more power- ful algorithm was needed. If the most severe constraints could be used early in the computation so as to eliminate the largest number of feasible solutions, the job could be performed much more quickly. Geoffrion (37) had suggested a method which uses an imbedded linear program to com- plete surrogate constraints which are as strong as possible. The use of the imbedded linear program had produced dramatic reductions in the computation times experienced by Geoffrion.

While Glover (39) and others have experimented with a similar approach, the limited computational experience available suggests that the Geoffrion approach is the most advanced technique available for the solution of this type problem.

A program using the Geoffrion algorithm was successful in obtaining solutions for both the constrained and the unconstrained example problems.

The constrained problem required 52 seconds using a UNIVAC 1108 computer for a complete implicit enumeration requiring 827 iterations. The unconstrained problem is more difficult to solve because it contains a larger number of feasible solutions. The solution time on the UNIVAC 1108 was 603 seconds and involved 4917 iterations. The solution time is seen to be very sensitive to the problem formulation.

Consider that approximately one minute and ten minutes were required for the solution of a relatively simple problem involving only nine events to be scheduled in one of ten time periods and involving only three resources. The task facing the Mission Operations group will require the scheduling of between 50 and 100 activities involving perhaps 50 resources to within one day during a one-year period. Even allowing for some sophisticated data compression, taking advantage of the fact that the Aij array is sparse, a limitation imposed by the memory available in most large computers is encountered. The large number of coefficients required would require the development of some automated translator to convert the problem into a zero-one formulation. If the computation time is nearly linear with problem size as claimed by Geoffrion (37), solution times on the order of at least several hours are expected for the constrained problem and perhaps ten times that for the unconstrained problem. Experience with these problems suggested that computation time is not linear for these problems, but some higher order polynomial function of the number of variables suggesting an even more pessimestic conclusion as to the practicality of optimal scheduling.

The program for the algorithm used successfully is not reproduced here because it would require too much space as it involves 869 Fortran statements, excluding the data which required 264 cards for the unconstrained problem. The author will provide a listing to anyone wishing to experiment with the problem.

CONCLUSIONS AND RECOMMENDATIONS

The zero-one formulation presented here, together with the Geoffrion, imbedded linear optimization, implicit enumeration, algorithm used are representative of the best available techniques for optimum scheduling. A projection of the results achieved to application of these techniques to problems of interest in the mission operations planning and scheduling activity is not encouraging.

1. The current state-of-the-art of integer program formulation requires a rather cumbersome formulation involving large numbers of variables and large numbers of constraining equations to represent scheduling problems.

2. The current state-of-the-art of solution techniques does not allow solution of the required size problem with sufficient speed to make the solution of realistic scheduling problems practical.

3. The feasibility of any optimal scheduling problems of real interest would require the development of a program translator to generate the coefficients for an integer formulation of the problem together with data compression techniques for handling the data within a computer. The computer storage requirements would, however, still be very great.

4. The optimal scheduling technique discussed here may be of interest in special problems of limited size.

5. The scheduling problems of interest are within the capacity of heuristic scheduling algorithms. While the results achieved will not necessarily be optimal, they will most likely be good enough. Many of these heuristic algorithms employ a Monte-Carlo approach which allows some trade-off of increased accuracy versus increased computation time.

6. The results obtained using heuristic algorithms are very sensitive to the problem formulation and it is extremely difficult to anticipate the result of using a given heuristic. It would be advantageous for anyone performing automated scheduling to obtain experience with as wide a range of heuristic programs as possible.

7.   Development of a heuristic scheduling program is now underway which assigns priorities based on the "minimum slack time first rule" in a stochastic manner.   The program incorporates a resource leveling feature to balance the resource utilization as much as possible , considering the costs associated with each resource.   Work on this program should complement work currently being done on other heuristic programs within NASA and help provide a range of experience and capability to meet diverse problems.   Work on this problem can be continued during the second year of this program.

REFERENCES

1. Kelly, Jr., J. E., _Industrial Scheduling_, Chapter 21, Muth, J. F., and Thompson, G. L., editors, Prentic-Hall, 1963.

2. Anonymous - I. E. du Pont de Nemours and Co., _Resource Allocation and Multi-Project Scheduling_, Wilmington, Delaware, 1961.

3. Brand, J. D., Meyer, W. L., and Schaffer, L. R., _The Resource Scheduling Problem in Construction_, Civil Engineering Studies Report No. 5, Department of Civil Engineering, University of Illinois, Urbana, Illinois, 1964.

4. Wiest, J. D., "The Scheduling of Large Projects with Limited Resources," unpublished PhD. thesis, Carnegie Institute of Technology, Pittsburgh, Pa., 1963.

5. Hadley, G., _Nonlinear and Dynamic Programming_, Section 8.8, Addison-Wesley, 1964.

6. Balas, E., "Project Scheduling with Resource Constraints," _Applications of Mathematical Programming Techniques_, Carnegie-Mellon University, Pittsburgh, Pa., 1970.

7. Wagner, H. M., Giglio, R. J., and Glaser, R. G., "Preventive Maintenance Scheduling by Mathematical Programming," _Management Science_, January, 1964.

8. Moodie, C. L., and Manderville, D. E., "Project Resource Balancing by Assembly Line Balancing Techniques," _Journal of Industrial Engineering_, July, 1965.

9. Elmaghraby, S. E., "The One Machine Sequencing Problem with Delay Costs," _Journal of Industrial Engineering_, February, 1968.

10. Burton, M. B., "Some Mathematical Models for the Allocation of Limited Resources to Critical Path Type Scheduling Problems," unpublished dissertation, University of Illinois, Urbana, Illinois, 1964.

11. Pritsker, A. A. B., Watters, L. J., and Wolfe, P. M., "Multi-Project Scheduling with Limited Resources: A Zero-One Programming Approach", _Management Science,_ September, 1969.

12. Watters, L. J., "Reduction of Integer Polynomial Programming Problems to Zero-One Linear Programming Problems," _Operations Research,_ Volume 15, No. 6, November-December, 1967.

13. Fisher, M. L., "Optimal Solution of Resource Constrained Network Scheduling Problems," Technical Report No. 56, Operations Research Center, Mass. Institute of Technology, 1970.

14. Davis, E. W., "Networks: Resource Allocation," _Industrial Engineering,_ Volume 6, No. 4, April, 1974.

15. Gomory, R. E., "An Algorithm for Integer Solutions to Linear Programs," PP269-302 in _Recent Advances in Mathematical Programming,_ R. L. Graves and P. Wolfe, editors , McGraw-Hill, 1963.

16. Gomory, R. E., "On the Relation Between Integer and Non-Linear Solutions to Linear Programs," _National Academy of Sciences,_ Volume 53, 1965.

17. Gomory, R. E., and Baumel, W. J., "Integer Programming and Pricing," _Econometrica,_ Volume 28, 1960.

18. Glover, F., "Stronger Cuts in Integer Programming," _Operations Research,_ Volume 15, 1967.

19. Glover, F., "A New Foundation for a Simplified Primal Integer Programming Algorithm," _Operations Research,_ Volume 16, 1968.

20. Dalton, R. E., and Llewellyn, R. W., "An Extension of the Gomory Mixed Integer Algorithm to Mixed-Discrete Variables," _Management Science,_ Volume 12, 1966.

21. Haldi, J., and Isaacson, L. M., "A Computer Code for Integer Solutions to Linear Problems," _Operations Research,_ Volume 13, 1965.

22. Markowitz, H. M., and Manne, A. S., "On the Solution of Discrete Programming Problems," _Econometrica,_ Volume 25, 1957.

23. Wilson, R. B., "Stronger Cuts in Gomory's All-Integer Integer Programming Algorithm," _Operations Research,_ Volume 15, 1967.

24. Young, R. D., "A Simplified Primal (All-Integer) Integer Programming Algorithm," Operations Research, Volume 16, 1968.

25. Lawler, E. L., and Wood, D. E., "Branch and Bound Methods - A Survey," Operations Research, July-August, 1966.

26. Mueller-Merbach, H., "Experience with Methods for Resource Scheduling in CPM Networks," INTERNET Conference, Vienna, 1967.

27. Johnson, T. J. R., "An Algorithm for the Resource Constrained Project Scheduling Problem," unpublished PhD. dissertation, Mass. Institute of Technology, August, 1967.

28. Davis, E. W., "An Exact Algorithm for the Multiple-Constrained Resource Project Scheduling Problem," unpublished dissertation, Yale University, New Haven, Conn., 1968.

29. Davis, E. W., and Heidon, G. E., "An Algorithm for Optimal Project Scheduling Under Multiple-Resource Constraints," Management Science, August, 1971.

30. Bennington, G. E., and McGinnis, L. F., "A Critique of Project Planning with Constrained Resources," Symposium on Scheduling Theory and Its Application, Raleigh, North Carolina, May, 1972.

31. Balas, E., "An Additive Algorithm for Solving Linear Programs with Zero-One Variables," Operations Research, Volume 13, 1965.

32. Balas, E., "Discrete Programming by the Filter Method," Operations Research, Volume 15, 1967.

33. Freeman, R. J., "Computational Experience with a 'Balasian' Integer Programming Algorithm," Operations Research, Volume 14, 1966.

34. Glover, F., "Surrogate Constraints," Operations Research, Volume 16, 1968.

35. Geoffrion, A. M., "Integer Programming by Implicit Enumeration and Balas' Methods," SIAM Review, Volume 9, 1967.

36. Lemke, C. E., and Spielberg, K., "Direct Search Algorithms for Zero-One and Mixed Integer Programming," Operations Research, Volume 15, 1967.

37. Geoffrion, A. M., "An Improved Implicit Enumeration Approach for Integer Programming," AM 5644-PR, The Rand Corporation, June, 1968.

38. Davis, E. W., "Project Scheduling Under Resource Constraints - Historical Review and Categorization of Procedures," AIIE Transactions, Volume 5, No. 4, December, 1973.

39. Glover, F., "A Multiphase - Dual - Algorithm for the Zero-One Integer Programming Problem," Operations Research, Volume 13, November - December, 1965.

40. Pritsker, A. A. B., and Watters, L. J., "A Zero-One Programming Approach to Scheduling with Limited Resources," RM 5561 PR, The Rand Corporation, January, 1966.

41. Jenett, E., "Experience with Evaluation of Critical Path Methods," Chemical Engineering, February 10, 1969.

42. Phillips, C. R., "Fifteen Key Features of Computer Programs for CPM and PERT," Journal of Industrial Engineering, January - February, 1964.

43. Fendly, L. G., "Toward the Development of a Complete Multi-Project Scheduling System," Journal of Industrial Engineering, October, 1968.

44. Wiest, J. D., "A Heuristic Scheduling and Resource Allocation Model for Evaluating Alternative Weapon System Programs," RM 5769 PR, The Rand Corporation, August, 1969.

45. Wiest, J. D., "Heuristic Programs for Decision Making," Harvard Business Review, September - October, 1965.

46. Wiest, J. D., "A Heuristic Model for Scheduling Large Projects with Limited Resources," Management Science, February, 1967.

47. Verhines, D. R., "Optimum Scheduling of Limited Resources," Engineering Progress, Volume 54, No. 3, March, 1963.

48. Shaffer, L. R., Ritter, J. B., and Meyer, W. L., The Critical Path Method, McGraw-Hill, 1964.

49. Levy, F. K., Thompson, G. L., and Wiest, J. D., "Multi-Ship, Multi-Shop, Workload Smoothing Program," Naval Research Logistics Quarterly, March, 1963.

50. Burgess, A. R., and Killebrew, J. B., "Variation in Activity Level on a Cyclic Arrow Diagram," Journal of Industrial Engineering, March - April, 1962.

51. Davis, E. W., "Resource Allocation in Project Network Models - A Survey," Journal of Industrial Engineering, Volume 17, No. 4, April, 1966.

52. Bowman, E. H., "The Schedule Sequencing Problem," Operations Research, Volume 13, No. 5, 1965.